ONR Award # N00014-7-1-1010

# FINAL REPORT

# BLAST AND IMPACT RESISTANT COMPOSITE STRUCTURES FOR NAVY SHIPS

Submitted by:

P. Raju Mantena, Ahmed Al-Ostaz, Alexander H.D. Cheng and A.M. Rajendran
Composite Structures and Nano-Engineering Research
The University of Mississippi, University, MS 38677

To:

Dr. Yapa D. S. Rajapakse
Program Manager, Solid Mechanics
Office of Naval Research (ONR 332)
One Liberty Center (Suite 1425)
875 North Randolph Street
Arlington, VA 22203-1995

20130321085

March 15, 2013

# REPORT DOCUMENTATION PAGE

*Form Approved*
**OMB No. 0704-0188**

Public raporting burden for this collection of information is astimated to everage 1 hour per response, including the time for reviewing instructions, searching data sources, gathering end meintaining the data needed, and complating and reviewing the collection of information. Send comments regarding this burden estimata or any other aspect of this collection of information, including suggestions for reducing this burden to Washington Headquarters Service, Directorate for Information Operetions and Raports, 1215 Jefferson Davis Highway, Suite 1204, Arlington, VA 22202-4302, end to the Office of Management and Budget, Paperwork Reduction Project (0704-0188) Washington, DC 20503.
**PLEASE DO NOT RETURN YOUR FORM TO THE ABOVE ADDRESS.**

| 1. REPORT DATE *(DD-MM-YYYY)* | 2. REPORT TYPE | 3. DATES COVERED *(From - To)* |
|---|---|---|
| 15-03-2013 | FINAL | 16-JUL-2007 - 31 DEC-2012 |

**4. TITLE AND SUBTITLE**
Blast and Impact Resistant Composite Structures for Navy Ships

**5a. CONTRACT NUMBER**
N/A

**5b. GRANT NUMBER**
N00014-07-1-1010

**5c. PROGRAM ELEMENT NUMBER**
N/A

**6. AUTHOR(S)**
Mantena, P. Raju
Al-Ostaz, Ahmed
Cheng, Alexander H. D.
Rajendran, A. M.

**5d. PROJECT NUMBER**
12PR04101-01

**5e. TASK NUMBER**
NA

**5f. WORK UNIT NUMBER**
N/A

**7. PERFORMING ORGANIZATION NAME(S) AND ADDRESS(ES)**
UNIVERSITY OF MISSISSIPPI
OFFICE OF RESEARCH
100 BARR HALL
UNIVERSITY, MS 38677-0907

**8. PERFORMING ORGANIZATION REPORT NUMBER**
N/A

**9. SPONSORING/MONITORING AGENCY NAME(S) AND ADDRESS(ES)**
Office of Naval Research, 875 North Randolph Street, Arlington, VA 22203-1995
ONR REG ADMIN ATLANTA-N66020, 100 ALABAMA STREET SW SUITE 4R15, ATLANTA, GA 30303-3104

**10. SPONSOR/MONITOR'S ACRONYM(S)**
ONR

**11. SPONSORING/MONITORING AGENCY REPORT NUMBER**
FINAL

**12. DISTRIBUTION AVAILABILITY STATEMENT**
Approved for Public Release; distribution is Unlimited.

**13. SUPPLEMENTARY NOTES**

**14. ABSTRACT**
The focus of our research efforts is on marine composite structures, particularly lightweight glass/carbon polymeric based composites, and innovative concepts for the mitigation of blast, shock and impact effects. Technical approach included researching low-cost fire resistant nanoclay and exfoliated graphite platelet reinforced glass and carbon polymeric based composites with fly ash and 3-D fiber reinforced foams; investigating their response to low-velocity impact, ballistic, shock and blast loads; dynamic mechanical analysis for modulus, damping, creep and stress relaxation; developing constitutive models and computer simulations; and evaluating their radar-absorbing and EM-shielding characteristics for improved stealth and safety. Research conducted under this ONR award would also impact the development of composite materials technology for the nation's critical infrastructure; body and modular armor designs for military and civilian vehicles; homeland security; JIEDDO (Joint Improvised Explosive Device Defeat Organization) and DTRA (Defense Threat Reduction Agency).

**15. SUBJECT TERMS**
Blast mitigation, shock, low-velocity impact, composite materials, nanoclay, exfoliated graphite, 3D fiber reinforced foams

| 16. SECURITY CLASSIFICATION OF: | | | 17. LIMITATION OF ABSTRACT | 18. NUMBER OF PAGES | 19a. NAME OF RESPONSIBLE PERSON |
|---|---|---|---|---|---|
| a. REPORT | b. ABSTRACT | c. THIS PAGE | | | P. Raju Mantena |
| U | U | U | UU | 295 | 19b. TELEPONE NUMBER *(Include area code)* 662.915.5990 |

## TABLE OF CONTENTS

1.0 PROJECT SUMMARY..... 1

2.0 MAJOR ACCOMPLISHMENTS AND OUTCOMES..... 3

3.0 SIGNIFICANCE OF RESEARCH AND NAVY RELEVANCE..... 5

4.0 COLLABORATION AND TRANSITIONS..... 5

5.0 ACKNOWLEDGEMENT..... 6

6.0 JOURNAL PUBLICATIONS AND CONFERENCE PROCEEDINGS..... 7

7.0 TECHNICAL REPORTS

7.1 2007 ONR Solid Mechanics Program Review..... 11

7.2 2008 ONR Solid Mechanics Program Review..... 13

7.3 2009 ONR Solid Mechanics Program Review..... 23

7.4 2010 ONR Solid Mechanics Program Review..... 35

7.5 2011 ONR Solid Mechanics Program Review..... 45

8.0 APPENDIX: Copies of Journal publications (A through V listed on page 7)..... 55

ONR Award # N00014-7-1-1010

# BLAST AND IMPACT RESISTANT COMPOSITE STRUCTURES FOR NAVY SHIPS

**P. Raju Mantena, Ahmed Al-Ostaz, Alexander H.D. Cheng and A.M. Rajendran**
Composite Structures and Nano-Engineering Research
The University of Mississippi, University, MS 38677

## PROJECT SUMMARY

Objective of this research is to develop stronger, safer and more cost-effective structures for the new generation naval ships; especially nanoparticle reinforced glass/carbon polymeric based composites and structural foams for blast, shock and impact mitigation. FRP composites are presently being used in US Navy Ships such as the Osprey class mine hunter, and for topside structures on large warships such as the Advanced Enclosed Mast System (AEMS). The navy also has plans to integrate more composites into the new generation CV(X) and DD(X) ship class designs.

The focus of our research has been on marine composite structures; particularly lightweight glass/carbon polymeric based composites, and innovative concepts for the mitigation of blast, shock and impact effects. Technical approach included researching low-cost fire resistant nanoclay and exfoliated graphite platelet reinforced glass and carbon polymeric based composites with fly ash and 3-D fiber reinforced foams; investigating their response to low-velocity impact, ballistic, shock and blast loads; dynamic mechanical analysis for modulus, damping, creep and stress relaxation; developing constitutive models and computer simulations; and evaluating their radar-absorbing and EM-shielding characteristics for improved stealth and safety.

The University of Mississippi (UM), Michigan State University (MSU), and University of New Orleans (UNO), supported by the US Army Corps Engineer Research and Development Center (ERDC) have utilized their research strengths in collaborating on the modeling, analysis, fabrication and testing of affordable blast, shock and impact resistant nanoparticle reinforced composite structures for the new generation of navy ships. University of Alabama-Birmingham (UAB) fabricated the large VARTM sandwich composite panels and performed quasi-static, fire and ballistic tests. North Carolina A&T State University (NC AT) provided their patented low-cost fire resistant fly ash based Eco-Core foams. Northrop Grumman Ship Building (NGSB), Gulfport, MS advised and facilitated these research efforts. WebCore Technologies, Miamisburg, OH provided their patented TYCOR® foam cores for layering in between glass or carbon composite face sheets; providing structures that offer optimal flexural rigidity, vibration damping and blast/shock/impact energy absorption along with reduced weight for the future generation naval structures or the retrofitting of existing ones.

Sandwich composites with balsa and foam cores are presently being featured in a number of navy applications such as in surface ship deck structures, radar mast and boat hulls. In the work reported here, several new and emerging cores in sandwich construction have been explored. Different core types considered include;

(a) Balsa wood which is a traditional core material being used in present generation ship structures. Balsa is a natural material, and is prone to local variation in properties due to cell size and cell thickness variations;

(b) Polyvinyl chloride (PVC) foam core which is being used in present generation ship structures for radar mast enclosures and boat hulls;

(c) Tycor (TYCOR® from Webcore Technologies), an engineered three-dimensional fiber reinforced damage tolerant core for sandwich structures, has the potential to provide improved blast and ballistic resistance. In this core, glass fiber is reinforced through the thickness of closed cell foam sheets to produce a web and truss structure; and

(d) Eco-core is an emerging fire resistant sandwich core. Fire damage in ship structures is of significant concern. The burn-through resistance and heat insulation characteristics of Eco-core makes it an attractive fire resistant core. The inexpensive fire resistant Eco-Core or other foams layered in between carbon nanotube or graphite platelet enhanced composite face plates will provide structures that offer optimal flexural rigidity, vibration damping and blast/shock/impact energy absorption along with reduced weight; for the future generation naval structures or the retrofitting of existing ones.

One of our research goals is to make use of the available experimental blast and shock response data, for performance prediction of sandwich composite panels under a wider range of operational loading conditions and threat scenarios, which would facilitate design decisions at the ship superstructure-system level. The P-I (Pressure-Impulse) diagram mathematically relates a specific damage level to a combination of blast pressure and impulse imposed on a particular structural element and allows reduced order modeling of the sandwich composite panel systems. P-I curves are also known as iso-damage curves with each curve representing a certain response level such as mid-span deflection or rotation at supports, etc. Experimental blast response and quasi-static material property data were generated for E-glass and carbon face skin sandwich composite panels with balsa, PVC foam and TYCOR® cores. The Pressure vs Impulse (P-I) curve methodology that was developed to represent estimated damage levels in civil infrastructure components subjected to blast loadings, has been adapted for analyzing these sandwich composite panels. Results show good correspondence between model predictions and experimental data for the performance evaluation of various sandwich composite panel configurations. This P-I curve methodology enables the generation of a database of performance envelopes for sandwich composite panels with a variety of skin and core material combinations under various blast and shock loading scenarios, for naval composite structural applications. The available experimental data, which is limited to only specific blast and shock loading scenarios, has been used for validating this computer simulation methodology.

Other complementary research efforts covered in this report include: a first-principles estimation of the shock response of nanoreinforced composite materials; creep, stress relaxation modeling and the effects of bromination on viscoelastic response of nanoclay and graphite platelet reinforced vinyl ester; determination of power law attenuation coefficients and the electromagnetic characteristics of carbon nanotubes. In the following sections; the major accomplishments and outcomes, journal articles and conference proceedings supported by this grant, and the technical details of this research (presented at the annual reviews) are provided.

## MAJOR ACCOMPLISHMENTS AND OUTCOMES:

**Shock Tube Apparatus**

**Split-Hopkinson Pressure Bars (tension and compression)**

- State-of-the-art shock tube and Split-Hopkinson Pressure Bars (tension and compression) commissioned in the Blast and Impact Dynamics laboratory at the University of Mississippi, for the high-strain rate evaluation of composite materials and sandwich structures.
- Researched new and emerging cores including low cost fire resistant fly ash based Eco-Core® and TYCOR® (an engineered three-dimensional fiber reinforced damage tolerant core); woven carbon and high-elongation HPG glass face skins in sandwich constructions.
- Large (8 feet x 4 feet) scale navy relevant sandwich composites with balsa, PVC foam, stitched polyurethane with glass and carbon / vinyl ester fabricated by the VARTM process as per Northrop Grumman Ship Building design specs.
- Glass and Carbon sandwich composite panels with balsa, PVC foam and TYCOR® cores were subjected to blast loads simulating approximate threat levels of 2000 lbs to 27,000 lbs of TNT, at the ERDC-Blast Load Simulator (BLS) facility.
- Developed and evaluated 12" x 12" x 2" thick fire resistant fly ash based Eco-Core panels, with and without chopped glass fibers, for use in sandwich structural applications. The effect of long term immersion of Eco-Core, balsa and PVC foam in sea and tap water was evaluated and found that Eco-Core is as good as PVC foam. The energy absorbing potential of Eco-Core as a sacrificial structural panel against a glass/vinyl ester composite panel has also been assessed.
- Low-cost and fire resistant nanoclay and graphite platelet reinforced panels manufactured.
- Creep and stress relaxation modeling, and the effects of bromination on viscoelastic response of nanoclay and graphite platelet reinforced vinyl ester.
- Low velocity punch-shear response of nanoclay and graphite platelet reinforced vinyl ester plates, laminated face sheets and sandwich composites.
- High-strain rate characteristics of nanoclay and graphite platelet reinforced vinyl ester panels.
- Shock tube analysis of sandwich composite beams and face skins performed.

- Ballistic and fire damage response of various sandwich composite configurations initiated.
- A first-principles estimation of the shock response of nanoreinforced composite materials developed.
- Molecular dynamics simulations of graphite-vinyl ester nanocomposites and its constituents.
- AUTODYN simulations of the shock response and finite element modeling of nanoclay and graphite platelet reinforced vinyl ester nanocomposites.
- The Pressure vs Impulse (P-I) curve methodology (developed to represent estimated damage levels in civil infrastructure components subjected to blast loadings) has been adapted for analyzing the sandwich composite panels and face skins.
- The power law attenuation coefficients and electromagnetic characteristics of carbon nanotubes were evaluated.
- Research findings published in twenty two journal articles (copies included in Appendix), and disseminated in eighteen conference presentations/proceedings.

## SIGNIFICANCE OF RESEARCH AND NAVY RELEVANCE:

Producing stronger, safer and more cost-effective platforms for the new generation naval ships requires innovative designs, new materials, and affordable/efficient processing and characterization technologies. This research will advance the development of blast, shock and impact resistant composites for navy ship structural applications; to achieve better mobility, survivability, stealth, safety, and at lower cost. Research conducted under this ONR award would also impact the development of composite materials technology for the nation's critical infrastructure; body and modular armor designs for military and civilian vehicles; homeland security; JIEDDO (Joint Improvised Explosive Device Defeat Organization) and DTRA (Defense Threat Reduction Agency).

## COLLABORATION AND TRANSITIONS:

Northrop Grumman Ship Building (NGSB) - Advanced Capabilities Group (ACG) has collaborated and facilitated this research effort on the development of advanced ship panel concepts. Webcore Technologies Inc., a small-scale industry in Dayton, OH worked closely with University of Mississippi to develop affordable and durable TYCOR® composite sandwich panels for ship structural applications. TYCOR® is currently being used in several military and commercial applications including refrigerated cargo floor for Navy cargo ships, Air Force tactical shelters, Air Force runway matting, vehicular bridge decks, railcar floors and wind turbine blades. The US Army Corps of Engineers - Engineer Research and Development Center (ERDC) in Vicksburg, MS has maintained a strong connection with our research team at Ole Miss. The results of this research have also been successfully leveraged for grants from other federal agencies, including the following:-

Alex Cheng (PI), Ahmed Al-Ostaz, Christopher Mullen and P. Raju Mantena; *Nano Particle Reinforced Composites for Critical Infrastructure Protection with Extension to Multiple Hazards;* **SERRI (Southeast Region Research Initiative)-Department of Homeland Security; $1,159,976;** 2007 to 2010.

Alex Cheng (PI), Chung Song, Ahmed Al-Ostaz and P. Raju Mantena; *Structural, Material, and Geotechnical Solutions to Levee and Floodwall Construction and Retrofitting*; **SERRI (Southeast Region Research Initiative)-Department of Homeland Security**; **$1,959,537;** Nov 1, 2007 to Aug 31, 2012.

Ahmed Al-Ostaz (PI), Alex Cheng, Chung Song, A.M. Rajendran; *Nano-enhanced and Bio-inspired Materials for Mitigation and Protection of TIH Railcars and Stationary Tanks against High-Power Impact;* **SERRI (Southeast Region Research Initiative)-Department of Homeland Security; $1,001,970**; 2010 to 2012.

A.M. Rajendran (PI), P. Raju Mantena and Ahmed Al-Ostaz; *Nano to Continuum Multi-Scale Modeling Techniques and Analysis for Cementitious Materials under Dynamic Loading*; **DOD-HBCUs PIRT; $900,000;** June 1, 2011 to May 31, 2016.

A.M. Rajendran (PI) and P. Raju Mantena; *Atomistic Modeling of Transparent Glass/Ceramic Materials*; **ARO-TARDEC; $199,960**; Nov 1, 2012 to April 30, 2014.

P. Raju Mantena (PI); *High-Strain Rate Experimental Characterization and Analytical Modeling of Nanoenhanced Functionally Graded Composites for Energy Dissipation under Shock and Impact Loading*, **ERDC-CERL; $50,000**; Sep 1, 2012 to Aug 31, 2013.

## ACKNOWLEDGEMENT:

This research was funded by ONR Grant # N00014-07-1-1010, Office of Naval Research, Solid Mechanics Program (Dr. Yapa D.S. Rajapakse, Program Manager). Partial funding received under a subcontract from the Department of Homeland Security sponsored Southeast Region Research Initiative (SERRI) at the Department of Energy's Oak Ridge National Laboratory, is also acknowledged.

We would like to thank the following collaborators for their very valuable contributions to this project:

Dr. Larry Drzal, Dr. Dahsin Liu and Dr. Goujing Li from Michigan State University, Lansing, MI

Dr. Uday Vaidya and Dr. Selvum Pillay from University of Alabama - Birmingham

Dr. Kunigal Shivakumar from North Carolina A&T State University, Greensboro, NC

Dr. David Hui and Mr. John Lair from University of New Orleans, New Orleans, LA

Dr. Rob Banerjee and Dr. Elias Toubia from Webcore Technologies, Dayton, OH

Mr. John Sullivan from Northrop Grumman Ship Building (NGSB-ACG), Gulfport, MS

Dr. Arun Shukla from University of Rhode Island, RI

Dr. Carol Johnson, Dr. Beverly DePaula and Dr. Reed Mosher from US Army - Engineer Research and Development Center (ERDC), Vicksburg, MS

Several faculty, graduate students and staff at the University of Mississippi deserve special credit for the successful execution of this project:

Dr. Elizabeth Ervin, Dr. Weiping Xu, Dr. Hunain Alkhateb, Dr. Mohammad Irshidat, Dr. G. Wang, Dr. Chirstopher Mullen, Dr. Joseph Gladden, Dr. Joel Mobley, Dr. Darko Kajfez, Dr. Ahmed Kishk, Dr. Tezeswi Tadepalli, Dr. Ahmad Almagableh, Mr. Swasti Gupta, Mr. Brahmananda Pramanik, Mr. Richard Mack, Mr. Damian Stoddard, Mr. Kiyun Kim, Mr. Ghanshyam Pal, Mr. S.M. Mikki, Mr. Shaya Karimkashi, Mr. Lynn Stewart, Mr. Andy Gossett, Mr. James McPhail, Mr. Gary Denning, Mr. Marty Hickman, Mr. Gene Walker, Mr. Tim Hall, Ms Janet McBride, Ms Dorothy Llyod, Ms Anita Randle, Ms Beth Snider, Ms Nancy Roberts and Ms Jeanette Long.

**JOURNAL PUBLICATIONS AND CONFERENCE PROCEEDINGS** – ONR supported:

**Journal publications** (copies of these articles are included in Appendix):

**(A)** Tadepalli.,T. and P. Raju Mantena (2012); "Numerical and Experimental Blast response Characterization of Sandwich Composite Structural Panels" *Journal of Sandwich Structures and Materials*; 15 (1) pp. 110-133.

**(B)** Pramanik, B., Tadepalli, T. and Mantena, P. R. (2012); "Surface fractal Analysis for Estimating the Fracture Energy Absorption of Nanoparticle Reinforced Composites" *Materials* 2012, 5, pp. 922-936.

**(C)** Brahmananda Pramanik and P. Raju Mantena (2012); "Energy Absorption of Nano-Reinforced and Sandwich Composites in Ballistic and Low-Velocity Punch-Shear" *Open Journal of Composite Materials*; Vol.2, No. 3, 2012; pp. 87-96. doi: 10.4236/ojcm.2012.23010.

**(D)** Almagableh, A. and Raju Mantena, P. (2012); "Experimental and Finite Element Modeling of Vinyl ester Nanocomposites under Blast and Quasi-static Flexural Loading" *J. Appl. Polym. Sci.*, 126: 1895–1905. doi: 10.1002/app.36897

**(E)** B. Pramanik and P. R. Mantena (2011); "Viscoelastic Response of Graphite Platelet and CTBN Reinforced Vinyl Ester Nanocomposites" *Materials Sciences and Applications*, Vol. 2, No. 11, November 2011, pp. 1667-1674.

**(F)** T. Tadepalli and P.R. Mantena (2011); "Blast Response of Sandwich Composite Structural Panels" *ASME - Early Career Technical Journal (ECTC)* Vol. 10, 2011, pp. 33-38, ISBN978-1-4507-9223-3

**(G)** Weiping Xu and Elizabeth Ervin (2011); "First Principles Estimation of Shock Tube Tests on Nanoreinforced Composite Materials" *ASME-Journal of Applied Materials*, Vol. 78 (6) Nov 2011.

**(H)** Swasti Gupta, P. Raju Mantena and Ahmed Al-Ostaz (2010); "Dynamic Mechanical and Impact Property Correlation of Nanoclay and Graphite Platelet Reinforced Vinyl Ester Nanocomposites" *Journal of Reinforced Plastics and Composites,* Vol. 29, No.13, 2010, pp. 2037- 47.

**(I)** Ahmad Almagableh and P. Raju Mantena (2010); "Effects of Environmental Aging On The Thermal and Mechanical Properties of Vinyl Ester Nanocomposites, *ASME Early Career Technical Journal 2010*, Oct.1-2, Atlanta, Georgia, USA, CD-ROM, Vol.9, pp.35-40.

**(J)** P. Raju Mantena, Ahmed Al-Ostaz and Alexander H.D. Cheng (2009); "Dynamic Response and Simulations of Nano-particle Enhanced Composites" *Composites Science and Technology* 69 (2009) 772-779.

**(K)** Almagableh A.M., Mantena P.R., Al-Ostaz A, Liu W., Drzal L.T. (2009); 'Effects of Bromination on the Viscoelastic Response of Vinyl ester Nanocomposites' *eXPRESS Polymer Letters,* Vol. 3, No. 11, (2009), 724-732.

**(L)** Ahmad Almagableh, P. Raju Mantena and Ahmed Al-Ostaz (2009); 'Creep and Stress Relaxation Modeling of Nanoclay and Graphite Platelet Reinforced Vinyl ester Nanocomposites' *Journal of Applied Polymer Science,* Vol. 115, Nov (2009), pp. 1635-1642.

**(M)** Pramanik B., and Mantena P.R. (2009); "Punch-shear Characteristics of Nanoclay and Graphite Platelet Reinforced Vinyl Ester Plates, Laminated face sheets and Sandwich Composites under Low-Velocity Impact" *ASME - Early Career Technical Journal,* Vol. 8, No.1, October 2009, pp. 8.1-8.8.

**(N)** Swasti Gupta, P. Raju Mantena, Ahmed Al-Ostaz and Christopher Mullen (2009); "Shock Response and Finite Element Modeling of Nanoclay and Graphite Platelet Reinforced Vinyl Ester Nanocomposites" *ASME-Early Career Technical Journal,* Vol. 8, No. 1, October 2009, pp. 7.1-7.8.

**(O)** Joel Mobley, Richard Mack, Joseph Gladden and P. Raju Mantena (2009); "Determination of Power-law Attenuation Coefficient and Dispersion Spectra in Multi-wall Carbon Nano Tube Composites using Kramers-Kronig Relations" *Journal of Acoustical Society of America* 126 (1), pp. 92-97, July 2009.

**(P)** G. Wang, A., Al-Ostaz, A., A. H.-D. Cheng and P. R. Mantena (2009); "A Macroscopic-level Hybrid Lattice Particle Modeliing of Mode-I Crack Propagation in Inelastic Materials with Varying Ductility" *International Journal of Solids and Structures* 46 (2009) 4054-4063.

**(Q)** G. Wang, A., Al-Ostaz, A., A. H.-D. Cheng, and P. R. Mantena (2009); "Hybrid Lattice Particle Modeling of Wave Propagation Induced Fracture of Solids" *Comput. Methods Appl. Mech. Engg.* 199 (2009) 197-209.

**(R)** G. Wang, A. Al-Ostaz, A.H.-D. Cheng and P.R. Mantena (2009); "Hybrid lattice particle modeling: Theoretical Considerations for a 2D Elastic Spring Network for Dynamic Fracture Simulations," *Computational Materials Science* 44 (2009) 1126–1134.

**(S)** Shaya Karimkashi, Darko Kajfez, Ahmed A. Kishk and Shalmalee Vaidya (2009); "Microwave Conductivity Measurements of Carbon Veil by Two Different Methods" *Microwave and Optical Technology Letters* Vol. 51, No. 10, October 2009, 2435-2438.

**(T)** Al-Ostaz A., Pal G., Mantena P.R. and Cheng A.H-D (2008); "Molecular Dynamics Simulation of SWCNT-Polymer Nanocomposite and its Constituents" *Journal of Materials Science*, Vol. 43, No.1, pp.164-173, 2008.

**(U)** S.M. Mikki and A.A. Kishk (2008); "A Symmetry-Based Formalism for the Electrodynamics of Nanotubes" *Progress in Electromagnetics Research, PIER 86*, 111-134, 2008.

**(V)** S.M. Mikki and A.A. Kishk (2008); "Derivation of the Carbon Nanotube Susceptibility Tensor Using Lattice Dynamics Formalism" *Progress in Electromagnetics Research B*, vol. 9, 1-26, 2008

**Conference Proceedings:**

**(1)** P. Raju Mantena and Tezeswi Tadepalli; "Blast Response of Sandwich Composite Panels: Experiments and Simulations" *Proceedings of the International Congress on Computational Mechanics and Simulations - ICCMS 2012*; IIT Hyderabad, India; 10-12 December 2012; CD ROM - Paper#421.

**(2)** T. Tadepalli and P. R. Mantena; "Computational Simulation and Experimental Characterization of Sandwich Composite Panels Subjected to Blast Loads" *Proceedings of the American Society for Composites Twenty-Sixth Technical Conference*; Montreal, Quebec, Canada, Sep 26-28, 2011; American Society for Composites CD-ROM paper # 1081, 15 pp.

**(3)** P. Raju Mantena and Tezeswi Tadepalli; Blast, Shock and Impact Resistant Nano-reinforced Panels and Sandwich Composites; *Proceedings of ICC-CFT 2011 International Conference on Composites for the 21st Century: Current and Future Trends*; Bangalore, India 4-7 January 2011; CD ROM Paper #C022

**(4)** A.Almagableh, S.Gupta, P.R.Mantena, and T.Tadepalli, "Mechanical Response and Finite Element Simulations of Vinyl Ester Nanocomposite Panels Under Shock and Quasi-static Flexural Loading" *Proceedings of the American Society for Composites: 25th Technical Conference*, Dayton, OH, Sept. 20-22, 2010, American Society for Composites, CD-ROM-19.

**(5)** Brahmananda Pramanik and P. Raju Mantena; "Low Velocity Punch-Shear response of Nanocaly and Graphite Platelet reinforced Vinyl Ester Plates, Laminated Face Sheets and Sandwich Composites" *Proceedings of ASME-IMECE 2009* (Paper #12180 on CD ROM), Lake Buena Vista, FL, Nov 13-19, 2009.

**(6)** Hunain Alkhateb, Ahmed Al-Ostaz, A. H-D. Cheng and P. Raju Mantena; "Molecular Dynamics Simulations of Graphite-Vinyl Ester Nanocomposites and its Constituents" *Proceedings of the 1st Joint Canadian and American Society for Composites 24th Technical Conference Technical Conference - ASC / CACSMA* (Paper on CD ROM-11), Newark, DE, Sep 15-17, 2009.

**(7)** Ahmad Almagableh, P. Raju Mantena and Ahmed Al-Ostaz; "Creep and Stress Relaxation Modeling of Nanoclay and Graphite Platelet Reinforced Vinyl Ester Nanocomposites" *Proceedings of the 1st Joint Canadian and American Society for Composites 24th Technical Conference - ASC / CACSMA* (Paper #16 on CD ROM-11), Newark, DE, Sep 15-17, 2009.

**(8)** Pramanik B. and P. Raju Mantena 'Punch-shear Response of Nanoclay and Graphite Platelet Reinforced Vinyl ester Nanocomposites' *Mid South Area Engineering Sciences Conference - MAESC 2009*, Memphis, TN,May2009.

**(9)** M. Irshidat, Ahmed Al-Ostaz, P. Raju Mantena, A.H-D. Cheng 'Blast Resistance of Sandwich Composites in Marine Applications' *2009 American Society for Composites - CACSMA Conference (ONR Session),* University of Delaware, DE, Sep 15-18, 2009.

**(10)** Kunigal Shivakumar, Shivalingappa Lingaiah, Huanchun Chen, Paul Akangah, Gowthaman Swaminathan and Larry Russell Jr.' Polymer Nanofabric Interleaved Composite Laminates' *2009 American Society for Composites - CACSMA Conference (ONR Session),* University of Delaware, DE, Sep 15-18, 2009.

**(11)** Kunigal Shivakumar, Shivalingappa Lingaiah, Huanchun Chen, Paul Akangah, Gowthaman Swaminathan and Larry Russell Jr.; 'Polymer Nanofabric Interleaved Composite Laminates' *2009 American*

*Society for Composites - CACSMA Conference (ONR Session),* University of Delaware, DE, Sep 15-18, 2009.

**(12)** Uday Vaidya; 'Effect of Clean Apertures and Ballistic Impact Damage to E-glass/VE Laminates' *ICCM 17*, Edinburgh, UK, 27-31 July, 2009.

**(13)** Kunigal Shivakumar and Huanchun Chen; 'Eco-Core and its Performance in Sandwich Structural Application' *ICCM 17*, Edinburgh, UK, 27-31, July 2009.

**(14)** Almagbleh, Mantena, P. R., Al-Ostaz; 'Creep and Stress Relaxation Modeling of Nanoclay and Graphite Platelet Reinforced Vinyl ester Nanocomposites' *Mid-South Area Engineering Sciences Conference - MAESC 2009*, Memphis, TN, May 5, 2009.

**(15)** P. Raju Mantena; "Structural Foams, Nano and Grid-Stiffened Composites for Optimizing Energy Absorption" *Proceedings of the International Conference on Computational Methods in Engineering and Sciences - CMES 2009*, Hyderabad, India, Jan 8-10, 2009, pp. 1 - 7.

**(16)** Ahmad Almagableh, Swasti Gupta, P. Raju Mantena and Ahmed Al-Ostaz; "Dynamic Mechanical Analysis of Graphite Platelets and Nanoclay Reinforced Vinyl ester, and MWCNT Reinforced Nylon 6,6 Nanocomposites" *Proceedings of the 2008 SAMPE Fall Technical Conference*, Memphis, TN, Sep 8-11, 2008.

**(17)** Swasti Gupta, P. Raju Mantena and Ahmed Al-Ostaz; "Effect of Strain Rates on Energy Absorption of Exfoliated Graphite Platelet and Cloisite Nanoclay Reinforced Vinyl ester Nanocomposites" *Proceedings of the American Society for Composites 23rd Technical Conference*, Memphis, TN, Sep 8-1, 2008.

**(18)** Ge Wang, Ahmed Al-Ostaz, Alexander Cheng and P. Raju Mantena; "Particle Modeling for Blast Simulation" *Proceedings of the 2008 SAMPE Fall Technical Conference*, Memphis, TN, Sep 8-11, 2008.

# BLAST AND IMPACT RESISTANT COMPOSITE STRUCTURES FOR NAVY SHIPS

P. Raju Mantena, Alexander H.D. Cheng and Ahmed Al-Ostaz
Composite Structures and Nano-Engineering Research
University of Mississippi, University, MS 38677

## OBJECTIVE

Composite materials are increasingly being used in the construction of naval ships to enhance operational efficiency and reduce the life time costs. Naval ships are potentially subjected to dynamic loading in the form of severe blast waves generated by high-power explosives, as experienced by the USS Cole (Figure 1). Producing stronger, safer and more cost effective platforms for the new generation of naval ships requires innovative designs, new materials, affordable/efficient processing and characterization technologies. This project addresses several of these issues which would be of considerable benefit to navy operations.

Figure 1: USS Cole subjected to high-power explosive blast loading.

## TECHNICAL APPROACH

University of Mississippi (UM), Michigan State University (MSU), and University of New Orleans (UNO), supported by the Survivability and Protective Structures Branch of the Army Corps of Engineers Research and Development Center (ERDC) will utilize their unique research strengths in modeling, analysis, fabrication and testing of affordable structural composites to develop blast and impact resistant composite structures for the new generation navy ships to achieve better mobility, survivability, stealth, safety, and lower cost. North Carolina A&T State University (NC AT) will provide their patented fly-ash based Eco-Core foams, and the University of Alabama-Birmingham (UAB) will fabricate VARTM sandwich panels and perform ballistic tests. Northrop Grumman Ship Systems (NGSS), Gulfport, MS will advise and facilitate UM on their research efforts.

Focus of the proposed research is on marine composite structures, especially lightweight glass/carbon polymeric based composites, and innovative concepts for the mitigation of blast/shock/impact effects. Research areas include: low-cost fire-resistant exfoliated graphite and nano clay reinforced composites; fly ash based structural foams; low-velocity and ballistic impact; blast response; accelerated testing for long-term durability; dynamic mechanical analysis; computational mechanics and simulation; radar-absorbing and EM-shielding nano coatings for improved stealth/safety.

Tasks to be performed by the various agencies associated with this project are as follows:

**University of Mississippi:** UM has the expertise and facilities for conducting research on nanocomposite materials; low-velocity impact; dynamic mechanical analysis; accelerated testing for long-term durability; computational mechanics and simulation; Resonant Ultrasound Spectroscopy (RUS); radar-absorbing and EM-shielding nano coatings for improved stealth/safety.

**Michigan State University, East Lansing, MI:** MSU will concentrate its research effort on the development of low-cost fire resistant exfoliated graphite and nano clay reinforced brominated vinyl ester (or other) resin panels, flexible films and coatings; interphase studies, and novel processing techniques for navy ship structural applications.

**University of New Orleans, New Orleans, LA:** UNO will work on Hopkinson bar high-strain rate experimental characterization; dynamic modeling and simulation for determining the response of large composite structures/panels to high energy blast loads, and proposing optimal design configurations

**University of Alabama-Birmingham, AL:** UAB will fabricate 4' x 8' VARTM E-glass / vinyl ester with Eco-Core foam and TYCOR core sandwich panels; perform intermediate (gas gun) and high-velocity (ballistic) projectile penetration testing of specimens with and without elastomeric or other nano coatings; flame retardation experiments, and microscopy quantification.

**North Carolina A&T State University, Greensboro, NC:** For this project, NC AT will focus their research on developing and supplying to UM lighter, stronger, impact and fire resistant 12" x 12" x 1" Eco-Core foam panels for navy ship applications; conduct mechanical (tension, compression and shear) tests and provide the data for other performance studies; explore scaling of the manufacturing process to 2ft x 2ft x 1in or larger panels; and identify potential tie-up with industry for commercialization.

**Engineer Research and Development Center (ERDC), Vicksburg, MS**: ERDC conducts research and development (R&D) in support of military construction, military engineering, civil works, Department of Defense, and others. ERDC will support UM research with its unique Blast Load Simulator (BLS) facility for evaluating the response of sandwich composite structures/panels to blast pressure waveforms of up to 20,000 lbs explosive yields and peak reflected pressures simulating blast loads from terrorist bombs.

**Northrop Grumman Ship Systems (NGSS), Gulfport, MS:** FRP composites are presently being used in US Navy Ships such as the Osprey class mine hunter, and for topside structures on large warships such as the Advanced Enclosed Mast System (AEMS). The navy also has plans to integrate more composites into the new generation CV(X) and DD(X) ship class designs. Almost half of the nation's naval ship building industries are located in the Gulf Coast, and most prominently Northrop Grumman Ship Systems in Mississippi and Louisiana. NGSS will advise and facilitate UM on their research efforts.

## RECENT ACCOMPLISHMENTS

The project has just been awarded and sub-contracts are being processed.

## NAVY RELEVANCE

Results from these investigations have significant potential in the development of nano-multifunctional materials and sandwich structure designs that would contribute to building lighter, stronger and faster ships for the US Navy. The inexpensive fire resistant Eco-Core or other foams layered in between carbon nanotube or graphite platelet enhanced composite face plates will provide structures that offer optimal flexural rigidity, vibration damping and blast/shock/impact energy absorption along with reduced weight; for the future generation naval structures or retrofitting of existing ones.

# BLAST AND IMPACT RESISTANT COMPOSITE STRUCTURES FOR NAVY SHIPS

**P. Raju Mantena, Alexander H.D. Cheng and Ahmed Al-Ostaz**
Composite Structures and Nano-Engineering
The University of Mississippi

## OBJECTIVE

Develop stronger, safer and more cost-effective structures for the new generation naval ships; especially nanoparticle reinforced glass/carbon polymeric based composites and structural foams for blast/shock/impact mitigation.

## TECHNICAL APPROACH

Focus of research is on marine composite structures; particularly lightweight glass/carbon polymeric based composites, and innovative concepts for the mitigation of blast/shock/impact effects. Sandwich composites with balsa and foam cores are presently being featured in number of navy applications such as in surface ship deck structures, radar mast and boat hulls. In the present work several new and emerging cores have been explored in sandwich construction. Different core types have been considered including; (a) Tycor (TYCOR® from Webcore Technologies), an engineered three-dimensional fiber reinforced damage tolerant core for sandwich structures, has the potential to provide improved blast and ballistic resistance. In this core, glass fiber is reinforced through the thickness of closed cell foam sheets to produce a web and truss structure; (b) Eco-core is an emerging fire resistant sandwich core. Fire damage in ship structures is of significant concern. The burn-through resistance and heat insulation characteristics of Eco-core makes it an attractive fire resistant core; (c) Balsa wood which is a traditional core material being used in present generation ship structures. Balsa is a natural material, and is prone to local variation in properties due to cell size and cell thickness variations; and (d) Polyvinyl chloride (PVC) foam core which is being used in present generation ship structures for radar mast enclosures and boat hulls.

Our research approach includes the characterization of low-cost fire resistant exfoliated graphite nanoplatelet reinforced glass/carbon polymeric based composites with fly ash and 3-D fiber reinforced foams; investigating their response to low-velocity impact, ballistic, shock and blast loads; dynamic mechanical analysis for modulus, damping, creep and stress relaxation; developing constitutive models and computer simulations; accelerated testing for long-term durability; and the radar-absorbing and EM-shielding characteristics for improved stealth/safety.

## RECENT ACCOMPLISHMENTS

E-glass / vinyl ester sandwich composite panels were designed and fabricated by the VARTM process as per Northrop Grumman Ship Building design specifications. These 4' x 8' x 2.32" thick sandwich panels are made up of 0.16" thick E-glass (90/0, 45/-45, 90/0, 45/-45), 90/0) face skins with Dow 510A-40 brominated vinyl ester resin and 2" thick Tycor, PVC foam and balsa cores. Two large panels were subjected to blast load waveforms and peak reflected pressures simulating terrorist threats. Trial blast tests, simulating an approximate threat level of about 27,000 lbs TNT at 184 feet, were conducted at the ERDC - Blast Load Simulator (BLS) facility in Vicksburg, MS. One 4' x 4' E-glass/Tycor panel (with all-around bolted b.c.) subjected to 80 psi pressure level was not breached, and there are no visible signs of damage. Another 64" x 34" E-glass/ Balsa core panel (two-sides pinned and two-sides free b.c.) subjected to about 60 psi slid through the supports and was completely damaged, with E-glass face skin on blast side shearing into two halves at the middle.

Instrumentation, data acquisition and specimen clamping issues are being resolved for future full-scale blast experiments. Smaller samples cut from the larger sandwich panels are undergoing shock tube and ballistic tests.

AUTODYN computer simulations of the response of composite structures/panels to blast loads, particle dynamics model of the impact event, and a first-principle shock model were developed. The modulus, damping and glass transition temperature of vinyl ester reinforced with graphite nano platelets and nanoclay have been characterized. Low-velocity impact, high-strain rate Hopkinson bar and shock-tube tests were performed on these nanoparticle reinforced specimens. Their radar-absorbing and EM shielding characteristics were also evaluated. 12" x 12" x 2" thick fly ash based Eco-core foam panels were manufactured and their static properties determined. Further details of these research investigations are given in the following sections.

**1. Dynamic Mechanical Analysis:** A *TA Instruments* Model Q800 DMA was used for characterizing the dynamic modulus, loss factor, $T_g$ , creep and stress relaxation properties of graphite platelet and nanoclay reinforced composites [1] proposed for naval ship structural applications. Peaks of the tan delta or loss modulus curves are found to be sensitive indicators of glass transition temperature and are associated with the impact properties of elastomeric materials. The time-temperature superposition principle is also employed for characterizing the long-term behavior of nanocomposites. From DMA testing, it was observed (Figure 1) that the storage modulus of pure nylon 6,6 is greater than that of pure vinyl ester, where as the glass transition temperature and loss factor are higher for pure vinyl ester compared to pure nylon 6,6. Storage modulus increased with increasing reinforcement in all the cases. It was also observed that storage modulus and glass transition temperature of 2.5 wt. percent graphite platelet reinforced vinyl ester is more than that of nanoclay reinforced vinyl ester, while loss factor is higher for the 2.5 wt. percent nanoclay reinforced vinyl ester.

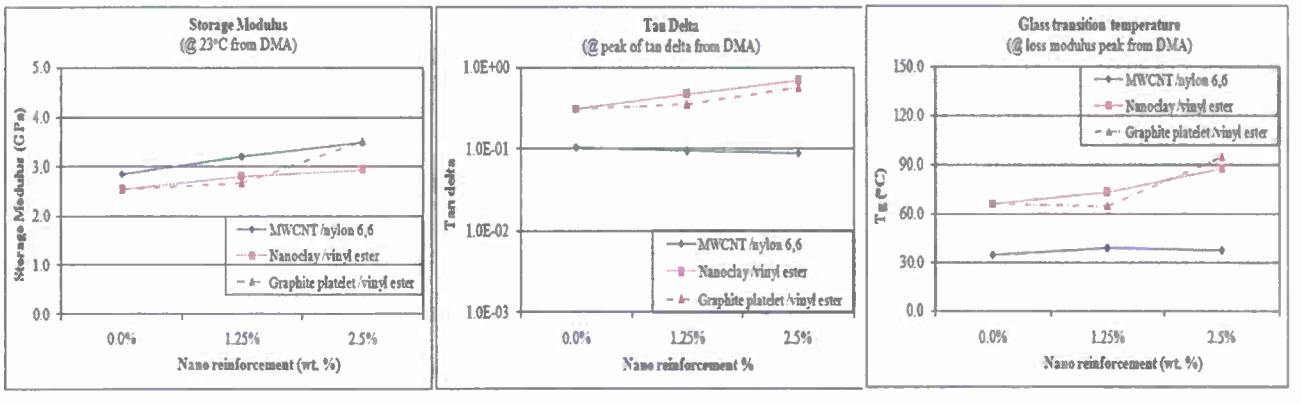


Figure 1. Storage modulus, damping and glass transition temperature for nylon 6,6 with MWCNTs; and vinyl ester reinforced with nanoclay and graphite platelets.

**2. Low-velocity Impact and Shock Response:** Low-velocity impact tests were performed on vinyl ester nanocomposites in a drop-weight instrumented impact test system (Dynatup Model 8250) as per ASTM D6110-06. From low-velocity impact testing it is observed (Figure 2) that for un-notched specimens, the energy absorption of pure vinyl ester almost doubled when reinforced with 2.5 wt. percent Cloisite 30B nanoclay and exfoliated graphite nano platelets [2]. However, notched specimens showed a 50% decrease in energy absorption for 2.5 wt. percent nanoclay and a 75% decrease with 2.5 wt. percent graphite platelet reinforcements, suggesting notch sensitivity.

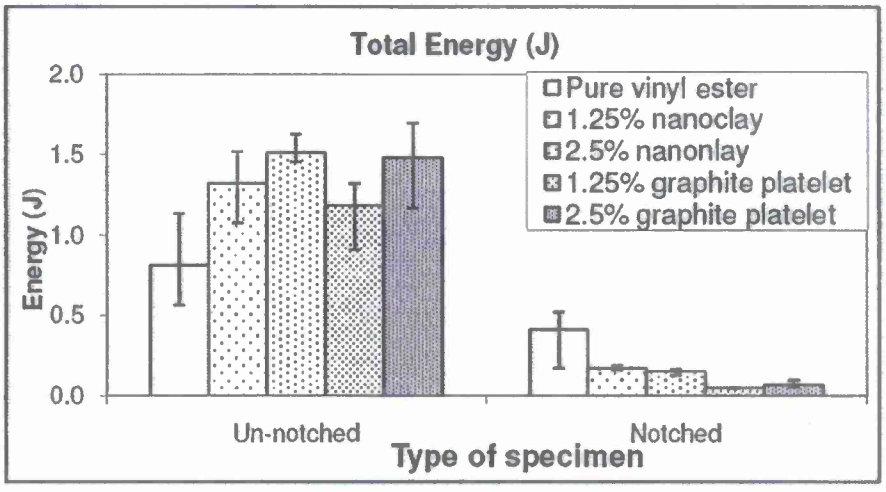


Figure 2. Energy absorbed by notched and un-notched pure vinyl ester, and with nanoclay and graphite platelet reinforcements under low-velocity impact.

Shock tube tests were conducted at the University of Rhode Island on nanocomposite panels of dimension 254 mm x 101.6 mm x 9.9 mm (10" x 4" x .39"). The panels were held under simply supported conditions so as to minimize damage due to gripping and clamping. The span of the simply supported plate was 152 mm (6") and the overhangs measured 50.8 mm (2") from each end. The center of the specimen was kept in line with the center of the shock tube. The ratio of the loading diameter to the span was 0.5. The specimens were blast loaded from the exit of the shock tube on the face opposite to the supports [3]. One panel from each configuration was subjected to 70 psi (482.3 kPa) and another at 120 psi (827.4 kPa) peak pressure. Samples subjected to 70 psi (482.3 kPa) peak pressure did not fracture, and all the samples subjected to 120 psi (827.4 kPa) peak pressure shattered into pieces(Figures 3 and 4).

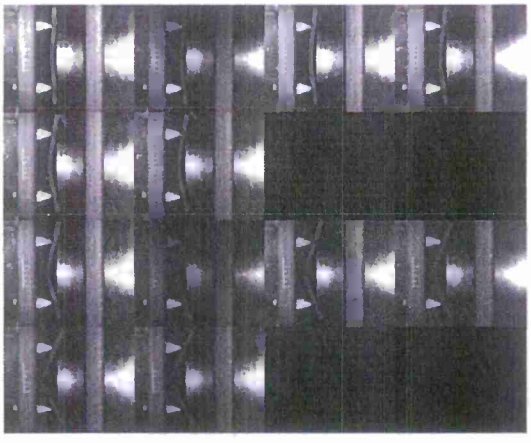

Figure 3. Real time image of 2.5 wt. % graphite platelet/vinyl ester specimen subjected to 120 psi peak pressure in shock tube [3].

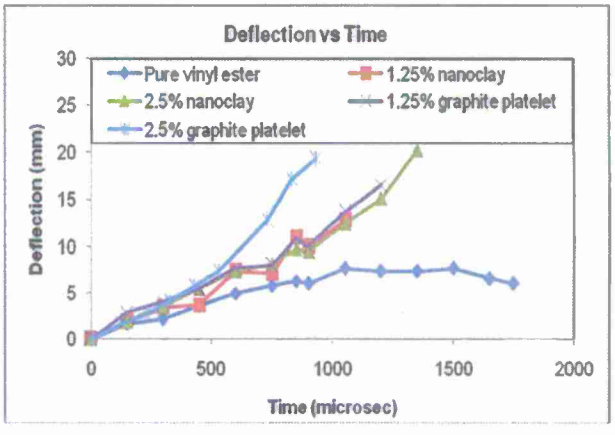


Figure 4. Deflection vs. time from high speed images for pure vinyl ester and nanocomposites at 120 psi peak pressure in shock tube [3].

For analyzing the material response to shock loading, quasi-static and dynamic approaches were adopted. In quasi-static method, the energy absorbed by each specimen is obtained by correlating the mid-span deflection with the pressure in terms of transient load. Pressure at respective time intervals was converted to transverse load exerted on the specimen by multiplying it with the effective area of the driven section (3" diameter). Transient loads obtained were plotted against the respective mid-span deflections. Energy absorbed was then computed with numerical integration up to the point of maximum deflection (failure) [3]. The energy absorbed up to failure for 120 psi peak pressure shock loading for pure vinyl ester and nanoclay and graphite platelet reinforced composites is shown in Figure 5. As per this approach, the 2.5 wt. percent graphite platelet reinforced vinyl ester appears to absorb maximum energy up to failure. It was also observed that shock tube response of nanocomposites showed a similar trend as that of the low-velocity impact tests. Results of shock tube tests are inconclusive at this stage as only one sample was tested in each case.

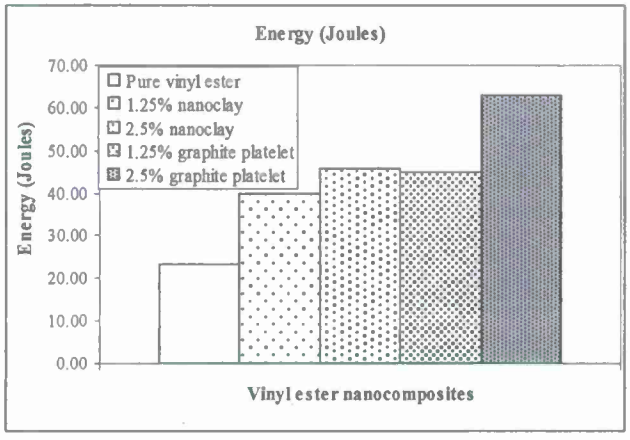


Figure 5. Energy absorption of pure vinyl ester and nanocomposites subjected to 120 psi (827.4 kPa) pressure in shock tube.

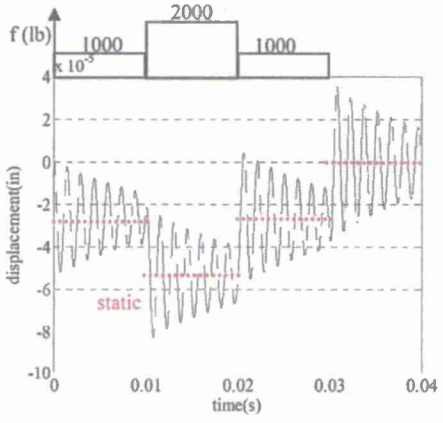


Figure 6. Centerline displacement from shock model of a sample beam subjected to three pulses (with 2% damping).

**3. First-Principle Shock Model:** Main purpose of this work is to obtain the response of a structure experiencing an arbitrary shock load through modal analysis. The selected model is an Euler-Bernoulli beam with both torsional and lateral springs at its ends so that the boundary conditions are adjustable. The beam is also connected to a foundation to which base excitation can be applied. Model input includes the gross properties of Young's modulus, material density, and physical geometry. The excitation force time history, or the shock pressure pulse, is discretized into sufficiently small time steps to capture the highest expected frequency content. Closed form equations have been employed to derive the eigenproblem that generates the structure's mode shapes and natural frequencies. A discrete number of orthonormalized mode shapes are used to obtain the time history response. An amount of damping is also estimated for each mode in the simulation. As shown in Figure 6, this method captures the transient behavior, specifically at each abrupt change in force. The approach is to match shock tube experiments using gross parameters of the composite materials and actual pressure pulses. Convergence studies will be important to ensure capture of the complex shock response. An additional Hertzian element will be added into this beam model to simulate any structural contact or as a preliminary model for fluid resistance. Eventually the impact dynamics of a beam subjected to shock in a fluid environment will be examined. The goal is to mimic a shock load on a segment of ship hull underwater.

**4. AUTODYN Simulations:** Finite element analysis of fluid structure interaction (FSI) was used to study blast resistance of sandwich composites. Commercially available hydrodynamic software AUTODYN 11.0 with either Lagrangian, Eulerian, Arbitrary Lagrangian-Eulerian (ALE) or SPH formulation was used. Data is being collected to establish Pressure-Impulse (PI) and iso-damage curves for sandwich composites made up of 0.16"

thick E-glass (90/0, 45/-45, 90/0, 45/-45), 90/0) face skins and 2" thick Tycor foam. Mechanical properties of Tycor (from the manufacturer) and skin properties (from literature) used in this study are summarized in Table 1.

Table 1: Properties of Tycor foam and E-glass / vinyl ester skins

| Foam properties | | | | | Skin properties ($v_f$ = 0.65) | | | |
|---|---|---|---|---|---|---|---|---|
| Stiffness | | Average strength | | Ultimate strain | Stiffness | | Average strength | |
| $E_L$ (MPa) | 351.6 | $T_L$ (MPa) | 5.52 | 1.57 % | $E_L$ (GPa) | 48.86 | $T_L$ (MPa) | 820 |
| $E_T$ (MPa) | 206.8 | $T_T$ (MPa) | 2.07 | 1.00 % | $E_T$ (GPa) | 16.17 | $T_T$ (MPa) | 45 |
| $E_Z$ (MPa) | 682.6 | $T_Z$ (MPa) | 4.48 | 0.66 % | $E_Z$ (GPa) | 16.17 | $C_L$ (MPa) | 490 |
| $\nu_{LZ}$ | 0.28 | $C_L$ (MPa) | 5.52 | 1.57 % | $\nu_{LT}$ | 0.263 | $C_T$ (MPa) | 110 |
| $\nu_{TZ}$ | 0.16 | $C_T$ (MPa) | 3.45 | 1.67 % | $\nu_{TZ}$ | 0.263 | $S_{LT}$ (MPa) | 55 |
| $\nu_{LT}$ | - 0.15 | $C_Z$ (MPa) | 15.2 | 2.22 % | $\nu_{ZL}$ | 0.088 | | |
| $G_{LZ}$ (MPa) | 227.5 | $S_{LZ}$ (MPa) | 2.90 | 1.27 % | $G_{LT}$ (GPa) | 7.831 | | |
| $G_{TZ}$ (MPa) | 179.4 | $S_{TZ}$ (MPa) | 3.52 | 1.96 % | $G_{TZ}$ (GPa) | 3.133 | | |
| $G_{LT}$ (MPa) | 2.76 | $S_{LT}$ (MPa) | 0.34 | 12.5 % | $G_{ZL}$ (GPa) | 7.831 | | |

Two cases of sandwich composites were simulated: (a) 36 in high and 36 in width sandwich composite panel with fixed all-around boundary condition, and (b) 52 in high and 34 in wide sandwich composite panel simply supported at two ends and free at other two ends. Schematic of these cases are shown in Figure 7. In the first case, 1040 eight-node brick elements were used to build the core and 10400 shell elements were used to build ten layers of skin. In the second case, 1040 eight-node brick elements were used to build the foam core and 10400 eight-node brick elements were used to build ten layers of skin. A 5 lb, 10 lb, 20 lb, or 50 lb charge of TNT explosive was placed at a fixed distance of 3 m from the face of the panel and detonated. Lagrangian formulation was used for the solid model and Eulerian formulation was used for the fluid simulation. Orthotropic equation of state and elastic strength model was used for the skin and the foam. For the air, ideal gas equation of state was used. Time history of midpoint displacement and the incident pressure were recorded at a gauge point placed at the center of the panel. Figures 8 and 9 show the recorded mid-point displacements and damage maps.

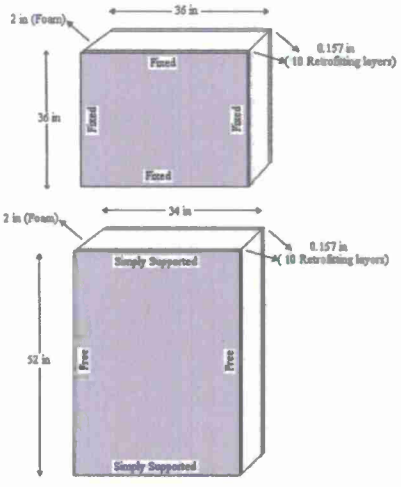


Figure 7: Schematic of the AUTODYN models used.

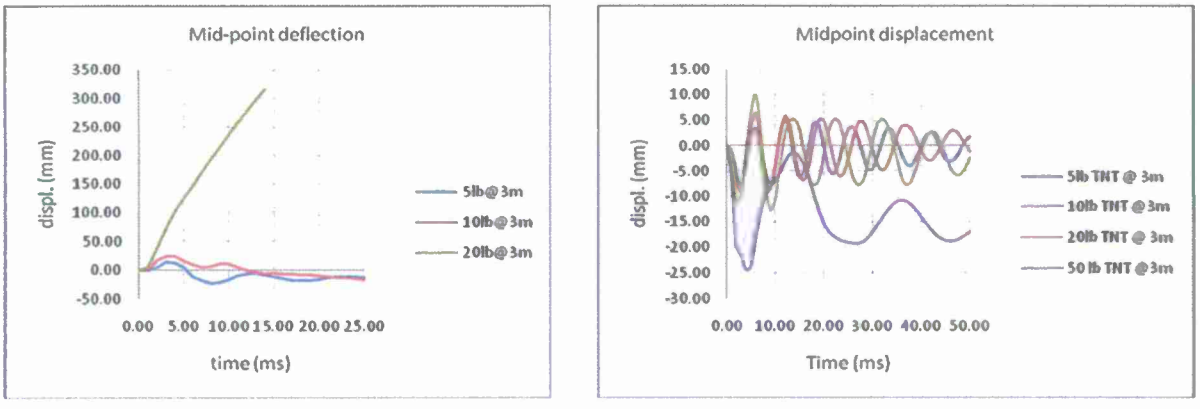


Figure 8: Time history of midpoint displacement for sandwich composites under different blast loads with (a) simply-supported on top and bottom, and (b) fixed all-around boundary conditions

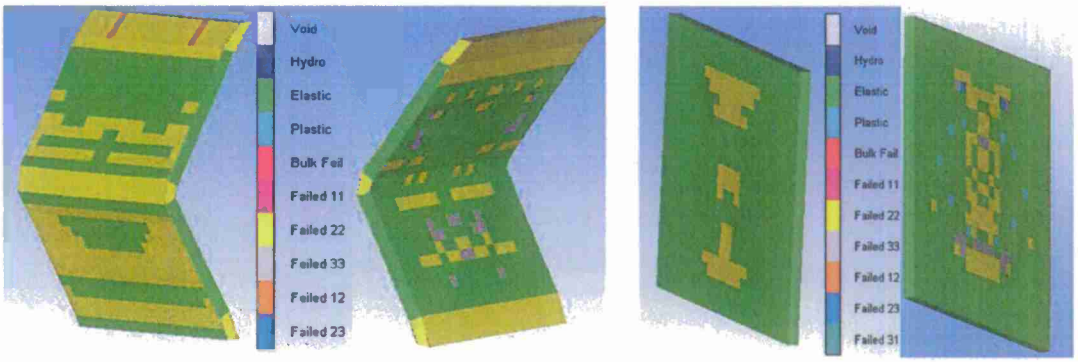


(a) (b)

Figure 9: AUTODYN simulation of damage region for E-glass / Tycor sandwich composite under 20lb TNT@3m with (a) simply supported on top and bottom (front face at right and back face at left), and (b) fixed all-around (front face at right and back face at left)

**5. Nanoreinforcement Modification of Composites:** (Dr. Larry Drzal, Michigan State University)

The goal is to develop a fundamental understanding of the interaction of graphite nanoplatelets with macro reinforcing fibers and polymer matrices, and how these interactions affect the mechanical properties and durability (fire, blast and environmental) of nanoparticle modified polymer composites. The objectives of of this project are: (1) quantify the effect of nanoparticle concentration and dispersion a) around and between individual reinforcing fibers (intralaminar) and b) between lamina in both unidirectional and woven fiber lamina (interlaminar). (2) optimize the improvement in mechanical properties and durability of a carbon fiber (or glass fiber) vinyl ester, nylon and polyurea matrix composite systems utilizing the addition of clay or exfoliated graphite nanoplatelets.

The nanoparticles that have shown beneficial property improvement in the first year of this study has been the exfoliated graphite. Research will be continued on brominated vinyl ester resin and polyurea matrix systems. Both E-glass fibers and carbon fibers will be sized with exfoliated graphite nanoplatelets for compatibility with these matrix systems in tow and woven mat form. Furthermore, 1 mil thick films containing orientated graphite nanoplatelets will be prepared and laminated into composite panels through compression molding to investigate fracture and energy absorption mechanisms and fire protection capability. The same material with suitable modifications will also be inserted between lamina in unidirectional composite panels to investigate their role as a composite toughening agent.

**6. High- Strain Rate Testing/Analysis:** (Dr. David Hui, University of New Orleans)

Split-Hopkinson Pressure Bar (SHPB) tests were performed on nanoclay and graphite platelet reinforced vinyl ester specimens with a set-up consisting of striker bar, incident bar, and transmission bar, all made of maraging steel with a diameter of 12.7 mm (0.5"). Length of striker, incident and transmission bar is 762 mm (30"), 1219.2 mm (48") and 2438.4 mm (96") long respectively. Circular specimen of dia. 9.9 mm (0.39") and thickness of 4.5 mm (0.18") is sandwiched in between the incident bar and the transmission bar. Strain gauges mounted on incident bar and transmission bar were used as signal indicators and the energy absorbed by samples was computed from their outputs.

Figure 10 shows the energy absorption of pure vinyl ester and nanocomposites at approximate strain rates of 2500 and 3500 per second. It should be noted that data at 3500 per second for the 1.25% nanoclay/vinyl ester specimen is not available at this time and more SHPB tests are in progress. Energy absorption is observed to be increasing with increasing strain rates for pure vinyl ester as well as with 2.5 wt. percent graphite platelet and nanoclay reinforcement. In SHPB testing, the energy absorption showed an increase of 50% with increasing strain rate for pure vinyl ester, while it reduced by 30% with addition of 1.25 wt. percent graphite platelets. Reinforcement of 2.5 wt. percent nanoclay in vinyl ester showed a 30% increase in energy absorption for both strain rates compared to pure vinyl ester. Further testing of samples with the SHPB apparatus is in progress.

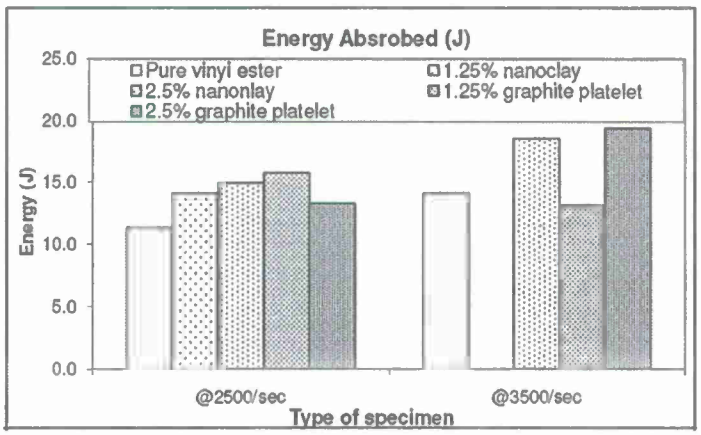


Figure 10. Energy absorption at 2500 and 3500 per second strain rates from SHPB testing of pure vinyl ester, and with nanoclay and graphite platelet reinforcement.

**7. VARTM Fabrication of Sandwich Composites and Ballistic Characterization:**
(Dr. Uday Vaidya, University of Alabama - Birmingham)

For this project UAB has fabricated large 8 ft x 4ft sandwich panels representative of ship structures using the vacuum assisted resin transfer molding (VARTM) process. In VARTM, single-sided flat plate tooling is adopted in conjunction with vacuum and infusion lines. The preform (i.e. fabric facesheet layers and the core) are encapsulated in a vacuum bag. Resin is infused with the aid of vacuum until full wet-out of the facesheets occurs. The sandwich panels utilized 5 layers for each facesheet made of E-glass fabric facesheets of a combination of plain weave [0/90] and [+/-45] angle ply architecture. Specifically the lay-up for each facesheet was as follows: E-glass fiber (90/0, 45/-45, 90/0, 45/-45, 90/0) and vinyl ester resin. The sandwich panel lay-up was co-infused (simultaneous wet-out of the top and bottom facesheet) with low viscosity, room temperature cure 510A-40 brominated vinyl ester resin system. Two 4ft x 8 ft sandwich panels with 2 " thick Tycor, and one panel each with balsa wood and PVC foam core, were fabricated. In all cases the areal density of the sandwich panels is maintained as close to each other as possible.

Ballistic tests compared the damage initiated by ballistic events on three sandwich structures with equivalent E-glass face sheets but with different core materials, namely Tycor, Balsa and Foam core. In order to compare the role of the core material, it was decided that the ballistic event should fully penetrate the structure. To this end NIJ level III was chosen as the threat level. Testing was conducted using a Universal Receiver equipped with a barrel to launch 0.30 caliber M80 ball round projectile(s). Projectiles were loaded to meet NIJ standard velocities for a level III impact. Other 0.30 caliber projectiles were manufactured to impact at lower

velocities in an attempt to determine the velocity threshold at which core differences would be realized, however the projectiles could not be 'loaded down' to a safe level to establish this threshold.

Table 2: Results of NIJ level III ballistic tests on sandwich panels with different core materials.

| | **E1B3VFP1 [ E-glass / Balsa Sandwich]** | | **E1P2VEP1 [ E-glass /PVC Sandwich]** | | **E1T1VDP1 [ E-glass /Tycor Sandwich]** | |
|---|---|---|---|---|---|---|
| Shot ID | Striking Velocity ft/s (m/s) | Residual Velocity ft/s (m/s) | Striking Velocity ft/s (m/s) | Residual Velocity ft/s (m/s) | Striking Velocity ft/s (m/s) | Residual Velocity ft/s (m/s) |
| 1 | 2919 (890) | 2871 (875) | 2935 (895) | 2927 (892) | 2925 (892) | 2443 (745) |
| 2 | - | 2897 (883) | 2950 (899) | 2865 (873) | 2898 (883) | - |
| 3 | 2911 (887) | 2890 (881) | 2961 (903) | - | 2969 (905) | - |
| 4 | 2888 (880) | 2843 (867) | 2970 (905) | - | 3007 (917) | - |
| 5 | 2951 (899) | - | 2978 (908) | - | 2948 (899) | - |
| 6 | 2885 (879) | - | | | | |
| | **Shot locations (Front view)** | | **Shot locations (Front view)** | | **Shot locations (Front view)** | |
| | 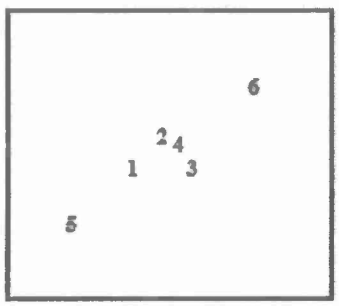 | | 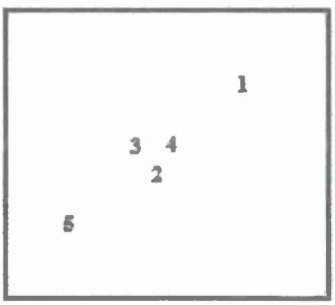 | | 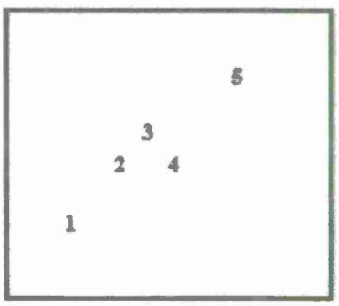 | |

Figure 11. Front, back, and side views of the E-glass / Tycor sandwich panel after projectile penetration.

Results of the ballistic tests conducted on all sandwich samples are shown in Table 2. The measurement of exit velocities from PVC foam and Tycor core sandwich panels was limited in most cases, due to extensive debris resulting from dislodged core particles. These cores, when damaged at high impact velocities, break up into very fine particles, and particles exit the panel. The exit of a large number of these particles passes through the exit chronographs and causes them to default. This has been observed in previous tests using brittle core materials as well. However comparing the damage zones on the back face (exit side) of the panels, the PVC had

very minimal damage on the exit face implying that the least amount of energy has been absorbed. The balsa core engages the projectile to a higher degree and hence higher interaction between the core and the face sheets. The back face damage is larger compared to the PVC core panel. The Tycor foam core provides the most interaction (Figure 11), if the projectile strikes at the intersection of a web i.e. the stiffening elements of the core. The damage zone size reduces if the projectile strikes one (either x or y) element of the core. If the projectile strikes between the stiffening elements of the core, the damage on the back face is very similar to the PVC foam core. Further evaluation of the tested panels need to be conducted for more conclusive analysis, for example tap testing, cross section microscopy, etc. Also post-mortem studies will evaluate effects of damage interaction from multisite impacts and their effect on residual strength of the sandwich panels.

**8. Fly Ash Based Eco-core Structural Foams:** (Dr. Kunigal Shivakumar, North Carolina A&T)

The current manufacturing capability of Eco-core is restricted to panel sizes of 6 x 6 x 1 in and 12 x 12x 1 in. Northrop Grumman Ship System suggested that they use 2 in thick cores in their ship structures application. Accordingly, the eco-core process was scaled-up to manufacture 2 in thick panels. Processability of different fibers such as chopped and milled from different vendors namely Johns Maniville, Owens Corning, Fibertech, PPG was evaluated. Based on this study 4.5% weight of JM3 (Johns Maniville) and OC2 (Owens Corning) were chosen as reinforcement for baseline eco-core. Six panels each of baseline (no fiber), JM3 reinforced, and OC2 reinforced eco-core were fabricated and shipped to University of Mississippi. Panel size was 14 x 14 x 2 in as molded and trimmed to 12 x 12 x 2 in. Separately, 1/2 in thick panels were made and characterized for compression, tension, shear, flexure and fracture properties. Table 3 lists the average value with standard deviation based on five tested samples.

Table 3. Mechanical Properties of Eco-cores

| Property | Baseline | Eco-Core - JM3 4.5 wt.% | Eco-Core - OC2 4.5 wt.% |
|---|---|---|---|
| **Density, g/cc** | 0.53 (0.02*) | 0.52 (0.02) | 0.52 (0.01) |
| **Compression** | | | |
| Strength, $F_c$, psi | 3,169 (193) | 2,177 (159) | 2,544 (320) |
| Modulus, $E_c$, msi | 0.17 (0.02) | 0.16 (0.01) | 0.12 (0.02) |
| **Tension** | | | |
| Strength, $F_t$, psi | 756 (94) | 881 (48) | 1,152 (211) |
| Modulus, $E_t$, msi | 0.38 (0.01) | 0.37 (0.02) | 0.40 (0.04) |
| **Shear** | | | |
| Strength, $F_s$, psi | 740 (59) | 777 (56) | 678 (116) |
| **Flexural** | | | |
| Strength, $F_b$, psi | 1,665 (129) | 1,145 (191) | 1,433 (136) |
| Modulus, $E_b$, msi | 0.42 (0.02) | 0.35 (0.03) | 0.39 (0.02) |
| **Fracture** toughness, $K_{Ic}$, psi-in$^{1/2}$ | 291 (36) | 419 (92) | 292.5 (8) |
| *Standard deviation | *Note: Based on 1/2" thick panel test* | | |

## TRANSITIONS

These research investigations have been leveraged with a concurrent grant: Nano-Particle Reinforced Composites for Critical Infrastructure Protection, from the Department of Homeland Security - Southeast Region Research Initiative (DHS-SERRI). Northrop Grumman Ship Building (NGSB) - Advanced Capabilities Group (ACG) facilitated this research effort on development of advanced ship panel concepts. Webcore Technologies Inc., a small-scale industry in Dayton, OH worked closely with University of Mississippi to develop affordable and durable TYCOR® composite sandwich panels for ship structural applications. TYCOR® is currently being used in several military and commercial applications including refrigerated cargo floor for Navy cargo ships, Air Force tactical shelters, Air Force runway matting, vehicular bridge decks, railcar floors and wind turbine blades.

## NAVY RELEVANCE

Producing stronger, safer and more cost-effective platforms for the new generation naval ships requires innovative designs, new materials, and affordable/efficient processing and characterization technologies. This research will advance the development of blast/shock/impact resistant composites for navy ship structural applications; to achieve better mobility, survivability, stealth, safety, and at lower cost.

## ACKNOWLEDGEMENT

This research was funded by ONR Grant #00014-07-1-1010, Office of Naval Research, Solid Mechanics Program (Dr. Yapa D.S. Rajapakse, Program Manager). Partial funding received under a subcontract from the Department of Homeland Security - sponsored Southeast Region Research Initiative (SERRI) at the Department of Energy's Oak Ridge National Laboratory is also acknowledged. We would like to thank Dr. Arun Shukla, University of Rhode Island for performing the shock tube tests, and Dr. Rob Banerjee, Webcore Technologies for providing their TYCOR® panels for this research.

## PUBLICATIONS (ONR-supported)

1. Ahmad Almagableh, Swasti Gupta, P. Raju Mantena and Ahmed Al-Ostaz "Dynamic Mechanical Analysis of Graphite Platelets and Nanoclay Reinforced Vinyl ester, and MWCNT Reinforced Nylon 6,6 Nanocomposites" *Proceedings of the 2008 SAMPE Fall Technical Conference*, Memphis, TN, Sep 8-11, 2008.
2. P. Raju Mantena, Ahmed Al-Ostaz and Alexander H-D Cheng "Dynamic Response and Simulation of Nano-particle Enhanced Composites" *Composites Science and Technology* (in press)
3. Swasti Gupta, P. Raju Mantena and Ahmed Al-Ostaz "Effect of Strain Rates on Energy Absorption of Exfoliated Graphite Platelet and Cloisite Nanoclay Reinforced Vinyl ester Nanocomposites" *Proceedings of the American Society for Composites 23rd Technical Conference*, Memphis, TN, Sep 8-1, 2008.
4. Al-Ostaz A., Pal G., Mantena P.R. and Cheng A.H-D "Molecular Dynamics Simulation of SWCNT-Polymer Nanocomposite and its Constituents" *Journal of Materials Science*, Vol. 43, No1, pp.164-173, 2008.
5. Ge Wang, Ahmed Al-Ostaz, Alexander Cheng and P. Raju Mantena "Particle Modeling for Blast Simulation" *Proceedings of the 2008 SAMPE Fall Technical Conference*, Memphis, TN, Sep 8-11, 2008.
6. Ge Wang, A. Al-Ostaz, A.H.-D. Cheng and P.R. Mantena (2008), Hybrid Lattice Particle Modeling: Theoretical Considerations for a 2-D Elastic Spring Network for Dynamic Fracture Simulations, Computational Materials Science (in press).
7. Ge Wang, A. Al-Ostaz, A.H.-D. Cheng and P. Radziszewski (2008), Particle modeling and its current success in the simulations of dynamic fragmentation of solids, in Strength of Materials: New Research Trends (Ed. Frank Columbus), Nova Science Publishers (Accepted)

# BLAST AND IMPACT RESISTANT COMPOSITE STRUCTURES FOR NAVY SHIPS

**P. Raju Mantena, Alexander H.D. Cheng, Ahmed Al-Ostaz and A.M. Rajendran**
Composite Structures and Nano-Engineering Research
The University of Mississippi

## OBJECTIVE

Develop stronger, safer and more cost-effective structures for the new generation naval ships; especially nanoparticle reinforced glass/carbon polymeric based composites and structural foams for blast, shock and impact mitigation.

## TECHNICAL APPROACH

Focus of research is on marine composite structures; particularly lightweight glass/carbon polymeric based composites, and innovative concepts for the mitigation of blast, shock and impact effects. Sandwich composites with balsa and foam cores are presently being featured in number of navy applications such as in surface ship deck structures, radar mast and boat hulls. In our work, other new and emerging cores including TYCOR® (an engineered three-dimensional fiber reinforced damage tolerant core) and the fire resistant Eco-Core® are also being explored in sandwich constructions.

Technical approach includes researching low-cost fire resistant nanoclay and exfoliated graphite platelet reinforced glass and carbon polymeric based composites with fly ash and 3-D fiber reinforced foams; investigating their response to low-velocity impact, ballistic, shock and blast loads; dynamic mechanical analysis for modulus, damping, creep and stress relaxation; developing constitutive models and computer simulations; accelerated testing for long-term durability; and evaluating their radar-absorbing and EM-shielding characteristics for improved stealth and safety.

## RECENT ACCOMPLISHMENTS

During Year-I of this project, several 4' x 8' x 2.25" thick sandwich composite panels made up of 0.125" thick E-glass (90/0, 45/-45, 90/0, 45/-45, 90/0) face skins with 2" thick TYCOR, PVC foam and balsa cores and Dow 510A-40 brominated vinyl ester resin were designed and fabricated by the VARTM process. Some of these large size panels were subjected to blast load waveforms and peak reflected pressures simulating terrorist threats at the ERDC - Blast Load Simulator (BLS) facility in Vicksburg, MS. Smaller samples are also being analyzed in shock tube, ballistic, and low-velocity tests. Results of preliminary investigations along with molecular dynamics modeling and computer simulations are given in References 1 and 2. The Year II research effort and accomplishments on blast loading of large sandwich composite panels; low velocity punch-shear characteristics of nanocaly and graphite platelet reinforced vinyl ester, laminated face sheets and sandwich composites; shock tube testing for design optimization; NDE and mechanical property characterization; constitutive modeling and computer simulations are described in the following sections:

**1) Blast Testing:** Two large 4' x 4' panels were subjected to blast load waveforms and peak reflected pressures simulating terrorist threats. Trial blast tests, simulating an approximate threat level of about 27,000 lbs TNT at 184 feet, were conducted at the ERDC-Blast Load Simulator (BLS) facility in Vicksburg, MS. One 4' x 4' E-glass/TYCOR sandwich panel, with all-sides bolted and subjected to about 80 psi peak pressure and 1000 psi-ms impulse, was not breached and there were no visible signs of damage [1]. Another 4' x 3' E-glass/TYCOR sandwich composite panel, bolted at top/bottom and two sides free, was subjected to 70 psi peak pressure and

900 psi-ms impulse loading. As seen in Figure 1, this panel offered significant resistance to the blast load with permanent deformation and only localized shear pullout damage at the bolt regions. Balsa and PVC foam core sandwich composite panels with E-glass, Owens Corning HPG glass and T700 FOE treated carbon face sheets are currently undergoing blast tests.

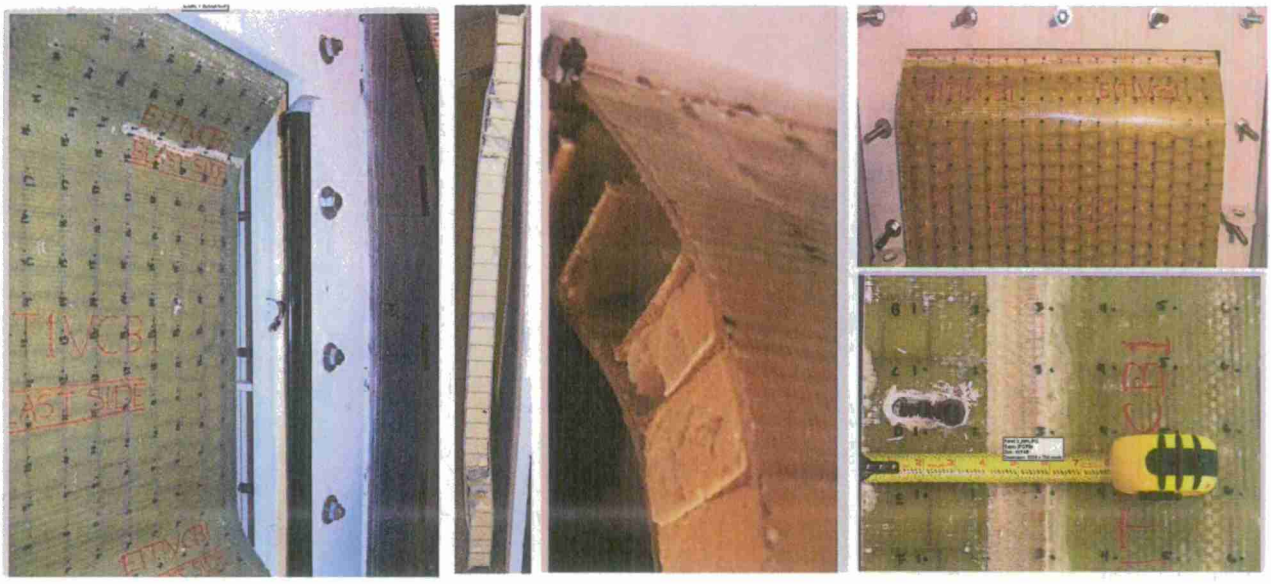

Figure1. E-glass/TYCOR sandwich composite panel bolted at top/bottom and two-sides free, after blast test.

**2. Punch-shear Characteristics of Nanoparticle Reinforced Vinyl ester Plates, Laminated Face Sheets and Sandwich Composites:** Low velocity punch-shear response of nanoparticle reinforced vinyl ester plates, laminated face sheets, and sandwich composites were analyzed on 4"× 4" square plate specimens with all around fixed circular boundary condition and impacted by a hemispherical-head plunger with added mass. Impact load, displacement and energy plots along with visual inspection of post-damage specimens depicted the punch-shear characteristics of these composites. Test results show more than 10% improvement in impact energy absorption with addition of 2.5 wt. pct. graphite platelets to pure vinyl ester (Figure 2). Maximum improvement in energy absorption (about 40%) was observed with Owens Corning HP ShieldStrand® glass fabric face sheets compared to the E-glass/vinyl ester (Figure 3).

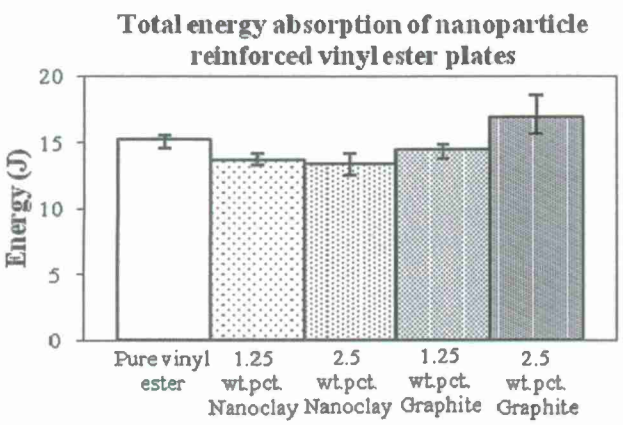


Figure 2. Total energy absorbed by nanoparticle reinforced vinyl ester plates during low velocity punch-shear.

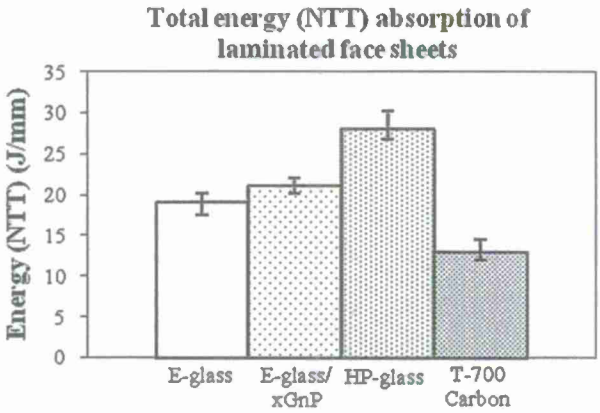


Figure 3. Total energy absorbed (NTT) by laminated face sheets during low velocity punch-shear.

A third set of low velocity punch-shear experiments showed that PVC and Balsa core sandwich composites absorbed more or less the same energy (Figure 4). TYCOR has glass fiber reinforced webs embedded in the foam core. The punch-shear energy absorption at the intersection of webs was observed to be double that in foam region. Response along web line was an average of that at other two locations. Spatial non-uniformity of the core resulted in larger data scatter, with the average response of TYCOR sandwich similar to that of PVC foam and Balsa wood. Fly ash based Eco-Core sandwiched in between E-glass/vinyl ester face sheets showed approximately 85% more energy absorption than with TYCOR, Balsa wood and PVC foam cores [3].

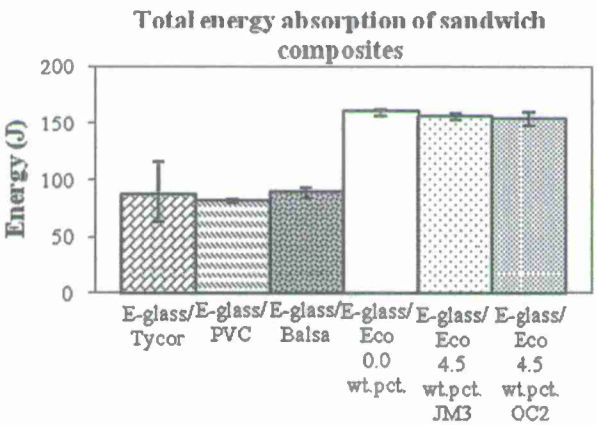


Figure 4. Total energy absorbed by sandwich composites during low velocity punch-shear.

**3. Shock Response of Nanoclay and Graphite Platelet Reinforced Vinyl ester Nanocomposites:** Shock tube tests were conducted at Univeristy of Rhode Island (Dr. Arun Shukla) on nanoclay and graphite platelet reinforced Derakane 411-350 (non-brominated) and 510A-40 (brominated) vinyl ester composite panels of dimensions 254 mm x 101.6 mm x 9.9 mm (10" x 4" x 0.39"). The panels were held under simply supported conditions and subjected to about 120 psi (827.4 kPa) peak pressure. Quasi-static and dynamic approaches were adopted for analyzing the material response to shock loading [4]. Figure 5 shows the energy absorbed up to failure for nanoclay and graphite platelet reinforced non-brominated 411-350 and brominated 510A-40 vinyl ester resin systems at about 120 psi peak pressure shock loading. As can be observed, bromination while significantly improving the shock resistance of pure vinyl ester has a deleterious effect, however, with the addition of nanoclay and graphite platelets.

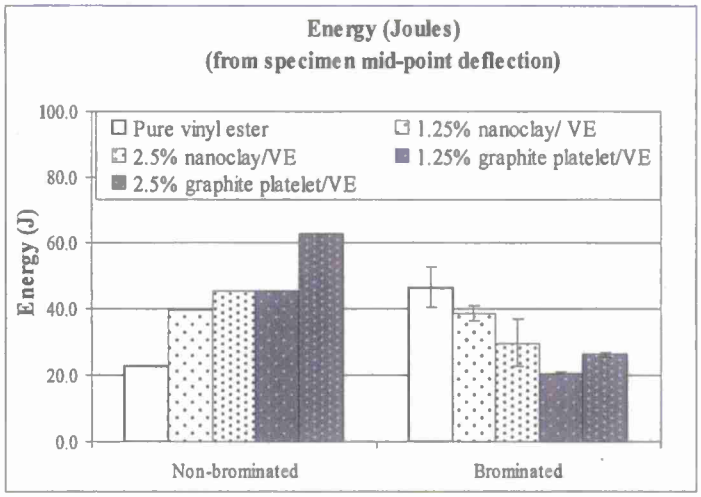


Figure 5. Shock response of the nanoclay and graphite platelet reinforced non-brominated 411-350 and brominated 510A-40 vinyl ester resin systems.

**4. Constitutive Modeling and Computer Simulations:** The objective of this phase of study is to develop computational-based design tools to optimize a wide range of materials for naval applications. For achieving this goal, multi-scale modeling ranging from quantum to continuum, have been adopted [1].

**Analysis of sandwich composite beams subjected to blast loading:** The focus here is to develop computationally-efficient models that can replicate with reasonable accuracy the experimental results of mid-point deflections and failure mechanisms for sandwich composite beams subjected to air blast loading.

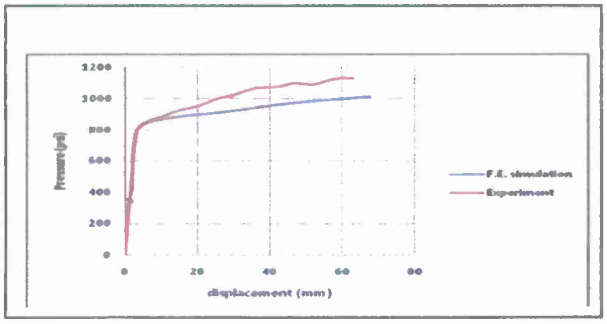


Figure 6: Mid-point deflection of sandwich composite beam with balsa core.

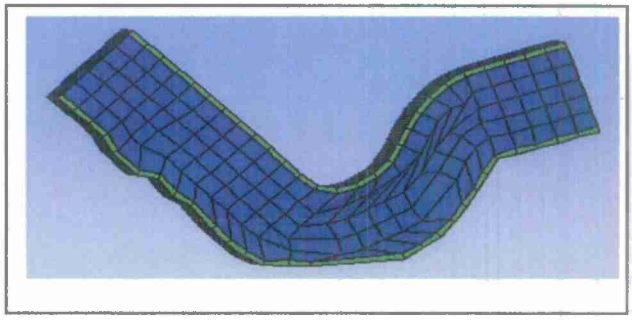

Figure 7: Side view of the deformed sandwich composite beam with balsa core.

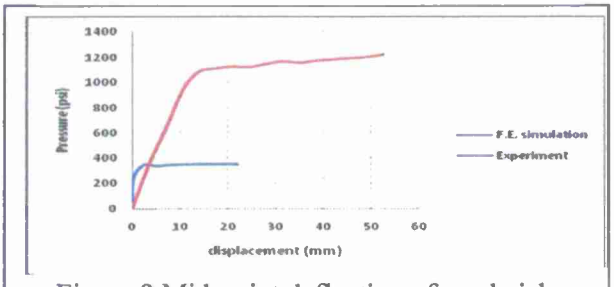


Figure 8:Mid-point deflection of sandwich composite beam with PVC core.

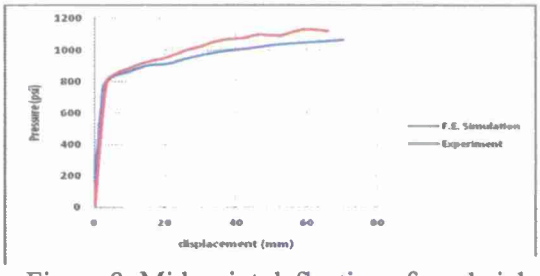


Figure 9: Mid-point deflection of sandwich composite beam with TYCOR core

ANSYS AUTODYN, an explicit hydrocode that uses finite difference, finite volume, and finite element techniques to solve a wide variety of non-linear dynamic problems in solids, fluids, gases, and their interactions, was used to model and analyze the sandwich composite beams under blast loading. Three types of sandwich composites were investigated in this research. Each sandwich composite was made of two faces and one core. The faces were made of E-glass woven fibers with vinyl ester matrix and the core was made of three different materials: TYCOR, Balsa and PVC. All specimens have the same 12" long and 4" wide dimensions, and similar b.c. as used in the shock tube experiments. Each case was loaded with the same pressure time-history obtained from shock tube experiments. AUTODYN analysis shows good agreement of midpoint-deflection (Figure 6) with the experimental shock response data, especially in the elastic range, for sandwich composite beam made with balsa core material. AUTODYN output of the deformed shape with balsa core is shown in Figure 7.

On the other hand, a large difference between experimental and numerical results was obtained in the case of PVC core material (Figure 8). This can be attributed to using incorrect equation of state, strength or failure models; and due to uncertainty of used material properties. These factors are currently under investigation. Figure 9 shows the mid-point deflection for sandwich composite beam with TYCOR core material. Good agreement between experimental and numerical results is achieved in the first part of the curve. After that more deflection is noticed numerically at the same applied pressure. Ongoing research work includes: modeling other core materials, obtaining iso-damage curves for range of pressure and impulse values, and developing computational-based design charts.

**Spall Crack Simulation Using Hybrid Lattice Particle Modeling (HLPM):** Spall crack occurs inside material body when a plate of material flyer impacts onto another plate at high speeds. Failure arises at the interaction of tension and compression waves. It is a highly dynamic problem with fragmentation, and offers a challenge to numerical models. Hybrid lattice particle modeling (HLPM) has been developed and adopted for this study. The HLPM combines the strengths of conventional lattice theory and an originally developed particle modeling (PM) technique. HLPM employs the interaction potentials of either linear (quadratic) or nonlinear (Lennard-Jones or polynomial) type with the axial/angular spring linkage in a regular or irregular lattice system. The defined spring constants are then mapped into the adopted lattice system, which are in turn matched with the material's continuum-level elastic moduli, strength and Poisson's ratio [6-9].

**High performance scalable computing and simulations:** A literature search is being performed to identify constitutive/damage theories suitable for describing the dynamic response of cellular, foam and nanoparticle based lightweight materials. Most models and theories are based on the quasi-static loading response of advanced composites and strain rate effects on strength and damage evolution are not addressed. Our efforts are focused on development of new models or the modification of existing models to accurately capture strain rate effects on deformation and failure processes. The latest version of the DoD parallel Lagrangian code - EPIC has been officially acquired from Army and installed on University of Mississippi computer platform. For baseline computations, an existing mechanics based strength model will be implemented into the EPIC code to simulate blast experiments on composite panels for Navy applications. A PhD student (female American citizen) has been specifically recruited to accomplish this task.

Other ongoing research by University of Mississippi investigators include: effects of geometric and simulation parameters on the elastic moduli of multi-walled carbon nanotubes using molecular dynamics approach [10]; a first-principles estimation of the shock response of nanoreinforced composite materials [11]; creep and stress relaxation modeling [12] and the effects of bromination on viscoelastic response [13] of nanoclay and graphite platelet reinforced vinyl ester; determination of power law attenuation coefficients [14] and the electromagnetic characteristics [15, 16] of carbon nanotubes.

**5. Shock Tube Pressure Tests:** (Dr. Dahsin Liu, Michigan State University)

Smaller beam specimens cut from the larger sandwich composite panels were subjected to high-pressure shock tube testing in a simply- supported condition. The specimens were trimmed to 12" long and 4" wide. During the shock testing, each specimen was simply-supported with 8.5"span. Three types of sandwich composites were investigated. Each simply-supported specimen was loaded with a pressure wave at the center of its 8.5" span. The pressure wave had a diameter of 3.15" and maximum pressure around 1.35 ksi. Besides pressure, the deformation history of composite specimens was also important to determine their resistance and energy absorption characteristics. A high-speed movie camera was used to record the images of specimen deformation along with an innovative finger sensor technique for acquiring quantitative measurements. The high-speed movie camera (4k frames/second) at an oblique angle from the specimen surface could measure the deformation and damage processes of composite specimens up to some extent.

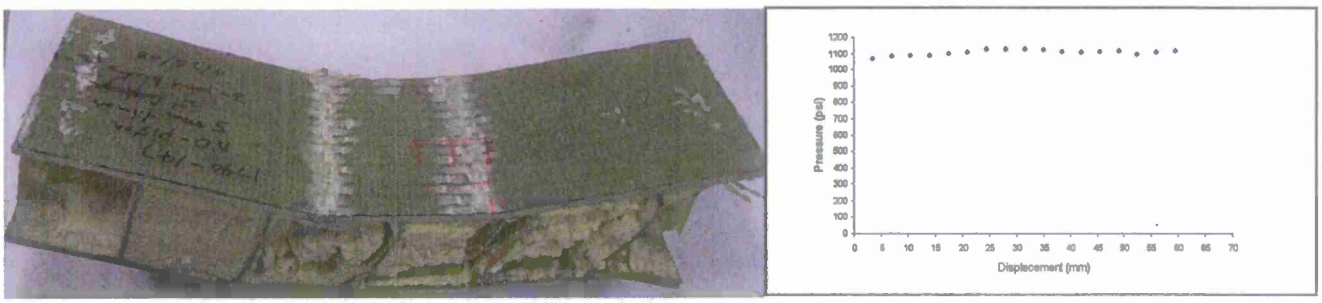


(a) E-glass / TYCOR sandwich composite beam specimen.

(b) E-glass / balsa sandwich composite beam specimen

(c) E-glass / PVC sandwich composite beam specimen

Figure 10. Photographs of (a) TYCOR, (b) balsa, and (c) PVC core sandwich composite beams after shock loading along with their pressure-displacement histories obtained from finger sensors

The 16-pin finger sensor installed behind the back side of each specimen could measure the specimen deformation when the fingers contacted the specimens. Figure 10 shows photographs of the TYCOR, balsa, and PVC core sandwich composite beams after shock loading along with their pressure-displacement histories obtained from finger sensors. Representative energy absorption for each sandwich composite beam, within the

0.5" circumference enclosed by finger sensors, was approximated by integrating the area under these curves. They are about 49 J for Tycor, 44 J for Balsa and 46 J for the PVC foam (up to 52 mm displacement). The energy absorption is highest for TYCOR due likely to its rigidity from the reinforcing webs. Both TYCOR and balsa appeared to have more internal damage compared to the PVC.

## 6. Optimizing TYCOR® Panel Design for Improved Blast Resistance:

(Dr. Rob Banerjee and Dr. Elias Tobia, WebCore Technologies)

The improvement of dynamic resistance and energy dissipation of sandwich structures using TYCOR as an engineered core is one of the goals of this naval research program. This phase, targets the experimental performance of using TYCOR core to design a lightweight and volumetrically-efficient composite structure with multifunctional structural load carrying and mitigation capability to absorb and dissipate the high energy impact induced by blast impulses. The effect of structural core layout is being assessed and studied. A series of physical and mechanical tests were performed and evaluated. The Table in Figure 11 shows strength benchmark data of TYCOR sandwich composite panel that was blast tested at ERDC with the top/bottom fixed and other two sides free b.c (see Figure 1).

| Core Strength Properties | TYCOR 158C1 | Test Method |
|---|---|---|
| $C_z$ (psi) Compression strength | 999 | ASTM-C 365 |
| $E_z$ (psi) Modulus | 70459 | |
| $T_z$ (psi) Tension strength | 365 | ASTM-C 297 |
| $E_z$ (psi) Modulus | 8811 | |
| $S_{LZ}$ (psi) Shear strength | 525 | ASTM-C 273 |
| $G_{LZ}$ (psi) Shear modulus | 25295 | |
| $S_{TZ}$ (psi) Shear strength | 435 | ASTM-C 273 |
| $G_{TZ}$ (psi) Shear modulus | 24750 | |

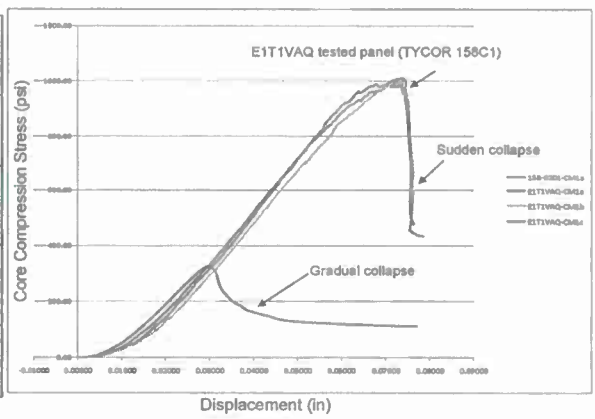


Figure 11: Core compression test of ductile vs. brittle TYCOR panel

The next generation blast-resistant panel will use WebCore's innovative 3-D design architecture and stitching technology with advanced materials including energy-absorbing viscoelastic foams. Figure 11 also shows the effect of highly ductile panel with a light weight unidirectional design controlling the collapse mode. The next candidate panel will have continuous unidirectional webs along the main span with transverse stitching. The unidirectional webs resist the plastic deformation in the core at the initial stage of loading, while the transverse stitching offers high compressibility characteristics intended to mitigate the remaining high dynamic loads. This core crushing capability will play an efficient role to maintain a larger face sheet separation at a certain stage under blast, and therefore, a higher bend resistance. This behavior can be achieved by refining the web weight, while using a highly ductile foam (such as ZOTEK foam) to engage the face sheet stretching contribution for energy absorption.

## 7. NDE, Mechanical Property Characterization, and Burn-through Fire Tests of Eco-Core:

(Dr. Uday Vaidya and Dr. Selvum Pillay, University of Alabama - Birmingham)

UAB supported the University of Mississippi under a sub-contract effort in 2008-2009 Year II period. During Year 1, various panels suggested by Ole Miss have been fabricated via VARTM and delivered as needed. This progress briefing summarizes three sub-tasks; (a) NDE tap tests of blast panels; (b) Mechanical property characterization of laminate face sheets; and (c) Burn-through fire testing of Eco-Core sandwich panels.

**Nondestructive tap testing to assess blast damage:** Laminated face sheets and sandwich composite panels with E-glass vinyl ester and nanographene platelets, Owens Corning HPG glass, T700 FOE treated carbon face sheets have been evaluated by tap testing non-destructive evaluation (NDE). The blast exposed and corresponding control panels have been evaluated. After a thorough study of the panels it was determined that there are obvious effects of blast loading. The pulse width was almost constant across the panel for the control panels. The blast panel readings show increase in pulse width indicative of through thickness damage. The pulse width increased by 6.76% for E-glass/VE with nanographene panel, 1.26% for the HPG/VE, 6.2% for the T700 carbon/VE laminated facesheets. For the E-glass/VE sandwich panels there was 32.8% on blast side, and 28.7% from opposite to blast side. These studies provide a means of quantifying blast damage in various panels non-destructively. The higher values of blast tested sandwich panels are more related to the interface damage between face sheets and core, which was extensive under blast.

**Mechanical Property Characterization Studies:** The face sheet constituents namely E-glass/VE, E-glass/VE with nanographene platelets, Owens Cornong HPG-glass/VE and T700 carbon/VE were characterized to generate the mechanical properties for these materials. These data sets will be used as input by Ole Miss in their modeling studies. Standard ASTM tests were adopted in generating the tensile and inter-laminar shear data on these materials. Shear, tension and Poisson's ratio tests were conducted on E-Glass (GVE), HPG glass (GHVE), and FOE Carbon (CVE). 5 layers were infused with vinyl ester (VE) resin. The average thickness was 2.70 mm for carbon CVE, 2.73 mm for GHVE, and 3.30 mm for GVE. The nanographene treated samples were not tested because of the inadequate filament level wet-out. The processing issues are being addressed to increase the filament level wet-out of the nanographene VE specimens. The E-glass/VE and Carbon/VE had comparable response in shear. HPG glass is very compliant in the shear mode with high elongation characteristics; hence it performs well in impact. The tension data indicates that HPG has significantly higher strength than E-glass, with tensile modulus comparable to E-glass. The T700 FOE treated carbon performed as expected - highest strength and modulus in tension.

**Burn-Through Fire Testing of Eco-Core Sandwich Panels:** Burn-through fire tests were conducted on 12" x 12" x 2.25" thick sandwich panels with E-glass/vinyl ester face skins bonded to the NC AT Eco-Core, both without and with some JM3 and OC2 chopped glass fiber reinforcement mixed in the fly ash based core with phenolic resin. Experimental conditions were set based on the David Taylor Research Center [DTRC] Burn-Through Test, MIL-STD-2031(Navy adopted standard). It was observed that the maximum back face temperature for Eco-Core specimens without chopped glass fiber reinforcement reached about 73 °C, where as for those with chopped glass fibers it was between 68 °C to 77 °C. No significant mass loss, damage, discoloration or delamination on back faces was observed.

**8. Nanoreinforcement Modification of Composites:** (Dr. Larry Drzal, Michigan State University)

The goal here is to develop a fundamental understanding of the interaction of graphite nanoplatelets with macro reinforcing fibers and polymer matrices, and how these interactions affect the mechanical properties and durability (fire, blast and environmental) of nanoparticle modified polymer composites. The objectives of this project are:

i. To quantify the effect of nanoparticle concentration and dispersion (a) around and between individual reinforcing fibers (intralaminar), and (b) between lamina in both unidirectional and woven fiber lamina (interlaminar).
ii. To optimize the improvement in mechanical properties and durability of a carbon fiber (or glass fiber) vinyl ester, nylon and polyurea matrix composite systems utilizing the addition of clay or exfoliated graphite nanoplatelets.

Nanoparticles including nanoclay and nanographite reinforced bromated vinyl ester nanocomposite plates were synthesized using an in-situ polymerization method. Nanographite reinforced flexible epoxy

nanocomposites plates were synthesized by dispersion in epoxy and polymerized. Nanographite reinforced epoxy nanocomposite coatings and nanographite reinforced polyurea/polyurethane nanocomposite coatings were applied to the surface of building blocks with different amount of nanographite in the coating. Samples were supplied to Ole Miss for further physical property tests and structural characterization.

The mechanical, thermal and electrical properties of nanographite reinforced flexible epoxy nanocomposites plates were measured (Figure 12). It was found that nanographite increased the tensile modulus of the reinforced epoxy nanocomposite, while the tensile strength of nanocomposites remained about the same as the base resin. Elongation of nanographite reinforced flexible epoxy and the impact strength decreased with increasing content of nanographite. Thermal conductivity of nanographite reinforced soft epoxy nanocomposite increased with increasing content. The percolation threshold of nanographite reinforced flexible epoxy around 4 wt%. At a concentration of about 6 wt.% nanographite, the reinforced flexible epoxy nanocomposite samples were semiconductive.

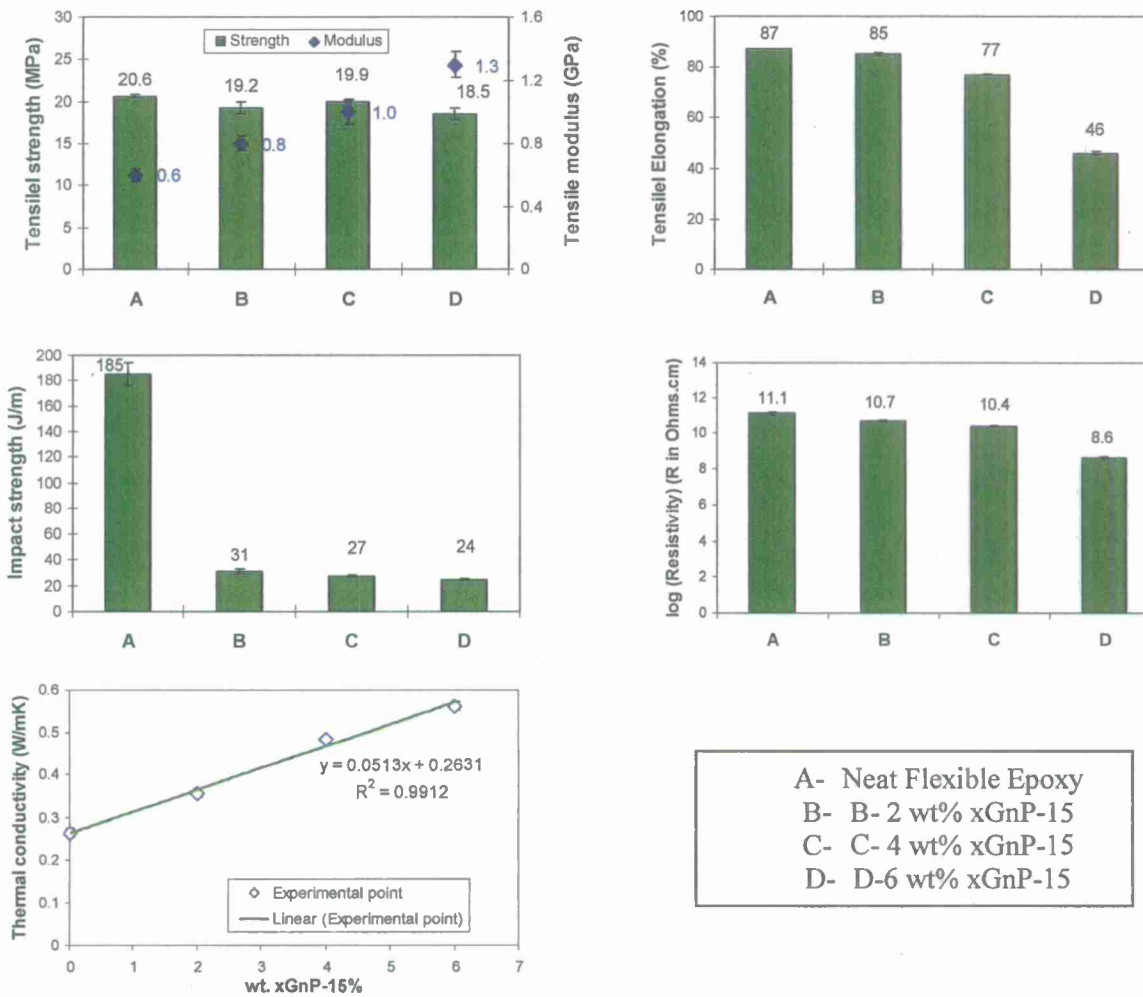


Figure 12. Physical Properties of Nanographite Reinforced Flexible Epoxy Nanocomposites. A- Neat Flexible Epoxy. B- 2 wt% xGnP-15. C- 4 wt% xGnP-15. D-6 wt% xGnP-15

Maleic anhydride (MA) was used to modify the surface of the nanographite by either coating or grafting (-g-), which was then used to fabricate brominated vinyl ester nanocomposites (Figure 13). It was found that the flexural modulus and flexural strength of the MA modified nanographite reinforced bromated vinyl ester nanocomposites did not change compared to the regular nanographite reinforced vinyl ester nanocomposite. However, the electrical conductivity decreased as a result of adding the MA modified nanographite as filler in the brominated vinyl ester nanocomposites system. This indicates that the maleic anhydride acts as a blocking agent preventing the nanographite particles from forming a conductive network and thereby reducing the electrical conductivity.

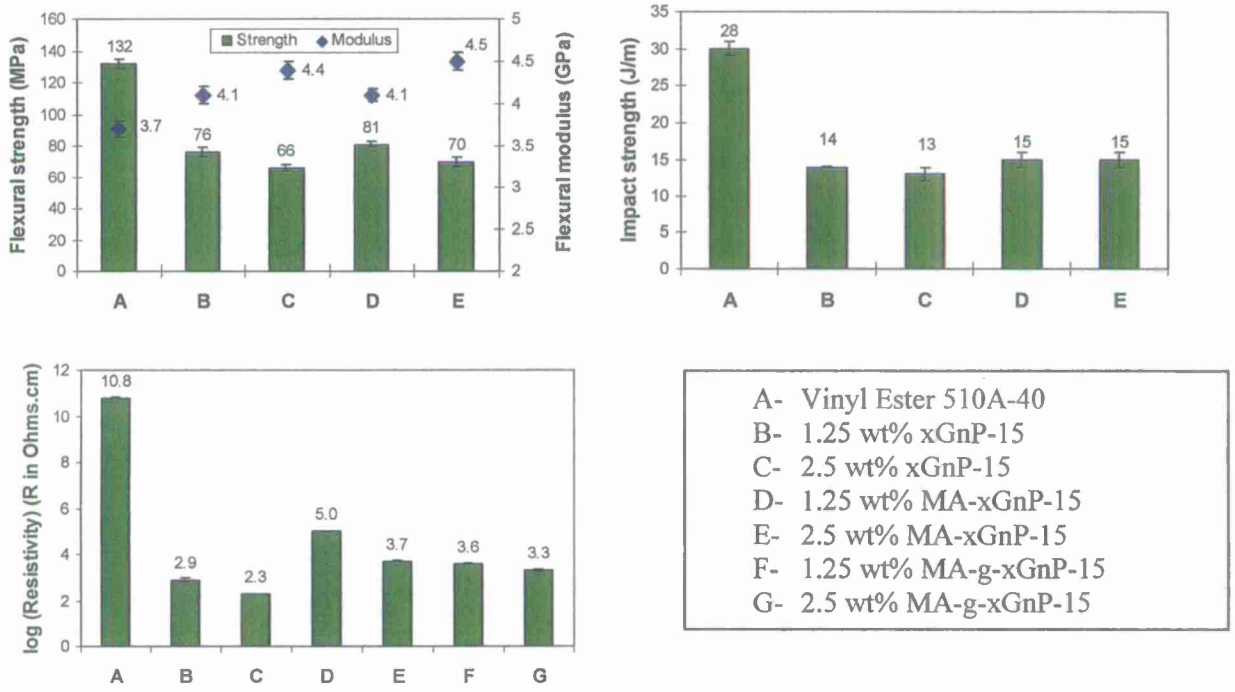


Figure 13. Physical Properties of Nanographite Reinforced Brominated Vinyl Ester Nanocomposites. A- Neat 510-40A Brominated Vinyl Ester. B- 1.25 wt% xGnP-15. C- 2.5 wt% xGnP-15. D-1.25 wt% MA-xGnP 15. E-2.5 wt% MA-xGnP-15. F-1.25 wt% MA-g-xGnP-15. G-2.5 wt% MA-g-xGnP-15

## TRANSITIONS

These research investigations have been leveraged with a concurrent grant: Nano-Particle Reinforced Composites for Critical Infrastructure Protection, from the Department of Homeland Security - Southeast Region Research Initiative (DHS-SERRI). Northrop Grumman Ship Building (NGSB) Advanced Capabilities Group is facilitating this research effort on development of advanced ship panel concepts. WebCore Technologies Inc., a small-scale industry in Dayton, OH is working closely with University of Mississippi to develop affordable and durable TYCOR® composite sandwich panels for navy ship structural applications. TYCOR® is currently being used in several military and commercial applications including refrigerated cargo floor for Navy cargo ships, Air Force tactical shelters, Air Force runway matting, vehicular bridge decks, railcar floors and wind turbine blades.

## NAVY RELEVANCE

Producing stronger, safer and more cost-effective platforms for the new generation naval ships requires innovative designs, new materials, and affordable/efficient processing and characterization technologies. This research will advance the development of blast, shock and impact resistant composites for navy ship structural applications; to achieve better mobility, survivability, stealth, safety, and at lower cost.

## ACKNOWLEDGEMENT

This research was funded by ONR Grant # 00014-07-1-1010, Office of Naval Research, Solid Mechanics Program (Dr. Yapa D.S. Rajapakse, Program Manager). Partial funding received under a subcontract from the Department of Homeland Security sponsored Southeast Region Research Initiative (SERRI) at the Department of Energy's Oak Ridge National Laboratory, is also acknowledged. We would like to thank Dr. Arun Shukla, University of Rhode Island for performing the shock tube tests on nanoclay and graphite platelet reinforced vinyl ester specimens.

## PUBLICATIONS (ONR-supported):

1) P. Raju Mantena, Alex Cheng and Ahmed Al-Ostaz "Blast and Impact Resistant Composite Structures for Navy Ships" *Proceedings of the 2008 ONR Solid Mechanics Program - Marine Composites and Sandwich Structures*, University of Maryland, Adelphi, MD, Sep 17-19, 2009, pp. 417-426.

2) P. Raju Mantena, Ahmed Al-Ostaz and Alexander H. D. Cheng "Dynamic Response and Simulations of Nanoparticle-Enhanced Composites" *Composites Science and Technology 69 (2009) 772-779.*

3) Pramanik B., Mantena P.R. "Punch-shear Characteristics of Nanoclay and Graphite Platelet Reinforced Vinyl Ester Plates, Laminated face sheets and Sandwich Composites under Low-Velocity Impact" *ASME - Early Career Technical Journal 2009* (in press)

4) Gupta S., Mantena P.R., Al-Ostaz A., Mullen C. "Shock Response and Finite Element Modeling of Nanoclay and Graphite Platelet Reinforced Vinyl Ester Nanocomposites" *ASME - Early Career Technical Journal 2009* (in press)

5) Swasti Gupta, P. Raju Mantena and Ahmed Al-Ostaz, "Dynamic Mechanical and Impact Property Correlation of Nanoclay and Graphite Platelet Reinforced Vinyl Ester Nanocomposites" *Journal of Reinforced Plastics and Composites* (in press).

6) G. Wang, A. Al-Ostaz, A.H.-D. Cheng and P.R. Mantena "Hybrid lattice particle modeling: Theoretical considerations for a 2D elastic spring network for dynamic fracture simulations," *Computational Materials Science* 44 (2009) 1126–1134.

7) G. Wang, A. Al-Ostaz, A. H.-D. Cheng, and P.R. Mantena, "A Macroscopic-Level Hybrid Lattice Particle Modeling of Mode-I Crack Propagation in inelastic materials with varying ductility" *International Journal of Solids and Structures* (revised).

8) Wang G, Al-Ostaz, Cheng, Mantena. P.R. "Hybrid Lattice Particle Modeling of Wave Propagation Induced Fracture of Solids" *Computer Methods in Applied Mechanics and Engineering* (under review)

9) G. Wang, A. Al-Ostaz, A.H.-D. Cheng, and P. Raju Mantena "Particle Modeling of Dynamic Fracture Simulations of a 2D Polymeric Material (nylon 6,6) Subject to the Impact of a Rigid Indenter" *Computational Materials Science* 44 (2008) 449–463.

10) Hunain Al-Khateb, Ahmed Al-Ostaz, Raju Mantena and Alex Cheng "Geometric and Simulation Parameter Effects on Elastic Moduli of Multi-Walled Carbon Nanotubes Using Molecular Dynamics Approach" *Journal of Materials Science* (revised).

11) Weiping Xu and Elizabeth Ervin "First Principles Estimation of the Shock Response of Nanoreinforced Composite Materials" *Journal of Structural Health Monitoring* (under review)

12) Ahmad Almagableh, P. Raju Mantena, and Ahmed Al-Ostaz, "Creep and Stress Relaxation Modeling of Nanoclay and Graphite Platelet Reinforced Vinyl ester Nanocomposites," *Journal of Applied Polymer Science* (accepted).

13) Ahmad Almagableh, P. Raju Mantena, and Ahmed Al-Ostaz, "Effect of Bromination on the Viscoelastic Response of Vinyl ester Nanocomposites," *eXPRESS Polymer Letters* (revised).
14) Mobley J., Mack R.A., Gladden J.R. and Mantena, P.R. "Determination of Power Law Attenuation Coefficient and Dispersion Spectra in Multi-wall Carbon Nanotube Composites Using Kramers-Kronig Relations" *Journal of Acoustical Society America* 126 (1), pp. 92-97, July 2009.
15) S.M. Mikki and A.A. Kishk "A Symmetry-Based Formalism for the Electrodynamics of Nanotubes" *Progress in Electromagnetics Research, PIER 86*, 111-134, 2008.
16) S.M. Mikki and A.A. Kishk "Derivation of the Carbon Nanotube Susceptibility Tensor Using Lattice Dynamics Formalism" *Progress in Electromagnetics Research B*, vol. 9, 1-26, 2008

## BLAST AND IMPACT RESISTANT COMPOSITE STRUCTURES FOR NAVY SHIPS

**P. Raju Mantena, A.M. Rajendran and Ahmed Al-Ostaz**
Composite Structures and Nano-Engineering Research
The University of Mississippi

**OBJECTIVE:** Develop stronger, safer and more cost-effective structures for the new generation naval ships; especially nanoparticle reinforced glass/carbon polymeric based composites and structural foams for blast, shock and impact mitigation.

**TECHNICAL APPROACH:** Focus of research is on marine composite structures; particularly lightweight glass/carbon polymeric based composites and innovative concepts for the mitigation of blast, shock and impact effects. Sandwich composites with balsa and foam cores are presently being featured in number of navy applications such as in surface ship deck structures, radar mast and boat hulls. In our work, other new and emerging cores including TYCOR® (an engineered three-dimensional fiber reinforced damage tolerant core) and the fire resistant fly ash based Eco-Core® are also being explored in sandwich constructions. Technical approach includes researching low-cost fire resistant nanoclay and exfoliated graphite platelet reinforced glass and carbon polymeric based composites with fly ash and 3-D fiber reinforced foams; investigating their response to low-velocity impact, ballistic, shock and blast loads; dynamic mechanical analysis for modulus, damping, creep and stress relaxation; developing constitutive models and computer simulations; accelerated testing for long-term durability; and evaluating their radar-absorbing and EM-shielding characteristics for improved stealth and safety.

### SUMMARY OF RECENT ACCOMPLISHMENTS

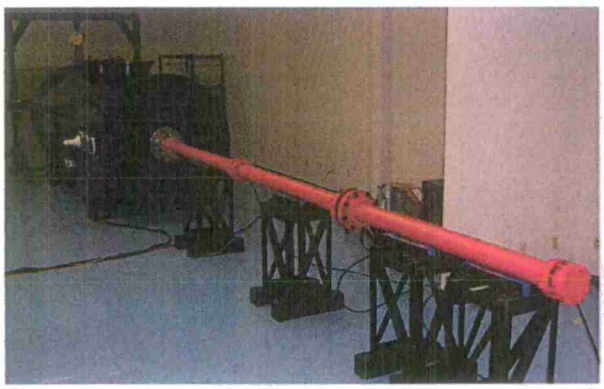

Shock Tube Apparatus

Split-Hopkinson (tension and compression) Pressure Bars

- Shock Tube and Split-Hopkinson Pressure Bar (tension and compression) test facilities have been commissioned at the University of Mississippi, for the high-strain rate evaluation of nano-reinforced panels and sandwich composites.
- Researched new and emerging cores including low cost fire resistant fly ash based Eco-Core® and TYCOR® (an engineered three-dimensional fiber reinforced damage tolerant core); woven carbon and high-elongation HPG glass face skins in sandwich constructions.

- Glass and Carbon sandwich composite panels with balsa, PVC foam and TYCOR® cores fabricated as per Northrop Grumman Ship Building design specs were subjected to blast loads simulating approximate threat levels of ~ 2000 lbs of TNT, at the ERDC-Blast Load Simulator (BLS) facility.
- Effects of bromination (for improved fire resistance) on the viscoelastic response of vinyl ester nanocomposites characterized and creep / stress relaxation.
- Low velocity punch-shear and high-strain rate characteristics of nanoclay and graphite platelet reinforced vinyl ester panels.
- Shock tube analysis of sandwich composites, and Eco-Core panel as sacrificial protection explored.
- Modeling and high-performance scalable computing for simulating the response of composite panels subjected to high energy blast loads.

## TECHNICAL DETAILS

**1. Introduction:** Several 4' x 4' x 2.25" thick sandwich composite panels made up of 0.125" thick E-glass, T700 FOE treated woven carbon and Owens Corning HPG glass face skins with 2" thick TYCOR, PVC foam and balsa cores were designed (as per Northrop Grumman Ship Building specs) and fabricated with Dow 510A-40 brominated vinyl ester resin by the VARTM process (more details in Section 8). Some of the large size panels were subjected to blast load waveforms and peak reflected pressures simulating terrorist threats at the ERDC - Blast Load Simulator (BLS) facility in Vicksburg, MS. Smaller samples were also analyzed in shock tube, ballistic and low-velocity impact tests. Results of previous investigations along with molecular dynamics modeling and computer simulations are given in References 1-3. Year II research efforts on the design, fabrication and blast loading of large sandwich composite panels; low velocity punch-shear and high-strain rate characteristics of nanoclay and graphite platelet reinforced vinyl ester; shock tube testing for design optimization; Eco-Core as sacrificial panel for blast mitigation; constitutive modeling and computer simulations are described in the following sections:

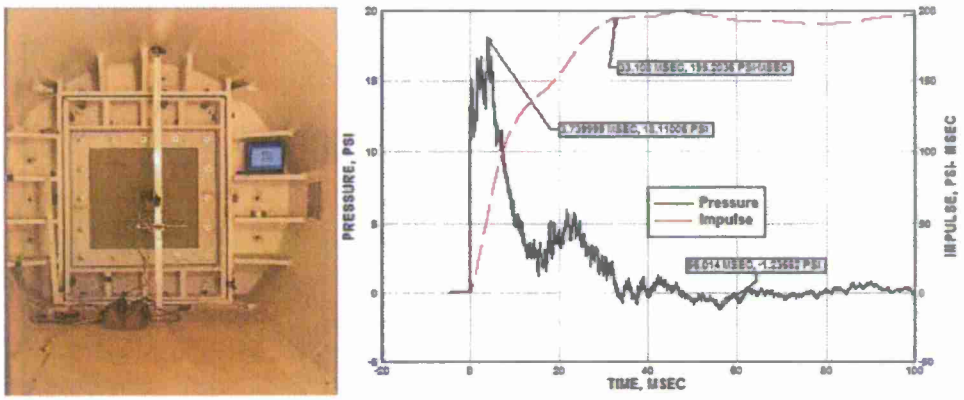


Figure 1. Sandwich composite panel bolted at top/bottom and two-sides free undergoing blast test of 16-18 psi peak pressure and 200 psi-ms impulse (equivalent to 2000 lbs of TNT at 140 feet).

**2. Blast Loading**: Trial blast tests, simulating an approximate threat level of about 27,000 lbs TNT at 184 feet, were conducted previously at the ERDC-Blast Load Simulator (BLS) facility in Vicksburg, MS. One 4' x 4' E-glass/TYCOR sandwich panel, with all-sides bolted and subjected to about 80 psi peak pressure and 1000 psi-ms impulse, was not breached and there were no visible signs of damage [2]. Another 4' x 3' E-glass/TYCOR sandwich composite panel, bolted at top/bottom and two sides free, was subjected to 70 psi peak pressure and

900 psi-ms impulse loading. This panel offered significant resistance to the blast load with permanent deformation and localized shear pullout damage at the bolt regions [3]. This year, six large 4' x 4' x 2.25" thick panels with Balsa, PVC, TYCOR foam cores and E-glass and T700 FOE treated carbon face sheets were subjected to blast load waveforms of 16-18 psi peak pressures and 200 psi-ms impulse (Figure 1), which represents an approximate threat level of 2000 lbs of TNT at 140 feet. The blast tested panels underwent 0.5 to 1.5 inches of mid-point deflection, with no visible signs of external damage. The blast response data is currently being analyzed.

**3. Punch-shear Characteristics of Nanoparticle Reinforced Vinyl ester Plates:** Low velocity (3 m/s) punch-shear response of nanoparticle reinforced vinyl ester plates, laminated face sheets, and sandwich composites were analyzed on 4"× 4" square plate specimens [4] with all around fixed circular boundary condition and impacted by a hemispherical-head plunger with added mass (ASTM D3763). Impact load, displacement and absorbed energy (Figure 2) along with visual inspection of post-damage specimens depicted the punch-shear failure characteristics (Figure 3) of these nanoclay and graphite platelet reinforced vinyl ester panels.

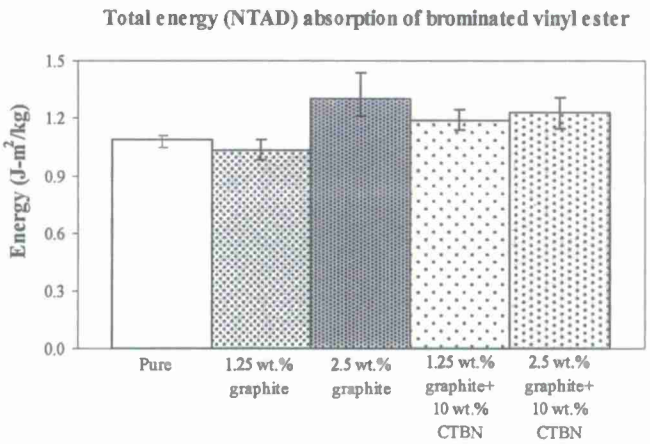


Figure 2. Total energy absorbed by vinyl ester nanocomposites under low velocity punch-shear.

Nanoparticle reinforced vinyl ester panels showed about 10% improvement in impact energy absorption with the addition of 2.5 wt% graphite platelets to brominated vinyl ester. Addition of 10 wt% CTBN (carboxy terminated butadiene nitrile rubber, see Section 9 for more details) to the 1.25 wt% graphite showed an improvement in punch-shear energy absorption, but was not useful in case of the 2.5 wt% graphite brominated vinyl ester.

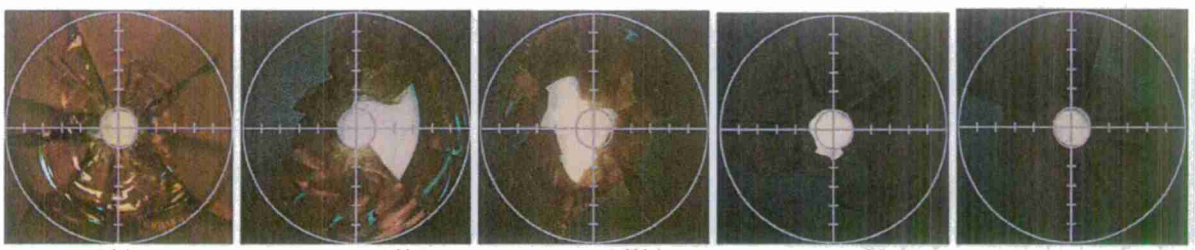


Figure 3. Back face fracture surfaces of nanoparticle reinforced brominated 510A-40 vinyl ester composite panels after drop weight punch-shear testing (i) brominated vinyl ester, (ii) 1.25 wt% nanoclay, (iii) 2.5 wt% nanoclay, (iv) 1.25 wt% graphite, and (v) 2.5 wt% graphite.

**4. Constitutive Modeling and Computer Simulations:** The objective of this phase of study is to develop computational-based design tools to optimize a wide range of materials for naval applications.

**Analysis of sandwich composite beams subjected to shock loading:** Focus here is to develop computationally-efficient models that can replicate with reasonable accuracy the experimental results of mid-point deflections and failure mechanisms for sandwich composite beams subjected to shock loading. ANSYS AUTODYN, an explicit hydrocode that uses finite difference, finite volume, and finite element techniques to solve a wide variety of non-linear dynamic problems in solids, fluids, gases, and their interactions, was used to model and analyze the sandwich composite beams under shock loading. Three types of sandwich composites were investigated. Each sandwich composite was made of two faces and one core. The faces were made of E-glass woven fibers with vinyl ester matrix and the core was made of three different materials: TYCOR, Balsa and PVC. All specimens have the same 12" long and 4" wide dimensions, similar b.c. and loaded with the same pressure time-history obtained from shock tube experiments. A large difference between experimental and numerical results was obtained initially in the case of PVC core material, which was attributed to using incorrect equation of state, strength or failure models and due to uncertainty of used material properties [3]. These factors have been resolved and AUTODYN analysis showed good agreement of the midpoint-deflection with experimental shock response data, as shown in Figure 4.

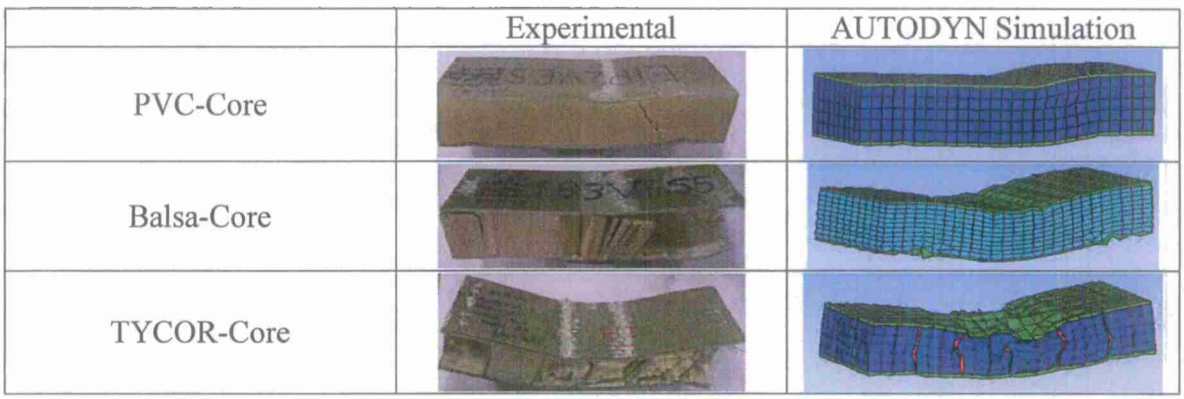


Figure 4. Failure shapes obtained experimentally and numerically for the case of sandwich composite beams under shock loading.

**High performance scalable computing and simulations:** Blast response of a vinyl ester plate was simulated using the DoD Lagrangian code EPIC acquired from the government. In preliminary modeling efforts, a circular plate with a time dependent surface pressure loading conditions was assumed. This assumption allows calculations using a two-dimensional axi-symmetric configuration. EPIC simulations considered a surface pressure-time history applied in a circular region. Results using a library constitutive model for the vinyl ester showed elastic deformation only. Further analysis indicated that the applied pressures were relatively very low when compared with the yield stress of pure vinyl ester. To capture the boundary conditions effect more accurately, EPIC simulations of a 3-D square plate with clamped edges were performed. The effective and volumetric strain levels in the plate were much lower than the failure measured strains in both quasi-static and split Hopkinson bar experiments. Based on these preliminary simulation results, it is speculated that in blast experiments the failure of vinyl ester plate is controlled by fracture mechanics rather than the strain to failure type criterion.

Unfortunately, most design codes employ Johnson-Cook type strength model and "effective plastic strain" based fracture model to describe most materials. Based on our current computational analysis, it is

concluded that a continuum damage mechanics (CDM) based constitutive model with "fracture mechanics" controlled parameters will be necessary to predict the vinyl ester plate failure under blast loading. The current modeling effort now is focused on identifying a CDM model with microcracks controlled failure criterion. An internal state variable based damage model that would explicitly consider a crack density evolution law to describe progressive damage in composite panels under blast loading is being developed.

**Other ongoing research at University of Mississippi:** modeling different core materials and face skins to obtain iso-damage P-I curves for developing computational-based design charts; creep and stress relaxation modeling [5]; effects of bromination on viscoelastic response [6]; finite element simulations of nanoclay and graphite platelet reinforced vinyl ester panels under shock and quasi-static flexural loading [7].

**5. Eco-Core as Sacrificial Panel for Shock Mitigation of Composite Structures:**
(Dr. Kunigal Shivakumar, North Carolina A&T State University)

High strain rate studies have shown that Eco-Core has significant energy absorption capability primarily because of the large amount of crushing strain. Both material porosity and hollowness of cenosphere contributes to this phenomenon. An experimental investigation to understand how an Eco-Core panel protects a composite primary structure under a blast condition was explored.

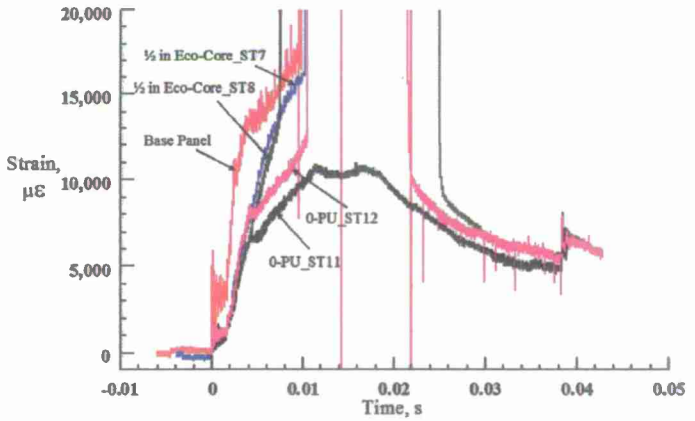


Figure 5. Strain vs. Time response of 1/4" thick $(0/90)_S$ glass/vinyl ester base panel with one-half inch thick Eco-Core and polyurea coated Eco-Core.

Strain and damage response of composite panel with and without Eco-Core bonded on the blast face were compared. Test cases consisted of: base 1/4 in thick FGI 1854 glass/Derakane vinyl ester $(0/90)_s$ panel and base panels faced Eco-Core panel. The Eco-Core panels included in the test study were: 1-in thick, 1/2-in thick, and 1/2-in thick Eco-Core face coated with a thin layer of polyurea. Tests were conducted at about 3,500 psi static chamber pressure at the Michigan State University (Dr. Dahsin Liu) shock tube test facility. Figure 5 shows the strain-time response at back-center of the composite panel for the four test cases considered. Several items to be noted are: peak strain, strain rate rise and strain decay after the peak strain. Peak strain was high for base panel and decreased to a lowest value for a panel with 1/2-in Eco-Core and surface coated with polyurea. Strain rise rate also decreased from base panel case to coated ones. Summary of these results indicate that Eco-Core as a sacrificial panel indeed has shock mitigation property, which is further enhanced by adding a thin polyurea coating. An exhaustive study is needed to further qualify the results and optimize the design.

**6. Shock Tube Pressure Tests:** (Dr. Dahsin Liu, Michigan State University)

Smaller 12" long and 4" wide beam specimens cut from the larger sandwich composite panels were subjected to high-pressure shock tube testing in a simply-supported condition. Six types of sandwich composites were investigated. Each simply-supported specimen was loaded with a 3.5" pressure wave at the center of its 8" span and about 1.2 ksi maximum generated pressure. A unique 20-pin finger sensor installed behind the back side of each specimen measured the out-of-plane deformations when fingers made contact with the center of non-loading surface. Figure 6 shows the failure mechanisms and energy absorption of TYCOR and balsa core sandwich composite beams with E-glass and T700 carbon face sheets after the shock loading, along with pressure-displacement histories obtained from finger sensors. The other sandwich beam configurations are currently undergoing shock tests.

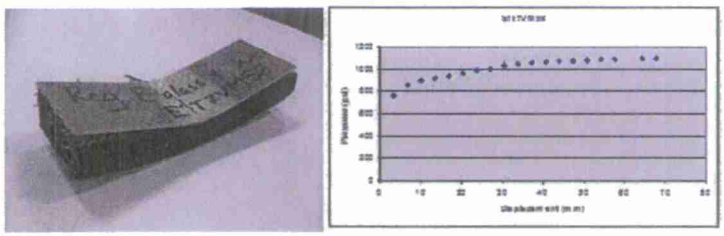

(a) Five ply E-glass / 158C4 stitched TYCOR® sandwich composite beam.

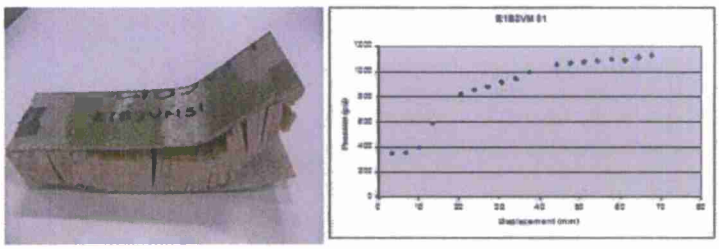

(b) Five ply E-glass / Balsa sandwich composite beam.

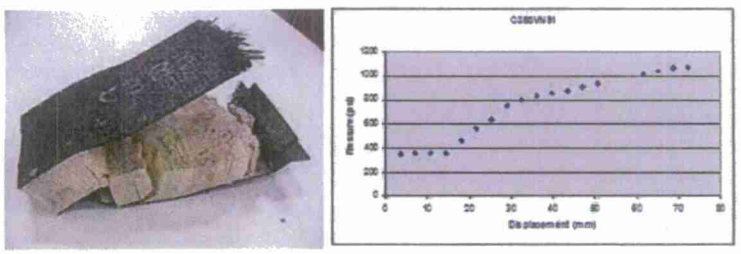

(c) Five Ply T700 Carbon / Balsa sandwich composite beam.

Figure 6. (a) E-glass / 158C4 stitched TYCOR®, (b) E-glass / Balsa, and (c) T700 Carbon / Balsa sandwich composite beams after the shock loading along with pressure-displacement histories.

**7. Optimizing TYCOR® Panel Design for Improved Blast Resistance:**
(Dr. Rob Banerjee and Dr. Elias Toubia, WebCore Technologies)

The improvement of dynamic resistance and energy dissipation of sandwich structures using TYCOR as an engineered core is one of the main goals. This research, targets the experimental performance of using TYCOR Core to design a lightweight and volumetrically-efficient composite structure with multifunctional

structural load carrying and mitigation capability to absorb and dissipate the high energy impact induced by blast impulses.

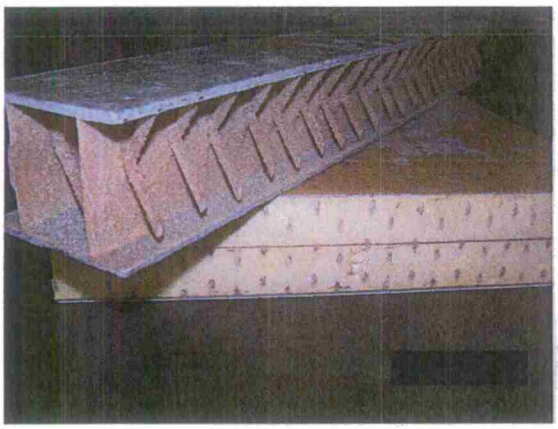

| Core Strength Properties | 158C4 Stitched TYCOR Predicted | 158C4 Unidirectional TYCOR Predicted | 158C1 Grid TYCOR Tested (Vicksburg, 2008) | Test Method |
|---|---|---|---|---|
| $C_z$ (psi) Compression strength | 900 | 560 | 999 | ASTM-C 365 |
| $E_z$ (psi) Modulus | 43000 | 35000 | 70459 | |
| $T_z$ (psi) Tension strength | 314 | 115 | 365 | ASTM-C 297 |
| $E_z$ (psi) Modulus | - | - | 8811 | |
| $S_{LZ}$ (psi) Shear strength | 310 | 310 | 525 | ASTM-C 273 |
| $G_{LZ}$ (psi) Shear modulus | 31000 | 31000 | 25295 | |
| $S_{TZ}$ (psi) Shear strength | 330 | 34 | 435 | ASTM-C 273 |
| $G_{TZ}$ (psi) Shear modulus | 33000 | 400 | 24750 | |

Figure 7. (a) 158C4 stitched TYCOR® core with foam removed to show the web architecture, and (b) core strength properties of the TYCOR® panels designed for blast mitigation.

The blast-resistant panels manufactured under this phase use WebCore's innovative 3-D design architecture and stitching technology with advanced materials including energy-absorbing foams. Figure 7 shows the stitching patterns of a light weight unidirectional design. This panel has continuous unidirectional webs along the main span with transverse stitching. The unidirectional webs resist the plastic deformation in the core at the initial stage of loading, while the transverse stitching offers high compressibility characteristics intended to mitigate the remaining high dynamic loads. Table also shows the predicted and tested core strength for all versions of manufactured panels.

**8. Fabrication of large size sandwich composite panels by VARTM:**
(Dr. Uday Vaidya and Dr. Selvum Pillay, University of Alabama - Birmingham)

Overall objectives of UAB in this phase was to fabricate large (4' x 4' and/or 8' x 4') scale navy relevant sandwich composites with balsa, PVC foam, stitched polyurethane with glass and carbon / vinyl ester facesheets for blast, shock, ballistic and impact characterization.

Technical approach implemented the Vacuum Assisted Resin Transfer Molding (VARTM) process with sequential co-infusion to fabricate large 4' x 4' or 4' x 8' laminated and sandwich panels. The fabrication work was undertaken in two stages: first, UAB procured materials and fabricated a set of sandwich panels. Following discussions with John Sullivan at Northrop Grumman Ship Building (NGSB), it was decided to use the kits supplied by NGSB for maintaining the same material as the navy is presently using. Kits were received from NGSB that included the core materials, the carbon and glass fabrics and supplies needed for fabricating these panels. A total of 6 variants (two 4' x 4' for each variant) were processed with varying face sheet material, core, and stacking sequence. Table 1 lists all the variants and constituent materials with details on phase sheet stacking sequence. Innovative aspects of this work include the cost-effective production of large sandwich panels for ship deck type structures. The work on carbon fiber sandwiches is entirely new and of high interest to the Navy. Physical phenomena of the synergistic role of new materials and material combinations will help create efficient and durable structures for the navy.

Table 1: Sandwich composite panels with varying core/face sheet materials fabricated by VARTM.

| | Face Sheet Material | Core | Number of Layers | Face sheet Stacking Sequence |
|---|---|---|---|---|
| 1 | E-Glass | WebCore | 5 | [0/90]/45/[0/90]/45/[0/90] |
| 2 | E-Glass | Balsa | 5 | [0/90]/45/[0/90]/45/[0/90] |
| 3 | Owens Corning HP Glass | Balsa | 5 | [0/90]/45/[0/90]/45/[0/90] |
| 4 | Carbon | Balsa | 5 | [0/90]/45/[0/90]/45/[0/90] |
| 5 | Carbon | Balsa | 8 | [0/90]/45/[0/90]/45/45/[0/90]/45/[0/90] |
| 6 | Carbon | PVC Foam | 8 | [0/90]/45/[0/90]/45/45/[0/90]/45/[0/90] |

**9. Nanoreinforcement Modification of Composites:** (Dr. Larry Drzal, Michigan State University)

The goal here is to develop a fundamental understanding of the interaction of graphite nanoplatelets with macro reinforcing fibers and polymer matrices, and how these interactions affect the mechanical properties and durability (fire, blast and environmental) of nanoparticle modified polymer composites. Functionalization of xGnP exfoliated graphite nanoparticles has been completed. Nanocomposites consisting of these functionalized nanoparticles were combined with 510A-40 vinyl ester resin to produce nanocomposites.

- Styrene was covalently bonded to the edges of the xGnP. The concentration was between 2 to 3 % of the grafted styrene oligomer. The unnotched Izod impact strength of this styrene functionalized xGnP reinforced 510A-40 nanocomposite is 30% higher than unmodified xGnP reinforced nanocomposite.
- An epoxy/amine adduct was used to covalently functionalize the edges of xGnP. The flexural strength and the un-notched Izod impact strength of the 510A-40 nanocomposites were also improved about between 30% and 160%. This functionalization approach reduced the electrical conductivity of the 510A-40 nanocomposite about 7 orders of magnitude however.
- An epoxy/ATBN adduct were used to covalently functionalize the edges of xGnP. Covalently functionalized epoxy and ATBN on xGnP improved the unnotched Izod impact strength of epoxy/ATBN xGnP reinforced 510A-40 VE nanocomposites about 80%.
- As an alternative to covalently attaching the functionalization to the edges of xGnP, a physical coating of the surfaces was also investigated. Physical coating of CTBN on xGnP surface at a concentration equivalent to one monolayer increased the unnotched Izod impact strength 70% and decreased the electrical conductivity of reinforced xGnP coated with CTBN in 510A-40 VE nanocomposites only about 150%.

The combination of unwoven glass fiber and the xGnP fillers to achieve improved mechanical strength and impact property improvements for blast and impact resistance was investigated. Glass fibers (GF) were combined with VE matrices at various volume fractions using a hand lay-up, resin impregnation and compression method. The electrical conductivity, flexural properties and notched izod impact strength of the GF/VE binary composites were investigated. xGnP nanoparticles at various concentrations were applied as coatings by spraying GF unwoven mats. Studies of the effect of xGnP loading concentration on mechanical properties of VE /GF composites were carried out with different xGnP contents (0.6%, 1.3%, and 3.3% by weight). The flexural properties, notched izod impact strength, and electro conductivity of the composites were

investigated respectively. The electrical conductivity was measured along the flow direction using a two-probe method. The results obtained to date include:

- The flexural properties and notched izod impact strength of the GF/VE binary composites improved by 3.5x and 50x respectively with increasing GF. The compression molded GF/VE composites shown better these properties than the samples that were not compression molded by 40%.
- xGnP coated GF/VE composites were observed to have better flexural strength (20%) and impact strength (15%) as well as higher electrical conductivity (9 orders) than those not coated with xGnP.
- Incorporation of xGnP into the unwoven GF composite has enhanced the mechanical properties of the composites. The flexural strength and impact strength showed the highest value for unwoven fabric-GF/VE-composite-filled xGnP (1.3 wt%) compared to the baseline woven-fabric-GF/VE composites without xGnP due to the ability of the xGnP fillers to enhance the plastic deformation of the composites.
- The flexural strength and modulus of the xGnP/GF/VE hybrid composites with optimum loading of xGnP (about 0.5 to 1.3 wt%) produced the highest values among the investigated samples (330 MPa and 14.5 GPa, respectively), but the impact strength and electro conductivity of the xGnP/GF/VE hybrid composites increased to values of (1450 J/M) and (resistivity $10^{1.4}$ ohms.cm) only after 4.5wt% xGnP was added to the system.
- xGnP sprayed on the GF surface in a 0.5 inch pattern produced a greater flexural strength (350 MPa) and impact strength (1590 J/M) in xGnP/GF/VE composites than uniformly sprayed xGnP on the GF/VE composites.

**10. High-strain Rate Evaluation of Nanoclay and Graphite Platelet Reinforced Vinyl Ester:**
(Dr. David Hui, University of New Orleans)

Small cylindrical specimens cut from the 1.25 and 2.5 wt% nano clay and graphite platelet reinforced plus the 10 wt% CTBN added brominated vinyl ester plate samples were subjected to high-strain rate compressive loading (~ 1200/sec) in Split-Hopkinson Pressure Bar apparatus. As seen in Figure 8, the failure strength of brominated vinyl ester (VC00FH) is reduced with nanoparticle reinforcement, even with the 10 wt% CTBN added. Absorbed energy showed marginal improvement for the 1.25 wt% graphite platelets (VG12FH) and also with 10 wt% CTBN added (VG12PH). However, energy absorption decreased with 2.5 wt% graphite platelets (VG25FH), even with the 10 wt% CTBN added (VG25PH). Tensile SHPB tests are currently in progress.

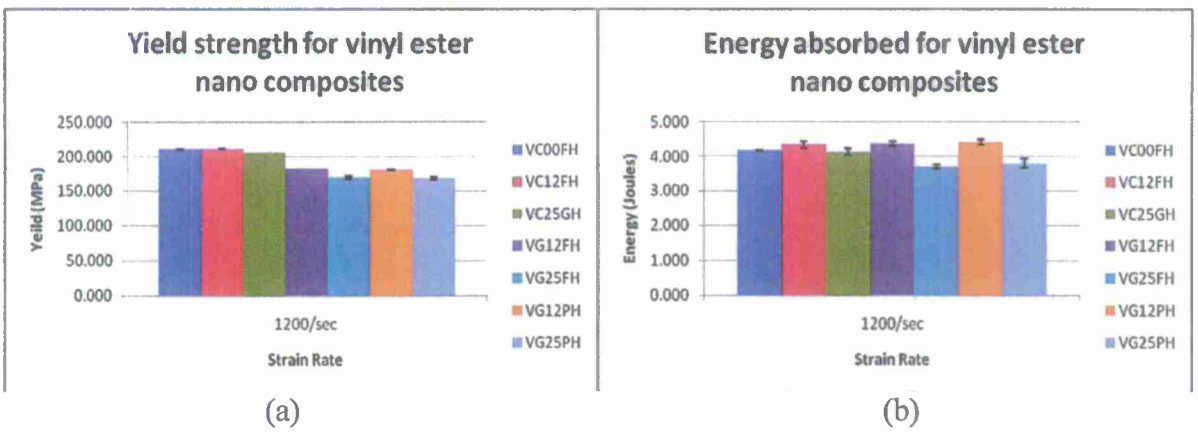


(a) (b)

Figure 8. (a) Yield Strength, and (b) energy absorption for vinyl ester nano composites under high-strain (1200/sec) compressive loading.

**11. References:**

[1] P. Raju Mantena, Ahmed Al-Ostaz and Alexander H.D. Cheng (2009); "Dynamic Response and Simulations of Nano-particle Enhanced Composites" *Composites Science and Technology* 69 (2009) 772-779.

[2] P. Raju Mantena, Alex Cheng and Ahmed Al-Ostaz "Blast and Impact Resistant Composite Structures for Navy Ships" *2008 Office of Naval Research - Solid Mechanics Program: Marine Composites and Sandwich Structures*, University of Maryland, Adelphi, MD, Sep 17-19, 2008, pp. 417-426.

[3] P. Raju Mantena, Alexander Cheng, Ahmed Al-Ostaz and A.M. Rajendran; "Blast and Impact Resistant Composite Structures for Navy Ships" *2009 Office of Naval Research - Solid Mechanics Program: Marine Composites and Sandwich Structures Conference*, University of Maryland, MD, Sep 23-25, 2009, pp. 363-374.

[4] Pramanik B., and Mantena P.R. (2009); "Punch-shear Characteristics of Nanoclay and Graphite Platelet Reinforced Vinyl Ester Plates, Laminated face sheets and Sandwich Composites under Low-Velocity Impact" *ASME - Early Career Technical Journal,* Vol. 8, No.1, October 2009, pp. 8.1-8.8.

[5] Ahmad Almagableh, P. Raju Mantena and Ahmed Al-Ostaz (2009); 'Creep and Stress Relaxation Modeling of Nanoclay and Graphite Platelet Reinforced Vinyl ester Nanocomposites' *Journal of Applied Polymer Science,* Vol. 115, Nov (2009), pp. 1635-1642.

[6] Almagableh A.M., Mantena P.R., Al-Ostaz A, Liu W., Drzal L.T. (2009); 'Effects of Bromination on the Viscoelastic Response of Vinyl ester Nanocomposites' *eXPRESS Polymer Letters,* Vol. 3, No. 11, (2009), 724-732.

[7] Ahmad Almagableh, Swasti Gupta, P. Raju Mantena and Tezeswi Tadepalli; 'Mechanical response and Finite Element Simulations of Vinyl ester Nanocomposite Panels under Shock and Quasi-static Flexural Loading' submitted for presentation and proceedings of the *Joint 25th Technical Conference of American Society for Composites & 14th US-Japan Conference on Composite Materials*, September 20-22, 2010, Dayton, OH.

**NAVY RELEVANCE:** Producing stronger, safer and more cost-effective platforms for the new generation naval ships requires innovative designs, new materials, and affordable/efficient processing and characterization technologies. This research will advance the development of blast, shock and impact resistant composites for navy ship structural applications; to achieve better mobility, survivability, stealth and safety at lower cost.

**TRANSITIONS:** These research investigations have been leveraged with a concurrent grant: Nano-Particle Reinforced Composites for Critical Infrastructure Protection, from the Department of Homeland Security - Southeast Region Research Initiative (DHS-SERRI). Northrop Grumman Ship Building (NGSB) Advanced Capabilities Group is facilitating this research effort on development of advanced ship panel concepts. WebCore Technologies Inc., a small-scale industry in Dayton, OH is working closely with University of Mississippi to develop affordable and durable TYCOR® composite sandwich panels for navy ship structural applications. TYCOR® is currently being used in several military and commercial applications including refrigerated cargo floor for Navy cargo ships, Air Force tactical shelters, Air Force runway matting, vehicular bridge decks, railcar floors and wind turbine blades.

**PUBLICATIONS (ONR-supported):**

Results of this research have been disseminated in eleven journal publications and ten conference presentations/proceedings during 2009-2010.

# BLAST AND IMPACT RESISTANT COMPOSITE STRUCTURES FOR NAVY SHIPS

**P. Raju Mantena and T. Tadepalli**
Composite Structures and Nano-Engineering Research
The University of Mississippi

## OBJECTIVE

Develop stronger, safer and more cost-effective structures for the new generation naval ships; especially nanoparticle reinforced glass/carbon polymeric based composites and structural foams for blast, shock and impact mitigation.

## TECHNICAL APPROACH

Experimental blast response and quasi-static material property data were generated for E-glass and carbon face skin sandwich composite panels with balsa, PVC foam and TYCOR® cores. The Pressure vs Impulse (P-I) curve methodology that was developed to represent estimated damage levels in civil infrastructure components subjected to blast loadings, has been adapted for analyzing these sandwich composite panels. Results show good correspondence between model predictions and experimental data for the performance evaluation of various sandwich composite panel configurations. This P-I curve methodology enables the generation of a database of performance envelopes for sandwich composite panels with a variety of skin and core material combinations under various blast and shock loading scenarios, for naval composite structural applications.

## SUMMARY OF RECENT ACCOMPLISHMENTS

- Numerical models have been developed for the performance evaluation of sandwich composite panels under various blast loading scenarios.
- The Pressure vs Impulse (P-I) curve methodology is implemented to facilitate the rapid analysis of component and system level response to blast and shock loading.

## TECHNICAL DETAILS

**1. Introduction:** The goal of this study is to make use of available experimental blast and shock response data for the performance prediction of sandwich composite panels under a wider range of operational loading conditions and threat scenarios, which would facilitate design decisions at the ship superstructure-system level. The available experimental data, which is limited to only specific blast and shock loading scenarios, is used for validating the proposed computer simulation methodology.

The P-I (Pressure-Impulse) diagram (Figure 1) mathematically relates a specific damage level to a combination of blast pressure and impulse imposed on a particular structural element and allows reduced order modeling of the sandwich composite panel systems. P-I curves are also known as iso-damage curves with each curve representing a certain response level such as mid-span deflection or rotation at supports, etc.

In a particular threat scenario, the pressure and impulse acting on a structure can be determined by using scaling laws based on the distance of the structure from the blast source [1]. Knowing the distribution of pressure and impulse due to a specific blast scenario, the damage to individual components in terms of ductility

demand can then be determined from the P-I chart [2, 3] and can also be further mapped onto a structure consisting of many such components.

Previous research conducted at University of Mississippi under the DHS-SERRI project "Nano-Particle Reinforced Composites for Critical Infrastructure Protection" involved the evaluation of strength and deformation capacity of civil infrastructure components subject to blast and extreme loading [4]. Pressure versus Impulse (P-I) curves were used to represent estimated damage levels in components subjected to blast or shock loadings. The adopted procedure and reflected blast pressure versus distance relation followed the TM 5-1300 Joint Forces military guidance [1]. A database of P-I curves for reinforced concrete components of various cross sections and reinforcement ratios was developed, including the benefits of nano-particle reinforcement. These simulations allow the planner to determine the likely location and extent of damage in building structures subject to blast loadings. This simplified methodology used for rapid damage and vulnerability assessment of critical infrastructure [5] has been adopted here for the performance evaluation of sandwich composite panels for naval ship structures [6].

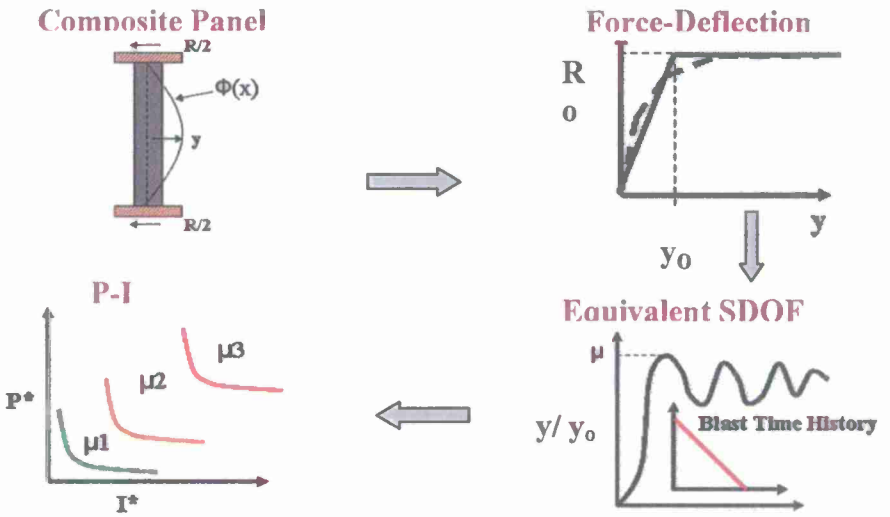


Figure 1. Procedure for generating the P-I curves numerically

**2. Fabrication Of Large Size Sandwich Composite Panels**: Large 4' x 4' and 8' x 4' size navy relevant sandwich composites with balsa, PVC, Tycor foam cores and glass and carbon / vinyl ester face sheets were fabricated for blast, shock, ballistic and impact characterization by the Vacuum Assisted Resin Transfer Molding (VARTM) process at the University of Alabama-Birmingham [6]. A total of 6 variants (two 4' x 4' for each variant) were processed with varying face sheet material, core, and stacking sequence.

Table I. SANDWICH COMPOSITE PANELS SUBJECTED TO BLAST LOADS.

| Sno | Material Code | Face Sheet Material | Core Material | Face-skin Stacking Sequence |
|---|---|---|---|---|
| 1 | E1B3VNB1 | E-Glass / vinyl ester | Balsa core type 9.7 pcf PB standard | [0/90]/45/[0/90]/45/[0/90] 5 plies |
| 2 | C3B3VNB1 | T-700 Carbon FOE treated / vinyl ester | Balsa core type 9.7 pcf PB standard | [0/90]/45/[0/90]/45/[0/90] 5 plies |
| 3 | C3B3V0B1 | T-700 Carbon FOE treated / vinyl ester | Balsa core type 9.7 pcf PB standard | [0/90]/45/[0/90]/$45_2$/[0/90]/45/[0/90] - 8 Plies |
| 4 | C3P2V0B1 | T-700 Carbon FOE treated / vinyl ester | PVC core type 8.1 pcf Divinycell H130 | [0/90]/45/[0/90]/$45_2$/[0/90]/45/[0/90] - 8 Plies |
| 5 | E1T7VMB2 | E-Glass / vinyl ester | Stitched TYCOR | [0/90]/45/[0/90]/45/[0/90]5 plies |
| 6 | E1T8VPB1 | E-Glass /vinyl ester | Non-Stitched TYCOR | [0/90]/45/[0/90]/45/[0/90] 5 plies |

Table I lists all the variants and constituent materials along with details on face sheet stacking sequence. In the work reported here, out of the six different sandwich composite panels described in Table I, only three panels which have equal face sheet and core thickness, i.e., the 5 ply E-glass/balsa, 8 ply Carbon/Balsa and 8 ply Carbon/PVC, are considered for computational simulation and analysis.

**3. Blast Testing:** The six large 4' x 4' x 2.25" thick panels with Balsa, PVC, TYCOR foam cores and E-glass and T700 FOE treated carbon face sheets (Table I) were mounted in the US Army Corps of Engineers ERDC Blast Load Simulator (Vicksburg, MS) such that the top and bottom were fixed and the other two sides were free.

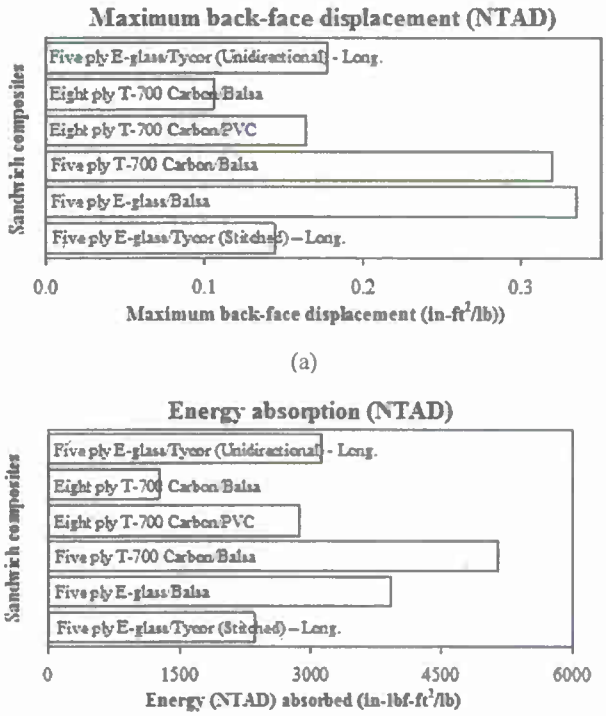


Figure 2. (a) Maximum back-face displacement, and (b) energy absorbed by sandwich composite panels subjected to blast load waveforms of 16-18 psi peak pressures and 200 psi-ms impulse.

These were subjected to blast load waveforms of 16-18 psi peak pressures and 200 psi-ms impulse which represents an approximate threat level of 2000 lbs of TNT at 140 feet. The blast tested panels underwent about 0.5 to 1.5 inches of mid-point deflection, with no visible signs of external damage. Figure 2 compares the experimental blast response characteristics of these sandwich panels [6] with respect to mid-point deflection and energy absorption (data normalized to areal density - NTAD).

**4. Finite Element Modeling**: The SAP2000 finite element model consists of layered nonlinear shell elements (Figure 3) and allows multiple layers of different thicknesses, each with a different material property, while avoiding shear locking behavior. The shell element also includes the effects of transverse shear deformation. Bulk material nonlinear–stress strain data obtained from quasi-static tensile and compressive testing of corresponding face sheet and core materials respectively is used as input for the material constitutive models. The quasi-static experimental data shows variation in material properties (Figure 4); hence the averaged

experimental and published material data consistent with the SAP2000 program requirements are used as input for the FE model [7].

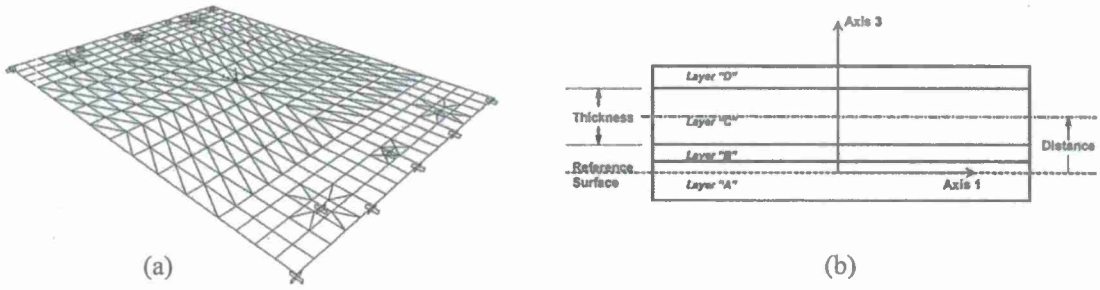


Figure 3. (a) FE model of sandwich composite panel mesh and boundary conditions, and (b) SAP2000 shell element

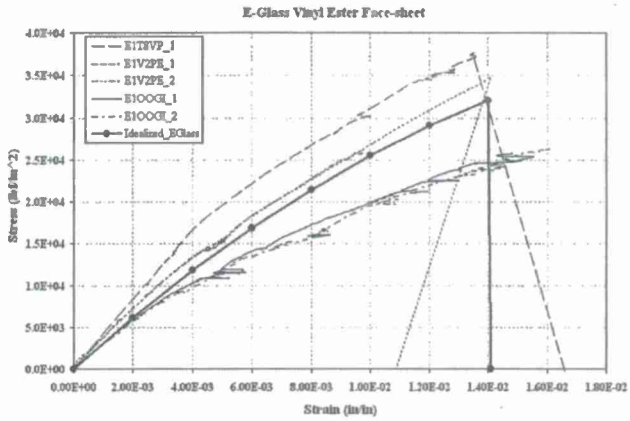


Figure 4. Experimental uni-axial stress-strain relation and idealization for (a) E-glass vinyl ester face sheets, and (b) Balsa wood core.

The strength vs deformation capacity of undamaged sandwich composite panels shown in Table I are established by nonlinear quasi-static finite element analysis [7], with each panel subjected to 1.5 inches of mid-span deformation under displacement control and boundary conditions simulating the complex interactions that occur during the actual blast tests.

**5. Equivalent Single Degree Of Freedom Idealization**: The nonlinear force deflection relationship obtained from FE modeling is initially idealized to an elastic-perfectly plastic force-deflection relationship by equating the work done, which is the area under the respective force-deflection curves (Figures 5, 7 and 9). The equivalent elastic stiffness $K_E$ and the equivalent maximum elastic deflection $y_o$ are then computed. Since there are non-unique solutions for the idealized curves, in this study the $K_E$ is constrained such that the elastic stiffness of the SDOF system is similar to the initial stiffness of the composite panel obtained from quasi-static nonlinear analysis. Based on these assumptions, the component is idealized as an equivalent single degree of freedom (SDOF) system [7].

The energy balance method (based on principle of conservation of mechanical energy) is commonly employed to obtain the quasi-static and impulsive asymptotes of P-I curves. To obtain the impulsive asymptote, the total energy imparted to the system is assumed to be in the form of kinetic energy and is equated to the total strain energy stored in the system at its maximum response. For the quasi-static regime, the load can be assumed to be constant before the maximum deformation is achieved and accordingly the quasi-static (Pressure) asymptote is obtained by equating the work done by the load and total strain energy in the system at maximum deformation.

P-I curves can also be generated numerically by simulating the dynamic response of the SDOF system to a large number of triangular impulse loads by using the implicit generalized Newmark method of time integration in Matlab. The time duration of the impulse ($t_d$); the time of rise ($t_r$), peak load and the impulse applied onto the component are varied. The maximum values of response to each loading are then computed, and if they match a certain desired response level, they are stored in an array along with the peak pressure and corresponding impulse.

The quasi-static and impulsive asymptotes for different ductility ratios ($\mu_i = y_i/y_o$) corresponding to critical stages in the component response for the 5 ply E-glass/Balsa, 8 ply Carbon/Balsa and 8 ply Carbon/PVC sandwich panels are plotted in the respective P-I space (Figures 6, 8, 10, 11). These numerical simulations of reduced order enable the construction of iso-damage curves that are suitable for damage prediction over a wider range of blast pressure and impulse combinations.

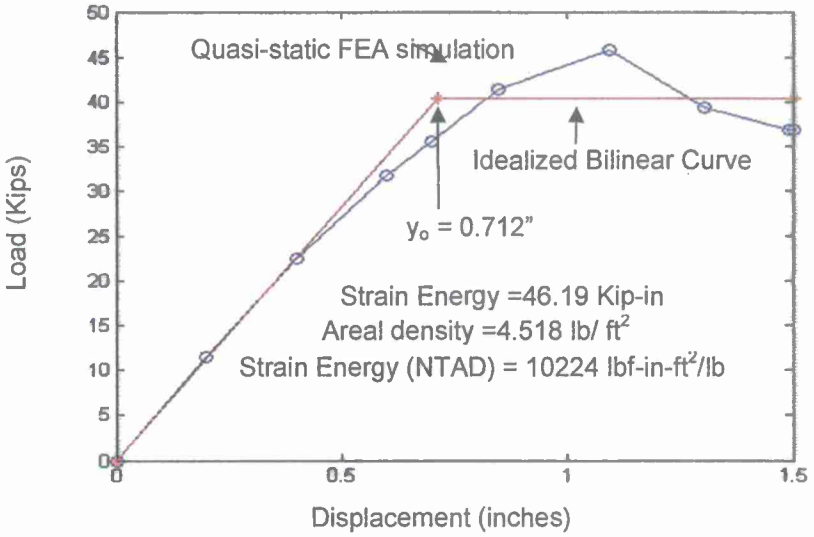


Figure 5. Simulated quasi-static force-displacement relation and equivalent bi-linear idealization for the 5 ply E-glass/Balsa sandwich panel (E1B3VNB1)

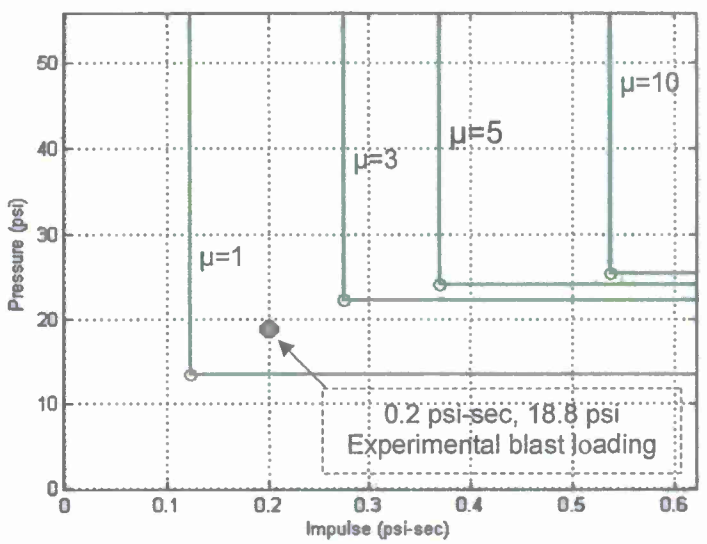


Figure 6. Pressure-Impulse curves for the 5 ply E-glass/Balsa sandwich panel (E1B3VNB1), for different ductility ratios ($\mu_i = y_i / y_o$)

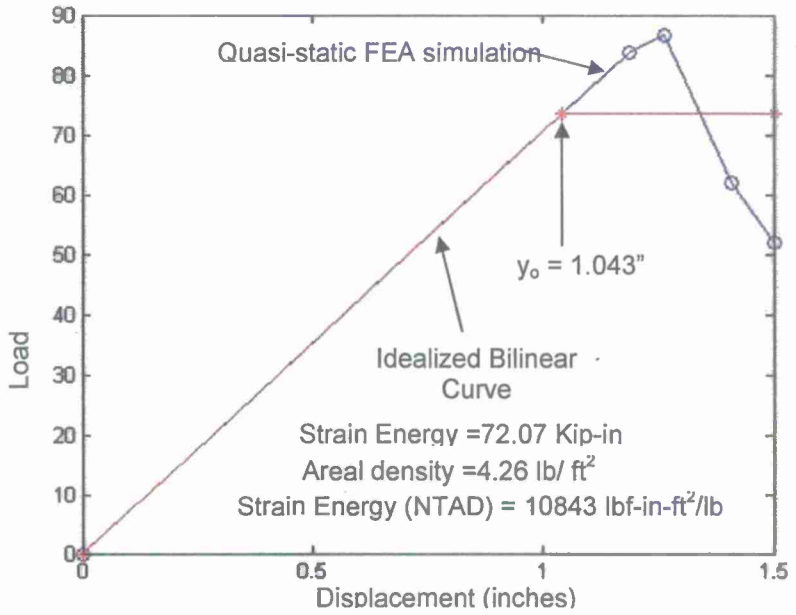


Figure 7. Simulated quasi-static force-displacement relation and equivalent bi-linear idealization for the 8 ply Carbon/Balsa sandwich panel (C3B3V0B1)

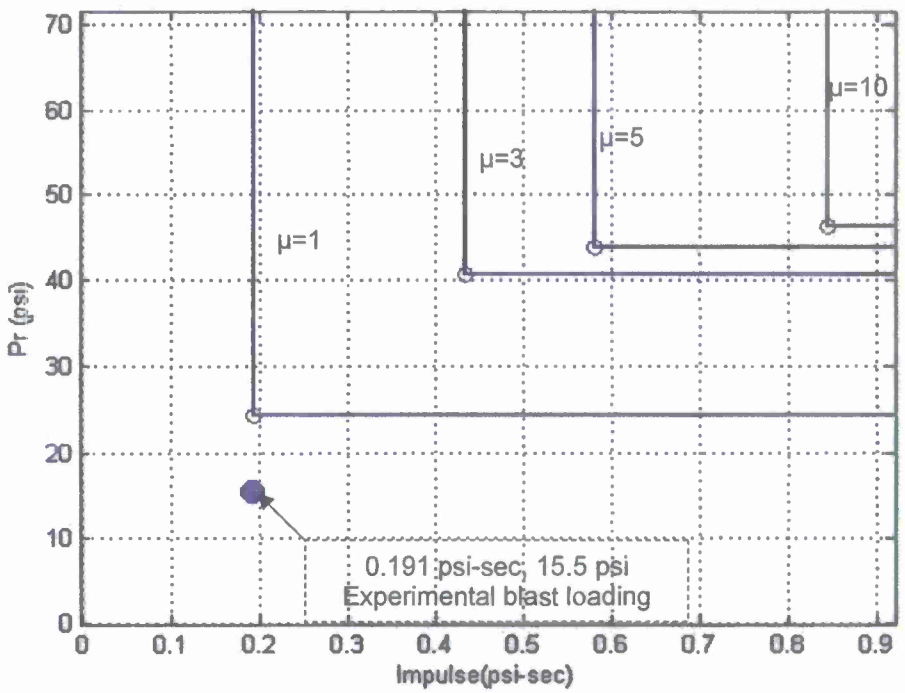


Figure 8. Pressure-Impulse curves for the 8 ply Carbon/Balsa sandwich panel (C3B3V0B1), for different ductility ratios ($\mu_i = y_i / y_o$)

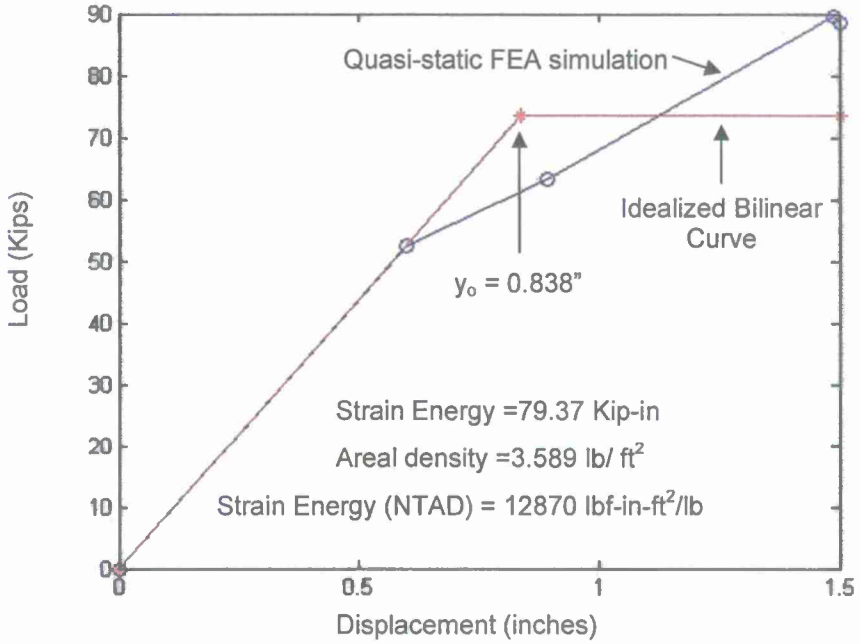


Figure 9. Simulated quasi-static force-displacement relation and equivalent bi-linear idealization for the 8 ply Carbon/PVC sandwich panel (C3P2V0B1)

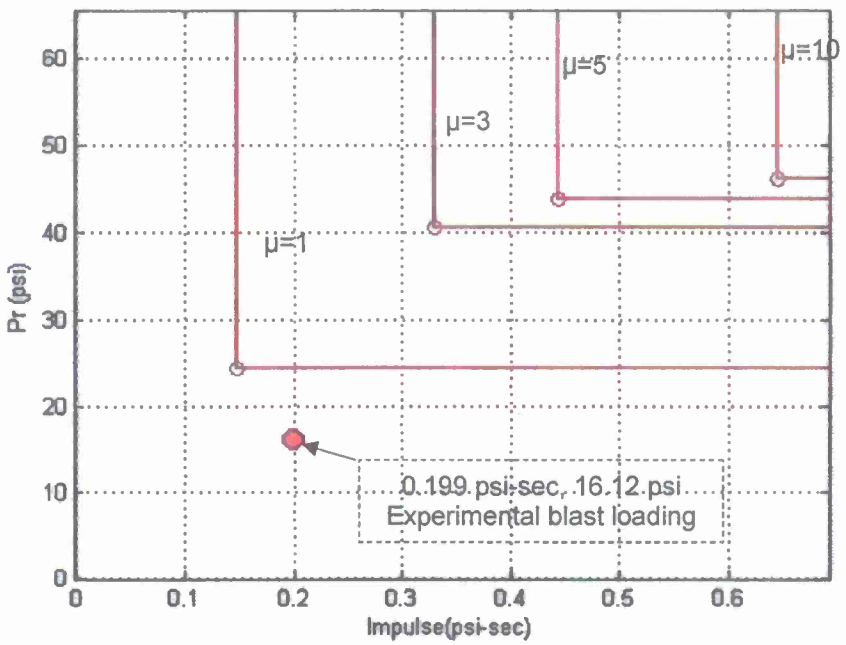


Figure 10. Pressure-Impulse curves for 8 ply Carbon/PVC sandwich panel (C3P2V0B1) for different ductility ratios ($\mu_i = y_i / y_o$)

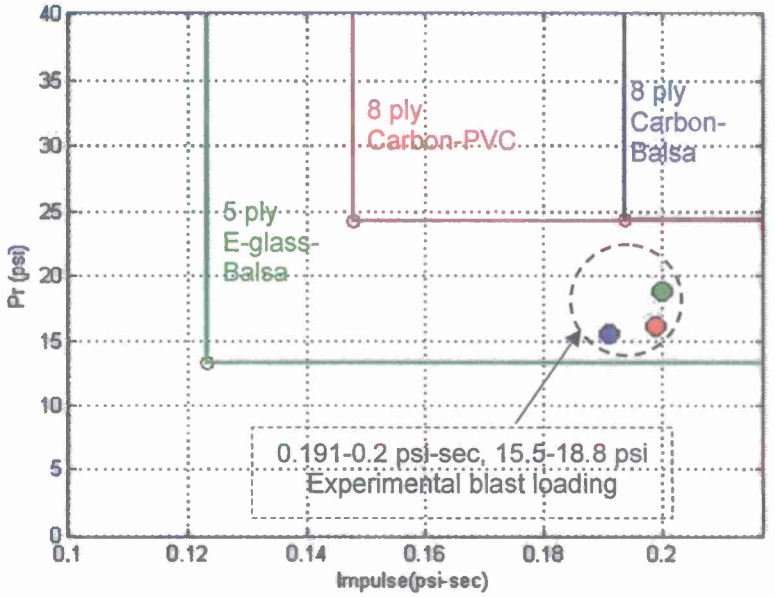


Figure 11. Comparison of Pressure-Impulse curves for the 5 ply E-glass/Balsa, 8 ply Carbon/Balsa and 8 ply Carbon/PVC, for the ductility ratio $\mu = 1$.

**6. Conclusions**: In this work, Pressure vs Impulse (P-I) curves are developed for sandwich composite panels with a variety of skin and core material combinations, to enable the generation of a database of performance envelopes under various blast loading scenarios. The strength vs deformation properties of the undamaged sandwich composite panels are established by nonlinear quasi-static finite element analysis (FEA) of the component subjected to mid-span deformation under displacement control, with boundary conditions simulating the actual blast tests and idealized for SDOF (single degree of freedom) modeling. Nonlinear quasi-static analysis indicates that the Carbon/PVC panel has the highest energy absorption (NTAD) capability followed by 8 ply Carbon/Balsa and E-glass/Balsa respectively, based on area under the simulated quasi-static load-deflection curves (Figures 5,7,9). From these force-deformation simulations it appears that for the 8 ply Carbon/Balsa and 8 ply Carbon/PVC panels (having the same face sheet material but different cores) the type of core material type dictates the deformation upto yield, being higher for Balsa than PVC core. However, the energy absorption under quasi-static loading is marginally higher for PVC than Balsa core. Comparison between 5 ply E-glass/Balsa and 8 ply Carbon/Balsa panels (which have the same core, but different face sheet materials) indicates that the face-sheet material determines the peak load resistance of the panel, which is higher for an 8 ply Carbon face sheet than a 5 ply E-glass face sheet of equal thickness.

In the pressure-impulse space, these simulations predict that the 8 ply Carbon/Balsa sandwich panel would require considerably higher blast pressure and impulse values to cause permanent deformation (as defined by the equivalent SDOF system) when compared to the E-Glass/Balsa and Carbon/PVC sandwich panels. For the experimental blast loading conducted at 15.5-18.8 psi pressure and 0.19-0.2 psi-sec impulse, the 5 ply E-glass/Balsa panel absorbs the most energy by virtue of larger plastic deformation, while the 8 ply Carbon/Balsa panel absorbs the least energy as it responds elastically. The analytical predictions are consistent with the experimental data obtained from blast tests. Analysis of the other three sandwich composite panel configurations i.e., the 5 ply Carbon/Balsa, E-glass/Non-Stitched Tycor and E-glass/Stitched Tycor shown in Table I, is currently ongoing.

## 7. References


[1] TM 5-1300/NAVFAC P-397, AFR 88-22 Nov. 1990. Structures to resist effects of accidental explosions.

[2] Tadepalli, T., 2010. "Performance Evaluation of Low-Rise Concrete Frame Building Structures in Moderate Seismic Zones Subject to External Blast Loading," Dissertation submitted in partial fulfillment of requirements of Doctor of Philosophy in Engineering Science, Department of Civil Engineering, University of Mississippi, Dec. 2010.

[3] Tadepalli,T. and Mullen,C.L., 2008, "Vulnerability of Low Rise Buildings to External Blast Events: Damage Mapping," *Proceedings of Inaugural Conference of the Engineering Mechanics Institute, EM08*, Minneapolis, MN.

[4] Cheng, A., Al-Ostaz, A., Mullen C.L. and Mantena, P.R., 2009, "Nano Particle Reinforced Composites for Critical Infrastructure Protection," Report submitted to Southeast Region Research Initiative, Managed by UT□Battelle for U.S. Department of Energy, supporting the Department of Homeland Security, Task Order: 4000055459, May 2009.

[5] Tadepalli, T. and Mullen, C.L, "Simplified blast simulation procedure for hazard mitigation planning," *Ninth International Conference on Structures Under Shock and Impact*, Wessex Institute of Technology, New Forest, Southampton, United Kingdom, 3 to 5 July 2006.

[6] Mantena, P. R., Rajendran, A.M. and Al-Ostaz, A. "Blast and Impact Resistant Composite Structures for Navy Ships" *2010 Office of Naval Research - Solid Mechanics Program: Marine Composites and Sandwich Structures Conference*, University of Maryland, MD, Sep 27-29, 2010, pp. 379-388

[7] Tadepalli,T. and Mantena,P.R., Computational simulation and experimental characterization of sandwich composite panels subjected to blast loads, *The 26th Annual American Society of Composites Technical Conference*, Montreal, Canada, Sept.26-28, 2011, Paper No. 1081.


**NAVY RELEVANCE:** Producing stronger, safer and more cost-effective platforms for the new generation naval ships requires innovative designs, new materials, and affordable/efficient processing and characterization technologies. This research will advance the development of blast, shock and impact resistant composites for navy ship structural applications; to achieve better mobility, survivability, stealth and safety at lower cost.

**TRANSITIONS:** Northrop Grumman Ship Building (NGSB) Advanced Capabilities Group is facilitating this research effort on development of advanced ship panel concepts. WebCore Technologies Inc., a small-scale industry in Dayton, OH is working closely with University of Mississippi to develop affordable and durable TYCOR® composite sandwich panels for navy ship structural applications. TYCOR® is currently being used in several military and commercial applications including refrigerated cargo floor for Navy cargo ships, Air Force tactical shelters, Air Force runway matting, vehicular bridge decks, railcar floors and wind turbine blades.

**PUBLICATIONS (ONR supported)**

**Journal Papers**

- Ahmad Almagableh and P. Raju Mantena, 2010 "Effects of Environmental Aging On The Thermal and Mechanical Properties of Vinyl Ester Nanocomposites, *ASME Early Career Technical Journal 2010*, Oct.1-2, Atlanta, Georgia, USA, CD-ROM, Vol.9, pp.35-40

**Conference Papers**

- A.Almagableh, S.Gupta, P.R.Mantena, and T.Tadepalli, "Mechanical Response and Finite Element Simulations of Vinyl Ester Nanocomposite Panels Under Shock and Quasi-static Flexural Loading" *Proceedings of the American Society for Composites: 25th Technical Conference*, Dayton, OH, Sept. 20-22, 2010, American Society for Composites, CD-ROM-19 pp.
- P. Raju Mantena and Tezeswi Tadepalli, "Blast, Shock and Impact Resistant Nano-reinforced Panels and Sandwich Composites" *Proceedings of ICC-CFT 2011: International Conference on Composites for 21st Century - Current and Future Trends*, Bangalore, India, 4-7 January 2011, CD ROM Paper #C022.

# APPENDIX

JOURNAL OF SANDWICH STRUCTURES & MATERIALS

Article

Journal of Sandwich Structures and Materials
15(1) 110–133
© The Author(s) 2012
Reprints and permissions:
sagepub.co.uk/JournalsPermissions.nav
DOI: 10.1177/1099636212460542
jsm.sagepub.com
SAGE

# Numerical and experimental blast response characterization of sandwich composite structural panels

**Tezeswi P Tadepalli and Prabhakar Raju Mantena**

## Abstract

Experimental blast response and quasi-static material property data were obtained for E-glass and carbon face skin sandwich composite panels with balsa, polyvinyl chloride foam, and TYCOR® cores. The pressure versus impulse (*P–I*) curve methodology enabled the generation of a database of performance envelopes for these sandwich composite panel configurations under different blast loading scenarios. The strength versus deformation properties of various undamaged sandwich composite panels are established numerically and idealized for single-degree-of-freedom modeling. Results show good correspondence between model predictions and experimental results for performance evaluation of the various sandwich composite structural panel configurations that were investigated.

## Keywords

Blast, *P–I* curves, sandwich composite panels, finite element analysis

## Introduction

The goal of this study is to make use of available experimental blast and shock response data for the performance prediction of sandwich composite panels under a wider range of operational loading conditions and threat scenarios, which would

Department of Mechanical Engineering, Composite Structures and Nano-Engineering Research, University of Mississippi, Oxford, USA

**Corresponding author:**
Tezeswi P Tadepalli, Department of Mechanical Engineering, Composite Structures and Nano-Engineering Research, University of Mississippi, University, Oxford, MS 38677, USA.
Email: tadepali@olemiss.edu

facilitate design decisions at the ship superstructure-system level. The available experimental data, which is limited to only specific blast and shock loading scenarios, is used for validating the proposed reduced order computer simulation methodology.

Several detailed studies have been conducted on the blast and shock response of sandwich composite panels [1–5]. These studies have examined the response and various failure modes of the panels such as core crushing, delamination, bending, and shear response. The focus of these studies has largely been limited to the response of a composite sandwich panel to a unique blast or shock loading scenario.

Our study focuses on implementation of the *P–I* (pressure vs. impulse) curve computational methodology to enable exploration of the design space, and for evaluating the response of available sandwich composite panel configurations to various blast loads. An attempt has been made to validate the computational methodology for predicting the performance of various sandwich composite panels based on limited available experimental data corresponding to specific blast load histories.

The *P–I* (pressure–impulse) diagram shown in Figure 1 relates a specific damage level to a combination of blast pressure and impulse imposed on a particular structural element, and allows the reduced order modeling of sandwich composite panel systems. *P–I* curves are also known as iso-damage curves with each curve

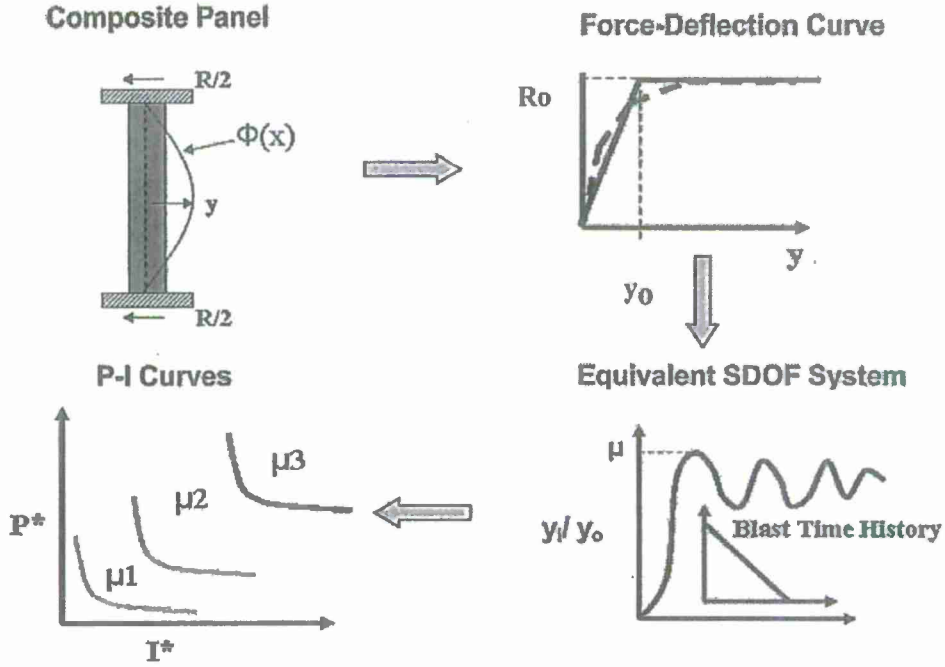


**Figure 1.** Procedure for generating the pressure–impulse (*P–I*) curves numerically.

representing a certain response level such as mid-span deflection or rotation at supports, etc.

In a particular threat scenario, the pressure and impulse acting on a structure can be determined using scaling laws based on the distance of the structure from the blast source [6]. Knowing the distribution of pressure and impulse due to a specific blast scenario, the damage to individual components in terms of ductility demand can then be determined from the *P–I* chart [7, 8], and can also be further mapped on to a structure consisting of many such components.

Previous research conducted at the University of Mississippi on nano-particle reinforced composites for critical infrastructure protection involved the evaluation of strength and deformation capacity of civil infrastructure components subject to blast and extreme loading [9]. Pressure vs impulse (*P–I*) curves were used to represent estimated damage levels in components subjected to blast or shock loadings. The adopted procedure and reflected blast pressure vs distance relation followed the TM 5-1300 Joint Forces military guidance [6]. A database of *P–I* curves for reinforced concrete components of various cross sections and reinforcement ratios was developed, including the benefits of nano-particle reinforcement. These simulations allow the planner to determine the likely location and extent of damage in building structures subject to blast loadings. This simplified methodology used for rapid damage and vulnerability assessment of critical infrastructure [10], has been adopted here for the performance evaluation of sandwich composite panels for naval ship structural applications [11].

## Fabrication of large size sandwich composite panels

Large $1.22 \times 1.22\,m^2$ ($4 \times 4\,ft^2$) and $2.44 \times 1.22\,m^2$ ($8' \times 4'$) size navy relevant sandwich composites with balsa, polyvinyl chloride (PVC), TYCOR® foam cores, and glass and carbon/vinyl ester face sheets were fabricated for blast, shock, ballistic, and impact characterization by the vacuum assisted resin transfer molding process at the University of Alabama–Birmingham [11]. A total of six variants (two $1.22 \times 1.22\,m^2$ panels for each variant) were processed with varying face sheet material, core, and stacking sequence. In the work reported here, these six different sandwich composite panels are considered for computational simulation and analysis. The layup and stacking sequence of these panels are described in Table 1.

## Blast testing

The six large $1.22 \times 1.22 \times 0.057\,m^3$ ($4\,ft \times 4\,ft \times 2.25\,in$) thick panels with balsa, PVC, TYCOR foam cores, and E-glass and T700 F0E-treated[i] carbon face sheets were mounted in the US Army Corps of Engineers ERDC Blast Load Simulator (Vicksburg, MS) such that the top and bottom were fixed and the other two sides were free (Figure 2). The blast simulator uses a He/Air mixture to simulate the effects of an explosion. Stiff steel edge plates of width 152 mm (6″) are used as front and back of the loading frame. These panels were subjected to blast load

**Table 1.** Sandwich composite panels subjected to blast loads

| S. no. | Material code | Face sheet material | Core material | Face skin stacking sequence |
|---|---|---|---|---|
| 1 | E1B3VNB1 | E-glass/vinyl ester | Balsa core type 9.7 pcf PB standard | [0°/90°]/45°/[0°/90°]/45°/[0°/90°] – five plies |
| 2 | C3B3VNB1 | T-700 carbon F0E-treated/vinyl ester | Balsa core type 9.7 pcf PB standard | [0°/90°]/45°/[0°/90°]/45°/[0°/90°] – five plies |
| 3 | C3B3V0B1 | T-700 carbon F0E-treated/vinyl ester | Balsa core type 9.7 pcf PB standard | $[0°/90°]/45°/[0°/90°]/45°_2$/[0°/90°]/45°/[0°/90°] – eight plies |
| 4 | C3P2V0B1 | T-700 carbon F0E-treated/vinyl ester | PVC core type 8.1 pcf Divinycell H130 | $[0°/90°]/45°/[0°/90°]/45°_2$/[0°/90°]/45°/[0°/90°] – eight plies |
| 5 | E1T7VMB2 | E-glass/vinyl ester | Stitched TYCOR | [0°/90°]/45°/[0°/90°]/45°/[0°/90°] – five plies |
| 6 | E1T8VPB1 | E-glass/vinyl ester | Non-stitched TYCOR | [0°/90°]/45°/[0°/90°]/45°/[0°/90°] – five plies |

PVC: polyvinyl chloride.

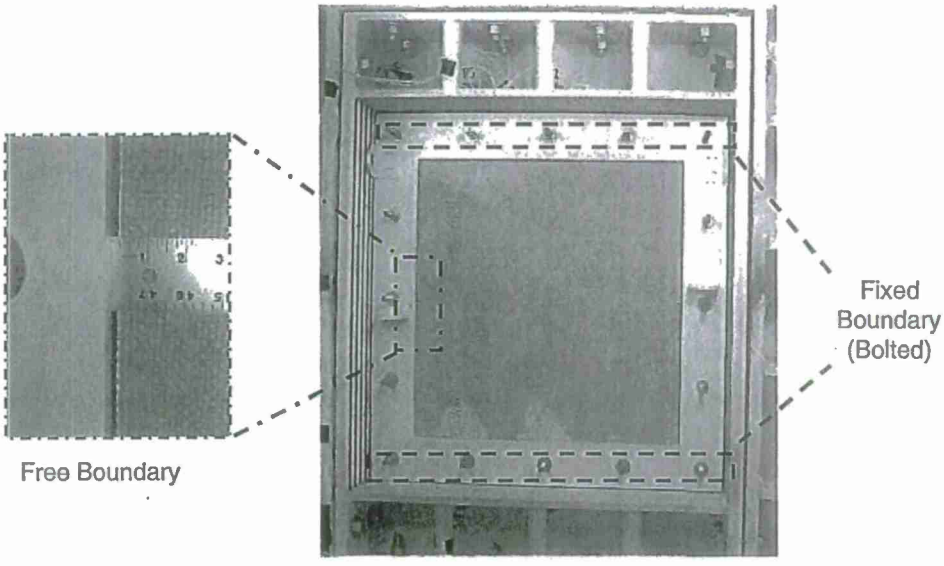


**Figure 2.** Fixed top/bottom and two sides free boundary condition of sandwich panel mounted in the ERDC blast load simulator.
ERDC: Engineer Research and Development Center.

| Panel 2 | |
|---|---|
| Driver Pressure | 250 psi |
| Driver Length | 5.5 ft |
| He/Air | 20/80 |
| Cascade Length (in) | 12 |
| Gaps (in) | 0 |

| Gage | P (psi) | I (psi-msec) |
|---|---|---|
| P1 | 16.4 | 192 |
| P2 | 16.1 | 198 |
| P3 | 16.1 | 195 |
| P4 | 22.8 | 219 |
| P5 | 17.7 | 194 |
| P6 | 16.8 | 195 |
| P7 | 17.8 | 191 |
| P8 | 20.4 | 212 |
| Sum | 150.1 | 1601 |
| Avg | 18.8 | 200 |

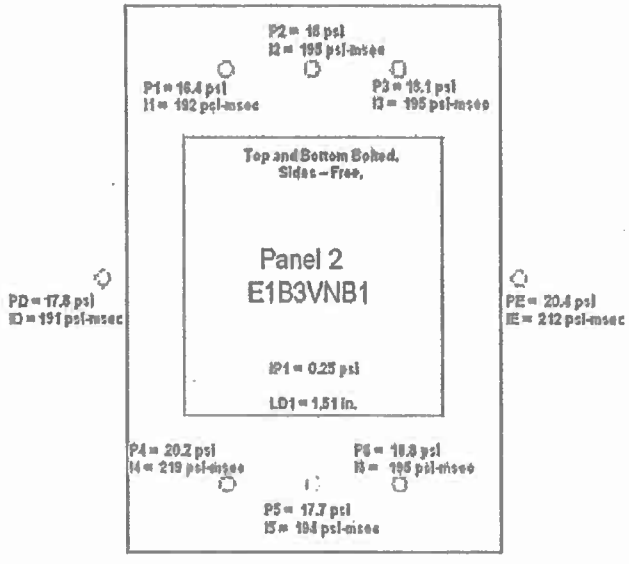


**Figure 3.** Typical peak reflected pressure and impulse distribution on five ply E-glass/balsa sandwich panel (E1B3VNB1).

waveforms of 106.8–129.6 kPa (15.5–18.8 lbf/in$^2$) peak over-pressures and 1.28–1.38 kPa s (185–200 lbf/in$^2$ ms) impulse which represents an approximate threat level of 907.2 kg (2000 lbs) of trinitrotoluene (TNT) at 42.7 m (140 ft) (Figures 3 and 4). Four high speed Phantom® cameras with a sampling rate of 1000 frames per second were positioned to capture the response of the rear face of the panel from various angles. A laser range finder (Acuity® AR4000-LIR) was used for recording the deflection time-history of the back face of the panels. Kulite® high pressure ruggedized dynamic response IS pressure transducer (HKS-11-375-100SG(M) series) was used for measuring the pressure time-histories at various locations around the panel (as shown in Figure 3). A HiTechniques® (HT600) data acquisition system sampled the events at 1 MHz and recorded for 131 ms for the pressure gages and 2 s on the laser.

These blast tested panels underwent about 12.7–38.1 mm (0.5–1.5 in.) of mid-point deflection, with no visible signs of external damage.

Figure 5 compares the experimental blast response characteristics of these sandwich panels [11]. To accommodate specific weight requirements, the reported experimental and numerical data have been normalized to areal density (NTAD) (kg/m$^2$); with respect to both mid-point deflection (m/kg/m$^2$) and the energy absorption (kJ/kg/m$^2$) capabilities.

## Finite element modeling

Various failure mechanisms may influence the response during blast loading of a sandwich composite panel. This study focuses only on the global flexural mode of failure, with the sandwich composite panel under a fixed–fixed boundary condition

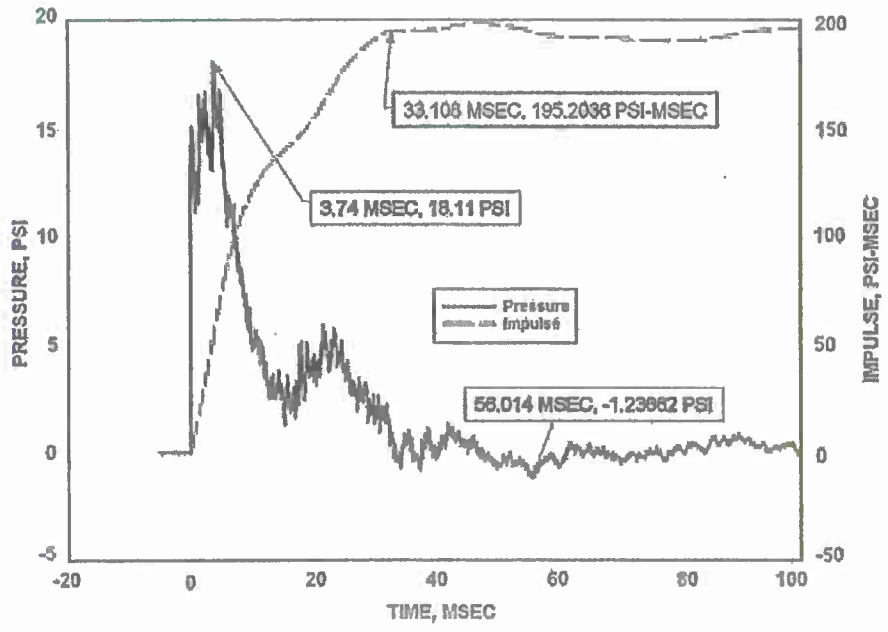


**Figure 4.** Typical blast load history on sandwich panels with 106.8–129.6 kPa (16–18 lbf/in$^2$) peak pressure and 1.28–1.38 kPa s (185–200 lbf/in$^2$ ms) impulse; equivalent to 907.2 kg (2000 lbs) of TNT at 42.7 m (140 ft).
TNT: trinitrotoluene.

at each support. The methodology described here, however, can be easily extended to accommodate other failure modes and boundary conditions.

The SAP2000® [12] finite element (FE) model consists of layered nonlinear shell elements (Figure 6(a)) and allows multiple layers of different thicknesses, each with a different material property, while avoiding shear locking behavior. The shell element also includes the effects of transverse shear deformation. Bulk material nonlinear–stress strain data obtained from quasi-static tensile and compressive testing of corresponding face sheet and core materials, respectively, is used as input for the material constitutive models. The quasi-static experimental data shows some variation in material properties for the face skin and core materials (Figures 7 to 9); hence both the averaged experimental and published material data that are consistent with the SAP2000 program requirements are used as input for the FE model [13–16].

A parameter study was initially conducted with the FE model, for closely similar boundary conditions, in order to simulate the complex interactions that occur during the actual blast tests (Figure 6(b)). The bolt locations are modeled as being fixed against displacement and rotation. The stiff back plate near the bolts (Figure 2) extends the support to the panel by 76 mm (3″). Figure 6(b) shows the effect of three different boundary conditions (simulating different degrees of restraint at the edge of the back plate) on the quasi-static force–deformation response (stiffness) of the panel. The free boundary condition at the plate edge was finally chosen, based on comparison of dynamic response of the equivalent

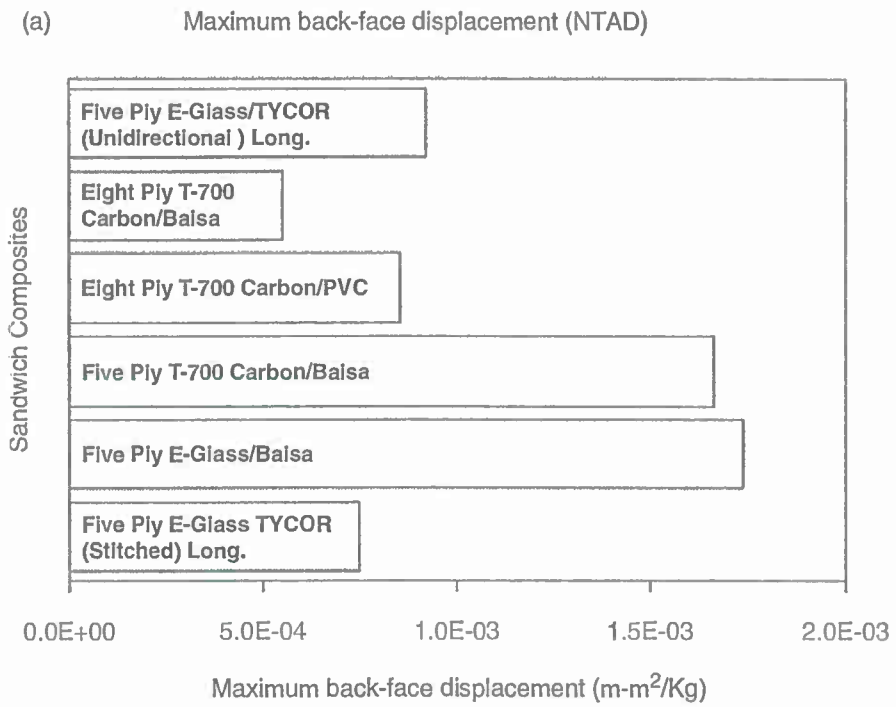


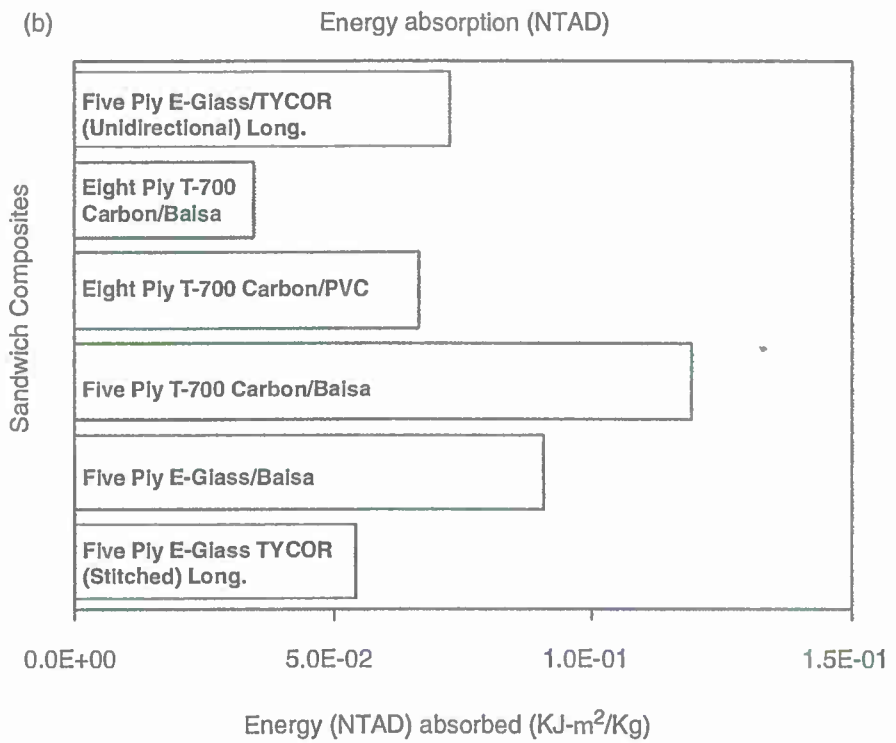


**Figure 5.** Experimentally obtained (a) maximum back-face displacement and (b) energy absorbed by sandwich composite panels subjected to blast load waveforms.

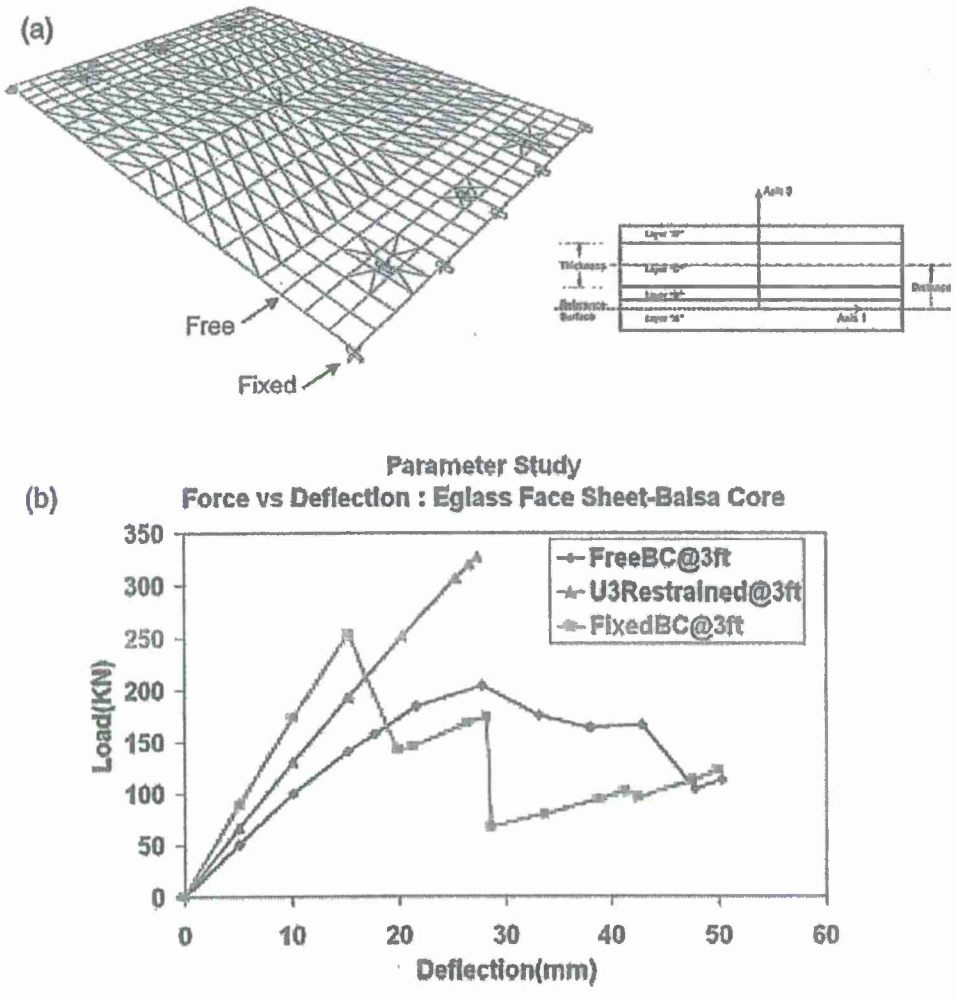


**Figure 6.** (a) FE model of sandwich composite panel mesh and (b) effect of boundary conditions on the quasi-static response of sandwich composite panels.
FE: finite element.

single-degree-of-freedom (SDOF) system with experimental observations for maximum back-face deflection.

The strength versus deformation capacity of undamaged sandwich composite panels shown in Table 1 are established by nonlinear quasi-static FE analysis [12], with each panel subjected to about 1.5 in. (38.1 mm) of mid-span deformation under displacement control.

## Equivalent SDOF idealization

The nonlinear force–deflection relationship obtained from FE modeling for each sandwich panel configuration is initially idealized to an elastic-perfectly plastic force–deflection relationship by equating the work done, which is the area under the respective force–deflection curves (Figures 10 to 15). The equivalent elastic

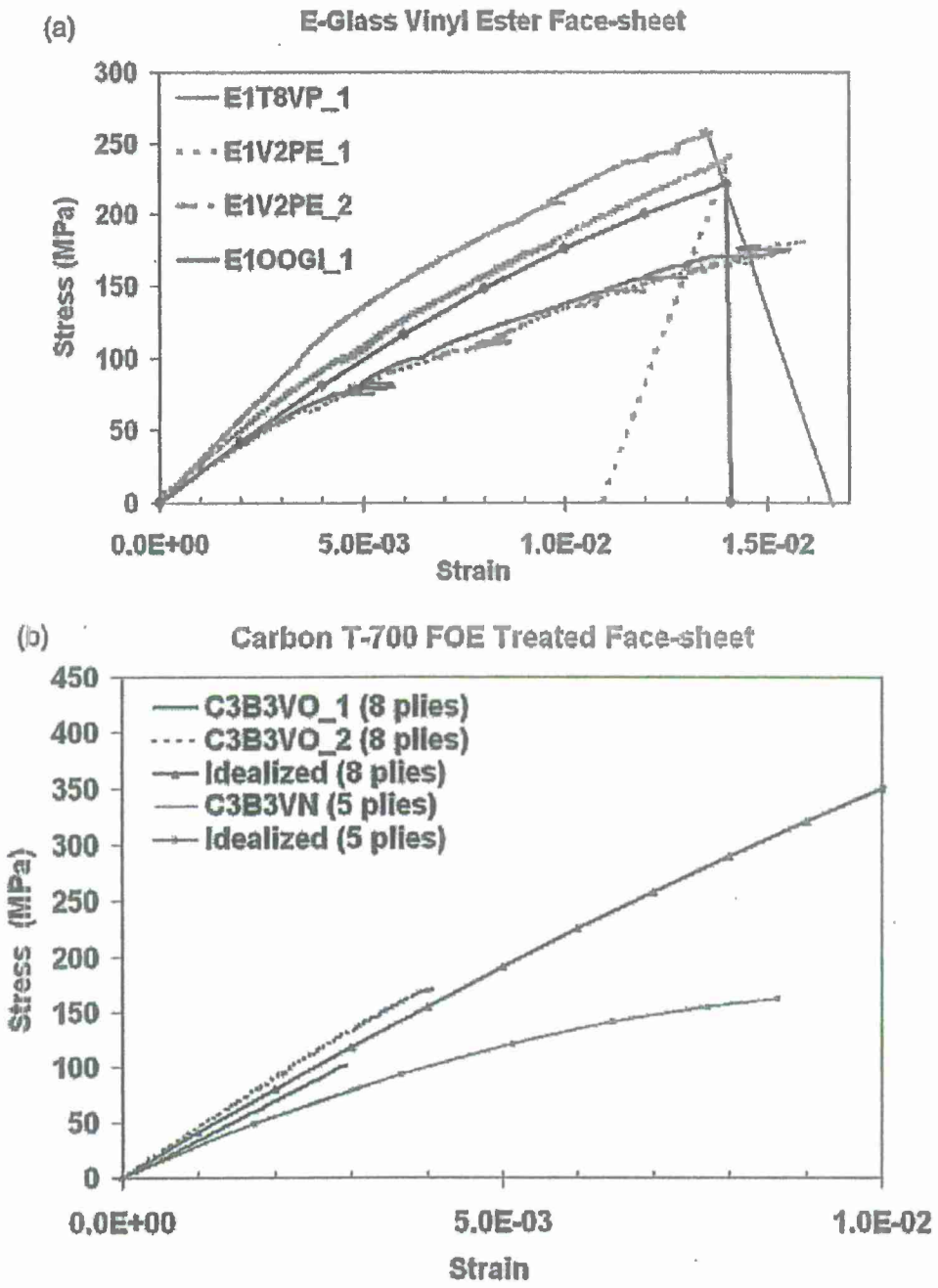


**Figure 7.** Experimental uniaxial stress–strain relation and idealization for (a) E-glass vinyl ester and (b) carbon T-700 FOE-treated face sheets.

stiffness, $k_e$, and the equivalent maximum elastic deflection, $y_o$, are then computed. Since there are non-unique solutions for these idealized curves; in this study the, $k_e$, is constrained such that the elastic stiffness of the SDOF system is similar to the initial stiffness of the composite panel obtained from quasi-static nonlinear

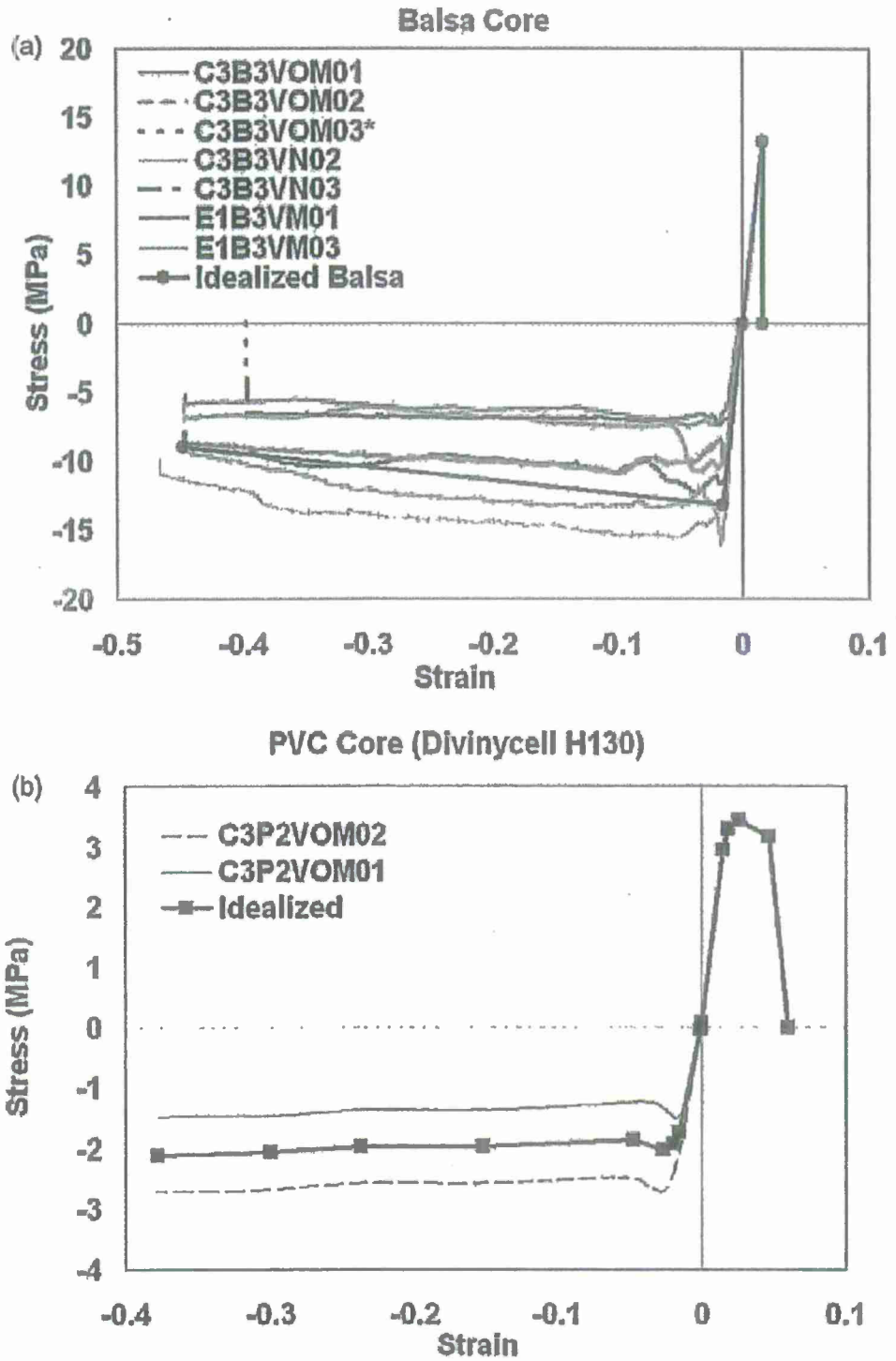


**Figure 8.** Experimental uniaxial stress–strain relation and idealization for (a) balsa wood core and (b) PVC foam core.
PVC: polyvinyl chloride.

A-65

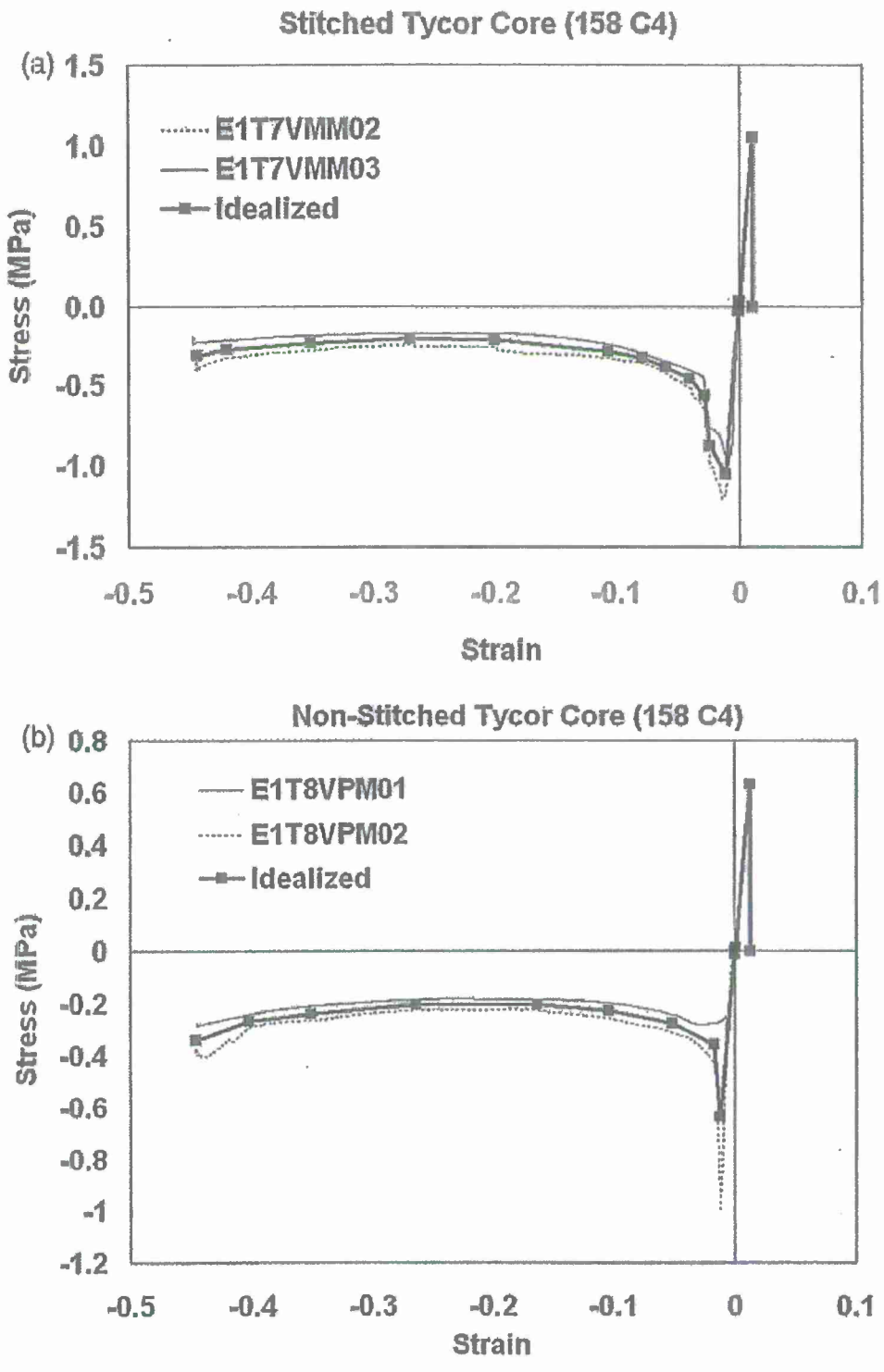


**Figure 9.** Experimental uniaxial stress–strain relation and idealization for (a) stitched and (b) non-stitched TYCOR cores.

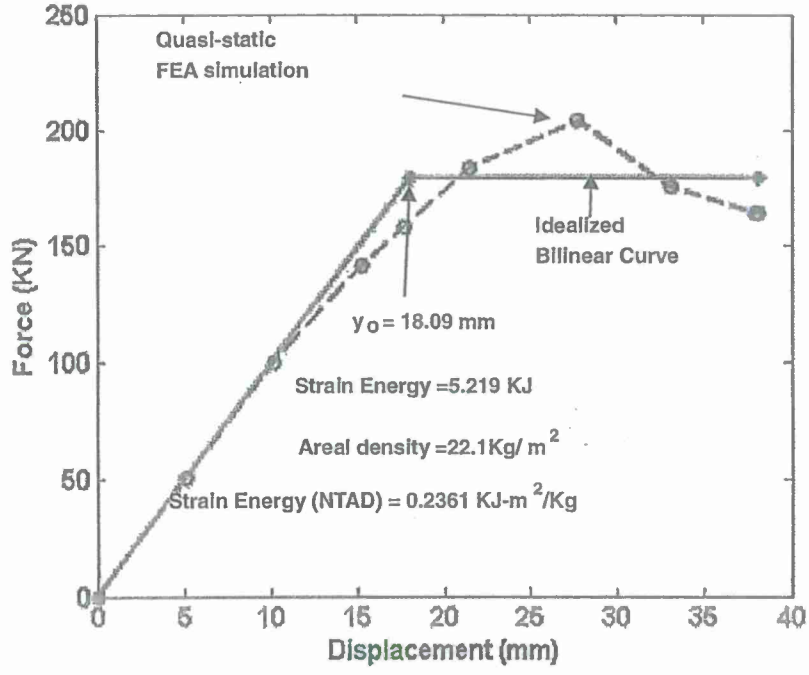


**Figure 10.** Simulated quasi-static force–displacement relation and equivalent bilinear idealization for the five ply E-glass/balsa sandwich panel (E1B3VNB1).

analysis. Based on these assumptions, the component is idealized as an equivalent SDOF system [17].

The energy balance method (based on principle of conservation of mechanical energy) is commonly employed to obtain the quasi-static and impulsive asymptotes of $P$–$I$ curves [17]. To obtain the impulsive asymptote, the maximum deflection of an SDOF system subject to a very short duration loading (relative to the natural period) is considered. The total energy imparted to the system is assumed to be in the form of kinetic energy and is equated to the total strain energy stored in the system at its maximum response. The loading is considered to be a pure impulse as shown below

$$i = F \cdot t_d \tag{1}$$

This impulse imparts an initial velocity ($v$) to the system of mass $M$

$$v = \dot{y} = \frac{i}{M} \tag{2}$$

Therefore, the kinetic energy imparted to the system is given by

$$K.E. = \frac{Mv^2}{2} = \frac{i^2}{2M} \tag{3}$$

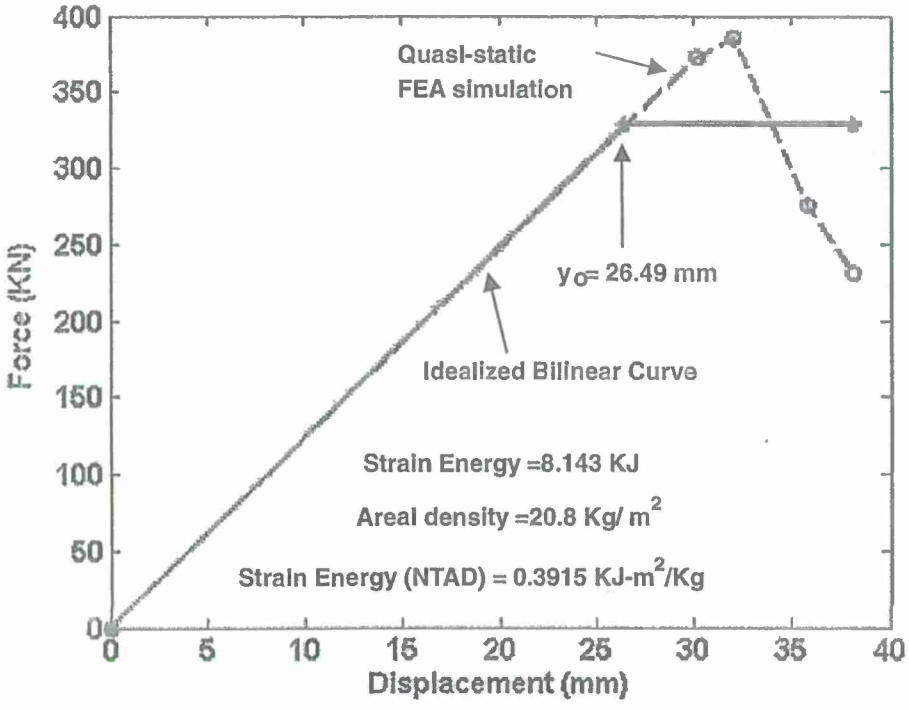


**Figure 11.** Simulated quasi-static force–displacement relation and equivalent bilinear idealization for the eight ply carbon/balsa sandwich panel (C3B3V0B1).

Since resistance is bilinear, strain energy at maximum deflection (i.e. total energy absorbed by the system) is equal to the area under the resistance curve given by

$$U = R_{\max} \cdot \left(y_{\max} - \frac{y_{el}}{2}\right) \tag{4}$$

where $U$ is the strain energy at maximum deflection, $R_{\max}$ the maximum resistance of the equivalent SDOF system, $y_{\max}$ the maximum deflection of the equivalent SDOF system, and $y_{el}$ the maximum elastic deflection of the equivalent SDOF system.

At maximum deflection the external energy is assumed to be completely absorbed by the SDOF system. Thus, equating external kinetic energy (equation (3)) to internal strain energy (equation (4)) and normalizing with respect to area, we obtain

$$i = \frac{(R_{\max}/A) \cdot \left(\sqrt{2\mu - 1}\right)}{\omega} \tag{5}$$

where $A$ is the exposed area ($36'' \times 42''$) of the sandwich panel, $\mu = \frac{y_{\max}}{y_{el}}$ the ductility ratio, and $\omega = \sqrt{\frac{K}{M}}$, $K = \frac{R_{\max}}{y_{el}}$.

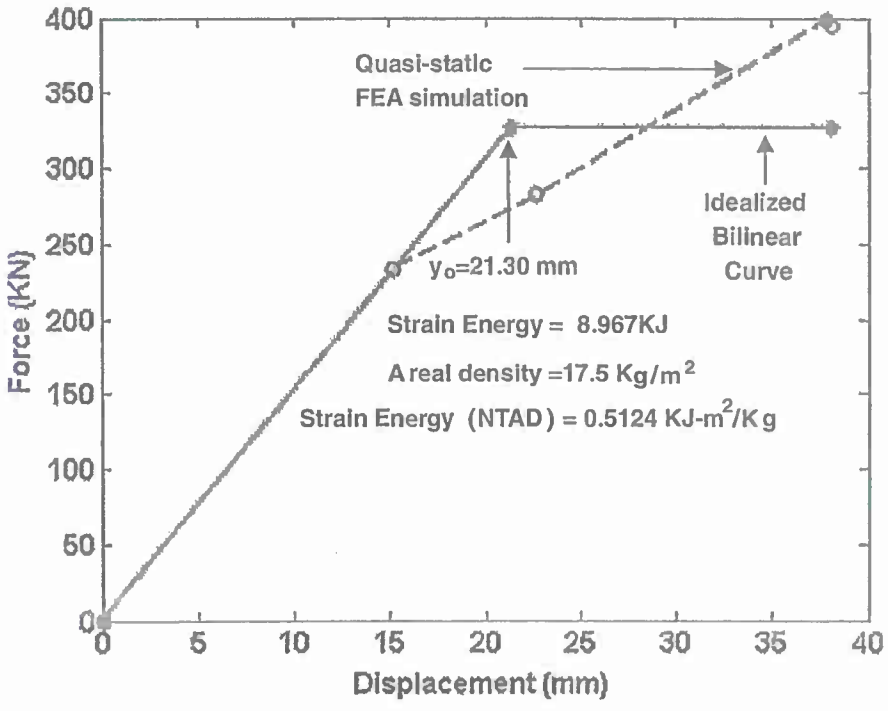


**Figure 12.** Simulated quasi-static force–displacement relation and equivalent bilinear idealization for the eight ply carbon/PVC sandwich panel (C3P2V0B1).
PVC: polyvinyl chloride.

To obtain the pressure asymptote, the quasi-static regime is considered; where the load can be assumed to be constant before the maximum deformation is achieved. Accordingly, the quasi-static (pressure) asymptote is obtained by equating the work done by the load and total strain energy in the system at maximum deformation as shown below

$$W = F \cdot y_{\max} \tag{6}$$

Equating the external energy (equation (6)) to internal energy (equation (4)) and normalizing with respect to area, we obtain

$$P = \frac{R_{\max}}{A} \cdot \left(\frac{\mu - 0.5}{\mu}\right) \tag{7}$$

*P–I* curves can also be generated numerically by simulating the dynamic response of the SDOF system to a large number of triangular impulse loads using the implicit generalized Newmark method of time integration in Matlab®. The time duration of the impulse ($t_d$); the time of rise ($t_r$), peak load, and the impulse applied onto the component are varied. The maximum values of response to each loading are then computed, and if they match a certain desired response level, they are

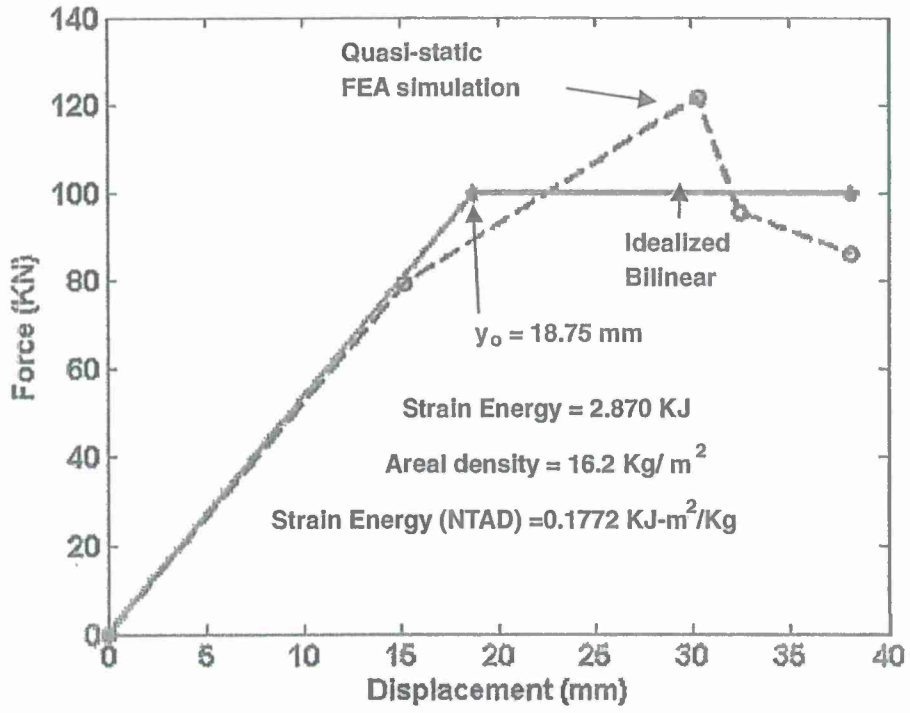


**Figure 13.** Simulated quasi-static force–displacement relation and equivalent bilinear idealization for the five ply carbon/balsa sandwich panel (C3B3VNB1).

stored in an array along with the peak pressure and corresponding impulse. A comparison of the energy balance method and the numerical approach (Figure 16) for a typical case shows that similar *P–I* curves are obtained by both these methods.

However, given the large variation in the material properties of the sandwich panel materials, as well as the complex boundary conditions, only the asymptotes of the *P–I* curves are computed in this study. These numerical simulations of reduced order enable the rapid construction of iso-damage curves that are suitable for damage prediction over a wider range of blast pressure and impulse combinations.

## Results and discussion

The quasi-static and impulsive asymptotes for different ductility ratios ($\mu_i = y_i/y_o$) corresponding to critical stages in component response for the six different composite sandwich panel configurations investigated are plotted in the respective *P–I* space (Figures 17 to 22). Figure 23 shows the comparative performance, in *P–I* space, of these six sandwich panel configurations, corresponding to first yield displacement ($\mu = 1$). The simulated responses are observed to concentrate under three groupings corresponding to relatively high, medium, and low overall blast resistance, in terms of the pressure and impulse these panels can withstand before

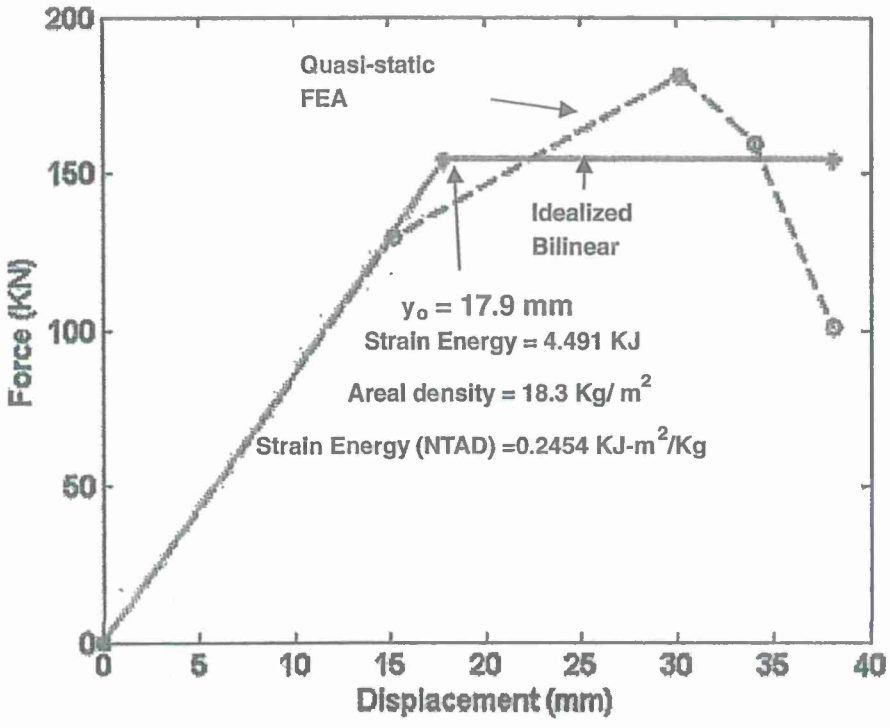


**Figure 14.** Simulated quasi-static force–displacement relation and equivalent bilinear idealization for the five ply E-glass/TYCOR (stitched) sandwich panel.

undergoing plastic deformation. The first group consisting of eight ply carbon/balsa (C3B3VOB1) and eight ply carbon/PVC (C3P2VOB1) shows the greatest overall resistance. The second group with five ply E-glass/balsa (E1B3VNB1), five ply E-glass/TYCOR® (unidirectional), and five ply E-glass/TYCOR® (stitched), each of which show relatively moderate resistance to blast. The five ply carbon/balsa (C3B3VNB1) is predicted to have the lowest overall blast resistance of all six sandwich panel configurations, as per this *P–I* curve methodology.

Nonlinear quasi-static analysis indicates that the five ply carbon/balsa has the highest energy absorption (NTAD) capability followed by five ply E-glass/balsa and five ply E-glass/TYCOR® (unidirectional)-Long., respectively, based on area under the simulated quasi-static load–deflection curves (Figure 24). From these force–deformation simulations it appears that for the eight ply carbon/balsa and eight ply carbon/PVC panels (which have the same face sheet material, but different cores of same thickness) the type of core material dictates the deformation up to yield (NTAD), being higher for PVC foam than the balsa core (Figure 24(a)). However, the energy absorption (NTAD) under quasi-static loading is marginally higher with balsa than PVC core (Figure 24(b)). A similar comparison between the five ply E-glass/balsa, five ply E-glass/TYCOR® (unidirectional) Long., and five ply E-glass/TYCOR® (stitched) Long., (which have the same face sheet materials, but different cores of same thickness) indicates that the five ply E-glass/balsa has

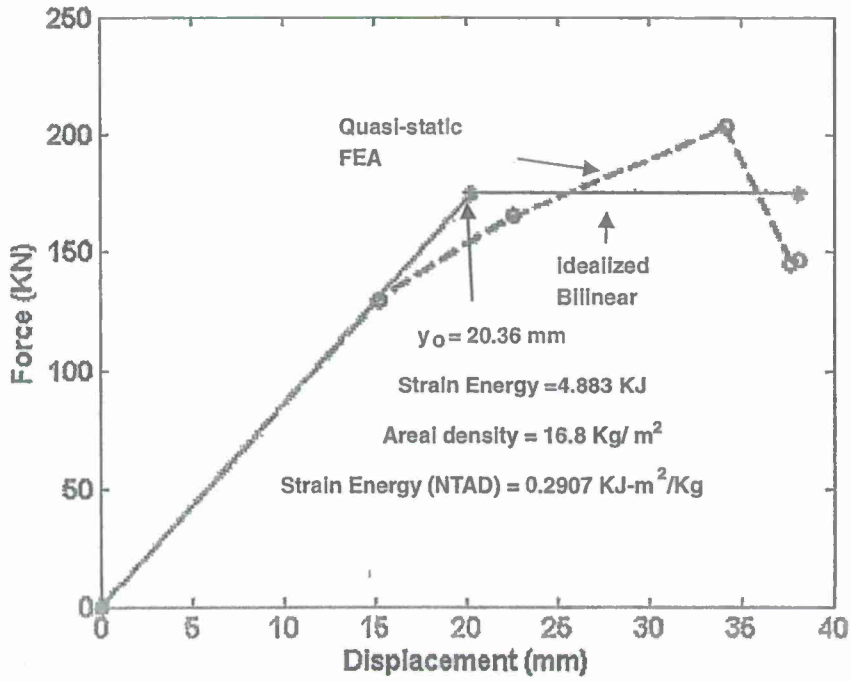


**Figure 15.** Simulated quasi-static force–displacement relation and equivalent bilinear idealization for the five ply E-glass/TYCOR (unidirectional) sandwich panel (E1T8VPB1).

the highest deformation up to yield (NTAD) among these three panel configurations, with the five ply E-glass TYCOR® (stitched) Long. panel having the lowest deformation up to yield (NTAD). Figure 24(b) indicates highest energy (NTAD) absorption, among these three, by the five ply E-glass panel with a balsa core. It is also observed that the five ply E-glass TYCOR® (stitched) panel absorbs less energy (NTAD) as compared to the five ply E-glass TYCOR® (unidirectional) Long. panel.

Comparison of all the panels with five ply E-glass face sheets and different cores of same thickness mentioned in the previous paragraph, gives similar values of peak load resistance (Figures 10, 14, and 15). Conversely, the eight ply carbon/balsa panel gives a higher peak load resistance (Figure 11) than a five ply E-glass/balsa panel (Figure 10) (which have the same core, but different face sheet materials of same thickness). This indicates correlation between the type of face sheet material and the peak load resistance of the panel. Overall these trends shown in Figure 24 are similar to those obtained from the experimental blast tests (shown previously in Figure 5).

In the pressure–impulse space, these simulations predict that the eight ply carbon/balsa and the eight ply carbon/PVC sandwich panels would require considerably higher blast pressure and impulse values to cause permanent deformation (as defined by the equivalent SDOF system), when compared with the five ply E-glass/balsa and five ply carbon/balsa and five ply E-glass/TYCOR® (both stitched

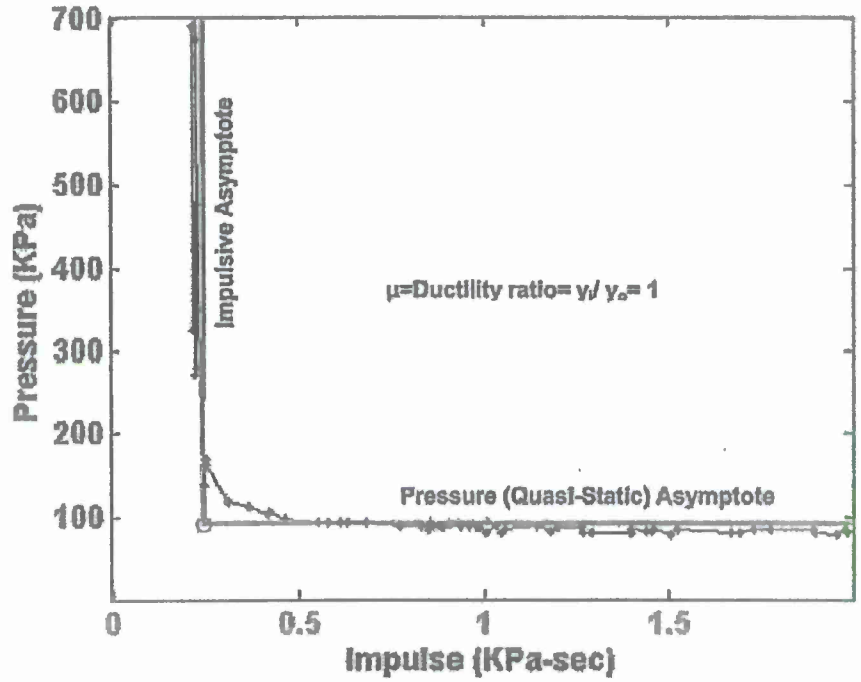


**Figure 16.** Typical *P–I* diagram showing the computed response curve ($\mu = 1$) and asymptotes for the five ply E-glass/balsa sandwich panel (E1B3VNB1).

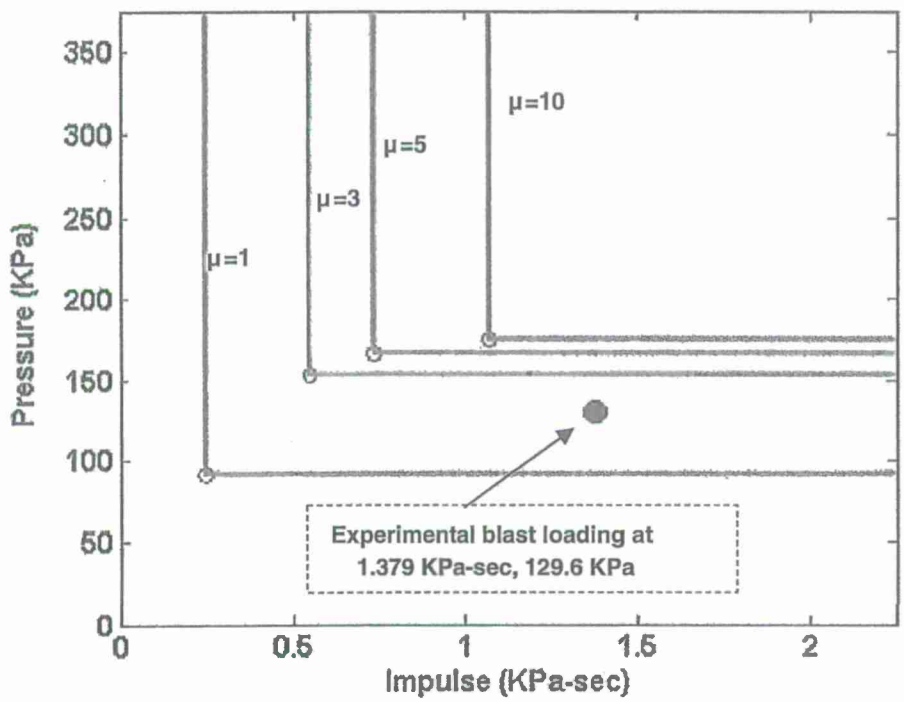


**Figure 17.** Pressure–impulse curves for the five ply E-glass/balsa sandwich panel (E1B3VNB1), for different ductility ratios ($\mu_i = y_i/y_o$).

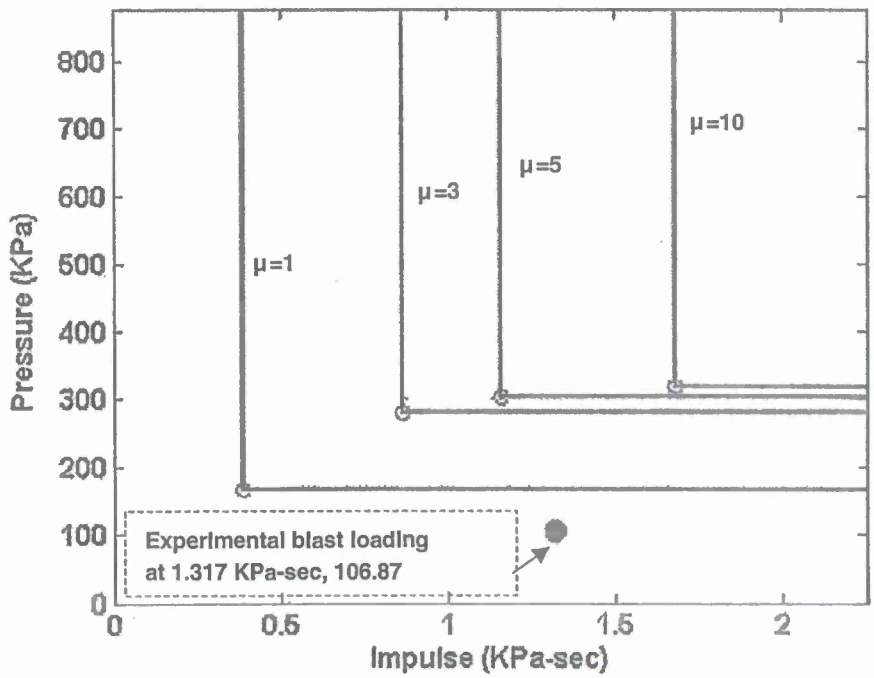


**Figure 18.** Pressure–impulse curves for the eight ply carbon/balsa sandwich panel (C3B3V0B1), for different ductility ratios ($\mu_i = y_i/y_o$).

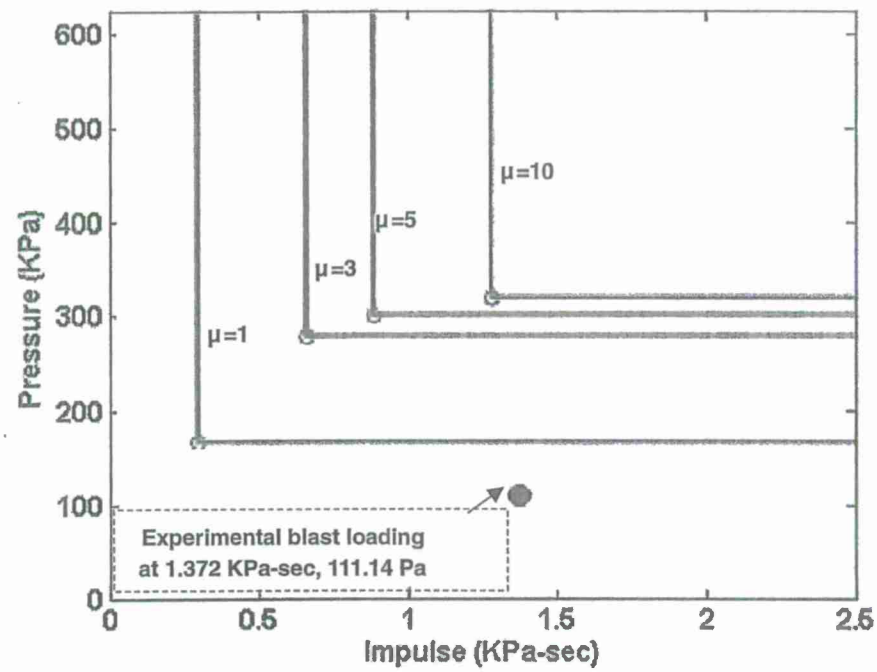


**Figure 19.** Pressure–impulse curves for eight ply carbon/PVC sandwich panel (C3P2V0B1) for different ductility ratios ($\mu_i = y_i/y_o$).
PVC: polyvinyl chloride.

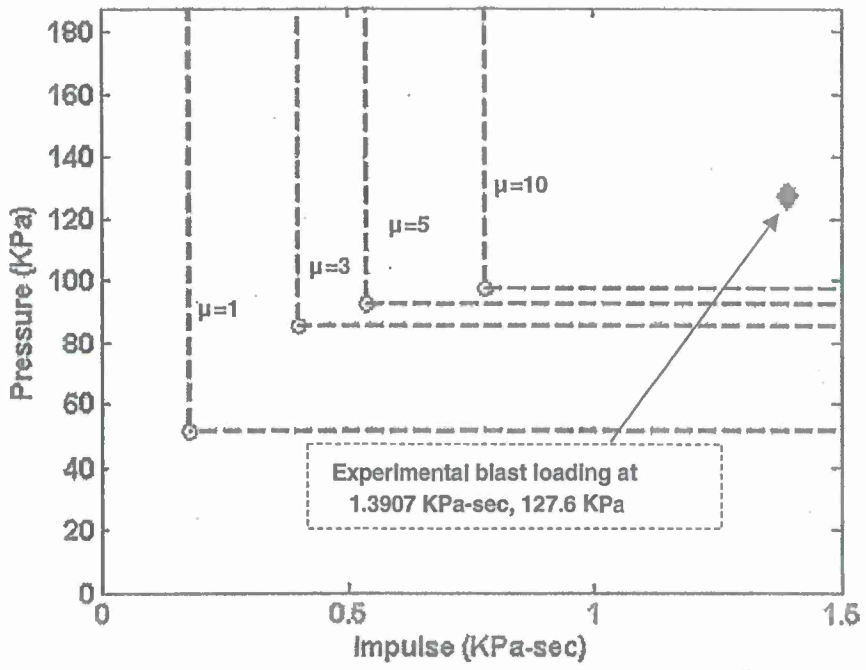


**Figure 20.** Pressure–impulse curves for the five ply carbon/balsa sandwich panel (C3B3VNB1), for different ductility ratios ($\mu_i = y_i/y_o$).

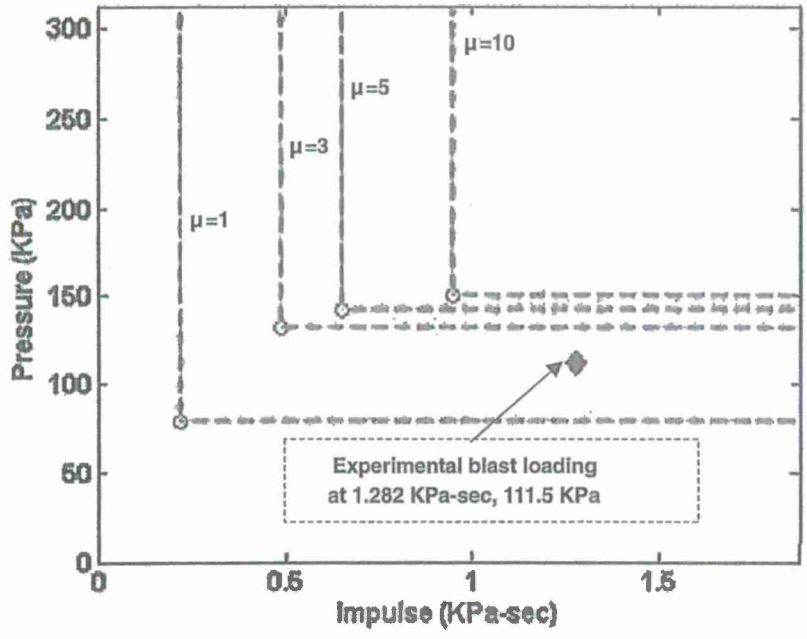


**Figure 21.** Pressure–impulse curves for the five ply E-glass/TYCOR (stitched) sandwich panel (E1T7VMB2), for different ductility ratios ($\mu_i = y_i/y_o$).

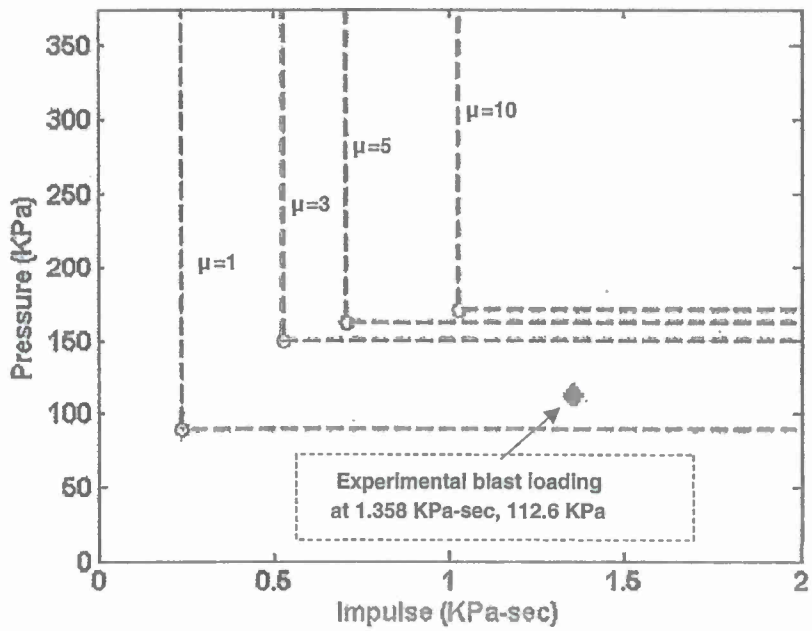


**Figure 22.** Pressure–impulse curves for the five ply E-glass/TYCOR (unidirectional) sandwich panel (E1T8VPB1), for different ductility ratios ($\mu_1 = y_f/y_o$).

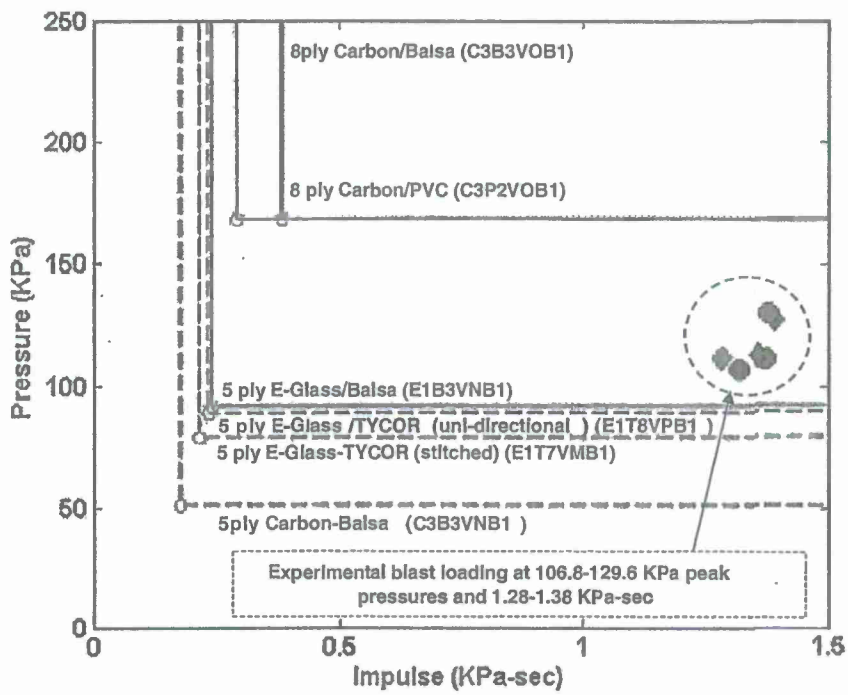


**Figure 23.** Comparison of pressure–impulse curves for the various sandwich composite panels, re-plotted for a ductility ratio $\mu = 1$.

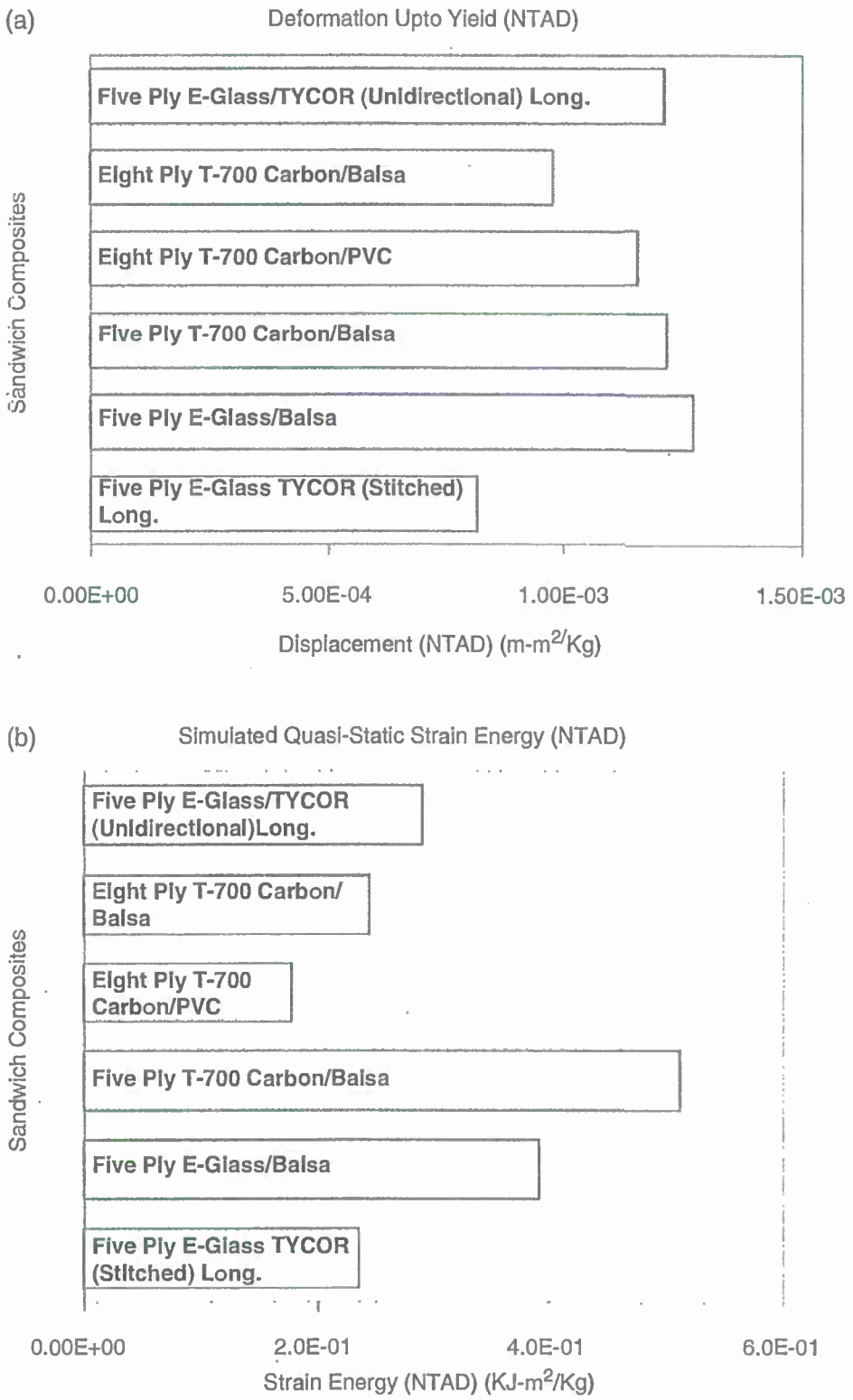


**Figure 24.** (a) Simulated deformation up to yield and (b) strain energy absorption under quasi-static loading for the various sandwich composite panels.

and unidirectional) sandwich panels. For the experimental blast loading conducted at 106.8–129.6 kPa (15.5–18.8 lbf/in$^2$) peak pressures and 1.38 kPa s (200 lbf/in$^2$ ms) impulse, the five ply carbon/balsa panel absorbs the most energy (NTAD) by virtue of plastic deformation at these blast pressure–impulse combinations, while the eight ply carbon/PVC panel absorbs the least energy as it responds more elastically.

Further implications of these findings are that in case of relatively stiffer panels, the supporting structural framing and connections need to be carefully designed such that they allow the maximum demand to be achieved in the panel so as to take full advantage of its energy absorption capability. The framing should also be designed to withstand the higher blast forces transmitted from these panels.

## Conclusions

In this study, pressure versus impulse ($P$–$I$) curves are developed for sandwich composite panels with a variety of skin and core material combinations, to enable the generation of a database of performance envelopes under various blast loading scenarios.

The strength versus deformation properties of the undamaged sandwich composite panels are established by nonlinear quasi-static FE analysis of the component subjected to mid-span deformation under displacement control, with boundary conditions simulating the actual blast tests and idealized to facilitate SDOF modeling.

The analytical predictions are consistent with the experimental data obtained from blast tests. The computational methodology described in this study can also be adopted for comparing the performance characteristics of various other hypothetical sandwich composite panel configurations with no experimental data corresponding to blast loading.

### Funding

This study was funded by ONR grant no. N00014-7-1-1010, Office of Naval Research, Solid Mechanics Program (Dr Yapa Rajapakse, Program Manager).

### Acknowledgment

The sandwich composite panels were fabricated by Dr Uday Vaidya and Dr Selvum Pillay at the University of Alabama, Birmingham.

### Note

i "F0E" are the last three characters of a product code used by manufacturers of the carbon fiber (TORAY), within the context of a surface treatment of carbon fibers, which allows the vinyl ester matrix to adhere to the surface of the otherwise smooth fiber. "F" is designation for sizing type; "0" is designation for surface treated; "E" designates the amount of surface treatment (sizing). Please see link for further details- http://www.toraycfa.com/pdfs/ExplanationofProductCode.pdf

## References


1. Tekalur SA, Bogdanovich AE and Shukla A. Shock loading response of sandwich panels with 3-D woven E-glass composite skins and stitched foam core. *Compos Sci Technol* 2009; 69(6): 736–753.
2. LeBlanc J, Shukla A, Rousseau C, et al. Shock loading of three-dimensional woven composite materials. *Compos Struct* 2007; 79(3): 344–355.
3. Zhu F and Lu G. A review of blast and impact of metallic and sandwich structures. *Electron J Struct Eng* 2007; Special Issue: Loading on Structures: 92–101.
4. Li QM and Meng H. Pulse loading shape effects on pressure–impulse diagram of an elastic–plastic, single-degree-of-freedom structural model. *Int J Mech Sci* 2002; 44: 1985–1998.
5. Fatt MSH and Palla L. Analytical modeling of composite sandwich panels under blast loads. *J Sandwich Struct Mater* 2009; 11(4): 357–380.
6. Departments of the Army, the Navy, and the Air Force. *Structures to resist effects of accidental explosions*. Report no. TM 5-1300/NAVFAC P-397/AFR 88-22, November 2011. Washington, DC: Departments of the Army, the Navy, and the Air Force.
7. Tadepalli T. *Performance evaluation of low-rise concrete frame building structures in moderate seismic zones subject to external blast loading*. PhD Dissertation, Department of Civil Engineering, University of Mississippi, MS, USA, 2010.
8. Tadepalli T and Mullen CL. Vulnerability of low rise buildings to external blast events: damage mapping. In: *Proceedings of inaugural conference of the engineering mechanics institute*, EM08, Minneapolis, MN, USA, 19–21 May 2008.
9. Cheng A, Al-Ostaz A, Mullen CL, et al. *Nano particle reinforced composites for critical infrastructure protection*. Report Submitted to Southeast Region Research Initiative, Managed by UT Battelle for US Department of Energy, Supporting the Department of Homeland Security. Task order. 4000055459, 2009.
10. Tadepalli T and Mullen CL. Simplified blast simulation procedure for hazard mitigation planning. In: *Ninth international conference on structures under shock and impact*, Wessex Institute of Technology, New Forest, Southampton, UK, 3–5 July 2006.
11. Mantena PR, Rajendran AM and Al-Ostaz A. Blast and impact resistant composite structures for navy ships. In: *2010 office of naval research – solid mechanics program: marine composites and sandwich structures conference*, University of Maryland, MD, USA, September 27–29, 2010, pp.379–388.
12. Computers & Structures Inc. Analysis reference manual, SAP 2000V14, Berkeley, USA, 2008.
13. Tadepalli T and Mantena PR. Computational simulation and experimental characterization of sandwich composite panels subjected to blast loads. In: *The 26th annual American society of composites technical conference*, Montreal, Canada, 26–28 September 2011, paper no. 1081.
14. DIAB Group AB. Divinycell H technical manual, October 2010, p.25.
15. Tagarielli VL, Deshpande VS and Fleck NA. The high strain rate response of PVC foams and end-grain balsa wood. *Composites Part B* 2008; 39: 83–91.
16. Walter TR and Subhash G. Density dependency of the mechanical behavior of sandwich core materials. In: *Proceedings of the XIth international congress and exposition*, Orlando, FL, USA, 2–5 June 2008. Bethel, CT: Society for Experimental Mechanics Inc.
17. Biggs JM. *Introduction to structural dynamics*, 1st edn. New York: McGraw-Hill Companies, 1964.

*Materials* 2012, *5*, 922-936; doi:10.3390/ma5050922

OPEN ACCESS

*materials*

ISSN 1996-1944

www.mdpi.com/journal/materials

*Article*

# Surface Fractal Analysis for Estimating the Fracture Energy Absorption of Nanoparticle Reinforced Composites

**Brahmananda Pramanik *, Tezeswi Tadepalli and P. Raju Mantena**

Department of Mechanical Engineering, University of Mississippi, University, MS 38677, USA; E-Mails: tadepali@olemiss.edu (T.T.); meprm@olemiss.edu (P.R.M.)

* Author to whom correspondence should be addressed; E-Mail: bpramani@olemiss.edu; Tel.: +1-662-915-5990; Fax: +1-662-915-1640.

*Received: 19 March 2012; in revised form: 8 May 2012 / Accepted: 11 May 2012 / Published: 23 May 2012*

**Abstract:** In this study, the fractal dimensions of failure surfaces of vinyl ester based nanocomposites are estimated using two classical methods, Vertical Section Method (VSM) and Slit Island Method (SIM), based on the processing of 3D digital microscopic images. Self-affine fractal geometry has been observed in the experimentally obtained failure surfaces of graphite platelet reinforced nanocomposites subjected to quasi-static uniaxial tensile and low velocity punch-shear loading. Fracture energy and fracture toughness are estimated analytically from the surface fractal dimensionality. Sensitivity studies show an exponential dependency of fracture energy and fracture toughness on the fractal dimensionality. Contribution of fracture energy to the total energy absorption of these nanoparticle reinforced composites is demonstrated. For the graphite platelet reinforced nanocomposites investigated, surface fractal analysis has depicted the probable ductile or brittle fracture propagation mechanism, depending upon the rate of loading.

**Keywords:** nanocomposites; low velocity punch-shear; fractured surface; digital microscopy; fractal dimension; fracture energy; fracture toughness

## 1. Introduction

Nanocomposites are being considered for applications in marine structures subjected to blast waves and impact loading. Impact energy mitigation is a requirement for these structures. Characterizing energy absorption response of materials at higher strain rates has gained increasing attention from

researchers. Figure 1 shows the fracture energy contribution as a part of the total absorbed energy during fracture propagation. It also indicates that a major portion of the total energy input to the system during loading is dissipated. Roughness of the fractured surface plays a major role in predicting fracture energy absorption.

**Figure 1.** Contribution of fracture energy to the total energy absorption mechanism during low-velocity impact.

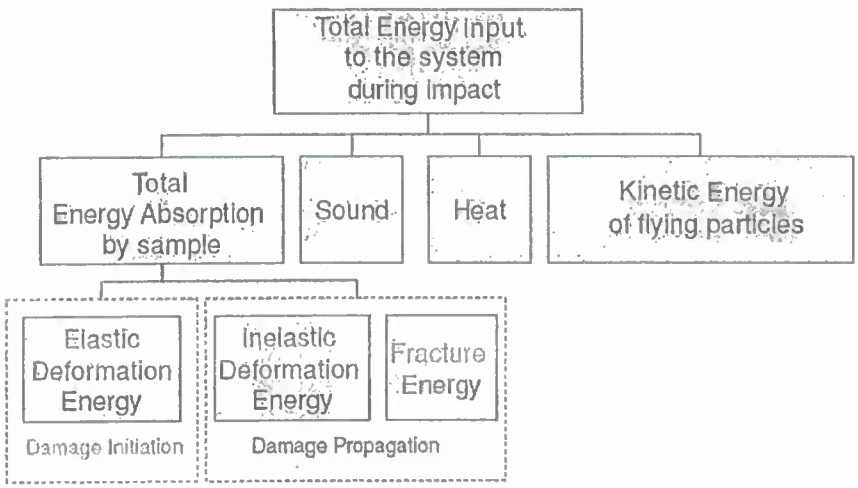


Beginning with the pioneering work by Mandelbrot *et al.* [1], numerous investigators have focused on statistical characterization of the roughness of fractured surfaces [1–10]. It is now evident that the topography of crack surfaces can be described as being self-affine [10]. Self affinity is defined and well-described in the context of fractals by Mandelbrot [2]. As the crack propagates, the scale of tortuosity varies in different axes, which leads to fractal self-affinity of the fractured surface. Hence determining invariant fractal dimensionality of the surface becomes more tedious and multiple scaled-sampling dependent. Griffith states that brittle fracture occurs when the released strain energy is greater than the fracture energy required to create new fracture surfaces [11]. Consequently a more tortuous fractured surface indicates greater fracture energy absorption during crack propagation.

Cherepanov *et al.* [3] discussed several achievements in the field of fractal geometry that influenced fracture mechanics. Hotar *et al.* [4] applied fractal geometry in combination with statistical tools for the classification of surface roughness. Mecholosky [5] showed how fractal geometry can be used in estimating the theoretical strength of materials based on crack tip geometry and generated fracture surface. The applicability of the fractal concept within fracture mechanics has also been discussed in several publications. Kozlov *et al.* [6] showed that the fundamental concepts of fractal fracture mechanics are applicable to polymeric composites. Rodrigues *et al.* [7] applied the concept of fractals to explain the crack deflection toughening mechanism in ceramic materials. Ficker [8] derived the relationship between mechanical strength and fractal characteristics of porous gels and verified with experimental data. Williford [9] expressed the similarity relationship between fracture energy and surface roughness using fractal dimensionality. Lu *et al.* [9,12–14] extended Williford's work to explain the uncertainties of predicting surface fractal dimensionality and illustrated (Figure 2) that the intuitive sense of tougher materials having rougher fracture surface is not commensurate with

experimental observations. The relationships between roughness of fracture surfaces measured by fractal dimensions and toughness are exactly opposite for ductile and brittle materials. Composite materials are reported to have both possibilities.

**Figure 2.** Relationship between fractal dimension of the fractured surface and fracture energy of different materials [9,12–14].

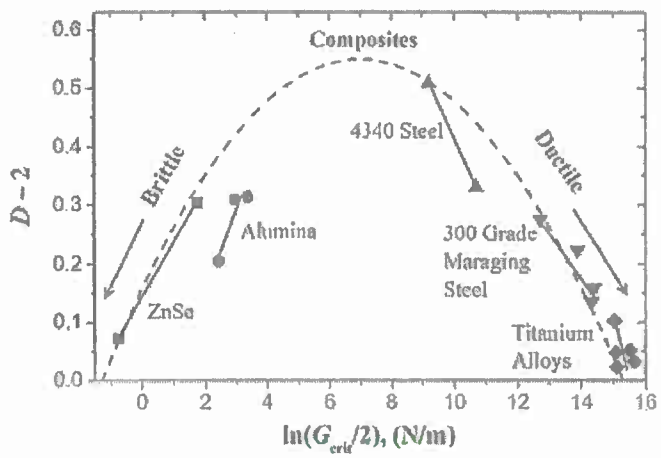


Objective of the work presented here is to quantify fractal dimensionality of the failure surfaces for predicting the fracture energy and toughness of vinyl ester based nanocomposites. The methodologies of estimating fractal dimension of the fractured surfaces are based on the classical Vertical Section Method (VSM) and the Slit Island Method (SIM) described in literature [3]. For our work these conventional methodologies have been adapted such that a digital microscope may be utilized to capture the surface images, which are then digitally processed to create the roughness profiles required for VSM, and the 2D cross sections required for SIM. This eliminates specimen preparation difficulties and increases repeatability. Energy absorption due to fracture and toughness under quasi-static uni-axial tensile and low velocity punch-shear loading is estimated analytically from the surface fractal dimension. To verify the validity of these two procedures, conventional hot rolled A36 steel and grey cast iron specimens that fractured under quasi-static axial tensile loading are also analyzed. A study is conducted to quantify the sensitivity of both fracture energy and predicted fracture toughness to the fractal dimension of the failed surface profile. An investigation on the viscoelastic response of similar nanocomposites reported that the storage modulus varies with temperature as well as frequency in multi-frequency Dynamic Mechanical Analyzer (DMA) [15]. Frequency dependent storage modulus indicates the possibility of different failure characteristics of nanoparticle reinforced composites at varied loading rates. The application of fractal analysis has been considered in the current research to observe the post-failure characteristics of nanocomposite specimens subjected to two different loading rates, *i.e.*, quasi-static and low velocity punch-shear tests. The research findings reported in later sections demonstrate the applicability of surface fractal analysis for nanocomposites.

## 2. Experimental Section

### *2.1. Materials and Methods of Investigation*

Pure Derakane 510A-40 brominated vinyl ester polymer is reinforced with 1.25 wt % xGnP (exfoliated graphite nanoplatelates) and 2.5 wt % xGnP in two different batches. Two batches are modified with a 10 wt % CTBN (Carboxy Terminated Butadiene Nitrile) rubbery toughening agent. The exfoliation and homogeneous dispersion of the nanoplatelets in polymer matrix are performed using sonication technique [16]. Coupons of these four different nanocomposite configurations are tested in quasi-static axial tensile and low velocity punch-shear loading according to ASTM standards D638 and D3763 respectively, and the improvement of mechanical properties is compared with respect to the pristine Derakane 510A-40 brominated vinyl ester polymer samples [17,18]. Specimens that are tested under low velocity punch-shear loading along with the corresponding material properties are shown in Table 1.

**Table 1.** Specimens tested in low velocity punch-shear loading with the corresponding quasi-static uniaxial tensile properties used for estimating fracture energy and fracture toughness [17,18].

| | Types of matrix | Type of reinforcement | Elastic modulus (GPa) | Ultimate strength (MPa) |
|---|---|---|---|---|
| | Brominated 510A-40 Vinyl ester | None | 3.35 | 73.45 |
| | Brominated 510A-40 Vinyl ester | 1.25 wt % xGnP | 3.67 | 40.96 |
| | Brominated 510A-40 Vinyl ester | 2.5 wt % xGnP | 3.38 | 41.96 |
| | Brominated 510A-40 Vinyl ester | 1.25 wt % xGnP + 10 wt % CTBN | 3.48 | 44.58 |
| | Brominated 510A-40 Vinyl ester | 2.5 wt % xGnP + 10 wt % CTBN | 4.68 | 27.68 |

### *2.2. Vertical Section Method*

The fracture surfaces of failed specimens are studied with a Keyence · VHX-600E digital microscope [19] which generates a series of 3D-images (Figure 3a) at optical magnifications of 500×, and 1000× to 5000× with 1000× increment. Global slope of the cracked surface may also contribute to the variation in computed fractal dimension. At each magnification level, the profile roughness (Figure 3b) is estimated by the ratio ($R_L$) of vertical section profile length (obtained from 3D Profile Measurement Software, VHX-H2MK Ver 1.1) to a fixed projection length of 50 μm, consistent for all cases. Surface roughness ($R_S$) is calculated using the following expression [3]:

$$R_s = \frac{4}{\pi}(R_L - 1) + 1 \quad (1)$$

The calibration factor, which is the constant horizontal distance between two consecutive data points on the vertical section profile at a specific magnification level, is used as measurement scale ($d$). The surface roughness ($R_S$) is related to surface fractal dimensionality ($D_S$) [3] as:

$$R_s(d) = Kd^{D_S - 2} \quad (2)$$

where $K$ is the model constant. The fractional part of $D_S$ is evaluated from the slope of linear regression of $R_S$ versus $d$, plotted on log-log scale (Figure 4).

**Figure 3.** (**a**) 3D image and (**b**) vertical section profile of a typical fractured surface.

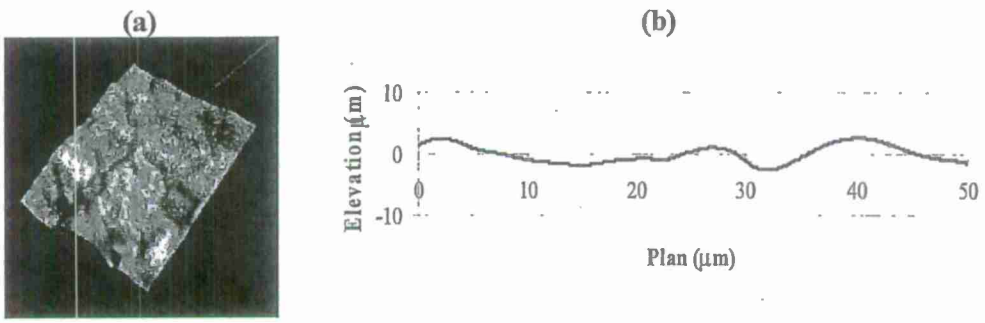


**Figure 4.** Typical fraction of surface fractal dimension from the slope of regression line in Vertical Section Method (VSM).

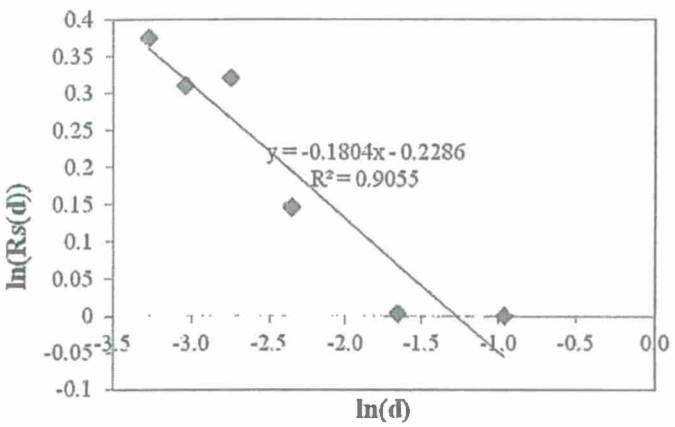

### *2.3. Slit Island Method*

The evident dependency of dimensionality on the ratio of area ($S$) and perimeter ($P$) is applied to estimate the fractional part of $D_S$. Multiple fractured surface 2D images are captured at 1000× magnification by varying the depth of the focal plane of the microscope in 1 micron increment up to a depth of 10 μm under ambient light source. These images represent the closed-loop contour lines at various focal depths. These images are converted to grayscale image for applying "Sobel" edge detection method which returns Black-and-White (BW) images with edges computed based on maximum image intensity gradient. A MATLAB® code, developed in-house, was used for performing image-summation of ten depth-wise consecutive images (Figure 5a) to obtain slit islands at an effective depth of 10 μm along with respective area and perimeter estimation. The image processing functions available in MATLAB® are applied to reduce noise. The white colored area in Figure 5b is considered to be the "Slit Island". The boundary of each island is plotted with a least-count that is one pixel long (0.16 μm), which is considered here as the 'yardstick' for the Richardson approach in estimating dimensionality of the fractured surface. The area of each island is obtained from the region within this boundary.

**Figure 5.** (**a**) 3D topography of a typical fractured surface; and (**b**) Black-and-White (BW) 2D summed-image (1600 × 1200 pixels in 250 μm × 228.8 μm viewport) at 10 μm depth representing islands.

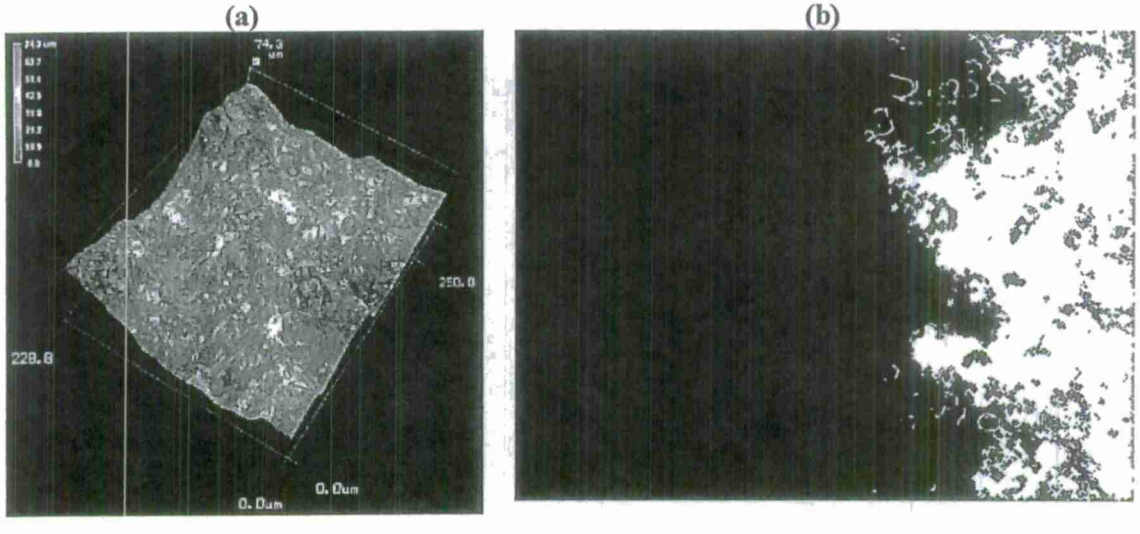


The coordinate of each vertex on the boundary line is determined and the perimeter of each island is estimated by the cumulative summation of the distances of two consecutive vertices. The area and perimeter of all islands are summed to obtain the corresponding total area ($S$) and perimeter ($P$) of fractal islands. The respective $S$ and $P$ are estimated using ten different 'yardsticks' of consecutively increasing length. The least-square fit line is drawn in spread sheet application through $S$ versus $P$ plotted on log-log scale (Figure 6). Slope of this line indicates the fractional part of the fractal dimension ($D_S$) for each crack surface [3].

**Figure 6.** Typical surface fractal dimension estimation from the slope of the regression line in Slit Island Method (SIM).

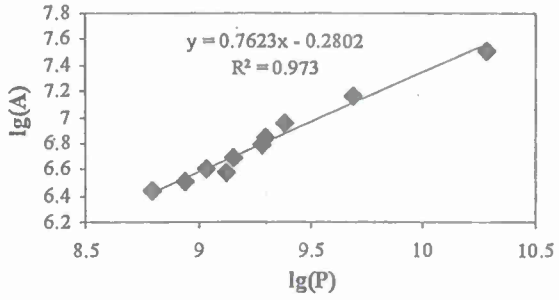


### *2.4. Fracture Energy and Toughness Estimation*

The fractal dimension ($D_S$) of the fracture surface described in the previous section, is used to determine fracture energy ($J_{IC}$) using the following Equations [20]:

$$J_{IC} = CL^{(D_S-2)} \tag{3}$$

where,

$$C = \frac{\pi S_Y^{\ 2}}{E} \tag{4}$$

$J_{IC}$ = fracture energy, $L$ = scale of observation (approximated by consistent dimensionality), $S_Y$ = Yield strength (ultimate strength for brittle materials), $E$ = Young's modulus. From the estimated fracture energy ($J_{IC}$), the toughness ($K_{IC}$) was evaluated using the following Equation [20]:

$$K_{IC} = \sqrt{J_{IC}E} \tag{5}$$

Parametric sensitivity of the fracture energy obtained from the fractal dimension has been investigated using the well established Equations 3 and 4. Results plotted in Figure 7 show that fracture energy decreases exponentially with linear increment of fractal dimension, indicating that the fracture energy is highly sensitive to the magnitude of the fractal dimension.

**Figure 7.** Theoretical relation of fracture energy with fractal dimension in parametric sensitivity study.

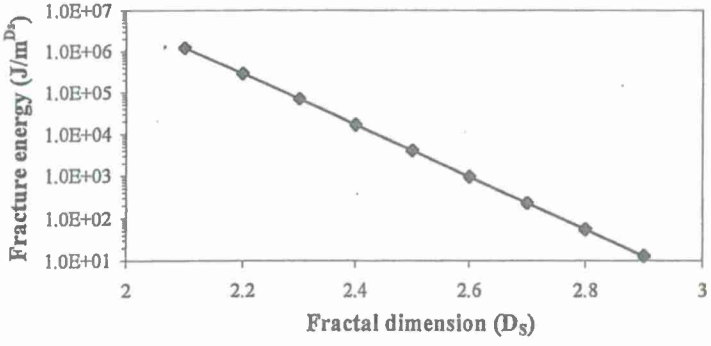


B-86

## 3. Results and Discussion

A series of experiments to determine fractal dimensionality of the nanoreinforced fractured surface are organized in two sections. The first section validates the applicability of the two methods to our investigation. VSM and SIM are used independently to determine the fractal dimension of conventional hot rolled steel and cast iron fractured under quasi-static axial tensile tests. Dimensionalities so obtained are compared with the trend of tortuosity evaluated using the concept explained in earlier studies [11,17]. A large difference is observed between the dimensionalities obtained from VSM and SIM. The possibility for systematic errors is higher in Vertical Section Method, which is based on surface fractal measurements covering a broad range of scales with limited steps of magnification. However, such errors are reduced in the case of Slit Island Method, but at the expense of introducing scale dependent estimates since the fractal dimensionality is estimated at a certain scale. The dimensionality values of cast iron and steel obtained by VSM method are found to be similar to values published in literatures [21,22], and follow a trend similar to that observed for tortuosity. Hence analysis for fracture energy and fracture toughness of all specimens in current investigation is based on the dimensionalities obtained from VSM. The second section determines the fractal dimensionality of nanoparticle reinforced composite specimens fractured under quasi-static tensile and under low velocity punch-shear loading. Average of fractal dimensionalities obtained from five locations on the fractured surface of each specimen is estimated for further analysis. The respective average fractal dimensionalities are shown in Table 2. In general, a higher dimensionality is observed in dynamically punch-sheared specimens as compared to specimens that failed under quasi-static axial tension.

**Table 2.** Surface fractal dimension of nanocomposites under quasi-static axial tensile and low velocity punch-shear loading.

| | Quasi-static axial tensile test | | | Low velocity punch-shear test | | |
|---|---|---|---|---|---|---|
| | VSM * | SIM * | Tortuosity # | VSM * | SIM * | Tortuosity # |
| A36 hot rolled Steel [18,19] | 0.078 | 0.700 | 0.037 | – | – | – |
| Cast Iron | 0.159 | 0.865 | 0.085 | – | – | – |
| Vinyl ester | 0.139 | 0.348 | 0.026 | 0.181 | 0.742 | 0.042 |
| Vinyl ester + 1.25 wt % xGnP | 0.161 | 0.463 | 0.034 | 0.269 | 0.766 | 0.075 |
| Vinyl ester + 2.5 wt % xGnP | 0.189 | 0.662 | 0.039 | 0.127 | 0.647 | 0.051 |
| Vinyl ester + 1.25 wt % xGnP + 10 wt % CTBN | 0.182 | 0.574 | 0.042 | 0.161 | 0.743 | 0.063 |
| Vinyl ester + 2.5 wt % xGnP + 10 wt % CTBN | 0.214 | 0.622 | 0.056 | 0.127 | 0.703 | 0.050 |

* Fractional part of fractal dimensions; # Surface roughness [11,17].

Experimental results obtained using VSM are further analyzed to study the correlation of surface fractal dimension (Figure 8) with fracture energy, as well as fracture toughness, under both quasi-static tensile and low velocity punch-shear loading. Nanocomposite specimens that fractured under quasi-static tensile loading show an increase in the fracture surface dimensionality with increasing graphite and CTBN reinforcement (Figure 8). Fracture energy and the corresponding fracture toughness (estimated from average fractal dimensionality using theoretical Equations 3 to 5, and

shown in Figure 9 (a,b) respectively) demonstrate a decrease in energy absorption due to fracture surface creation with increase in nanoparticle reinforcement.

**Figure 8.** Surface fractal dimension (from VSM) of nanocomposites under quasi-static axial tensile loading.

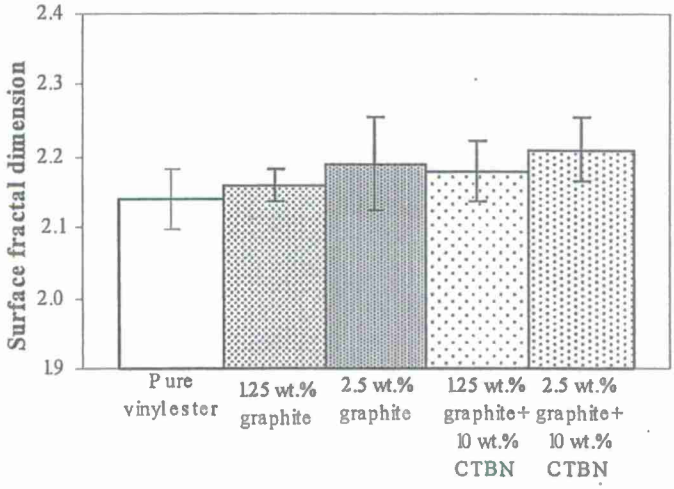


**Figure 9.** Theoretically estimated (**a**) fracture energy and (**b**) fracture toughness of nanocomposites under quasi-static axial tensile loading.

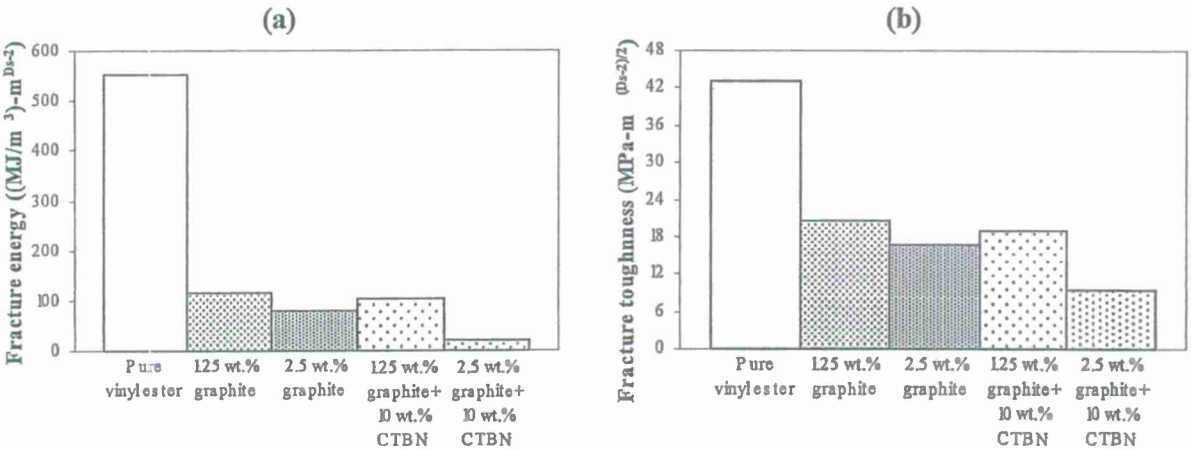


Area under the experimental load-deflection response curve (Figure 10a) provides the total energy absorption corresponding to all failure mechanisms (Figure 10b) under quasi-static tensile loading. It is to be noted that all experimental data has been normalized to the respective specimen areal density-NTAD [17,18].

Though fracture contributes to only a part of this total energy absorption, overall trend between the theoretically estimated fracture energy and experimentally obtained total energy absorption are not in good agreement for quasi-static axial tensile loading.

**Figure 10.** Experimentally obtained (**a**) load-deflection response; and (**b**) total energy (NTAD) absorption of nanocomposites under quasi-static axial tensile loading.

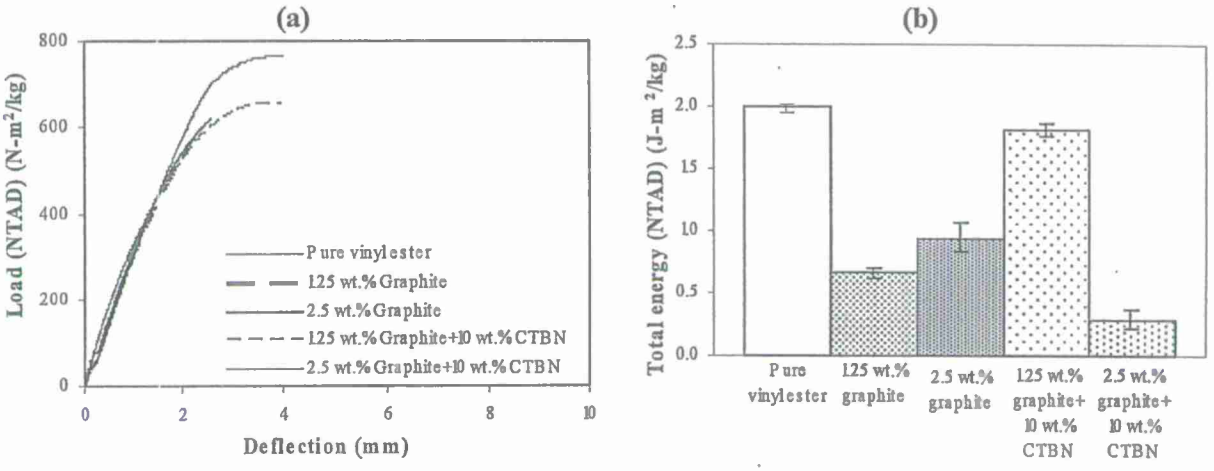


In the case of low velocity punch-shear, the correspondence between surface fractal dimensionality and nanoreinforcement is somewhat decreasing (Figure 11) except 1.25 wt % xGnP reinforced nanocomposite which is indicating that the fracture surface for this nanocomposite configuration was the most tortuous. The fractal dimension decreases, however, when this reinforcement is supplemented with 10 wt % CTBN toughening agent.

**Figure 11.** Surface fractal dimension (from VSM) of nanocomposites under low velocity punch-shear loading.

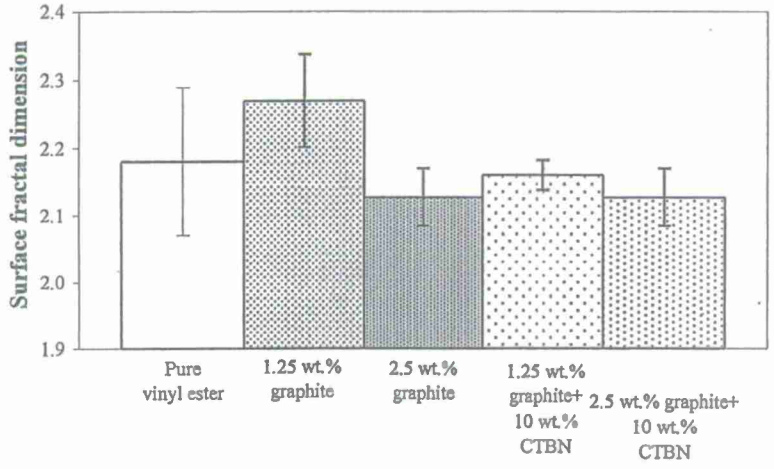


Figure 12a compares the nanoreinforced fracture energy and toughness estimated theoretically using Equations 3 to 5 for each material configuration. It reflects a similar decreasing trend with respect to the experimentally obtained fractal dimension shown in Figure 11, except for the 1.25 wt % graphite reinforcement. Figure 12b illustrates the fracture toughness of these nanocomposites estimated from Equation 5, and shows the same trend as fracture energy (Figure 12a).

**Figure 12.** Theoretically estimated (**a**) fracture energy; and (**b**) fracture toughness of nanocomposites under low velocity punch-shear.

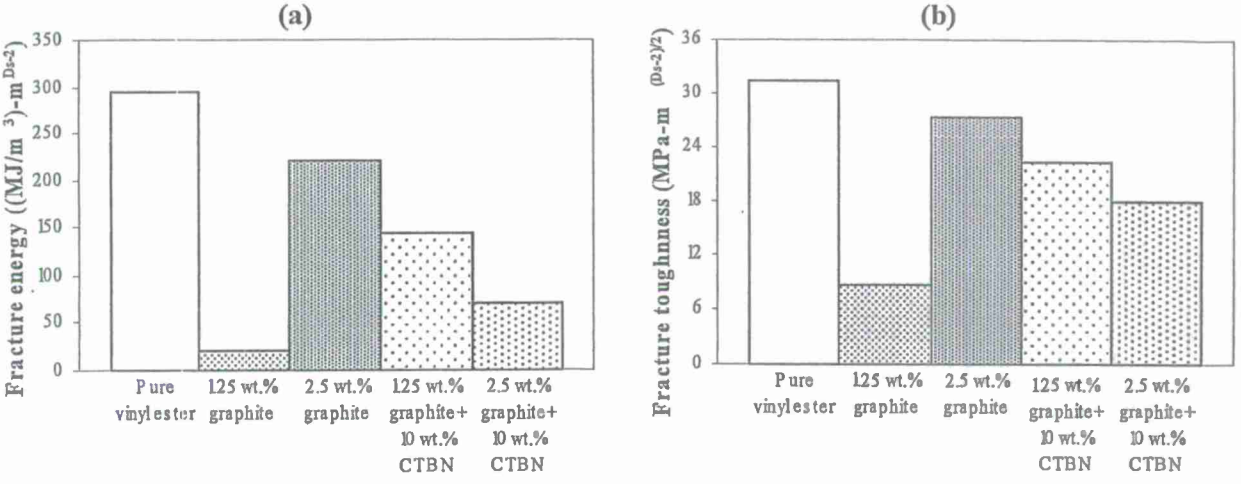


In low velocity punch-shear tests, damage propagation due to puncture is observed to occur after the first peak load of the load-deflection response. Hence, as shown in Figure 13a, and also described in Figure 1, the total load-deflection response is divided into two phases, *i.e.*, damage initiation phase and damage propagation phase. The load-deflection response (Figure 13b) from low velocity punch-shear tests on the same set of nanocomposites was studied in a previous investigation [17]. The amount of energy absorbed during each phase is the area under the corresponding portion of the load-deflection curve. Fracture energy is only a part of the total energy absorbed during the puncture propagation phase. In the post-test fractured specimens investigated here, the theoretically estimated fracture energy (shown in Figure 12a) does not show a trend similar to either energy absorption due to damage propagation (Figure 14a), or the total energy absorption (Figure 14b).

**Figure 13.** (**a**) Damage initiation and puncture propagation phase on a typical load-deflection response of nanocomposites under low velocity punch-shear; and (**b**) Experimentally obtained load (NTAD)-deflection response [17].

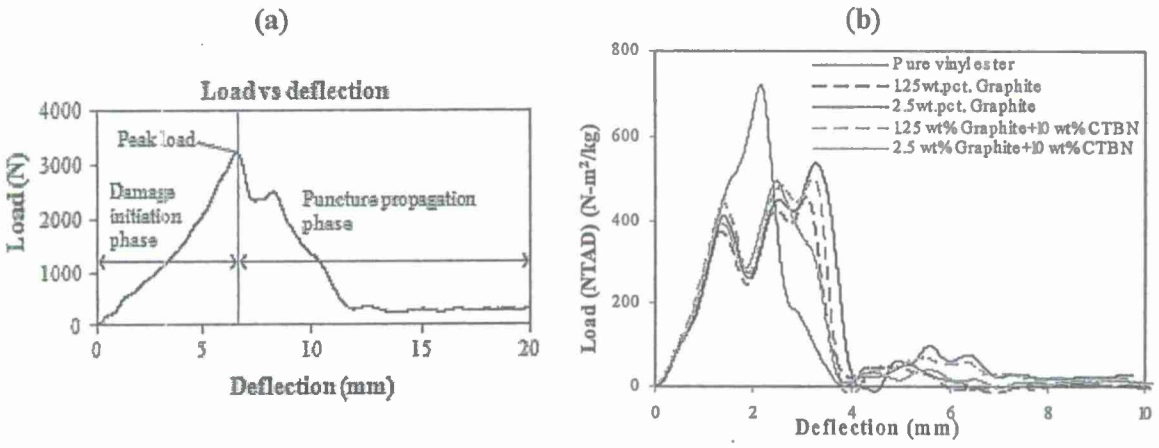

**Figure 14.** Experimentally obtained (**a**) Energy (NTAD) absorption during puncture propagation, and (**b**) total energy (NTAD) absorption of nanocomposites under low-velocity impact.

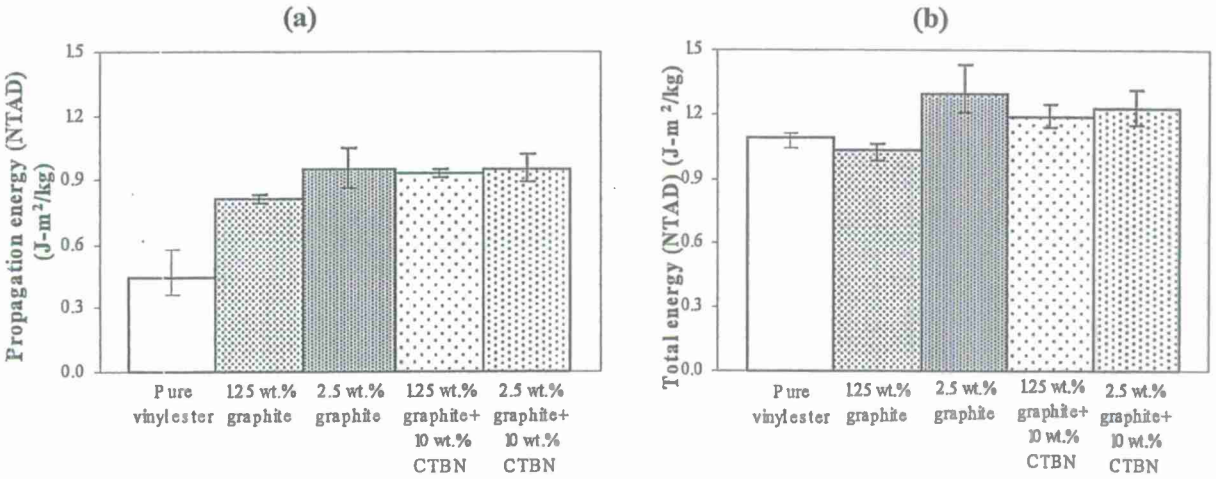


Figure 15 shows the ultimate strength of these graphite platelet reinforced nanocomposites obtained experimentally from quasi-static uniaxial tensile tests. It is observed that the ultimate strength is decreasing with increasing nanoreinforcement, similar to the theoretically estimated fracture energy (shown in Figure 9a and Figure 12a), for both quasi-static and punch-shear failed specimens. The surface fractal dimensionality (shown in Figure 8) increases with decreasing fracture energy and toughness, for quasi-static tensile (Figure 9) loading. This trend is consistent with the ductile response reported in literature [12], and as shown on the right side of Figure 2. On the other hand, low velocity punch-shear tested specimens illustrate decreasing trend for both surface dimensionality (Figure 11) and the fracture energy (Figure 12), which is in agreement with the brittle response shown on the left side of Figure 2. These two different trends between the fracture energy and surface fractal dimensionality for quasi-static and punch-shear loading are conceivable for composite materials [12].

**Figure 15.** Ultimate strength of vinyl ester nanocomposites from quasi-static axial tensile tests.

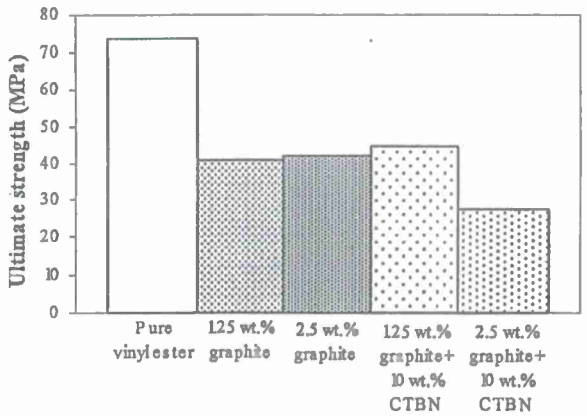

## 4. Conclusions

Applicability of fractal analysis to the study of fractured surfaces in nanoparticle reinforced composites has been investigated. During crack propagation, tortuosity varies at different scales, due to which the fractured surface becomes self-affine at the nano, micro and macro-levels, whereas the currently accepted methodologies are based on self-similar fractals. Hence, dimensionality varies with measuring scales and/or magnification factors and different definitions of dimensionality as well. Determining an invariant fractal dimensionality of the surface becomes dependent on sampling at multiple scales and thus, more tedious.

In the case of nanoparticle reinforced composite materials, heterogeneity of the fracture surface morphology at multiple scales dictates the possible uncertainty in determining an overall fractal dimensionality. In Vertical Section Method, which is based on surface fractal measurements covering a broad range of scales with limited steps of magnification, the possibility for systematic errors is higher. In the case of Slit Island Method, however, since the fractal dimensionality is estimated at a certain scale, such errors are reduced but at the expense of introducing scale dependent estimates. In the work reported here the Vertical Section Method has been used.

In the work reported here, it is observed that the fracture energy and toughness are highly sensitive to fractal dimensionality. The fractal dimensionality increases with wt % increase in xGnP reinforcement under quasi-static uniaxial tensile loading, whereas low velocity punch-shear tested specimens show decreasing trend. An anomaly is observed, however, with 1.25 wt % xGnP which shows the highest dimensionality in case of low velocity punch-shear. The estimated fracture energy and toughness decrease with nanoreinforcement increment for the specimens failed in both quasi-static tensile and low velocity punch-shear loading. This decreasing trend is similar with that of the ultimate strength obtained from quasi-static tensile test. For the graphite platelet reinforced nanocomposites investigated, surface fractal analysis has depicted the probable ductile or brittle fracture propagation mechanism, depending upon the rate of loading.

## Acknowledgments

This investigation was supported by ONR Grant N00014-07-1-1010, Office of Naval Research, Solid Mechanics Program (Yapa D.S. Rajapakse, Program Manager). Graphite platelet vinyl ester composite plates were manufactured by Larry Drzal's group at Michigan State University—Composite Materials and Structures Center.

## References

1. Mandelbrot, B.B.; Passoja, D.E.; Paullay, A.J. Fractal character of fracture surfaces of metals. *Nature* **1984**, *308*, 721–722.
2. Mandelbrot, B.B. Self-affine fractals and fractal dimension. *Phys. Scr.* **1985**, *32*, 257.
3. Cherepanov, G.P.; Balankin, A.S.; Ivanova, V.S. Fractal fracture mechanics—A review. *Eng. Fracture Mech.* **1995**, *51*, 997–1033.

4. Hotar, V.; Novotny, F. Surface profile evaluation by fractal dimension and statistical tools. In *Proceedings of 11th International Conference on Fracture*, Turin, Italy, 20–25 March 2005.
5. Mecholskey, J.J. Estimating theoretical strength of brittle materials using fractal geometry. *Mater. Lett.* **2006**, *60*, 2485–2488.
6. Kozlov, H.V.; Burya, O.; Aloev, V.Z. Application of fractal fracture mechanics to polymers and polymeric composites. *Mater. Sci.* **2004**, *40*, 491–496.
7. Rodrigues, J.A.; Pandolfelli, V.C. Insights on fractal-fracture behavior relationship. *Mat. Res.* **1998**, *1*, 47–52.
8. Ficker, T. Fractal strength of cement gels and universal dimension of fracture surfaces. *Theor. Appl. Fract. Mech.* **2008**, *50*, 167–171.
9. Williford, R.E. Multifractal fracture. *Scr. Metall.* **1988**, *22*, 1749–1754.
10. Schmittbuhl, J.; Roux, S.; Berthaud, Y. Development of roughness in crack propagation. *Europhys. Lett.* **1994**, *28*, 585–590.
11. Griffith, A.A. The phenomenon of rupture and flow in solids. *Phil. Trans. Roy. Soc. London A* **1921**, *221*, 163–198.
12. Lu, C. Some notes on the study of fractals in fracture. In *Proceedings of 5th Australasian Congress on Applied Mechanics*, ACAM 2007, Brisbane, Australia, 10–12 December 2007; pp. 234–239.
13. Bai, Y.L.; Lu, C.; Ke, F.J.; Xie, M.F. Evolution induced catastrophe. *Phys. Lett. A* **1994**, *185*, 196–200.
14. Lu, C.; Ke, F.J.; Bai, Y.L.; Xia, M.F. Numerical simulation of evolution induced catastrophe, *Sci. China Ser. A* **1995**, *38*, 462–471.
15. Pramanik, B.; Mantena, P.R. Viscoelastic response of graphite platelet and CTBN reinforced vinyl ester nanocomposites. *Mater. Sci. Appl.* **2011**, *2*, 1667–1674.
16. Drzal, L.T.; Fukushima, H. Exfoliated graphite nanoplatelets (xGnP): A carbon nanotube alternative. In *Proceedings of NSTI Nanotechnology Coneference and Trade Show*, Boston, MA, USA, 7–11 May 2006.
17. Pramanik, B.; Mantena, P.R. Punch-shear characteristics of nanoclay and graphite platelet reinforced vinyl ester plates, laminated face sheets and sandwich composites under low velocity impact. *ASME Early Career Tech. J.* **2009**, *8*, 56–63.
18. Mantena, P.R.; Cheng, A.H.D.; Al-Ostaz, A.; Rajendran, A.M. Blast and impact resistant composite structures for navy ships. In *the Proceedings of 2009 ONR-Solid Mechanics Program Review*, Adelphi, MD, USA, 21–23 September 2009.
19. *User's Manual 96M00189*; Digital Microscope VHX-600E; Keyence Corp.: Elmwood Park, NJ, USA, 2007.
20. Williford, R.E. Procedure for Estimating Fracture Energy from Fracture Surface Roughness. U.S. Patent 4,860,589, 29 August 1989.
21. Lung, C.W.; Mu, Z.Q. Fractal dimension measured with perimeter-area relation and toughness of materials. *Phys. Rev. B* **1988**, *38*, 781–784.

22. Dlouhy, I.; Strnadle, B. The effect of crack propagation mechanism on the fractal dimension of fracture surfaces of steels. *Eng. Fracture Mech.* **2008**, *75*, 726–738.

© 2012 by the authors; licensee MDPI, Basel, Switzerland. This article is an open access article distributed under the terms and conditions of the Creative Commons Attribution license (http://creativecommons.org/licenses/by/3.0/).

*Open Journal of Composite Materials*, 2012, 2, 87-96
doi:10.4236/ojcm.2012.23010 Published Online July 2012 (http://www.SciRP.org/journal/ojcm)

Scientific Research

# Energy Absorption of Nano-Reinforced and Sandwich Composites in Ballistic and Low-Velocity Punch-Shear

**Brahmananda Pramanik, P. Raju Mantena***

Department of Mechanical Engineering, University of Mississippi, Oxford, USA.
Email: *meprm@olemiss.edu

Received January 25th, 2012; revised February 24th, 2012; accepted March 9th, 2012

## ABSTRACT

This paper presents an investigation on energy absorption characteristics of nano-reinforced panels, laminated face sheets and sandwich composites in high velocity ballistic and low velocity punch-shear experiments. The vinyl ester panels were reinforced with 1.25 and 2.5 wt. percent nanoclay and exfoliated graphite platelets. Three different face sheets were manufactured with E-glass, Owens Corning HP ShieldStrand® glass and T-700 Carbon woven fabric in vinyl ester; and one with the E-glass and graphite platelets impregnated vinyl ester matrix. The sandwich composites were fabricated with balsa, PVC foam, 3D-fiber reinforced Tycor® and fire resistant fly-ash based Eco-Core® cores in between E-glass/vinyl ester face sheets. Ballistic tests were conducted according to NIJ level III using a universal receiver equipped with a barrel to launch 0.308 caliber M80 ball round projectile at about 890 m/s. Low velocity punch-shear tests were performed at around 3 m/s according to ASTM D3763 Standard using a drop-weight impact test system. The tortuosity of the fractured surface in nanocomposite specimens has been investigated using digital microscope. In ballistic tests, the 3-D fiber reinforced Tycor® core provided the most resistance when projectile strikes at the web-flange interface region. The 2.5 wt. pct. graphite platelet reinforced nanocomposite, HP ShieldStrand® glass vinyl ester face sheets, and E-glass/Eco-Core® sandwich composite showed the best energy absorption under low velocity punch-shear.

**Keywords:** Energy Absorption, Tortuosity; Ballistic; Punch-Shear; Nanocomposites; Sandwich Composites

## 1. Introduction

This research is primarily focused on developing stronger, safer and more cost-effective structures for the new generation naval ships; especially nanoparticle reinforced glass/carbon polymeric based composites and structural sandwich composites for blast, shock and impact mitigation. These blast resistant structures must endure the high stresses produced by not only shocks and ballistic, but also low velocity impacts. Minimal damage, with high energy absorption and penetration resistance is desired.

Gama *et al.* [1,2] and Xiao *et al.* [3] performed quasi-static, ballistic and low velocity impact punch-shear tests to define the elastic and absorbed energies of composites as a function of penetration displacement. Shaker *et al.* [4] studied the failure mechanism of basket weave and 3-D braided Kevlar-fabric reinforced epoxy composites under low and high velocity impacts. Hosur *et al.* [5] carried out low velocity impact tests on quasi-isotropic CFRP composite laminates. Deka *et al.* [6] explained the multi-site impact response of laminate composites. The ballistic and punch-shear response of nanoparticle reinforced vinyl ester panels, laminated face sheets and sandwich composites has been investigated in the present work.

NIJ level III Standard [7] was adopted for the high velocity ballistic tests where a universal receiver equipped with a barrel was used to launch 0.308 caliber M80 ball round projectile at about 890 m/s. Dynatup 8250 drop-weight impact test system was used for low velocity punch shear tests according to ASTM D3763 Standard [8]. Low velocity tests were performed on 101.6 mm × 101.6 mm (4" × 4") square panel specimens with fixed circular boundary condition and impacted by a hemi-spherical-head plunger with added mass. The impact load, displacement, energy plots and visual inspection of the post damaged specimen described the punch shear response and failure characteristics of these composites.

## 2. Material Description

Five different DERAKANE 510A-40 vinyl ester thermoset nanocomposite panels, reinforced with 1.25 and 2.5 wt. percent Cloisite 30B nanoclay and exfoliated graphite (xGnP) nanoplatelets, were considered for the nanocomposite specimen characterization. DERAKANE

*Corresponding author.

Copyright © 2012 SciRes.

510A-40 is a brominated bisphenol-A based vinyl ester [9] consisting of 38 wt. pct. styrene, added with Butanone peroxide, N, N-Dimethylaniline, Cobalt Naphthenate and 2-4-Pentanedione additives to impart maximum fire retardance and chemical resistance with toughness. The samples were prepared (at Michigan State University) by dispersing of 510A-40 vinyl ester resin solution with different percentages of nanoclay or nanographite in a container for 4 hours, followed by multiple passes through a flow cell connected to a 100 W sonicator for sufficient exfoliation. The well-mixed vinyl ester resin solution with nanoclay or nanographite was poured into a mold, let stand for 30 minutes at room temperature and then was post cured at 80°C for 3 hours.

Four different woven fabric laminated composite face sheets were fabricated (at University of Alabama, Birmingham) with Dow Derakane 510A-40 brominated vinyl ester resin by the VARTM process. The base specimen is a five-ply E-glass woven fabric with laminate schedule [(0/90)/(+45/–45)/(0/90)/(+45/–45)/(0/90)]. The second face sheet was prepared with same laminate configuration, but with 2.0 wt. pct. xGnP-15 exfoliated graphite platelets pre-mixed in the vinyl ester resin before fabrication. The third face sheet was made with five-layers of Owens Corning high performance HP Shield-Strand® glass fabric with similar laminate schedule and resin. The fourth face sheet was made with only three plies of FOE treated T-700 carbon fabric [(0/90)/(+45/–45)/(0/90)] laminate schedule in same matrix. Here the number of plies was reduced from five to three to keep stiffness of this carbon fabric laminate consistent with the other glass fabric face sheets.

Six different types of sandwich composites fabricated with 2" thick Tycor® (an engineered 3-D fiber reinforced damage tolerant core from WebCore Technologies), poly-vinyl chloride (PVC) foam, balsa-wood and three types of fire-resistant Eco-Core® (fly-ash based core material mixed with chopped JM3 and OC2 glass-fibers) sandwiched in between the five-ply E-glass/vinyl ester face sheets were fabricated (at University of Alabama, Birmingham) using VARTM process.

Areal density is one of the important parameters used for comparing the blast resistance of different composites with respect to steel [10]. All specimens investigated are of lesser areal density than that of a 6.35 mm (0.25") thick structural steel plate with 48.8 kg/m$^2$ (10 lb/ft$^2$) areal density (Table 1). The dynamic responses are reported here by normalizing the load and energy absorption data to their respective areal densities (NTAD).

## 3. Experimentation

The high velocity ballistic experiments were conducted

**Table 1. Arcal densities of nanocomposites, laminated face sheets and sandwich composites.**

| | | *Volume Density* | | *Areal Density* | | *Thickness* | |
|---|---|---|---|---|---|---|---|
| | | (kg/m$^3$) | (lb/in$^3$) | (kg/m$^2$) | (lb/ft$^2$) | (mm) | (in) |
| Nano-composites | Pure vinyl ester | 1338 | 0.048 | 14.0 | 2.867 | 10.0 | 0.39 |
| | 1.25 wt. pct. nanoclay | 1347 | 0.049 | 14.0 | 2.867 | 10.0 | 0.39 |
| | 2.5 wt. pct. nanoclay | 1352 | 0.049 | 14.0 | 2.867 | 10.0 | 0.39 |
| | 1.25 wt. pct. graphite | 1352 | 0.049 | 14.0 | 2.867 | 10.0 | 0.39 |
| | 2.5 wt. pct. graphite | 1363 | 0.049 | 13.0 | 2.663 | 10.0 | 0.39 |
| Laminated face sheets | E-glass | 1875 | 0.068 | 6.10 | 1.258 | 3.30 | 0.13 |
| | E-glass/xGnP | 1747 | 0.063 | 8.40 | 1.721 | 4.80 | 0.19 |
| | HP-glass | 1833 | 0.066 | 5.50 | 1.123 | 3.00 | 0.12 |
| | T-700 Carbon | 1398 | 0.051 | 2.20 | 0.449 | 1.60 | 0.06 |
| Sandwiches | E-glass/Tycor | 386 | 0.014 | 22.6 | 4.623 | 57.2 | 2.25 |
| | E-glass/PVC | 360 | 0.013 | 20.4 | 4.187 | 57.2 | 2.25 |
| | E-glass/Balsa | 471 | 0.017 | 27.1 | 5.556 | 57.2 | 2.25 |
| | E-glass/Eco 0.0wt.pct. | 637 | 0.023 | 36.8 | 7.540 | 57.2 | 2.25 |
| | E-glass/Eco4.5wt.pct.CO2 | 664 | 0.024 | 37.8 | 7.738 | 57.2 | 2.25 |
| | E-glass/Eco4.5wt.pct. JM3 | 664 | 0.024 | 38.3 | 7.837 | 57.2 | 2.25 |
| Structural steel (for comparison) | | 7861 | 0.284 | 48.8 | 10.00 | 6.35 | 0.25 |

Copyright © 2012 SciRes. 

in accordance to the National Institute of Justice (NIJ) Threat Level III (M80) Standard [7]. The test weapon with an unvented velocity test barrel was mounted in the Universal Receiver (**Figure 1**). The receiver was attached to a table with sufficient restraint to ensure accurate shooting of repetitively fired rounds. Manually-loaded bullets of 9.6 grams (147 grains), 7.62 mm (0.308") nominal diameter and 28.2 mm (1.11") length were covered with an electro-deposited copper jacket.

Five specific shot locations were marked on each of the sandwich composite panels, three of them were closely located to get the relative ballistic interaction for sequential shots. For the Tycor® sandwich panel two target marks were at the web-intersection and other three marks were at the foam core region, to characterize the responses from different regions of the 3D-stitched core sandwich. The infrared ballistic screens and the proof chronograph captured striking and residual velocities respectively to determine the energy absorption characteristics of the sandwich panels.

Low velocity punch-shear experiments were performed using Dynatup 8250 drop weight impact test system according to ASTM D3763 Standard [8]. The specimen clamp assembly (**Figure 2**) consists of parallel rigid steel plates with a 76.2 mm (3") diameter hole in the center. Sufficient clamping force was applied to prevent slippage of the specimen during impact. Plunger assembly consists of a 12.70 mm (0.5") diameter steel rod of 50.8 mm (2") length with a hemispherical end of the same diameter positioned perpendicular to, and centered on the clamp hole.

Three samples from each type of nanoparticle reinforced vinyl ester panels, laminated face sheets and sandwich composites were tested under low velocity impact and the average data was considered for this investigation. A steel plunger was used for penetrating the specimens with the required impact energy and velocity. Impact drop weight and height were determined such that velocity slowdown at peak load point was less than 20% of impact point and the applied impact energy was at least three times the energy absorbed by the specimen at peak load [8]. This configuration provided about 38 J of impact energy and 3.6 m/s impact velocity for the nanocomposites and about 185 J impact energy and 4 m/s impact velocity for the laminated face sheets and sandwich composites.

## 4. Results and Discussion

High velocity ballistic damage was observed to have maximum destruction in through thickness cross-sectional view of Tycor® sandwich panel (**Figure 3**). The projectile, in this particular case, penetrated the sandwich panel at

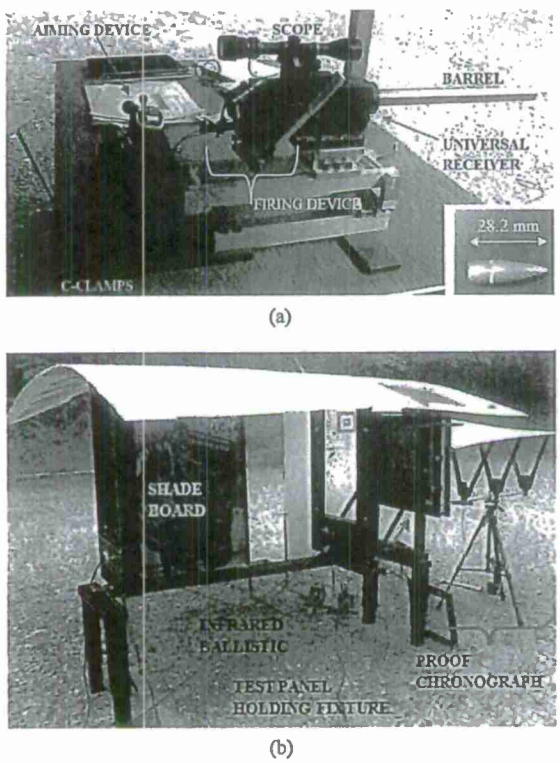


**Figure 1. (a) Ballistic test weapon and projectile (inset); (b) Sandwich test specimen fixture and data acquisition system.**

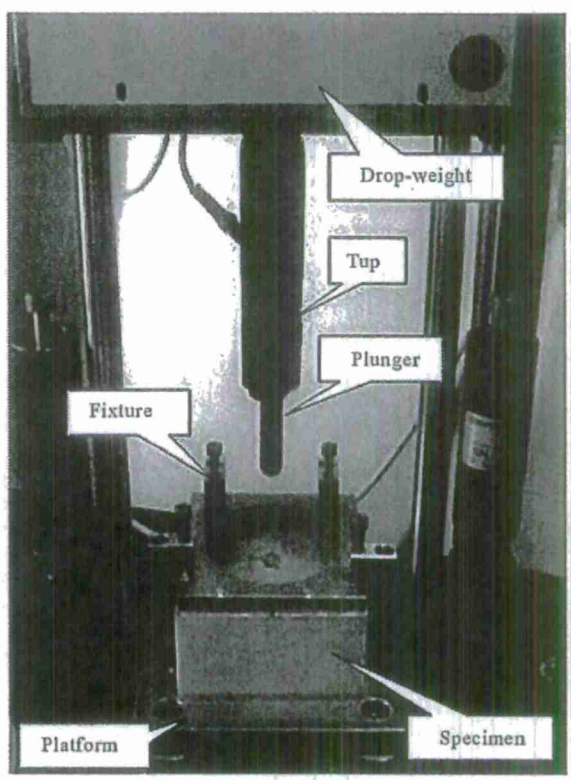


**Figure 2. Low velocity punch-shear test system.**

Copyright © 2012 SciRes.

web-intersection region. The projectile of only 0.308" (7.8 mm) diameter penetrated the panel at about 890 m/s velocity and created a inverted cone shaped damage through the thickness of the panel. It punctured the first face sheet leaving a small damage area on the skin. As in punch-shear testing, the web-intersection region of Tycor® provided significant resistance to the projectile and deflected the penetration path randomly. The projectile with high kinetic energy ripped off the web fibers and foam pieces from their original locations. Large amount of foam pieces came out from the core system bursting out through the other end of face sheet, unweaving the fiber strands and with fiber breakage over a large area on the face skins. PVC, Balsa and Eco-Core® sandwiches showed similar type of face sheet penetration on impact side and back face side (**Figure 3**). The projectile with high kinetic energy punctured the face sheets without much delamination and permanent flexure. Only the fibers were ripped off from the path of projectile. The soft PVC, Balsa cores and brittle Eco-Core® did not offer significant resistance to the projectile. The transversely compressed PVC foam core was decompressed after ballistic penetration. Hence the projectile path was observed to be narrower than the size of projectile. Balsa sandwich allowed the projectile to penetrate through its balsa core with easy fiber-shear and transverse compaction, hence the penetration hole had the same diameter of the projectile. Eco-Core® fragments were dislodged from the cylindrical path of the projectile creating a cylindrical penetration hole of larger diameter.

A drop in the projectile velocities during complete penetration through each sandwich panel was observed. The kinetic energy (KE in J) absorbed by the target panel was calculated [4] using Equation (1):

$$KE = \frac{1}{2} m\left(V_S - V_R\right) \quad (1)$$

where, $m$ = projectile mass (kg), $V_S$ = striking velocity (m/s) and $V_R$ = residual velocity (m/s).

**Figure 4** illustrates the overall energy absorption capacity (normalized to areal density) of the sandwich panels. It shows that Tycor® core sandwich panel absorbed maximum kinetic energy, whereas Balsa core and Eco-Core® with 4.5 wt. pct. OC2 chopped glass fibers sandwich panel took the least. PVC foam core sandwich absorbed slightly higher energy than Balsa core sandwich but much less than the Tycor® core sandwich panel.

Residual velocities of the projectiles were not recorded for last three shots on PVC foam core panel and last four shots of Tycor® foam core panel, which would have given a better understanding of the material behavior. Debris and other small particles from the punctured foam masked these residual velocity measurements. This did not happen in case of Balsa wood core panels. It is to be

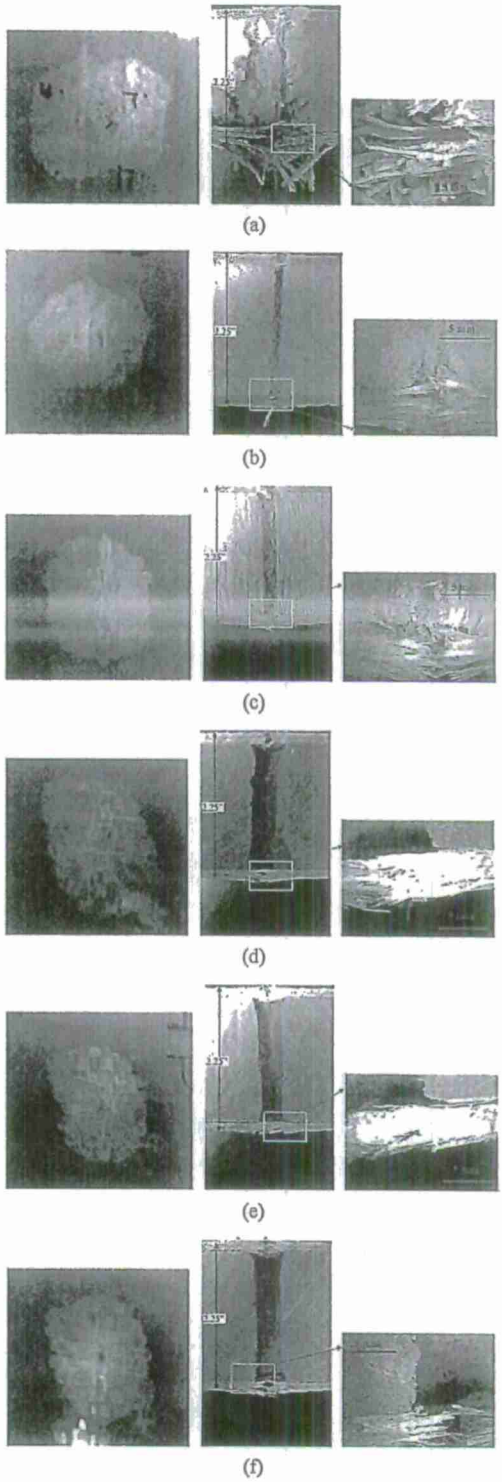


**Figure 3. Sandwich composites made with five-ply E-glass face sheets and light-weight cores after ballistic impact (a) E-glass/Tycor impacted web-intersection; (b) E-glass/PVC; (c) E-glass/Balsa; (d) E-glass/EcoCore 0.0 wt. pct.; (e) E-glass/EcoCore 4.5 wt. pct. JM3 and (f) E-glass/Eco-Core 4.5 wt. pct. OC2.**

Copyright © 2012 SciRes.

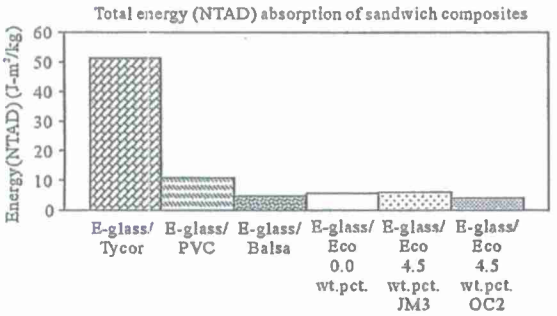


**Figure 4. Energy absorption of sandwich composites in ballistic tests.**

noted that Shot ID 4 in Tycor® foam core panel shows higher residual velocity as well as the back face of panel shows large opening of the fractured skin at the shot location, which indicates that the projectile momentum was partly transferred to the large but light weight particle of foam which moved faster than the bullet during exit. The proof chronograph captured the higher velocity of the particle and not that of the projectile. Under these circumstances, the proof chronograph was triggered by the particle velocity which was higher than the projectile, causing erroneous results.

In low velocity punch-shear tests, the radial growth of damage in brominated 510A-40 vinyl ester nanoparticle reinforced composite panels; centering impact point was less for pure vinyl ester than its nanocomposites (**Figure 5**). Nanoclay reinforced composites were damaged equally on both faces, whereas graphite platelet reinforced composites showed more damage on the rear than impact side. In some cases of graphite platelet reinforced nanocomposites, fracture propagated very less on impact side. Penetration of plunger through the specimen required some more load due to the shearing friction between plunger wall and the inner surface of the punch through hole, which resulted in additional energy absorption.

Post-test views (**Figure 6**) of laminated woven fabric composite face sheets showed that radial growth of delamination was less for the E-glass/vinyl ester face sheet than HP-glass/vinyl ester face sheet and occurred on reverse side for both. Due to opacity of E-glass/xGnP-vinyl ester and T-700 Carbon/vinyl ester face sheets, the occurrence of delamination was not visible. In case of T-700 Carbon/vinyl ester face sheets, carbon fiber strands were peeled off partially from back side. The shredded fibers due to plunger penetration were clogged inside the puncture hole.

The visual inspection (**Figure 7**) of sandwich composites made with five-ply E-glass face sheets and lightweight cores showed that the radial growth of delamination is least in tougher core, and more in case of softer cores. E-glass/Tycor sandwich shows three different

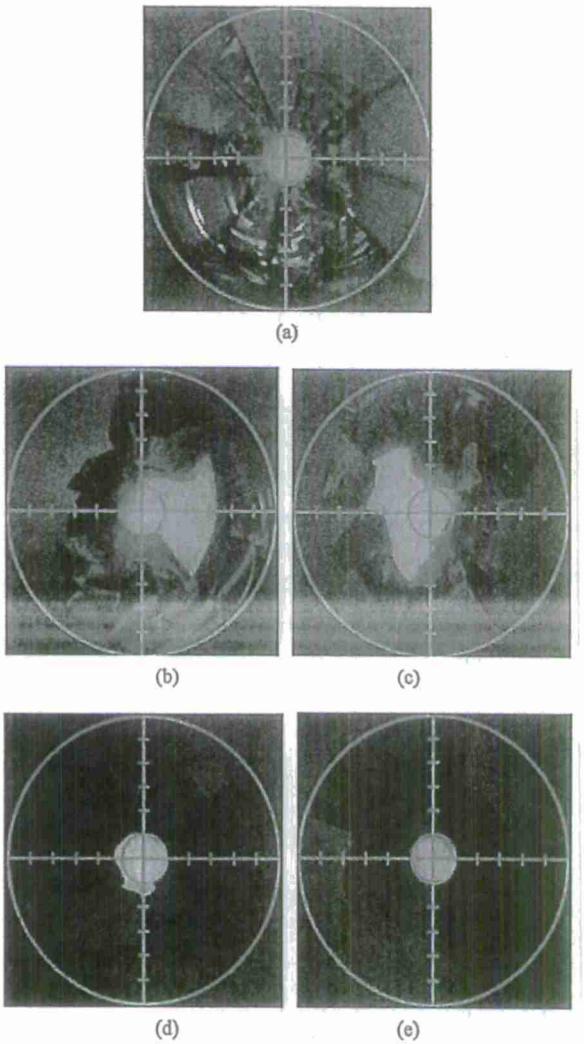


**Figure 5. Back face fracture surfaces of brominated 510A-40 vinyl ester nanoparticle reinforced composite panels after drop weight punch-shear testing. (a) Pure vinyl ester; (b) 1.25 wt. pct. nanoclay; (c) 2.5 wt. pct. nanoclay; (d) 1.25 wt. pct. graphite; (e) 2.5 wt. pct. Graphite.**

modes of failure due to impact at web-intersection, web-line and direct foam zones respectively. It can be observed that the softest foam-zone showed maximum delamination whereas the web-intersection allowed least delamination. Fly-ash based Eco-Core® is the toughest but also has highest density among all. It showed less delamination as well as less depth of penetration. PVC and Balsa cores showed average performance with respect to delamination and puncture.

Tortuosity of the fracture surface contributes to overall energy absorption during fracture propagation [11]. For brittle materials, Griffith criterion suggests that the energy absorbed by the crack growth is proportional to the new surface formed due to crack propagation [12], *i.e.*,

Copyright © 2012 SciRes. 

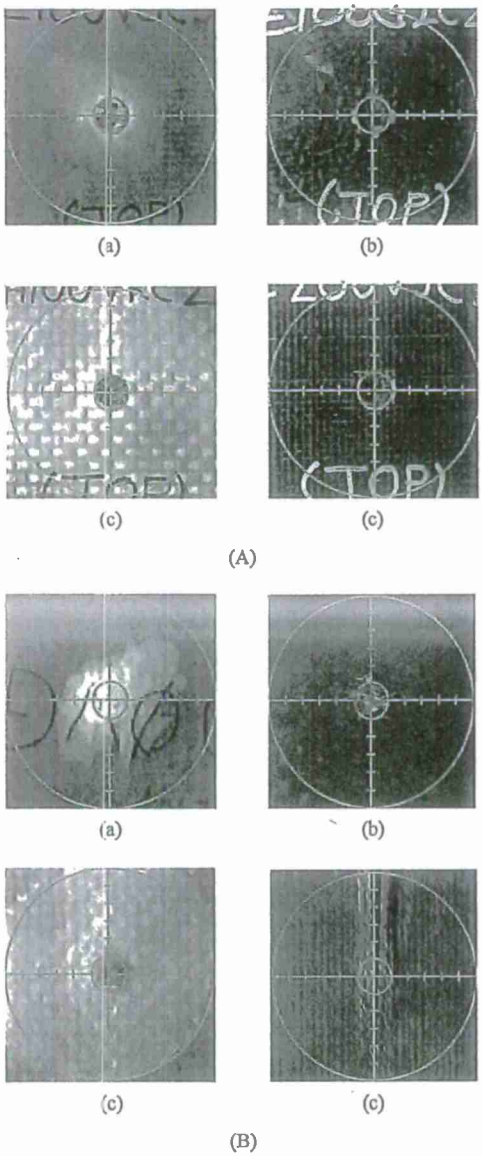


**Figure 6. Laminated woven fabric composite face sheets after punch-shear tests [(A) impact side and (B) reverse side]. (a) E-glass; (b) E-glass/xGnP-15; (c) HP-glass; (d) T-700 Carbon.**

$$E = \int P dx \approx W = 2\gamma a \qquad (2)$$

where, $\gamma$ = specific surface energy (depends on molecular bonding of materials), $a$ = fracture surface area. This surface energy ($W$) contributes significantly to overall energy ($E$) absorption.

In this research, the fracture surface area and the fracture surface roughness of post-test nano-reinforced specimens were estimated using a Keyence VHX-600E digital microscope [13] with a view port of 228.8 μm × 305.0 μm. The fine depth composition function of this

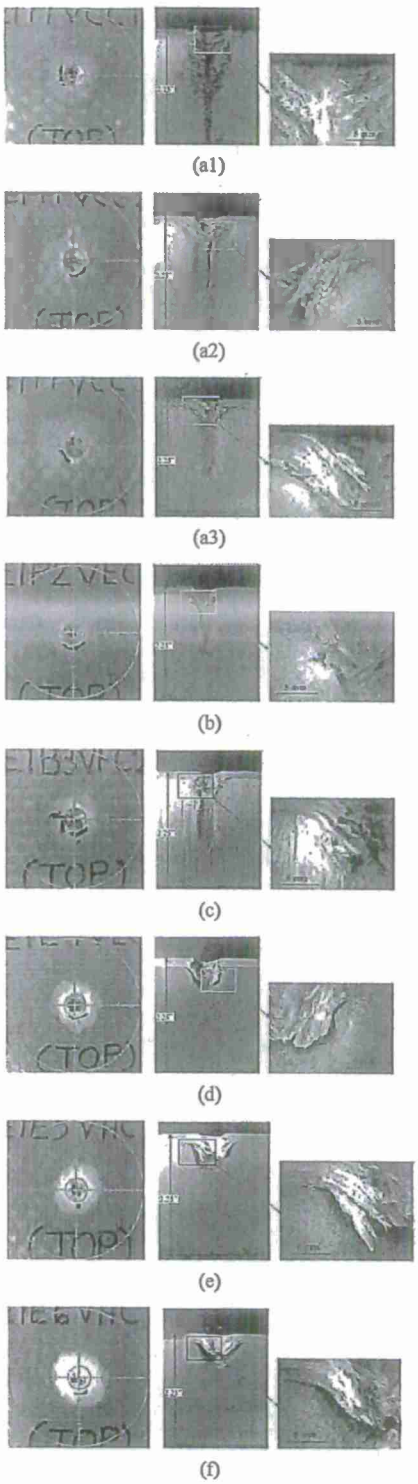


**Figure 7. Sandwich composites made with five-ply E-glass face sheets and light-weight cores after punch-shear tests (a) E-glass/Tycor [impacted at (a1) web-intersection, (a2) web-line, and (a3) foam-region]; (b) E-glass/PVC; (c) E-glass/Balsa; (d) E-glass/EcoCore 0.0 wt. pct.; (e) E-glass/Eco-Core 4.5 wt. pct. JM3 and (f) E-glass/Eco-Core 4.5 wt. pct. OC2.**

Copyright © 2012 SciRes.

microscope system captured multiple images that focused on $70 \times 10^3$ μm$^2$ areas with 20 μm increments of height for focul point and composed them into single 1000 times magnified 3D image. It created the 3-D data points of the fractured surface included in the observation area. These 3-D data points mapped the actual topography of fracture surface and estimated the tortuous surface area of crack propagation under the view port [14]. The longitudinal elevation ($z(x)$) of the surface topography was used to plot fracture surface profile ($L$) [15] and estimated the fracture surface roughness using Equation (3).

$$R_a = \frac{1}{L}\int_0^L |z(x)|dx \quad (3)$$

Surface area and roughness were estimated at 5 different locations on the back face of the post impacted specimen. The average data was considered statistically reasonable for fracture analysis of the nanocomposite specimens.

Pure vinyl ester showed the smoothest fracture surface with an average 3.6 μm roughness and least $85.98 \times 10^3$ μm$^2$ surface area. Nanoclay reinforcement increased the roughness a little more [9.2 μm and 11.2 μm]. Inclusion of graphite platelet reinforcement showed very rough fracture surface. Reinforcement with 2.5 wt. pct. graphite platelet has 29.6 μm surface roughness with $143.71 \times 10^3$ μm$^2$ fracture surface area. Large data scatter showed the heterogeneity of the fracture surface and the structure which is considered inherent to composites.

The Dynatup impulse data acquisition software provided instantaneous impact point displacement and applied load data. The load versus deflection data were plotted up to failure point for each tested sample. Corresponding cumulative energy absorption data were generated using approximate integration method (trapezoidal rule) (Equation (4)) [16].

$$E = \int_{x_{i-1}}^{x_{i+1}} P(x)dx \approx \frac{\Delta x}{2}\left[P(x_{i-1}) + 2P(x) + P(x_{i+1})\right] \quad (4)$$

where, $P$ = instantaneous applied load and $\Delta x$ = increment of material deformation.

Load versus deflection plot showed two distinct phases of failure propagation for complete puncture [2,14]. These two phases are damage initiation, the phase up to the peak load and puncture propagation, the phase of rapid load reduction after peak load. The total energy absorption was calculated as the sum of the energy absorbed for damage initiation and puncture propagation phases up to complete failure of the specimen. The total energy absorptions are normalized to areal density (NTAD) and shown in the form of bar charts to investigate the punch shear response of vinyl ester nanocomposites, laminated face sheets and sandwich composites under low velocity impact.

Pure vinyl ester and nanoclay reinforced vinyl ester showed stiff but linear load-deflection response at damage initiation stage. A little change of slope explained fracture initiations and plastic flow. Graphite platelet reinforced vinyl ester had distinctive multi-peak load fluctuations at this phase. This response showed large fracture generation at the rear side of the specimen. Energy absorption was carried out mainly at this phase. Vinyl ester nanocomposite panels showed sharp and smooth load-reduction. Comparatively harder and brittle graphite platelet reinforced nanocomposites absorbed less energy in puncture propagation phase. Puncture propagation phase absorbed less energy due to short duration and material fragmentation occurred severely with some hinging effects (**Figure 8(a)**). Nanoparticle reinforced vinyl ester panels showed more than 10% improvement in impact energy absorption with the addition of 2.5 wt. pct. graphite platelets to pure vinyl ester. However, the nanoclay and 1.25 wt. pct. graphite platelet reinforcements showed a detrimental effect (**Figure 8(b)**). Fracture surface area and respective fracture surface

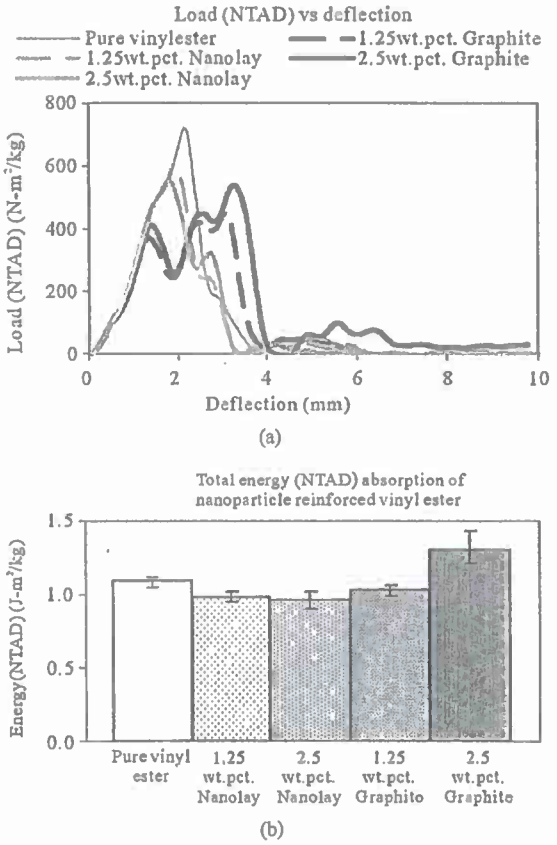


**Figure 8. (a) Load (NTAD)-deflection response, and (b) Total energy (NTAD) absorbed for punch-shear test of vinyl ester nanocomposites.**

Copyright © 2012 SciRes.

roughness (**Figure 9**) show their contribution to total energy absorption. Maximum fracture surface area and surface roughness for 2.5 wt. pct. graphite reinforced nanocomposite contributed to highest energy absorption. For rest of nano-reinforcement, the correlation between fracture surface roughness/area and the total energy absorption is however not that good.

All laminated face sheets showed a smooth elastic deformation with close initial stiffness. NTAD result for T-700 carbon fabric face sheet showed the highest stiffness in later stage than that of the other configurations. HP-glass/vinyl ester face sheet sustained maximum peak load among all. E-glass/vinyl ester and T-700 Carbon/vinyl ester face sheets took more or less same amount of load before puncture. E-glass/xGnP-vinyl ester composite took least load in this phase. However, this face sheet fairly deflected during the damage initiation phase and hence absorbed maximum energy up to peak load same as HP-glass/vinyl ester face sheet; whereas T-700 Carbon/vinyl ester absorbed least energy. Some prominent hinging effects of attached fiber fragments with the surface of the plunger are observed in case of all laminated face sheets. Only E-glass/xGnP-vinyl ester composite showed comparatively smooth puncture propagation. HP-glass/vinyl ester composite face sheet provided lot of resistance after peak load and continued to cause delamination. Hence the load-deflection plot shows a distinctive wavy plateau region at peak load (**Figure 10(a)**). Laminated woven fabric composite face sheets showed that the addition of graphite platelets in vinyl ester matrix absorbed approx. 10% more energy than reference E-glass face sheet; whereas the FOE treated T-700 carbon fabric displayed lowest energy absorption. Maximum improvement in energy absorption (about 40%) was observed with Owens Corning HP Shield-Strand® glass fabric face sheets compared to the E-glass/vinyl ester (**Figure 10(b)**).

The sandwich composites showed (**Figures 11(a)**) five clear peaks indicating failure of each woven fiber lamina on the impact side of face sheets up to peak load. PVC sandwich fails at minimum peak load. All other sandwiches took approximately same amount of load at this phase. In case of sandwich composites, load reduction was very less and slow. Plunger could not penetrate much in the 2.25" thick sandwich specimens. Lot of hinges demonstrated uneven resistance due to ripped

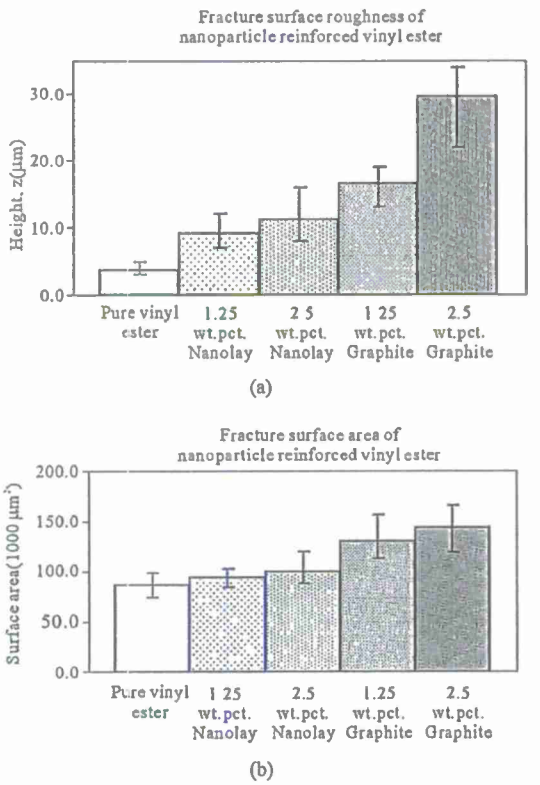


**Figure 9. (a) Fracture surface roughnesses and (b) Fracture surface areas of vinyl ester nanocomposites.**

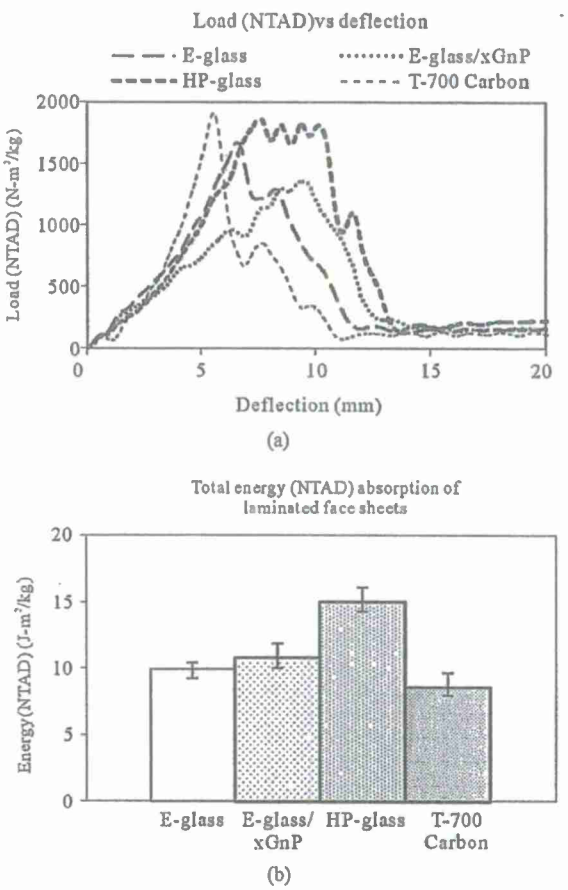


**Figure 10. (a) Load (NTAD)-deflection response, and (b) Total energy (NTAD) absorbed for punch-shear test of laminated face sheets.**

Copyright © 2012 SciRes.

c-102

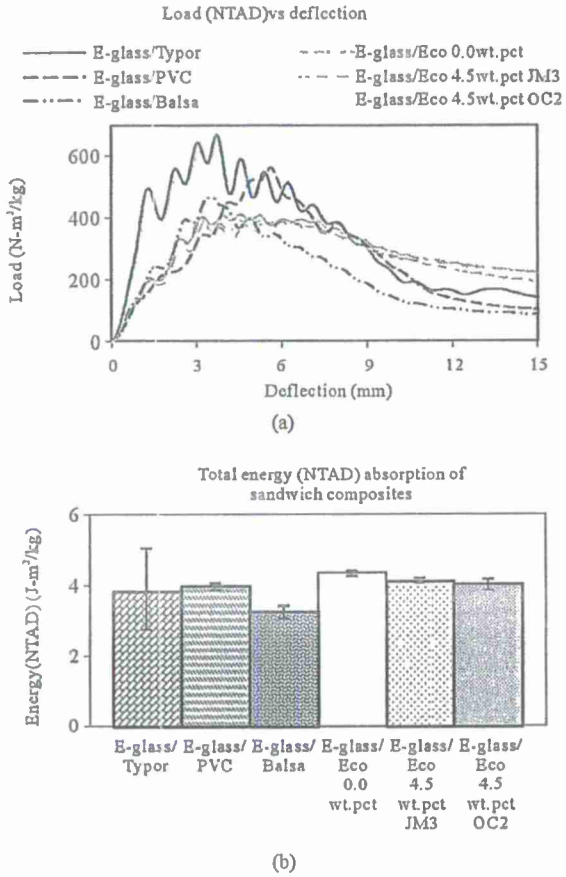


**Figure 11. (a) Load (NTAD)-deflection response, and (b) Total energy (NTAD) absorbed for punch-shear test of sandwich composites.**

fiber and core materials which influenced significant energy absorption after peak load. Sandwich composites made with five-ply E-glass face sheets and light-weight cores showed that PVC and Balsa sandwiches absorbed more or less same energy. The Tycor® sandwich composite has glass fiber webs embedded in the foam core. The punch-shear energy absorption at the intersection of the webs was observed to be double of that at foam-region.

The response at web line was an average of that at other two locations. Spatial non-uniformity of the core resulted in large data scatter, with the average response of Tycor® sandwich composite similar to that of PVC foam and balsa wood sandwich composites. The higher density of Eco-Core® core provided significant resistance to plunger penetration during impact which resulted in higher energy absorption than other sandwich composites made with light-weight and softer core. The energy absorption normalized to areal density (NTAD) showed (**Figure 11(b)**) Eco-Core® sandwich composite having 10% better energy absorption among all, though the chopped glass fiber reinforcement in core did not contribute much in energy absorption improvement. Tycor® sandwich composite absorbed maximum energy only when plunger impacted at web intersection region.

## 5. Conclusions

Sandwich composites were tested under both low velocity punch-shear and high velocity ballistic loading. On impact at the web-reinforcement intersection region, Tycor® sandwich absorbed significant amount of energy in both punch-shear and ballistic tests. However considering overall average performance of the samples, Eco-Core® performed the best in energy absorption during punch-shear tests, but performed poorly in ballistic tests.

High velocity impact loading by a small projectile was observed to be more detrimental to the integrity of a composite structure than low velocity drop weight punch-shear impact loading. Intra-lamina delamination, fiber breakage, face sheet-core separation were more visible in case of high velocity ballistic impact than low velocity punch-shear. The larger impact plunger with lower impact energy damaged the core system lesser than the high velocity projectile. Ballistic penetration occurred in Eco-Core® sandwich by dislodging brittle core fragments and creating a through cylindrical hole. Punch-shear test-plunger could not even penetrate more than 0.6" in 2.25" thick Eco-Core® sandwich composites.

Multi-site high velocity projectile impact testing was conducted on sandwich panels of E-glass/vinyl ester skins with different core materials. The residual velocity of the projectile was highly influenced by the energy absorbability of core materials. Sequential impact caused an increase in delamination damage along with complete core perforation and fiber breakage. The visual analysis of post-impact composite panels concludes that projectiles passed through the panel thickness, tearing and delaminating the E-glass/Vinyl ester skin and penetrating core materials. The delamination and puncture of the skin due to penetration occupied more area at the back face with respect to the front face due to high deceleration rate. Less deceleration of the projectiles was observed for sandwich specimens with balsa and PVC and Eco-Core® cores. Minimally damaged regions indicate lower energy absorption capacity. These unreinforced cores offer less shear resistance at high velocities, while energy absorption enhances with core reinforcement. Tycor® core sandwich panel absorbed maximum kinetic energy, whereas other sandwich panels performed worse in energy absorption. PVC foam core sandwich panel absorbed little bit more energy than other sandwich panel. Eco-Core® sandwich panels could not absorb much kinetic energy of the projectile.

Low velocity punch-shear test results show more than

Copyright © 2012 SciRes.

10% improvement in impact energy absorption with addition of 2.5 wt. pct. graphite platelets to pure vinyl ester, whereas addition of nanoclay and 1.25 wt. pct. graphite platelet reinforcements showed detrimental effect. Owens Corning HP ShieldStrand® glass fabric face sheets showed maximum improvement in energy absorption (about 40%) compared to the E-glass/vinyl ester. High areal density of Eco-Core® sandwich composites showed very high energy absorption among all of the sandwich specimens. The even assessment of energy absorption among these panels have been carried out by normalizing their load taking capacity and energy absorptions to their respective areal densities (NTAD). Eco-Core® sandwiches performed the best in energy absorption; with chopped fiber reinforcements not providing any improvement. Normalized test results showed that Tycor® sandwich composite absorbed higher energy at the web intersection regions.

## 6. Acknowledgements

This investigation was supported by ONR Grant N00014-07-1-1010, Office of Naval Research, Solid Mechanics Program (Dr. Yapa D. S. Rajapakse, Program Manager). The nanoclay and graphite platelet vinyl ester composite panels were manufactured by Dr. Larry Drzal's group at Michigan State University. HP ShieldStrand® glass fabric was supplied by Owens Corning. Composite face sheets and sandwich panels were manufactured and ballistic tests were performed by Dr. Uday Vaidya's group at University of Alabama-Birmingham. Tycor® cores were supplied by WebCore Technologies, Miamisburg, OH. Fly-ash based Eco-Core® cores were manufactured by Dr. Kunigal Shivakumar at North Carolina A & T State University.

## REFERENCES

[1] B. A. Gama and J. W. Gillespie Jr., "Punch Shear Based Penetration Model of Ballistic Impact of Thick-Section Composites," *Composite Structures*, Vol. 86, No. 4, 2008, pp. 356-369. doi:10.1016/j.compstruct.2007.11.001

[2] B. A. Gama, S. M. W. Islam, M. Rahman, J. W. Gillespie Jr., T. A. Bogetti, B. A. Cheeseman, C. Yen and C. P. R. Hoppel, "Punch Shear Behavior of Thick-Section Composites under Quasi-Static, Low Velocity, and Ballistic Impact Loading," *SAMPE Journal*, Vol. 41, No. 4, 2005, pp. 6-13.

[3] J. R. Xiao, B. A. Gama and J. W. Gillespie Jr., "Progressive Damage And Delamination in Plain Weave S-2 glass/SC-15 Composites under Quasi-Static Punch-Shear Loading," *Composite Structures*, Vol. 78, No. 2, 2007, pp. 182-196. doi:10.1016/j.compstruct.2005.09.001

[4] M. Shaker, F. Ko and J. Song, "Comparison of the Low and High Velocity Impact Response of Kevlar Fiber-Reinforced Epoxy Composites," *Journal of Composites Technology and Research (JCTR)*, Vol. 21, No. 4, 1999, pp. 224-229. doi:10.1520/CTR10985J

[5] M. V. Hosur, C. R. L. Murthy and T. S. Ramamurthy, "Low-Velocity Impact Response and Evaluation of Delamination Damage in CFRP Laminates," *Noise Control and Acoustics Division, ASME*, Vol. 24, 1997, pp. 203-214.

[6] L. J. Deka, S. D. Bartus and U. K. Vaidya, "Multi-Site Impact Response of S2-glass/epoxy Composite Laminates," *Composite Science and Technology*, Vol. 69, No. 6, 2009, pp. 725-735. doi:10.1016/j.compscitech.2008.03.002

[7] J. E. Samuels and K. M. Higgins, "Ballistic Resistance of Personal Body Armor, NIJ Standard – 0101.04," *National Institute of Justice* and *National Institute of Standards and Technology*, 2000, Gaithersburg.

[8] ASTM Standard D3763, "Standard Test Method for High Speed Puncture Properties of Plastics Using Load and Displacement Sensors," *ASTM International*, 2006, West Conshohocken.

[9] L. T. Drzal and H. Fukushima, "Expanded Graphite Products Produced Therefrom," US Patent No.7550529, 2009.

[10] E. Wang, N. Gardner and A. Shukla, "The Blast Resistance of Sandwich Composites with Stepwise Graded Cores," *International Journal of Solids and Structures*, Vol. 46, No. 18-19, 2009, pp. 3492-3502.

[11] R. L. Smith, J. J. Mecholsky and S. W. Freiman, "Estimation of Fracture Energy from the Work of Fracture and Fracture Area: I. Stable Crack Growth," *International Journal of Fracture*, Vol. 156, No. 1, 2009, pp. 97-102. doi:10.1007/s10704-009-9350-7

[12] D. Broek, "Elementary Engineering Fracture Mechanics," Martinus Nijhoff Publishers, Leiden, 1982. doi:10.1007/978-94-011-9055-8

[13] Keyence Corporation, "User's Manual 96MOO189, Digital Microscope VHX-600E," Keyence Corporation, 2007, Elmwood Park.

[14] B. Pramanik, "Punch-Shear and Ballistic Energy Absorption Characteristics of Nano-Reinforced Panels, Laminated Face Sheets and Sandwich Composites," M.S. Thesis, University of Mississippi, Oxford, 2010.

[15] M. S. Lou, J. C. Chen and C. M. Li, "Surface Roughness Prediction Technique for CNC End-Milling," *Industrial Technology*, Vol. 15, No. 1, 1999, pp. 1-6.

[16] D. Hyde, "DPlot User Manual," HydeSoft Computing, LLC, 2008, Vicksburg.

Copyright © 2012 SciRes.

# Experimental and Finite Element Modeling of Vinyl Ester Nanocomposites Under Blast and Quasi-Static Flexural Loading

**Ahmad Almagableh,[1] P. Raju Mantena[2]**

[1]*Al-Balqa Applied University, Faculty of Engineering Technology, Mechanical Engineering, Amman 11134, Jordan*
[2]*Composite Structures and Nano-Engineering Research Group, Mechanical Engineering Department, The University of Mississippi, University, Mississippi 38677*

Received 18 August 2011; accepted 26 January 2012
DOI 10.1002/app.36897
Published online 18 May 2012 in Wiley Online Library (wileyonlinelibrary.com).

**ABSTRACT:** Materials used in blast, penetration, and impact loaded structural applications require high strength and toughness under high strain rate loading. 510A-40 brominated bisphenol-A-based vinyl ester resin was developed and reinforced with different loadings of nanoclay and exfoliated graphite platelet to produce composites with optimal flexural rigidity, vibration damping, and enhanced energy absorption. As these reinforced polymeric materials are viscoelastic in principle, the mechanical behavior was characterized under two extremes of strain rate loading. In this article, the macroscopic response of brominated vinyl ester reinforced with 1.25 and 2.5 wt % nanoclay and exfoliated graphite platelet is considered. Air-blast experiment was conducted by subjecting these specimens to a high-transient pressure in a shock-tube with flexural loading configuration. The axial response was investigated quasi-statically in a uniaxial tension/compression test and dynamically in a compression Split-Hopkinson bar test. The servo-hydraulic MTS system was used to simulate the shock-tube testing in a flexural quasi-static loading configuration. High strain rate properties obtained from shock-tube experiment are compared with that of characterized under the simulated quasi-static flexural loading. Further, a computational finite element analysis model was developed in ANSYS LSDYNA to predict with reasonable accuracy the dynamic response of shock-loaded nanoreinforced specimens. Drop in both failure strain and energy absorption was observed with the addition of nanoparticles to pristine vinyl ester. However, an improvement in energy absorption was observed in case of shock-tube loading at high strain rates as compared to that loaded quasi-statically. © 2012 Wiley Periodicals, Inc. J Appl Polym Sci 126: 1895–1905, 2012

Key words: nanocomposites; reinforcement; clay

## INTRODUCTION

Traditional composite materials are no longer capable of satisfying rigorous requirements for materials with enhanced mechanical and thermal properties, nor can they be engineered to control properties at the atomic scale. The essence of such control in properties has derived from the fact that the bulk properties of materials under external loading such as impact pressure or temperature are largely dictated by their molecular level orientation. Eventually, nanocomposite systems could be built at the molecular level to create large structures with primarily new molecular organizations.

What makes nanocomposites attractive is the extremely great interaction between small-scale particles and the matrix resin within the nanostructure. An interphase of 1-nm thick represents about 30% of the total volume in case of nanocomposites where as it reaches to 0.3% of the total volume of polymer in case of microparticle-filled composites.[1] The large interfaces within the nanostructure also enhance adhesion energy which translates into increase molecular bonding, and this increase in chemical bonding develops the polymer crosslinking and improves both mechanical and thermal properties. Conversely, a negligible contribution made by the interphase provides diverse possibilities of performance tailoring and is able to influence the properties of the matrices to a much greater extent under rather low nanofiller loading.

In addition to possessing extremely high mechanical properties (strength and modulus),[2] which are the apparent advantages for polymeric nanocomposites, nanotubes, for instance, are predicted to have an interesting mode of plastic behavior, that is experience a step-wise diameter reduction (local necking) and lattice orientation change.[3] Such highly bendable elastic stretching is extremely useful and could play an important role in increasing the toughness of nanotube-filled composites by increasing the energy absorbed during deformation. Significant improvement in the

*Correspondence to:* A. Almagableh (amalmag1@gmail.com).
Contract grant sponsor: Office of Naval Research, Solid Mechanics Program; contract grant number: N00014-07-1-1010.


© 2012 Wiley Periodicals, Inc.

tensile properties of polypropylene composites has also been reported in terms of stiffening, strengthening, and toughening with a low-filled content of about 0.5%.[4]

Scope of this investigation is to study this class of nanocomposite system against blast loading applications. Applications involve marine composite structures; particularly, lightweight glass/carbon polymeric-based composites, and innovative concepts for the mitigation of blast/shock/impact effects. Sandwich composites with balsa and foam cores are presently being featured in the number of navy applications such as in surface ship deck structures, radar mast, and boat hulls. Several new and emerging cores have been explored in sandwich construction. Different core types have been considered including Tycor (TYCOR® from Webcore Technologies) is an engineered three-dimensional fiber reinforced damage tolerant core for sandwich structures and has the potential to provide improved blast and ballistic resistance. This article presents our recent results on processing of brominated vinyl ester structural composites with nanoreinforcement for marine composite applications. Instead of using the commercial Derakane 411-350 vinyl ester resin, a 510A-40 brominated bisphenol-A-based vinyl ester consisting of 33 wt % styrene was developed and modified to produce the maximum degree of fire retardancy combined with enhanced chemical resistance and toughness. These brominated 510A-40 vinyl ester resin systems are planned to be used in the composite face sheets of sandwich structures with fire-resistant foam layered in between to further reduce flammability along with optimal flexural rigidity, vibration damping, and enhanced energy absorption.

Bromination of vinyl ester resin was found to exhibit good corrosion resistance, toughness, and imparts retardancy of fire, smoke, and toxicity which are of significant concern in ship structures.[5]

Effects of bromination on the viscoelastic properties of Derakane vinyl ester reinforced with 1.25 and 2.5 wt % nanoclay and graphite nanoplatelets were investigated using DMA.[6] Frequency sweep across three decades: 0.01, 0.1, 1, and 10 Hz was performed over temperature range from 30 to 150°C at a step rate of 4°C/min. The time–temperature superposition principle was applied to create master curves of dynamic storage modulus at a reference temperature. Results revealed drop in initial storage modulus with bromination for all the tested specimens; however, pure vinyl ester and nanocomposites with bromination exhibited higher glass transition temperature and damping (Tan $\delta$ peak).

Bromination outcome on punch shear characteristics for laminated face sheets and sandwich composites of vinyl ester nanocomposites was investigated using Dynatup 8250 drop-weight impact instrument.[7] Test results showed that more than 10% improvement in impact energy absorption with addition of 2.5 wt % graphite platelets to brominated resin.

Understanding the panel response to shock loads, and developing accurate mechanical models will help in establishing future design criteria. In this article, the shock response of brominated 510 A-40 vinyl ester with 1.25 and 2.5 wt% nanoclay and graphite platelet is studied. The Split-Hopkinson bar, shock-tube, and the servo-hydraulic Material Testing System were used to characterize the mechanical response of these nanocomposites. A computational efficient FEA model is developed to predict the shock response of these nanoreinforced specimens. Further, the FEA approach was implemented to validate the conducted experiments.

## EXPERIMENTAL

### Materials and sample preparation

The matrix used here is a DERAKANE 510A-40 vinyl ester resin (manufactured and supplied by Ashland specialty chemical, Division of Ashland INC, Columbus, OH). This DERAKANE 510A-40 vinyl ester resin is a brominated bisphenol-A-based vinyl ester consisting of 38 wt % styrene, and modified to produce the maximum degree of fire retardancy combined with enhanced chemical resistance and toughness. These additives are butanone peroxide, *N,N*-dimethylaniline, cobalt naphthenate, and 2,4-pentanedione, all supplied from Sigma Aldrich, St. Louis, MO.

Exfoliated graphite nanoplatelets (xGnP) were produced at Michigan State University according to the method described in Ref. [8] The nanoclay was Cloisite 30B from Southern Clay Products, Gonzales, TX. The xGnP nanocomposites have exfoliated and dispersed graphite platelets with 1-nm thickness and several hundred nanometers widths. Distance between layers is in the range of 10–30 Å and size of the layered graphite extends from several hundred nanometers to several microns. Figure 1(a,b) shows morphology using TEM and SEM for xGnP inside the matrix and Figure 1(c) shows nanoclay dispersion.

Specimens were prepared by dispersing about 6.6 lbs of epoxy vinyl ester resin solution with different percentages of nanoclay/nanographite in a 1-gal container for 4 h, followed by four passes through a flow cell connected to a 100-W sonicator. In brief, 1% butanone peroxide, 0.2% of 2,4-pentanedione, 0.1% *N,N*-dimethylaniline, and 0.2% cobalt naphthenate were added to the mixed vinyl ester resin solution in order and mixed for 10 min. The above

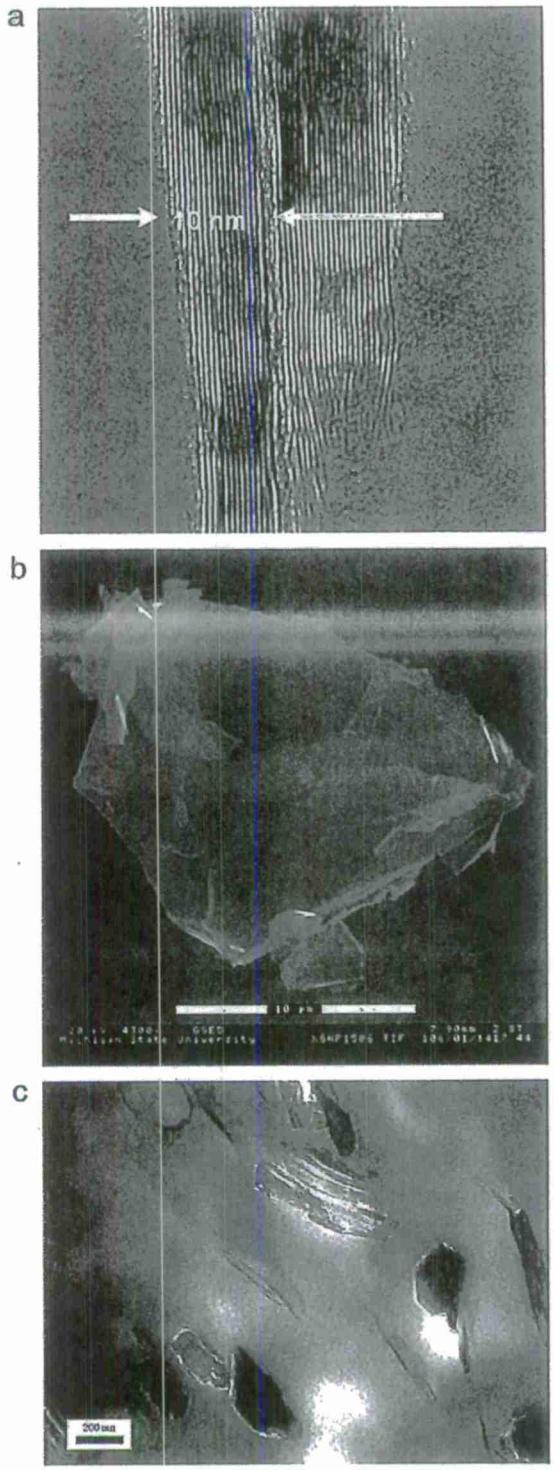


Figure 1 Morphology of nanoparticles dispersion (a) edge view (TEM) of xGnP, (b) lateral view (SEM) of xGnP, and (c) Cloisite® nanoclay.[14]

mixed resin solution was mixed for 2 min with FlackTek speed mixer at 3000 rpm. The well-mixed vinyl ester resin solution with nanoclay/nanographite was poured into a 13" × 13" × 0.4" mold, let stand for 30 min at room temperature, and then was postcured at 80°C for 3 h.

### Quasi-static axial test

Tensile Quasi-static tests on 10-in long specimens were carried out on the Material test system Model 3180 (MTS System, Minnesota, MN) operating at a cross-head speed of 0.05 in/min (corresponding to a strain rate of 0.001/s). Tests were carried out according to ASTM D 638-08 ASTM.[9] An extensometer was employed to measure plastic deformation, and lubricant was applied between the specimen and the loading platens to reduce friction.

Compressive tests on another set of 5.5-in specimens were performed on same machine operating at similar crosshead speed as in tensile test. The compressive force was introduced to the specimen by a typical combined loading compression test fixture according to ASTM D 6641.[10] A strain gauge was attached to the specimen in the compression test setup to measure axial deformation up to 3% strain from which the compressive modulus was estimated.

### Hopkinson bar tests

Split-Hopkinson Pressure Bar (SHPB) is utilized in the high-strain-rate testing of these nanomaterials at a strain rate of 1500/s. The pressure bar consists of a striker bar, an incident bar, and a transmission bar made of steel. Schematic diagram of the SHPB is shown in Figure 2.

A 0.5-in diameter testing specimen is placed between the incident bar and the transmission bar. When the striker bar impacts the incident bar, an elastic compressive stress pulse (shock wave), referred to as the incident wave, is generated and travels along the incident bar toward the specimen. The pulse duration equals the round-trip time of longitudinal elastic bar-wave in the striker bar. When the incident wave reaches the specimen, part of the pulse is reflected back in the incident bar owing to impedance mismatch at the bar/specimen interface, and the outstanding is transmitted through the specimen into the transmission bar.

Strain gages are mounted on the bars; provide time measures of the pulses in the incident and the transmission bars. Dynamic stress–strain and strain rate are calculated based on a one-dimensional elastic bar-wave theory for pulse propagation using Lagrangian diagram.[11]

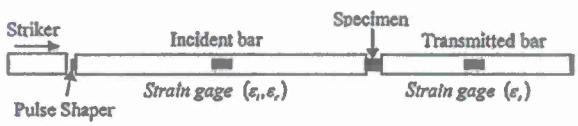


Figure 2 Schematic of Split-Hopkinson pressure bar.

D-107

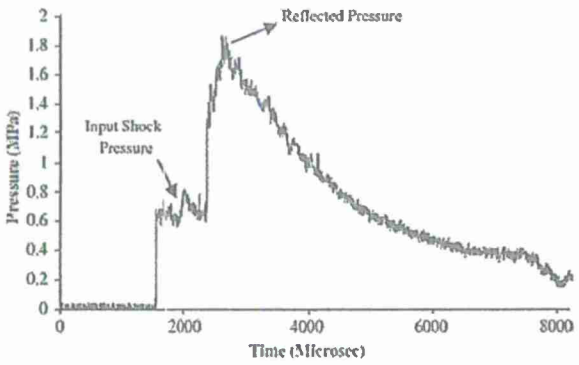


Figure 3 Typical shock pressure profile obtained in shock tube. [Color figure can be viewed in the online issue, which is available at wileyonlinelibrary.com.]

### Air blast loading

A shock tube typically consists of high-pressure (driver) and low-pressure (driven) sections separated by a diaphragm. The driver and driven sections have a 6-in inner diameter and the converging section begins as 6-in diameter and ends 3 in. The tube is operated by pressurizing the high pressure section until the pressure difference across the diaphragm reaches a critical value and it ruptures. This rapid release of gas creates a shock wave that propagates down the tube to impart air blast loading on a specimen.

The shock-loaded brominated nanoreinforced panels were rectangular plates of 10-in long, (4-in wide and 0.39-in thickness). These plates were held under simply supported boundary conditions so as to minimize damage owing to gripping and clamping. The span of the simply supported plate was 6 in, and the overhangs measured 2 in along each end. The center of the specimen was kept in line with the center of the shock tube and the ratio of the loading diameter to the span was 0.5. The specimens were blast loaded from the muzzle of the shock tube on the face opposite to the supports.

The shock tube is instrumented with pressure and velocity measurements to provide real-time data about the shock pressure and shock velocity. A PCB 134A23 dynamic pressure sensor is mounted at the muzzle section of the shock tube and graphite rods are used to measure the shock velocity.

A typical pressure history obtained from shock tube is shown in Figure 3. The first peak pressures obtained in such experiments are called as "input shock pressure." The second peak is the "reflected shock pressure" from the specimen that the shock blast is impinged upon.

### Flexural quasi-static test

The Material Test System machine operating at a crosshead speed of 0.05 in/min (corresponding to a strain rate of 0.001/s) was again used to evaluate the material response under flexural loading with similar boundary and loading configuration as in shock tube experiment. Specimen dimensions and span length of the simply supported conditions were kept similar to shock tube experiment. Quasi-static experiments were conducted under flexural deformation loading using a three-point bending fixture. A 3-in diameter steel cylinder was attached to the load cell through a threaded stud, creating a circular loading configuration (match the shock pressure). The steel cylinder is then embedded inside a bag filled partially with sand in the bottom to simulate uniform pressure distribution up to failure of the specimen. Figure 4(a,b) shows this experimental setup in the MTS system, with and without the sand-bag attached. Loading conditions in Figure 4(b) simulate distributed loading conditions (similar to shock tube test), whereas the load in Figure 4(a) simulates a four-point loading configuration.

A C-clamp fixture was used to mount two external linear variable-differential transformers (LVDTs) at the middle on both sides of the specimen to capture midspan deflection and connected via a strain

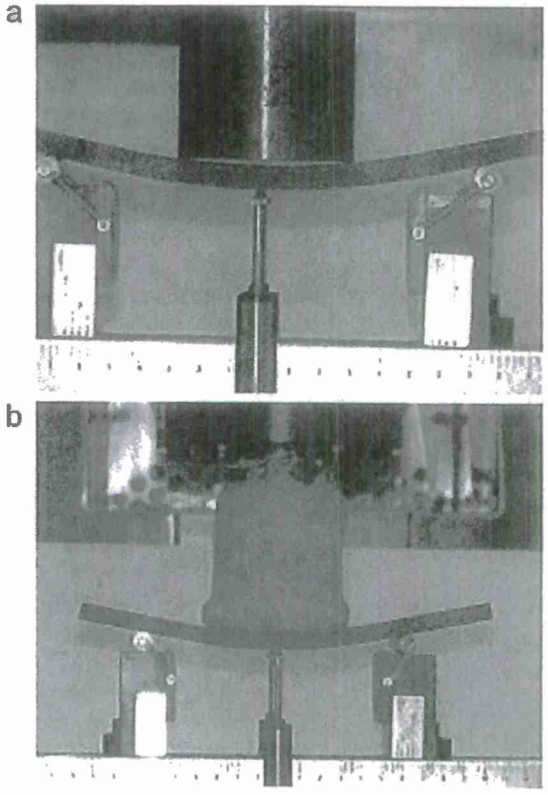


Figure 4 Quasi-static loading of nanoreinforced specimen, (a) without a sand bag, and (b) with the sand bag (to simulate distributed shock tube pressure loading). [Color figure can be viewed in the online issue, which is available at wileyonlinelibrary.com.]



D-108

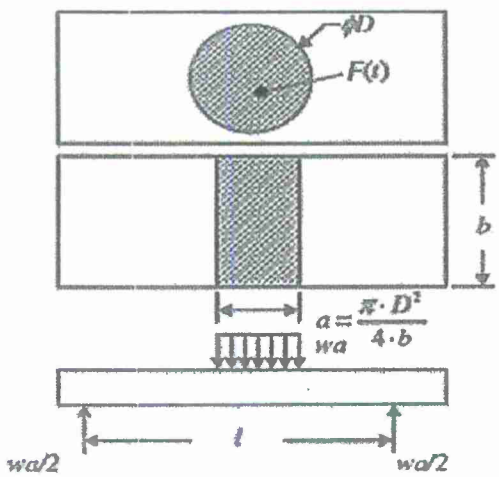


Figure 5 Boundary conditions for shock and flexural quasi-static tests..[11]

indicator box. Load and stroke displacement were obtained from the load cell and actuator movement. It should be noted that the midspan deflection (measured by LVDTs) was not the same as the stroke displacement of the system crosshead, and the two data sets have been synchronized independently over time.

## Strain rate analysis

An approximation of the strain rate under quasi-static flexural loading is computed[12] using bending moment analysis to assess numerical work. The quasi-static flexural strain, $\varepsilon(t)$ can be obtained from Hooks law as:

$$\varepsilon(t) = \frac{M y}{E I} \tag{1}$$

where $E$ and $I$ are young modulus and area moment of inertia, respectively, and $y$ is the distance from the neutral axis. The induced bending moment, $M(t)$, was computed from the load time history obtained at each time step ($t$). The load ($F$) applied on the circular region was approximated as a distributed loading, $w$, (Newton/meter) acting on a rectangular area along the beam width of length, $a$, and width, $b$, as shown in Figure 5.

With this approximation, the maximum bending moment at the midspan is given by:

$$M(t) = \frac{1}{8} F\,(2l - a) \tag{2}$$

Substituting the values of $M(t)$, $y$ and $I$ into eq. (1), $\varepsilon(t)$ is given as:

$$\varepsilon(t) = \frac{1}{8} \frac{F(t)\,(2l - a)\,(d/2)}{E\,(bd^3/12)} \tag{3}$$

where $d$ is the beam thickness. The strain versus time evaluated as a function of the load history, $F(t)$, was plotted using eq. (3) for both the quasi-static flexural and the shock loading. The only difference is that the pressure data obtained as an output from shock have been converted into force by multiplying with the effective area. It should be noted that this is only an approximation as the Young modulus ($E$) obtained from quasi-static tensile testing was used in eq. (3) for obtaining transient strain history.

A graph showing the computed strain versus time for brominated vinyl ester under quasi-static and shock loading is shown in Figures 6 and 7, respectively. Vinyl ester specimen was observed to posses relativley higher strain over longer duration of time under quasi-static loading. As per this approach, the

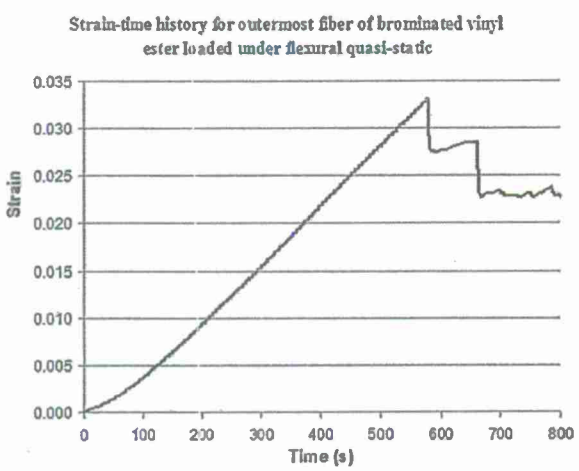


Figure 6 Transient strain history for the outermost fiber of brominated vinyl ester, loaded under flexural quasi-static test.

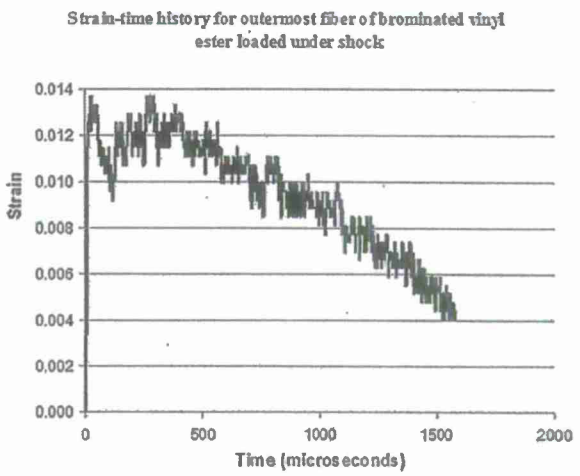


Figure 7 Transient strain history for the outermost fiber of brominated vinyl ester, loaded under shock.

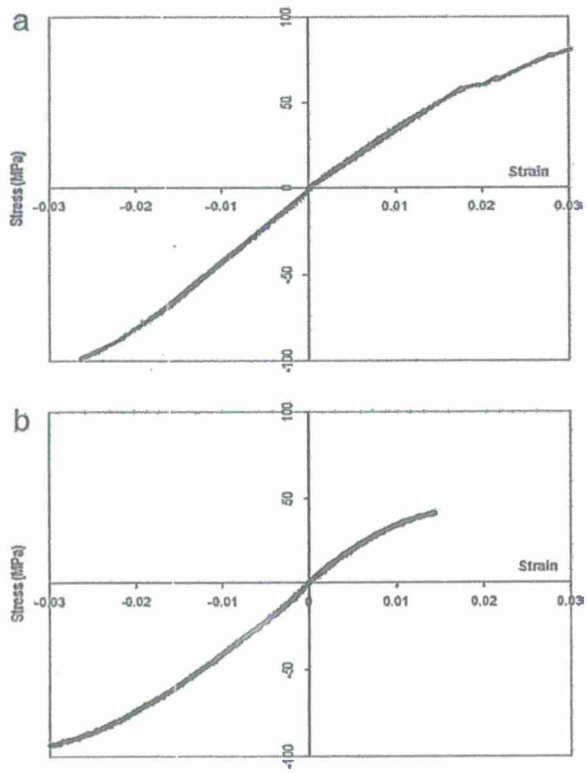


Figure 8 Tension and compression stress–strain data for (a) brominated vinyl ester, and (b) brominated vinyl ester with 2.5 wt % xGnP.

strain rates computed for quasi-static and shock loading were 0.0001 and 1000/s, respectively.

## EXPERIMENTAL RESULTS

In general, failure mechanism of nanoreinforced composites is more complicated than common fiber/laminate composites. This is because the fact that the distribution of nanoparticles in the matrix can be either random or in preferred orientations, and thus the stress distribution within the nanostructure can be extremely complex.

For a viscoelastic material, rate of loading is a fundamental characteristic, as energy absorption up to failure may vary for different strain rates. Therefore, the mechanical response and energy absorption characteristics under different strain rate loading were considered.

### Quasi-static tension and compression

Typical stress–strain curves for both tension and compression of some nanocomposite specimens are shown in Figure 8. In fact, the system with 2.5% xGnP infusion has both the lowest strength and the lowest failure strain [Fig. 8(b)] but stable stiffness among the two systems was observed. That was not surprising much owing to the fact that the previous studies with nanoparticle[13] did not show such improvement.

Possible reasons for drop in failure strain could be that the xGnP reinforcement did not contribute much to the elongation, and that the failure was mostly controlled by nucleation of cracks (inclusions) which are the predominant forms of damage during failure under quasi-static loading. These cracks begin to nucleate either at inhomogeneities such as nanoparticle sites and interact with defects (pores) within the resin neat creating a larger crack area with more energy dissipated.

### Shock loading

Theory of shock wave propagation indicates that rupture occurs when successive shock waves meet after multiple reflections over an interface (nanoparticles), which results in what so-called spalling. The deflection history of the shock-loaded nanocomposite samples was captured in frames of 150 microsecond time duration as shown in Figure 9. The shock loading is observed to induce maximum deflection at the center of the panels and reduced gradually toward the end.

Viscoelastic material is typically become stiff when subjected to high strain rate loading. This is typically observed in most of the nanoreinforced systems. Increase in stiffness at high strain rate was also dictated from stress–strain curves obtained using the SHPB. The stiffer material can lead to a lower deflection which in turn shows lesser energy absorption.

### Energy absorption

The energy absorbed by vinyl ester nanocomposites obtained from numerical integration of the load versus midpoint deflection is shown in Figure 10. Energy absorption is studied at different strain rates by comparing behavior of nanocomposites in case of shock with those simulated flexurally in MTS. As mentioned before, loading configuration (distributed pressure profile) was kept the same in both experiments. All specimens loaded quasi-statically were observed to have less mid-deflection as compared to those tested in shock. For example, specimens with xGnP showed an increase in energy absorption up to 150% in shock as compared to quasi-static. Conversely, in case of both shock and quasi-static loading, addition of either nanoparticles (nanoclay and xGnP) to brominated resin resulted in drop in failure strain and energy absorption capability.

In case of shock loading, energy behavior varies from nanocomposite system to another based on type and amount (wt %) of nanoparticle used. For example, comparing the central deflection in Figure 10,



D-110

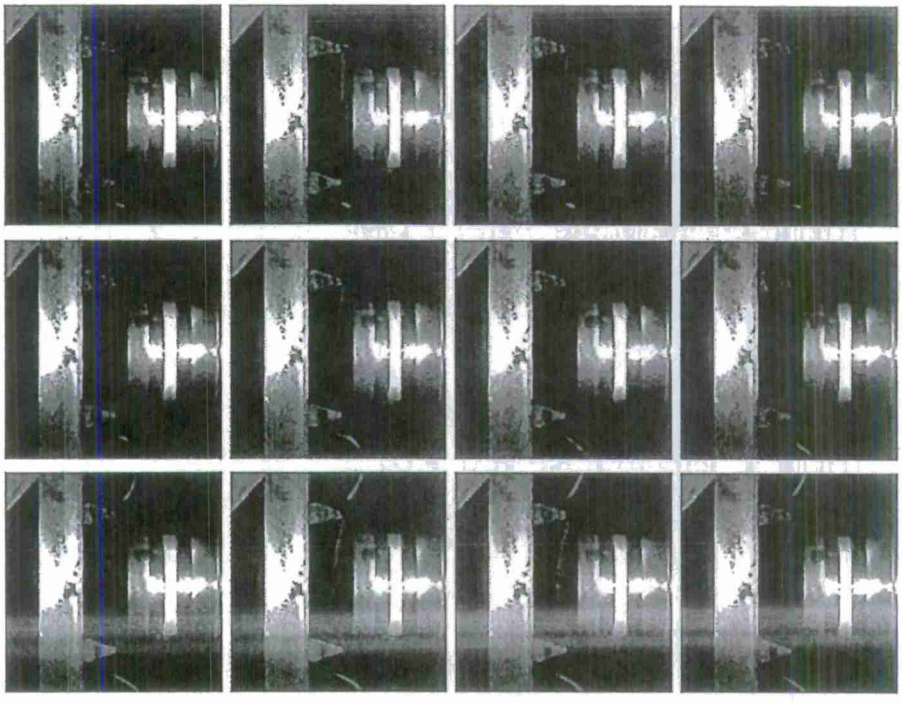

Figure 9 Typical real time images for vinyl ester under shock loading.

nanoclay system exhibited greater deflection as compared to xGnP of the same weight loading (black bars). In contrast, the energy behavior is about the same for both systems with 2.5 wt % nanoclay and 2.5 wt % xGnP as shown in Figure 11. This phenomenon can be owing to some error/uncertainty in processing energy absorption out from force–deflection data set for the two experiments.

To sum up, addition of nanoparticles of either xGnP or nanoclay to brominated resin did not show such improvement in deflection and energy absorption quantities. Moreover, tremendous drop in mechanical properties (energy absorption) is more pronounced with adding xGnP rather than that associated with nanoclay reinforcement. On the contrary, another study reported 10% improvement in impact energy absorption with addition of 2.5 wt % graphite platelets to brominated resin.[7]

## Finite element approach

Finite element modeling of brominated vinyl ester nanocomposite beam specimens subjected to both

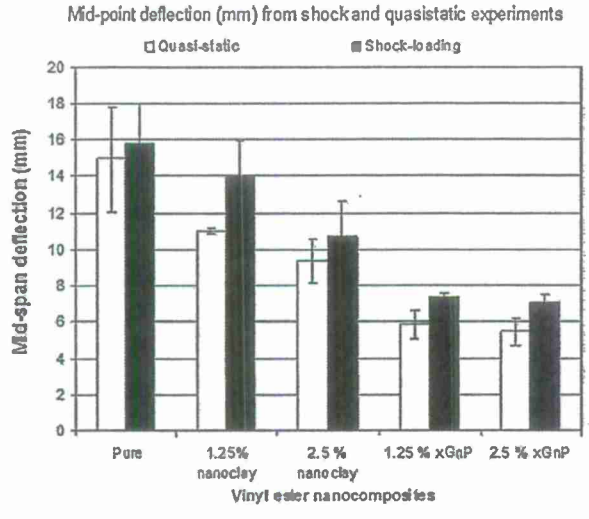


Figure 10 Midpoint deflection at failure under both quasi-static flexural and shock experiments.

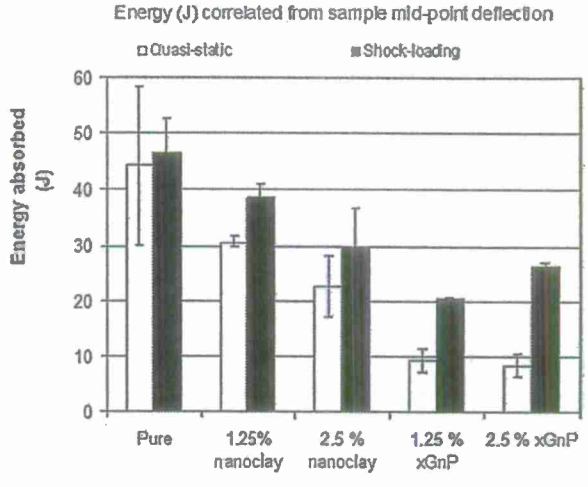


Figure 11 Energy absorption characteristics for both quasi-static flexural and shock experiments.

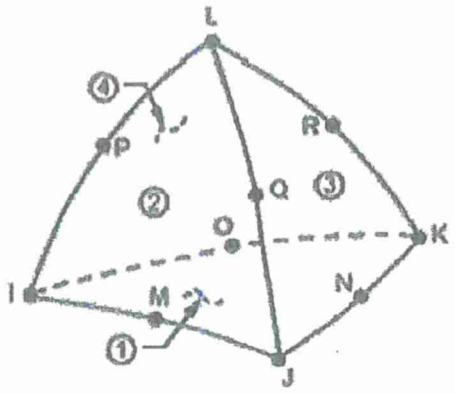


Figure 12 Solid 168 element geometry.

shock and quasi-static flexural loading was attempted in this study. The nanocomposite materials are considered isotropic because the nanoparticles are randomly dispersed in the vinyl ester matrix. ANSYS LS-DYNA with explicit analysis was used to predict the dynamic response of the shock-loaded materials, whereas ANSYS was applied for modeling the quasi-static flexural experiment. Solid 168, a higher order 3D, 10 node tetrahedral structural solid explicit dynamic element was used for modeling (Fig. 12).

Modeling of the beam structure was established by connecting appropriate key points in the same way as in shock tube setup. A refined mesh in the loading area (circular) and a course one in the outer regions were applied. As the specimen was held under a simply supported boundary condition with a 6-in span length, the respective lines in the model were restrained to move in the (loading) z-direction. Also, the center (origin) node on the specimen and the center of the left support were restrained to move in *xy*-plane to avoid twisting mechanism as shown in Figure 13. Deformed shape of the structure owing to load applications under both experiments with midpoint deflection was captured from the finite element simulations.

### Shock tube analysis

A nodal load was applied in the shock experiments on all nodes of the circular region owing to the inherent problems in applying area load in a 3D element under explicit ANSYS-LSDYNA analysis. Load on the nodes on periphery of the circle (external nodes) was half in magnitude to that on nodes inside the circular region (internal nodes). There were totally 4965 internal nodes and 240 external nodes on the loading area of which the FEA solution stabilized. Load was applied with the discreet values obtained from the pressure profile curve and was divided in 5085 (4965 + 240/2) equal parts. Load was applied in the form of two arrays with one row containing time data and the other row containing the respective load values. Two more arrays were generated, one for internal nodes and one for external nodes. Time at which maximum deflection was observed in shock experiments has been defined as the time at end of the load step.

Two different material models have been applied in FEA to simulate the shock response of these nanocomposites. The first material model used was the standard piecewise material model. This model provides a multilinear elastic–plastic material behavior that allows stress versus strain curve and strain rate dependency. Engineering stress–strain and failure strain were obtained from high strain data (Hopkinson bar) and converted to true stress-true plastic strain, defined as a material input. The failure criterion is defined by the effective failure plastic strain.

The linear viscoelastic material model introduced by Herrmann and Peterson was applied in the FEA analysis of shock tube loading. This principle asserts that the total strain (stress) resulting from the application of a sequence of stresses (strains) is equals to the sum of strains (stresses) caused by individual stresses (strains). To define a linearly viscoelastic constitutive model in FEA, the experimental stress relaxation data obtained from DMA tests over a wide range of temperatures were shifted to a room temperature, and then fitted into eq. (4) as shown in Figure 14. According to this model, the parameters $G_\infty$ (relaxation modulus at $\infty$ time), $G_o$ (initial relaxation modulus), $K$ (bulk modulus), and the constant, $\beta$, are required to define the linear viscoelastic model in ANSYS LSDYNA.

$$\phi(t) = G_\infty + (G_o - G_\infty)e^{-\beta t} \quad (4)$$

The elastic bulk behavior is assumed when calculating the incrementally integrated pressure ($P$) from

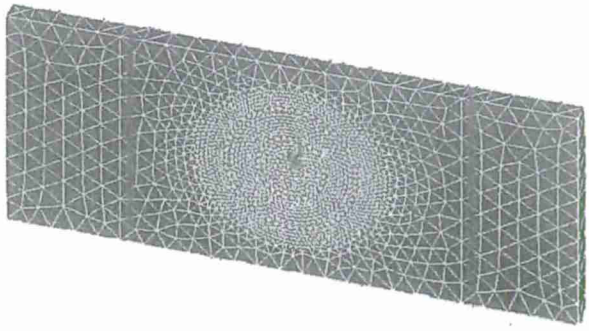

Figure 13 Finite element model of shock tube experiment with boundary conditions. [Color figure can be viewed in the online issue, which is available at wileyonlinelibrary.com.]



D-112

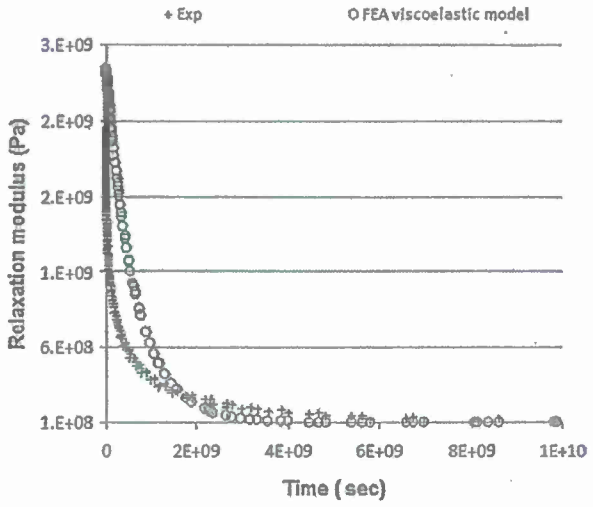


Figure 14 Shear relaxation modulus for vinyl ester as function of time from DMA.

volume ($v$). Thus, the total stress calculated based on the linear viscoelastic model is given as:

$$\sigma_{ij} = 2\int_0^t \phi(t-\tau)\left[\frac{\partial \varepsilon_{ij}(\tau)}{\partial \tau}\right]d\tau + (K \ln v)\delta_{ij} \qquad (5)$$

Following maps as in the previous analysis (Fig. 7), a transient strain history of the outmost fiber for vinyl ester modeled under shock is shown in Figure 15. FEA results in terms of the maximum strain and strain rate of the outermost fiber do agree well with that obtained experimentally as per the linear bending approach (Fig. 7).

Figure 16 shows the deformation of pure vinyl ester subjected to 120 psi peak pressure obtained from finite element modeling.

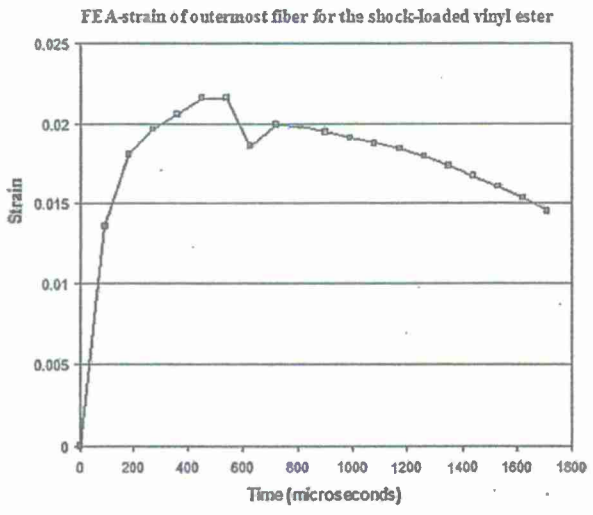


Figure 15 FEA strain of outermost fiber for the vinyl ester specimen under shock.

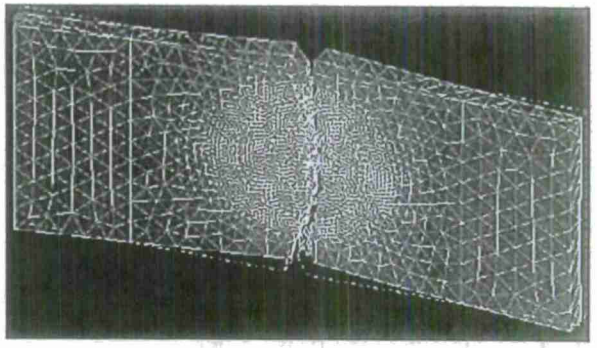

Figure 16 Deformation of pure vinyl ester subjected to 120 psi pressure in a shock tube. [Color figure can be viewed in the online issue, which is available at wileyonlinelibrary.com.]

Figures 17 and 18 show midpoint deflection (outermost fiber) at failure for brominated vinyl ester with nanoclay and graphite platelet nanoreinforcements, subjected to 120 psi peak pressure and also the predictions obtained from finite element analysis using both piecewise linear (high strain rates data) and viscoelastic response as input parameters. It is observed that the viscoelastic model gives a marginally better prediction of sample midpoint deflection compared to the piecewise (high strain rate) linear material models. The time–temperature superposition principle applied in shifting the viscoelastic property used in FEA-LSDYNA is based on the fact that processes involved in molecular motion occur at larger rates at elevated temperatures. Thus, these materials proved to react in a linearly viscoelastic behavior although subjected to a high strain rate loading (shock) over microseconds. That is to say, the short time duration of the shock pulse imposed

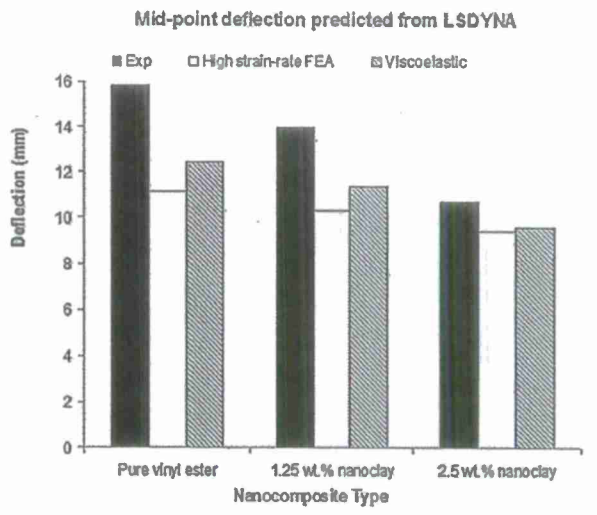


Figure 17 FEA predictive and experimental midpoint deflection for nanoclay reinforced vinyl ester.

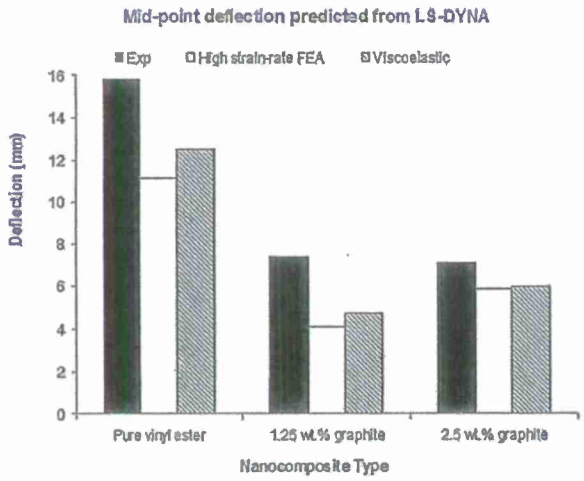


**Figure 18** FEA predictive and experimental midpoint deflection for graphite reinforced vinyl ester.

on the viscoelastic material is theoretically compensated by the time–temperature superposition which accelerates molecular motion as if occurs at elevated temperatures and elevated strain rate.

## Quasi-static flexural analysis

The quasi-static flexural experiments (with sand-bag) conducted on a given nanocomposite sample in the MTS test system were modeled and validated in ANSYS. The element type, model geometry, boundary conditions, and loading configuration are kept exactly similar to those used for simulating the shock tube response. Both the tension and the compression engineering stress–strain data were defined as constitutive material models under the nonlinear with large deformation analysis method. The experimental maximum load from MTS was converted to a uniform pressure and applied in ANSYS in constant increments over a certain number of substeps. Failure model in ANSYS is based on Von Mises criterion which assumes that yielding will occur only when the second invariant of the deviatoric stress reaches a critical value (strength). Failure occurrence is dictated from postprocessing of Von Mises stress data, and cannot be directly dictated or shown from solution interface.

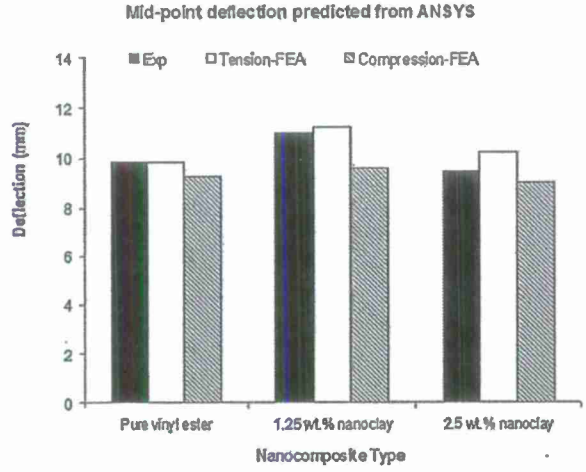


**Figure 19** FEA predictive and experimental midpoint deflection for nanoclay/510A-40 vinyl ester under quasi-static flexural loading.

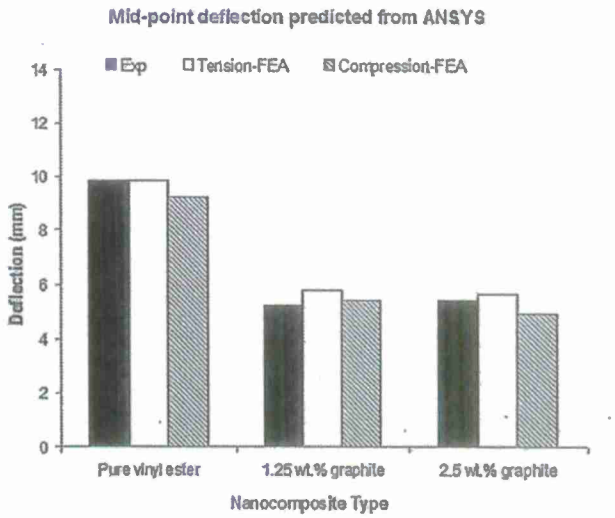


**Figure 20** FEA predictive and experimental midpoint deflection for graphite platelet/510A-40 vinyl ester under quasi-static flexural loading.

FEA midpoint deflection results for the nanocomposites loaded under quasi-static (with the sand-bag) are shown in Figures 19 and 20. It should be noted that tension and compression data obtained from the two independent quasi-static tests (described earlier) were used for defining the material constitutive models. From ANSYS results, the quasi-static flexural experiment conducted with the sand bag to simulate the distributed shock pressure was modeled and validated.

## CONCLUSIONS

Brominated vinyl ester nanocomposite systems are viscoelastic materials in basis which are sensitive to the rate of loading applied, time, and temperature dependent as well. Therefore, the mechanical response had been investigated over two extremes of strain rates loading. The high strain rate response of nanoclay and graphite platelet reinforced 510A-40 vinyl ester was first studied by conducting air blast loading using the shock tube. On the other extreme, the servo-hydraulic MTS test system was used to study the material behavior under quasi-static loading, with boundary conditions and loading configuration similar to shock tube experiments.

Experimental results showed that addition of nanoparticles to brominated resin adversely affected the energy absorption capability under shock loading. These nanoreinforced materials become stiffer and exhibited drop in failure strain when subjected to shock. Moreover, this increase in stiffness under shock was also dictated from stress–strain curves obtained using the Hopkinson bar. On comparing the loading rate, all the nanosystems tested were observed to absorb greater energy under high strain rate (shock) as compared to the quasi-static flexural mode.

Lesser energy absorbed within the low strain rate as compared to shock loading could be owing to role of nanoparticles toward failure. Cracks under quasi-static may begin to grow over the nanoparticles sites (inclusions), and then these small size cracks interact with pores within the vinyl ester matrix making larger cracks with larger stress concentrations. On the other hand, failure mechanism of nanoreinforced specimens under shock loading could be owing to complex shock wave propagation.

Finite element modeling of the shock tube loading showed that the linear viscoelastic model gives marginally better prediction of sample midpoint deflection compared to the high strain rate piecewise linear material model. As a result, these materials proved to react in a linearly viscoelastic behavior although subjected to a high strain loading (shock) over microseconds. The short time duration of the shock pulse imposed on the viscoelastic material is theoretically compensated by the time–temperature superposition which accelerates molecular motion as if occurs at elevated temperatures and elevated strain rate. The quasi-static flexural experiment conducted with the sand bag to simulate the distributed shock pressure was modeled and validated in ANSYS.

The nanoclay and graphite platelet vinyl ester composite panels were manufactured by Dr. Lawrence T. Drzal's group at Michigan State University.

## References

1. Kojima, Y.; Fukimori, K.; Usuki, A.; Okada, A.; Karauchi, T. J Mater Sci Lett 1993, 12, 889.
2. Xu, X.; Thwe, M.; Shearwood, C; Liao, K. J Appl Phys Lett 2002, 81, 2833.
3. Dresselhaus, M. S.; Dresselhaus, G.; Avouris, P. Carbon Nanotubes, Synthesis, Structure, Properties, and Application; Springer: New York, 2001.
4. LeBaron, P. C.; Wang, Z; Pinnavaia, T. J. J Appl Clay Sci 1999, 15, 11.
5. Sorathia, U.; Ness, J.; Blum, M. J Comp A: Appl Sci Manuf 1999, 30, 707.
6. Almagableh, A.; Mantena, P. R.; Alostaz, A.; Liu, W; Drzal, L. T. J eXPRESS Polym Lett 2009, 3, 724.
7. Pramanik, B; Mantena, P. R. J ASME Early Career Tech 2010, 8, 1.
8. Kalaitzidou, K.; Fukushima, H.; Askeland, P.; Drzal, L. T. J Mater Sci 2008, 43, 2895.
9. Laboratory of Polymer Technology-Polymer Blends, Available at: http://polymeeri.tkk.fi, 1/21/ 2010.
10. ASTM Standard D 638–08. Standard Test Method for Tensile Properties of Plastics; ASTM International: West Conshohocken, PA, 2008.
11. ASTM Standard D 6641/D 6641M. Standard Test Method for Determining the Compressive Properties of Polymeric Matrix Composite Laminates Using a Combined Loading Compression (CLC) Test Fixture; ASTM International, 2007.
12. Almagableh, A. Viscoelastic and shock response of nanoclay and graphite platelet reinforced vinyl ester nanocomposites, PhD Dissertation, 2010, Department of Mechanical Engineering, University of Mississippi.
13. Gupta, S. "Energy absorption characteristics of MWCNT/Nylon 6,6; and nanoclay and graphite platelet/vinyl ester nanocomposites", Master's Thesis. 2009, Department of Mechanical Engineering, University of Mississlppi
14. Shiner, C.; Timmerman, J.; Ebonee, P. M.; Williams; Seferis, J. 48th International SAMPE Symposium, 2003, 2539.

*Materials Sciences and Applications*, 2011, 2, 1667-1674
doi:10.4236/msa.2011.211222 Published Online November 2011 (http://www.SciRP.org/journal/msa)

Scientific Research

# Viscoelastic Response of Graphite Platelet and CTBN Reinforced Vinyl Ester Nanocomposites

**Brahmananda Pramanik, P. Raju Mantena***

Department of Mechanical Engineering, University of Mississippi, Oxford, USA.
Email: *meprm@olemiss.edu

Received August 20th, 2011; revised October 3rd, 2011; accepted October 17th, 2011.

## ABSTRACT

*Developing stronger, safer and more cost-effective structural materials for the new generation naval ships is the focus of ongoing research at University of Mississippi. The light-weight nanoparticle reinforced glass/carbon polymeric based composites and structural foams for blast, shock and impact mitigation are emphasized in this research. Derakane 510A-40 brominated vinyl ester nanocomposite resin systems are considered to be used in the composite face sheets of sandwich structures with fire-resistant foam core to reduce flammability along with optimal flexural rigidity, vibrational damping and enhanced energy absorption. In this work, the viscoelastic performance of 1.25 and 2.5 weight percent exfoliated graphite nanoplatelet (xGnP) added with 10 weight percent Carboxy Terminated Butadiene Nitrile (CTBN) reinforced brominated vinyl ester nanocomposites are studied. A Dynamic Mechanical Analyzer (DMA)—TA Instruments Model Q800 was used to obtain the viscoelastic properties, modulus (stiffness), creep/stress relaxation, and damping (energy dissipation), of the exfoliated graphite platelet and CTBN reinforced brominated vinyl ester. Effects of frequency (time) on the viscoelastic behavior were investigated by sweeping the frequency over three decades: 0.01, 0.1, 1.0 and 10 Hz, temperature range from 30˚C to 15˚C at 4˚C per minute step rate. Master curves were generated by time-temperature superpositioning (TTS) of the experimental data at 50˚C reference temperature. Addition of CTBN in xGnP reinforced brominated vinyl ester composites resulted in greater intrinsic material damping, indicating the possibility of higher energy absorption with the new configuration.*

*Keywords*: *Nanocomposite, CTBN, Viscoelastic, TTS, Material Damping, Energy Absorption*

## 1. Introduction

The objective of ongoing research at University of Mississippi is developing stronger, safer and more cost-effective structural materials for the new generation naval ships. The emphasis is on the light-weight nanoparticle reinforced glass/carbon polymeric based composites and structural foams for blast, shock and impact mitigation. The optimal flexural rigidity, vibrational damping and enhanced energy absorption characteristics of composite structures are extensively investigated in this research.

Thermoset resins, such as vinyl ester, are typically brittle. To improve their fracture resistance or toughness, they are usually blended or reacted with different additives and modifiers, which generally forms a second dispersed phase. The most frequently used modifiers are liquid rubbers. The morphology of the final modified thermoset can significantly affect the toughening mechanism and consequently its fracture toughness [1-3].

Auad *et al.* [1] investigated the mechanical behavior of vinyl ester resin cured with styrene and modified with liquid rubber CTBN. A sharp drop in density causing detrimental fracture toughness was observed in higher CTBN concentrations (>10 wt%). Balakrishnan *et al.* [2] examined the fracture behavior of rubber dispersed epoxy and inferred cavitations, yielding, plastic deformation of matrix, crack diversion and energy dissipation caused by rubber particles which contribute to the improvement of the ductility of the epoxy nanocomposite system. Frohlich *et al.* [3] suggested the compatibility matching as the key to novel phase-separated nanocomposites with significantly improved toughness.

The study of time dependent deformation process is highly relevant when long-term applications are in consideration. Polymeric composites are viscoelastic in nature and show the time-temperature dependant behavior. The time-dependent deformation of materials subjected to a constant stress is defined as creep [4]. In multiple literatures, the creep behavior of polymer/clay nanocom-

Copyright © 2011 SciRes. 

posites have been modeled [4-9], and proposed that nanoparticles improve the creep resistance of polymer matrices depending on success in level of exfoliation.

The fatigue strength, cyclic deformation and strain incompatibility of clay-reinforced nylon have been demonstrated by Yang *et al.* [4] Fatigue strength slightly increased by addition of clay reinforcement to nylon 6. The cyclic deformation has been examined applying stress-strain hysteresis loops. The strain incompatibility near the phase boundary caused both relaxation of three dimensional stress field and extraction of clay platelets in the nano-composites under study.

Tensile compliance of the nano-clay reinforced Polyethylene composites was investigated by Pegoretti *et al.* [5]. The viscoelastic component is low corresponding only to a few percent of the compliance even at relatively high stresses. The compliance of the composites is only slightly lower than that of the neat rPET, the Cloisite® 25A reinforcement being somewhat stronger. Both clays were illustrated beneficial effect on the dimensional stability of the composites as compared to the neat rPE, the creep rate did not rise at long time periods.

Galgali *et al.* [6] presented an experimental investigation on the creep behavior of molten polypropylene organically modified clay nanocomposites and concluded that the solid-like rheological response of this nanocomposite develops from large frictional interactions of the clay crystallites. Compatibilizer showed a significant influence in modifying the rheological behavior.

Non-linear time dependent creep of polyethylene (PE) montmorillonite layered silicate (MLS) nanocomposites was investigated by Ranade *et al.* [7]. Non-linearity in the creep response was modeled using the Burger model and the tensile-creep response was attributed to dispersion effects with marginal effects of crystallinity.

Perez *et al.* [8] studied the clay content and temeperature dependent creep behavior of biodegradable composites based on starch/polycaprolactone commercial blends reinforced with organo-modified nanoclay, processed by melt-intercalation. The experimental response was correlated with Findlay's power law and Burger's model. This investigation showed that the addition of clay to the neat matrix leads to a significant improvement of creep resistance.

The effects of incorporating various montmorillonite nanoclays into several starch samples were by rheologically examined by Chiou *et al.* [9]. Frequency sweep and creep results for starch–nanoclay samples at room temperature indicated that the Cloisite Na+ samples formed more gel-like materials than the other nanoclay samples. The Cloisite Na+ samples exhibited a large increase in modulus at higher temperature. In contrast, the more hydrophobic nanoclay samples had comparable modulus values to the pure starch sample. These results suggested that during gelatinization, the leached amylose interacted with the Cloisite Na+ interlayer, producing better reinforcement and higher modulus values.

These multiple studies showed the significance of characterizing visoelastic behavior of nanocomposites in their respective application fields. Hence, investigating time-temperature depended response of rubber-toughened nanocomposites is an important consideration. The aim of this paper is to describe the viscoelastic behavior of vinyl ester nanoreinforced composites added with an almost unreactive liquid carboxy terminated butadiene nitrile (CTBN) rubber, a toughening agent for thermoset resins. The viscoelastic response of Carboxy Terminated Butadiene Nitrile (CTBN) on the viscoelastic behavior of Derakane 510A-40 brominated vinyl ester reinforced with 1.25 and 2.5 wt% exfoliated graphite nano platelets was studied using dynamic mechanical analyzer (DMA). Single frequency and frequency sweep across 3 decades: 0.01, 0.1, 1.0 and 10 Hz were applied over 30˚C to 150˚C temperature range at a 4˚C/min step rate. The time- temperature superposition (TTS) principle was applied to develop master curves of the dynamic storage modulus at a reference temperature of 50˚C.

## 2. Experimental Techniques

### 2.1. Dynamic Mechanical Analyzer (DMA)

DMA tests were performed in accordance with ASTM D4065-01 standard [10]. TA Instruments Model Q 800 DMA (**Figure 1**) is a stress-controlled Combined Motor and Transducer (CMT) machine where the motor applies a force and displacement sensors measure strain, force and amplitude in the form of raw signals recorded by the machine [11]. Experiments were performed using the single-cantilever clamp. Hence the most of the strain oc-

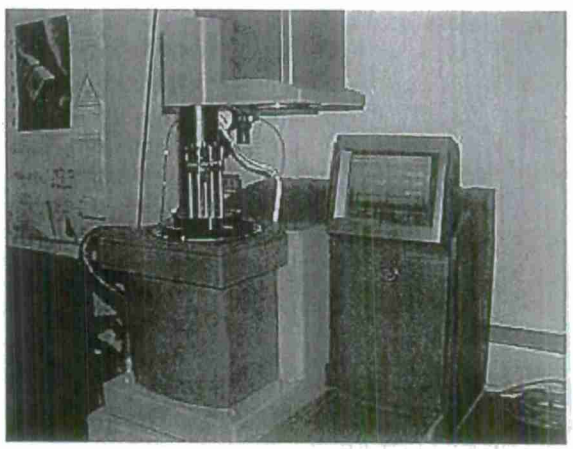

**Figure 1. TA Instruments Model Q800 DMA for dynamic tests [11].**

Copyright © 2011 SciRes. 

curred at the sample surface, while the center experienced no strain. The stress and strain equations, applied in these experiments, are based on theory of linear visoelasticity of the materials (Equations (1) to (4)).

$$E = \frac{K_s}{F_c} \cdot \frac{L^3}{12I}\left[1+\frac{12}{5}(1+\upsilon)\left(\frac{t}{L}\right)^2\right] \quad (1)$$

$$F_c = 0.7616 - 0.02713\sqrt{\frac{L}{t}} + 0.1038\ln\left(\frac{L}{t}\right) \quad (2)$$

$$\sigma_x = \frac{6PL}{wt^2} \quad (3)$$

$$\varepsilon_x = \frac{3\delta t F_c}{L^2\left[1+\frac{12}{5}(1+\upsilon)\left(\frac{t}{L}\right)^2\right]} \quad (4)$$

where, $E$ = elastic modulus, $K_s$ = measured stiffnes, $F_c$ = clamping correction factor, $L$ = clamp span length, $I$ = sample moment of inertia, $\upsilon$ = Poisson's ratio, $t$ = sample thickness, $\sigma_x$ = stress, $P$ = applied load, $w$ = width of the specimen, $\varepsilon_x$ = strain, $\delta$ = amplitude of deformation.

The viscoelastic properties, such as, modulus (stiffness) and damping (energy dissipation), of the exfoliated graphite platelet added with CTBN reinforced brominated vinyl ester were studied over a range of temperature and frequency. Creep and stress relaxation experiments were also conducted using DMA.

## 2.2. Single Frequency Dynamic Test

Dynamic mechanical analysis was carried out using the TA Instrument model DMA Q800 V7.5 on rectangular cross-sectioned specimens under single-cantilever clamping mode, with a span length of 17.5 mm. The 1.25 and 2.5 weight percent nanoclay, graphite platelet and graphite platelet added with 10 weight percent Carboxy Terminated Butadiene Nitrile (CTBN) reinforced brominated vinyl ester nanocomposites were characterized and compared with the base pure brominated vinyl ester thermoset composite under single frequency—temperature ramp method. Samples of 35 mm × 10 mm × 1.6 mm thick were clamped with 30 gm clamp mass and subjected to 1 Hz single frequency with 25 μm displacement amplitude assuming linear visco-elastic characterization. Test temperature was equilibrated at 30˚C and maintained isothermal for 5 minutes, and then elevated with 3˚C/min steps up to 150˚C in test duration. Three specimens were tested from each configuration of the nanocomposites. The output data were processed by Rheology data analysis software to produce characteristic graphs [11].

## 2.3. Multi-Frequency Dynamic Test

DMA measurements included frequency sweep with time temperature steps, to which time-temperature super-position (TTS) was applied to predict the long-term time dependent properties of the material. The dynamic storage modulus ($E'$) and damping of nano-reinforced brominated 510A-40 vinyl ester specimens were characterized as a function of temperature and frequencies. Dynamic mechanical testing was used to perform multi-frequency measurements with accelerated temperature and theoretical time-temperature superposition post-processing of the data. Effects of CTBN inclusion in exfoliated graphite platelet reinforcement were investigated.

Vinyl ester nanocomposites were characterized by performing a multi-frequency isothermal mode test, in which the sample is equilibrated at different temperatures and subjected to a series of frequencies. Specimens with dimensions of 35 mm × 10 mm × 1.6 mm were subjected to frequencies of 0.01, 0.1, 1.0 and 10 Hz with a temperature step rate of 4˚C per minute starting from 30˚C (RT) to 150˚C. Only 25 μm displacement amplitude was applied for the test since the analysis assumes linear domain for viscoelastic characterization, and two specimens were tested from each configuration. The raw data was then processed using the Rheology data analysis software to generate the master curves.

## 2.4. Creep and Stress Relaxation

The creep and stress-relaxation response of brominated vinyl ester and its nanocomposites was investigated using the DMA. Nano-reinforced brominated 510A-40 vinyl ester specimens were tested in a TA Instruments Model Q800 DMA using single-cantilever clamp with a span of 17.5 mm and pre-load stress of 3 MPa. The preload stress of 3 MPa was chosen due to apply the linear viscoelastic theory at low stresses. Two samples were tested from each configuration.

Short term creep tests were carried out by subjecting the samples to a constant load over 30 minutes duration at isothermal temperatures in the DMA. The room temperature (RT) varied between 30˚C and 32˚C. A temperature range of 30˚C through 100˚C was chosen, as this covered the glass transition temperature for all the nanocomposites considered in this research. The sample was initially equilibrated at 30˚C for about 4 minutes to make sure that the sample temperature settles down. After equilibrium, the sample was subjected to a fixed stress of 3 MPa for about 30 minutes. The temperature was then incremented by 4˚C and the above procedure repeated till the final temperature of 100˚C.

In the stress relaxation mode, the sample was held at a constant strain and the stress level measured as a function

Copyright © 2011 SciRes. 

of time over the same temperature range. The method segments executed during the relaxation test was the same as that used in creep. The sample is initially equilibrated at RT for about 4 minutes, and then displaced 0.01 strain for 30 minutes. The temperature was then incremented by 4°C and the process repeated until the final temperature of 100°C.

## 3. Analysis and Computation

### 3.1. Linear Viscoelastic Theory

A viscoelastic material is characterized by possessing both viscous and elastic behavior. Elastic material is one which returns all the energy stored during loading after the load is removed [12]. As a result, the stress and strain response for elastic materials moves totally in phase. For elastic materials, Hook's law applies, where the stress is proportional to the strain, and the modulus is defined at the ratio of stress and strain. A purely viscous material returns none of the energy stored during loading. All the energy dissipated as "pure bending" once the load is removed. In this situation, the stress is proportional to the strain rate rather than strain. These materials, known as inelastic materials, have only damping, instead of stiffness. Both of these two types are ideal in existence. The real-life materials fall into neither of the above categories. These are called viscoelastic materials. Some of the energy stored in a viscoelastic system is recovered upon removal of the load; and the remainder is dissipated as heat [12]. **Figure 2** [12] describes the cyclic stress at a loading frequency of $\omega$ is out-of-phase with the strain by certain angle $\phi$, where $0 < \phi < \pi/2$. The angle $\phi$ is a measure of the materials damping level; the larger angle denotes greater damping. The viscoelastic modulus is represented by a complex quantity. The real part of this complex parameter, known as storage modulus ($E_1$), relates the elastic behavior of the material, and defines the stiffness. The imaginary component, known as loss modulus ($E_2$), explains the material's viscous behavior, and defines the ability of energy dissipation of the material. The complex viscoelastic modulus ($E^*$) is defined as:

$$E^* = E_1 + iE_2 = \frac{\sigma_0}{\varepsilon_0} e^{i\varphi} \tag{5}$$

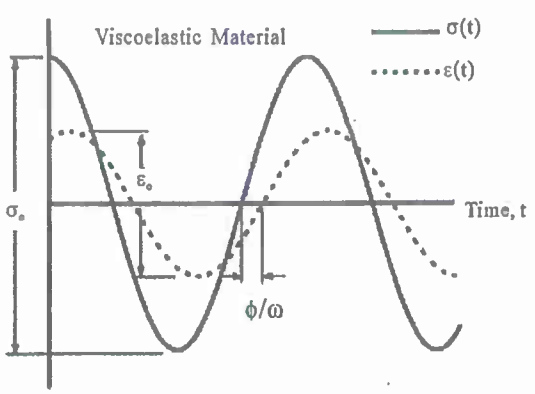


**Figure 2. Cyclic stress and strain curves vs. time for a viscoelastic material [12].**

### 3.2. Time-Temperature Superposition (TTS)

Molecular motion in materials occurs at larger rates under elevated temperatures. The time-temperature superposition principle is based on this temperature dependent response of the materials. The change in property which occurs relatively quickly at higher temperatures can be made to appear as if they occurred at longer times or lower frequencies simply by shifting the data with respect to time (1/frequency) [11]. By shifting the data with respect to frequency to a reference curve, a master curve is generated, which covers time (frequencies) outside the accessible range. The shifting mechanism used to shift a set of data upon a reference curve follows WLF [11] model. This model assumes that the fractional free volume increases linearly with respect to temperature in the transition region, and when the free volume increases, its viscosity decreases. In this model, the degree of shifting is calculated according to Equation (6):

$$\log(a_T) = \frac{-C_1(T - T_0)}{C_1 + (T - T_0)} \tag{6}$$

## 4. Results and Discussion

### 4.1. Modulus

**Figures 3** shows the storage modulus variations with temperature for brominated vinyl ester nanocomposites with the single-frequency test. Addition of CTBN to graphite reinforcement shifted the drop of storage modulus to higher temperature.

**Figure 4** shows the detrimental effect of CTBN reinforcement in storage modulus with respect to xGnP presented at 30°C. **Figures 5** and **6** show the storage modulus variations with temperature for brominated vinyl ester nanocomposites with the multi-frequency tests. It can be observed that the modulus remains higher at higher frequency up to the glass transition temperature.

### 4.2. Glass Transition

**Figures 7** shows the loss factor variation with temperature for brominated vinyl ester nanocomposites at single frequency. **Figure 8** shows a marginal increase of glass transition temperature in nanocomposites with CTBN addition.

Copyright © 2011 SciRes. 

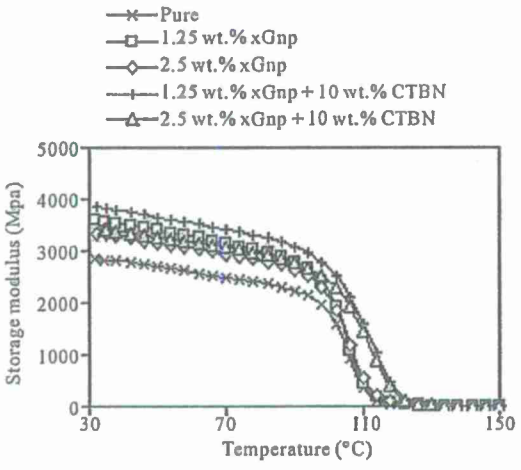


Figure 3. Storage modulus for brominated vinyl ester nanocomposites at single-frequency.

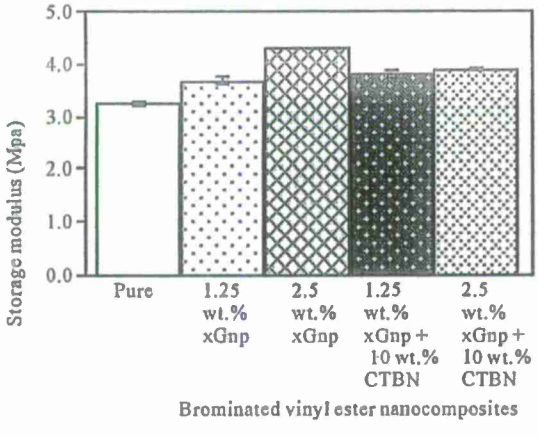


Figure 4. Storage modulus at initial temperature for brominated vinyl ester nanocomposite.

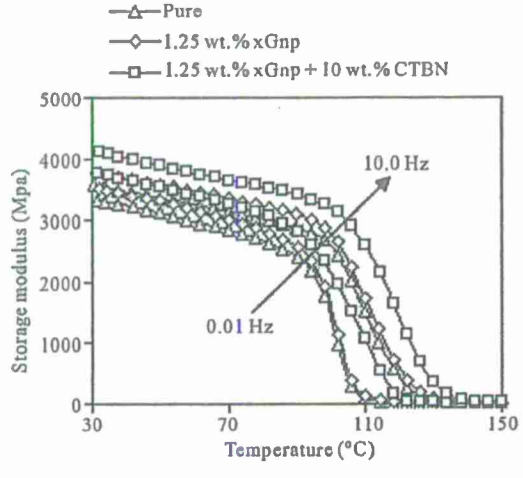


Figure 5. Storage modulus for 1.25 wt% reinforced brominated vinyl ester nanocomposites at multi-frequency.

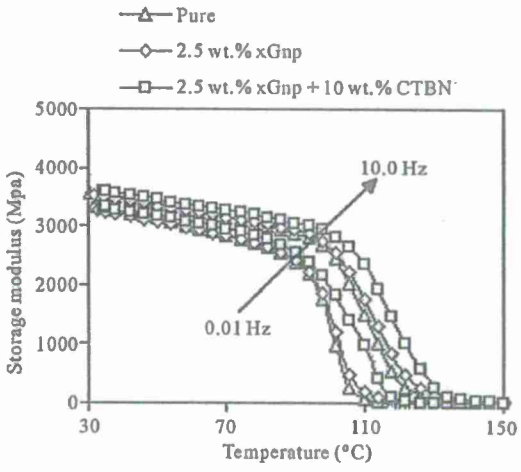


Figure 6. Storage modulus for 2.5 wt% reinforced brominated vinyl ester nanocomposites at multi-frequency.

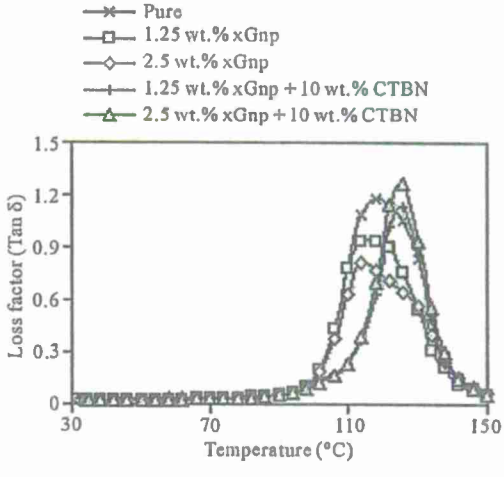


Figure 7. Loss factor for brominated vinyl ester nanocomposites at single-frequency.

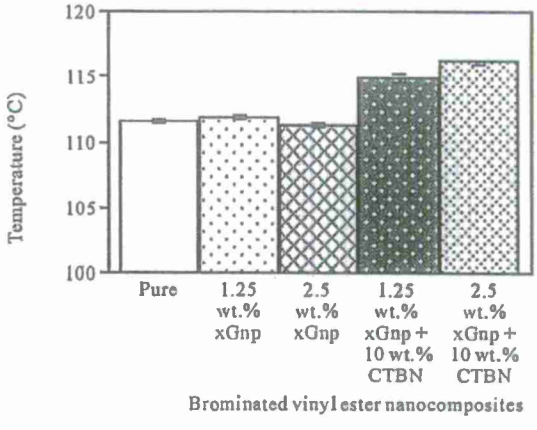


Figure 8. Glass transition temperature for brominated vinyl ester nanocomposites.

Copyright © 2011 SciRes. 

E-120

**Figures 9** and **10** show the loss factor variations in multi-frequency tests. CTBN inclusion in graphite reinforcement contributed in maintaining the peak loss factor within a higher temperature range during glass transition (114°C to 116°C).

### 4.3. Damping

Tan-delta, defined as the ratio of loss modulus to storage modulus, is a measure of inherent material damping. Peak of Tan-delta is the region over which material experiences a transition from glassy to a leathery behavior, associated with the onset of short range molecular segments motion, of which all are initially frozen [12,13]. CTBN addition resulted in greater value of Tan δ peak showing more inherent material damping as shown in **Figure 11**, indicating the possibility of higher energy absorption.

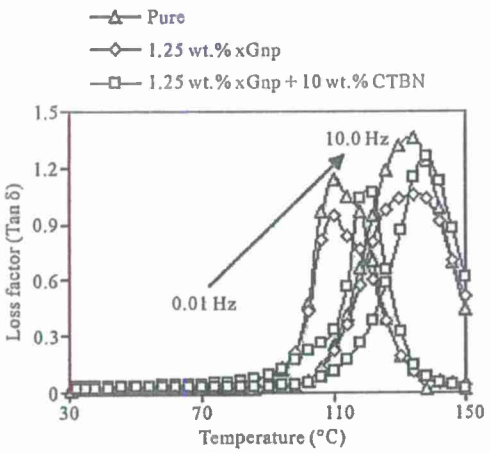


**Figure 9. Loss factor for 1.25 wt% reinforced brominated vinyl ester nanocomposites at multi-frequency.**

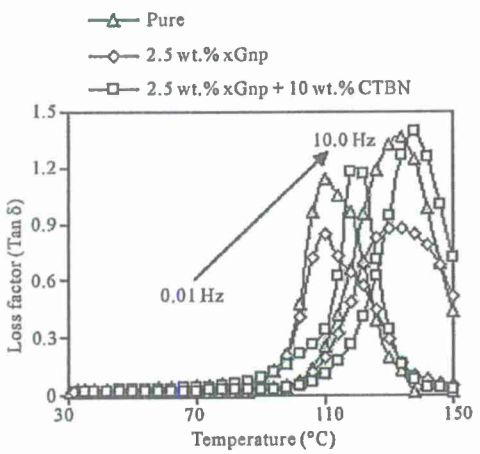


**Figure 10. Loss factor for 2.5 wt% reinforced brominated vinyl ester nanocompposites at single-frequency.**

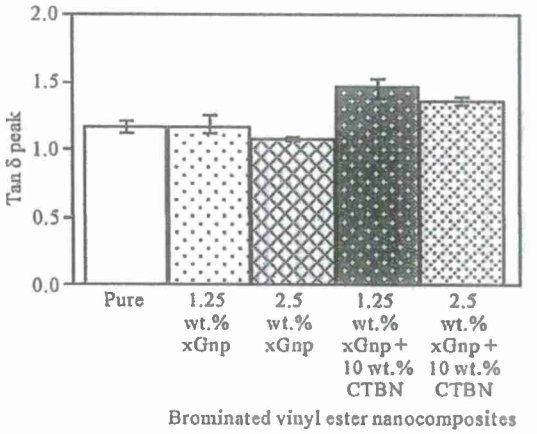


**Figure 11. Tan-delta peaks for brominated vinyl ester nanocomposites.**

### 4.4. Long-Term Dynamic Properties

Since the glass transition temperature for nanocomposites is observed to be variable for different compositions, a reference temperature of 50°C was chosen to generate master curves for storage modulus. To perform this, data from higher temperature experiments in the lower portion of the plot are shifted to the left (lower frequencies) and curves corresponding to the temperatures lower than 50°C are shifted to the right [11].

**Figure 12** shows the generated master curves of storage modulus over an extended period of time. From **Figure 12**, all vinyl ester nanocomposites were observed to maintain their rigidity (at 50°C) with an average dynamic storage modulus of (2.5 GPa) over a period of $10^{10}$ sec (321.5 years), from where the vinyl ester nanocomposites impregnated with CTBN starts to show improvement. This is significant on the long term behavior of reinforced vinyl ester with CTBN.

### 4.5. Creep and Stress-Relaxation

Shape of the creep and relaxation curves for brominated vinyl ester is strongly dependent on temperature observed in this experiment (**Figures 13** and **14**). The effect of temperature on creep and relaxation behavior of brominated vinyl ester, 1.25 wt percent × GnP, 2.5 × GnP reinforced samples with 10 wt percent CTBN additives over 30 minutes duration were also showed similar trend. The creep deformations in the initial portion, which are pure elastic, are relatively small and associated with bending and stretching of intermolecular bonds. However, the deformation beyond the proportional limit is same as a stretching of the wrinkled molecular chains which is not recoverable instantly. Hence, the mechanical response exists in the viscoelastic linear region, where no intermolecular slippage causes permanent deformation [12,13].

Copyright © 2011 SciRes. 

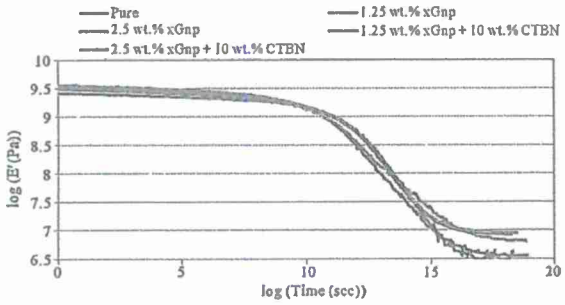


**Figure 12. Master curves for brominated vinyl ester nanocompposites.**

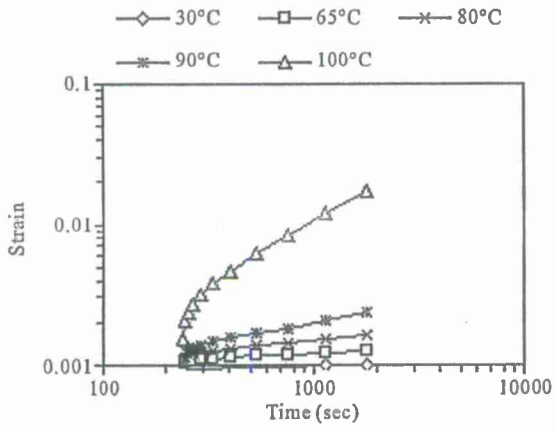


**Figure 13. Creep-strain for pure brominated vinyl ester.**

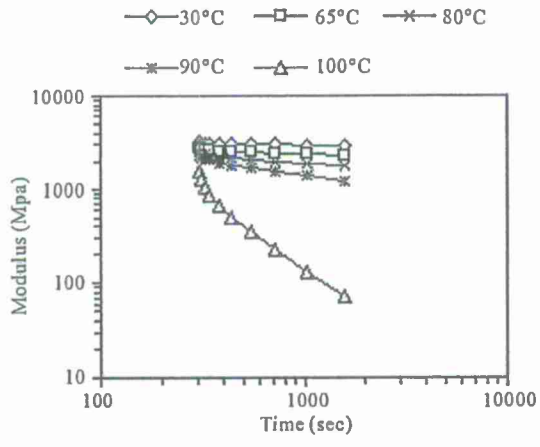


**Figure 14. Relaxation modulus for pure brominated vinyl ester.**

It has been observed that at 100°C, both increment of creep-strain and decrement of modulus in stress-relaxation are less with the addition of toughening agent (**Figures 15** and **16**). Accordingly, addition of CTBN to × GnP reinforcement improves the creep resistance.

## 5. Conclusions

The effect of carboxy terminated butadiene nitrile (CTBN) on the viscoelastic behavior of Derakane 510A-40 brominated vinyl ester reinforced with 1.25 and 2.5 wt percent exfoliated graphite platelets was investigated using dynamic mechanical analyzer (DMA). Single frequency and frequency sweep across 3 decades: 0.01, 0.1, 1.0 and 10 Hz were applied over 30°C to 150°C temperature range at a 4°C/min step rate. The time-temperature superposition principle was used to develop master curves of dynamic storage modulus at a reference temperature of 50°C.

The elastic modulus was observed to decrease by a small amount with addition of CTBN to the reinforcement; along with marginal increase of the glass transition

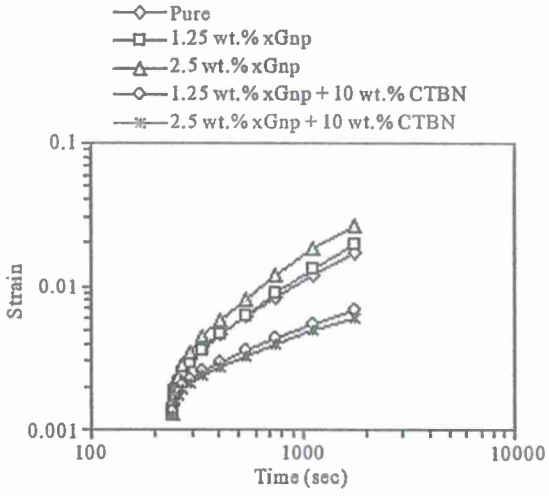


**Figure 15. Creep-strain for nanocomposites at 100°C.**

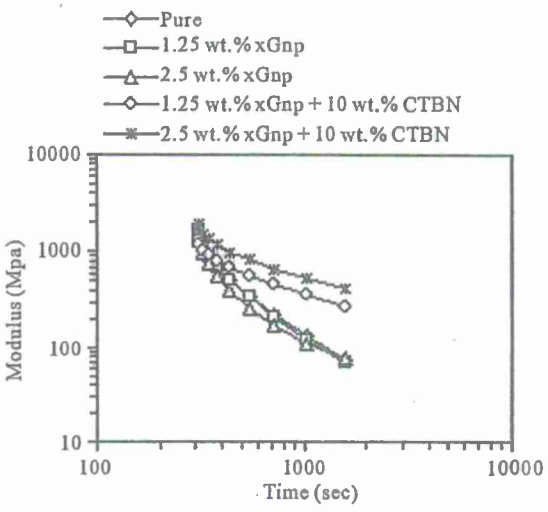


**Figure 16. Relaxation modulus for nanocomposites at 100°C.**

Copyright © 2011 SciRes. 

temperature. CTBN addition also resulted in greater value of Tan $\delta$ peak showing more inherent material damping with the possibility of higher energy absorption. Creep and relaxation curves showed the improvement of creep resistance due to the CTBN inclusion in the nano-reinforcement.

## 6. Acknowledgements

The support from ONR Grant N00014-07-1-1010, Office of Naval Research, Solid Mechanics Program (Dr. Yapa D.S. Rajapakse, Program Manager) has been acknowledged. The nanoclay and graphite platelet reinforced vinyl ester composite panels were manufactured by Dr. Larry Drzal's group at Michigan State University.

## REFERENCES

[1] M. L. Auad, P. M. Frontini, J. Borrajo and M. I. Aranguren, "Liquid Rubber Modified Vinyl Ester Resins: Fracture and Mechanical Behavior," *Polymer*, Vol. 42, No. 8, 2001, pp. 3723-3730. doi:10.1016/S0032-3861(00)00773-4

[2] S. Balakrishnan, P. R. Start, D. Raghavan and S. D. Hudson, "The Influence of Clay and Elastomer Concentration on the Morphology and Fracture Energy of Preformed Acrylic Rubber Dispersed Clay Filled Epoxy Nanocomposites," *Polymer*, Vol. 46, No. 25, 2005, pp. 11255-11262. doi:10.1016/j.polymer.2005.10.053

[3] J. Fröhlich, R. Thomann and R. Mülhaupt, "Toughened Epoxy Hybrid Nanocomposites Containing Both an Organophilic Layered Silicate Filler and a Compatibilized Liquid Rubber," *Macromolecules*, Vol. 36, No. 19, 2003, pp. 7205-7211. doi:10.1021/ma035004d

[4] J. L. Yang, Z. Zhang, A. K. Schlarb and K. Friedrich, "On the Characterization of Tensile Creep Resistance of Polyamide 66 Nanocomposites. Part II: Modeling and Prediction of Long-Term Performance," *Polymer*, Vol. 47, No. 19, 2006, pp. 6745-6758. doi:10.1016/j.polymer.2006.07.060

[5] A. Pegoretti, J. Kolarik, C. Peroni and C. Migliaresi, "Recycled Polyethylene Terephthalate Layered Silicate Nanocomposites: Morphology and Tensile Mechanical Properties," *Polymer*, Vol. 45, No. 8, 2001, pp. 2751-2759. doi:10.1016/j.polymer.2004.02.015

[6] G. Galgali, C. Ramesh and A. Lele, "A Rheological Study on the Kinetics of Hybrid Formation in Polypropylene Nanocomposites," *Macromolecules*, Vol. 34, No. 4, 2001, pp. 852-858. doi:10.1021/ma000565f

[7] A. Ranade, K. Nayak, D. Fairbrother and N. A. D'Souza, "Maleated and Non-Maleated Polyethylene Montmorillonite Layered Silicate Blown Films: Creep, Dispersion and Crystallinity," *Polymer*, Vol. 46, No. 18, 2005, pp. 7323-7333. doi:10.1016/j.polymer.2005.04.085

[8] J. Perez, V. A. Alvarez and A. Vasquez, "Creep Behavior of Layered Silicate/Starch Polycaprolacton Blends Nanocomposites," *Materials Science and Engineering. A, Structural Materials: Properties, Microstructure and Processing*, Vol. 480, No. 1-2, 2008, pp. 259-265.

[9] B. S. Chiou, E. Yee, G. Glenn and W. Orts, "Rheology of Starch—Clay Nanocomposites," *Carbohydrate Polymers*, Vol. 59, No. 4, 2005, pp. 467-475. doi:10.1016/j.carbpol.2004.11.001

[10] ASTM Standard D-4065-01, "Standard Practice for Plastics: Dynamic Mechanical Properties: Determination and Report of Procedure," ASTM International, 2000.

[11] TA Instruments, "Dynamic Mechanical Analyzer, Q SeriesTM, Getting Started Guide," Revision F, New Castle, 2004. http://www.adhesivesmag.com

[12] J. D. Ferry, "Viscoelastic Properties of Polymers", 3rd Edition, John Wiley & Sons Inc., New York, 1980.

[13] A. Almagableh, P. R. Mantena and A. Alostaz, "Creep and Stress Relaxation Modeling of Nanoclay and Graphite Platelet Reinforced Vinyl Ester Nanocomposites," *Journal of Applied Polymer Science*, Vol. 115, No. 3, 2009, pp. 1635-1642. doi:10.1002/app.31152

Copyright © 2011 SciRes. 

ASME Early Career Technical Journal
2011 ASME Early Career Technical Conference, ASME ECTC
November 4 – 5, Atlanta, Georgia USA

# BLAST RESPONSE OF SANDWICH COMPOSITE STRUCTURAL PANELS

**Tezeswi P. Tadepalli, Research Associate**
Department of Mechanical Engineering,
Composite Structures and Nano-Engineering Research
The University of Mississippi
University, MS-38677, USA

**P. Raju Mantena, Professor**
Department of Mechanical Engineering,
Composite Structures and Nano-Engineering Research
The University of Mississippi
University, MS-38677, USA

## ABSTRACT

Experimental blast response and quasi-static material property data were generated for E-glass and carbon face skin sandwich composite panels with balsa, PVC foam and TYCOR® cores. The Pressure vs Impulse (P-I) curve methodology that was developed to represent estimated damage levels in civil infrastructure components subjected to blast loadings, has been adapted for analyzing these sandwich composite panels. Results show good correspondence between model predictions and experimental data for the performance evaluation of various sandwich composite panel configurations.

This P-I curve methodology enables the generation of a database of performance envelopes for sandwich composite panels with a variety of skin and core material combinations under various blast and shock loading scenarios, for naval composite structural applications.

## INTRODUCTION

The goal of this study is to make use of available experimental blast and shock response data for the performance prediction of sandwich composite panels under a wider range of operational loading conditions and threat scenarios, which would facilitate design decisions at the ship superstructure-system level. The available experimental data, which is limited to only specific blast and shock loading scenarios, is used for validating the proposed computer simulation methodology.

Several detailed studies have been conducted on the blast and shock response of sandwich composite panels [1,2,3,4,5]. These studies have examined the response and various failure modes of the panels such as core crushing, delamination, bending and shear response. The focus of these studies has largely been on the response of a composite sandwich panel to a unique blast or shock loading scenario.

Here we have focused on implementation of the PI (Pressure vs Impulse) curve computational methodology to enable exploration of the design space and for evaluating response of the available sandwich composite panels to various blast loads. An attempt has been made to validate the computational methodology for predicting the performance of sandwich composite panels based on limited experimental data corresponding to specific blast loads.

The P-I (Pressure-Impulse) diagram (Figure 1) relates a specific damage level to a combination of blast pressure and impulse imposed on a particular structural element, and allows reduced order modeling of the sandwich composite panel systems. P-I curves are also known as iso-damage curves with each curve representing a certain response level such as mid-span deflection or rotation at supports, etc.

In a particular threat scenario, the pressure and impulse acting on a structure can be determined by using scaling laws based on the distance of the structure from the blast source [6]. Knowing the distribution of pressure and impulse due to a specific blast scenario, the damage to individual components in terms of ductility demand can then be determined from the P-I chart [7,8] and can also be further mapped onto a structure consisting of many such components.

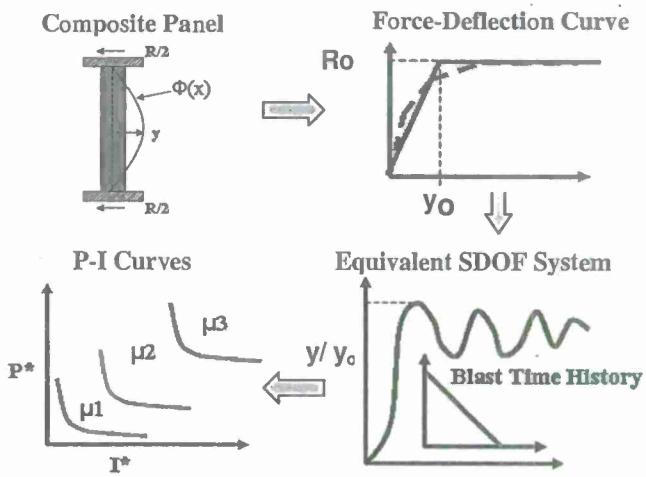


Figure 1. Procedure for generating the P-I curve numerically

Previous research conducted at University of Mississippi under the DHS-SERRI project "Nano-Particle Reinforced Composites for Critical Infrastructure Protection" involved the evaluation of strength and deformation capacity of civil infrastructure components subject to blast and extreme loading



F-124

[9]. Pressure versus Impulse (P-I) curves were used to represent estimated damage levels in components subjected to blast or shock loadings. The adopted procedure and reflected blast pressure versus distance relation followed the TM 5-1300 Joint Forces military guidance [6]. A database of P-I curves for reinforced concrete components of various cross sections and reinforcement ratios was developed, including the benefits of nano-particle reinforcement. These simulations allow the planner to determine the likely location and extent of damage in building structures subject to blast loadings. This simplified methodology used for rapid damage and vulnerability assessment of critical infrastructure [10] has been adopted here for the performance evaluation of sandwich composite panels for naval ship structures [11].

## FABRICATION OF LARGE SIZE SANDWICH COMPOSITE PANELS

Large 4' x 4' and 8' x 4' size navy relevant sandwich composites with balsa, PVC, Tycor foam cores and glass and carbon / vinyl ester face sheets were fabricated for blast, shock, ballistic and impact characterization by the Vacuum Assisted Resin Transfer Molding (VARTM) process at the University of Alabama-Birmingham [11]. A total of 6 variants (two 4' x 4' for each variant) were processed with varying face sheet material, core, and stacking sequence.

In the work reported here, out of the six different sandwich composite panels, only three panels which have equal face sheet and core thickness, i.e., the 5 ply E-glass/balsa, 8 ply Carbon/Balsa and 8 ply Carbon/PVC, are considered for computational simulation and analysis. The layup and stacking sequences of these are described in Table I.

Table I. Sandwich Composite Panels Subjected To Blast Loads

| Sno | Face Sheet Material | Core Material | Face-skin Stacking Sequence |
|---|---|---|---|
| 1 | E-Glass/ vinyl ester | Balsa core type 9.7 pcf PB standard | [0/90]/45/[0/90]/45/[0/90] 5 Plies |
| 2 | T-700 Carbon FOE treated/ vinyl ester | Balsa core type 9.7 pcf PB standard | [0/90]/45/[0/90]/$45_2$/[0/90]/ 45/[0/90] 8 Plies |
| 3 | T-700 Carbon FOE treated/ vinyl ester | PVC core type 8.1 pcf Divinycell H130 | [0/90]/45/[0/90]/$45_2$/[0/90]/ 45/[0/90] 8 Plies |

## BLAST TESTING

The six large 4' x 4' x 2.25" thick panels with Balsa, PVC, TYCOR foam cores and E-glass and T700 FOE treated carbon face sheets were mounted in the US Army Corps of Engineers ERDC Blast Load Simulator (Vicksburg, MS) such that the top and bottom were fixed and the other two sides were free. These were subjected to blast load waveforms of 16-18 psi peak pressures and 200 psi-ms impulse which represents an approximate threat level of 2000 lbs of TNT at 140 feet. The blast tested panels underwent about 0.5 to 1.5 inches of mid-point deflection, with no visible signs of external damage.

Figure 2 compares the experimental blast response characteristics of these sandwich panels [11] with respect to mid-point deflection and energy absorption (data normalized to areal density - NTAD).

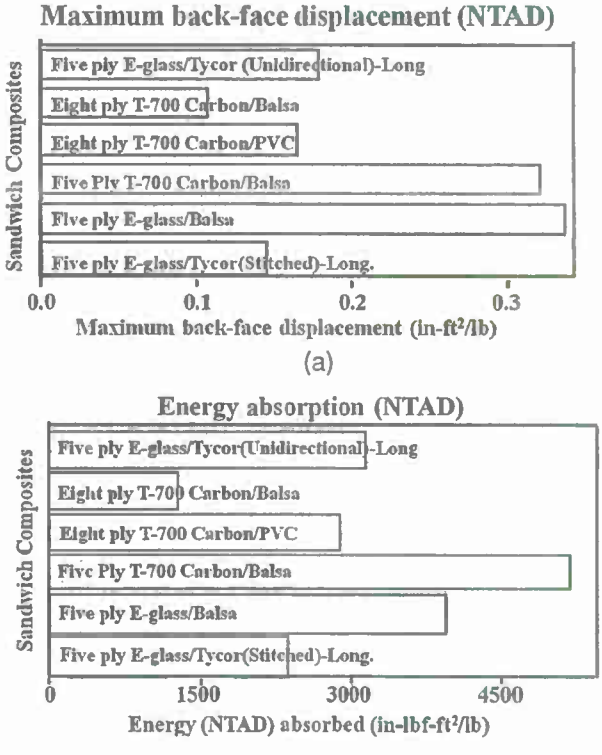


Figure 2. (a) Maximum back-face displacement, and (b) energy absorbed by sandwich composite panels subjected to blast load waveforms of 16-18 psi peak pressures and 200 psi-ms impulse

## FINITE ELEMENT MODELING

The SAP2000 finite element model consists of layered nonlinear shell elements (Figure 3) and allows multiple layers of different thicknesses, each with a different material property, while avoiding shear locking behavior. The shell element also includes the effects of transverse shear deformation. Bulk material nonlinear–stress strain data obtained from quasi-static

tensile and compressive testing of corresponding face sheet and core materials respectively is used as input for the material constitutive models. The quasi-static experimental data shows variation in material properties (Figure 4); hence the averaged experimental and published material data consistent with the SAP2000 program requirements are used as input for the FE model [12].

The strength vs deformation capacity of undamaged sandwich composite panels shown in Table I are established by nonlinear quasi-static finite element analysis [12], with each panel subjected to 1.5 inches of mid-span deformation under displacement control and boundary conditions simulating the complex interactions that occur during the actual blast tests.

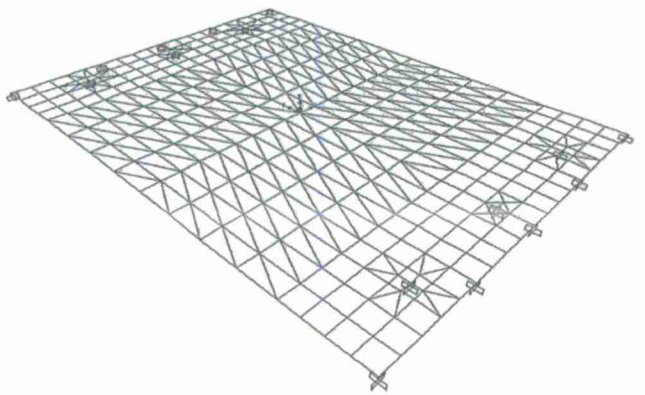

(a)

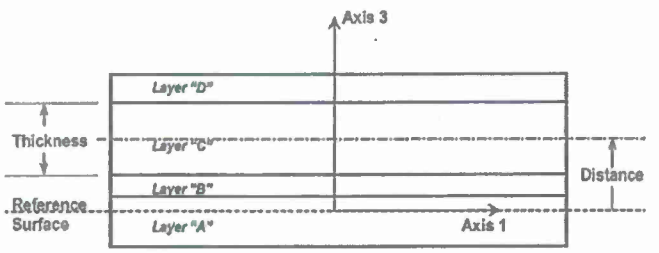


(b)

Figure 3. (a) FE model of sandwich composite panel mesh and boundary conditions, and (b) SAP2000 shell element

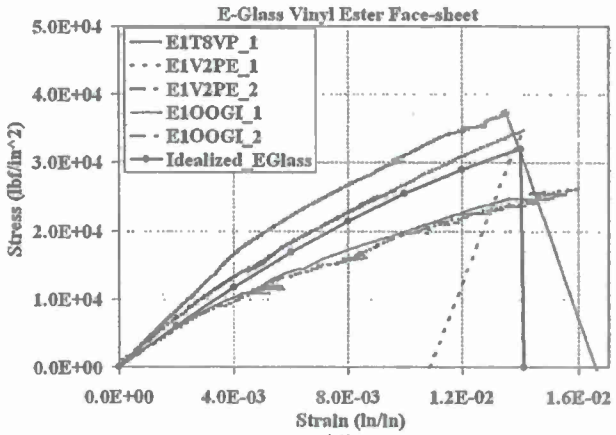


(a)

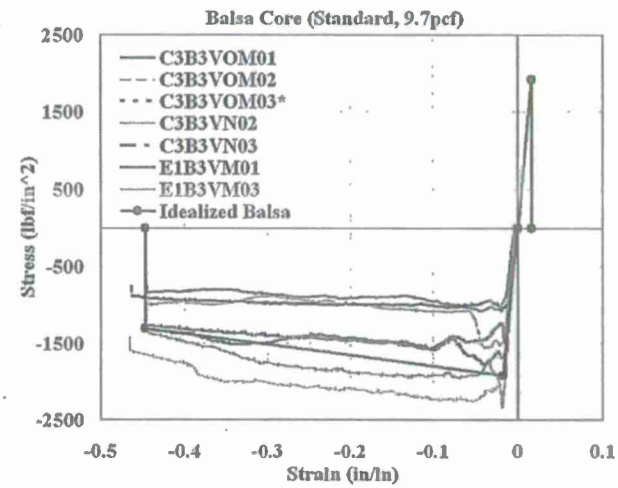


(b)

Figure 4. Experimental uni-axial stress-strain relation and idealization for (a) E-glass vinyl ester face sheets, and (b) Balsa wood core.

## EQUIVALENT SINGLE DEGREE OF FREEDOM IDEALIZATION

The nonlinear force deflection relationship obtained from FE modeling is initially idealized to an elastic-perfectly plastic force-deflection relationship by equating the work done, which is the area under the respective force-deflection curves (figures 5, 7 and 9). The equivalent elastic stiffness $k_e$ and the equivalent maximum elastic deflection $y_o$ are then computed. Since there are non-unique solutions for the idealized curves, in this study the $k_e$ is constrained such that the elastic stiffness of the sdof system is similar to the initial stiffness of the composite panel obtained from quasi-static nonlinear analysis. Based on these assumptions, the component is idealized as an equivalent single degree of freedom (sdof) system [12].

The energy balance method (based on principle of conservation of mechanical energy) is commonly employed to obtain the quasi-static and impulsive asymptotes of P-I curves.



F-126

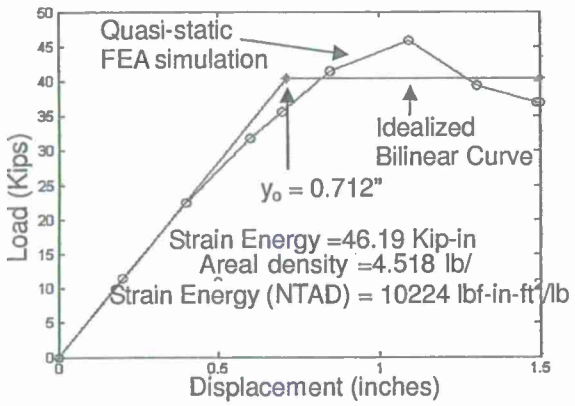


Figure 5. Simulated quasi-static force-displacement relation and equivalent bi-linear idealization for the 5 ply E-glass/Balsa

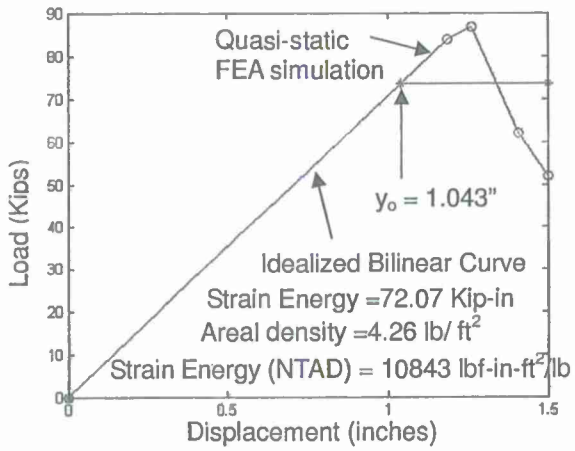


Figure 7. Simulated quasi-static force-displacement relation and equivalent bi-linear idealization for the 8 ply Carbon/Balsa sandwich

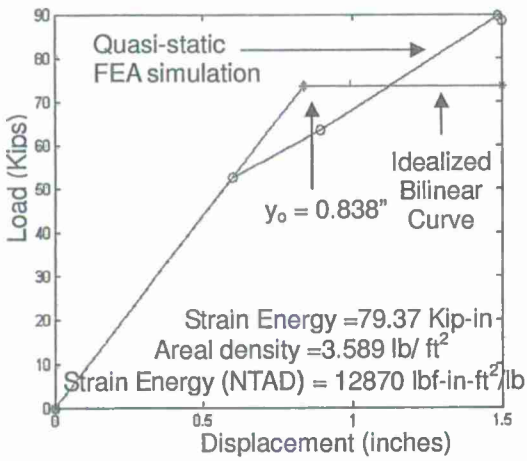


Figure 9. Simulated quasi-static force-displacement relation and equivalent bi-linear idealization for the 8 ply Carbon/PVC sandwich

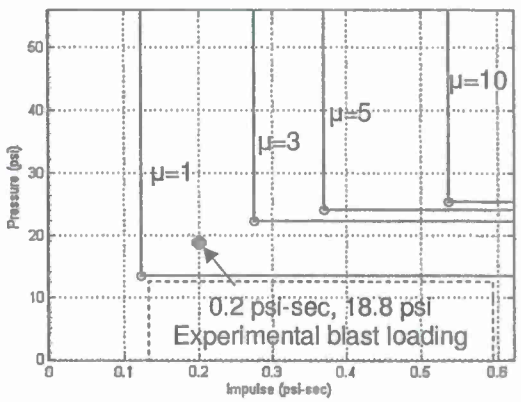


Figure 6. Pressure-Impulse curves for the 5 ply E-glass/Balsa sandwich panel (E1B3VNB1), for different ductility ratios ($\mu_i=y_i/y_o$)

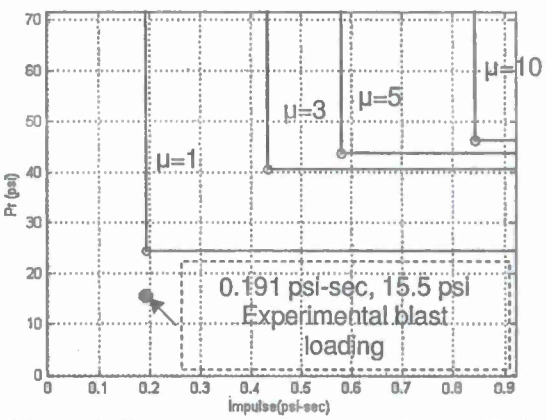


Figure 8. Pressure-Impulse curves for the 8 ply Carbon/Balsa sandwich panel (C3B3V0B1), for different ductility ratios ($\mu_i=y_i/y_o$)

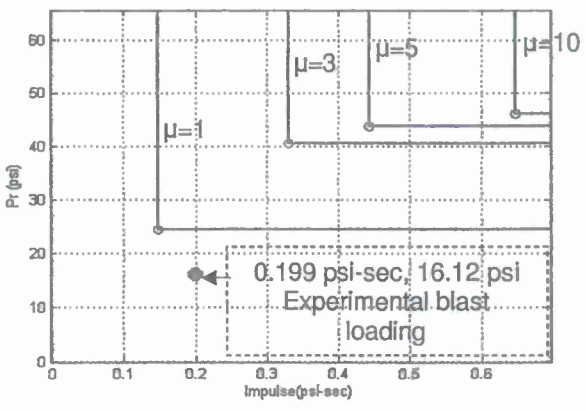


Figure 10. Pressure-Impulse curves for 8 ply Carbon/PVC sandwich panel (C3P2V0B1) for different ductility ratios ($\mu_i=y_i/y_o$)



F-127

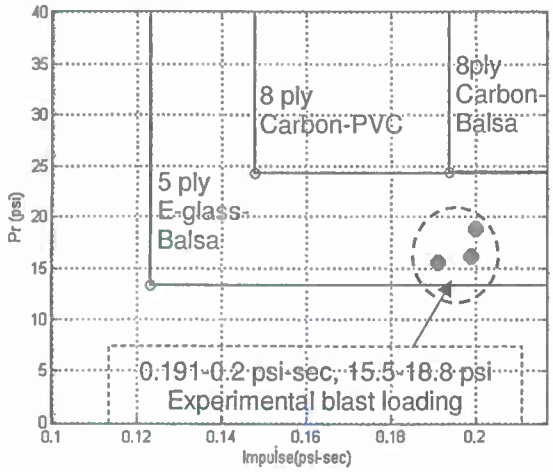


Figure 11. Comparison of Pressure-Impulse curves for the 5 ply E-glass/Balsa, 8 ply Carbon/Balsa and 8 ply Carbon/PVC, for the ductility ratio $\mu = 1$.

To obtain the impulsive asymptote, the total energy imparted to the system is assumed to be in the form of kinetic energy and is equated to the total strain energy stored in the system at its maximum response. For the quasi-static regime, the load can be assumed to be constant before the maximum deformation is achieved and accordingly the quasi-static (Pressure) asymptote is obtained by equating the work done by the load and total strain energy in the system at maximum deformation.

P-I curves can also be generated numerically by simulating the dynamic response of the SDOF system to a large number of triangular impulse loads by using the implicit generalized Newmark method of time integration in Matlab. The time duration of the impulse ($t_d$); the time of rise ($t_r$), peak load and the impulse applied onto the component are varied. The maximum values of response to each loading are then computed, and if they match a certain desired response level, they are stored in an array along with the peak pressure and corresponding impulse.

The quasi-static and impulsive asymptotes for different ductility ratios ($\mu_i = y_i/y_o$) corresponding to critical stages in the component response for the 5 ply E-glass/Balsa, 8 ply Carbon/Balsa and 8 ply Carbon/PVC sandwich panels are plotted in the respective P-I space (Figures 6, 8, 10, 11). These numerical simulations of reduced order enable the construction of iso-damage curves that are suitable for damage prediction over a wider range of blast pressure and impulse combinations.

## CONCLUSIONS

In this work, Pressure vs Impulse (P-I) curves are developed for sandwich composite panels with a variety of skin and core material combinations, to enable the generation of a database of performance envelopes under various blast loading scenarios.

The strength vs deformation properties of the undamaged sandwich composite panels are established by nonlinear quasi-static finite element analysis (FEA) of the component subjected to mid-span deformation under displacement control, with boundary conditions simulating the actual blast tests and idealized for SDOF (single degree of freedom) modeling.

Nonlinear quasi-static analysis indicates that the Carbon/PVC panel has the highest energy absorption (NTAD) capability followed by 8 ply Carbon/Balsa and E-glass/Balsa respectively, based on area under the simulated quasi-static load-deflection curves (Figures 5,7,9). From these force-deformation simulations it appears that for the 8 ply Carbon/Balsa and 8 ply Carbon/PVC panels (having the same face sheet material but different cores) the type of core material type dictates the deformation upto yield, being higher for Balsa than PVC core. However, the energy absorption under quasi-static loading is marginally higher for PVC than Balsa core. Comparison between 5 ply E-glass/Balsa and 8 ply Carbon/Balsa panels (which have the same core, but different face sheet materials) indicates that the face-sheet material determines the peak load resistance of the panel, which is higher for an 8 ply Carbon face sheet than a 5 ply E-glass face sheet of equal thickness.

In the pressure-impulse space, these simulations predict that the 8 ply Carbon/Balsa sandwich panel would require considerably higher blast pressure and impulse values to cause permanent deformation (as defined by the equivalent SDOF system) when compared to the E-Glass/Balsa and Carbon/PVC sandwich panels. For the experimental blast loading conducted at 15.5-18.8 psi pressure and 0.19-0.2 psi-sec impulse, the 5 ply E-glass/Balsa panel absorbs the most energy by virtue of larger plastic deformation, while the 8 ply Carbon/Balsa panel absorbs the least energy as it responds elastically. The analytical predictions are consistent with the experimental data obtained from blast tests. Analysis of the other three sandwich composite panel configurations i.e., the 5 ply Carbon/Balsa, E-glass/Non-Stitched Tycor and E-glass/Stitched Tycor, is currently ongoing.

## REFERENCES

[1] S. A. Tekalur, A. E. Bogdanovich, and A. Shukla, 2009 "Shock Loading Response of Sandwich Panels with 3-D Woven E-Glass Composite Skins and Stitched Foam Core", Composites Science and Technology, Vol. 69, Issue 6, pp. 736-753

[2] J. LeBlanc, A. Shukla, C. Rousseau, and A. Bogdanovich, 2007, "Shock Loading of Three-dimensional Woven Composite Materials", Composite Structures, Vol. 79, No. 3, pp. 344-355.

[3] F. Zhu & G. Lu, 2007, "A Review of Blast and Impact of Metallic and Sandwich Structures", EJSE Special Issue: Loading on Structures

[4] Li, Q.M., and Meng, H., 2002, "Pulse loading shape effects on pressure-impulse diagram of an elastic-plastic, single-degree-of-freedom structural model", International Journal of Mechanical Sciences; 44: pp.1985-1998.

[5] Hoo Fatt MS, Palla L., 2009, "Analytical Modeling of Composite Sandwich Panels under Blast Loads", Journal of Sandwich Structures and Materials, 11(4):357-380.
[6] TM 5-1300/NAVFAC P-397, AFR 88-22 Nov. 1990. Structures to resist effects of accidental explosions.
[7] Tadepalli, T., 2010, "Performance Evaluation of Low-Rise Concrete Frame Building Structures in Moderate Seismic Zones Subject to External Blast Loading," Dissertation, Department of Civil Engineering, University of Mississippi.
[8] Tadepalli,T. and Mullen,C.L., 2008, "Vulnerability of Low Rise Buildings to External Blast Events: Damage Mapping," Proceedings of Inaugural Conference of the Engineering Mechanics Institute, EM08, Minneapolis, MN.
[9] Cheng, A., Al-Ostaz, A., Mullen C.L. and Mantena, P.R., 2009, "Nano Particle Reinforced Composites for Critical Infrastructure Protection," Report submitted to Southeast Region Research Initiative, Managed by UT Battelle for U.S. Department of Energy, supporting the Department of Homeland Security, Task Order: 4000055459.
[10] Tadepalli, T. and Mullen, C.L, 2006, "Simplified blast simulation procedure for hazard mitigation planning," Ninth International Conference on Structures Under Shock and Impact, Wessex Institute of Technology, New Forest, Southampton, United Kingdom.
[11] Mantena, P. R., Rajendran, A.M. and Al-Ostaz, A., 2010, "Blast and Impact Resistant Composite Structures for Navy Ships", 2010 Office of Naval Research - Solid Mechanics Program: Marine Composites and Sandwich Structures Conference, University of Maryland, MD, pp. 379-388.
[12] Tadepalli,T. and Mantena,P.R., 2011, "Computational simulation and experimental characterization of sandwich composite panels subjected to blast loads", The 26th Annual American Society of Composites Technical Conference, Montreal, Canada, Paper No. 1081.

## ACKNOWLEDGEMENTS

This research was supported by ONR Grant No. N00014-7-1-1010, Office of Naval Research, Solid Mechanics Program (Dr. Yapa Rajapakse, Program Manager). The sandwich composite panels were fabricated by Dr. Uday Vaidya and Dr. Selvum Pillay at the University of Alabama-Birmingham.

J_ID: AMJ DOI: 10.1115/1.4004536 Date: 14-July-11 Stage: Page: 1 Total Pages: 7

PROOF COPY [JAM-10-1036] 029105AMJ

ASME-JOURNAL OF APPLIED MECHANICS, Vol 78 (6), NOV 2011

# First Principles Estimation of Shock Tube Tests on Nanoreinforced Composite Materials

**Weiping Xu**
Lecturer, Civil Engineering
Southwest Jiaotong University,
Room 402, Building C,
144 Jiaoda Road Southwest Jiaotong Science Park,
Jinniu District Chengdu City,
Sichuan Province, China 610031
e-mail: weipingxu2010@gmail.com

**Elizabeth K. Ervin**
Assistant Professor, Civil Engineering
203 Carrier Hall, P.O. Box 1848,
University of Mississippi,
University, MS 38677-1848
e-mail: eke@olemiss.edu

*Extreme loads events can cause enormous human and infrastructure losses. Camputer modeling is the key to reducing the high cast af dynamic monitoring and experimentatian. Engineers in various fields have undertaken camplicated madeling for structures under abnarmal loads. However, an efficient and accurate model is necessary ta mare rapidly address dangeraus shock prablems. Campasite materials have replaced metals in variaus applicatians thanks ta their superiar shock resistance praperties. This investigatian particularly relates ta their usage on naval ships ta achieve improved blast survivability with the additional benefit of lower cost. A relatively simple model is detailed far the appraximate centerline respanse predictian of the specific camplex case of campasite materials tested in a shack tube. A modal analysis simulatian af a beam is perfarmed using grass praperties as well as physical geometry and arbitrary shack. Clased form equatians have been emplayed to derive the eigenprablem that generates mode shapes and natural frequencies, and the resulting respanses are campared ta experimental shack tube test results. The best outcome was generated by the simplest model consisting af a shock pressure pulse averaged in two divisions and applied over the entire beam span. For this case, the simulatian and experimental respanses had reasanable correlation far fractured E-glass/vinyl-ester compasite specimens with bath nanaclay and graphite platelet reinfarcement. This madel is also a canservative estimate for the transient test deflection range for all other specimens.* [DOI: 10.1115/1.4004536]

*Keywords: closed-farm, shack tube, compasite, nanoreinforcement*

## 1 Introduction

Extreme loads such as earthquakes and explosions can cause enormous human and infrastructure losses. Considering the high cost of dynamic monitoring and experimentation, computer models are the keys to reducing physical test requirements. With improved computational capacities, engineers in various fields have undertaken complicated modeling for structures under abnormal loads. However, an efficient and accurate model is necessary to more rapidly address dangerous shock problems. A relatively simple model will be detailed herein for the response prediction of the specific complex case of composite materials tested in a shock tube.

Thanks to superior properties, composite materials have replaced metals in various engineering applications. Composites offer numerous advantages such as high strength/weight ratio, low cost, corrosion performance, and improved stealth. Due to enhanced shock resistance, there is a specific demand for composite materials in defense applications. This investigation particularly relates to the usage on naval ships to achieve better blast survivability with the additional benefit of lower cost. While Gibson discussed the basic concepts, mechanical properties and test methods for composite materials in [1], shock damage evolution within a composite is still actively being investigated [2]. For instance, Bogdanovich applied geometrically nonlinear theory, dynamic deformation, and failure analysis methods to laminated composite cylindrical shells exposed to longitudinal and lateral blast-type loading [3]. While these complex theories are useful, testing is still required to validate and verify model results.

Experimental investigations have been performed to induce shock damage in composite materials. Shock tests can be realized mainly by explosive or air blasts, both of which are costly and time consuming. The more reusable test apparatus, shock tubes generate air shocks on specimens by using an inert gas either inside or outside a driving piston [4]. Utilized in this work, the shock tube constructed by Dr. Arun Shukla at the University of Rhode Island uses simply supported test specimens of 256 mm by 102 mm. The span of the experimental plate was 152 mm, and the overhangs were 50.8 mm at each end. Each specimen is placed into an instrumented driven section of the tube. In the adjoining driven section, helium pressure builds until a mylar diaphragm ruptures, sending an air blast that imparts a shock wave to the specimen [5].

Many researchers focus on finding computer models for such shock problems. Lall has developed an approach for analyze the shock damage initiation and progression, based on closed-form energy models, explicit finite elements, and statistical pattern [6]. Using a linear acoustic plane wave assumption, Li and Hua approximately solved the transient vibration of an elastic laminated composite cylindrical shell with infinite length exposed to an underwater shock wave [7]. Applying the finite element program Abaqus/Explicit together with a user material subroutine, large woven roving E-glass/vinyl-ester composite panels subjected to shock loads have also been modeled by Johnson et al. [8]. Through both three-dimensional X-ray microstructural investigation and a parallel series of shock experiments using a 50 mm ballistic gas gun, McDonald and Millett worked to link microstructure and simulation to predict the shock performance of a composite material [9]. The propagating disturbance of breaking

Contributed by the Applied Mechanics Division of ASME for publication in the JOURNAL OF APPLIED MECHANICS. Manuscript received February 8, 2010; final manuscript received July 6, 2011; published online XX XX XXXX. Assoc. Editor: Vikram Deshpande.

 Copyright © 2011 by ASME 

G-130

ID: sambasivamt Time: 11:04 I Path: O:/3b2/AM/#Vol00000/110046/APPFile/AI-AM/#110046

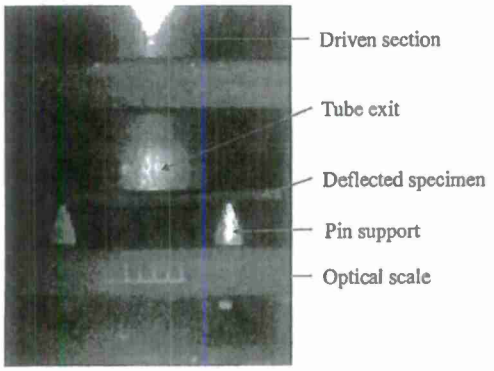


**Fig. 1 A still photograph of a loaded test specimen**

fibers has been generated by Goeke and McClintock to find the critical fracture location of three-dimensional graphite composites undergoing shock [10]. In a quite complicated manner, Raimondo et al. worked to join low velocity constitutive failure models, including delamination, with orthotropic state equations [11].

The main purpose of this paper is to obtain structural response to an arbitrary shock load through a modal analysis simulation, which is reasonably accurate and responsive as compared to complex models. Model input includes the gross properties of Young's modulus and material density as well as physical geometry and arbitrary shock load. Closed form equations have been employed to derive the eigenproblem that generates mode shapes and natural frequencies, and the aim is to estimate experimental responses of composite materials to actual shock tube results.

## 2 Model Case Studies

Six different cases are used in this work to model a composite specimen's response to transient pressure. The modeled cases differ by applied load (cases 1, 2, and 3) and boundary conditions (cases 4, 5, and 6) in order to determine the most accurate model.

**2.1 Description.** Obtained via high-speed photography, a specimen view of the shock tube test configuration is shown in Fig. 1. The longitudinal centerline section of the plate is simulated as a beam, and any transverse relative motion is neglected. Presuming linear elasticity, the employed Euler-Bernoulli beam model is provided in Fig. 2. Permitting multiple boundary conditions, $K_{t1}$ and $K_{t2}$ are torsional springs while $k_1$ and $k_2$ are lateral springs. The width of the cross section is 101.6 mm, and the thickness is 9.525 mm. The gross material parameters used in the simulation are provided in Table 1; note that the elastic modulus is determined through three-point bend beam impact testing at the University of Mississippi. Base excitation $f(t)$ can be considered, but it is converted herein to an effective distributed force which

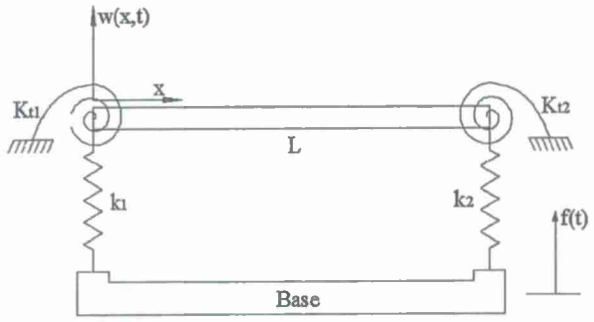


**Fig. 2 First principles beam model**

**Table 1 Measured E-glass/vinyl-ester specimen properties**

| Sample name | Reinforcement | Density ($kg/m^3$) | Flexural modulus (GPa) | Weight |
|---|---|---|---|---|
| VC00AS01 | none | 1112.44 | 2.56 | — |
| VC00AS01t2 | none | | | — |
| VC12BS01 | nanoclay | 1132.99 | 2.24 | 1.25% |
| VC12BS02 | | | | |
| VC25BS01 | | 1139.65 | 2.55 | 2.5% |
| VC25BS02 | | | | |
| VG12BS01 | graphite platelets | 1117.29 | 2.73 | 1.25% |
| VG12BS02 | | | | |
| VG25BS01 | | 1133.58 | 3.56 | 2.5% |
| VG25BS02 | | | | |

simulates the shock tube pressure. Discrete test data has been provided for the midspan displacement $w(L/2, t)$ using optical means.

**2.2 Case Studies.** The applied impulse and boundary conditions are herein detailed for each simulated case.

*2.2.1 Case 1.* In case 1, the entire excitation force is distributed over the entire beam length, as shown in Fig. 3. This neglects that the exit tube does not extend over the free span and the plate overhangs the simple supports. Ideal pinned boundary conditions are also assumed.

The cross sectional area of the shock tube at the 76.2 mm driven section $A_{sec}$ is 4560.4 $mm^2$. Thus, the excitation force $F(t)$ is

$$F(t) = P(t)A_{sec}$$

and the distributed pressure load $q(t)$ is

$$q(t) = \frac{F(t)}{l}$$

Shown in Fig. 4(*a*), the applied pressure for case 1 is simulated by dividing the measured pressure profile into two constant regions of average magnitude. Thus, the effective force is 21 and 19.25 N s/mm of beam length as shown in Fig. 4(*b*).

Modal analysis is employed to apply the equivalent force to the model. First, the closed-form beam equation is solved to obtain mode coefficients and natural frequencies. The first three calculated natural frequencies of the specimen VC00AS01 are 282.8, 1131.4, and 2545.5 Hz. For an exact solution, an infinite number of modes are required in the modal analysis, but this is computationally unrealistic. Thus, convergence studies are employed to ensure that enough modes are used in the simulation. As provided in Fig. 5, the results for this case converge at just two modes.

*2.2.2 Case 2.* In the actual shock tube tests, the ratio of the loading diameter to the span was the significant proportion of one-half as shown in Fig. 6(*a*). For case 2, the distributed equivalent force is based upon the driven section diameter of 3 in. as provided in Fig. 6(*b*).

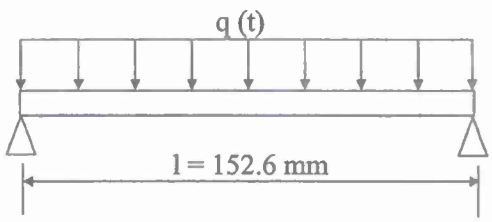


**Fig. 3 Distributed load model of case 1**



G-131

ID: sambasivamt Time: 11:04 I Path: O:/3b2/AMJ/#Vol00000/110046/APPFile/AI-AMJ/#110046

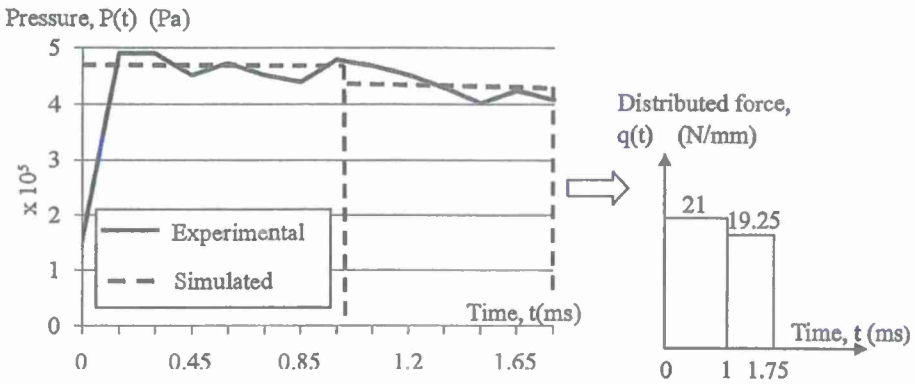


Fig. 4 (*a*) Applied pressure $P(t)$ and (*b*) excitation force for VC00AS01 case 1

To evenly distribute the pressure over the entire beam, an equivalent deflection of case 1 to case 2 at the middle point is desired. The static midspan deflection in case 1 is

$$\delta_1 = \frac{5}{384}\frac{q_1 l^2}{EI}$$

and for case 2 is

$$\delta_2 = \frac{11}{2048}\frac{q_2 l^2}{EI}$$

In order to have the same deflection at the middle point, or $\delta_1 = \delta_2$, the equivalent distributed force is

$$q_1(t) = 0.4124 q_2(t)$$

After applying this equivalence to the excitation of case 1, the forces in case 2 are shown in Fig. 7.

*2.2.3 Case 3.* The effective excitation force for case 3 is obtained in the same manner as in case 2. However, the excitation pressure is discretized into smaller constant time intervals, as shown in Fig. 8. The difference among cases 1, 2, and 3 is strictly excitation force; thus, the models will converge similarly.

*2.2.4 Case 4.* Case 4 is similar to case 3 in excitation but has different boundary conditions. End moments are added to simulate the effect of the test specimens overhanging the supports.

As shown in Fig. 9(*b*), the moment induced is

$$M = \frac{1}{2}\rho A L^2 g = 13.6\ \text{N} - \text{mm}$$

where $\rho$ is the material density, $A$ is the cross sectional area of the plate, $L$ is the length of the overhang, and $g$ is gravitational acceleration. These moments are enforced as constant $K_{t1}$ and $K_{t2}$ (Fig. 2) and prove to be relatively small compared to the threshold of $1.13 \times 10^8$ N mm/rad for fixed-fixed boundary conditions. The VC00AS01 case 4 natural frequencies are less than 1% different from previous cases, and the response also converges at two modes.

*2.2.5 Case 5.* In case 5, additional boundary conditions are considered. The supports were not attached to the specimens and relative motion may occur, specifically when pinned only on one side as in Fig. 1. Thus, the values for the lateral springs $k_1$ and $k_2$ are adjusted to simulate this possible condition. With $1.8 \times 10^5$ N/mm being the threshold for pinned ends, both lateral spring constants of $1.8 \times 10^3$ N/mm were selected to allow limited motion. The first three natural frequencies of the specimen VC00AS01 are 267.1, 896.2, and 1572.6 Hz. With identical excitation force as in case 4, convergence was again reached at two modes.

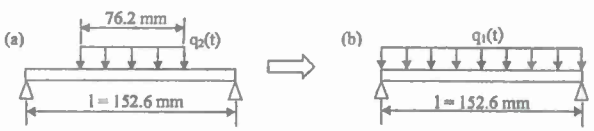


Fig. 6 Configuration of (*a*) experimental specimen and (*b*) simulated model

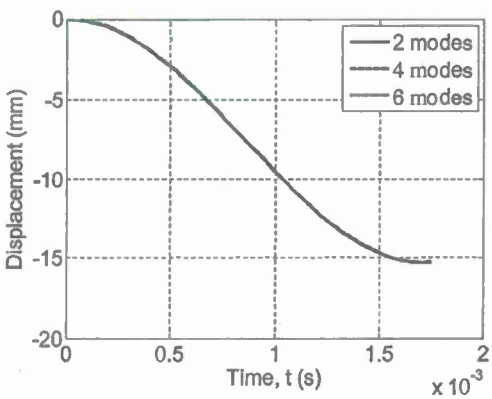


Fig. 5 Convergence study for VC00AS01 case 1

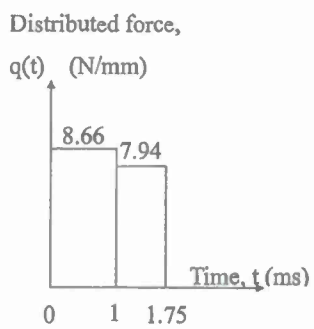


Fig. 7 Equivalent force values for case 2



G-132

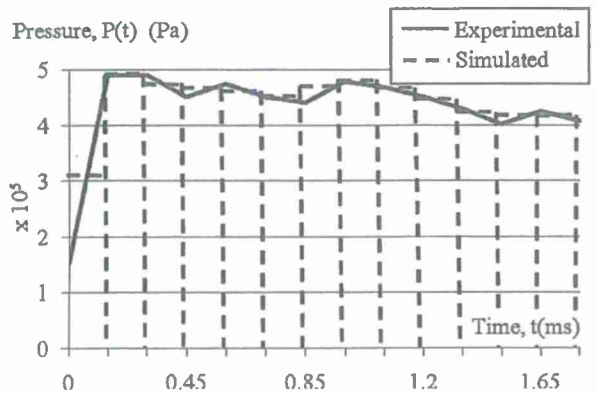


Fig. 8 Excitation pressure for VC00AS01 case 3

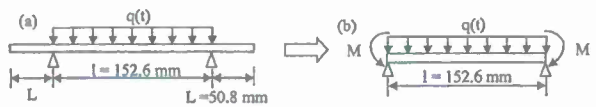


Fig. 9 Beam model for case 4

*2.2.6 Case 6.* For case 6, possible asymmetric boundary conditions were simulated as differing the lateral spring constants $k_1$ and $k_2$ of $1.8 \times 10^3$ and $1.8 \times 10^7$ N/mm, respectively. The first three natural frequencies of the specimen VC00AS01 are 274.5, 987.1, and 1878.7 Hz. The results for VC00AS01 case 6 converge at two modes as well.

## 3 Results

The six cases are plotted for VC00AS01 in Fig. 10. Since cases 3 and 4 are quite similar, the overhanging portions do not induce significant boundary changes. Case 1 shows a significantly greater deflection, indicating an overestimation of load. Case 1 is the most diverse as compared with all others; Case 2 through case 6 are less than 5% different. As case 5 is the most complex symmetric case, cases 1 and 5 are used for further comparisons to experimental data. The results for the ten different materials are provided in Figs. 11 through 20.

The results of the case studies as contrasted with the experimental shock tube results are provided in Table 2. In order to quantify the disparity, the root mean square (rms) relative difference of the model ($y$) to the test ($x$) response was calculated by

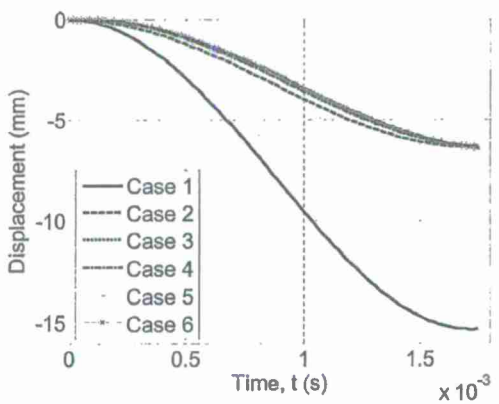


Fig. 10 Comparison of the midspan deflection of the six cases for VC00AS01

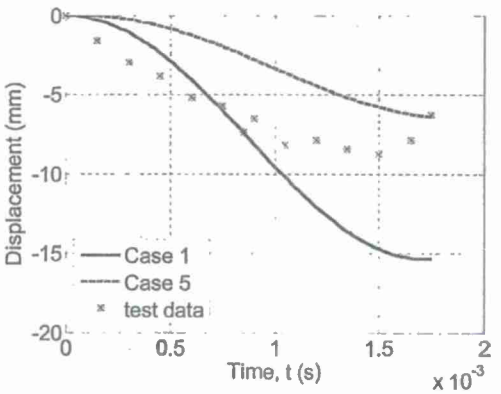


Fig. 11 Midspan deflection for VC00AS01

$$\sqrt{\frac{1}{n}\sum_{i=1}^{n}\left(\frac{y_i - x_i}{x_i}\right)^2}$$

where $n$ is the number of discrete data points.

## 4 Discussion

As discussed in the following subsections, three main conclusions can be characterized from these results. Note that the peak pressure in the shock tube was approximately 0.5 MPa and faded over 14 ms, inducing an average velocity of approximately 6 m/s in the specimens.

**4.1 Case 1 Applicability.** Unexpectedly the simplest case is the most accurate for broken specimens. Case 1 is a reasonable model for all fractured specimens with nanoreinforcement. This may be because using an elastic model does not consider the plastic deformation of the specimen. The consideration of the shock impulse spanning the entire beam compensates for the neglect of plasticity in the model. Similar results were obtained as well in the impact tests of [12]. For the unbroken specimens, it is not clear which case is a better model as it depends on whether the specimen has entered the plastic range. In short, case 1 is an advisable model choice for response approximation for any case: the result is a conservative overestimate of deflection.

**4.2 Case 5 Underestimation.** For most cases the model underestimates the deflection. This implies that either the force is underestimated or the plate stiffness may be overestimated. Another possible explanation is that, although the driver section is

**Table 2 rms comparison of model to data and resulting conclusions**

| Sample name | Post test condition (load) | rms difference Case 1 | rms difference Case 5 | Applicable section(s) |
|---|---|---|---|---|
| VC00AS01 | unbroken (0.48 MPa) | 0.648 | 0.624 | 4.2, 4.3 |
| VC00AS01t2 | broken (0.83 MPa) | 1.540 | 0.509 | 4.2, 4.3 |
| VC12BS01 | unbroken (0.48 MPa) | 0.959 | 0.619 | 4.2, 4.3 |
| VC12BS02 | broken (0.83 MPa) | 0.374 | 0.718 | 4.1 |
| VC25BS01 | unbroken (0.48 MPa) | 1.104 | 0.593 | 4.2, 4.3 |
| VC25BS02 | broken (0.83 MPa) | 0.734 | 0.898 | 4.1, 4.2 |
| VG12BS01 | unbroken (0.48 MPa) | 0.563 | 0.579 | 4.2, 4.3 |
| VG12BS02 | broken (0.83 MPa) | 0.402 | 0.746 | 4.1 |
| VG25BS01 | unbroken (0.48 MPa) | 0.585 | 0.716 | 4.2, 4.3 |
| VG25BS02 | broken (0.83 MPa) | 0.631 | 0.929 | 4.1 |

PROOF COPY [JAM-10-1036] 029105AMJ

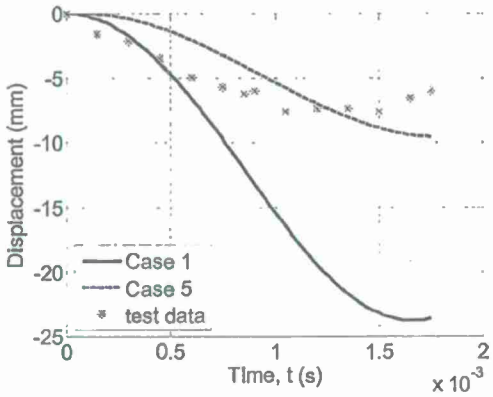


Fig. 12 Midspan deflection for VC00AS01t2

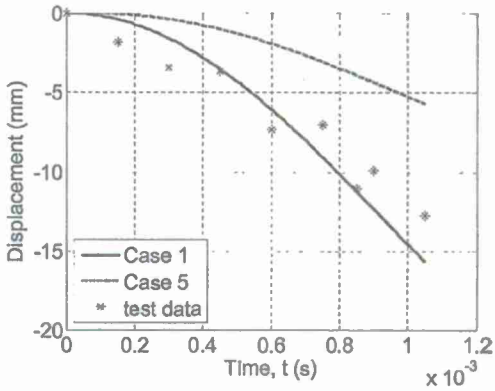


Fig. 14 Midspan deflection for VC12BS02

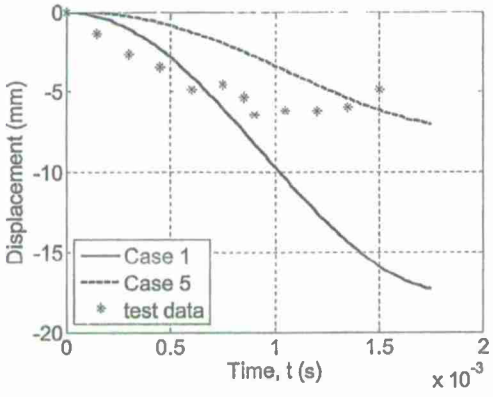


Fig. 13 Midspan deflection for VC12BS01

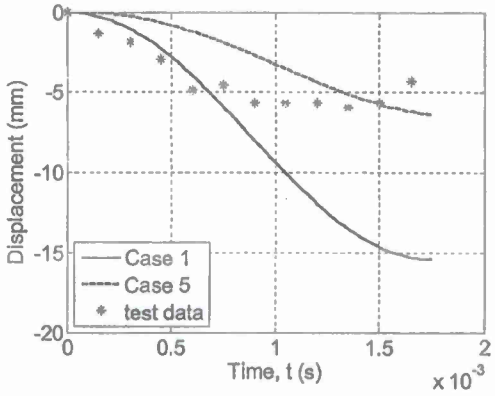


Fig. 15 Midspan deflection for VC25BS01

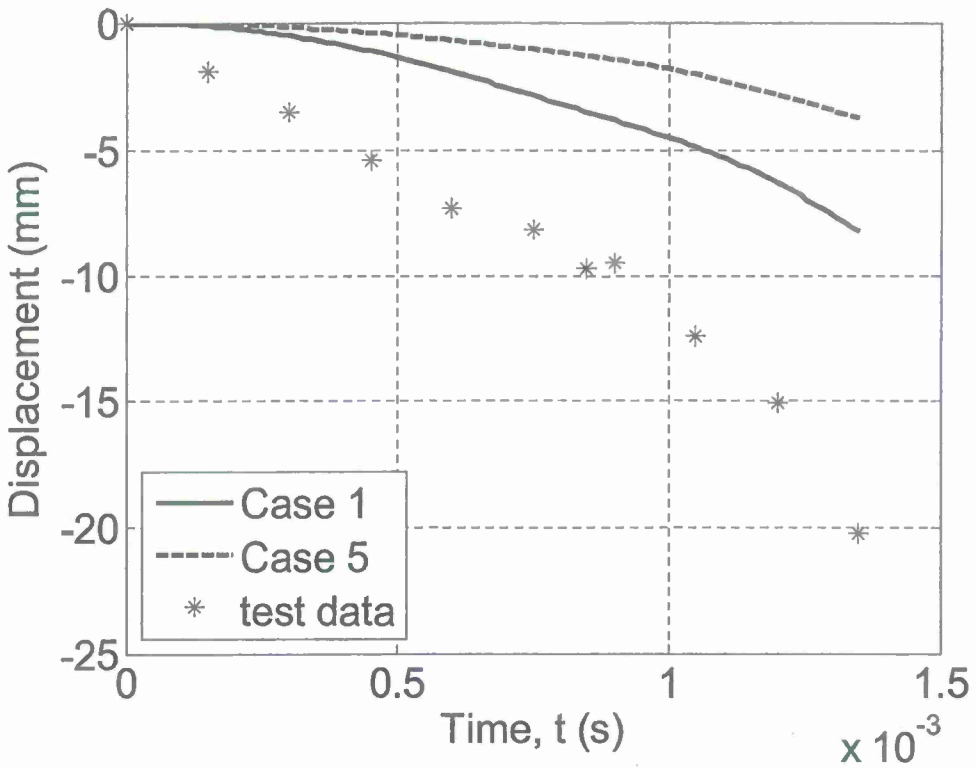


Fig. 16 Midspan deflection for VC25BS02



G-134

ID: sambasivamt Time: 11:05 I Path: Q:/3b2/AMJ/#Vol00000/110046/APPFile/AI-AMJ#110046

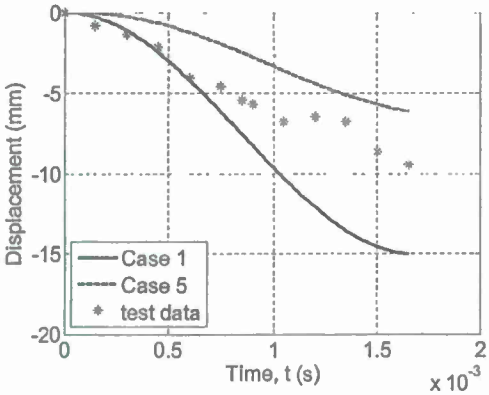


Fig. 17 Midspan deflection for VG12BS01

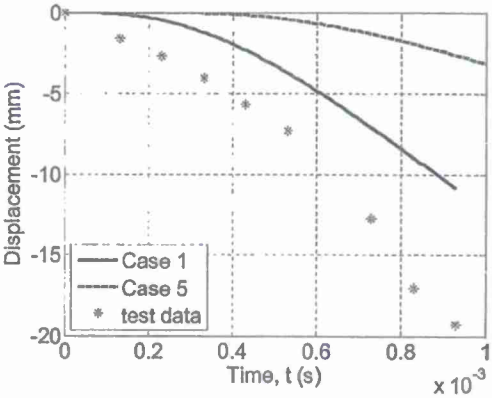


Fig. 20 Midspan deflection for VG25BS02

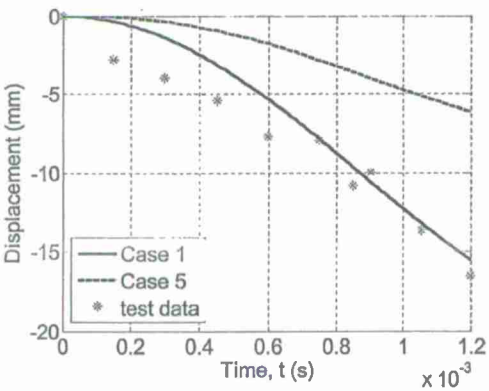


Fig. 18 Midspan deflection for VG12BS02

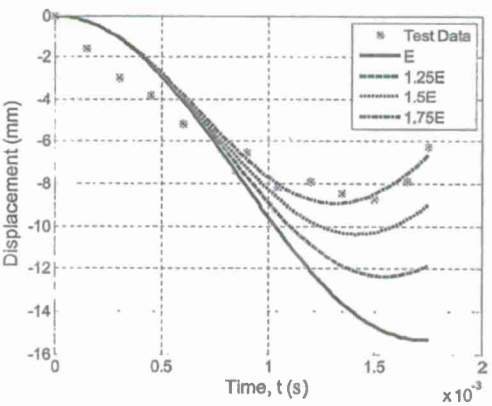


Fig. 21 Midspan displacement of case 1 VC00AS01 with changing elastic modulus

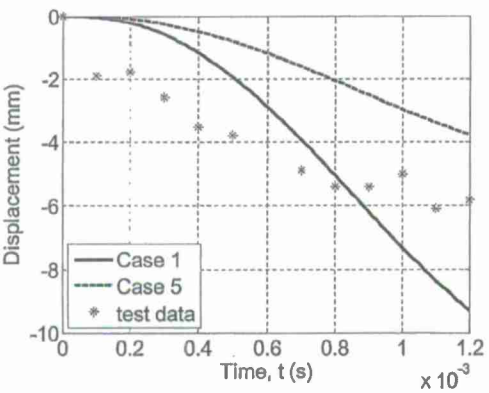


Fig. 19 Midspan deflection for VG25BS01

close to contacting the specimen, leakage may exist which could allow the pressure pulse to spread to other areas besides the driver section. This would have a considerable effect as the linear model is quite sensitive to the applied force. Additionally, the beam model does not consider any transverse or directional plate properties. The layup of the E-glass fibers is also neglected as the gross material properties are employed.

**4.3 Frequency Underestimation.** For every experimental test, the measured data points reveal an upward trend before 1.75 ms have elapsed. The rebounding behavior implies that the model underestimates the natural frequencies of the plate. While this could be due to transverse modal coupling, the gross elastic modulus is a more likely cause. As it is universally proportional to the model's natural frequencies, the elastic modulus measured by the impact machine may undervalue the effective modulus in the shock tube tests. The results of a parameter study for the unreinforced specimen VC00AS01 is shown in Fig. 21. Case 1 shows the best agreement with the test data when the modulus used for the simulation is 1.75 times bigger of the given value. Note that another source of higher frequencies may be contact with the supports, which will be examined in the future. Case 5 provides the same trend but does not improve its accordance as the elastic modulus increases.

## 5 Summary

The structural response to an arbitrary shock load has been obtained through a modal analysis simulation. Model input includes the gross material properties, physical geometry, and shock tube pressure. Closed form equations have been employed to generate the mode shapes and natural frequencies that correspond to ten different composite material configurations. After considering a variety of boundary conditions and impulse discretizations, simulation responses show that a uniform full-span load generated from an averaged pressure model provides a fairly accurate model. This case specifically applies for all fractured specimens with reinforcement, and it is an advisable and conservative choice for all other specimens as well. The model is strictly linear; however, the specimens enter a nonlinear plasticity or fracture



G-135

state. All specimens are composite, so an isotropic beam model will result in additional disparity. Despite these simplifications, the results with the closed-form beam model are similar in range with the experimental results. Thus, this quick and efficient tool estimates experimental shock tube test response with reasonable accordance.

## Acknowledgment

The research was funded by ONR Grant N00014-07-1010, Office of Naval Research, Solid Mechanics Program (Dr. Yapa D.S. Rajapakse, Program Manager). We would like to thank Dr. Arun Shukla at the University of Rhode Island for performing the shock tube tests.

## References

[1] Gibson, R. F., 2007, *Principles of Composite Material Mechanics*, 2nd ed., CRC, Boca Raton, FL.

[2] Tekalur, S. A., Shivakumar, K., and Shukla, A., 2008, "Mechanical Behavior and Damage Evolution in E-Glass/Vinyl-Ester and Carbon Composites Subjected to Static and Blast Loads," Composites: Part B, 39, pp. 57–65.

[3] Bogdanovich, A., 1993, *Non-linear Dynamic Problems for Composite Cylindrical Shells*, Elsevier Applied Science, London.

[4] Glenn, D. H., and Croeley, B. K., 1971, "Analysis of a High-Explosive Shock-Tube Experiment," Journal of Applied Physics, 42(5), pp. 2099–2105.

[5] Tekalur, S. A., Shukla, A., and Shivakumar, K., 2008, "Blast Resistance of Polyurea Based Layered Composite Materials," Composite Structures, 84, pp. 271–281.

[6] Lall, P., Choudhary, P., Gupte, S., and Suhling, J., 2006, "Health Monitoring for Damage Initiation & Progression During Mechanical Shock in Electronic Assemblies," *2006 Electronic Components and Technology Conference*, San Diego, California, pp. 85–94.

[7] Li, J., and Hua, H., 2009, "Transient Vibration of Laminated Composite Cylindrical Shells Exposed to Underwater Shock Waves," Engineering Structures, 31, pp. 738–748.

[8] Johnson, H. E., Louca, L. A., and Mouring, S. E., 2006, "Current Research Into Modeling of Shock Damage to Large Scale Composite Panels," Journal of Material Science, 41, pp. 6655–6672.

[9] McDonald, S. A., and Millett, J. C. F., 2007, "The Shock Response, Simulation and Microstructural Determination of a Model Composite Material," Journal of Material Science, 42, pp. 9671–9678.

[10] Goeke, E. C., and McClintock, F. A., 1975, "Fracture of Graphite Composites Under Shock Loading," Journal of Applied Physics, 46(11), pp. 4671–4673.

[11] Raimondo, L., Lannucci, L., Robinson, P., Curtis, P. T., and Wells, C. M., 2005, "Shock Modeling of Multi-phase Materials: Advances and Challenges," *2005 ASME Pressure Vessels and Piping Division Conference*, Denver, Colorado, pp. 807–817.

[12] Mouring, S. B., Louca, L., and Levis, W., 2005, "Structural Response of Impact-Damaged Composite Panels," *Proceedings of MTS/IEEE OCEANS 2005*, 2, pp. 1370–1373.

# Dynamic Mechanical and Impact Property Correlation of Nanoclay and Graphite Platelet Reinforced Vinyl Ester Nanocomposites

SWASTI GUPTA AND P. RAJU MANTENA*
*Department of Mechanical Engineering, University of Mississippi, Mississippi, MS, USA*

AHMED AL-OSTAZ
*Department of Civil Engineering, University of Mississippi, Mississippi, MS, USA*

**ABSTRACT:** An experimental investigation was carried out to correlate the impact response of nanocomposites with the dynamic, inherent damping, and glass transition properties of Derakane 411-350 vinyl ester thermoset reinforced with 1.25 and 2.5 wt% Cloisite 30B nanoclay and exfoliated graphite nanoplatelets (xGnP).

Dynamic mechanical analysis was performed to obtain the visco-elastic properties such as storage modulus ($E'$), loss modulus ($E''$), glass transition temperature ($T_g$) and loss factor (Tan $\delta$). Low velocity impact tests were performed at an approximate strain rate of $15\,s^{-1}$ on notched and unnotched Charpy samples using a drop-tower impact test system. Storage modulus was observed to increase with increasing nano reinforcements (max 40% for graphite platelet/vinyl ester nanocomposite). Loss factor also showed a significant increase of 80% with the addition of nanoclay, and 125% with graphite platelet. Glass transition temperature and loss modulus of nanoclay and graphite platelet reinforced nanocomposites also showed significant improvements over the pristine polymer. Low-velocity impact tests showed an increase of almost 100% energy absorption for unnotched samples with increasing nano reinforcement. However, a 70–90% reduction was observed in the case of notched samples. A direct correlation between impact response and dynamic mechanical properties for these vinyl ester nanocomposites was observed.

**KEY WORDS:** dynamic mechanical analysis, low-velocity impact, storage and loss modulus, vinyl ester nanocomposites, damping and glass transition.

## INTRODUCTION

IN THE PAST decade several polymer composites have been developed with different fiber reinforcement to improve modulus, strength, fatigue, corrosion mitigation, durability, flammability, and viscoelastic response. It is reported that mechanical and thermomechanical properties of composites are vastly improved by reinforcing the polymer with nano-sized rather than micron-sized particles of the same material [1]. One of the reasons attributed to this is fewer defects in the filler particle at the nano level as compared to

*Author to whom correspondence should be addressed. E-mail: meprm@olemiss.edu
Figures 1–5 and 7 appear in color online: http://jrp.sagepub.com



0731-6844/10/13 2037–11 $10.00/0 DOI: 10.1177/0731684409341762
© The Author(s), 2010. Reprints and permissions:
http://www.sagepub.co.uk/journalsPermissions.nav

H-137

micro or macro level [2]. Further, many important chemical and physical interactions are governed by surfaces and surface properties [3]. Hence, nanoreinforcements having very high surface-to-volume ratio exhibit substantially different composite properties.

These new class of composites are increasingly being studied for their application in structures such as spacecrafts, airplanes, warships etc. which require high stiffness-to-weight ratio along with high damping. Nanoclay [4–7] and graphite platelets [8–12] are some of the nano scale inclusions proposed as filler materials showing promise for structural applications, and have been investigated in this work for naval ships and homeland security applications. It is well known and documented that stress state in composites could be multi-axial and nonuniform even under a uniaxial loading due to complex interaction between the fiber and matrix. Hence, a detailed study into the dynamic behavior and the principles guiding them is a must before putting these nanocomposites in use. It includes understanding the elastic and fracture properties as well as interaction between fiber/matrix interface.

It is well known that composites loose significant properties above the glass transition temperature. Structural materials subjected to dynamic loading should ideally have high stiffness along with high damping to be effective in blast/shock/impact loading. Further, high storage modulus to enhance the ability to absorb energy before failure as well as high loss modulus to dissipate the energy are advantageous. High damping or loss factor (tan $\delta$) expressed as the ratio of loss modulus to the storage modulus, is also desirable to avoid catastrophic failure.

The objective of this work is to study the impact and dynamic properties of nanoclay/vinyl ester and graphite platelet/vinyl ester nanocomposites with 1.25 and 2.5 wt% nano reinforcements and comparison with the pure polymer. These nanocomposites are proposed as face plates of sandwich composite structure with fire-resistant foam layered in between to enhance the energy absorption along with optimal flexural rigidity, vibration damping and reduced flammability. This new class of material is expected to make the structure blast/shock/impact resistant with reduced weight for naval ships and homeland security applications. An attempt is made to investigate the correlation between dynamic mechanical and impact properties, which can reduce the need for more expensive impact testing.

## EXPERIMENTS

### Specimen Preparation

For this research, Derakane 411-350 vinyl ester thermoset plates of dimension 280 mm × 280 mm × 10 mm (10″ × 10″ × 0.39″) were manufactured at Michigan State University with 1.25 and 2.5 wt% of cloisite 30B nanoclay and exfoliated graphite nanoplatelets (xGnP). High viscosity of vinyl ester resin restricted the higher percentage of nano reinforcement due to the problems with removal of entrapped air and improper mixing.

Dynamic mechanical analysis was performed in single cantilever deformation mode with fixed-fixed boundary condition using a clamp having a span of 17.5 mm (0.69″). Prismatic samples with nominal dimension of 10.0 mm width × 1.6 mm thick. (0.39″ × 0.06″) were milled from the manufacturer supplied plates and cut to a length of ~30 mm (1.18″) to provide sufficient overhang for clamping. It is to be noted that in all the samples, thickness of supplied plate (10 mm) was used as width for the DMA sample. Two samples were tested from each configuration.

Low-velocity impact tests were performed in flexure mode using simply supported fixture with a span of 95.25 mm (3.75″). Impact samples were milled to the dimensions of 127 × 10.0 × 12.7 mm (5″ × 0.39″ × 0.5″), as per ASTM D-6110-06 [13] test requirements. Five samples were tested from each configuration with and without notch. The notch, where applicable, was cut by specially made milling cutter with an angle of 45° and a depth of 2.54 mm (0.1″) from top of plate, maintaining a dimension of 10.16 ± 0.05 mm (0.400″ ± 0.002″) for thickness under notch. It is to be noted that thickness of the specified plate (10 mm) was used as width for impact sample.

### Dynamic Mechanical Analysis

Dynamic mechanical analyzer (DMA) is used to characterize the dynamic properties of material as a function of temperature and frequency. It is a powerful technique used to characterize the storage modulus, loss modulus, damping and glass transition temperature of viscoelastic materials by subjecting small samples to an oscillatory load under a controlled temperature program. Material under testing is vibrated in flexure at varying temperature; and force and amplitude are recorded to obtain the dynamic properties.

DMA tests were performed in accordance with ASTM D4065-01: 'Standard Practice for Plastics: Dynamic Mechanical Properties: Determination and Report Procedures' [14] using model Q800 DMA (TA Instruments, USA) and recommendations of the machine manufacturer [15,16].

DMA Q800 is a controlled stress with a combined motor and transducer (CMT) machine in which the motor applies a force and displacement sensors measure strain. Force and amplitude are the raw signals recorded by the machine. Stiffness is calculated directly from force and amplitude and modulus is calculated by multiplying the stiffness by an appropriate geometry factor. The geometry factor for a single-cantilever clamp is calculated by [15].

$$GF = \frac{1}{F}\left[\frac{L^3}{12I} + 2S(1+\upsilon)\frac{L}{A}\right] \tag{1}$$

where:

$L$ = sample span length of one side (mm)
$A$ = sample cross sectional area ($mm^2$)
$I$ = geometric moment ($mm^4$) = ($bh^3/12$)
$h$ = sample thickness (mm)
$b$ = sample width (mm)
$F$ = clamping factor (nominally 0.9)
$S$ = shearing factor (nominally 1.5)
$\upsilon$ = Poisson's ratio (nominally 0.44)

As can be seen from the formula, the geometry factor is an exponential function of span length and thickness. Hence, it is important that due care is taken in preparation and measurement of the samples. A digital vernier caliper with a least-count of 0.01 mm (0.0005″) was used in this test, and the average of width and thickness at five different locations was recorded. A variation of <0.03 mm was observed in the dimensions of the individual sample.

After several trial runs, single cantilever clamp was used for experiments. Three-point bend clamp was first tried because of the advantage of nullifying friction and clamping effects, but stiffness of vinyl ester nanocomposites was dropping below working range of machine for larger sample required in three-point bend clamp.

Testing of all the specimens were done at a frequency of 1 Hz and displacement amplitude of 25 μm. Temperature range of −50 to 150°C with a temperature ramp of 3°C/min was used for characterization. Samples were clamped with a torque of 1.13 N m (10 lb in.) and two samples were tested from each configuration.

### Low-velocity Impact Test

Low-velocity impact tests were performed in a drop-weight instrumented impact test system (Instron Model 8250) and the test method used was comparable to that of ASTM D6110-06 [13]. The difference being that a drop-weight system was used instead of pendulum type machine recommended in the standard.

The sample dimensions were used as input in the Instron software for calculation of normalized-to-thickness values of absorbed energy. For this purpose, all the dimensions except that of notch were measured using digital vernier caliper with least count of 0.01 mm (0.0005″). Notch dimensions of random specimens were verified on comparator for angle, depth, and radius. In all other samples, notch depth was measured using vernier caliper and a straight edge. Straight edge was kept on top of the surface and depth was measured using inside jaws of vernier caliper with one jaw on straight edge and another on end of notch.

Specimens of dimensions as specified earlier were kept on a steel support fixture having central span of 95.25 mm (3.75″) with notch (where applicable) facing down, simulating a simply supported beam configuration. These specimens were impacted with a steel charpy tup from a suitable drop height. It was ensured that the steel tup hits the specimen at the middle both lengthwise as well as widthwise by providing appropriate stoppers in the fixture.

After several trial runs, the cross head weight was set at 2.364 kg (5.2 lbs) providing a total drop weight of 3.318 kg (7.3 lbs) with a drop height of 177.8 mm (7″). Load range used for tests was standardized to 4.448 kN (1000 lbs). Filter was set at 4 kHz and time for data collection was set to 20 mS. Velocity slowdown of <20% was observed in all the results.

## RESULTS AND DISCUSSION

Figures 1 and 2 show typical outputs of storage modulus, loss modulus, and loss factor as a function of temperature for pure vinyl ester and 2.5 wt% graphite platelet/vinyl ester nanocomposites. Figures 3–5 show the comparison of storage modulus, loss modulus, and loss factor with respect to temperature for the vinyl ester nanocomposites. Glass transition temperature reported here is from the peak of loss modulus, as per ASTM D4065-01 [13], and loss factor from peak of tan $\delta$ curve. These figures show the results for one sample, and the $\alpha$ transition has been used for reporting the peak tan $\delta$ value. It is also to be noted that only one distinct tan $\delta$ peak was observed in case of the 2.5 wt% graphite platelet reinforced vinyl ester, while other configurations showed two tan δ peaks.

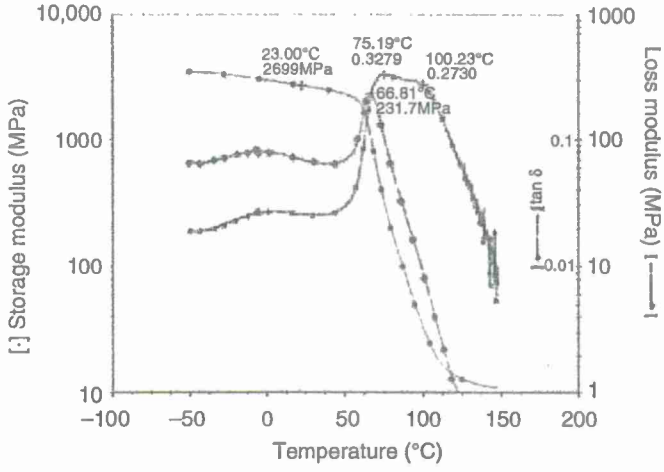


***Figure 1.*** *Typical dynamic modulus and damping for pure vinyl ester.*

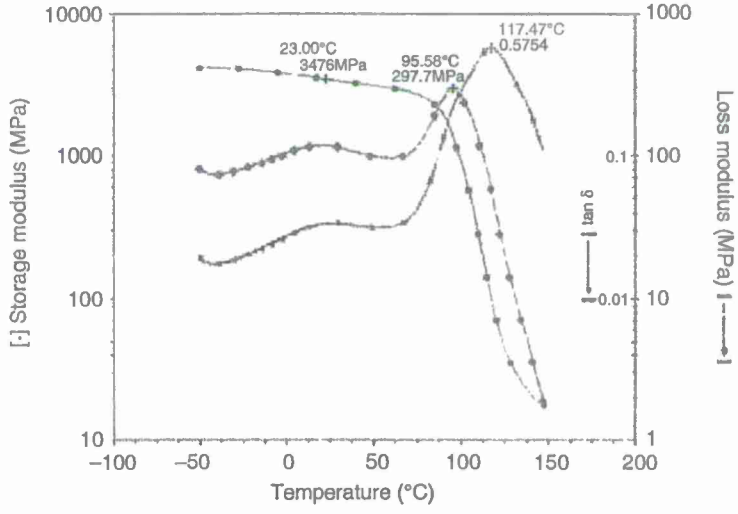


***Figure 2.*** *Typical dynamic modulus and damping for vinyl ester with 2.5 wt% graphite platelets.*

It is observed that storage modulus increases gradually with increase in nanoclay reinforcement in vinyl ester. However, 2.5 wt% graphite platelet reinforcement showed significant improvement (~30%) in storage modulus as compared to 1.25 wt% reinforcement. Area under the tan $\delta$ curve (Figure 5(c)), which is believed to be a good indicator of the energy absorption capacity of the material [17], glass transition temperature, and loss factor also showed an increase with increasing reinforcement for both nanoclay and graphite platelets.

Figure 6 shows the total energy absorption up to failure, for pure vinyl ester and their nanocomposites, when subjected to low-velocity impact. It is observed that for un-notched specimens, the energy absorption doubled when reinforced with 2.5 wt% Cloisite 30B nanoclay, and graphite platelets. However, notched specimens showed a 50% decrease

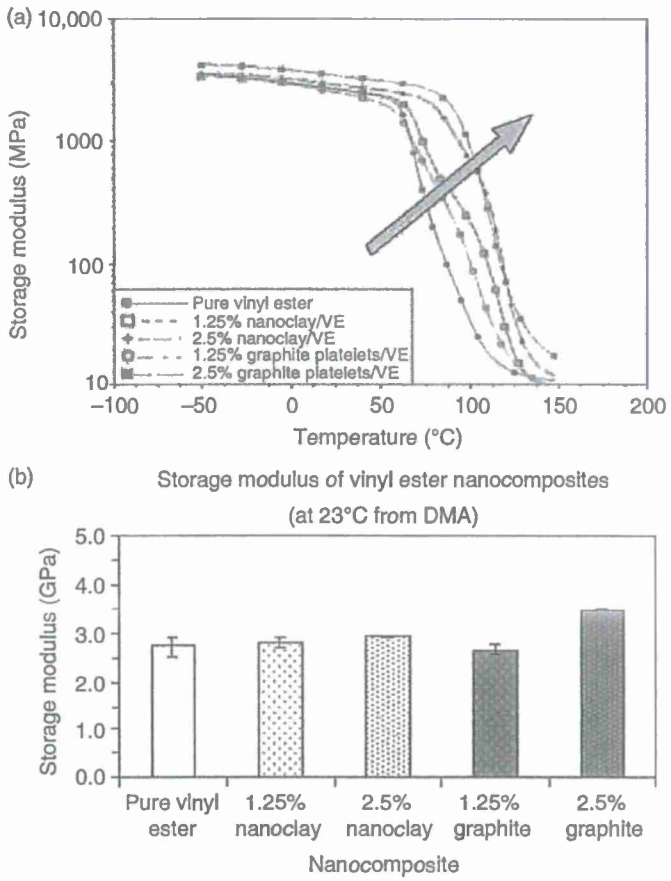


*Figure 3. (a) Storage modulus vs. temperature of vinyl ester nanocomposites, (b) Storage modulus of vinyl ester nanocomposites, at 23°C.*

in energy absorption for 2.5 wt% nanoclay reinforcement, and a 75% decrease for 2.5 wt% graphite platelet reinforcement, suggesting their notch sensitivity. Notch sensitivity shown with nanoreinforcement may be attributed to the interfacial stress transfer phenomenon noted by Roy Xu et al. [18,19] due to stress singularity at the fiber–matrix interface, and inefficient interfacial shear stress transfer in discontinuous fiber because of the high stiffness property mismatch.

The main objective of this research was to investigate the correlation between the dynamic and impact properties of the material. Properties of a polymer are dependent on its cross-linking and molecular mobility, which can be obtained by performing dynamic tests. Storage modulus and loss modulus are indicators of energy absorbing and dissipating capacity of a material. The area under the tan $\delta$ curve is another indicator of the degree of molecular mobility and, hence the damping properties of the material. Higher damping will increase the energy absorption and dissipating capacity of the material.

A correlation between the dynamic mechanical and impact properties was attempted which may be helpful in determining impact properties without performing the more expensive and destructive impact experiments. Figure 7 shows the correlation of total

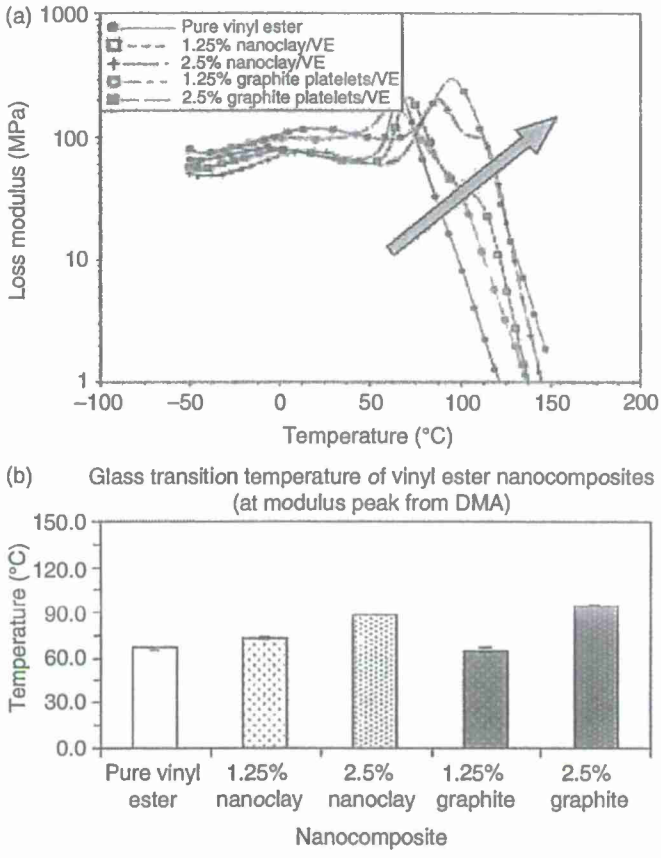


***Figure 4.*** *(a) Loss modulus vs. temperature of vinyl ester nanocomposites, (b) Glass transition temperature of vinyl ester nanocomposites, at loss modulus peak.*

absorbed energy (from impact tests) with respect to area under tan $\delta$ curve (from the DMA tests) along with proportional variability in the output values using the square of correlation coefficient, $R^2$.

Similar correlation of total impact energy was attempted with storage modulus at room temperature; loss modulus at room temperature; loss factor at peak of tan $\delta$; and glass transition temperature, and is summarized in Table 1.

Results demonstrate that an increase in area under the tan $\delta$ curve will most likely improve the impact energy absorption. Loss modulus at room temperature, and high loss factor peak also show good correlation with the impact energy absorption. However, the percentage increase is different for nanoclay and graphite platelet reinforcement, with nanoclay showing more sensitivity (higher slopes of the linear fit line, Table 1). Storage modulus and glass transition temperature also show some correlation with the impact energy. This is better than previously conducted experiments on sheet molding compound (SMC) glass resin composite formulations which showed marginal correlation of impact properties with the dynamic mechanical properties [20]. Further studies using different matrices and reinforcement material are required to establish a distinct relationship between the dynamic and impact properties.

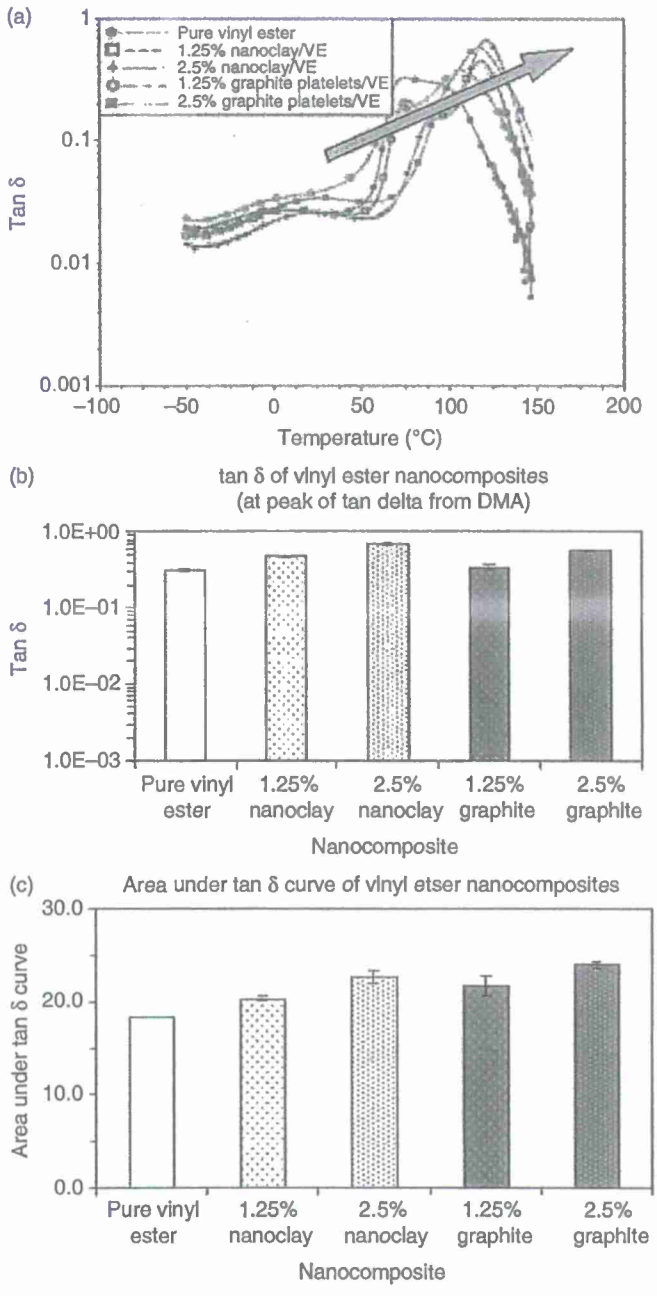


***Figure 5.*** *(a) Tan δ vs. temperature of vinyl ester nanocomposites, (b) Loss factor of vinyl ester nanocomposites, at peak of tan δ, (c) Area under tan δ curve for vinyl ester nanocomposites over a temperature range of −50 to 150°C.*

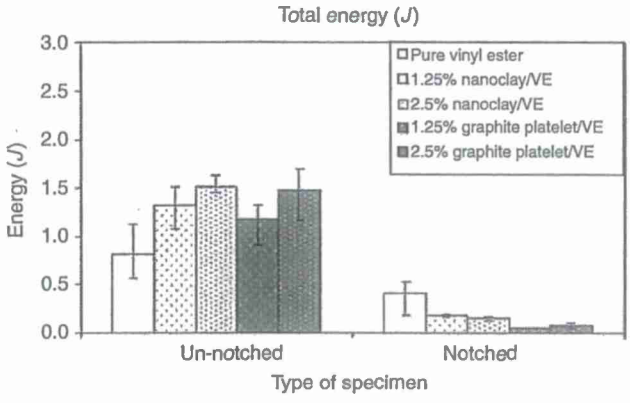


***Figure 6.*** *Total energy for notched and un-notched pure vinyl ester and nanoclay and graphite platelets reinforced nanocomposites.*

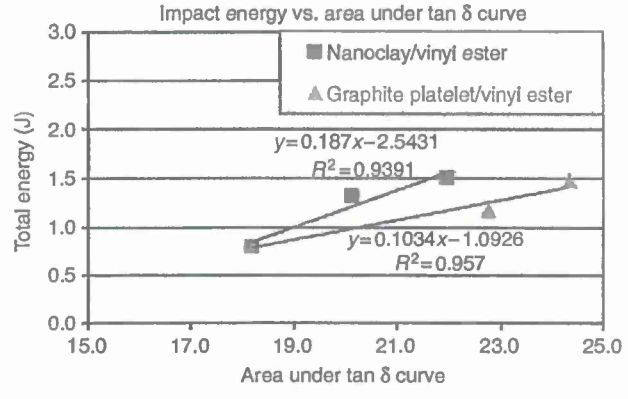


***Figure 7.*** *Total energy (from impact) vs. area under tan δ curve (from DMA, Integrated over the temperature range of −50 – 150°C) for vinyl ester nanocomposites.*

***Table 1. Correlation (linear) of total energy (from impact) with the dynamic mechanical properties (from DMA).***

| Nanocomposite | Nanoclay/Vinyl ester | | | | Graphite platelet/Vinyl ester | | | |
|---|---|---|---|---|---|---|---|---|
| Reinf. Wt% | 0% | 1.25% | 2.50% | Correlation | 0% | 1.25% | 2.50% | Correlation |
| Total energy | 0.808 | 1.323 | 1.510 | coefficient, $R^2$ (and slope) | 0.808 | 1.182 | 1.480 | coefficient, $R^2$ (and slope) |
| Storage modulus | 2.717 | 2.790 | 2.924 | 0.827 (3.149) | 2.717 | 2.661 | 3.491 | 0.635 (0.578) |
| Loss modulus | 71.16 | 72.13 | 73.59 | 0.863 (0.276) | 71.16 | 90.89 | 117.6 | 0.977 (0.014) |
| Loss factor | 0.311 | 0.466 | 0.693 | 0.867 (1.760) | 0.311 | 0.351 | 0.560 | 0.818 (2.276) |
| Area under tan δ | 18.20 | 20.12 | 21.96 | 0.939 (0.187) | 18.20 | 22.76 | 24.33 | 0.957 (0.103) |
| Glass transition temp. | 66.16 | 72.78 | 87.82 | 0.783 (0.029) | 66.16 | 64.82 | 94.69 | 0.654 (0.016) |

## CONCLUSIONS

From DMA experiments, graphite platelet reinforcement showed a greater improvement in storage modulus, loss modulus, and glass transition temperature as compared to nanoclay, where as nanoclay shows higher loss factor compared to graphite platelet reinforcement. Area under the tan $\delta$ curve, and energy absorption up to failure show similar improvement for both nanoclay and graphite platelet reinforcement. Impact energy was observed to have a good correlation with area under the tan $\delta$ curve. Some relationship with loss modulus at room temperature for nanoclay and graphite platelet reinforcement as well as with loss factor was observed, but with different levels of sensitivity. These nanoparticle reinforced composites appear to be good candidates for proposed application as blast/shock/impact resistant structures.

## ACKNOWLEDGMENTS

The authors would like to acknowledge the support received from the Department of Civil Engineering at the University of Mississippi, and funding received under a subcontract from the Department of Homeland Security-sponsored Southeast Region Research Initiative (SERRI) at the Department of Energy's Oak Ridge National Laboratory. Support for this research by ONR Grant # N00014-07-1-1010, Office of Naval Research, Solid Mechanics Program (Dr Yapa D.S. Rajapakse, Program Manager) is also acknowledged. The nano clay and graphite platelet/vinyl ester composite plates were manufactured by Dr Larry Drzal's group at Michigan State University- Composite Materials and Structures Center.

## REFERENCES

1. Sumita, M., Tsukumo, Y., Miyasaka, K. and Ishikawa, K. (1983). Tensile Yield Stress of Polypropelene Composites Filled with Ultrafine Particles, *Journal of Materials Science*, **18**: 1758–1764.
2. Fischer, H. (2003). Polymer Nanocomposites: From Fundamental Research to Specific Applications, *Material Science and Engineering*, **23**: 763–772.
3. Hussain, F., Hojjati, M., Okamoto, M. and Gorga, R. E. (2006). Polymer-Matrix Nanocomposites, Processing, Manufacturing, and Application: An Overview, *Journal of Composite Materials*, **40**: 1511–1575.
4. Schmidt, D., Shah, D. and Giannelis, E. P. (2002). New Advances in Polymer/Layered Silicate Nanocomposites, *Current Opinion in Solid State and Materials Science*, 6(3): 205–212.
5. Ray, S. S. and Okamoto, M. (2003). Polymer/Layered Silicate Nanocomposite: A Review from Preparation to Processing, *Progress in Polymer Science*, **28**: 1539–1641.
6. Bhat, G., Hegdel, R. R., Kamath, M. G. and Deshpande, B. (2008). Nanoclay Reinforced Fibers and Nonwovens, *Journal of Engineered Fibers and Fabrics*, **3**(3): 22–34.
7. Alexandre, M. and Dubois, P. (2000). Polymer-layered Silicate Nanocomposites: Preparation, Properties and Uses of a New Class of Materials, *Material Science and Engineering*, **28**: 1–63.
8. Shen, J. W., Chen, X. M. and Huang, W. Y. (2003). Structure and Electrical Properties of Grafted Polypropylene/Graphite Nanocomposites Prepared by Solution Intercalation, *Journal of Applied Polymer Science*, **88**: 1864–1869.
9. Yasmin, A., Luo, J. and Daniel, I. M. (2006). Processing of Expanded Graphite Reinforced Polymer Nanocomposites, *Composites Science and Technology*, **66**(9): 1182–1189.
10. Yasmin, A. and Daniel, I. (2004). Mechanical and Thermal Properties of Graphite Platelet/Epoxy Composites, *Polymer*, **45**(24): 8211–8219.
11. Xiao, P., Xiao, M. and Gong, K. (2001). Preparation of Exfoliated Graphite/Polystyrene Composite by Polymerization-filling Technique, *Polymer*, **42**: 4813–4816.

12. Fukushima, H. and Drzal, L.T. 2002. Graphite Nanoplatelets as Reinforcement for Polymers: Structural and Electrical Properties, In: *Proceedings of 17th American Society of Composites Technical Conference*, 21–23 October, Lafayette, IN.
13. ASTM Standard D-6110-06 (2006). Standard Test Method for Determining the Charpy Impact Resistance of Notched Specimens of Plastics, ASTM International.
14. ASTM Standard D-4065-01 (2000). Standard Practice for Plastics: Dynamic Mechanical Properties: Determination and Report of Procedures, ASTM International.
15. Dynamic Mechanical Analyzer, Q SeriesTM, (2004). Getting Started Guide, Revision F, Issued January TA Instruments, New Castle, Delaware.
16. DMA Theory and Applications Training Course (2007). TA Instruments, New Castle, Delaware.
17. Kuzak, S. G. and Shanmugam, A. (1999). Dynamic Mechanical Analysis of Fiber-reinforced Phenolics, *Journal of Applied Polymer Science*, **73**: 649–658.
18. Xu, L. R. and Sengupta, S. (2005). Interfacial Stress Transfer and Property Mismatch in Discontinuous Nanofiber/Nanotube Composite Materials, *Journal of Nanoscience and Nanotechnology*, **5**(4): 620–626.
19. Xu, L. R., Li, L., Charles, M. L. and Kuai, H. (2007). Mechanical Characterization of Nanofiber-reinforced Composite Adhesives, *Journal of Nanoscience and Nanotechnology*, 7(7): 2546–2548.
20. Mantena, P. R., Mann, R. and Nori, C. (2001). Low-velocity Impact Response and Dynamic Characteristics of Glass-Resin Composites, *Journal of Reinforced Plastics and Composites*, 20(6): 513–553.

ASME Early Career Technical Journal
2010 ASME Early Career Technical Conference, ASME ECTC
October 1-2, Atlanta, Georgia USA

# EFFECTS OF ENVIRONMENTAL AGING ON THE THERMAL AND MECHANICAL PROPERTIES OF VINYL ESTER NANOCOMPOSITES

**Ahmad Almagableh, P. Raju Mantena**
Dept. of Mechanical Eng., Univ. of Mississippi
University, MS 38677 USA

## ABSTRACT

*In this paper, the Dynamic Mechanical Analyzer is used to study the effects of hygrothermal exposure on material properties of graphite platelet and nanoclay reinforced vinyl ester nanocomposites. An attempt is made to empirically model the change in glass transition temperature under hygrothermal effects. Aged specimens were observed to have drop in glass transition temperature as well as a reduction in the damping peak magnitude, indicating possible formation of microcavities (irreversible morphological changes) mainly in the vinyl ester with nanoclay reinforcements. A dominant trend of drop in the room temperature storage modulus in all nanocomposites was also observed, though the drop is more pronounced in nanoclay specimens and increases with duration of aging exposure. Empirical Predictions of degraded modulus as a function of temperature did agree quiet well with experimental data from DMA, and error between modeled data and the experimental is becoming more pronounced in the rubbery region for nano-reinforced specimens.*

## INTRODUCTION

Accurate prediction of the durability or life of composite structures in service environments is a major concern. Service environments are temperature, moisture, mechanical loads (static or cyclic) or a combination of these, known as hygrothermomechanical environments. Plasticization of polymer based composites by water absorption leads to a drop in the glass transition temperature, $T_g$, and further degradation of composite mechanical properties. Warm, moist environments can considerably change the performance of a material as demonstrated in several polymeric systems [1].

The available free volume (pores) in a resin alters the water equilibrium concentration and can, in addition, occupy micro-voids and other morphological defects. Water absorbed in the polymer is generally grouped into free water and bound water [1].Water molecules, which are gathered in the free volume of the polymer and are relatively free to travel through the microvoids and pores, are identified as free water, while water molecules that are dispersed in the polymer matrix and linked to the polar groups of the polymer are designated as bound water. A loosely bound water within the polymer network is recognized as the one which can be released easily upon heating [2], and strongly bound water (frozen) is difficult to remove from the polymer network.

Moisture uptake in a polymeric composite can lead to chemical degradation effects, both reversible and irreversible, including weakening the intermolecular bonds among the functional groups of the chains (plasticization) [3], debonding at filler-matrix interfaces [4], leaching of unreacted functional groups [5], micro-structural damage such as cavities or pores in the matrix [6], increased crosslinking [7], and degradation of the matrix properties due to hydrolysis and oxidation during long-term exposure to water [5].

Mechanical and thermal behavior could also be affected due to moisture absorption, the thermal properties such as the glass transition temperature and damping properties, and mechanical properties including tensile strength, modulus, failure strain [8] and fracture toughness [9] can be significantly altered.

The kinetics of water diffusion is assumed to follow the one-dimensional Fick's second law, which considers that the driving force of diffusion is the water concentration gradient. Some other models have also been applied to describe more complex diffusion processes. A two-phase model has been utilized to interpret the Langmuir diffusion process [10], in which the absorbed water is divided into a free phase and a strongly bound phase.

Alvarez and Vazquez [11] have studied the effect of water absorption on the behavior of vinylester (VE) and polyester–glass fiber composites at two different temperatures. A relation was found between the glass transition temperature ($T_g$), the bath temperature and the plasticization of the network-structure. Poor fiber–matrix interfaces were observed by a scanning electron microscope (SEM) due to water absorption. Extraction of silane coupling in composite materials was observed at a temperature of 80 C. In addition, unsaturated polyester matrix absorbs more water than VE due to its higher

hydrophilic character and void content. It was observed that mechanical properties (flexural modulus and interfacial shear strength) decrease remarkably with immersion time at high temperatures.

Plasticization of polymeric based composites under water absorption leads to a drop in the glass transition temperature, $T_g$, and further degradation of composite properties [12]. In this study, the effect of hygrothermal exposure on glass transition temperature and damping of nanoclay and graphite platelet reinforced vinyl ester nanocomposites are characterized and modeled empirically.

## MATERIALS AND ENVIRONMENTAL AGING

The polymeric matrix used was a vinyl ester resin (Ashland specialty chemical, Division of Ashland INC, Columbus, OH). DERAKANE 510A-40 vinyl ester resin is a brominated bisphenol-A based vinyl ester consisting of 38 wt. % styrene, and modified to produce the maximum degree of fire retardancy combined with enhanced chemical resistance and toughness. These additives are Butanone peroxide, N,N-Dimethylaniline, Cobalt Naphthenate, and 2-4-Pentanedione, all supplied from Sigma Aldrich (St. Louis, Mo).

Exfoliated graphite nanoplatelets (xGnP) were produced according to the method described in Ref [13]. Figure 1 (a) shows a TEM morphology for edge view of xGnP inside the matrix. These xGnP nanocomposites have exfoliated and dispersed graphite platelets with 1 nm thickness and several hundred nanometers widths. The distance between layers is in the range of 10~30 Å and the size of the layered graphite extends from several hundred nanometers to several microns. The nanoclay was Cloisite 30B from Southern Clay Products, Inc as shown in Figure1 (b).

Nanocomposites were prepared by dispersing about 3000 gm of epoxy vinyl ester resin solution with different percentages of nanoclay or nanographite in a 1 gal container for 4 hours, followed by 4 passes through a flow cell connected to a 100 W sonicator. 1% Butanone peroxide, 0.2% of 2-4 Pentanedione, 0.1% N,N-Dimethylaniline, and 0.2% Cobalt Naphthenate were added to the mixed vinyl ester resin solution in order and mixed for 10 min. The above mixed resin solution was mixed for 2 min with FlackTek speed mixer at 3000 RPM. The well-mixed vinyl ester resin solution with nanoclay or nanographite was poured into a 13"×13"×0.4" mold, let stand for 30 minutes at room temperature and then was post cured at 80 °C for 3 hours. Prismatic samples with nominal dimension of 35 x 10 x 1.6 mm size were prepared from these plates and tested before and after environmental aging in a DMA using the single-cantilever clamp fixture.

The hygrothermal aging effect on both mechanical and thermal properties was studied through conducting a freeze-thaw cycling, in which a specimen is submerged in a water bath, subjected to a temperature cycling from 15 F to 45 F each over a 6 hour period. Aged Specimens were divided into two sets based on the immersion time. The first set was taken out after 60 days and tested and the other is left inside the environmental chamber for 60 more days. Specimens subjected to freeze-thaw cycling were tested using the TA Instruments model Q800 Dynamic Mechanical Analyzer to obtain viscoelastic properties.

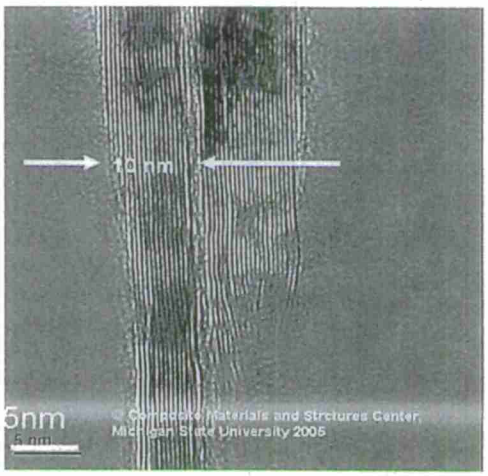


(a)

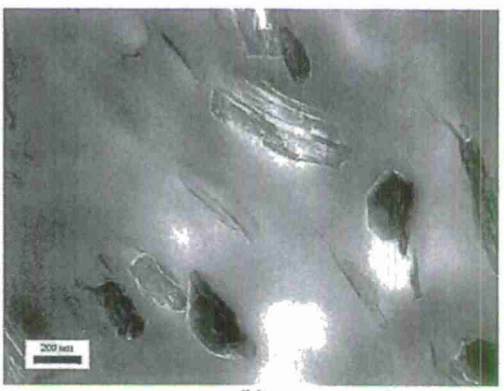

(b)

Figure 1. TEM images of nanoparticle dispersion for (a) xGnP, and (b) Cloisite® nanoclay [14].

## MOISTURE UPTAKE

It should be noted that nano-specimens were weighed before and after aging exposure, using digital meter with a 1% gm resolution, thus moisture measurements using this technique might be not sufficient accurate with relative to the weight of water molecules absorbed. Water absorption (percent) as a function of immersion time was determined using the following Equation:

$$M\% = \frac{M_t - M_o}{M_o} \times 100 \quad (1)$$

where $M_t$ is the weight at a time, t, and $M_o$ is the weight at dry conditions. Table 1 lists moisture absorbed by weight percentage versus immersion time.

Table 1. Moisture absorption (wt. %) for vinyl ester nanocomposites as a function of immersion time.

| Material | M (%) after 60 days | M (%) after 120 days |
|---|---|---|
| Vinyl ester matrix (VE) | 3.0 | 4.5 |
| VE+1.25wt. percent nanoclay | 1.4 | 2.8 |
| VE+2.5 wt. percent nanoclay | 1.4 | 5.5 |
| VE+1.25wt. percent xGnP | 1.2 | 2.5 |
| VE+2.5 wt. percent xGnP | 1.4 | 2.8 |

## DYNAMIC MECHANICAL ANALYZER

To obtain the thermal transition characteristics of the vinyl ester nanocomposites, both prior to and after environmental aging, dynamic measurements were carried out using the TA Instrument model Q800 DMA on prismatic specimens with 0, 1.25 and 2.5 wt. percent graphite nanoplatelet (xGnP) and nanoclay reinforcements. Specimens were deformed at constant amplitude ($25\,\mu m$) over a 1 Hz single frequency, with temperature ramped at 3°C per minute starting from 30°C (RT) to 150°C.

## EXPERIMENTAL RESULTS

Moisture uptake by resin causes hydrolysis and chain scission over the long term and plasticization in the short term due to moisture absorption, which generally results in a decrease in storage modulus (E') as well as drop in the glass-transition temperatures, linked to the degree of molecular mobility [15]. Vinyl ester nanocomposites exhibited a reduction in $T_g$ as a function of immersion time except for the case of 2.5 wt. percent xGnP (Table 2). A drop in the room temperature storage modulus in the nanocomposites was also observed which is more pronounced in nanoclay specimens and increases with duration of aging exposure, whereas those reinforced with xGnP experienced steady modulus variation insensitive to aging time. For example, pure vinyl ester resin had a maximum drop of about 400 MPa in room temperature modulus compared to 150 MPa for those reinforced with 1.25 wt. % xGnP based upon 120 days of immersion time.

Intermolecular hydrogen bonding by water molecules (plasticization) can be manifested by a decrease in the room temperature modulus which is found in nanoclay composites. However, it is clear that stress relaxation allows increased molecular movement, which in turn allows further cross-linking to occur. In fact, the water uptake process at the outset is quite complex due to the competing effects of plasticization and crosslinking and the mechanism is further complicated due to a possible cure progression under immersion in aqueous solution which cause higher modulus and increased brittleness [15]. Data scatter tends to be greater between aged specimens than those unaged, with a tendency towards greater scatter with longer aging exposure. The reason may be because of uneven plasticization taking place or specimen shrinkage during temperature ramp in DMA tests.

Table 2. Viscoelastic properties for vinyl ester nanocomposites before and after aging exposure.

| Material | Conditions | $T_g$ (°C) | Peak of loss factor | Initial modulus (MPa) |
|---|---|---|---|---|
| Vinyl ester VE | Dry | 125 | 1.23 | 2950 |
| | 60 days | 124 | 1.08 | 2950 |
| | 120 days | 117.5 | 0.93 | 2600 |
| 1.25 % nanoclay/VE | Dry | 122 | 1.2 | 2900 |
| | 60 days | 122 | 1 | 3400 |
| | 120 days | 119 | 1 | 2700 |
| 2.5 % nanoclay/VE | Dry | 124 | 1.25 | 3100 |
| | 60 days | 121 | 0.96 | 3000 |
| | 120 days | 121 | 0.9 | 2700 |
| 1.25 % xGnP/VE | Dry | 126 | 1 | 3500 |
| | 60 days | 121 | 1 | 3300 |
| | 120 days | 122 | 1 | 3350 |
| 2.5 % xGnP/VE | Dry | 129 | 0.94 | 3800 |
| | 60 days | 123 | 0.7 | 3700 |
| | 120 days | 128 | 0.83 | 3500 |

Unlike the trend observed for nanoclay specimens, Tg was initially reduced in xGnP specimens and then rose again with further moisture absorption, in some cases it becomes close to the original dry $T_g$ of the material. Comyn [16] also reports similar behavior for epoxy where, Tg initially reduced and then it went up again with further moisture absorption. These xGnP reinforced specimens show a more considerable increase in Tg (120 days compared to 60 days), which could be evidence of embrittlement or antiplasticization phenomena. Antiplasticization is basically leaching of free (non-crosslinked) styrene monomer residues that act as a

plasticizer in the material after longer immersion time in water. In addition to the above effects, it is believed that major effect occurs due to rapid heating induced by the DMA test, which has also been observed by Akay et al. [17].

## MODELING GLASS TRANSITION TEMPERATURE

The hygrothermal degradation based on plasticization of vinyl ester nanocomposites is modeled based on the following empirical Equation 2. Equation 2 is based on the experimental observation that degradation in property (stiffness) is gradual until the temperature T approaches $T_{gw}$ [12]. The value of $T_{gw}$ is obtained from DMA experiments as the peak of loss-factor (Tan δ peak).

$$\frac{E(T)}{E_o} = \left[\frac{T_{gw} - T}{T_{gO} - T_O}\right]^{1/2} \quad (2)$$

Where
E= matrix stiffness after hygrothermal degradation.
$E_o$= matrix stiffness before degradation (baseline).
T= temperature at which E is to be predicted (F).
$T_{go}$= glass transition temperature for reference dry condition.
$T_{gw}$=glass transition temperature at fully saturated conditions (120 aging days).
$T_o$= test temperature at which Eo was measured (room temperature).

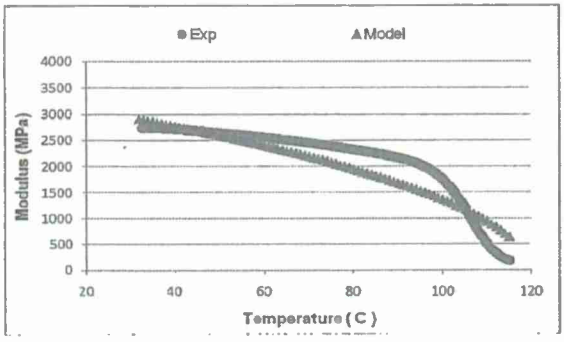


(a)

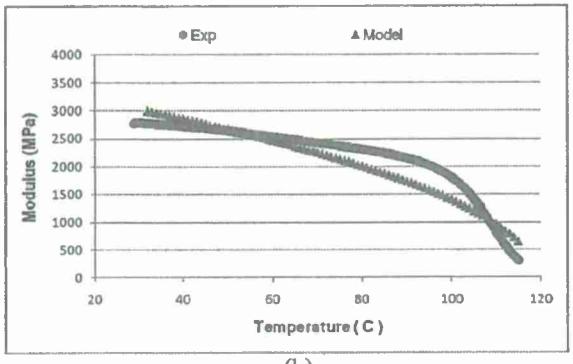


(b)

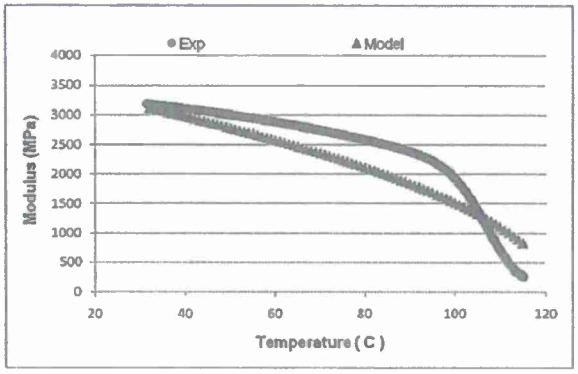


(c)

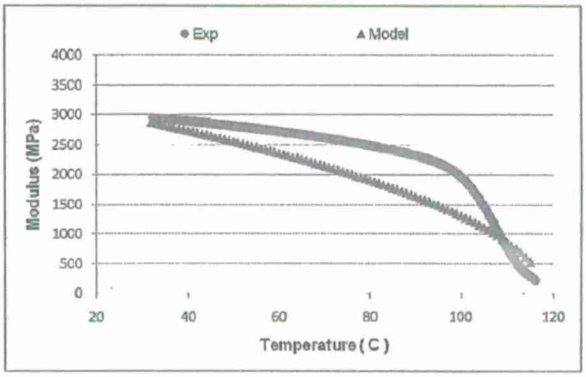


(d)

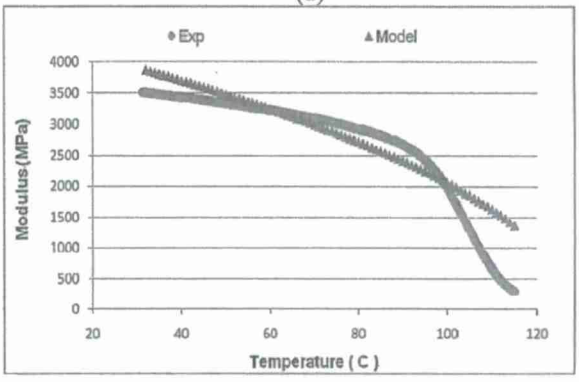


(e)

Figure 2. Emperical model predictions and experimental results of modulus vs temperature for (a) brominated vinyl ester (VE), (b)1.25 wt.% nanoclay/ VE, (c) 2.5 wt. % nanoclay/ VE, (d) 1.25 wt. % xGnP/ VE and (e) 2.5 wt. % xGnP/ VE.

The degraded modulus as a function of temperature obtained from DMA along with that predicted at approximately fully saturated conditions (Equation 2) is plotted in Figures 2 (a-e). The predicted degradation of modulus as a function of temperature did agree quite well

with experimental data from DMA; however, the degraded modulus based on model prediction was generally less than the experimental modulus for all specimens tested. Moreover, error between modeled and experimental data in the rubbery region is more pronounced for nano-reinforced specimens especially with 2.5 wt. %. Again, this can be an indication of irreversible damage taking place in the form of fiber–matrix debonding (cross-linking) which can be directly assessed from the rubbery region [18].

## CONCLUSIONS

Hygrothermal aging effect on graphite platelet and nanoclay reinforced vinyl ester nanocomposites was studied by conducting a freeze-thaw cycling, in which a specimen is submerged in a water bath, subjected to a temperature cycling from 15 F to 45 F for 60 and 120 days. Aged specimens were observed to have drop in Tg as well as a reduction in the damping peak magnitude, indicating possible formation of microcavities (irreversible morphological changes) mainly in the vinyl ester with nanoclay reinforcements. A dominant trend of drop in the room temperature storage modulus in all nanocomposites was also observed, though, the drop is more pronounced in nanoclay specimens and increases with duration of aging exposure.

For xGnP specimens, Tg, was initially reduced and then rose again with further moisture absorption, which could be an evidence of embrittlement or antiplasticization phenomena. Furthermore, stable variation of initial storage modulus as a function of aging time because of possible cross-linking (antiplasticization) in xGnP specimens, and there is some recovery in properties of these aged specimens compared to ambient as they are heated during the DMA test.

The hygrothermal degraded stiffness (storage modulus) as a function of temperature was modeled empirically. Prediction of degraded modulus as a function of temperature did agree quiet well with experimental data from DMA, however, degraded modulus based on the model prediction was generally less than the experimental modulus for all specimens tested and error between modeled data and the experimental is becoming more pronounced in the rubbery region for nano-reinforced specimens.

Further work involves empirical modeling of mechanical properties (strength and stiffness) for brominated vinyl ester nanocomposites under hot-wet conditions.

## ACKNOWLEDGMENTS

This investigation was supported by ONR Grant N00014-07-1-1010, Office of Naval Research, Solid Mechanics Program (Dr. Yapa D.S. Rajapakse, Program Manager). The nanoclay and graphite platelet vinyl ester composite plates were manufactured by Dr. Larry Drzal's group at Michigan State University.

## REFERENCES

[1] Diamant, Y., Marom, G., and Broutman, L. J., 1981, "The Effect of Network Structure on Moisture Absorption of Epoxy Resins," J. Appl. Polymer Science., 26, pp. 3015-3025.

[2] Maggana, C., and Pissis, P., 1999, "Water Sorption and Diffusion Studies in an Epoxy Resin System," J. Polymer Science: Part B: Polymer Physics., 37, pp. 1165-1182.

[3] Ivanova, K. I., Pethrick, R. A., and Affrossman, S., 2000, "Investigation of Hydrothermal Ageing of a Filled Rubber Toughened Epoxy Resin Using Dynamic Mechanical Thermal Analysis and Dielectric Spectroscopy," J. Polymer, 41, pp. 6787-6796.

[4] Bowditch, M. R., 1996, "The Durability of Adhesive Joints in the Presence of Water," International Journal of Adhesion and Adhesives., 16 (2), pp. 73-79.

[5] Antoon, M .K., and Koenig, J. L., 1981, " Irreversible Effects of Moisture on the Epoxy Matrix in Glass-Reinforced Composites," Journal of Polymer Science: Polymer Physics Edition, 19, pp.197-212.

[6] Apicella, A., Nicolais, L., Astarita, G., and Drioli, E., 1979, "Effect of Thermal History on Water Sorption, Elastic Properties and the Glass Transition of Epoxy Resins," J. Polymer, 20, pp. 1143-1148.

[7] Liu, J., Lai, Z., Kristiansen, H., and Khoo, C., 1998, "Overview of Conductive Adhesive Joining Technology in Electronics Packaging Applications," Proc. 3rd International Conference on Adhesive Joining and Coating Technology in Electronics Manufacturing, IEEE, pp.1-18.

[8] Kasturiarachchi, K. A., and Pritchard, G., 1985, "Scanning Electron Microscopy of Epoxy-glass Laminates Exposed to Humid Conditions," Journal of Materials Science., 20, pp. 2038-2044.

[9] Butkus, L. M., Mathern, P. D., and Johnson, W. S., 1998, "Tensile Properties and Plane-Stress Fracture Toughness of Thin Film Aerospace Adhesives," Journal of Adhesion., 66, pp. 251- 273.

[10] Bonniau, P., and Bunsell, A. R., 1981, "A Comparative Study of Water Absorption Theories Applied to Glass Epoxy Composites," Journal of Composite Materials., 15 (3), pp. 272-293.

[11] Alvarez, V., and Vazquez, A., 2007, "Cyclic Water Absorption Behavior of Glass–Vinylester and Glass–Epoxy Composites," Journal of Composite Materials., 41, pp. 1275-1289.

[12] Chamis, C., and Sinclair, J., 1982, "Durability/ Life of Fiber Composites in Hygrothermomechanical Environments," Journal of Composite material, testing and design, ASTM STP 787, pp. 498-512.

[13] Drzal, L.T., Fukushima H., "Expanded Graphite Products Produced Therefrom," US Patent No. 7, 550-529.

[14] "Laboratory of Polymer Technology-Polymer Blends", http://polymeeri.tkk.fi.
[15] Karbhari, V., 2006, "Dynamic Mechanical Analysis of the Effect of Water on E-glass–Vinyl ester Composites," Journal of Reinforced Plastics and Composites., 25, pp. 631-644.
[16] Comyn, J., 1989, "Interaction of water with epoxy resins, Polymers in a marine environment," 2nd Conference, (IMarE), pp. 153-162.
[17] Akay, M., Kongahmun, S., and Stanley, A., 1997, "Influence of moisture on the thermal and mechanical properties of autoclaved and oven-cured Kevlar 49/epoxy laminates," J. Composite Science Technology., 57, pp. 565- 571.
[18] Almagableh, A., Mantena, P. R., Alostaz, A., Liu, W., and Drzal, L.T., 2009 "Effects of Bromination on the Viscoelastic Response of Vinyl ester Nanocomposites,", J. eXPRESS Polymer Letters., 3 (11), pp. 724–732.

Composites Science and Technology 69 (2009) 772–779

Contents lists available at ScienceDirect

Composites Science and Technology

journal homepage: www.elsevier.com/locate/compscitech

# Dynamic response and simulations of nanoparticle-enhanced composites

P. Raju Mantena *, Ahmed Al-Ostaz, Alexander H.D. Cheng

*Composite Structures and Nano-Engineering Research, University of Mississippi, University, MS 38677, USA*

ARTICLE INFO

*Article history:*
Received 5 December 2007
Received in revised form 26 February 2008
Accepted 26 February 2008
Available online 20 March 2008

*Keywords:*
A. Nanostructure
A. Polymer
A. Polymer matrix composites

ABSTRACT

The dynamic modulus and damping, low-velocity impact and high-strain (Hopkinson bar) response of nanoparticle-enhanced composites and fly ash based fire resistant structural foams have been characterized. Molecular Dynamic (MD) simulations were also used for obtaining the elastic constants for different matrices reinforced with single and multi-wall carbon nanotubes (MWCNT). Experimental results on the dynamic and impact response of nylon 6,6 with MWCNT, vinyl ester with nanoclay and graphite platelets, and Eco-Core® foams are presented; along with some of the predictions from molecular simulations. An increase in dynamic modulus and marginal drop in damping was observed with the addition of multi-wall carbon nanotubes to pristine nylon 6,6. Addition of MWCNT was detrimental to the maximum load and energy absorption under low-velocity impact. However, an improvement in strength and energy absorption was observed with Hopkinson pressure bar apparatus at high-strain rates under compressive loading. Results obtained from molecular simulations show that MWCNTs are transversely isotropic, and the transverse properties are comparatively poor.

Published by Elsevier Ltd.

## 1. Introduction

Fiber-reinforced polymer (FRP) composites are increasingly being used in naval platforms for improving the stealth and reducing topside weight, corrosion mitigation, fatigue, maintenance and operational costs. FRP composites are presently being used in US Navy Ships such as the Osprey class mine hunter, and for topside structures on large warships such as the Advanced Enclosed Mast System (AEMS). The navy also has plans to integrate more composites into the new generation CV(X) and DD(X) ship class designs. Structures in these applications are often subjected to high-strain rates due to impact by hard objects, mine blasts, projectile penetration and collisions.

On the other hand, the emergence of nano-sciences during the last decade has drastically altered the landscape of scientific research and technology development. Nanoreinforcement of engineering materials can impart dramatic structural (e.g. stiffness) and physical (e.g. reduced CTE) property benefits without adding significant weight. The essence of nanotechnology is the ability to work at a scale of about 1–100 nanometers, in order to create, manipulate, and use materials, devices, and systems that have novel properties and functions. Nanoparticle reinforced materials often have superior mechanical, thermal, electrical, magnetic, and electromagnetic properties. This is why nanotechnology finds applications in biomedical, biochemical, pharmaceutical, genetic engineering, materials, polymer science, electronics, composites, and other engineering areas. Carbon nanotubes (CNT) have become a primary focus in nanotechnology research due to their exceptionally high stiffness and strength. Many experimental and theoretical studies have been performed on single and multi-wall nanotubes. In particular, deformation modes and overall tube stiffness have been examined. This problem will be even more challenging in the case of nanocomposites in which carbon nanotubes are dispersed randomly in a polymeric matrix. Since the length-to-diameter ratio of CNTs exceeds 1,000,000 and they can be up to several millimeters in length, their presence may affect the dynamic response of such nanocomposites.

The Composite Structures and Nano-Engineering Research Group at University of Mississippi is conducting research on dynamic and acoustic response, freeze–thaw effects, and molecular dynamic simulations of nanoparticle-enhanced composites and fly-ash based fire resistant structural foams that are being developed for the future generation naval structures, or retrofitting of existing ones. Results from molecular simulations and experimental data on the dynamic and impact response of nylon 6,6 thermoplastic with different weight-percents of multi-wall carbon nanotubes (MWCNT), vinyl ester with nanoclay and graphite platelets, and Eco-Core® structural foams are presented in this paper.

## 2. Nanoparticle-enhanced composite and Eco-Core foam plates

For this research, several 305 mm × 305 mm × 9.5 mm (12″ × 12′ × 0.375″) thick nylon 6,6 thermoplastic plates reinforced with 1.25, 2.5, 5 and 10 wt.% multi-wall carbon nanotubes (MWCNT, supplied by Hyperion Catalysis) were prepared by

* Corresponding author. Tel.: +1 662 915 5990; fax: +1 662 915 5523.
*E-mail address:* meprm@olemiss.edu (P. Raju Mantena).

0266-3538/$ - see front matter Published by Elsevier Ltd.
doi:10.1016/j.compscitech.2008.02.035

J-154

Ensinger Inc. using a proprietary pressure extrusion process. A higher 20 wt.% loading of MWCNT resulted in plate fracture after extruding. Attempts were also made to manufacture vinyl ester (VE) resins containing multi-wall carbon nanotubes at the Michigan State University – Composite Materials and Structures Center. Two loading levels were investigated, namely, 1.25 and 2.50 wt.% MWCNT in Derakane 411-350 vinyl ester resin. Each blend exhibited very high viscosity and tackiness, presenting significant processing challenges to uniformly distribute the curative package and remove entrapped air during consolidation. Smaller plates of 89 mm × 152 mm × 9.5 mm (3.5″ × 6″ × 0.375″) were initially attempted; however, these contained large voids and non-uniform properties across the parts. The high viscosity of the MWCNT-vinyl ester resin restricted the removal of entrapped air, and plaques with acceptable quality were not produced. Derakane 411-350 vinyl ester thermoset plates 280 mm × 280 mm × 9.5 mm (11″ × 11″ × 0.375″) thick reinforced with 1.25 and 2.5 wt.% Cloisite 30B nanoclay and exfoliated graphite nanoplatelets (xGnP) were successfully fabricated at Michigan State University.

Fly ash based Eco-Core foam plates supplied by North Carolina A&T State University were designated as OM11, OM12, OM16, OM21, OM18 and OM19. Plates OM11 and OM12 consist of fly ash with phenolic resin (no added fibers) + 1 ply phenolic resin-coated glass fiber veil (on top/bottom surface). Plate OM16 consists of fly ash w/phenolic resin (0 wt.% 0.125-in chopped glass fiber) and no covering. Plate OM21 consisted of fly ash with phenolic resin (+6 wt.% 0.125-in chopped glass fibers) and no covering. Plates OM18 and OM19 consisted of fly ash with phenolic resin (+6 wt.% 0.125-in chopped glass fibers) and 1-ply covering of phenolic resin-coated glass fiber veil (on top/bottom surface).

The densities of nylon 6,6 reinforced with MWCNT, and vinyl ester reinforced with Cloisite nanoclay and graphite platelets, are shown in Fig. 1. Theoretical densities calculated by the rule of mixtures were within 5% of experimental values. As can be observed, the densities of vinyl ester reinforced with graphite platelets is lower than their counterpart nylon 6,6 reinforced with MWCNT.

## 3. Flexural/extensional modulus and damping characterization

A non-destructive impulse-frequency response vibration technique [1–3] was used for characterizing the dynamic flexural/extensional modulus and damping of nanocomposites and Eco-Core foams. The frequency response function (FRF) obtained from the impact and accelerometer signals was used for computing the dynamic flexural modulus from resonant frequency and loss factor (measure of damping) is calculated from the 3 dB half-power bandwidth. The same samples used for dynamic flexural testing were also used for extensional characterization (Fig. 2). In this case, end-masses are added for lowering frequency. The software program used takes these masses into account for computing extensional modulus from the resulting FRF. Results of the flexural vibration tests are reported here.

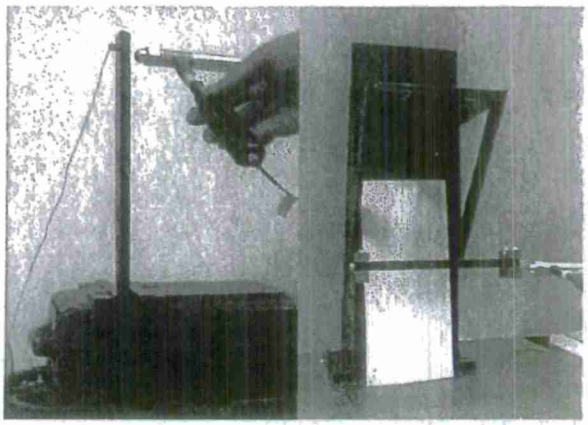

Fig. 2. Experimental set-up for flexural and extensional dynamic tests.

As shown in Fig. 3, a 15% increase in dynamic flexural modulus and marginal drop in damping was observed with the addition of 1.25–2.5 wt.% MWCNT compared to pristine nylon 6,6. The 20 wt.% nanocomposite exhibited both high flexural dynamic modulus and damping; however, this very high loading of MWCNT also resulted in plate fracture during the extrusion manufacturing process.

A 40% increase in flexural dynamic modulus without drop in damping was observed with the addition of 2.5 wt.% graphite platelets to vinyl ester (Fig. 4). The nanoclay reinforcement did not show any improvement in flexural modulus and damping.

Eco-Core foam samples OM18 and OM19, which consist of fly ash with phenolic resin (+6 wt.% 0.125-in chopped glass fibers) and 1-ply covering of phenolic resin-coated glass fiber veil (on top/bottom surface), exhibited both high flexural dynamic modulus and damping (Fig. 5).

## 4. Low-velocity impact characterization

Nanoparticle-enhanced and Eco-Core foam samples were prepared and tested in accordance with ASTM D-6110-06 Standard test method for determining the charpy impact resistance of notched specimens of plastics. Tests were performed at 2 m/s (4.5 mph) velocity in an Instron Model 8250 drop-weight instrumented impact system, with five notched and un-notched samples tested for each MWCNT weight percent.

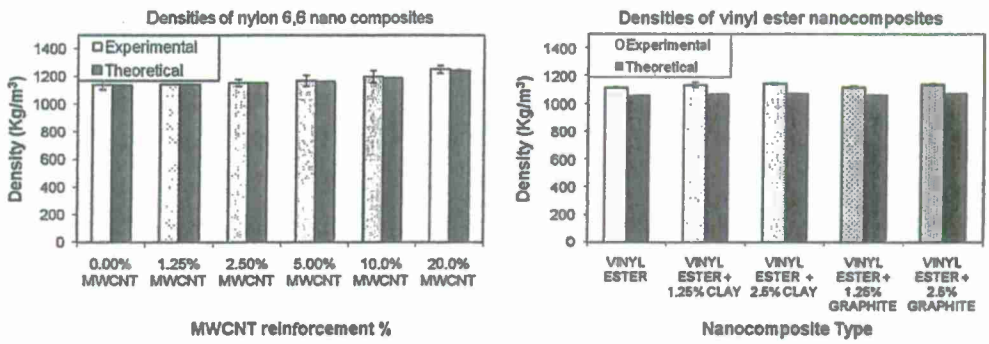


Fig. 1. Densities of nanoparticle-enhanced (a) nylon 6,6 and (b) vinyl ester composites.

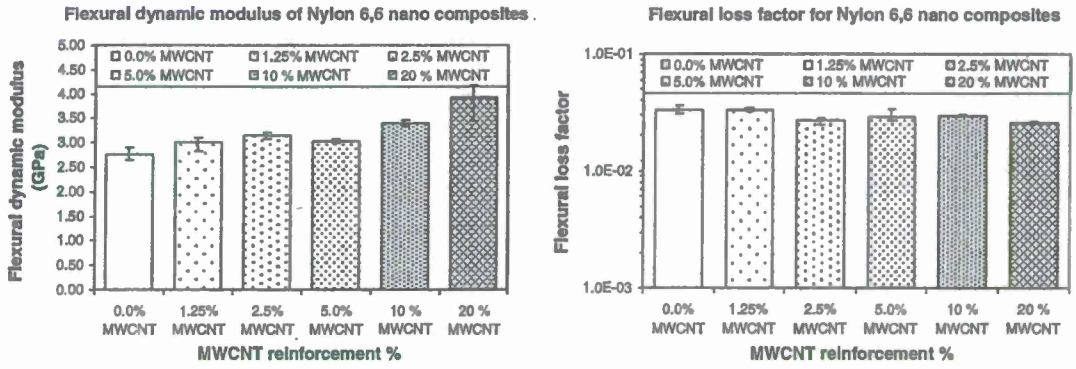


Fig. 3. Flexural modulus and damping of nylon 6,6 nanocomposites.

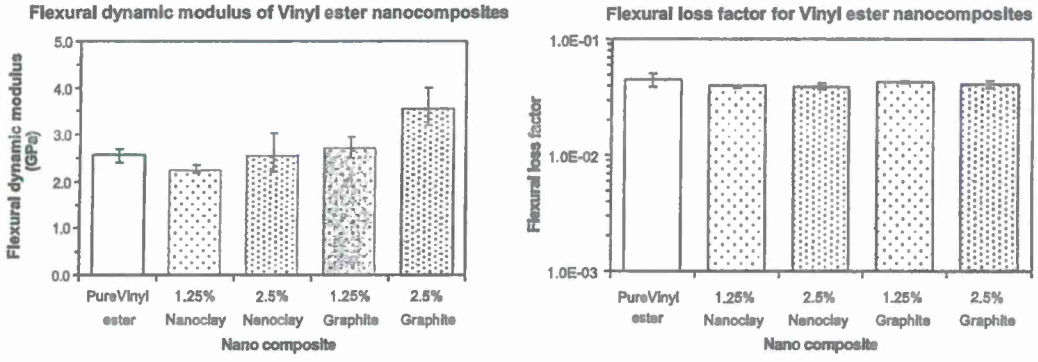


Fig. 4. Flexural modulus and damping of vinyl ester nanocomposites.

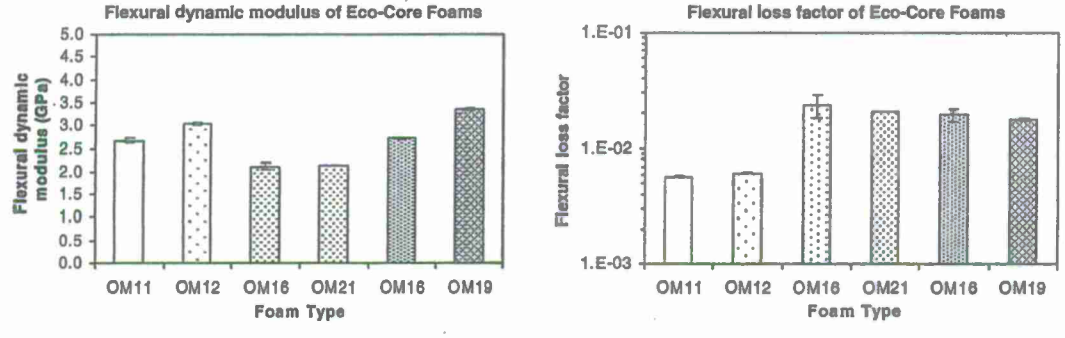


Fig. 5. Flexural modulus and damping of Eco-Core foams.

As seen in Fig. 6, pure nylon 6,6 absorbed more load and energy to failure than MWCNT reinforced nanocomposites for both notched and un-notched specimens, with the 5 wt.% being lower than the rest. Un-notched samples showed larger data scatter.

Addition of 1.25–2.5 wt.% nanoclay or graphite platelets to vinyl ester improved the maximum impact load by 60% and absorbed energy by 130%, for un-notched samples (Fig. 7). For notched specimens this trend is reversed, however, with graphite platelet reinforcement exhibiting greater notch-sensitivity.

Eco-Core foams OM18 and OM19, which consisted of fly ash with phenolic resin (+6 wt.% 0.125-in chopped glass fibers) and 1-ply covering of phenolic resin-coated glass fiber veil (on top/bottom surface), appear to have maximum load and maximum energy absorption to failure, for both notched and un-notched specimens (Fig. 8). It was observed that the maximum load and energy absorbed by Eco-Core foams are very low compared to nylon 6,6 and vinyl ester nanocomposites.

## 5. High-strain rate (Hopkinson bar) compression tests

Small samples cut from 0, 2.5, 5 and 10 wt.% nylon 6,6 nanocomposite plates were subjected to high-strain rate compression testing using a Split-Hopkinson Pressure Bar (SHPB) apparatus. The strain rate for these tests was around 950/s at 30 psi pressure. The 1.25 wt.% nylon 6,6; vinyl ester with nanoclay and graphite

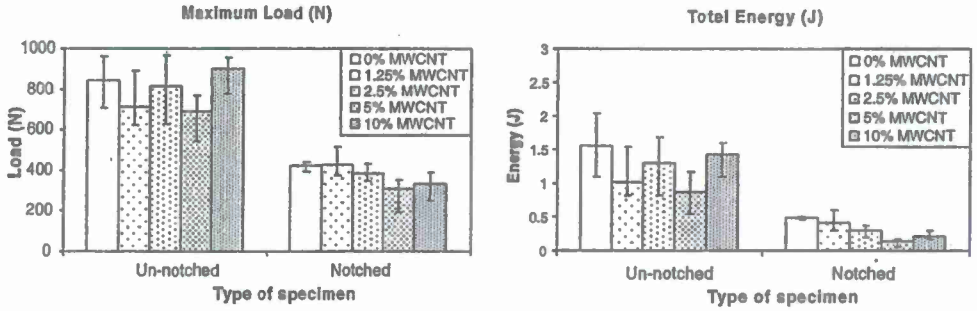


Fig. 6. Maximum load and energy absorbed by nylon 6,6 nanocomposites.

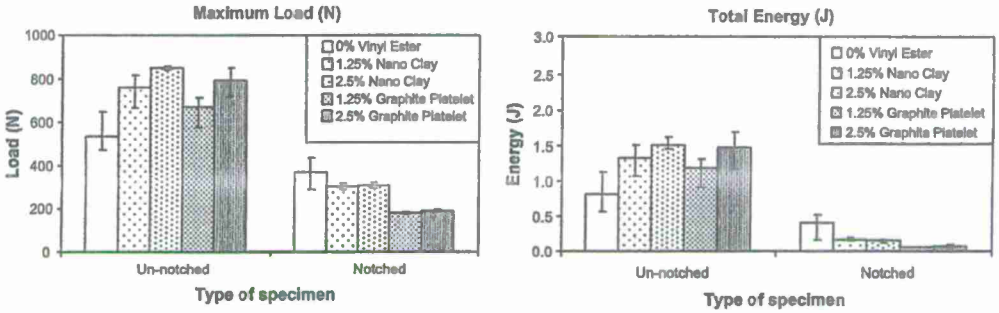


Fig. 7. Maximum load and energy absorbed by vinyl ester nanocomposites.

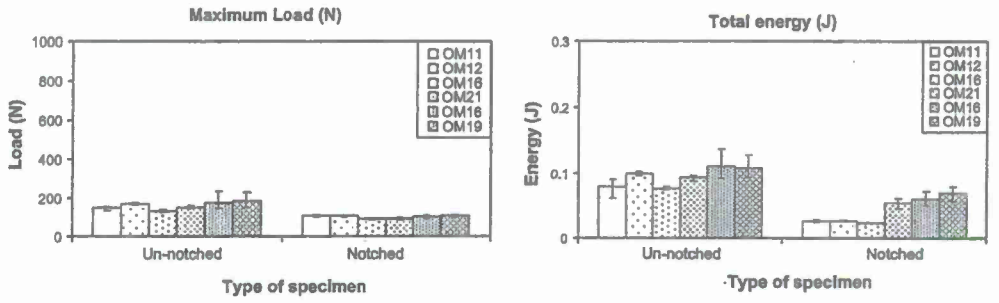


Fig. 8. Maximum load and energy absorbed by Eco-Core foams.

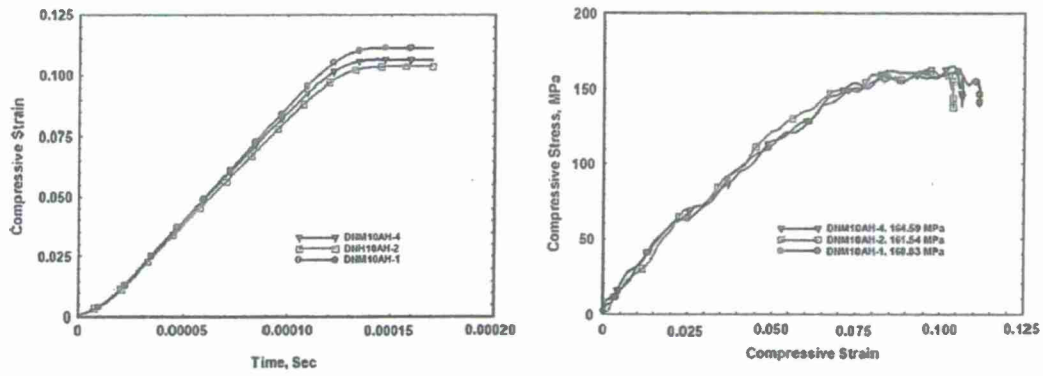


Fig. 9. Typical response of nylon 6,6 nanocomposites at high-strain rate.

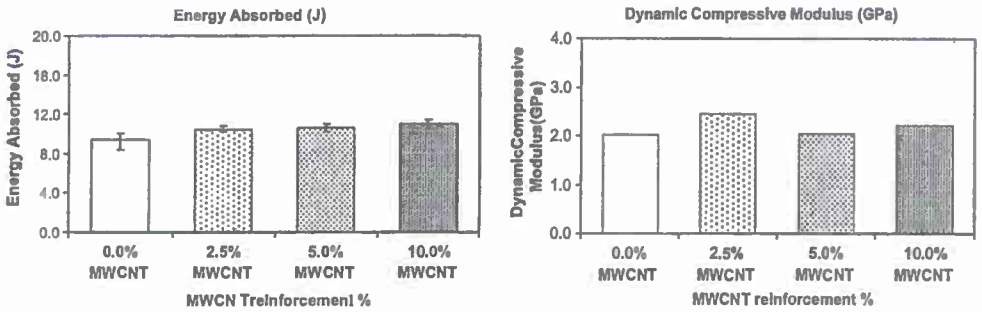


**Fig. 10.** Energy absorbed and compressive modulus of nylon 6,6 nanocomposites at high-strain rate.

platelet; and Eco-Core foam samples were not available at the time of high-strain rate testing and are therefore not reported here. Typical responses of nylon 6,6 nanocomposites to high-strain loading are shown in Fig. 9.

Addition of 2.5 wt.% MWCNT to pure nylon 6,6 showed 10–20% improvement in strength and energy absorption at high-strain rates (Fig. 10). A higher weight percent of MWCNT did not proportionately improve the strength or energy absorption. The dynamic compressive modulus for 5 wt.% nanocomposite is about the same as pristine nylon 6,6 at these high-strain rates. All the nano samples, including pure nylon 6,6, exhibited a permanent-set deformation under Hopkinson bar high-strain compressive loading, with none shattering.

## 6. Molecular dynamic simulations of nanocomposites

Many researchers have attempted to model the mechanical behavior of single wall carbon nanotube (SWCNT) taking input from molecular mechanics. Several new computational methods and their applications to nanostructures have been developed: equivalent continuum models [4–6], quasi-continuum models [7–14] using Tersoff and Brenner interatomic potential [15,16], and molecular dynamics simulations [17,18]. In this paper we focus on modeling and simulation of MWCNT composites using molecular dynamics approach.

Molecular Modeling is a computational technique to model or mimic the behavior of the molecules. Force fields of computational chemistry and material science are applied for studying small chemical molecular systems and material assemblies. The common feature of molecular modeling techniques is the atomistic level systems, this is in contrast to quantum chemistry. The main benefit of molecular modeling is that it allows more atoms to be considered during the simulation. Starting with a small number of molecules, and keep increasing the unit cell size, until one reaches a periodic system, which represents the full scale material properties. It is recommended to simulate unit cells with 3000 atoms or more, to describe the behavior of any material in order to get the periodic unit cell which represents the infinite system.

The commercially available Material Studio Software® [19] has been used for performing molecular dynamic simulations of single- and multi-wall carbon nanotube reinforced polymers to predict their mechanical properties. This was accomplished by using bulk amorphous polymer structures are generated by constructing polymeric chains in a periodic cell, taking into account the bond torsion probabilities and bulk packing requirements. Models are then equilibrated by a series of energy minimization and molecular dynamic runs. Crystal structures for semi-crystalline and amorphous polymers are generated [20,21] and the simulated bulk structures are subjected to three different methods for evaluating their mechanical behavior: the static method; the fluctuation method; and the dynamic method. In this paper we used the static method to illustrate the feasibility of using MD technique for predicting mechanical properties of nanocomposites. The dynamic method is still under investigation by the authors.

After molecular dynamics simulation has been performed, the resulting deformed molecular structure is analyzed for determining elastic constants. Elastic constants of the final atomic configuration are computed using the static approach suggested by Theodorou and Suter [22]. The elastic constants in this approach are defined as

$$C_{lmnk} = \left.\frac{\partial \sigma_{lm}}{\partial \varepsilon_{nk}}\right|_{T,\sigma_{nk}} = \frac{1}{V_0}\left.\frac{\partial^2 A}{\partial \varepsilon_{lm}\partial \varepsilon_{nk}}\right|_{T,\sigma_{lm},\sigma_{nk}}, \tag{1}$$

where $A$ denotes the Helmholtz free energy, $\varepsilon$ is the strain component, $\sigma$ is the stress component and $V_0$ is the volume of the simulation cell in the undeformed configuration. It is assumed that contributions originating from changes in configurational entropy on deformation, and from the strain dependence of the vibrational frequencies are negligible for glassy polymers. Thus, it is possible to estimate the elastic stiffness coefficients from numerical estimates as

$$\mathrm{d}^2U/\mathrm{d}\varepsilon_i \cdot \mathrm{d}\varepsilon_i = [\mathrm{d}\sigma_i/\mathrm{d}\varepsilon_j], \tag{2}$$

where $U$ is the potential energy of the system.

For each configuration submitted for analysis of static elastic constants, the first step consists of energy minimization using conjugate gradients method. In this study, the target minimum derivative for the initial step is 0.1 kcal/Å. However, to reduce the time required for the calculation, a maximum of 1000 steps were performed in attempting to satisfy the convergence criterion. Following the initial stage, three tensile and three pure shear deformations of magnitude ±0.0005 were applied to the minimized system and the system was re-minimized following each deformation. The internal stress tensor was then obtained from the analytically calculated virial and used to obtain estimates of the 6 × 6 elastic stiffness coefficient matrices.

As a result of these simulations, the elastic stiffness coefficients could be obtained by estimating the second derivatives of the deformation energy with respect to strain using a finite difference formula (for diagonal components only), and by calculating $\Delta\sigma_i/\Delta\varepsilon_j$ for each of the applied strains, where $\sigma_i$ represents, in vector notation, elements of the stress tensor obtained analytically using the following expression:

$$\sigma = -\frac{1}{V_0}\left[\left(\sum_{i=1}^{N} m_i(\mathrm{v}_i\mathrm{v}_i^T)\right) + \left(\sum_{i<j} r_{ij}f_{ij}^T\right)\right], \tag{3}$$

where index $i$ runs over all particles 1 through $N$; $m_i$, $\mathrm{v}_i$ and $f_i$ denote the mass, velocity and force acting on particle $i$; and $V_0$ denotes the

(undeformed) system volume. In an atomistic calculation, this expression for internal stress tensor is called virial expression.

Generally, it is assumed that the numerical estimation of second derivatives (of the energy) will be less precise than estimation of the first derivatives (of the stress). Therefore, the latter method has been used here for calculating the elastic constants. This approach creates the foundation of calculating elastic constants; however, the potential energy expression can alter depending upon the ensemble of thermodynamic variables of the simulation experiment.

In this paper we used COMPASS force field [23] because it supports all the energy interaction terms, in the material simulated. Different ensembles were applied for the different dynamic thermostat or barostat steps, such as NVT, Constant-volume/constant-temperature dynamics, NPT, Constant-pressure/constant-temperature dynamics.

The equations of motion were solved with Anderson, Berendsen or Parrinello velocity algorithms. The time step of integration was set to 1 fs in all cases. The summation methods for van der Waals and Coulomb forces were all atom based (cutoff, spline width and buffer width was 9.5 Å). The Discover program within Materials Studio Software was used. Discover provides several methods for controlling temperature and pressure. Depending on which state variables (for example, the energy $E$, volume $V$, temperature $T$, pressure $P$, and number of particles $N$) are kept fixed, different statistical ensembles can be generated. A variety of structural, energetic, and dynamic properties can then be calculated from the averages or the fluctuations of these quantities over the ensemble generated.

### 6.1. MWCNT

Two ensembles were applied for the dynamics steps, either NVT (Anderson thermostat), or NPT (Berendsen barostat and Parrinello thermostat). Temperature was set to 298 K and was raised till 400 K equilibrated back to room temperature to calculate the elastic constants of different multi-wall carbon nanotubes, of different chiralties, varying the number of walls, for both isobaric and isochoric ensembles. The MD trajectory was obtained by saving the coordinates and velocities of all atoms at each 100 fs (i.e. output a frame every 100 fs). MS static elastic properties were calculated by applying three tensile, and three shear strains of a magnitude ±0.0005 to the minimized equilibrated system and the system is reminimized following each deformation. The internal stress tensor is then obtained from the analytically calculated virial and used to obtain estimates of the elastic stiffness coefficients matrix.

Two types of simulations are used: sequential or assigned (individual). In the sequential simulation, the number of walls, chirality of inner tube and the minimum separation distance between carbon walls were specified without specifying the chiralty of the rest of the walls, the program automatically calculates chirality of subsequent layers. In the assigned simulation, the chiralty of each wall in the MWCNT is specified without over lapping the minimum distance, which is the thickness of a graphine sheet, (3.347 Å).

Various trial runs were carried out for the simulation of multi-wall carbon nanotubes. An assumption of transverse isotropy was used in calculating engineering constants of MWCNT [24]. Fig. 11 shows the effect of number of CNT layers on longitudinal Young's modulus. It shows that after three layers the properties are almost constant. Therefore, a MWCNT with three walls was used for the composite simulations. To study the effect of MCNT length on engineering constants, various MWCNT lengths were simulated using three walls by varying the number of super cell units and using NPT ensemble (Table 1).

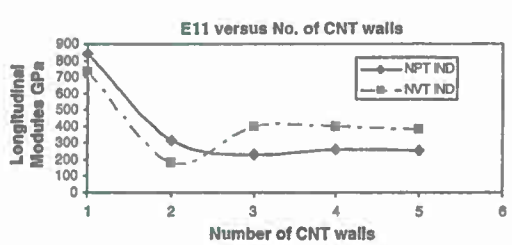


**Fig. 11.** Effect of the number of carbon layers on Young's modulus of MWCNT using MD Simulation with Berendsen thermostat and Berendsen barostat for NPT and NVT ensembles.

### 6.2. Nylon 6,6

For nylon-6,6, first a single chain of twenty monomers is built, and minimized using the conjugate gradient method. A rectangular unit cell of dimensions 33.3 Å × 33.3 Å × 33.3 Å was constructed from 10 polymer chains with 3820 atoms and a target density of 1.07 gm/cc. The unit cell was minimized for 150 ps at a rate of 1 fs under both NPT and NVT using COMPASS force field. Then, dynamic temperature loading was applied on the unit cell as follows: First, the temperature was increased from room temperature to 80 °C, which is beyond the glass transition temperature of nylon-6,6. This was done in two steps at a rate of 150 ps per step, then cooled to room temperature. Results of MD simulation for nylon 6,6 are shown in Fig. 12. Calculated engineering constants are summarized in Table 2.

### 6.3. MWCNT–nylon 6,6 composites

An infinite crystal of the MWCNT reinforced nylon 6,6 containing a given mass/volume fraction of the nanotube reinforcements is constructed using a box-shape unit cell of corresponding dimensions. The periodic boundary conditions across all the faces of the cell are applied. The MWCNT is generated sequentially with the inner diameter having the chirality 5–5. Different volume fractions of reinforcements are being considered: 5%, 10%, and 20%. Lower weight fractions (2.5 and 1.25) resulted in a very large system which is beyond the capabilities of the used software. The three edges ($a$, $b$ and c) of the cell are aligned respectively with the three coordinate axes ($x$, $y$ and $z$). The nanotube axis is aligned with the $z$ cell edge lengths, respectively. The atomic configuration within the cell corresponding to the cross-linked molecules of the nylon matrix and the MWCNT are generated using the following procedure:

**Table 1**
Effect of MWCNT length on engineering constants

| | Length (Å) | $L/d$ ratio (inner tube) | $L/d$ ratio (outer tube) | $E_{11}$ (GPa) | $E_{22}$ (GPa) | $\nu_{12}$ | $\mu_{23}$ (GPa) | $K_{23}$ (GPa) |
|---|---|---|---|---|---|---|---|---|
| 2 Units | 4.92 | 0.72 | 0.25 | 439 | 36 | 0.2 | 11 | 47.3 |
| 4 Units | 9.84 | 1.5 | 0.5 | 493 | 36 | 0.26 | 7.7 | 47.15 |
| 30 Units | 73.8 | 11 | 3.6 | 690 | 27.5 | .33 | 7.9 | 52.6 |
| 40 Units | 98.4 | 14.4 | 4.8 | 720 | 28.6 | .33 | 8.3 | 54.9 |

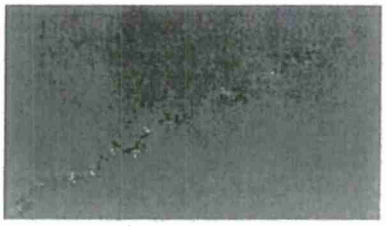

(a) Single chain of 20 molecules

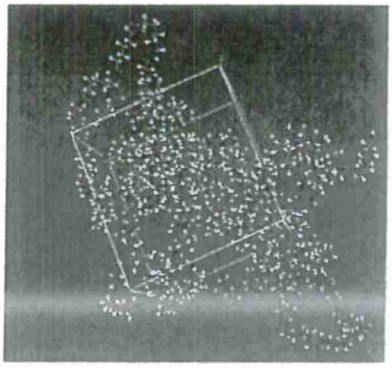

(b) Ten chains of nylon 6,6

NPT Cut off point: 9.5 A

$$C_{ij} = \begin{bmatrix} 4.1 & 1.9 & 2.2 & 0 & 0 & 0 \\ 2.1 & 4.82 & 2.1 & 0 & 0 & 0 \\ 3 & 2.6 & 4.8 & 0 & 0 & 0 \\ 0 & 0 & 0 & 1 & 0 & 0 \\ 0 & 0 & 0 & 0 & 1.3 & 0 \\ 0 & 0 & 0 & 0 & 0 & 1.2 \end{bmatrix} \text{GPa}$$

NPT Cut off point: 6.5 A

$$C_{ij} = \begin{bmatrix} 3.6 & 1.5 & 1.6 & 0 & 0 & 0 \\ 1.5 & 3.8 & 1.6 & 0 & 0 & 0 \\ 1.4 & 1.6 & 3.5 & 0 & 0 & 0 \\ 0 & 0 & 0 & 0 & 1.1 & 0 \\ 0 & 0 & 0 & 0 & 1.1 & 0 \\ 0 & 0 & 0 & 0 & 0 & 1 \end{bmatrix} GPa$$

NVT Cut off point: 6.5 A

$$C_{ij} = \begin{bmatrix} 5.3 & 2.7 & 2.8 & 0 & 0 & 0 \\ 2.7 & 5.2 & 2. & 0 & 0 & 0 \\ 2.8 & 2.1 & 4.8 & 0 & 0 & 0 \\ 0 & 0 & 0 & 1.3 & 0 & 0 \\ 0 & 0 & 0 & 0 & 1.2 & 0 \\ 0 & 0 & 0 & 0 & 0 & 1.1 \end{bmatrix} GPa$$

**Fig. 12.** MD simulation of nylon 6,6 matrix.

**Table 2**
Engineering constants of nylon 6,6 for different ensembles and different cut-off points

| Engineering constants (GPA) | NPT 9.5 A | NPT 6.5 A | NVT 6.5 A |
|---|---|---|---|
| $E_{11}$ | 4.0 | 2.8 | 3.4 |
| $\nu_{12}$ | 0.24 | 0.28 | 0.37 |
| $\mu_{23}$ | 3.9 | 2.7 | 3.6 |
| $K_{23}$ | 1.25 | 1.1 | 1.6 |

(a) A single molecule of the nylon is first constructed using the Visualizer [19] program from Accelrys, Fig. 12a;
(b) Next, the molecule generated in (a) is duplicated several times depending on the weight fraction of interest, Fig. 12b;
(c) The nylon-6,6 molecules generated in (b) are used as fragments within the Amorphous Cell program from Accelrys [2] to generate a box-shape computational cell of a given size containing the nylon 6,6 of a specified density;
(d) The atomic configuration corresponding to the MWCNT is then constructed using the procedure described earlier;
(e) The atomic configuration obtained in (e) is subjected to a series of energy minimization and dynamic relaxations under NPT condition starting with 20 ps for 1 fs time step. The temperature was raised from room temperature to 80 °C (beyond the glass transition temperature of nylon 6,6), then cooled down to room temperature.

**Table 3**
Engineering constants for MWCNT-nylon 6,6 composites with 5, 10 and 20 wt.% fractions

| Engineering constants (GPA) | 5% | 10% | 20% |
|---|---|---|---|
| $E_{11}$ | 5.5 | 13.6 | 73.5 |
| $E_{22}$ | 5 | 9.6 | 40.6 |
| $\nu_{12}$ | 0.32 | .31 | - |
| $\mu_{23}$ | 1.8 | 6.3 | 8.6 |
| $K_{23}$ | 5.3 | 10.5 | 18 |

Results of molecular dynamic simulations for MWCNT–nylon 6,6 composites with different weight fractions are shown in Table 3.

## 7. Concluding remarks

Non-destructive vibration response results show that the dynamic stiffness of nylon 6,6 nanocomposites increases with MWCNT loadings and the damping is reduced. In general, the 10 wt.% and 20 wt.% MWCNT/nylon 6,6 composites exhibited highest stiffness and damping. The 20 wt.% nano composite plates had broken into pieces during extrusion manufacturing process, and are therefore not considered practical. Addition of MWCNT was detrimental to the maximum load and energy absorption under low-velocity impact. However, there was an improvement in strength and energy absorption at high-strain rates under compressive loading with Hopkinson pressure bar apparatus.

A 40% increase in flexural dynamic modulus without drop in damping, along with improved low-velocity impact energy absorption was observed with the addition of 2.5 wt.% graphite platelets to vinyl ester. The nanoclay reinforcement did not show any improvement in flexural modulus and damping. Eco-Core foams with chopped glass fibers exhibited higher flexural modulus, damping and impact energy absorption compared to those without chopped glass fibers.

Results of molecular simulations with various types of loadings applied to MWCNTs show that the MWCNT is transversely isotropic. The transverse properties are comparatively poor. Molecular dynamic simulation is an effective technique that may be employed for obtaining composite properties.

## Acknowledgements

Authors wish to acknowledge support for this research by ONR Grant# N00014-06-1-0577, Office of Naval Research, Solid

Author's personal copy



Mechanics Program (Dr. Yapa D.S. Rajapakse, Program Manager). Ravi Zalani, Swasti Gupta and Hunain Alkhateb are the graduate students who worked on this Project. The nano clay and graphite plateiet reinforced vinyl ester plates were manufactured by Dr. Larry Drzal's group at Michigan State University. Eco-Core foam samples were supplied by Dr. Kunigal Shivkumar at North Carolina A&T State University. Hopkinson bar high-strain rate testing was performed by Dr. David Hui's group at University of New Orleans.

## References

[1] Mantena PR, Mann R, Nori C. Low-velocity impact response and dynamic characteristics of glass resin composites. J Reinf Plast Compos 2001;20(6):513–34.
[2] Nori C, Mantena PR, McCarty TA. Experimental and finite element analysis of pultruded glass-graphite/epoxy hybrids in axial and flexural modes of vibration. J Compos Mater 1996;30(18):1996–2018.
[3] Suarez SA, Gibson RF. Improved impulse-frequency response techniques for measurement of dynamic mechanical properties of composite materials. J Test Eval 1987;15:114–21.
[4] Odegard GM, Gates TS, Nicholson LM, Wise C. Equivalent continuum modeling with application to carbon nanotubes. NASA ICASE report NASA/TM-2002-211454; March 2002.
[5] Odegard GM, Gates TS, Nicholson LM, Wise C. Equivalent continuum modeling of nano-structured materials. NASA ICASE report NASA/TM-2001-210863; May 2001.
[6] Li C, Chou T. A structural mechanics approach for the analysis of carbon nanotubes. Int J Solids Struct 2003;40:2487–99.
[7] Zhang P, Huang Y, Geubelle PH, Klein PA, Hwang K. The elastic modulus of single-wall carbon nanotubes: a continuum analysis incorporating interatomic potentials. Int J Solids Struct 2002;39:3893–906.
[8] Zhang P, Huang Y, Gao H, Hwang K. Fracture nucleation in single-wall carbon nanotubes under tension: a continuum analysis incorporating interatomic potentials. Trans ASME 2002;69:454–8.
[9] Arroyo M, Belytschko T. Finite crystal elasticity of carbon nanotubes based on the exponential Cauchy–Born rule. Phys Rev B 2004;69:11541S.1–11541S.11.
[10] Zhang P, Jiang H, Huang Y, Geubelle PH, Hwang KC. An atomistic-based continuum theory for carbon nanotubes: analysis of fracture nucleation. J Mech Phys Solids 2004;52:977–98.
[11] Jiang H, Zhang P, Liu B, Huang Y, Geubelle PH, Gao H, et al. The effect of nanotube radius on the constitutive model for carbon nanotubes. Comput Mater Sci 2003;28:429–42.
[12] Jiang H, Feng XQ, Huang Y, Hwang KC, Wu PD. Defect nucleation in carbon nanotubes under tension and torsion: Stone–Wales transformation. Comp Meth Appl Mech Eng 2004;193:3419–29.
[13] Jiang LY, Huang Y, Jiang H, Ravichandran G, Gao H, Hwang KC, et al. A cohesive law for carbon nanotube/polymer interfaces based on the van der Waals force. J Mech Phys Solids 2006;54:2436–52.
[14] Arroyo M, Belytschko T. Nonlinear mechanical response and rippling of thick multiwalled carbon nanotubes. Phys Rev Lett 2004;91(21): 215505.1–5.4.
[15] Tersoff J. New empirical approach for the structure and energy of covalent systems. Phys Rev B 1988;37:6991–7000.
[16] Brenner DW. Empirical potential for hydrocarbons for use in simulating chemical vapor deposition of diamond films. Phys Rev B 42: 9458–71.
[17] Yakobson BI, Cambell MP, Brabec CJ, Bernholc J. High strain rate fracture and C-chain unrevealing in the carbon nanotubes. Comput Mater Sci 1997;8: 341–8.
[18] Belytschko T, Xiao SP, Schatz GC, Ruoff RS. Atomistic simulations of carbon nanotube fracture. Phys Rev B 2002;65(23):235430.1–0.7.
[19] MS modeling 4.0 online help manual, Accelrys Inc.; 2005.
[20] Pal G, Al-Ostaz A, Mantena PR, Cheng A, Song C. Molecular dynamic simulations of SWCNT–polymer nanocomposite and its constituents. in: Proceedings of the 21st annual technical conference of the American society for composites, Dearborn, MI, Paper #136 on CD ROM; 2006.
[21] Ahmed Al-Ostaz, Ghanshyam Pal P, Raju Mantena, Alex Cheng. Molecular dynamics simulation of SWCNT – polymer nanocomposite and its constituents. J Mater Sci 2008;43(1):164–73.
[22] Theodorou DN, Suter UW. Atomistic modeling of mechanical properties of polymeric glasses. Macromolecules 1986;19:139–54.
[23] Sun H. COMPASS: an ab initio force-field optimized for condensed-phase applications – overview with details on alkane and benzene compounds. J Phys Chem B 1998;102:7338–64.
[24] Christensen R. Mechanics of composite materials. Malbar (Fl): Krieger Publishing Company; 1991. p. 74–8.

*eXPRESS Polymer Letters Vol.3, No.11 (2009) 724–732*
*Available online at www.expresspolymlett.com*
*DOI: 10.3144/expresspolymlett.2009.90*

# Effects of bromination on the viscoelastic response of vinyl ester nanocomposites

*A. Almagableh[1*], P. R. Mantena[2], A. Alostaz[3], W. Liu[4], L. T. Drzal[4]*

[1]University of Mississippi, PO. Box 3967, MS 38677, USA
[2]University of Mississippi, 201 D Carrier Hall, MS 38677, USA
[3]University of Mississippi, 202 Carrier Hall, MS 38677, USA
[4]Composite Materials and Structures Center, Michigan State University, 2100 Engineering Bldg, East Lansing, MI 48824, USA

*Received 25 May 2009; accepted in revised form 1 September 2009*

Abstract. Fire, smoke and toxicity are of significant concern for composite materials used in marine applications. Bromination of vinyl ester resin imparts fire retardancy as manifested by a reduction in the amount of smoke, carbon monoxide, and corrosive combustion products. In this research, the viscoelastic properties, modulus (stiffness) and damping (energy dissipation), of 1.25 and 2.5 wt. percent nanoclay and exfoliated graphite nanoplatelet (xGnP) reinforced non-brominated and brominated vinyl ester have been studied over a range of temperature and frequency. Effects of frequency on the viscoelastic behavior were investigated using a Dynamic Mechanical Analyzer (DMA) by sweeping the frequency over three decades: 0.01, 0.1, 1 and 10 Hz, and temperature range from 30–150°C at a step rate of 4°C per minute. Master curves were generated by time-temperature superposing the experimental data at a reference temperature. The nano reinforced composites showed a drop in initial storage modulus with bromination. Nanocomposites with 1.25 and 2.5 wt. percent graphite had the highest storage modulus among brominated specimens. Bromination was also found to significantly increase the glass transition temperature ($T_g$) and damping for all nanocomposites. Among the brominated specimens, 1.25 wt. percent graphite platelet reinforced vinyl ester exhibited the best viscoelastic response with high damping and glass transition temperature, along with superior storage modulus over a longer time period.

*Keywords: nanocomposites, viscoelastic properties, bromination*

## 1. Introduction

Thermoset vinyl ester matrices are becoming increasingly important in industrial applications due to their enhanced mechanical properties. They exhibit characteristics similar to epoxy resins, as well as unsaturated polyester resins. Advantages include high tensile strength and stiffness, low cost, process versatility and good chemical resistance. However, vinyl ester still has some challenges like poor resistance to crack propagation, brittleness and large shrinkage that occurs during polymerization. Therefore, introducing good interfacial bonding between nanofillers and the resin is often used to alleviate volume shrinkage, void formation and improving surface dispersion along with toughness. Methods of incorporating nanoparticles into polymer matrices could be *ex-situ*, like dispersion of the synthesized nanoparticles into resin solution, or *in-situ* monomer polymerization process in the presence of the nanoparticles [1]. The interaction between the nanoparticles and matrix for the *ex-situ* fabricated composites are normally van der waals

*Corresponding author, e-mail: amalmag1@olemiss.edu
© BME-PT



K-162

forces, steric interaction. However, the *in-situ* synthesis methods may create strong chemical bonding within the composite.

Optical and mechanical properties of vinyl ester polymer reinforced with ZnO nanoparticles, functionalized with a bi-functional coupling agent methacryloxypropyl-trimethoxysilane (MPS) were investigated by Guo *et al.* [2]. The existence of MPS at the interface between the matrix and particles results in improved interfacial interaction which in turn improves UV shielding, modulus and strength significantly.

The physical properties of vinyl ester reinforced with unmodified CuO nanoparticles and those functionalized with a bi-functional coupling agent methacryloxypropyl-trimethoxysilane (MPS) were studied by Guo *et al.* [3]. Increase in both thermal stability and mechanical properties were attributed to good nanoparticles dispersion at the interface and the resulting chemical bonding between the functionalized nanoparticles and the matrix.

Vinyl ester thermosetting nanocomposites reinforced with iron oxide nanoparticles were prepared and characterized by Guo *et al.* [4]. Iron oxide nanoparticles functionalized with a bi-functional coupling agent was observed to increase the adhesion and dispersion of the nano filler into the matrix resulting in increased thermal stability, lower curing temperature and improved mechanical properties. The nanocomposites became also magnetically stronger and were independent of particles functionalization.

Schroeder *et al.* [5] analyzed morphologically thermoset materials obtained from styrene/vinyl ester resins of different molecular weights modified with polymethyl methacrylate (PMMA). It was found that different morphologies including dispersion of thermoplastic rich particles in a thermoset resin, continuity of network structure were highly dependent on molecular weight of vinyl ester, curing temperature and concentration of the PMMA additives. The addition of the thermoplastic PMMA increased the fracture resistance without significantly affecting both volume shrinkage reduction and the thermal-mechanical properties of the modified thermosets.

Recent interest in the use of organic-matrix composite materials in US Navy submarines and ships has generated the requirement for significant improvement in the flammability performance of these materials including reduction in the amount of smoke, carbon monoxide, and corrosive combustion products. New fire retardant approaches for organic-matrix composite materials are needed to address the smoke issues and to further reduce the flammability of these composites. Focus of our research is on developing stronger, safer and more cost-effective structures for the new generation naval ships; especially nanoparticle reinforced glass/carbon polymeric based composites and structural foams for blast/shock/impact mitigation. Fire, smoke and toxicity are of significant concern in ship structures. The US Navy is currently using brominated vinyl ester matrix resin with glass reinforcement for composite applications in topside surface ship structures [6]. This matrix resin was selected due to its good corrosion resistance and toughness. Bromine is an effective flame retardant, especially when combined with antimony oxide. Bromination of vinyl ester resin imparts fire retardancy as manifested by flame spread and lower heat release rates. However, this fire-retardant system functions primarily in the gas phase causing incomplete combustion. As such, brominated resins produce dense smoke, an increase in the yield of carbon monoxide, and hydrogen bromide.

The work reported here is an extension of previous work [7] on the viscoelastic behavior of non-brominated vinyl ester nanocomposites. DMA measurements are usually carried out under constant displacement amplitude in a fixed-frequency deformation mode, in which the mechanical properties are function of temperature only. Other measurements that provide more information may include frequency sweep with temperature steps, to which time-temperature superposition (TTS) applied to predict the long-term time dependent properties of the material [8]. An attempt has been made to experimentally characterize the dynamic storage modulus ($E'$) and damping of brominated and non-brominated vinyl ester reinforced with 1.25 and 2.5 wt. percent nano-clay and exfoliated graphite nanoplatelets (xGnP) as a function of temperature and frequencies. Dynamic mechanical testing has been used to perform multi-frequency (accelerated temperature measurements) and theoretical time-temperature superposition treatment of the data. Effects of bromination on the viscoelastic response of these vinyl ester nanocomposites are discussed.



K-163

## 2. Theory

The time-temperature superposition principle is based on the fact that processes involved in molecular motion occur at larger rates at elevated temperatures. The change in property which occurs relatively quickly at higher temperatures can be made to appear as if they occurred at longer times or lower frequencies simply by shifting the data with respect to time (1/frequency) [8]. By shifting the data with respect to frequency to a reference curve, a master curve is generated, which covers time (frequencies) outside the accessible range.

The shifting mechanism used to shift a set of data upon a reference curve follows WLF [8] model. This model assumes that the fractional free volume increases linearly with respect to temperature in the transition region, and when the free volume increases, its viscosity decreases. In this model, the degree of shifting was calculated according to Equation (1);

$$\log a_T = \frac{-C_1(T-T_0)}{C_2+(T-T_0)} \tag{1}$$

For both resin systems (with and without bromination), $C_1$ and $C_2$ were found to be around 103.9 and 399 K, respectively. Relationship between the shifting factor ($a_T$) versus $T$ is plotted in Figure 1 for pure and brominated vinyl ester.

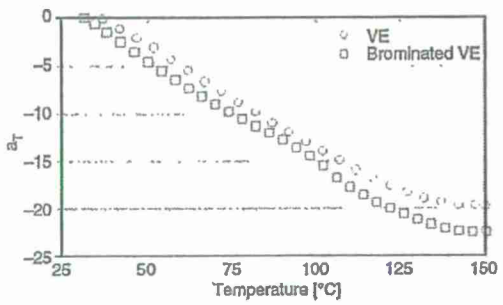


**Figure 1.** Relationship between shifting factor ($a_T$) and temperature for pure and brominated vinyl ester based on the WLF model

## 3. Experimental

### 3.1. DMA setup

Dynamic measurements were carried out using the TA Instrument model Q800 DMA on prismatic specimens deformed in a single-cantilever clamping mode, with a span length of 17.5 mm. Stress and strain with the single-cantilever clamp used in model Q800 DMA are calculated with Equations (2) and (3), respectively [8], assuming linear viscoelastic behavior.

$$\sigma_x = \frac{6PL}{wt^2} \tag{2}$$

$$\varepsilon_x = \frac{3\delta t F_c}{L^2\left[1+\frac{12}{5}(1+\upsilon)\left(\frac{t}{L}\right)^2\right]} \tag{3}$$

where $L$ – clamp span length
$t$ – sample thickness
$w$ – width of the specimen
$\nu$ – Poisson's ratio
$F_c$ – clamping correction factor
$\sigma_x$ – stress
$\varepsilon_x$ – strain
$P$ – applied force
$\delta$ – amplitude of deformation

### 3.2. Test description

The 1.25 and 2.5 wt. percent nanocaly and xGnP reinforced non-brominated and brominated vinyl ester nanocomposites were characterized by performing a multi-frequency isothermal mode, in which the sample is equilibrated at different temperatures and subjected to a series of frequencies. Specimens with dimensions of 35×10×1.6 mm were subjected to frequencies of: 0.01, 0.1, 1 and 10 Hz with a temperature step rate of 4°C per minute starting from 30°C (RT) to 150°C. A very small displacement amplitude (25 μm was applied since the analysis assumes linear viscoelastic characterization, and two specimens were tested from each configuration. The raw data was then fed to the Rheology data analysis software to generate the master curves.

### 3.3. Materials and sample preparations

The polymeric matrix used was a vinyl ester resin (manufactured and supplied by Ashland specialty chemical, Division of Ashland INC (Columbus, OH)). DERAKANE 411-350-(non-brominated) is a mixture of 45 wt.% styrene and 55 wt.% vinyl ester. Styrene allows the chain extension because of its single unsaturated carbon-carbon double bond, while the vinyl ester resin with two reactive vinyl



k-164

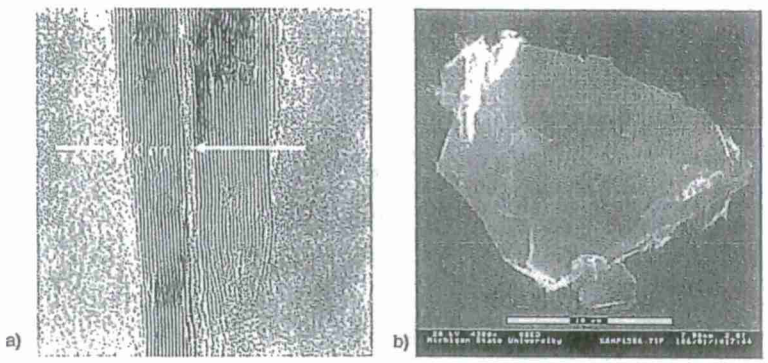

Figure 2. Morphology of xGnP using (a) edge view (TEM), and (b) Lateral view (SEM)

end groups enables the crosslinking for network. DERAKANE 510A-40 (brominated) vinyl ester resin is a brominated bisphenol-A based vinyl ester consisting of 38 wt.% styrene, and modified to produce the maximum degree of fire retardancy combined with enhanced chemical resistance and toughness. These additives are Butanone peroxide, N,N-Dimethylaniline, Cobalt Naphthenate, and 2-4-Pentanedione, all supplied from Sigma Aldrich (St. Louis, Mo).

Exfoliated graphite nanoplatelets (xGnP) were produced according to the method described in [9]. The nanoclay was Cloisite 30B from Southern Clay Products, Inc (Gonzales, TX). Figures 2a and 2b show a morphology using TEM and SEM for both edge and lateral views of xGnP inside a polymer. These xGnP nanocomposites have exfoliated and dispersed graphite platelets with 1 nm thickness and several hundred nanometers widths. Distance between layers is in the range of 10~30 Å and size of the layered graphite extends from several hundred nanometers to several microns.

The samples were prepared by dispersing about 3000 g of epoxy vinyl ester resin solution with different percentages of nanoclay or nanographite in a 1 gal container for 4 hours, followed by 4 passes through a flow cell connected to a 100 W sonicator. 1% Butanone peroxide, 0.2% of 2-4 Pentanedione, 0.1% N,N-Dimethylaniline, and 0.2% Cobalt Naphthenate were added to the mixed vinyl ester resin solution in order and mixed for 10 min. The above mixed resin solution was mixed for 2 min with FlackTek speed mixer at 3000 RPM. The well-mixed vinyl ester resin solution with nanoclay or nanographite was poured into a 13×13×0.4" mold, let stand for 30 minutes at room temperature and then was post cured at 80°C for 3 hours. Prismatic samples with nominal dimension of 35×10×1.6 mm size were prepared from these plates and tested in a DMA using the single-cantilever clamp fixture.

## 4. Results and discussion

### 4.1. Densities

As shown in Figure 3, the densities of brominated vinyl ester nanocomposites are greater than that of the non-brominated samples. It should be noted that bromine is a heavy atom and there are four bromine atoms bonded in one molecule, which results in density being higher for brominated specimens. Specific gravity of 510A-40 brominated vinyl ester is about 1.23 while that of the non-brominated version 411-350 is 1.046.

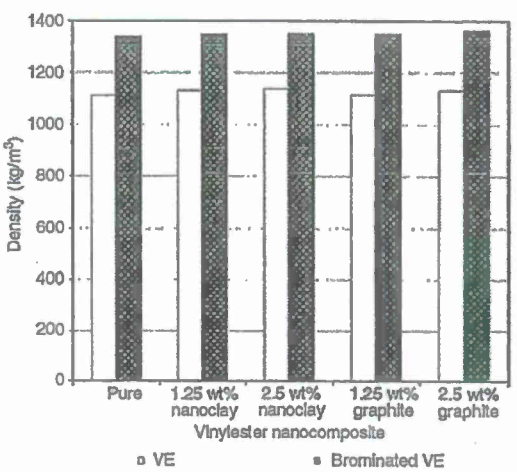


Figure 3. Densites of non-brominated (411-350) and brominated (510A-40) vinyl ester nanocomposites



K-165

### 4.2. Modulus

The storage modulus versus temperature curve provides valuable information about the stiffness of a material as a function of temperature, and it is sensitive to structural changes such as molecular weight, fiber-matrix bonding and degree of crosslinking density. Crosslink density, typically given as the average molecular weight between crosslinks ($M_c$), is an important factor governing the physical properties of cured thermoset resins. Moreover, it can be changed by adjusting the styrene content in the resins, molecular weight of vinyl ester oligomers, altering the state of conversion, and control of the cure conditions [10]. Crosslinking densities of the two resin systems (non-brominated and brominated) resulting from different styrene contents were calculated [10] as 1116 and 597 mol/m$^3$, respectively, based on Equation (4):

$$V = \frac{G_0^n}{RT} \tag{4}$$

where $V$ – crosslinking density
$R$ – gas constant
$G_0^n$ – plateau modulus from master curve of the shear modulus versus frequency.

Calculation of crosslinking density for nanocomposites using this equation is invalid, because contribution of nanoparticles in the crosslinking mechanism is unknown.

Higher initial storage modulus in fiber reinforced composite materials are in general attributed to good fiber/matrix bonding (cross linking), or higher initial molecular weight [11]. Figure 4 shows initial storage modulus (30°C) for vinyl ester nanocomposites, with and without bromination. Initial modulus was observed to increase with addition of nanoparticles in the non-brominated system. On the other hand, bromination resulted in a reduction of the initial storage modulus with addition of nanoparticles. Among the brominated specimens, gain in glassy (initial) modulus was observed with xGnP reinforcement, and a loss in glassy modulus was associated with the addition of nanoclay particles. Loss in storage moduli with the brominated nanoclay composites could be due to weak interfacial bonding between the nanoclay particles and brominated resin. However, the 1.25 wt.% xGnP appears to be bonding better with the brominated resin resulting in higher storage modulus compared to pure brominated vinyl ester.

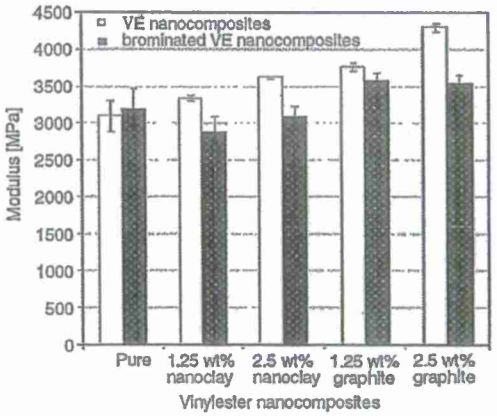


**Figure 4.** Initial storage modulus for non-brominated and brominated nanocompsoites at 1 Hz frequency

Figures 5–7 show the storage modulus ($E'$) evolution with temperature for some of the vinyl ester nanocomposites, with and without bromination. Bromination effect modifies the dynamic mechanical behavior for VE and its nanocomposites. Drop

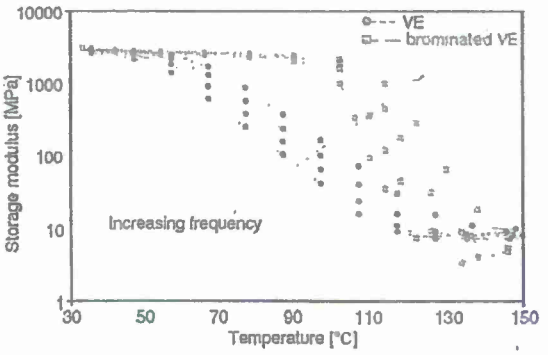


**Figure 5.** Storage modulus for pure vinyl ester with and without bromination

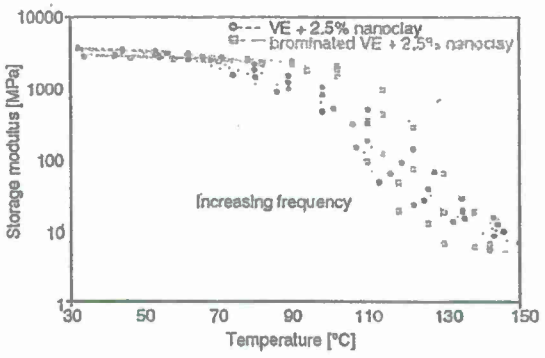


**Figure 6.** Storage modulus for 2.5 wt. percent nanoclay reinforced vinyl ester with and without bromination



k-166

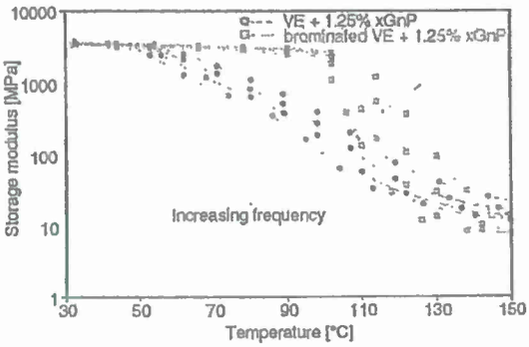


Figure 7. Storage modulus for 1.25 wt. percent xGnP reinforced vinyl ester with and without bromination

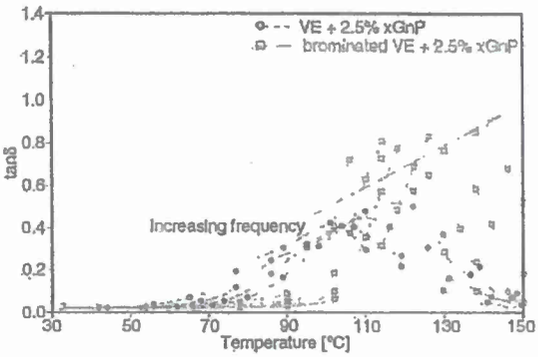


Figure 9. Tanδ curves for vinyl ester reinforced with 2.5 wt.% xGnP, with and without bromination

in modulus in the transition region is shifted to higher temperature. It is interesting to note that no major variation appears in the value of the rubbery modulus in both systems (brominated and non-brominated) with the addition of nanoparticles. This indicates that the crosslinking density of both networks has not been significantly affected with the addition of nanoparticles.

### 4.3. Damping

Tanδ, defined as the ratio of loss modulus to storage modulus, is a measure of the inherent material damping. Peak of tanδ is the region over which the material experiences a transition from glassy to a leathery behavior, associated with the onset of short range molecular segments motion, of which all are initially fixed. Bromination in general resulted in greater value of tanδ peak for all the nano reinforcements including pure vinyl ester (300% increase) suggesting that more material is involved in the relaxation (Figures 8–10). Two relaxations were observed for non-brominated vinyl ester, one at around 60°C and another between 110–120°C, which corresponds to the transition of St-resin rich phase at higher temperature. Varying the nanoclay concentration from 0 to 2.5 wt. percent produced a significant increment in the height of the corresponding loss factor peak (Figure not shown). However, significant drop of tanδ peak was associated with the addition of 2.5 wt.% xGnP to brominated resin. The greater amount of xGnP added to the brominated resin, more brittle material behavior was observed.

Area under tanδ curve (with units of °C) over the temperature range (30–150°C) was also calculated, as it is another good indicator of the total energy absorbed by the material [12]. The higher the area under tanδ curve, the greater the degree of molecular rearrangement, which enables the material to better absorb and dissipate energy. Brominated nanocomposites in general exhibited higher area under tanδ curves compared to the non-brominated

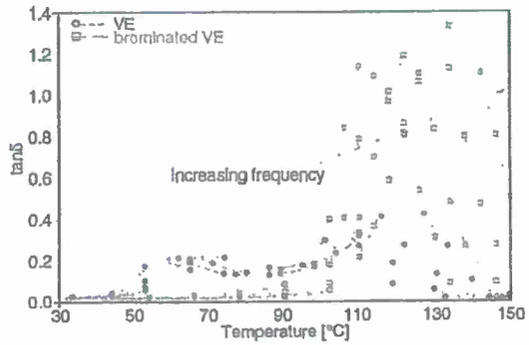


Figure 8. Tanδ curves for pure vinyl ester, with and without bromination

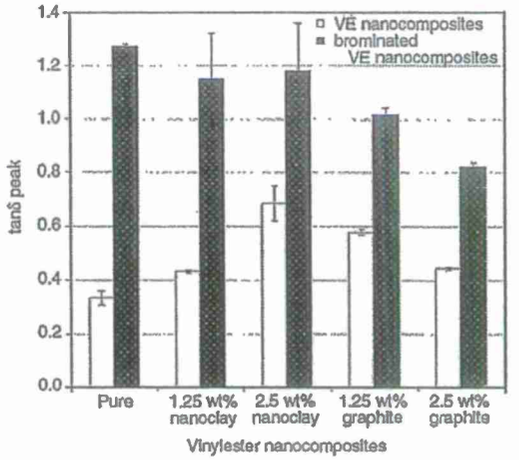


Figure 10. Tanδ peak for brominated and non-brominated vinyl ester nanocomposites at 1 Hz frequency



K-167

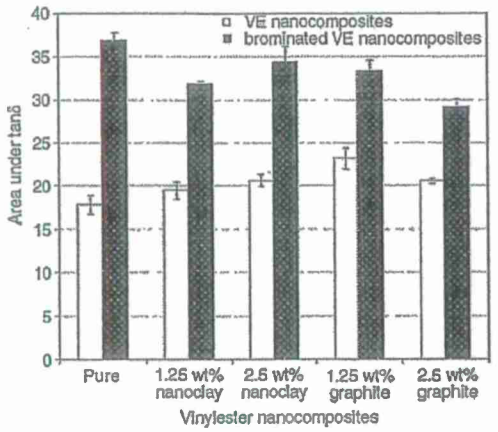


**Figure 11.** Area under tanδ curves for brominated and non-brominated vinyl ester nanocomposites at 1 Hz frequency

samples (Figure 11). From Figure 10, the higher tanδ peak value observed with the addition of 2.5 wt. percent nanoclay compared to 2.5 wt. percent graphite for brominated specimens, indicates greater molecular mobility in nanoclay brominated composites. Besides, the greatest loss in storage modulus along with the superior tanδ peak associated with the addition of nanoclay particles to brominated resin indicates that this reinforcement may be adversely affecting the interfacial bonding. Consequently, graphite nanoplatelets appear to form better interfacial bonding with brominated resin than nanoclay reinforcements.

## 4.4. Glass transition temperature, $T_g$

Figure 12 shows the loss modulus curves for the pure and brominated vinyl ester, as a function of frequency. Brominaton system produced network

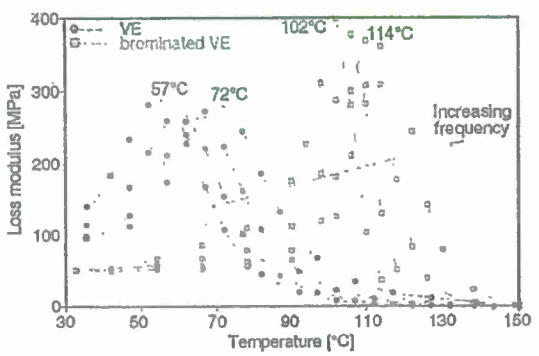


**Figure 12.** Loss modulus for pure vinyl ester, with and without bromination, as a function of frequency

with higher glass transition temperature (temperature corresponding to peak of loss modulus) than the non-brominated case. For example, $T_g$, for pure vinyl ester increased by about 80% with bromination. Glass transition temperature for the non-brominated vinyl ester nanocomposite system increased with increasing content of nanoparticles. Whereas in case of brominated vinyl ester nanocomposite system, it did not change with addition of nanoparticles. Furthermore, the glass transition temperature of the brominated samples for both pure resin and the nanocomposites was still higher than that of the non-brominated samples.

The significant increase in, $T_g$, achieved with bromination is probably due to higher initial density (molecular weight). As molecular weight increases with bromination, the glass transition region is displaced to longer time or temperature, because chain movement is expected to suppress when molecular entanglement is increased [13].

## 4.5. Time-temperature superposition

Since the glass transition temperature for nanocomposites with and without bromination is found to be varying, for this work a reference temperature of 50°C was chosen to generate master curves for the storage modulus. To perform this, data from higher temperature experiments in the lower portion of the plot are shifted to the left (lower frequencies) and curves corresponding to the temperatures lower than 50°C are shifted to the right [8]. Figure 13 shows the generated master curves of storage modulus over an extended period of time. From Figure 13a, the brominated vinyl ester is observed to maintain its rigidity (at 50°C) with an average dynamic storage modulus of (2.5 GPa) over a period of $10^{10}$ secs (321.5 years), where as the non-brominated vinyl ester starts to loose it's stiffness gradually just after $10^3$ secs (17 minutes). This is a significant improvement on the long term behavior of vinyl ester with bromination. Similarly, the brominated 1.25 wt. percent xGnP reinforced specimens exhibit superior average modulus of 2.7 GPa over 321.5 years (Figure 13b). In contrast, all the specimens with 2.5 wt. percent nanoreinforcement, both with and without bromination, show a stable dynamic response with an average storage modulus of 2.5 GPa (Figure 13c) for the first $10^8$ sec (3.2 years) only.



k-168

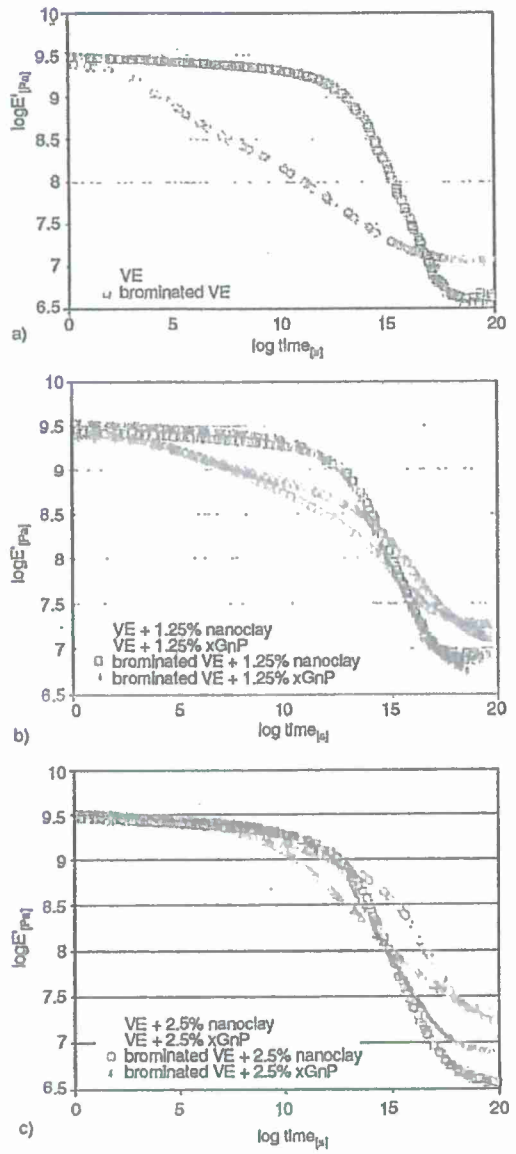


**Figure 13.** Master curves of storage modulus at a reference temperature of 50°C as a function of log time for a) pure vinyl ester, b) 1.25 wt. percent and c) 2.5 wt. percent nanoparticles

## 5. Conclusions

Bromination of vinyl ester resin imparts fire retardancy as manifested by a reduction in the amount of smoke, carbon monoxide, and corrosive combustion products. The effect of bromination on the viscoelastic behavior of Derakane 411-350 (non-brominated) vinyl ester reinforced with 1.25 and 2.5 wt. percent nanoclay and graphite nanoplatelets was investigated with a DMA. Frequency sweep across three decades: 0.01, 0.1, 1 and 10 Hz was performed over temperature range from 30 to 150°C at a step rate of 4°C/min. The time-temperature superposition principle was applied to create master curves of dynamic storage modulus at a reference temperature of 50°C.

Initial modulus was observed to increase with addition of nanoparticles in the non-brominated system. However, bromination resulted in a reduction of initial storage modulus with the addition of nanoparticles. Among the brominated specimens, gain in glassy (initial) modulus was observed with xGnP reinforcement, and a loss in glassy modulus was associated with the addition of nanoclay particles.

Both the pure vinyl ester and nanocomposites with bromination exhibited higher tanδ peak values and larger areas under the tanδ curves. From the storage modulus and damping results, it is surmised that graphite platelets appear to form better interfacial bonding with the brominated resin than the nanoclay reinforcements. Brominaton was also found to significantly increase the glass transition temperature for both pure vinyl ester (up to 80%) and the nanocomposites. The brominated vinyl ester reinforced with 1.25 wt. percent graphite platelets exhibited the best viscoelastic response with high damping and glass transition temperature, along with superior storage modulus over a longer time period.

## Acknowledgements

The authors would like to acknowledge the support received from the Department of Civil Engineering at the University of Mississippi, and funding received under a subcontract from the Department of Homeland Security-sponsored Southeast Region Research Initiative (SERRI) at the Department of Energy's Oak Ridge National Laboratory. Support for this research by ONR Grant # N00014-07-1-1010, Office of Naval Research, Solid Mechanics Program (Dr. Yapa D.S. Rajapakse, Program Manager) is also acknowledged.

## References

[1] Schroeder W. F., Borrajo J., Aranguren M. I.: Poly (methyl methacrylate)-modified vinylester thermosets: Morphology, volume shrinkage and mechanical properties. Journal of Applied Polymer Science, **106**, 4007–4017 (2007).
DOI: 10.1002/app.27006



K-169

[2] Guo Z., Wei S., Shedd B., Scaffaro R., Pereira T., Hahn H. T.: Particle surface engineering effect on the mechanical, optical and photoluminescent properties of ZnO/vinyl-ester resin nanocomposites. Materials Chemistry, **17**, 806–813 (2007).
DOI: 10.1039/b613286c

[3] Guo Z., Liang X., Scaffaro R., Pereira T., Hahn H. T.: CuO nanoparticle filled vinyl-ester resin nanocomposites: Fabrication, characterization and property analysis. Composites Science and Technology, **67**, 2036–2044 (2007).
DOI: 10.1016/j.compscitech.2006.11.017

[4] Guo Z., Lei K., Li Y., Wai Ng H., Prikhodko S., Hahn H. T.: Fabrication and characterization of iron oxide nanoparticles reinforced vinyl-ester resin nanocomposites. Composites Science and Technology, **68**, 1513–1520 (2008).
DOI: 10.1016/j.compscitech.2007.10.018

[5] Schroeder W. F., Auad M. L., Vico M. A. B., Borrajo J., Aranguren M. I.: Thermodynamic, morphological, mechanical and fracture properties of poly(methyl methacrylate)(PMMA) modified divinylester(DVE)/styrene(St) thermosets. Polymer, **46**, 2306–2319 (2005).
DOI: 10.1016/j.polymer.2005.01.019

[6] Sorathia U., Ness J., Blum M.: Fire safety of composites in the US Navy. Composites Part A: Applied Science and Manufacturing, **30**, 707–713 (1999).
DOI: 10.1016/S1359-835X(98)00112-2

[7] Almagableh A., Gupta S., Mantena P. R., Alostaz A.: Dynamic mechanical analysis of graphite platelet and nanoclay reinforced vinyl ester, and MWCNT reinforced nylon 6,6 nanocomposites. in 'Proceeding of SAMPE Fall Technical Conference, Memphis, USA', M034 p.19 (2008).

[8] TA Instruments.: Thermal analysis application brief, 144: Application of time-temperature superposition principles to DMA. TA Instruments, Newcastle (2004).

[9] Drzal L. T., Fukushima H.: Expanded graphite products produced therefrom. US Patent 7550529, USA (2009).

[10] Li H., Burts E., Bears K., Ji Q., Lesko J. J., Dillard D. A., Riffle J. S., Puckett P. M.: Network structure and properties of dimethacrylate-styrene matrix materials. Journal of Composite Materials, **34**, 1512–1528 (2000).
DOI: 10.1106/Q064-0U44-FWDJ-9LET

[11] Kuzak S. G., Shanmugam A.: Dynamic mechanical analysis of fiber-reinforced phenolic. Journal of Applied Polymer Science, **73**, 649–658 (1999).
DOI: 10.1002/(SICI)1097-4628(19990801)73:5<649::AID-APP5>3.0.CO;2-B

[12] Gupta S., Mantena P. R., Al-Ostaz A.: Dynamic mechanical and impact property correlation of nanoclay and graphite platelet reinforced vinyl ester nanocomposites. Journal of Reinforced Plastics and Composites, in press, (2009).
DOI: 10.1177/0731684409341762

[13] Hertzberg W. R.: Deformation and fracture mechanics of engineering materials. Wiley, New York (1989).



K-170

# Creep and Stress Relaxation Modeling of Vinyl Ester Nanocomposites Reinforced by Nanoclay and Graphite Platelets

**Ahmad Almagableh, P. Raju Mantena, Ahmed Alostaz**

*Composite Structures and Nano-Engineering Research, University of Mississippi, University, Mississippi 38677*

Received 4 March 2009; accepted 18 July 2009
DOI 10.1002/app.31152
Published online 00 Month 2009 in Wiley InterScience (www.interscience.wiley.com).

**ABSTRACT:** This article discusses the viscoelastic behavior of a vinyl ester (Derakane 411-350) reinforced with 1.25 and 2.5 wt % nanoclay and exfoliated graphite nanoplatelets during short-term creep and relaxation tests with a dynamic mechanical analyzer. Linear viscoelastic models are generally composed of one or more elements such as dashpots and springs that represent the viscous and elastic properties. Stress relaxation data from the dynamic mechanical analyzer have been used to obtain the elastic parameters based on model constitutive equations. The standard linear solid model, which is a physical model, has been used for predicting the creep deformation behavior of the vinyl ester nanocomposites over a wide temperature range. Some correlations have been made with the mechanical model, such as the effect of temperature on the deformation behavior, which is well explained by the dashpot mechanism. At lower temperatures, higher creep compliance has been observed for the vinyl ester versus the nanocomposites, whereas at temperatures near the glass-transition temperature of the vinyl ester, creep compliance in the nanocomposites is closer in magnitude to that for the vinyl ester. The creep response of the pure vinyl ester and its nanocomposites appears to be modeled reasonably well at temperatures lower than their glass-transition temperatures. A comparison of the predictions and experimental data from the creep tests has demonstrated that this model can represent the long-term deformation behavior of these nanoreinforced materials reasonably well. © 2009 Wiley Periodicals, Inc. J Appl Polym Sci 000: 000–000, 2009

Key words: nanocomposites; viscoelastic properties AQ2

## INTRODUCTION

Composite materials with polymer matrices exhibit viscoelastic behavior that is directly related to the molecular structure and formulation differences. A polymer at a specific temperature and with a specific molecular weight may behave as a liquid or a solid according to the timescale at which its molecules are deformed. In crosslinked polymers, the crosslinking acts to decrease the viscous component of viscoelastic behavior because the chains are prevented from slipping past one another.

Understanding the viscoelastic properties of composite materials is essential for the design and analysis of advanced structures. To determine the creep behavior of a given material, a constant stress is applied to a specimen maintained at a constant temperature, and the strain data are collected as a function of time. When a load is applied, instantaneous deformation occurs as a pure elastic response. This deformation is followed by rapidly decreasing deformation called primary deformation.[1] This is then followed by steady-state linear deformation called secondary deformation. The creep behavior of a polymer also depends heavily on the material temperature during testing, and the highest rate of deformation occurs around the glass-transition temperature ($T_g$).

The creep behavior of many plastics has been fitted to an analytical relationship similar to those proposed for metals. Findley[2] demonstrated that the creep strain ($\varepsilon$) and time ($t$) could be related by the following equation:

$$\varepsilon(t) = \varepsilon_O + mt^n \quad (1)$$

where $\varepsilon_O$ is the instantaneous strain and $m$ and $n$ are material constants that depend on both the stress and temperature. The restriction of this approach is that it does not provide a physical representation for creep deformation behavior under different loading conditions.

*Correspondence to:* A. Almagableh (amalmag1@olemiss.edu).

Contract grant sponsor: Department of Civil Engineering, University of Mississippi.
Contract grant sponsor: Southeast Region Research Initiative (sponsored by the Department of Homeland Security).
Contract grant sponsor: Solid Mechanics Program, Office of Naval Research; contract grant number: N00014-07-1-1010.


© 2009 Wiley Periodicals, Inc.



ID: selvarajn | Black Lining: [ON] | Time: 12:23 | Path: N:/3b2/APP#/Vol00000/091732/APPFile/C2APP#091732

J_ID: Z8E Customer A_ID: APP31152 Date: 11-September-09 Stage: Page: 2



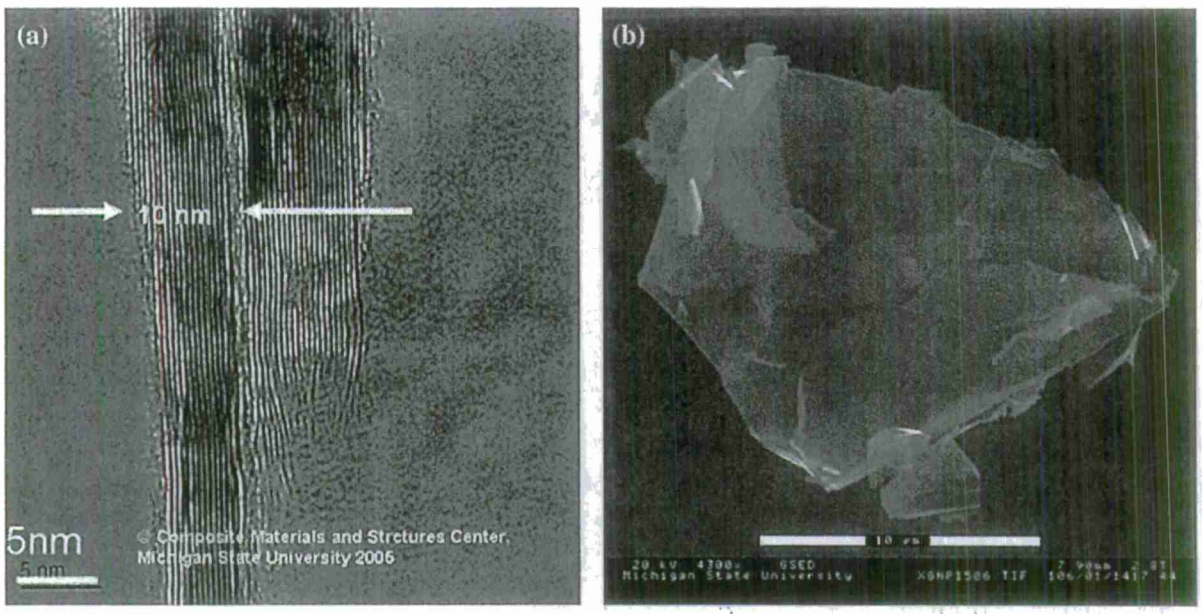


Figure 1 Morphology of xGnPs: (a) edge view (transmission electron microscopy) and (b) lateral view (scanning electron microscopy).[8]

Bakis and Temple-Boyer[3] studied the tensile creep response of coupon-type specimens made of epoxy reinforced with single-walled carbon nanotubes (up to 3 wt %). Master creep compliance curves were constructed at a reference temperature of 40°C on the basis of the time–temperature superposition principle, and a Findley-type creep law for the creep strain was fit to the master curves according to eq. (1).

Many physical models have described the time-dependent mechanical behavior of polymers. Most of these models have been developed to characterize the strain rate dependence, creep, and stress relaxation over the viscoelastic regime.[4–6] Linear viscoelastic models are generally composed of one or several elements such as dashpots and springs that represent the viscous and elastic properties. The Kelvin model, which is one of the simplest models, consists of a linear spring and a dashpot in parallel, and this model can be used to represent the behavior of a solid polymer component at the beginning of loading.[1] At longer times, the predicted deformation approaches a fixed value, and it returns to an undeformed condition after load removal.

Thermoset vinyl ester matrices are becoming increasingly important in industrial applications because of their enhanced mechanical properties. They exhibit characteristics similar to those of epoxy resins as well as unsaturated polyester resins. Advantages include a high tensile strength and stiffness, low cost, process versatility, and good chemical resistance. The deformation behavior of a vinyl ester polymer over a wide range of strain rates (0.0001–1/s) and over a wide range of temperatures [room temperature (RT) to 100°C] was investigated by Plaseied and Fatemi[7] under monotonic tensile loading and relaxation conditions. In our work, the effect of temperature on the creep deformation behavior of a vinyl ester (Derakane 411-350) and its nanocomposites with 1.25 and 2.5 wt % nanoclay and exfoliated graphite nanoplatelets (xGnPs) was investigated. The objective was to develop constitutive models to describe the viscoelastic behavior and characterize the temperature-dependent mechanical response of vinyl ester nanocomposites.

## EXPERIMENTAL

### Material preparation

Clay and graphite in conventional composites exist as layered materials, with the layers held together by van der Waals forces without any intercalation or exfoliation. Exfoliated nanocomposites, however, have exfoliated and dispersed graphite platelets with a 1-nm thickness and widths of several hundred nanometers. Figure 1(a,b) shows the morphology with transmission electron microscopy and scanning electron microscopy from both the edge and lateral views of xGnPs inside a polymer.[8] The distance between the layers was in the range of 10–30 Å, and the size of the layered graphite extended from several hundred nanometers to several micrometers. F1



L-172

ID: selvarajn | Black Lining: [ON] | Time: 12:23 | Path: N:/3b2/APP#/Vol00000/091732/APPFile/C2APP#091732

Square plates of the Derakane 411-350 vinyl ester and its nanocomposites with nominal dimensions of 254 × 254 × 9.9 $mm^3$ (10″ × 10″ × 0.39″) were prepared at the Composite Materials and Structures Center of Michigan State University. Prismatic samples with nominal dimensions of 35 × 10 × 1.6 $mm^3$ were prepared from these plates and tested with a dynamic mechanical analyzer with a single-cantilever clamp fixture.

### Experimental setup

Because a material's modulus is independent of its geometry, equations relating the sample stiffness to the modulus depend on the clamping conditions, sample shape, and deformation mode. The stiffness calculation for the single-cantilever clamp used in AQ1 the TA Instruments model Q800 dynamic mechanical analyzer along with the appropriate correction factor is described. Also included are stress and strain equations calculated from the force and deformation amplitude. The maximum level of strain occurs at the sample surface, whereas the center experiences no strain at all, provided that the stress and strain equations assume linear viscoelastic behavior. The stiffness model and maximum stress and strain level equations for a rectangular cross-section sample, analyzed on a single-cantilever clamp,[9] are as follows:

$$E = \frac{K_S}{F_C}\frac{L^3}{12I}\left[1+\frac{12}{5}(1+\upsilon)\left(\frac{t}{l}\right)^2\right] \quad (2)$$

$$F_C = 0.7616 - 0.02713\sqrt{\frac{L}{t}} + 0.1083\ln\left(\frac{L}{t}\right) \quad (3)$$

$$\sigma_x = \frac{6PL}{wt^2} \quad (4)$$

AQ3

$$\varepsilon_x = \frac{3\delta t F_C}{L^2\left[1+\frac{12}{5}(1+\upsilon)\left(\frac{t}{l}\right)^2\right]} \quad (5)$$

where $E$ is the elastic modulus, $L$ is the clamp span length, $K_s$ is the measured stiffness, $t$ is the sample thickness, $I$ is the sample moment of inertia, $\upsilon$ is Poisson's ratio, $F_C$ is the clamping correction factor, $\sigma_x$ is the stress, $\varepsilon_x$ is the strain, $P$ is the applied force, and $\delta$ is the amplitude of deformation.

### Test description

Derakane 411-350 vinyl ester samples with 1.25 and 2.5 wt % nanoclay and xGnPs were tested in a TA Instruments model Q800 dynamic mechanical analyzer using a single-cantilever clamp with a span of 17.5 mm and a preload stress of 3 MPa. The preload stress of 3 MPa was chosen because the linear viscoelastic theory is applicable when stresses are low. Two samples were tested from each configuration.

Short-term creep tests were carried out by the subjection of the samples to a constant load over 30 min at isothermal temperatures in the dynamic mechanical analyzer. RT fluctuated between 28 and 30°C. A temperature range of 28–100°C was chosen as this covered $T_g$ for all the nanocomposites that were investigated. The sample was initially equilibrated at 28°C for about 4 min to ensure that the sample temperature settled down. After equilibrium, the sample was subjected to a fixed stress of 3 MPa for about 30 min. The temperature was then increased by 4°C, and the aforementioned procedure was repeated until the final temperature of 100°C.

In the stress relaxation mode, the sample was held at a constant strain, and the stress level was measured as a function of time over the same temperature range. The method segments executed during the relaxation test were the same as those used in the creep test. The sample was initially equilibrated at RT for about 4 min and then displaced 0.1 mm for 30 min. The temperature was then increased by 4°C, and the process was repeated until the final temperature of 100°C.

## MODEL FORMULATION

The Maxwell model is a basic deformation behavior model for polymers; other models such as the Kelvin model and standard linear solid (SLS) are modifications of this model designed to better describe the deformation behavior.[1] Figure 2 shows the SLS F2 model consisting of a Maxwell element (a linear spring and a dashpot in series) and a linear spring in parallel. This model has been chosen because it can describe stress relaxation and creep behavior and also can explain the two main deformations of plastics;[10] the spring represents deformations due to bending and stretching of intermolecular bonds, whereas the dashpot represents deformation due to a viscous effect. Some correlations have been made with the mechanical model, such as the effect of temperature on the mechanical behavior, which is well explained by the dashpot mechanism. For instance, at high temperatures, the viscosity in the dashpot decreases, and this results in greater extensions, whereas at lower temperatures, the dashpot becomes more viscous, and less deformation takes place; this is similar to the creep response observed at RT.

In the SLS model, the total stress ($\sigma_{tot}$) is decom- AQ4 posed into the rate-dependent stress component in the spring ($E_2$) and dashpot ($\eta$) and the rate-independent equilibrium stress ($\sigma_1$) in the spring ($E_1$). The strain in the Maxwell element ($E_2$,$\eta$) is the same

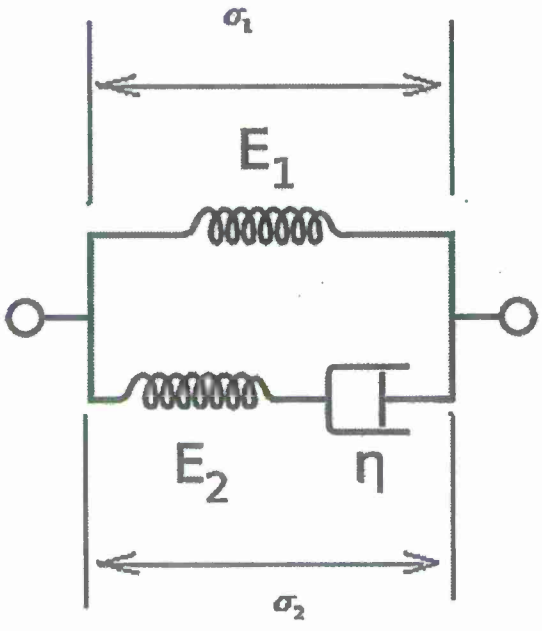


Figure 2 Schematic of the SLS model.

as that in the elastic spring parallel to it and can be substituted by the total strain (ε).[7]

The elastic constitutive equation in the spring follows Hooke's law:

$$\sigma_1 = E_1\varepsilon \tag{6}$$

$$\sigma_{tot} = \sigma_1 + \sigma_2 \tag{7}$$

The governing equation for the Maxwell element is

$$\frac{\sigma_2}{\eta} + \frac{1}{E_2}\sigma_2' = \varepsilon' \tag{8}$$

where $\varepsilon'$ and $\sigma_2'$ are time derivatives of the total strain and the stress component in the Maxwell element, respectively. With eqs. (6)–(8), the governing equation for the total stress in the SLS model can be obtained as follows:

$$\frac{d\varepsilon}{dt} = \frac{(d\sigma_{tot}/dt) + \frac{E_2}{\eta}(\sigma_{tot} - E_1\varepsilon)}{E_1 + E_2} \tag{9}$$

The solution of eq. (9) defines the stress–strain relationship at a constant strain rate for the proposed model, whereas the creep behavior can also be modeled with eq. (9), with $d\sigma_{tot}/dt = 0$ and $\sigma_{tot} = \sigma_0$. Then, the governing equations for this model under creep and stress relaxation are reduced to the forms given in eqs. (10) and (11), respectively:

$$\sigma_o = E_1\varepsilon + \frac{\eta}{E_2}(E_1 + E_2)\varepsilon' \tag{10}$$

$$0 = \frac{d\sigma}{dt} + \frac{E_2}{\eta}(\sigma - E_1\varepsilon) \tag{11}$$

## RESULTS AND DISCUSSION

The initial portion of a typical stress–strain curve for plastics loaded in tension under a constant strain rate is linear and follows Hooke's law.[3] As expected, the shape of the creep and relaxation curves for these vinyl ester nanocomposites is strongly dependent on the temperature. As an illustration, the effect of temperature on the creep and relaxation behavior of the pure vinyl ester and the 2.5 wt % nanoclay reinforced samples over 30 min is shown in Figures 3(a,b) and 4(a,b), respectively. The creep deformations in the initial (pure elastic) portion are relatively

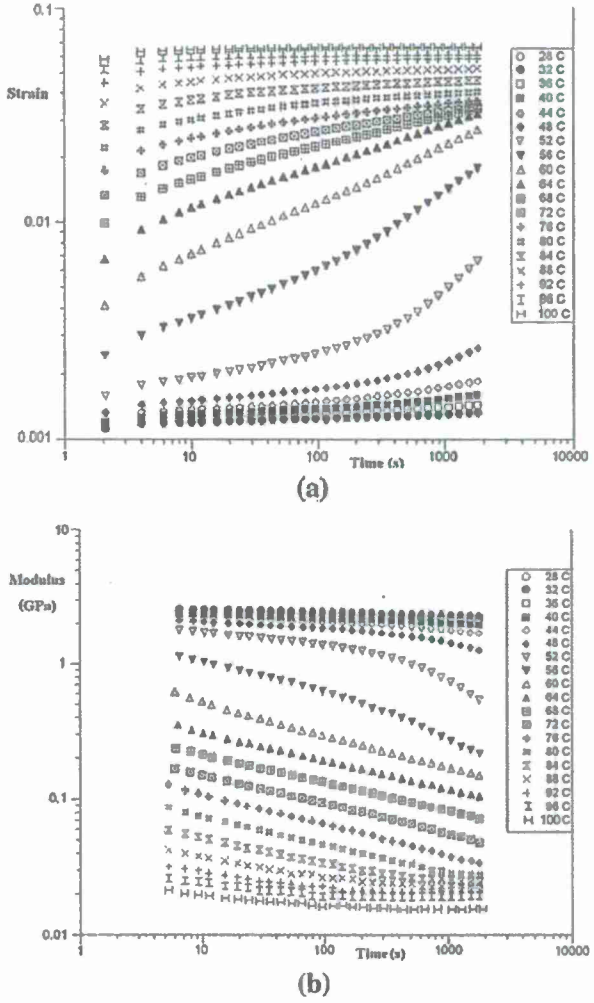


Figure 3 (a) Creep strain and (b) relaxation modulus for the pure vinyl ester.

J_ID: Z8E Customer A_ID: APP31152 Date: 11-September-09 Stage: Page: 5



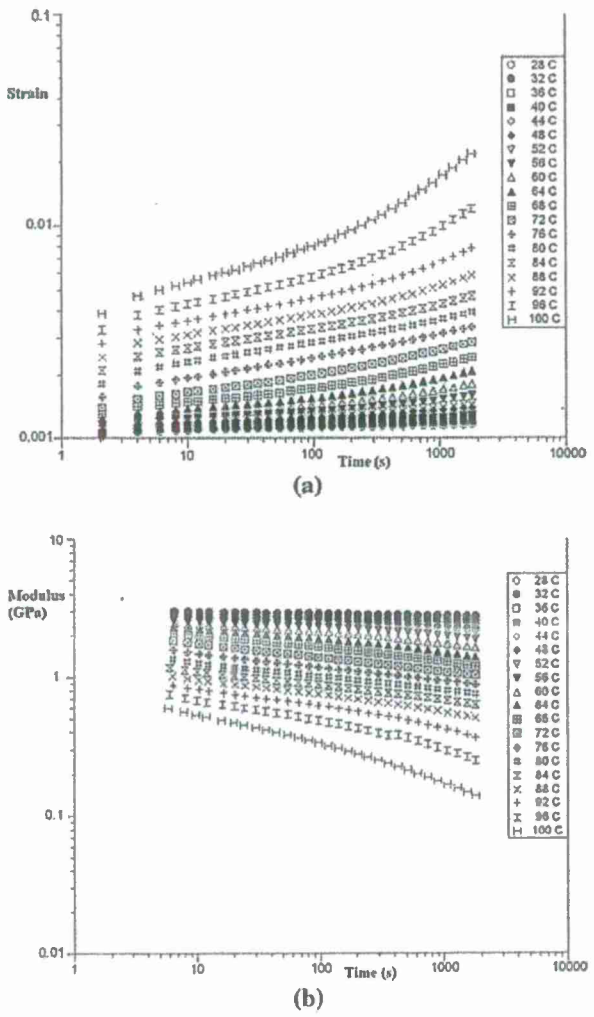


Figure 4 (a) Creep strain and (b) relaxation modulus for 2.5 wt % nanoclay vinyl ester.

small and are associated with bending and stretching of intermolecular bonds. However, the deformation that occurs beyond the proportional limit is similar to a straightening of the folded molecular chains, which is recoverable but not instantaneously. Thus, the mechanical response appears to exist in the viscoelastic linear region, in which no permanent deformation due to intermolecular slippage occurs.

At a lower temperature, much higher creep compliance was observed for the vinyl ester in comparison with the nanocomposites. At temperatures beyond $T_g$ of the pure vinyl ester, creep compliance in the nanocomposites became closer in magnitude to that for the vinyl ester. Also, the rubbery region was more prominent for the pure vinyl ester, as indicated by the dramatic drop in the modulus at temperatures greater than its $T_g$ (66°C). The 2.5 wt % nanoclay vinyl ester, however, still behaved as a solid with a modulus around 0.3 GPa beyond its glass transition.

## Development of the modified SLS model

Data from the relaxation experiments at a given temperature were used to calculate $E_1$ in the SLS model, which was associated with the rate-independent equilibrium stress or was approximately the same as the stress–strain curve without any viscosity effect. The initial modulus of the given model ($E$) is the sum of the moduli of the two linear springs, that is, $E_1 + E_2$, which is also obtained from relaxation data at a time equal to zero. The relationship between $E_1 + E_2$ and $E$ as a function of temperature was determined for the pure vinyl ester by the curve fitting of the relaxation data:

$$E = -10^{-6}T^4 + 0.0004T^3 - 0.034T^2 + 1.27T - 13.5 \quad (12)$$

$$E_1 = 29.86\exp(-0.082T) \quad (13)$$

$E_2$ was subsequently derived by the subtraction of $E_1$ in eq. (13) from $E$ in eq. (12) at different temperatures. The variation of $E_2$ with temperature is thus given by

$$E_2 = -10^{-6}T^4 + 0.0004T^3 - 0.034T^2 + 1.27T - 13.5 - 29.86\exp(-0.082T) \quad (14)$$

On the basis of this analysis, the solution of eq. (10) defines the creep strain response as per the SLS model:

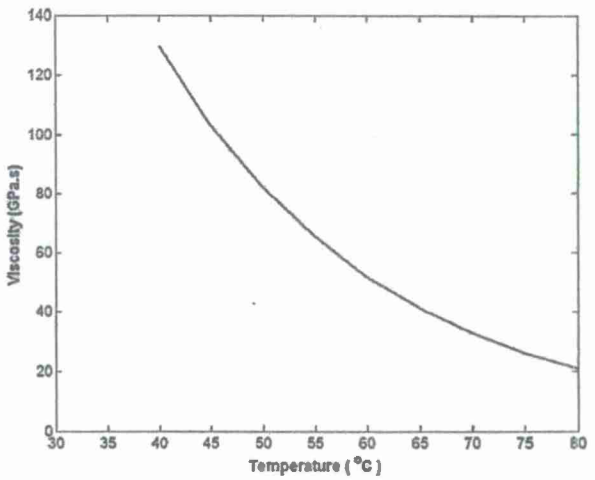


Figure 5 Relationship between η and the test temperature (°C) in the SLS model for the pure vinyl ester.



L-175

ID: selvarajn | Black Lining: [ON] | Time: 12:24 | Path: N:/3b2/APP#/Vol00000/091732/APPFile/C2APP#091732

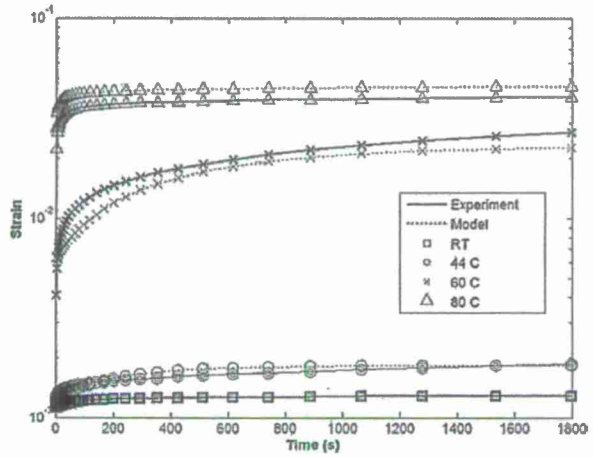


Figure 6 Predicted and experimental results of the creep strain versus time for the pure vinyl ester at selected temperatures on the basis of the viscoelastic model.

$$\varepsilon(t) = \frac{\sigma_o}{E_1}\left[1 - \frac{E_2}{E_1 + E_2}\exp(-t/\rho)\right] \quad (15)$$

where

$$\rho = (\eta/E_1E_2)(E_1 + E_2) \quad (16)$$

The parameter ρ is a constant proportional to the viscous effect in the model as expressed in eq. (16). To find an optimized value for ρ, a least-squares curve-fitting program in Microsoft Excel was applied to fit eq. (15) for all vinyl ester nanocomposites to the creep strain data curves obtained from creep experiments at room temperature ($T_r$). The viscosity parameter (ρ) was then modified in a way similar to that suggested by Khan et al.[11] to predict the actual creep behavior of all the nanocomposites at a specific operating temperature ($T$):

$$\rho = \text{Constant}\left(\frac{T_r}{T}\right)^m \quad (17)$$

The value of $m$ was calculated to be 0.44 from the least-squares curve fitting. Figure 5 shows η as a function of temperature for the pure vinyl ester, and as expected, η decreased when the temperature increased and vice versa, reflecting the physical behavior of the dashpot mechanism.

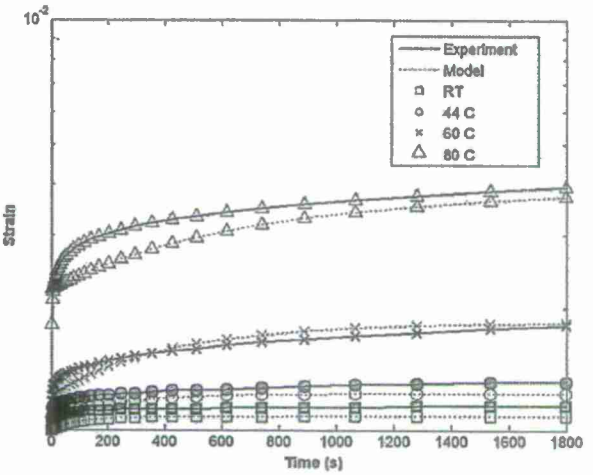


Figure 8 Predicted and experimental results of the creep strain versus time for the 2.5 wt % nanoclay vinyl ester at selected temperatures on the basis of the viscoelastic model.

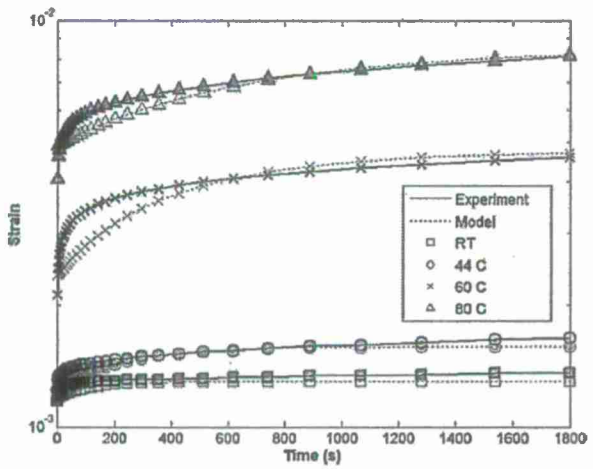


Figure 7 Predicted and experimental results of the creep strain versus time for the 1.25 wt % nanoclay vinyl ester at selected temperatures on the basis of the viscoelastic model.

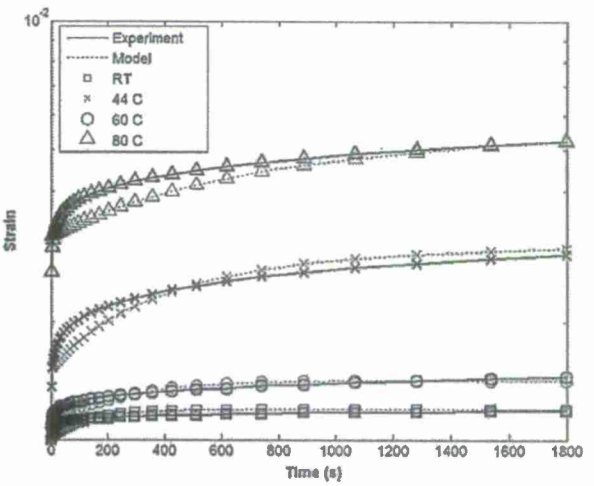


Figure 9 Predicted and experimental results of the creep strain versus time for the 1.25 wt % graphite platelet vinyl ester at selected temperatures on the basis of the viscoelastic model.

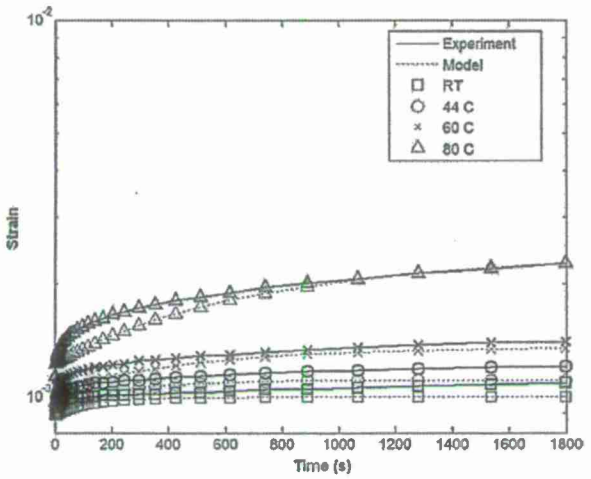


Figure 10 Predicted and experimental results of the creep strain versus time for the 2.5 wt % graphite platelet vinyl ester at selected temperatures on the basis of the viscoelastic model.

### Comparison of the model predictions with the dynamic mechanical analysis test results

Creep strain data at representative temperatures F6 obtained from the creep tests are plotted in Figure 6 along with the strain predicted from eq. (15), including the modified effect of viscosity in eq. (17). As can be seen from this figure, the model can predict the strain–time behavior of the pure vinyl ester reasonably well except at high temperatures (>66°C), at which the onset of the rubbery region started earlier with complete motion of molecular segments occurring for the pure vinyl ester polymer in comparison with the nanocomposites. Again, the elastic constants ($E_1$ and $E_2$) for 1.25 and 2.5 wt % nanoclay and graphite platelet reinforced vinyl ester materials were obtained from their respective relaxation data; the viscosity constant (ρ) developed in eq. (17), however, varied with the temperature. Agreement between the model predictions and creep data for the nanocomposites was better than that for the pure F7-F10 vinyl ester, as shown in Figures 7–10.

## CONCLUSIONS

The viscoelastic behavior of vinyl ester nanocomposites was characterized with creep and relaxation tests using a DMA Q800 at various isothermal temperatures. The SLS model was used in this study to model the creep behavior of the vinyl ester nanocomposites. This physical model is a modification of the Kelvin and Maxwell model, consisting of a Maxwell model with a linear spring and a dashpot in series together and then both in parallel with a linear spring. After the elastic constants for this model were obtained from relaxation test data at various isothermal temperatures, predictions of creep strain behavior were performed and shown to be in reasonable agreement with the experimental data for the vinyl ester nanocomposites. The dashpot parameter of the SLS model was then modified to reflect the variation of the deformation behavior with the temperature. The predicted creep behavior based on the modified constants showed good correlations with the experimental results, especially at temperatures lower than the sample's $T_g$. In summary, the modified SLS model provides a good representation of the constitutive behavior of vinyl ester nanoclay and graphite platelet nanocomposites in viscoelastic deformation regimes as a function of temperature.

The nanoclay and graphite platelet/vinyl ester composite plates were manufactured by Larry Drzal's group at Michigan State University Composite Materials and Structures Center.

## References

1. Plaseied, A.; Fatemi, A. J Reinforced Plast Compos 2008. AQ5
2. Findley, W. N. SPEJ 1960, 16, 57.
3. Bakis, C. E.; Temple-Boyer, C. F. In Proceedings of the 14th International Conference on Composite Materials; Hahn, H. T.; Martin, M. J., Eds.; Society for Manufacturing Engineers: Dearborn, MI, 2003; Paper No. 2019 (CD ROM).
4. Ward, I. M. Mechanical Properties of Solid Polymers, 2nd ed.; Wiley: New York, 1983.
5. Osswald, T. A.; Menges, G. Material Science of Polymers for Engineers, 2nd ed.; Hanser: Munich. AQ6
6. Bardenhagen, S. G.; Stout, M. G.; Gray, G. T. Mech Mater 1997, 25, 235.
7. Plaseied, A.; Fatemi, A. J Mater Sci 2008. AQ5
8. Drzal, L. T.Michigan State University. Private communication, 2009.
9. Dynamic Mechanical Analyzer, Q Series, Getting Started Guide, Revision F; TA Instruments: New Castle, DE, 2004.
10. Shah, V. Handbook of Plastics Testing Technology; Wiley: New York, 1984.
11. Khan, A. S.; Lopez-Pamies, O.; Kazmi, R. Int J Plast 2006, 22, 581.



ID: selvarajn | Black Lining: [ON] | Time: 12:24 | Path: N:/3b2/APP#/Vol00000/091732/APPFile/C2APP#091732

ASME Early Career Technical Journal
2009 ASME Early Career Technical Conference, ASME ECTC
October 2-3, 2009, Tuscaloosa, Alabama, USA

# PUNCH-SHEAR CHARACTERISTICS OF NANOCLAY AND GRAPHITE PLATELET REINFORCED VINYL ESTER PLATES, LAMINATED FACE SHEETS AND SANDWICH COMPOSITES UNDER LOW VELOCITY IMPACT

**Brahmananda Pramanik, P. Raju Mantena**
Dept. of Mechanical Engg., Univ. of Mississippi, University, MS 38677 USA

## ABSTRACT

*This work describes the punch-shear response of nanoparticle reinforced vinyl ester plates, laminated face sheets and sandwich composites using Dynatup 8250 drop-weight impact test instrument according to the ASTM D3763 Standard. Tests were performed on 4"× 4" square plate specimens with fixed circular boundary condition, impacted by a hemispherical-head plunger with added mass. The impact load, displacement, energy plots and visual inspection of the post damaged specimens depicted the punch-shear characteristics of these composites.*

*Test results show more than 10% improvement in impact energy absorption with addition of 2.5 wt. pct. graphite platelets to pure vinyl ester. Maximum improvement in energy absorption (about 40%) was observed with Owens Corning HP ShieldStrand® glass fabric face sheets compared to the E-glass/vinyl ester. In another set of experiments with fly-ash based EcoCore® sandwiched in between E-glass/vinyl ester face sheets showed approximately 85% more energy absorption than with Tycor®, Balsa wood and PVC foam cores.*

## INTRODUCTION

Nanoparticle reinforced glass/carbon polymeric based composites and structural foams are being considered for use in military, new generation naval ships and critical infrastructure applications where lightweight damage tolerant structures are essential for blast, shock, impact mitigation. Prediction of damage, energy absorption and penetration resistance are important to develop stronger, safer and more cost-effective structures. Analyzing the rate sensitivity of these new material systems is essential for applications involving wide range of dynamic loading conditions. Gama et al. [1, 2] and Xiao et al. [3] performed quasi-static, ballistic and low velocity impact punch-shear tests to define the elastic and absorbed energies of composites as a function of penetration displacement. Shaker et al. [4] studied the failure mechanism of basket weave and 3-D braided Kevlar-fabric reinforced epoxy composites under low and high velocity impacts. Hosur et al. [5] carried out low velocity impact tests on quasi-isotropic CFRP composite laminates. This paper describes the punch-shear response of nanoparticle reinforced vinyl ester plates, laminated face sheets and sandwich composites using Dynatup 8250 drop-weight impact test system according to ASTM D3763 Standard [6]. Low velocity tests were performed on 4" × 4" square plate specimens with fixed circular boundary condition and impacted by a hemispherical-head plunger with added mass. The impact load, displacement, energy plots and visual inspection of the post damaged specimen described the failure characteristics and punch shear response of these composites.

## MATERIAL DESCRIPTION

*510A-40 brominated vinyl ester nanoparticle reinforced composite plates:* Five different Derakane 510A-40 vinyl ester thermoset nanocomposites, reinforced with 1.25 and 2.5 wt. percent Cloisite 30B nanoclay and exfoliated graphite (xGnP) nanoplatelets, were manufactured at Michigan State University - Composite Materials and Structures Center.

*Laminated woven fabric composite face sheets:* Four different woven fiber fabric laminated composite face sheets were fabricated with Dow Derakane 510A-40 brominated vinyl ester resin by the VARTM process at the University of Alabama - Birmingham. The base specimen is a five-ply E-glass woven fabric with laminate schedule [(0/90)/(+45/-45)/(90/0)/(-45/+45)/(0/90)]. The second face sheet was prepared with same laminate configuration, but with 2.0 wt. pct. xGnP-15 exfoliated graphite platelets pre-mixed in the vinyl ester resin before fabrication. The third face sheet was made with five-layers of Owens Corning high performance HP ShieldStrand® glass fabric with similar laminate schedule and resin. The fourth face sheet was made with only three plies of FOE treated T-700 carbon fabric [(0/90)/(+45/-45)/(0/90)] laminate schedule in same matrix. Here the number of plies was reduced from five to three to keep stiffness of this carbon fabric laminate consistent with the other glass fabric face sheets.

*Sandwich composites made with five-ply E-glass face sheets and light-weight cores*: Six different kind of sandwich composites fabricated with 2" thick Tycor® (an



M-178

engineered 3-D fiber reinforced damage tolerant core from WebCore Technologies), poly-vinyl chloride (PVC) foam, balsa-wood and three types of fire-resistant EcoCore®(fly-ash based core material mixed with chopped JM3 and OC2 glass-fibers) sandwiched in between the five-ply E-glass/vinyl ester face sheets were fabricated at University of Alabama – Birmingham. The impact test specimens were cut in size of 4"x 4" (101.6 mm x 101.6 mm) each using bench saw from individual fabricated panels.

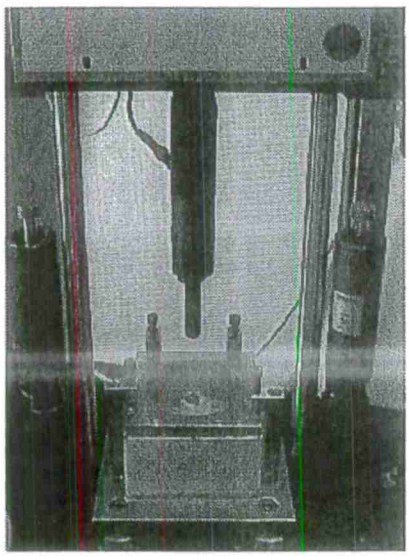

Figure 1. Low velocity impact test system

## LOW VELOCITY IMPACT TESTS

The experiments were performed using Dynatup 8250 drop weight impact test system [Figure 1], according to the ASTM D3763 Standard. Specimen clamp assembly consists of parallel rigid steel plates with a 3" (76.2 mm) diameter hole in the center of each. Sufficient clamping force was applied to prevent slippage of the specimen during impact. Plunger assembly consists of a ½" (12.70 mm) diameter steel rod of 2" (50.8 mm) length with a hemispherical end of the same diameter positioned perpendicular to, and centered on, the clamp hole. Dynatup Impulse™ data acquisition systems are equipped with load and velocity transducers to provide data collection, analysis and reporting. Using an instrumented tup, the data acquisition hardware captures instantaneous load signals and transfers to the impulse software for further data processing. The velocity at impact is measured just prior to impact using a photoelectric-diode and flag system.

## EXPERIMENTAL PROCEDURE

Three samples from each type of nanoparticle reinforced vinyl ester plates, laminated face sheets and sandwich composites were tested under low velocity impact and the average data considered for this investigation. Impact drop weight and height were determined such that velocity slowdown is less than 20% during the impact event as well as the applied impact energy was at least three times the energy absorbed by the specimen at peak load [1]. This configuration provided about 38 J of impact energy and 3.6 m/s impact velocity for the nanoparticle reinforced vinyl ester plates and about 185 J impact energy and 4 m/s impact velocity for the laminated face sheets and sandwich composites. A steel plunger with hemispherical end (0.5" dia. × 2" long) was used for penetrating the specimens with the required impact energy and velocity.

## VISUAL INSPECTION

*510A-40 brominated vinyl ester nanoparticle reinforced composite plates:* The visual inspection of the specimen illustrates that the radial growth of damage centering impact point is less for pure vinyl ester [Figure 2.(i)] than its nanocomposites. Nanoclay reinforced composites are damaged equally on both faces [Figures 2.(ii) and 2.(iii)], whereas graphite platelet reinforced composites showed more damage on the rear than impact side [Figures 2.(iv) and 2.(v)]. In some cases of graphite platelet reinforced nanocomposites, fracture propagates very less on impact side. Penetration of plunger through the specimen required some more load due to the shearing friction between plunger wall and the inner surface of the punch through hole, which resulted to additional energy absorption.

*Laminated woven fabric composite face sheets:* Visual inspection of these specimens confirms that the radial growth of delamination was less for E-glass/vinyl ester face sheet [Figure 3.(i.b)] than HP- glass/vinyl ester face sheet [Figure 3.(iii.b)] and occurred at reverse side for both sheets. Due to opacity of E-glass/xGnP-vinyl ester and T-700 Carbon/vinyl ester face sheets, the occurrence of delamination was not visible [Figures 3.(ii) and 3.(iv)]. In case of T-700 Carbon/vinyl ester face sheets, carbon fiber strands were peeled off partially from back side [Figure 3(iv.b)]. The shredded fibers due to plunger penetration were clogged in the puncture hole.

*Sandwich composites made with five-ply E-glass face sheets and light-weight cores:* The visual inspection of the specimen depicts that the radial growth of delamination is least in tough core, whereas more in case of softer cores. E-glass/Tycor sandwich [Figures 4.(i.a) to 4.(i.c)] shows three different modes of failure due to impact on web-intersection, web-line and direct foam zones respectively. It can be observed that the softest foam-zone showed maximum delamination whereas the web-intersection allowed least delamination. Fly-ash based EcoCore is the toughest and has highest density among all. It showed less delamination as well as less depth of penetration [Figures 4.(iv) to 4.(vi)]. PVC and Balsa cores showed average performance with respect to delamination and puncture [Figures 4.(ii) and 4.(iii)].

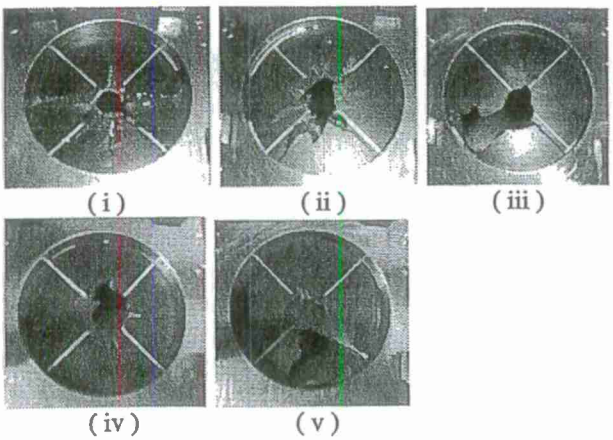


Figure 2. 510A-40 brominated vinyl ester nanoparticle reinforced composite plates after impact ( i ) Pure vinyl ester, ( ii ) 1.25 wt.pct. Nanoclay, ( iii ) 2.5 wt.pct. Nanoclay, ( iv ) 1.25 wt.pct. Graphite, ( v ) 2.5 wt.pct. Graphite.

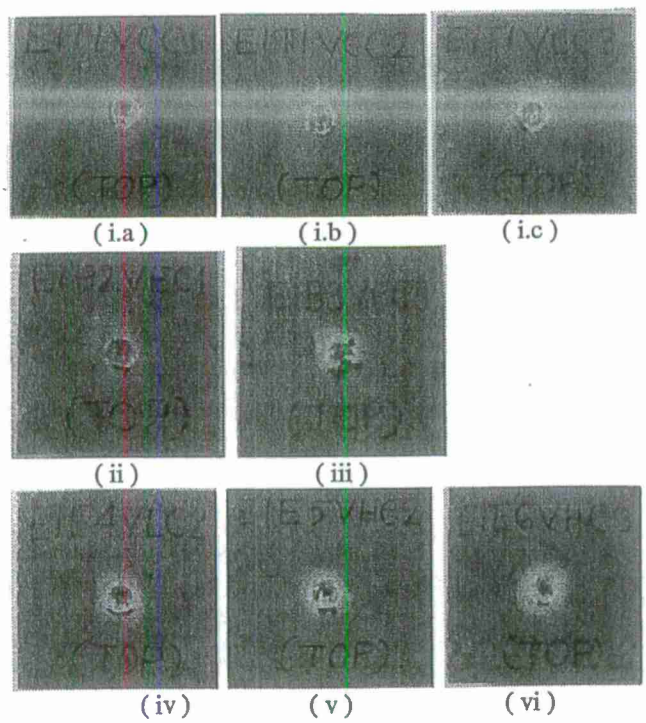


Figure 4. Sandwich composites made with five-ply E-glass face sheets and light-weight cores after impact ( i ) E-glass/Tycor [impacted at ( a ) web-intersection, ( b ) web-line and ( c ) foam-region], ( ii ) E-glass/PVC, ( iii ) E-glass/Balsa, ( iv ) E-glass/EcoCore 0.0 wt.pct., ( v ) E-glass/EcoCore 4.5 wt.pct. JM3 and ( vi ) E-glass/EcoCore 4.5 wt.pct.

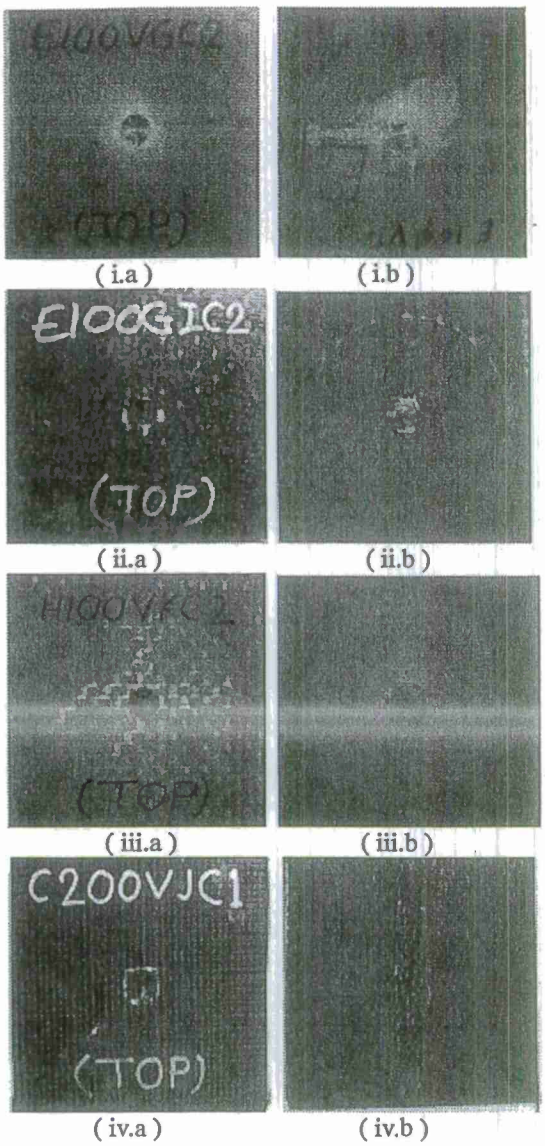


Figure 3. Laminated woven fabric composite face sheets after impact [( a ) impact side and ( b) reverse side] ( i ) E-glass, ( ii ) E-glass/xGnP-15, ( iii ) HP-glass, ( iv ) T-700 Carbon.

## RESULTS AND DISCUSSION

The Dynatup impulse data acquisition software provided instantaneous impact point displacement and applied load data. The load versus deflection data were plotted up to failure point for each tested sample. Corresponding cumulative energy absorption data were generated using Trapezoidal numerical integration method (Equation 1). In case of laminated woven fabric composite face sheets, absorbed energy was normalized-to-thickness (NTT) to eliminate the effects of specimen thickness variations and plotted accordingly.

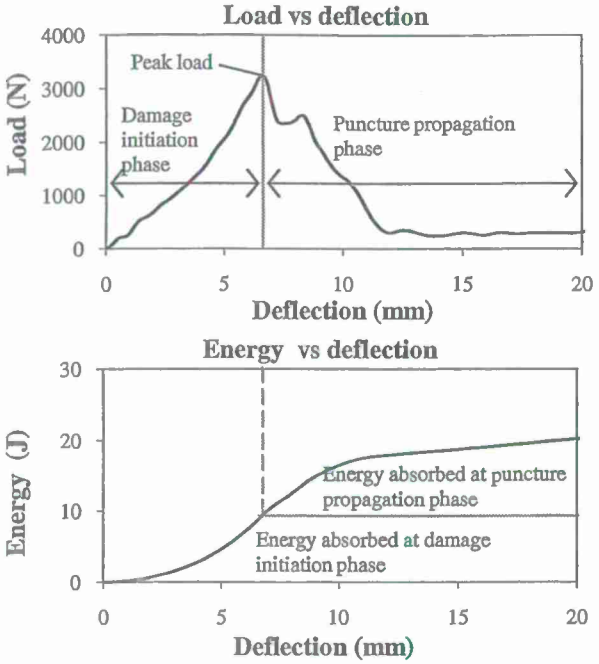


Figure 5. Punch-shear failure phases in puncture-deflection frame [Ref. 2]

$$E(1) = E(-1) + 0.5 \times [L(1) + L(-1)] \times [D(1) - D(-1)] \quad \ldots (1)$$

Where,

E(1) = Energy absorbed up to the current displacement data point,

E(-1) = Energy absorbed up to the immediate former displacement data point,

L(1) = Required load for the current displacement data point,

L(-1) = Required load for the immediate former displacement data point,

D(1) = Current displacement data point, and

D(-1) = Immediate former displacement data point

Figures 6, 11, 16 show the superimposed load response and Figures 7, 12, 17 show energy response with respect to tup deflection. Load versus deflection plot shows two distinct phases of failure propagation for complete puncture [2]. These two phases are damage initiation and puncture propagation.

*Damage initiation phase:* The first phase, named as damage initiation phase, is observed from the moment of impact to the point of peak load, where the damage initiates with almost uniform deflection with some initial fracture peaks [Figure 5].

Pure vinyl ester and nanoclay reinforced vinyl ester show stiff but linear load-deflection response at this stage. A little change of slope explains fracture initiations and plastic flow [Figure 6]. Graphite platelet reinforced vinyl ester has distinctive multi-peak load fluctuations at this phase. This response showed large fracture generation at the rear side of the specimen. Energy absorption is carried out mainly at this phase [Figure 8].

All laminated face sheets showed a smooth elastic deformation with clollse stiffness [Figure 11]. E-glass/vinyl ester face sheet showed marginally higher stiffness than that of the other configurations. HP-glass/vinyl ester face sheet sustained maximum peak load among all. E-glass/vinyl ester and T-700 Carbon/vinyl ester face sheets took more or less same amount of load before puncture. E-glass/xGnP-vinyl ester composite took least load in this phase. However, this face sheet fairly deflected during the damage initiation phase and hence absorbed maximum energy up to peak load same as HP-glass/vinyl ester face sheet; whereas T-700 Carbon/vinyl ester absorbed least energy [Figure 13].

The sandwich composites show five clear peaks indicating failure of each fiber lamina of the impact side face sheets up to peak load [Figure 16]. PVC sandwich fails at minimum peak load. All other sandwiches took approximately same amount of load at this phase. Energy absorption remained less for all sandwiches [Figure 18].

*Puncture propagation phase:* At the point of peak load, puncture is initiated and accomplished by rapid load-reduction. This phase can be identified as puncture propagation phase [Figure 5].

Vinyl ester nanocomposite plates showed sharp and smooth load-reduction. Comparatively harder and brittle graphite platelet reinforced nanocomposites absorbed less energy in this phase. Puncture propagation phase absorbed less energy due to short duration and material fragmentation occurred severely with some hinging effects [Figures 6 and 9].

Some prominent hinging effects of attached fiber fragments with the surface of the plunger are observed in case of all laminated face sheets. Only E-glass/xGnP vinyl ester composite showed comparatively smooth puncture propagation [Figure 11]. HP-glass/vinyl ester composite face sheet provided lot of resistance after peak load and continued to cause delamination. Hence the load-deflection plot shows a distinctive wavy plateau region at peak load. HP-glass/vinyl ester face sheet absorbed 60% more energy than E-glass/vinyl ester face sheet during the puncture propagation phase. E-glass/xGnP-vinyl ester and T-700 Carbon/vinyl ester showed comparative less energy absorption [Figure 14].

In case of sandwich composites, load reduction is very less and slow. Plunger could not penetrate the 2.25" thick sandwich specimen deeper than 0.6" (15 mm). Lot of hinges [Figure 16] depicts uneven resistance due to ripped fiber and core materials which influenced significant energy absorption after peak load. EcoCore showed the best energy absorption in this phase [Figure 19].

Table 1. Energy absorption of composite samples

| Impact energy = 38 J | | | |
|---|---|---|---|
| Impact velocity = 3.6 m/s | | | |
| **510A-40 brominated vinyl ester nanoparticle reinforced composite plates** | **Energy absorption (J)** | | |
| | **Damage Initiation** | **Puncture propagation** | **Total** |
| Pure vinyl ester | 9.05 | 6.22 | 15.27 |
| 1.25 wt.pct. Nanoclay | 6.63 | 7.09 | 13.72 |
| 2.5 wt.pct. Nanoclay | 5.65 | 7.78 | 13.42 |
| 1.25 wt.pct. Graphite | 11.56 | 2.88 | 14.43 |
| 2.5 wt.pct. Graphite | 13.65 | 3.26 | 16.90 |
| Impact energy = 185 J | | | |
| Impact velocity = 4 m/s | | | |
| **Laminated woven fabric composite face sheets** | **Energy absorption (NTT) (J)** | | |
| | **Damage Initiation** | **Puncture propagation** | **Total** |
| E-glass | 9.14 | 9.98 | 19.12 |
| E-glass/xGnP-15 | 12.81 | 8.35 | 21.16 |
| HP-glass | 12.13 | 16.00 | 28.13 |
| T-700 Carbon | 5.45 | 7.53 | 12.98 |
| Impact energy = 185 J | | | |
| Impact velocity = 4 m/s | | | |
| **Sandwich composites made with five-ply E-glass face sheets and light-weight cores** | **Energy absorption (J)** | | |
| | **Damage Initiation** | **Puncture propagation** | **Total** |
| E-glass/ Tycor | 32.70 | 54.30 | 87.00 |
| E-glass/ PVC | 29.22 | 52.28 | 81.50 |
| E-glass/ Balsa | 24.61 | 63.87 | 88.48 |
| E-glass/EcoCore 0 wt.pct. | 47.80 | 113.00 | 160.80 |
| E-glass/EcoCore 4.5 wt.pct. JM3 | 34.65 | 121.10 | 155.75 |
| E-glass/EcoCore 4.5 wt.pct. OC2 | 23.89 | 130.40 | 154.29 |

*Total Energy absorption*: The total energy absorption was calculated as the sum of the energy absorbed for damage initiation and puncture propagation phases up to complete failure of the specimen.

Table 1 and bar charts [Figures 8-10, 13-15 and 18-20] of energy absorption at damage initiation and puncture propagation phases as well as the total energy absorption are provided for comparative investigation of the punch shear response of all types of vinyl ester nanocomposites, laminated face sheets and sandwich composites under low velocity impact.

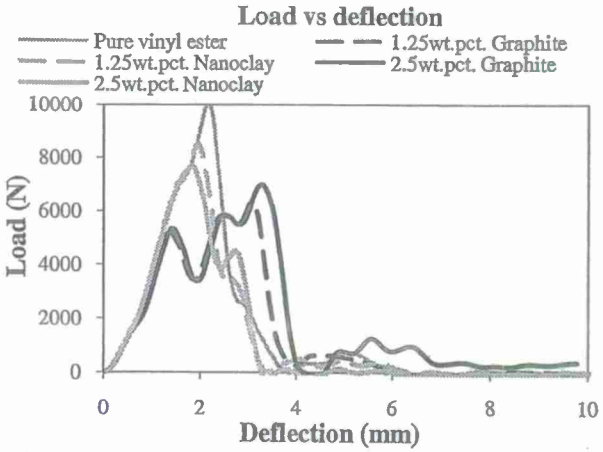


Figure 6. Load-deflection response of vinyl ester nanocomposites

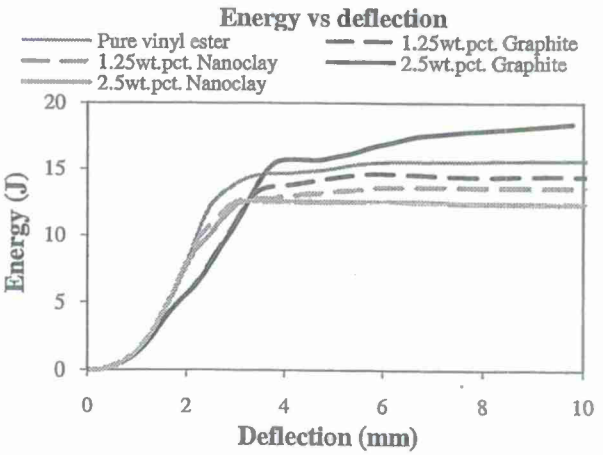


Figure 7. Energy-deflection response of vinyl ester nanocomposites

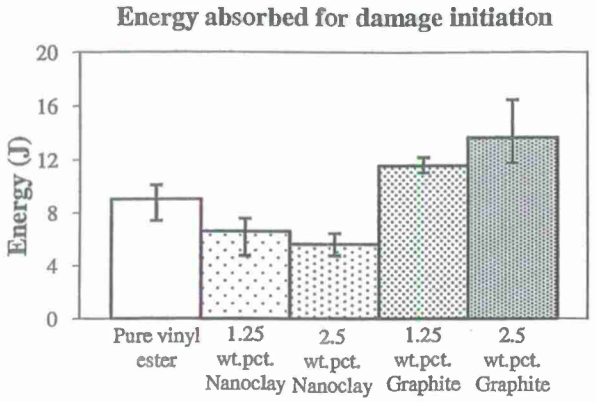


Figure 8. Energy absorbed for damage initiation (up to max. load ) of vinyl ester nanocomposites

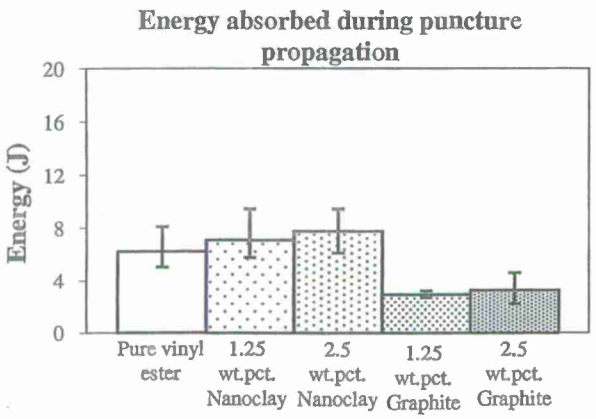


Figure 9. Energy absorbed during puncture propagation (from max. load to zero load ) of vinyl ester nanocomposites

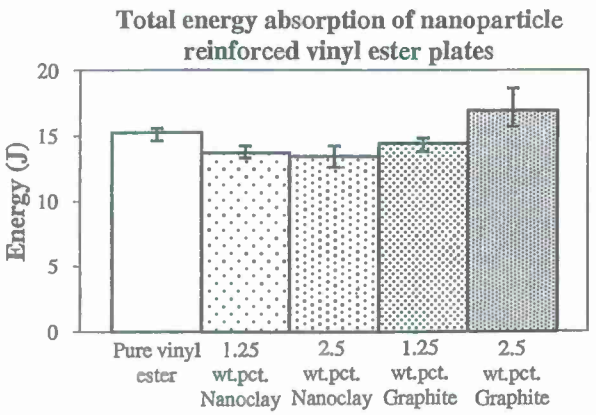


Figure 10. Total absorbed energy during punch-shear test of vinyl ester nanocomposites

*Nanoparticle reinforced vinyl ester plates:* The first set of experiments on nanoparticle reinforced vinyl ester plates showed more than 10% improvement in impact energy absorption with the addition of 2.5 wt. pct. graphite platelets to pure vinyl ester. However, the nanoclay and 1.25 wt. pct. graphite platelet reinforcements showed a detrimental effect [Figure 10].

*Laminated woven fabric composite face sheet:* The second set of experiments on laminated composite face sheets showed thickness dependent punch-shear response. In this case the absorbed energy was normalized-to-thickness (NTT) to eliminate the effects of specimen thickness variations. Addition of graphite platelets in vinyl ester matrix showed approx. 10% better energy absorption than reference E-glass face sheet; whereas the FOE treated T-700 carbon fabric displayed lowest energy absorption. Maximum improvement (about 40%) in energy absorption was observed with Owens Corning HP ShieldStrand® glass fabric face sheets compared to the E-glass/vinyl ester [Figure 15].

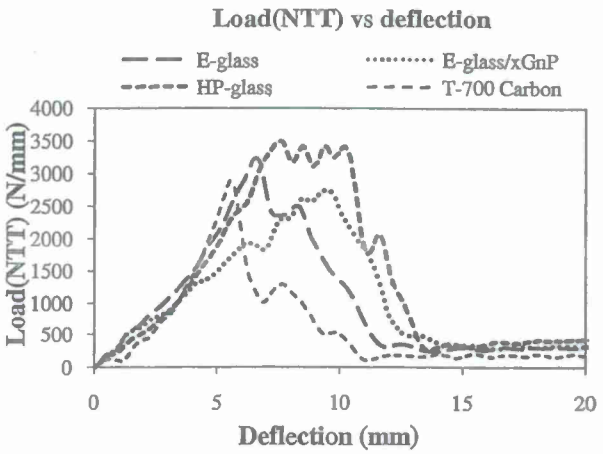


Figure 11. Load(NTT)-deflection response of laminated face sheets

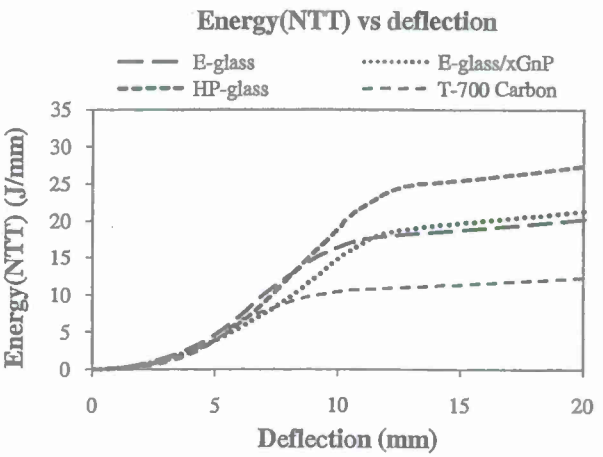


Figure 12. Energy(NTT)-deflection response of laminated face sheets



M-183

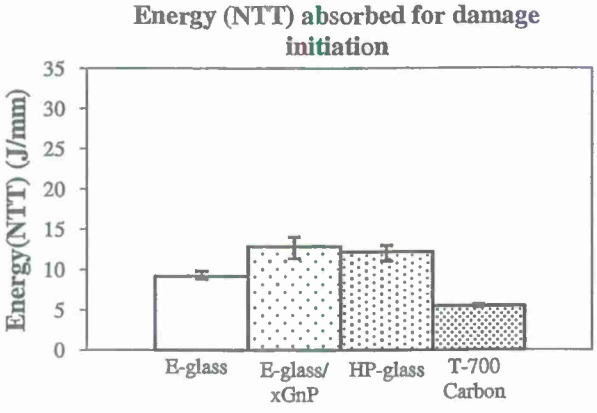


Figure 13. Energy (NTT) absorbed for damage initiation (up to max. load) of laminated face sheets

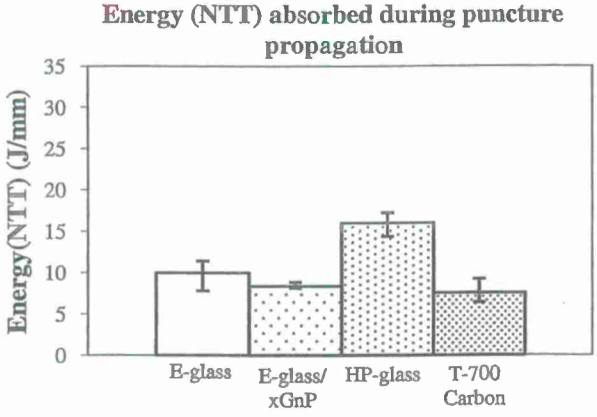


Figure 14. Energy (NTT) absorbed during puncture propagation (from max. load up to 20 mm deflection) of laminated face sheets

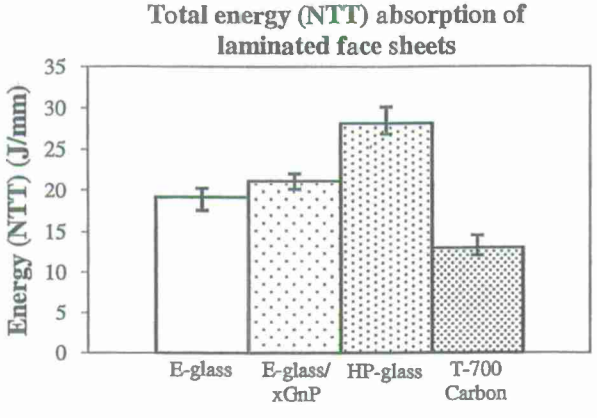


Figure 15. Total energy (NTT) absorbed for punch-shear test of laminated face sheets

*Sandwich composites made with five-ply E-glass face sheets and light-weight cores:* The third set of low velocity punch-shear tests showed that PVC and Balsa sandwiches absorbed more or less same energy. The Tycor® sandwich composite has glass fiber webs embedded in the foam core. The punch-shear energy absorption at the intersection of the webs was observed to be double of that at foam-region. The response at web line was an average of that at other two locations. Spatial non-uniformity of the core resulted in larger data scatter, with the average response of Tycor® sandwich composite similar to that of PVC foam and balsa wood sandwich composites. EcoCore® sandwich composites absorbed approximately 85% more energy than Tycor, PVC and Balsa sandwiches. The higher density of EcoCore® core provided significant resistance to plunger penetration during impact which resulted in higher energy absorption than other sandwich composites made with light-weight and softer core [Figure 20].

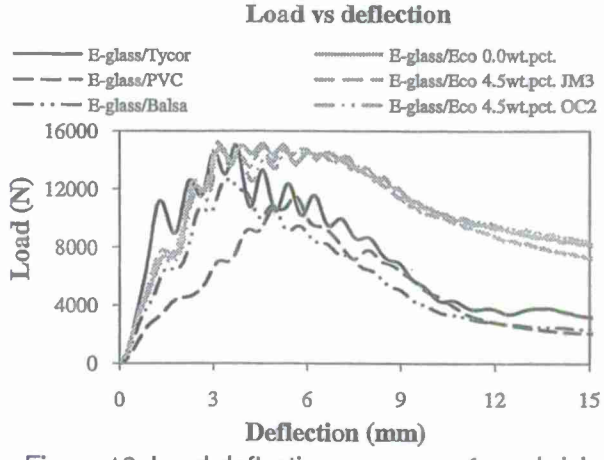


Figure 16. Load-deflection response of sandwich composites

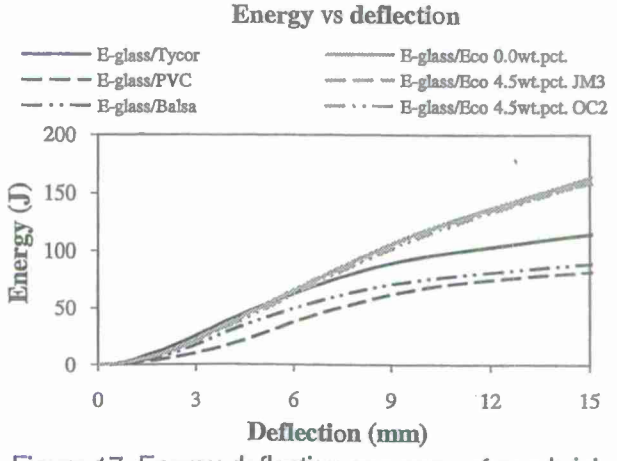


Figure 17. Energy-deflection response of sandwich composites

## CONCLUSIONS

Test results show more than 10% improvement in impact energy absorption with addition of 2.5 wt. pct. graphite platelets to pure vinyl ester, whereas addition of nanoclay and 1.25 wt. pct. graphite platelet reinforcements showed

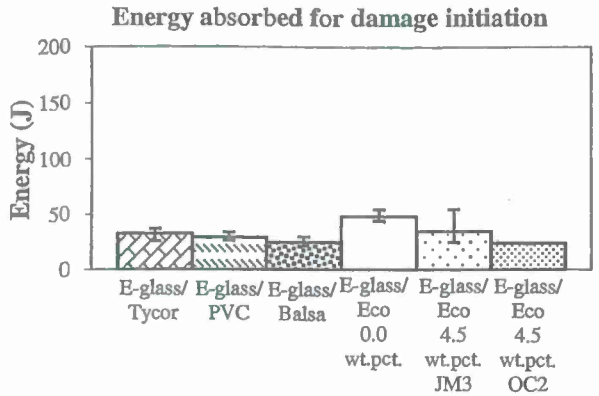


Figure 18. Energy absorbed for damage initiation (up to max. load) of sandwich composites

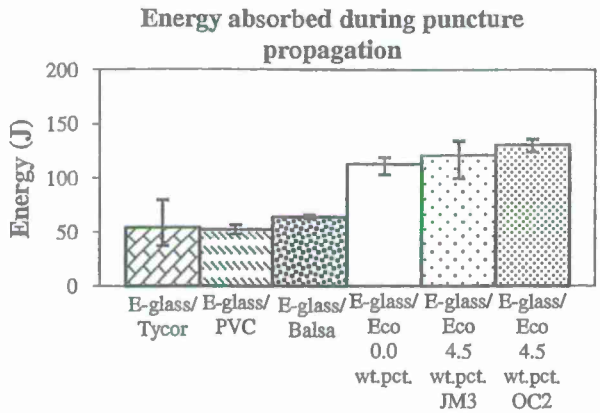


Figure 19. Energy absorbed during puncture propagation (from max. load up to 15 mm deflection) of sandwich composites

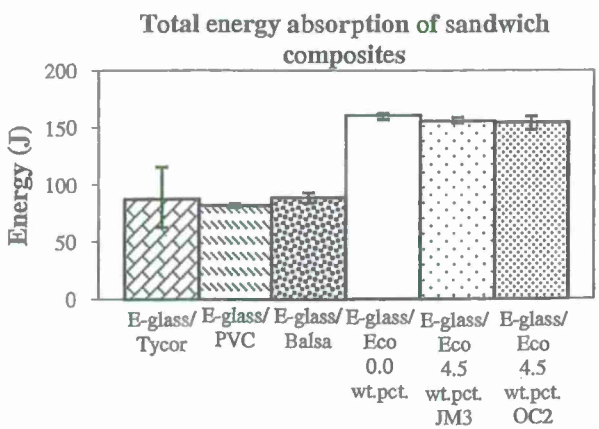


Figure 20. Total energy absorbed during punch-shear test of sandwich composites

detrimental effect. Owens Corning HP ShieldStrand® glass fabric face sheets showed maximum improvement in energy absorption (about 40%) compared to the E-glass/vinyl ester. Fly-ash based EcoCore® sandwiched in between E-glass/vinyl ester face sheets absorbed about 85% more energy than with Tycor®, Balsa wood and PVC foam cores. Cross section microscopy of the damaged samples is ongoing for a better understanding of the energy absorption mechanisms.

## ACKNOWLEDGMENTS

This investigation was supported by ONR Grant N00014-07-1-1010, Office of Naval Research, Solid Mechanics Program (Dr. Yapa D.S. Rajapakse, Program Manager). Partial funding received for this work under a sub-contract from DHS sponsored Southeast Region Research Initiative (SERRI) at the Department of Energy's Oak Ridge National Laboratory is gratefully acknowledged. The nanoclay and graphite platelet vinyl ester composite plates were manufactured by Dr. Larry Drzal's group at Michigan State University. HP ShieldStrand® glass fabric was supplied by Owens Corning. Composite face sheets and sandwich panels were manufactured by Dr. Uday Vaidya's group at University of Alabama-Birmingham. Tycor® cores were supplied by WebCore Technologies, Miamisburg, OH. EcoCore® cores were manufactured by Dr. Kunigal Shivakumar at North Carolina A&T State University.

## REFERENCES

[1] Gama, B. A., Gillespie Jr., J. W., 2008, "Punch shear based penetration model of ballistic impact of thick-section composites", Composite Structures, 86, pp.356-369.

[2] Gama, B. A., Waliul Islam, S. M., Rahman, M., Gillespie Jr., J. W., Bogetti, T. A., Cheeseman, B. A., Yen, C., Hoppel, C. P. R., 2005, "Punch shear behavior of Thick-section composites under quasi-static, low velocity, and ballistic impact loading", SAMPE Journal, Vol. 41, No. 4, pp. 6-13 .

[3] Xiao, J. R., Gama, B. A., Gillespie Jr., J. W., 2007, "Progressive damagae and delamination in plain weave S-2 glass/SC-15 composites under quasi-static punch-shear loading", Composite Structures 78, pp. 182-196.

[4] Shaker, M., Ko, F., Song, 1999, "Comparison of the Low and High Velocity Impact Response of Kevlar Fiber-Reinforced Epoxy Composites", Journal of Composites Technology and Research (JCTR), Vol. 21, Issue 4, pp. 224-229.

[5] Hosur, M. V., Murthy, C. R. L., Ramamurthy, T. S., 1997, "Low-velocity impact response and evaluation of delamination damage in CFRP Laminates", Noise Control and Acoustics Div. ASME Vol. 24, pp. 203-214.

[6] ASTM Standard: D3763-06 Standard test method for high speed puncture properties of plastics using load and displacement sensors, ASTM International, D20 Plastics D20.10 Mechanical Properties, September 2006.

ASME Early Career Technical Journa
2009 ASME Early Career Technical Conference, ASME ECT(
October 2-3, 2009, Tuscaloosa, Alabama, US/

# SHOCK RESPONSE AND FINITE ELEMENT MODELING OF NANOCLAY AND GRAPHITE PLATELET REINFORCED VINYL ESTER NANOCOMPOSITES

**Swasti Gupta, P. Raju Mantena**
Mechanical Engineering, University of Mississippi
University, MS, USA

**Ahmed Al-Ostaz, Christopher L. Mullen**
Civil Engineering, University of Mississippi
University, MS, USA

## ABSTRACT

*The shock response of Derakane 411-350 vinyl ester thermoset beam specimens with 1.25 and 2.5 wt. percent randomly distributed exfoliated graphite nanoplatelets and Cloisite 30B nanoclay were investigated. Shock tube apparatus was used to study the material response at a peak pressure of 70 psi (482.6 kPa), and approximate strain rate of 1000 per second; and 120 psi (827.4 kPa), and approximate strain rate of 1400 per second. Shock tube experiments were also modeled using the explicit finite element program, ANSYS LS-DYNA.*

*The energy absorption improved by about 150 percent with increasing nano reinforcement, for shock tests conducted at 120 psi peak pressure. A close agreement was observed between experimental data and finite element modeling of the shock response.*

## INTRODUCTION

Nanocomposites are often touted as the material of the 21st century finding applications in almost all industries including automobiles, electronics, space, chemicals, sensors, storage systems, health care, and structural applications among others. These new class of composites are increasingly being studied for their application in structures such as spacecrafts, airplanes, warships etc. which requires high stiffness-to-weight ratio along with high damping. Nanoclay [1-4] and graphite platelets [5-9] are some of the nano scale inclusions proposed as filler materials showing promise for structural applications, and have been investigated in this work for naval ships and homeland security applications.

The objective of this work is to study the shock response of nanoclay/ vinyl ester; and graphite platelet/ vinyl ester nanocomposites with 1.25 and 2.5 wt. percent reinforcement in comparison with the pure polymer. These nanocomposites are planned to be used as face plates of sandwich composite structure with fire-resistant foam layered in between to further enhance the energy absorption along with optimal flexural rigidity, vibration, damping and reduced flammability. These new materials are being developed to make structures blast/shock/impact resistant with reduced weight for naval ships and homeland security applications.

## SHOCK TESTS

A simple shock tube consists of two halves isolated from each other by a diaphragm with high gas pressure on the driver side of the shock tube [10-11]. Diaphragm is controlled to burst at the required pressure difference which develops a shock wave. This shock wave propagates into the test section (low pressure or driven section) of the tube. At the same time, an expansion wave develops and propagates in the driver side of the tube. If a test specimen is kept in the driven section (low pressure region) of the shock tube, the specimen undergoes this shock which simulates the rush of gas after an explosion. The shock tube test facility at University of Rhode Island was utilized in the current study.

Shock tube tests were conducted on plates of dimension 254 mm x 101.6 mm x 9.9 mm (10" x 4" x .39"). One panel from each configuration was subjected to 70 psi (482.3 kPa) and another at 120 psi (827.4 kPa) peak pressure. It is to be noted that pure vinyl ester specimen was first shock loaded with 70 psi (482.3 kPa) peak pressure and then with 120 psi (827.4 kPa) peak pressure. It was reported that samples subjected to 70 psi (482.3 kPa) peak pressure did not fracture. However, post-test samples received show hairline fractures for 1.25 and 2.5 wt percent graphite platelet samples subjected to 70 psi peak pressure. All the samples subjected to 120 psi (827.4 kPa) peak pressure fragmented into pieces.

The nanocomposite panels were held under simply supported conditions so as to minimize damage due to gripping and clamping. The span of the simply supported plate was 152 mm (6") and the overhangs measured 50.8 mm (2") along each end. The center of the specimen was kept in line with the center of the shock tube. The ratio of the loading diameter to the span was 0.5. The specimens were blast loaded from the exit of the shock tube on the face opposite to the supports [11].

Dynamic pressure sensor (PCB Piezotronics A123) mounted near the exit of the shock wave measures the shock pressure and reflected pressure history. Shock velocities are measured using break circuits and adequate calibration data is also available for the same. The shock wave velocities for the experiments conducted in this study were 500 m/s for a peak pressure of 70 psi (482.3 kPa) and 600 m/s with a peak pressure of about 120 psi (827.4 kPa). Images of the specimens loaded by the shock wave were captured in real time intervals of 100-150 microseconds [11] by using a high-speed IMACON 2000 camera.

## Strain Rate Approximation

For viscoelastic materials, the rate of loading is an important characteristic since energy absorbed before failure may vary for different strain rates. Viscoelastic materials typically become stiff at high strain rates with a reduction in strength and vice versa. An approximation of the transient strain rate under shock tube testing has been obtained using the bending moment equation under quasi-static load conditions.

The quasi-static bending moment equation was used for computing the flexural stress (σ):

$$\sigma = \frac{M \cdot y}{I} \tag{1}$$

Transient bending strain, ε(t) as a function of the instantaneous transient load, is obtained from:

$$\varepsilon(t) = \frac{\sigma(t)}{E} \tag{2}$$

The transient bending moment, $M$(t), was computed from transient load, $P$(t) obtained from pressure profile curve at each time step, t by multiplying it with the effective area of the driven section (3" Diameter) as shown in Figure 1. The transient shock load in this test was applied on a circular region which was approximated as a rectangular zone along the beam width as shown in Figure 2.

Boundary conditions are approximated as a simply-supported beam. Substituting value of σ from Equation (1), to obtain the, ε at each time step, t.

$$\varepsilon(t) = \frac{M(t) \cdot y}{E \cdot I} \tag{3}$$

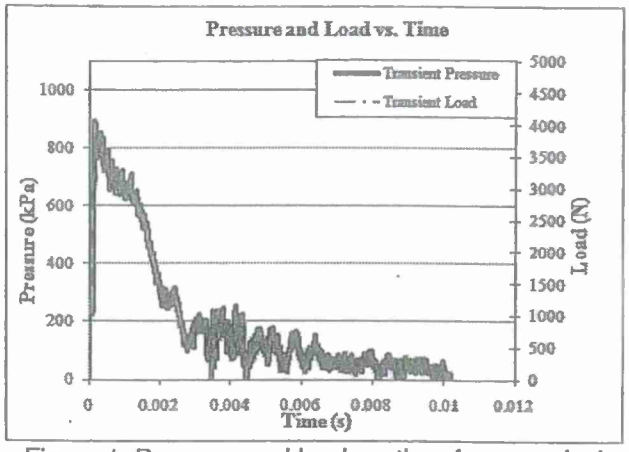


Figure 1. Pressure and load vs. time for pure vinyl ester specimen obtained from shock tube test

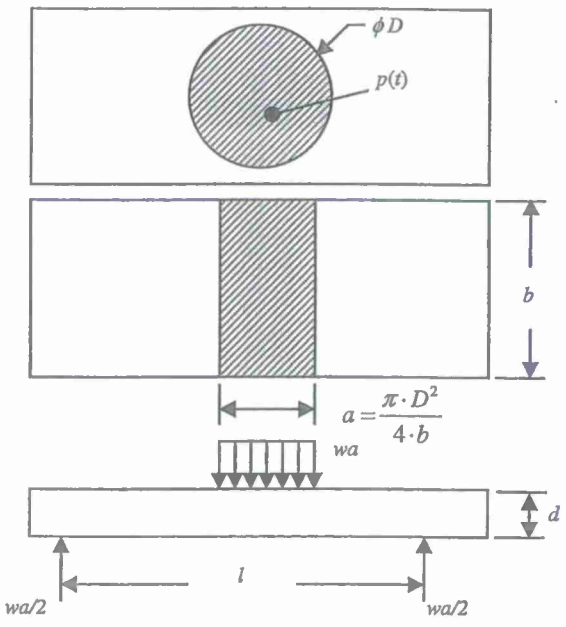


Figure 2. Boundary condition for Shock Test

Maximum bending moment at the center is given by:

$$M(t) = \frac{1}{8} wa \cdot (2l - a)$$

$$= \frac{1}{8} (p(t) \cdot b) \cdot \left( \frac{\pi \cdot D^2}{4b} \right) \cdot (2l - a)$$

$$M(t) = \frac{1}{8} p(t) \cdot (2l - a) \tag{4}$$

where $p(t)$ = Transient pressure
and $P(t)$ = Transient load



N-187

The area moment of inertia for rectangular beam specimen is given by:

$$I = \frac{b \cdot d^3}{12} \tag{5}$$

With the maximum flexural stress occurring at the outermost bottom layer of the specimen:

$$y = \frac{d}{2} \tag{6}$$

Substituting value of $M(t)$, $I$, and $y$ from equation (4), (5), (6) respectively in equation (3) gives:

$$\varepsilon(t) = \frac{\frac{1}{8} P(t) \cdot (2l - a) \cdot \frac{d}{2}}{E \cdot \frac{bd^3}{12}} = \frac{3}{4}\left(\frac{P(t) \cdot (2l - a)}{E \cdot b \cdot d^2}\right) \tag{7}$$

or

$$\varepsilon(t) = K \cdot P(t) \tag{8}$$

where

$$K = \frac{3}{4}\left(\frac{(2l - a)}{E \cdot b \cdot d^2}\right) \tag{9}$$

$K$ will be a constant based on the experimental set-up and type of material tested. The transient strain computed as a function of the transient load using equation (8) is plotted with time on the x-axis. A typical graph of transient strain versus time (and load versus time) for pure vinyl ester is shown in Figure 3.

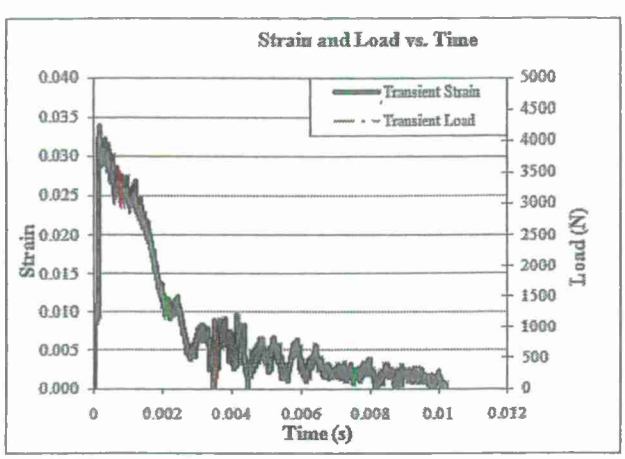


Figure 3. Strain and load vs. time for pure vinyl ester specimen obtained from shock tube test

Strain rate was then computed based on the initial slope. A typical graph for the slope of strain curve from shock tube for a peak pressure of 120 psi for pure vinyl ester is shown in Figure 4 with a linear fit line in the initial portion where maximum increase in pressure is observed. An approximate strain rate of 1000 per second and 1400 per second respectively for the 70 psi and 120 psi peak pressure was computed for the shock tube tests.

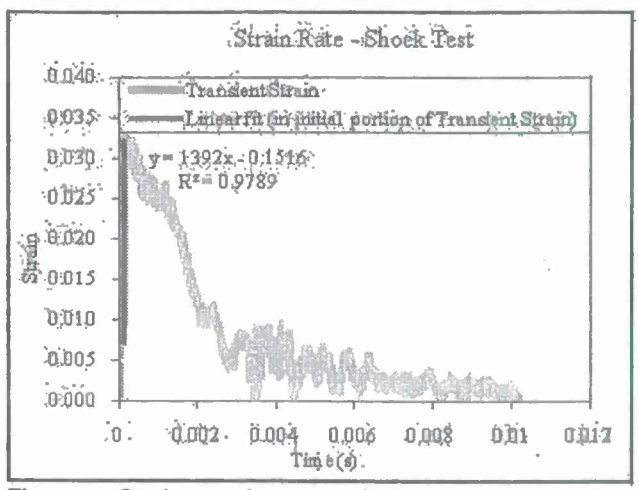


Figure 4. Strain rate for pure vinyl ester specimen for a shock tube test with a peak pressure of 120 psi

## Analysis of Shock Tube Test Data

The pressure profile curve, real time images, post-test visual examination and deflection data of vinyl ester nanocomposites were reported by the University of Rhode Island [11]. No failure was reported in the vinyl ester specimens subjected to 70 psi peak pressure, while specimens subjected to 120 psi peak pressure were shattered in pieces.

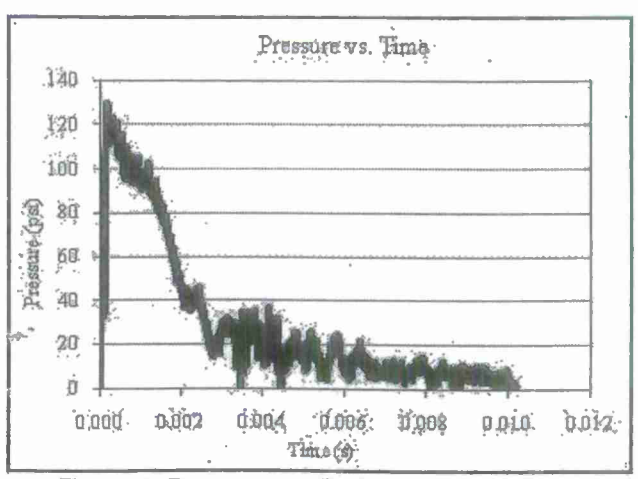


Figure 5. Pressure profile for pure vinyl ester subjected to 120 psi peak pressure [11]

The typical pressure profile curve, real time images and the post-test images for pure vinyl ester specimen subjected to 120 psi peak pressure is shown in Figures 5 to 7 and the response deflection versus time graph is shown in Figures 8 and 9. It is to be noted that in the case of pure vinyl ester, the same specimen was used for both 70 psi and 120 psi peak pressure.

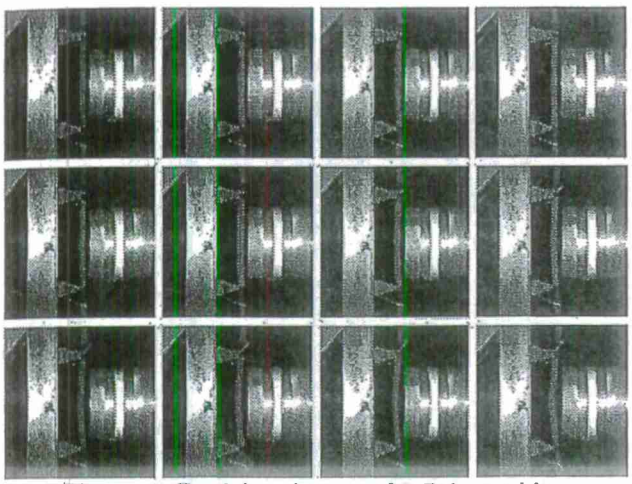

Figure 6. Real time image of 2.5% graphite platelet/vinyl ester subjected to 120 psi peak pressure in shock tube [11]

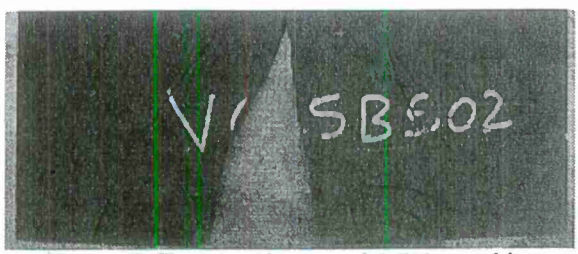

Figure 7. Post-test image of 2.5% graphite platelet/vinyl ester specimen subjected to 120 psi peak pressure in shock tube [11]

In order to analyze the material response to shock loading, quasi-static approach was adopted. In the quasi-static method, energy absorbed by each specimen is obtained by correlating the mid-span deflection with the pressure in terms of transient load. Pressure at respective time intervals was converted to transient load exerted on the specimen by multiplying it with the effective cross-sectional area of the driven section (3" Diameter). Transient load thus obtained was plotted against respective mid-span deflection. Energy absorbed was then computed with numerical integration up to the point of maximum deflection (failure). For this numerical integration, DPlot software [12] was used which employs trapezoidal rule to do the integration.

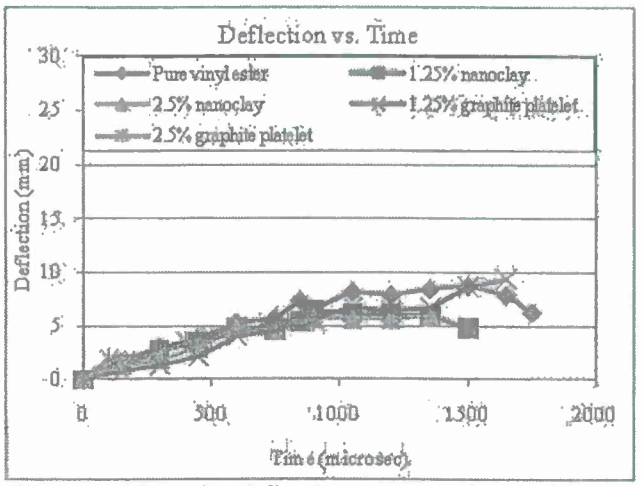


Figure 8. Mid-point deflection vs. time obtained from high speed images for vinyl ester panels with and without nano reinforcement at 70 psi peak pressure

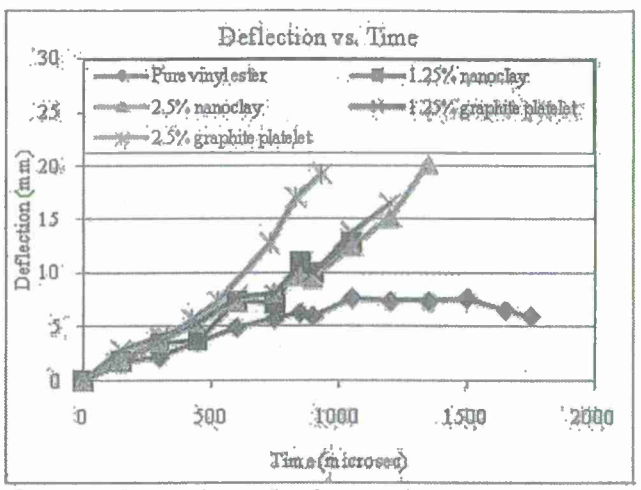


Figure 9. Mid-point deflection vs. time obtained from high speed images for vinyl ester panels with and without nano reinforcement at 120 psi peak pressure

## Finite Element Analysis of Shock Tube Test

Finite element modeling using ANSYS LS-DYNA of vinyl ester nanocomposite beam specimens subjected to shock loading was attempted. ANSYS LS-DYNA has the advantage of having explicit finite element program which provides faster solutions for large deformation and multiple nonlinearities problems [13].

The material to be analyzed is approximated to be randomly distributed nanoparticles in an isotropic matrix and the structure is supposed to have large deformations and complex loading through the thickness. Solid 168, a higher order 3D, 10 node tetrahedral structural solid, explicit dynamic element was used for modeling. The element is defined by ten nodes each having three degree of freedom at each node for translation motion in x, y, and

z direction. No real constants need to be defined for this element as everything is defined in the material property.

Standard piecewise material model was used for defining the material properties. This model provides a multi-linear elastic-plastic material option that allows input of stress-strain curve at different strain rates and effective failure plastic strain can be defined for defining failure point [13]. This material model required true stress-true plastic strain curve, density, and effective failure plastic strain as input. Engineering stress-strain and failure strain was obtained from quasi-static test and was converted to true stress-true plastic strain for input in the material model [14]. It is to be noted that the quasi-static test were conducted on nanocomposites produced using brominated 510A-40 vinyl ester resin as opposed to the non-brominated Derakane 411-350 vinyl ester resin used for shock tube experiments. Density of non-brominated Derakane 411-350 vinyl ester resin nanocomposites was used in finite element modeling [14].

Model of the structure was created using appropriate key points exactly in the same way as in shock tube experimental setup. A dense meshing in the loading area and a coarse meshing in outer area was employed. A total of 51786 elements with 76596 nodes were created.

Proper restraints were then assigned to define the boundary condition to match the experimental set-up as shown in Figure 10. As the test specimen was simply supported at a span of 150 mm (6") with an overhang of 50 mm (2") at both ends, the respective lines in the model were restrained to move in z-direction. To avoid twisting of the specimen, node at the center of the specimen and center of the left support were restrained to move in x and y direction.

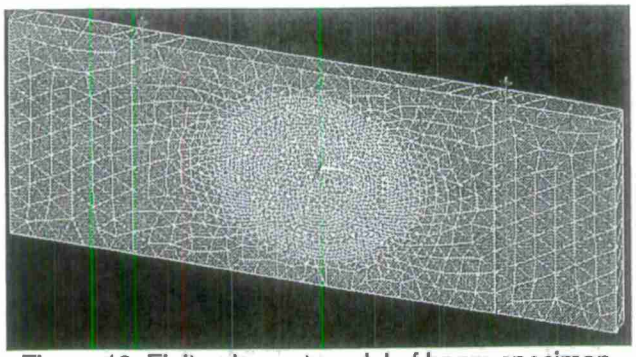

Figure 10. Finite element model of beam specimen for shock response characterization with boundary condition

Load applied in the experiments was by the shock coming out of a tubular section. This load was approximated to be equally distributed in the circular region of the same area. Due to the inherent problem with 3D Tet-Solid 168 element on applying uniformly distributed load [15], a nodal load was applied instead on all the nodes of the circular region. It was assumed that all the nodes are equidistant in the loading area. Load on the nodes on periphery of the circle (external nodes) was half in magnitude to that of load on nodes inside the circular region (internal nodes).

Solution was then obtained for transient analysis using explicit dynamics method. Time at the end of the load step was defined to be the time at which maximum deflection was observed in the experiments. Deformed view of the structure due to the applied load was captured and mid-point deflection was obtained to compare with the experimental results.

## EXPERIMENTAL RESULTS

The energy absorbed by vinyl ester nanocomposites obtained from numerical integration of the load vs. mid-point deflection is tabulated in Table 1, and the trend shown in Figure 11. It is to be noted that specimens subjected to 70 psi peak pressure did not fail while all other specimens fragmented into pieces. Further, in case of pure vinyl ester the same specimen was used for both 70 psi as well as 120 psi peak pressure.

Table 1. Energy absorption for nanoclay and graphite platelet/ vinyl ester nanocomposites for peak pressure of 70 psi and 120 psi

| Specimen | Energy absorption (J) | |
|---|---|---|
| | 70 psi | 120 psi |
| Pure vinyl ester | 16.95 | 22.94 |
| 1.25% nanoclay/ VE | 12.54 | 39.33 |
| 2.5% nanoclay/VE | 11.34 | 45.50 |
| 1.25% graphite platelet/VE | 19.43 | 45.53 |
| 2.5% graphite platelet/VE | 9.58 | 62.81 |

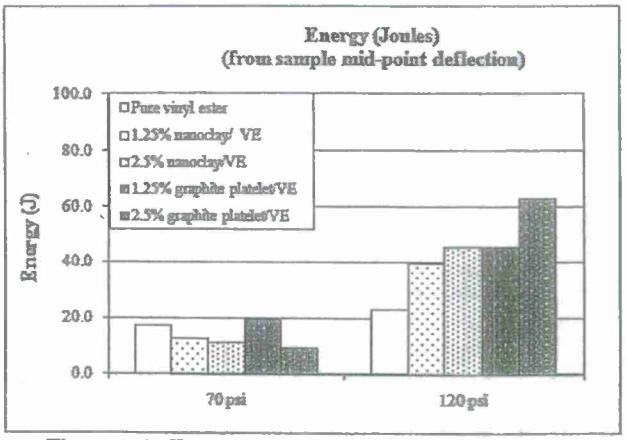


Figure 11. Energy absorption for nanoclay and graphite platelet/ vinyl ester nanocomposites for peak pressure of 70 psi and 120 psi

It was concluded that the energy absorption characteristics of vinyl ester specimens that did not fail when subjected to 70 psi peak pressure was not an appropriate measure of total energy absorption as high stiffness of material can lead to lower deflection which in turn may show lesser energy absorption. The trend of energy absorbed for the 120 psi peak pressure (where samples fragmented into pieces) is shown to be increasing with increasing reinforcement, with 2.5 wt. percent graphite platelet showing maximum improvement.

Figures 12 and 13 show the deformation of pure vinyl ester nanocomposites subjected to 70 psi and 120 psi peak pressure obtained from finite element modeling. Figures 14 and 15 show the deflection with respect to time obtained from finite element model and comparison with the experimental results.

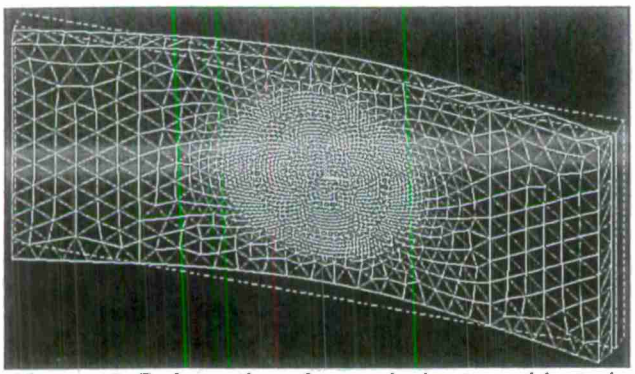

Figure 12. Deformation of pure vinyl ester subjected to 70 psi peak pressure from FEA

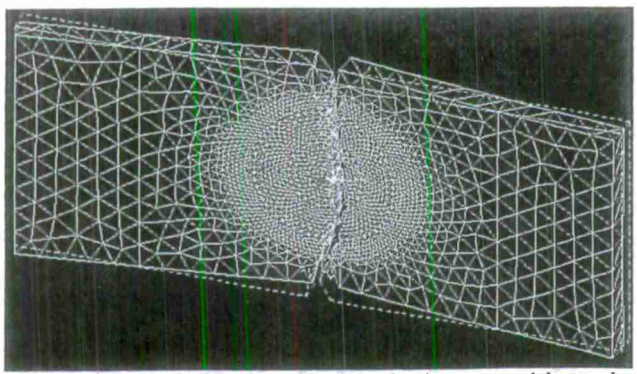

Figure 13. Deformation of pure vinyl ester subjected to 120 psi peak pressure from FEA

For 70 psi peak pressure experiments, it is observed that the FEA model of graphite platelet reinforcement showed failure occurring contrary to the experimental tests conducted and reported by University of Rhode Island [11]. The experimental deflections and those obtained from finite element model are observed to be close. Further, the post-test samples of graphite platelet received from University of Rhode Island did show some hairline fracture.

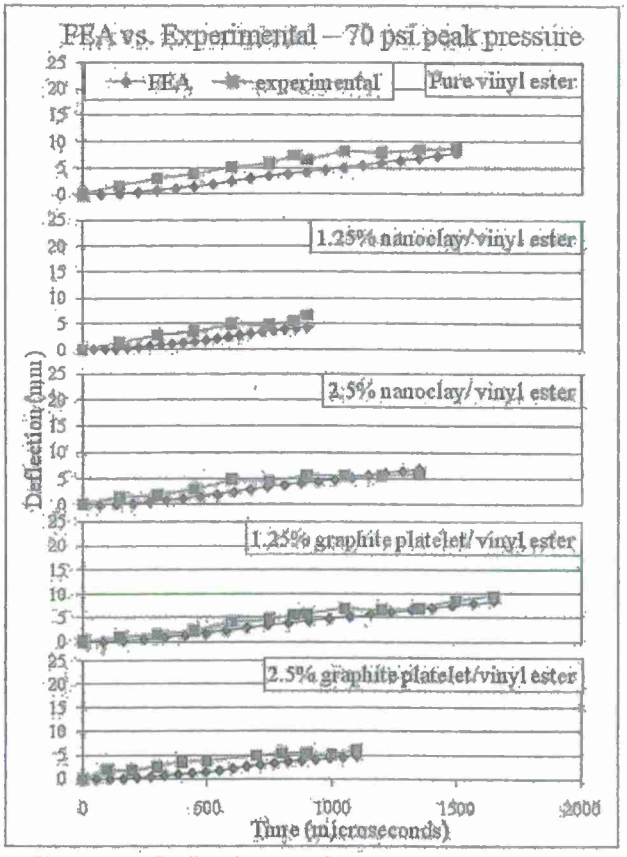


Figure 14. Deflection vs. time obtained from finite element model and shock tube experiments for nanoclay and graphite platelet/ vinyl ester subject to 70 psi peak pressure

For 120 psi peak pressure experiments, it is observed that the 2.5 wt. percent nanoclay reinforced vinyl ester does not show failure in the FEA model as opposed to the experimental tests conducted and reported by University of Rhode Island [11]. A larger variation between the experimental and finite element model deflections is observed for 2.5 wt. percent reinforcement of nanoclay and graphite platelet as shown in Figure 15. It is suspected that the pressure profile curve recorded for these cases are erroneous. It is also noted that brominated 510A-40 vinyl ester resin was used for defining the material model in finite element analysis instead of the non-brominated derakane 411-350 vinyl ester resin which was actually tested in shock tube. This might also be the reason for discrepancy as 2.5 wt. percent reinforcement of nanoclay and graphite platelet are showing inferior properties with brominated 510A-40 vinyl ester resin. Variation in

deflection of pure vinyl ester is also attributed to the reuse of same sample that was used for 70 psi peak pressure testing in the subsequent 120 psi peak pressure testing.

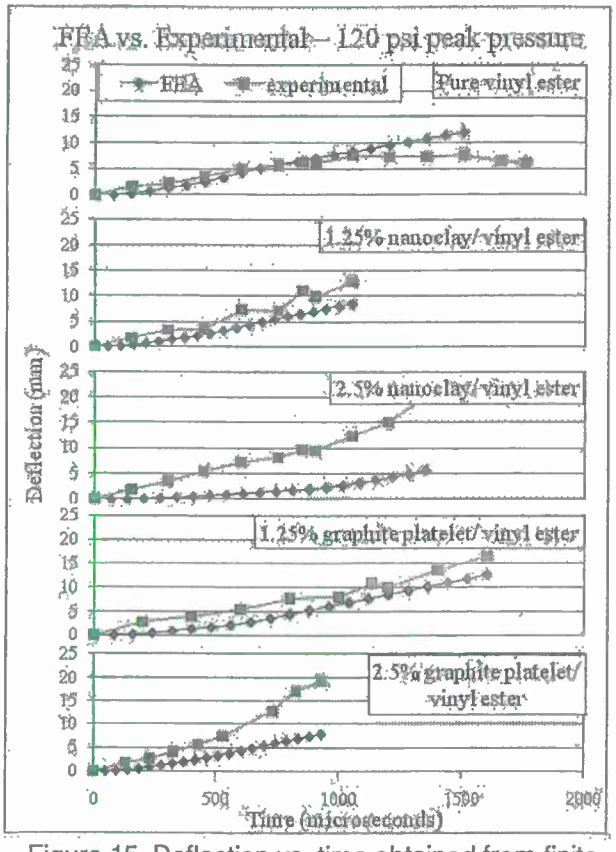


Figure 15. Deflection vs. time obtained from finite element model and shock tube experiments for nanoclay and graphite platelet/ vinyl ester subject to 120 psi peak pressure

## CONCLUSION

Energy absorption under shock testing is shown to be increasing for nanoclay and graphite platelet reinforced vinyl ester nanocomposites tested at a strain rate of 1400 per second (120 psi peak pressure). Graphite platelet reinforced vinyl ester nanocomposites also showed very good improvement in material response under shock testing obtained using dynamic approach.

For most of the cases, a good agreement with experimental deflection-time obtained from shock tube tests and finite element model was observed. Discrepancies in the results are attributed to the brominated 510A-40 vinyl ester resin used to define the material model, instead of derakane 411-350 vinyl ester resin which was actually used in the specimens that were subjected to shock tube testing. Shock tube experiments on brominated 510A-40 vinyl ester resin nanocomposites are underway to resolve these discrepancies.

## ACKNOWLEDGEMENT

The authors would like to acknowledge the support received from the Department of Civil Engineering at the University of Mississippi, and funding received under a subcontract from the Department of Homeland Security-sponsored Southeast Region Research Initiative (SERRI) at the Department of Energy's Oak Ridge National Laboratory. Partial support for this research by ONR Grant # N00014-07-1-1010, Office of Naval Research, Solid Mechanics Program (Dr. Yapa D.S. Rajapakse, Program Manager) is also acknowledged.

Authors would also like to acknowledge the support of Dr. Larry Drzal, Michigan State University for providing the nano samples, and Dr. Arun Shukla, University of Rhode Island for performing the shock tube tests.

## REFERENCES

[1] Schmidt, D., Shah, D. and Giannelis, E.P., 2002, "New Advances in Polymer/Layered Silicate Nanocomposites", Current Opinion in Solid State and Materials Science, 6(3), pp. 205–212.

[2] Ray, S.S. and Okamoto, M. , 2003, "Polymer/layered Silicate Nanocomposite: A Review from Preparation to Processing", Prog. Polymer Sci., 28, pp. 1539–1641.

[3] Bhat G., Hegde1 R. R., Kamath M.G., and Deshpande B., 2008, "Nanoclay Reinforced Fibers and Nonwovens", Journal of Engineered Fibers and Fabrics, 3(3), pp. 22-34.

[4] Alexandre M., Dubois P., 2000, "Polymer-layered silicate nanocomposites: preparation, properties and uses of a new class of materials", Material Science and Engineering; 28, pp. 1-63.

[5] Shen, J.W., Chen, X.M. and Huang, W.Y., 2003, "Structure and Electrical Properties of Grafted Polypropylene/Graphite Nanocomposites Prepared by Solution Intercalation", Journal of Applied Polymer Science, 88, pp. 1864–1869.

[6] Yasmin, A., Luo, J. and Daniel, I.M., 2006, Processing of Expanded Graphite Reinforced Polymer Nanocomposites, Composites Science and Technology, 66(9), pp. 1182–1189.

[7] Asma Yasmin, Isaac Daniel., 2004, "Mechanical and thermal properties of graphite platelet/ epoxy composites," Polymer 45, 24, pp. 8211-8219.

[8] Peng Xiao, Min Xiao, Gong K., 2001, "Preparation of exfoliated graphite/ polystyrene composite by polymerization-filling technique" Polymer, 42, pp. 4813-4816.

[9] Fukushima H., and Drzal L.T, 2004, "Graphite nanoplatelets as reinforcement for polymers: structural and

electrical properties" Proc. 17th International Conference on American Society for composites, September 9-11, 2004.
[10] University of Rhode Island website, http://www.advance.uri.edu/pacer/october2004/story10.htm, accessed on December 13, 2007 at 13:00 hours.
[11] Arun Shukla, September 2007, "Shock Testing of Reinforced Vinyl Ester Materials", Internal report, Department of Mechanical Engineering, University of Mississippi, University, MS.
[12] DPlot Version 2.2.1.1, Copyright © 2001-2008 by Hydesoft Computing, LLC.
[13] ANSYS LS-DYNA User's Guide. ANSYS Release 10.0.002184 © SAP IP, Inc.
[14] Swasti Gupta., 2009, "Energy Absorption Characteristics of MWCNT/ Nylon 6,6; and Nanoclay and Graphite Platelet/ Vinyl Ester Nanocomposites," MS thesis, University of Mississippi, University, MS.
[15] E-mail communication between Dr. Ahmed Al-Ostaz and Mr. Bill Bulat for incident number 826775 dated November 12, 2008.

# Determination of power-law attenuation coefficient and dispersion spectra in multi-wall carbon nanotube composites using Kramers–Kronig relations

Joel Mobley[a)]
*Department of Physics and Astronomy and Jamie Whitten National Center for Physical Acoustics, University of Mississippi, 1 Coliseum Drive, University, Mississippi 38677*

Richard A. Mack
*Jamie Whitten National Center for Physical Acoustics, University of Mississippi, 1 Coliseum Drive, University, Mississippi 38677*

Joseph R. Gladden
*Department of Physics and Astronomy, University of Mississippi, 108 Lewis Hall, University, Mississippi 38677*

P. Raju Mantena
*Department of Mechanical Engineering, University of Mississippi, 201D Carrier Hall, University, Mississippi 38677*

(Received 14 October 2008; revised 2 January 2009; accepted 2 April 2009)

Using a broadband through-transmission technique, the attenuation coefficient and phase velocity spectra have been measured for a set of multi-wall carbon nanotube (MWCNT)-nylon composites (from pure nylon to 20% MWCNT by weight) in the ultrasonic frequency band from 4 to 14 MHz. The samples were found to be effectively homogeneous on spatial scales from the low end of ultrasonic wavelengths investigated and up (>0.2 mm). Using Kramers–Kronig relations, the attenuation and dispersion data were found to be consistent with a power-law attenuation model with a range of exponents from $y=1.12$ to $y=1.19$ over the measurement bandwidth. The attenuation coefficients of the respective samples are found to decrease with increasing MWCNT content and a similar trend holds also for the dispersion. In contrast, the mean phase velocities for the samples rise with increasing MWCNT content indicating an increase in the mechanical moduli.
© *2009 Acoustical Society of America.* [DOI: 10.1121/1.3125323]

PACS number(s): 43.35.Cg, 43.20.Jr, 43.35.Yb, 43.35.Zc [RLW] Pages: 92–97

## I. INTRODUCTION

Since the discovery of carbon nanotubes (CNTs) by Iijima in 1991,[1] significant efforts have been made to incorporate these nanoparticles with conventional materials in order to improve the mechanical strength and stiffness or other physical properties (e.g., electrical and thermal conductance) of the resulting composite.[2–4] CNTs include both single- and multi-walled (MWCNT) structures, with the former having typical outside diameter (OD) of 1–2 nm while the latter an OD of 8–12 nm. Their lengths range from the typical 10 $\mu$m to as much as 100 $\mu$m with very high aspect ratios (length-to-diameter) of order 1000:1. CNTs have about 50 times the tensile strength of stainless steel (100 GPa vs 2 GPa) and five times the thermal conductivity of copper. Incorporating nano-scale particles into a matrix to construct a macro-scale composite can potentially offer improved performance over composites with larger inclusions (e.g., conventional carbon fibers) for several reasons, including the increased effective surface area of contact between the nanoparticles and the matrix, and higher crystallinity. CNT composites aim to capitalize on both the extraordinary mechanical properties of the individual CNTs and the potential advantages of nanoscale reinforcing particles. Research on CNT composites is diverse incorporating a variety of matrix materials and CNT types and sizes. Realizing the promise of enhanced mechanical properties relies on the ability to disperse the CNTs uniformly in the host material and on achieving good interfacial bonding for transferring loads across the matrix-fiber interface.[2–4] The dynamic properties of composite materials in the ultrasonic region of the spectrum can provide information about the mechanical moduli, fiber/matrix coupling, and structural integrity of composite materials.[5–8] The attenuation spectra of ultrasonic stress waves are sensitive to the coupling of the matrix and reinforcing inclusion as well as the homogeneity over length scales relevant for structural applications. The phase velocity spectra can be used to determine the dynamic mechanical moduli of a material, while the velocity dispersion is linked to the attenuation (as discussed below) and thus sensitive to a similar list of properties. Nonlinear mechanical properties of composites can also be used to find signs of microstructural degradation.[9]

Broadband ultrasonic spectroscopy is a technique utilizing time-localized signals to determine the phase velocity and attenuation coefficient spectra over a range of frequen-

a)Author to whom correspondence should be addressed. Electronic mail: jmobley@olemiss.edu

 0001-4966/2009/126(1)/92/6/$25.00 © 2009 Acoustical Society of America

cies simultaneously.[10] The attenuation coefficient and phase velocity spectra are components of the complex wavenumber and are further interlinked through the Kramers–Kronig (KK) relations. Fundamentally rooted in causality, KK relations provide linkages between the physical properties that govern the response of matter and materials to external stimuli. Due to their general foundations[11] KK relations have proven to be adaptable and applicable to a wide array of tasks which include measuring fundamental material parameters, establishing the consistency of laboratory data, and building causally-consistent physical models. KK relations between components of the complex wavenumber using the method of subtractions have been established for both homogeneous and inhomogeneous materials.[12] One complication in adapting KK relations for the analysis of data is the knowledge gap that exists between the infinite bandwidth required by the KK integrals and the measured data which are inherently bandlimited. The impact of this gap on KK calculations depends on many factors, both general and system-dependent. However, finite bandwidth approximations to the KK relations have proven to be applicable to measured ultrasonic attenuation and velocity spectra for suspensions exhibiting resonant features,[13–16] and have also proven accurate for the analysis of systems exhibiting monotonic behavior where the attenuation varies as a frequency power-law over limited experimental bandwidths.[17,18] For the power-law attenuation, the KK relations predict that the velocity dispersion also varies as a power-law (or logarithmically in the case that the attenuation is linear in frequency), although with a scaling factor that is a function of the power-law exponent.[17,19] Due to convergence problems with a KK formulation in use at the time, these results were first derived with an alternate technique, known as the time-causal method.[19] Using the method of subtractions,[12,20] the convergence problems were circumvented permitting valid KK calculations to be performed. In this work, we present data for the attenuation coefficient and phase velocity spectra of longitudinal mode elastic waves in the ultrasonic frequency regime for a series of nylon matrix materials containing various concentrations of MWCNTs. The attenuation coefficient spectra for the samples examined in this work are found to follow a power-law dependence on frequency and the dispersion data exhibits the variation predicted by the KK relations.

## II. THEORY

In a variety of media (including some liquids, soft mammalian tissues, and solid polymers) over a finite bandwidth, the attenuation coefficient of ultrasonic waves appears to be adequately modeled by a power-law dependence on frequency

$$\alpha(f) = \alpha_0 |f|^y, \tag{1}$$

where $\alpha_0$ and $y$ are real constants, with $1 \le y \le 2$. The frequency response of a medium of thickness $h$ can be characterized by its transfer function

TABLE I. The densities of the samples examined in this work.

| Sample | Density (g/cm$^3$) |
|---|---|
| 20% MWCNT | 1.25 |
| 10% MWCNT | 1.20 |
| 5% MWCNT | 1.17 |
| Nylon (0% MWCNT) | 1.14 |

$$H(f,h) = \exp[iK(f)h], \tag{2}$$

where

$$K(f) = \frac{2\pi f}{c_p(f)} + i\alpha(f) \tag{3}$$

is the conventional complex wavenumber, and $c_p(f)$ is the phase velocity. Given that the power-law attenuation persists throughout the spectrum, the KK relations predict that the phase velocities at two frequencies $f$ and $f_0$ have the following relationship:[17,19]

$$\frac{1}{c_p(f)} = \frac{1}{c_p(f_0)} + \frac{\alpha_0}{2\pi}\tan\left(y\frac{\pi}{2}\right)(|f|^{y-1} - |f_0|^{y-1}) \quad \text{for} \quad 1 < y \le 2, \tag{4a}$$

which takes the form

$$\frac{1}{c_p(f)} = \frac{1}{c_p(f_0)} - \frac{\alpha_0}{\pi^2}\ln\left|\frac{f}{f_0}\right| \quad \text{in the limit } y \to 1. \tag{4b}$$

These causally-consistent functional forms for the attenuation and phase velocity spectra have been shown to accurately describe the behavior of real materials over band limited windows in the low-megahertz region of the acoustic spectrum.[17–19]

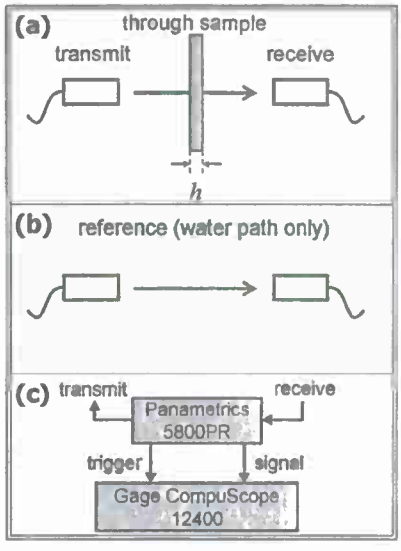


FIG. 1. (Color online) (a) The through sample and (b) reference (water path only) signal acquisition steps of the substitution method. (c) Schematic diagram of the instrumentation in the measurement system.



0-195

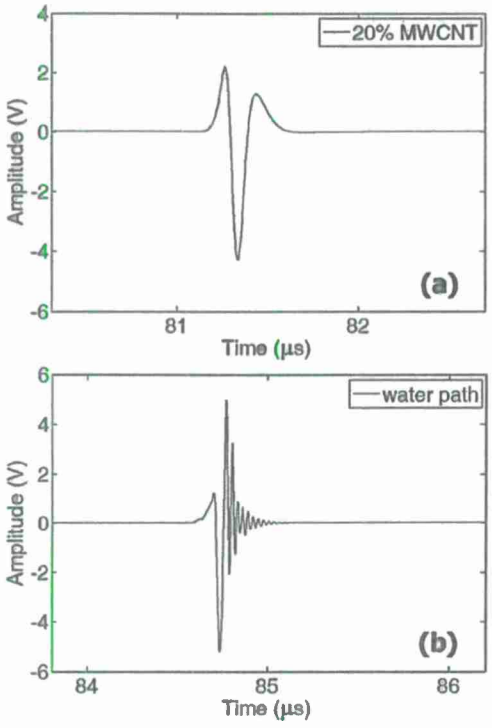


FIG. 2. (Color online) Representative waveforms captured during (a) through-sample acquisition (20% MWCNT sample) and (b) reference (water path only) acquisition.

## III. MATERIALS

The samples were provided as extruded plates by Ensinger Inc. with weight fractions of MWCNTs of 0% (pure nylon), 5%, 10%, and 20%. The polymer matrix for the samples is nylon 6,6. The MWCNTs were produced by Hyperion Catalysis International, Inc. (Cambridge, MA). The densities of the samples are shown in Table I.

## IV. DATA ACQUISITION AND ANALYSIS

The velocity and attenuation data were determined using the broadband ultrasonic spectroscopy technique implemented in a through-transmission set-up, as shown in Fig. 1. The ultrasound was generated and received by a pair of PVDF transducers (Olympus NDT/Panametrics) immersed in a water bath and separated by 12.5 cm. The transmitter was excited by a broadband pulser/receiver unit (Olympus NDT/Panametrics 5800). The received signals were captured by a digital oscilloscope (GaGe Applied Compuscope 12400) where they were digitized to 12 bits at a rate of 400 Msamples/s. For each sample, through-transmitted ultrasonic signals were acquired [Fig. 1(a)] from five sites at normal incidence. A representative through-sample waveform is shown in Fig. 2(a). In addition to the through-sample acquisitions, waterpath only waveforms were captured to serve as the reference data in the analysis, as shown in Fig. 1(b). A captured signal from a waterpath only acquisition is shown in Fig. 2(b). Sample thicknesses were measured ultrasonically at each acquisition site on the sample and are derived from time-of-flight measurements from pulse-echo signals off the near sample face for each transducer and a waterpath

TABLE II. The fit values for the attenuation constant, the exponent of the power law attenuation coefficients, and the offset $a_0$ for the four samples.

| Sample | $\alpha_0$ (Np mm$^{-1}$ MHz$^{-\gamma}$) | $\gamma$ | $a_0$ (Np/mm) |
|---|---|---|---|
| 20% MWCNT | 0.0217 | 1.169 | 0.0108 |
| 10% MWCNT | 0.0272 | 1.123 | −0.0048 |
| 5% MWCNT | 0.0264 | 1.154 | −0.0046 |
| Nylon (0% MWCNT) | 0.0267 | 1.187 | −0.0038 |

only through-transmission acquisition.[21] Waveform data were acquired by accumulating 5000 raw signals and the accumulated signal was recorded to disk for further processing. The discrete Fourier transforms of the through-transmitted and waterpath signals were taken, and the amplitude and phase spectra from each were then used to compute the attenuation coefficient and phase velocity for each site on a given sample. The attenuation coefficient was determined using the following relation:

$$\alpha(f) = \alpha_w(f) + \frac{\ln\dfrac{A_{\mathrm{ref}}(f)}{A_{\mathrm{thru}}(f)} + \ln T}{h}, \tag{5}$$

where $\alpha_w(f)$ is the attenuation coefficient for water, $A_{\mathrm{thru}}(f)$ and $A_{\mathrm{ref}}(f)$ are the Fourier amplitude spectra of the through-sample and reference waveforms, respectively, $h$ is the sample thickness, and $T=4Z_wZ_s/(Z_w+Z_s)^2$ is the single-pass

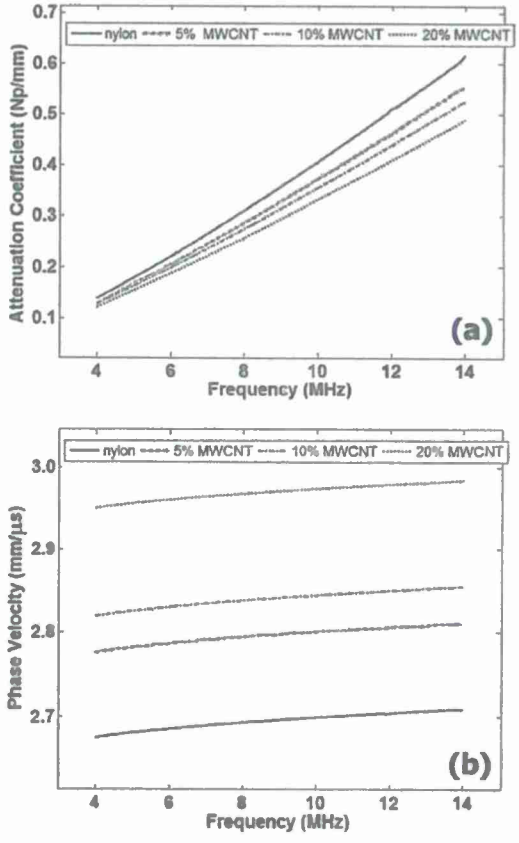


FIG. 3. (Color online) The measured (a) attenuation coefficient and (b) phase velocity spectra for the four samples studied in this work.



0-196

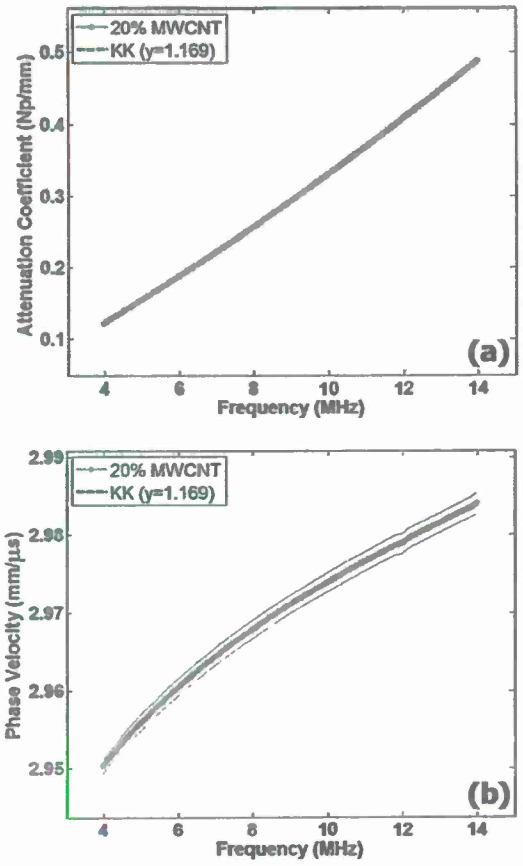


FIG. 4. (Color online) The experimental attenuation coefficient and phase velocity spectra for the 20% MWCNT sample with their associated KK predicted curves. The solid lines in the bottom panel are the standard deviation limits of the measured quantities. (The standard deviation limits for the attenuation data are smaller than the width of the plotted curve.)

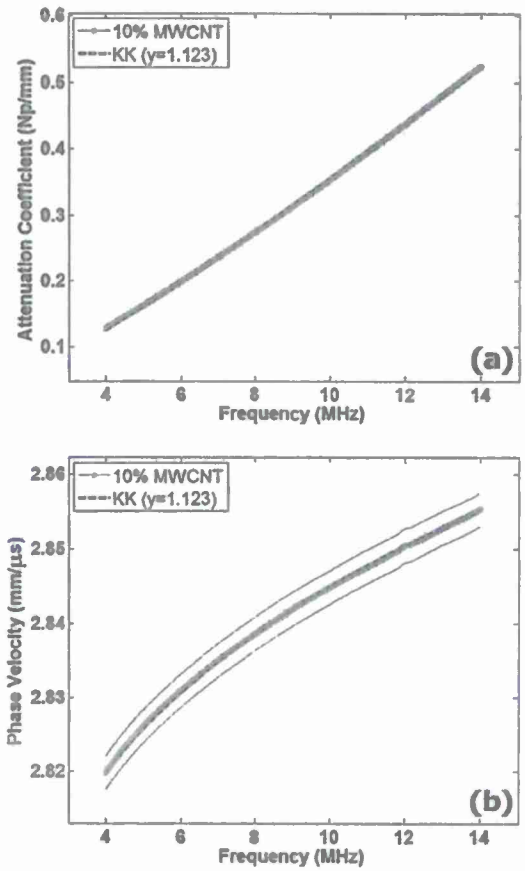


FIG. 5. (Color online) The experimental attenuation coefficient and phase velocity spectra for the 10% MWCNT sample with their associated KK predicted curves. The solid lines in the bottom panel are the standard deviation limits of the measured quantities. (The standard deviation limits for the attenuation data are smaller than the width of the plotted curve.)

amplitude transmission coefficient including both the entry and exit water/sample interfaces, where $Z_w=\rho_w c_w$ and $Z_w=\rho_s c_p(f)$ are the characteristic acoustic impedances of the water and the sample, respectively (the sample densities, $\{\rho_s\}$, are given in Table I). The phase velocity relation is

$$c(f)=\frac{c_w}{1-c_w\dfrac{\Delta\phi(f)}{2\pi fh}}, \tag{6}$$

where $\Delta\phi(f)=\phi_{\text{thru}}(f)-\phi_{\text{ref}}(f)$ is the difference in the unwrapped phase spectra from the two signals compensated for sheet offsets. The speed of sound in water, $c_w$, was determined by the water temperature using the formula from Ref. 22.

After the attenuation coefficient and phase velocity spectra were measured at five sites on a given sample, the spectra were averaged across the sites to yield a single attenuation and velocity spectrum for each sample. To determine the parameters $\alpha_0$ and $y$ in each case, the attenuation data were fitted to a model function of the form $\alpha(f)=a_0+\alpha_0 f^y$, where $a_0$ is the offset of the attenuation data at zero frequency (beyond the low frequency limits of the measurement spectrum). This was done over a range of exponents from $y=1.001$ to $y=1.349$, and the exponent $y$ and associated coefficient $\alpha_0$ that gave the best fit to the dispersion data using Eq. (4a) were used. The values for the parameters $\alpha_0$ and $y$ as determined by this procedure are given in Table II. (See Table III for phase velocity values at $f_{\text{low}}=4$ MHz.)

## V. RESULTS AND DISCUSSION

The results for the attenuation coefficient and phase velocity for all four samples are shown together in the panels of Fig. 3. The comparisons of the measured attenuation and dispersion data with the KK power-law model predictions are shown for each respective sample in Figs. 4–7. The top panel in each of Figs. 4–7 shows the attenuation coefficient and its power-law fit. The bottom panel in each figure compares the measured phase velocity spectra with the KK prediction in the form of Eq. (4a) using the parameters from the attenuation fit.

The attenuation coefficient spectrum for the pure nylon sample exhibited the highest values throughout the measurement bandwidth, and across the samples the attenuation was found to decrease with increasing MWCNT content (in the same way as with the dispersion as discussed below), as shown in Fig. 3(a). The attenuation coefficient of the nylon-only sample also exhibited the steepest rise with frequency, and the largest power-law exponent of about 1.19. The at-



0-197

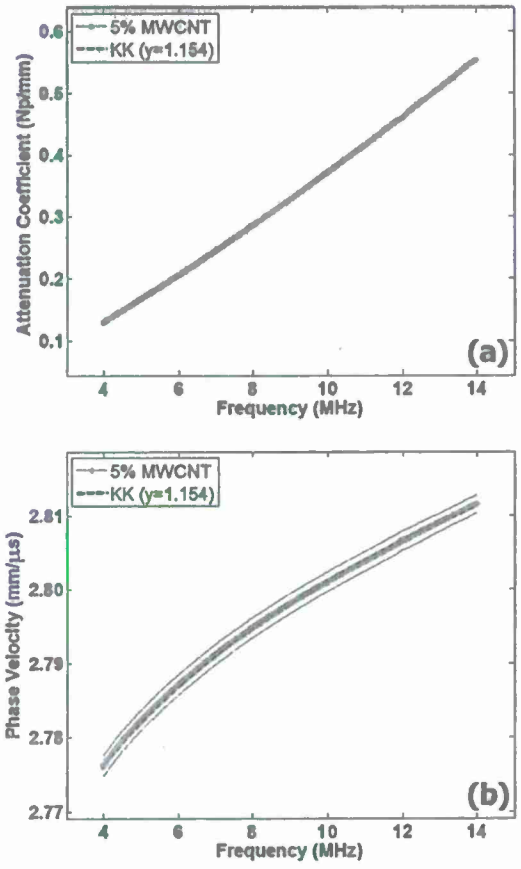


FIG. 6. (Color online) The experimental attenuation coefficient and phase velocity spectra for the 5% MWCNT sample with their associated KK predicted curves. The solid lines in the bottom panel are the standard deviation limits of the measured quantities. (The standard deviation limits for the attenuation data are smaller than the width of the plotted curve.)

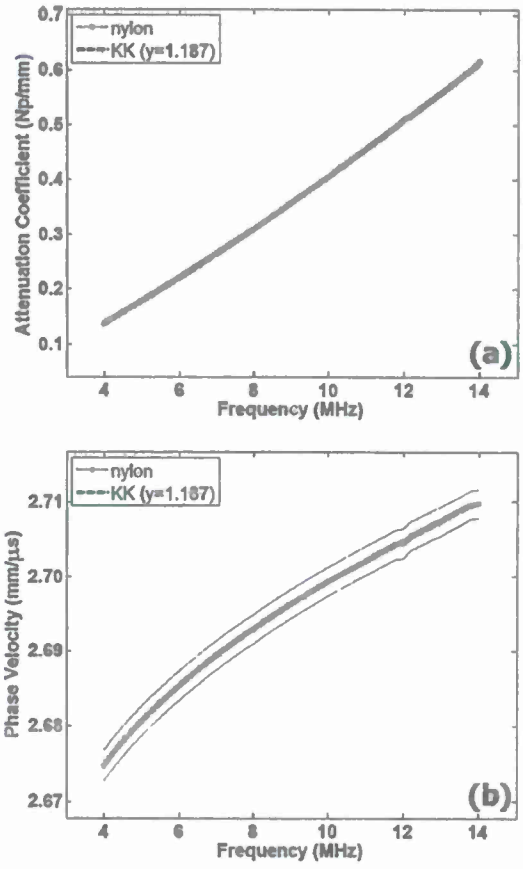


FIG. 7. (Color online) The experimental attenuation coefficient and phase velocity spectra for the nylon (0% MWCNT) sample with their associated KK predicted curves. The solid lines in the bottom panel are the standard deviation limits of the measured quantities. (The standard deviation limits for the attenuation data are smaller than the width of the plotted curve.)

tenuation coefficient of the 20% MWCNT sample was the smallest among the samples across the spectrum and the slowest rise with frequency. The power-law exponent of the 5% MWCNT sample and 10% MWCNT sample fell monotonically from the nylon value, but the 20% MWCNT sample had a greater exponent than both the 5% and 10% MWCNTs while still remaining lower than the nylon-only. The reasons for the monotonic decrease in attenuation with increasing MWCNT concentration are not clear, although this could due to differences in the bulk attenuation of the two media (volume related effect) or some aspect of the coupling between the two phases (interphase boundary effects and scaling with the interphase surface area). Simple series- and parallel-type volumetric law of mixtures models were unable to account for the differences in attenuation among the samples. It is likely that a combination of factors contributes to the observed trend, but a more definitive judgment on this manner is beyond the scope of the present work.

The phase velocity and dispersion results are summarized in Table III. The mean phase velocities (averaged across the 4–14 MHz bandwidth) for the four samples exhibit an increase as MWCNT content rises, starting from a value of 2.695 mm/$\mu$s for the pure nylon (0% MWCNT) sample up to 2.970 mm/$\mu$s for the 20% MWCNT sample. This is indicative of an increase in the Young's modulus of about 28% from pure nylon to the composite with the highest fraction of MWCNT, assuming that nylon's Poisson's ratio of about 0.39 continues to hold.[23] The dispersion, defined as $\Delta(1/c)=[1/c(f_{\text{low}})]-[1/c(f_{\text{high}})]$ [as is natural based on the form predicted in Eq. (4)], varies from sample to sample with the dispersion decreasing with increasing MWCNT content. This is the same trend as seen with the attenuation data as expected from the causally-consistent forms of Eqs. (3) and (4). (An interesting observation is that the change in phase velocity, $\Delta c=c(f_{\text{high}})-c(f_{\text{low}})$, as dispersion is often defined, did not change significantly from sample to sample.) The pure nylon exhibited the greatest dispersion, with a variation in $\Delta(1/c)$ about 1.26 times higher than that of the 20% MWCNT sample. These dispersion data are also consistent with the attenuation coefficient determinations as linked by the KK relations, as can be seen in the Figs. 4(b), 5(b), 6(b), and 7(b). In each case the KK prediction is almost indistinguishable from the measured phase velocity. It is clear that the KK predicted forms are quantitatively consistent with these data. It is not clear, however, how far beyond the measurement bandwidth one could expect these forms to continue to hold.

## VI. CONCLUSION

The phase velocity and attenuation coefficient spectra of composite materials with varying amounts of MWCNT con-



0-198

TABLE III. Phase velocity measurements from the four samples. The first three columns are the values at 4, 9, and 14 MHz, respectively. The fourth column is the phase velocity averaged over the entire bandwidth, and the last column is the dispersion.

| Sample | $c_p(f_{low})$ (mm/$\mu$s) | $c_p(f_{median})$ (mm/$\mu$s) | $c_p(f_{high})$ (mm/$\mu$s) | $\bar{c}_p$ (mm/$\mu$s) | $1/c_p(f_{low})-1/c_p(f_{high})$ $(mm/\mu s)^{-1}$ |
|---|---|---|---|---|---|
| 20% MWCNT | 2.950 | 2.971 | 2.984 | 2.970 | $3.83\times10^{-3}$ |
| 10% MWCNT | 2.820 | 2.842 | 2.855 | 2.840 | $4.40\times10^{-3}$ |
| 5% MWCNT | 2.776 | 2.798 | 2.812 | 2.797 | $4.53\times10^{-3}$ |
| Nylon (0% MWCNT) | 2.675 | 2.696 | 2.710 | 2.695 | $4.82\times10^{-3}$ |

tent (from 0 to 20% by weight) were measured using a broadband technique. The samples were found to be effectively homogeneous on spatial scales from the low end of ultrasonic wavelengths investigated and up (>0.2 mm). Over the measurement bandwidth, these spectra were found to be a consistent KK model that utilizes a frequency power-law form for the attenuation coefficient. The mean phase velocity increased monotonically with the rising MWCNT content, indicating an increase in the mechanical moduli with MWCNT concentration. The attenuation coefficient and the dispersion both showed the opposite trend, decreasing with increasing MWCNT content, consistent with the predictions of the KK model.

## ACKNOWLEDGMENT

Support for this research by the Office of Naval Research, Solid Mechanics Program, ONR Grant No N00014-07-1-1010 (Dr. Yapa D. S. Rajapakse, Program Manager), is acknowledged.

[1]S. Iijima, "Helical microtubules of graphitic carbon," Nature (London) **354**, 56–58 (1991).
[2]P. J. F. Harris, "Carbon nanotube composites," Int. Mater. Rev. **49**, 31–43 (2004).
[3]J. N. Coleman, U. Khan, W. J. Blau, and Y. K. I. Gun'ko, "Small but strong: A review of the mechanical properties of carbon nanotube-polymer composites," Carbon **44**, 1624–1652 (2006).
[4]J. Njuguna, K. Pielichowski, and J. R. Alcock, "Epoxy-based fibre reinforced nanocomposites," Adv. Eng. Mater. **9**, 835–847 (2007).
[5]S. I. Rokhlin, W. Huang, and Y. C. Chu, "Ultrasonic scattering and velocity methods for characterization of fiber-matrix interphases," Ultrasonics **33**, 351–364 (1995).
[6]Y. C. Chu and S. I. Rokhlin, "Determination of macromechanical and micromechanical and interfacial elastic properties of composites from ultrasonic data," J. Acoust. Soc. Am. **92**, 920–931 (1992).
[7]K. Balasubramaniam, S. Alluri, P. Nidumolu, P. R. Mantena, J. G. Vaughan, and M. Kowsika, "Ultrasonic and vibration methods for the characterization of pultruded composites," Composites Eng. **5**, 1433–1451 (1995).
[8]J. Wu, C. Layman, S. Murthy, and R.-B. Yang, "Determine mechanical properties of particulate composite using ultrasound spectroscopy," Ultrasonics **44**, e793–e800 (2006).
[9]K. Y. Jhang, "Applications of nonlinear ultrasonics to the NDE of material degradation," IEEE Trans. Ultrason. Ferroelectr. Freq. Control **47**, 540–548 (2000).
[10]W. Sachse and Y.-H. Pao, "On the determination of phase and group velocities of dispersive waves in solids," J. Appl. Phys. **49**, 4320–4327 (1978).
[11]J. S. Toll, "Causality and the dispersion relations: Logical foundations," Phys. Rev. **104**, 1760–1770 (1956).
[12]R. L. Weaver and Y.-H. Pao, "Dispersion relations for linear wave propagation in homogeneous and inhomogeneous media," J. Math. Phys. **22**, 1909–1918 (1981).
[13]J. Mobley, "Finite-bandwidth Kramers-Kronig relations for acoustic group velocity and attenuation derivative applied to encapsulated microbubble suspensions," J. Acoust. Soc. Am. **121**, 1916–1923 (2007).
[14]J. Mobley, K. R. Waters, and J. G. Miller, "Causal determination of acoustic group velocity and frequency derivative of attenuation with finite-bandwidth Kramers-Kronig relations," Phys. Rev. E **72**, 016604 (2005).
[15]J. Mobley, K. R. Waters, M. S. Hughes, C. S. Hall, J. N. Marsh, G. H. Brandenburger, and J. G. Miller, "Kramers-Kronig relations applied to finite bandwidth data from suspensions of encapsulated microbubbles," J. Acoust. Soc. Am. **108**, 2091–2106 (2000); "Erratum: 'Kramers-Kronig relations applied to finite bandwidth data from suspensions of encapsulated microbubbles [J. Acoust. Soc. Am. 108, 2091–2106 (2000)]'," J. Acoust. Soc. Am. **112**, 760–761 (2002).
[16]J. Mobley and R. E. Heithaus, "Ultrasonic properties of a suspension of microspheres supporting negative group velocities," Phys. Rev. Lett. **99**, 124301 (2007).
[17]K. R. Waters, M. S. Hughes, J. Mobley, G. H. Brandenburger, and J. G. Miller, "On the applicability of Kramers–Kronig relations for media with ultrasonic attenuation obeying a frequency power law," J. Acoust. Soc. Am. **108**, 556–563 (2000).
[18]K. R. Waters, M. S. Hughes, J. Mobley, and J. G. Miller, "Differential forms of the Kramers–Kronig dispersion relations," IEEE Trans. Ultrason. Ferroelectr. Freq. Control **50**, 68–76 (2003).
[19]T. L. Szabo, "Causal theories and data for acoustic attenuation obeying a frequency power law," J. Acoust. Soc. Am. **97**, 14–24 (1995).
[20]H. M. Nussenzveig, *Causality and Dispersion Relations* (Academic, New York, 1972).
[21]D. K. Hsu and M. S. Hughes, "Simultaneous ultrasonic velocity and sample thickness measurement and application in composites," J. Acoust. Soc. Am. **92**, 669–675 (1992).
[22]W. Marczak, "Water as a standard in the measurements of speed of sound in liquids," J. Acoust. Soc. Am. **102**, 2776–2779 (1997).
[23]G. S. Kino, *Acoustic Waves: Devices, Imaging, and Analog Signal Processing* (Prentice-Hall, Inc., Englewood Cliffs, NJ, 1987), p. 550.



0-199

International Journal of Solids and Structures 46 (2009) 4054–4063

Contents lists available at ScienceDirect

International Journal of Solids and Structures

journal homepage: www.elsevier.com/locate/ijsolstr

# A macroscopic-level hybrid lattice particle modeling of mode-I crack propagation in inelastic materials with varying ductility

G. Wang [a,*], A. Al-Ostaz [a], A.H.-D. Cheng [a], P.R. Mantena [b]

[a] Department of Civil Engineering, University of Mississippi, Oxford, MS 38677-1848, USA
[b] Department of Mechanical Engineering, University of Mississippi, Oxford, MS 38677-1848, USA

ARTICLE INFO

*Article history:*
Received 5 January 2009
Received in revised form 22 June 2009
Available online 6 August 2009

*Keywords:*
Fracture mechanics
Cracks
Lattice model
Particle model
Hybrid lattice particle model
Constitutive relations

ABSTRACT

This paper presents a numerical method, known as hybrid lattice particle modeling (HLPM), for the study of mode-I crack formation and propagation in two-dimensional geometry subject to a fixed-grip condition. The HLPM combines the strength of two numerical techniques, particle model (PM) and lattice model (LM), for the purpose of solving dynamic fragmentation of solids within a various Poisson's ratio range. A Lennard-Jones-type potential is employed to describe the nonlinear dynamic interaction of each macroscopic-size particle with its nearest-neighbors. Crack initiation and propagation is investigated for materials with different Young's modulus, tensile strength and varying ductility. It is demonstrated that crack patterns and propagation closely match the anticipated physical behavior of inelastic materials. Finally, the HLPM is applied to the investigation of a functionally designed composite material of an elastic–brittle infrastructure material coated with a ductile layer for the protection of fracture propagation. The ultimate application is aimed at the retrofitting of failing infrastructure.

© 2009 Elsevier Ltd. All rights reserved.

## 1. Introduction

Dynamic fracture is a complex and multi-scale physical phenomenon. From the microscopic point of view, fracturing is a process that material becomes separated due to the successive breakage of atomic bonds. Since the intrinsic strength properties at atomic structure level are available, molecular dynamics (MD) analysis has been the primary tool at the nano scale. Moreover, a discrete microscopic description in MD also allows defining local temperatures, potential energies, stress distributions and other quantities. These parameters present a precise physical meaning and are the key to understanding fracture. Thus, MD can provide a more fundamental insight into material behavior and its interactions. However, although MD simulation has benefitted from the rapid development of computing power and is becoming increasingly popular, the present state of computer technology is still far from being able to meet the demands of the macroscopic tasks. For example, we currently still cannot simulate a $1 \times 1 \times 1$ cm$^3$ cubic copper body at atomic level because the body consists of $10^{24}$ copper atoms, a number so large that no computer in the world can handle it. The second difficulty is its incapability in reaching the practical time scales. For instance, the laboratory dynamic fracture experiments generally last in microseconds (1 ms = $10^{-6}$ s), while the MD model time steps are typically in the nano ($10^{-9}$) or pico ($10^{-12}$) second range. As such, the MD is limited to a narrow range of solving nano- to micrometer scale problems. For this reason, a numerical tool for the modeling of dynamic fracture at macroscopic level is needed.

To successfully solve the dynamic fracture of materials at macroscopic level, it is critical if the model can deal with the uncertain evaluation of material body – large deformation or even fragmentation at a very high rate. In the other word, a successful dynamic fracture solver lies in an efficient solution of "re-meshing" in computation. The current numerical approaches for dynamic fracture simulation at macroscopic level can be generally classified into two categories – a continuum mechanics based approach (CMBA for short) and a discrete element based approach (DEBA for short). In brief, the CMBA is built up regarding the material body as one continuum media. Numerically, such models, e.g., finite element method (FEM), use space-averaging to set up constitutive equations within each element. In contrast, the DEBA shares a common concept of "discrete material", and the constitutive equations are assigned to define the interaction among the discrete neighbors. Examining the state-of-the-art of the research, we conclude that FEM, the most widely used CMBA, has difficulty in solving dynamic fracture problems, particularly in simulating collapse/fragmentation of materials under extreme loadings. Although FEM has constantly been developed to meet such requirements and several re-meshing techniques, i.e., Lagrange, Euler and Arbitrary Lagrange Euler, have been well established, fragmentation of materials is still unable to be well simulated. In contrast, the discrete element

* Corresponding author. Tel.: +1 662 915 5369; fax: +1 662 915 5523.
*E-mail address:* gewang@olemiss.edu (G. Wang).

0020-7683/$ - see front matter © 2009 Elsevier Ltd. All rights reserved.
doi:10.1016/j.ijsolstr.2009.08.001

based, or meshless, approach is robust in solving the re-meshing. Fig. 1 illustrates a material impact simulation by using FEM accounting for different re-meshing skills and by a meshless model, smoothed particle hydrodynamics (SPH) (Quan et al., 2003). It is clearly shown that the DEBA is superior to the CMBA in solving the fragmentation of materials; hence, it attracts increasing interests.

Particle modeling (PM) is the one among a number of the branches of DEBAs (Cundall, 1988; Meguro and Tagel-Din, 2000; Oñate et al., 2004; Monaghan, 2005). The PM was originally proposed by Greenspan (1997). In essence, PM, treating each computation cell as a particle with the mass lumped to its center, can be regarded as an upscale MD, but applied to large length scale and time scale problems. However, Greenspan (1997) developed such model with in mind more fluid modeling than solid modeling. As a consequence, there was no direct linkage to the solid material properties, making PM an empirical model without demonstrated validation with real engineering problems.

Lattice model (LM), on the other hand, has a long history of success in modeling micromechanics solid problems (Askar, 1985; Noor, 1988; Ostoja-Starzewski, 2002, 2007; Bolander and Sukumar, 2005; Berton and Bolander, 2006). The LM, however, does not have the flexibility of particle models, in which the particles can be subjected to very large deformation (displacement) and even fragmentation. Such limitation of LM comes from a fact of that it adopts a conjugate gradient method with respect to minimizing the total potential energy stored in all spring bonds to determine the displacement. Consequently, only one bond is allowed to fracture during each computational cycle (Alkhateb et al., 2009). Hence, the LM has so far been restricted to small motions. It is basically a *static/quasi-static* model, and does not model the *dynamic* fracture process. In Table 1, the strengths and weaknesses of the traditional LM and PM are summarized and compared.

To extend the capability of both LM and PM, and to allow the modeling of dynamic fracture and fragmentation of materials caused by impact, blasting and other extreme loadings, a hybrid lattice particle model (HLPM) has been developed based on Wang and Ostoja-Starzewski's PM (2005). As demonstrated in Table 1, the HLPM has been proposed that combines the strengths of LM and PM (Wang et al., 2009), in which the interaction potential can be described by employing either linear (quadratic) or nonlinear (Lennard-Jones or polynomial) type to the axial/angular linkage. The defined spring constants are then mapped into lattice system, which are in turn matched with the material's continuum-level elastic moduli and strength. The HLPM can readily simulate dynamic behaviors of materials at macro-scales with a varying Poisson's ratio range (Wang et al., 2009). The principle of HLPM can be described as follows: the particle–particle interaction is derived from lattice modeling (LM) theory whereas the computational scheme follows particle modeling (PM) technique. Once the translational strength is exceeded, the spring is broken and a fracture is created.

The advantages of HLPM over the existing discrete element based methods can be summarized as follows:

(1) Easy for the determination of input parameters. Four conservative/equivalent rules (mass, potential energy, Young's modulus and tensile/compression strength) are required to determine the material properties for the input datasheet.
(2) Easy for implementation. Since the physical size of each particle is ignored other than its equivalent mass, the algorithm of coding a HLPM computation is fairly easy.

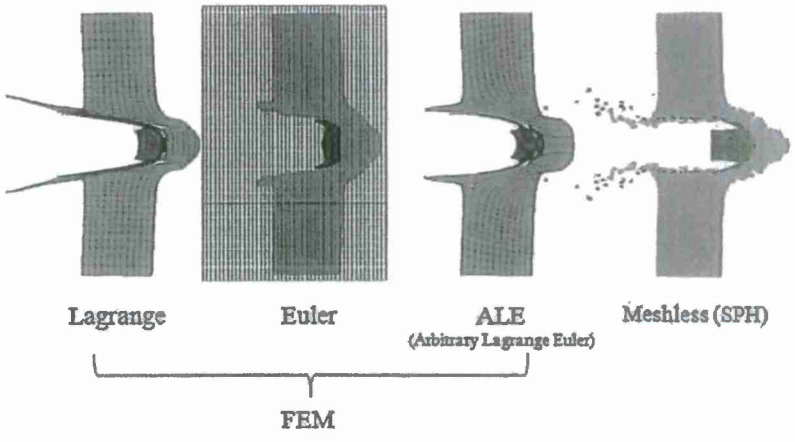


Fig. 1. A material impact simulation by using FEM accounting for different re-meshing skills, Lagrange, Euler and Arbitrary Lagrange Euler (ALE), and smoothed particle hydrodynamics (SPH) (Quan et al., 2003).

Table 1
Comparison of the lattice model (LM), the particle model (PM), and the hybrid lattice particle model (HLPM).

| | Lattice model (LM) | Particle model (PM) | Hybrid lattice particle model (HLPM) |
|---|---|---|---|
| Particle interaction | Spring (axial/angular), beam, etc. | Lennard-Jones potential (axial only) | Spring (axial/angular) mimicking the Lennard-Jones potential |
| Interaction neighborhood | Not limited to nearest neighbor | Nearest neighbor only | Not limited to nearest neighbor |
| Mesh system | Small deformation | Large deformation | Large deformation |
| Poisson's ratio | Flexible | Fixed | Flexible |
| Time process | Static | Dynamic based on Newton's second law | Dynamic based on Newton's second law |
| Force–displacement relation | Displacement (strain) interpreted from force (stress) | Force interpreted from displacement (distance between particles) | Force interpreted from displacement (distance between particles) |

A successful HLPM simulation have been achieved in predicting the fracture pattern of an epoxy plate with randomly distributed holes in tension, shown in Fig. 2(a) and (b) (Ostoja-Starzewski and Wang, 2006). Here is pointed out that, in the simulation, the Poisson's ratio of epoxy was set to 1/3. This is a special case of HLPM in which all the angular interactions are absent (Wang et al., 2009). As the figure illustrates, compared with the experimental observation, HLPM prediction of crack pattern seems more accurate than that of the FEM solution. Moreover, two successful qualitative comparisons currently have been completed with the dynamic failure experiments of polymeric material (nylon-6,6 and vinyl ester) indentation, shown in Fig. 3(a) and (b) (Wang et al., 2008a) and Fig. 4(a) and (b) (Wang, 2009), respectively.

After gaining the confidence of HLPM from the above-mentioned fracture study cases, in this paper, we step forward to investigate the modeling capability of the HLPM on the initiation and propagation of mode-I fracture in inelastic materials with different ductility employing a fixed-grip condition. As the mechanism for fracture formation and propagation in the lattice and the particle model is very different from that of the continuum mechanics based fracture mechanics model, it is not clear that the physical phenomenon of stable and unstable fracture growth can be correctly predicted. In short, the continuum model uses the stress intensity factor and energy release rate concepts for fracture creation and propagation; while the discrete HLPM uses the tensile/compression strength between bonds and the first principle based dynamic interaction among the particles. To have confidence in these models for simulating dynamic fracture problems, both numerical models need to be tested and validated.

In what follows, we first briefly introduce the HLPM algorithm. It is then applied to several two-dimensional dynamic fracture problems. Particularly, the stable and unstable fracture growth corresponding to the inelastic materials with varying ductility can be faithfully reproduced, using only the physically interpreted Lennard-Jones-type potential constants. Then, the HLPM is applied to the investigation of a functionally designed composite material of an elastic–brittle infrastructure material coated with a ductile layer for the protection of fracture propagation. The ultimate application is aimed at the retrofitting of failing infrastructure.

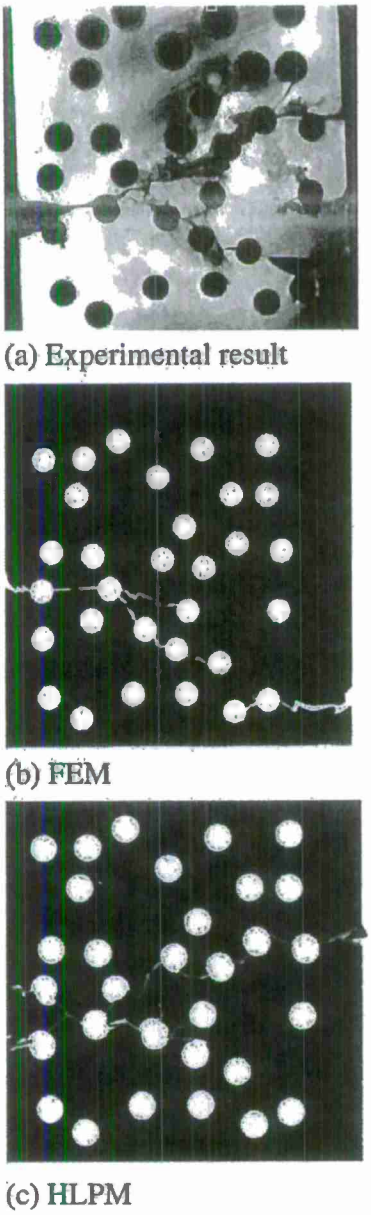


Fig. 2. Experimental and modeling results of epoxy in tension: (a) experiment (Al-Ostaz and Jasiuk, 1997) and (b) HLPM simulation (Ostoja-Starzewski and Wang, 2006).

## 2. Model description

The hybrid lattice particle model (HLPM) – also called lattice particle simulation, discrete modeling, or quasi-molecular modeling – is a dynamic simulation model that typically uses a relatively small number of particles of macroscopic sizes, representing solid and/or fluid mass. The particles' location and velocity evolves according to the laws of Newtonian mechanics. The axial force interaction between particles is modeled after Wang and Ostoja-Starzewski (2005) (reason: conventional LM only works for linear considerations), which is matched up with the Young's modulus and tensile strength of the material as well as energy and mass. The angular force interaction between the adjacent sides of each particle is after Wang et al. (2009). In principle, the distance of particle spacing can decrease to a few angstroms; in that case we recover a molecular dynamics like model. Hence the HLPM is fairly flexible in modeling physical phenomena of all sizes, limited only by the number of particles needed in the modeling (computational power).

The theoretical derivation of non-thermal-based HLPM can be briefly reviewed as follows.

In HLPM, the nonlinear axial interaction force between neighboring (quasi-) particles, $F$, can alternatively take the same form as in MD:

$$F = -\frac{G}{r^p} + \frac{H}{r^q} \tag{1}$$

Here $G$, $H$, $p$ and $q$ are positive constants, and $q > p \geqslant 1$ to obtain the repulsive effect that is necessarily (much) stronger than the attractive one, r being the distance between two particles.

Ashby and Jones (1980) presented a simple method to evaluate continuum-type Young's modulus $E$ and tensile stress $\sigma(r)$ of the material from $F(r)$, namely

$$E = \frac{S_0}{r_0} \tag{2}$$

and

$$\sigma(r) = NF(r) \tag{3}$$

where $S_0 = (dF/dr)_{r=r_0}$, and $r_0$ is the equilibrium spacing between contiguous particles. $N$ is the number of bonds/unit area, equal to $1/r_0^2$. Tensile strength, $\sigma_{TS}$, results when $dF(r_d)/dr = 0$, that yields,

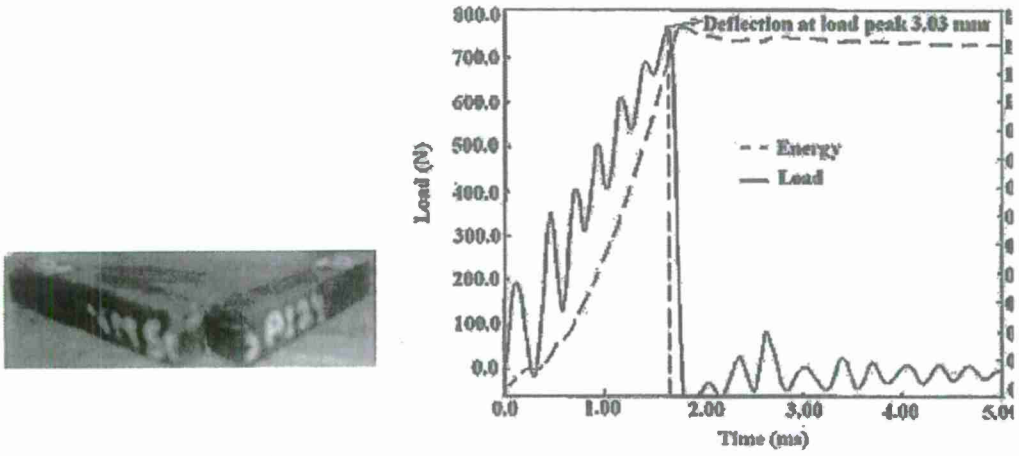


Fig. 3. The study of the failure of nylon-6,6 due to the impact of a rigid indenter (a) experimental results; (b) HLPM results. Maximum drop velocity of indenter is 1.87 m/s (Wang et al., 2008b).

$$\sigma_{TS} = NF(r_d) \tag{4}$$

Note that Eq. (2) has been demonstrated to be completely consistent with LM derivation (Wang et al., 2009).

Just as in MD, the nonlinear dynamical equation of motion for each particle $P_i$ of the PM system is given by

$$m_i \frac{d^2\vec{r}_i}{dt^2} = \sum_{j=1}^{K} \left[ \left( -\frac{G_i}{r_{ij}^p} + \frac{H_i}{r_{ij}^q} \right) \frac{\vec{r}_{ji}}{r_{ij}} \right], \quad i \neq j \tag{5}$$

where $m_i$ and $\vec{r}_{ji}$ are mass of $P_i$ and the vector from $P_j$ to $P_i$; $K$ is the total number of ambient particles interacting with particle $i$. In the present study, only the nearest neighboring particles are considered which is addressed by Wang and Ostoja-Starzewski (2005).

The derivation of four parameters in Eq. (1) from MD structures is conducted on a cubic body with volume $V(= A \times B \times C)$ (Wang and Ostoja-Starzewski, 2005). A face-centered cubic (fcc) lattice for both atomic and quasi-particle structures is chosen. If $p$, $q$ and $r_0$ are given, then, by conditions of mass and energy conservation, $G$ and $H$ can be derived. Consequently, Young's modulus is evaluated by Eq. (2) and tensile strength by Eq. (4). To represent an expected material property, we would have to do many sets of testing until a unique $(p, q)$ is found to match both Young's modulus and tensile strength of the material. The complete derivation process is described below.

First, for the atomic structure (MD model), we have:

Interaction potential energy (ergs):

$$\phi_a = \left( \frac{G_a r^{1-p_a}}{1-p_a} + \frac{H_a r^{1-q_a}}{1-q_a} \right) \times 10^{-8} \tag{6}$$

Young's modulus (GPa) is obtained from Eq. (2) and tensile strength (MPa) from Eq. (4).

Total number of atoms in $A \times B \times C$ cubic material body:

$$N^* = \left( \frac{A \times 10^8}{r_a} + 1 \right) \times \left( \frac{B \times 10^8}{r_a \sin 60^0} + 1 \right) \times \left( \frac{C \times 10^8}{r_a \sqrt{6}/3} + 1 \right) \tag{7}$$

In Eqs. (6) and (7), $r_a$ is equilibrium position of the simulated material in atomic structure, and $p_a, q_a$ are the exponential parameters in atomic structure. Note that, for a Lennard-Jones interaction case, $p_a = 7$ and $q_a = 13$.

Next, for the quasi-particle structure (PM model), we have interaction force (dynes) as in Eq. (1).

Interaction potential energy (ergs):

$$\phi = \frac{G_r^{1-p}}{1-p} + \frac{H_r^{1-q}}{1-q}, \text{ for } p > 1; \quad \phi = G \ln r + \frac{H_r^{1-q}}{1-q}, \text{ for } p = 1 \tag{8}$$

Total number of quasi-particles in PM system:

$$N = i_{max} \times j_{max} \times k_{max} \tag{9}$$

P-203

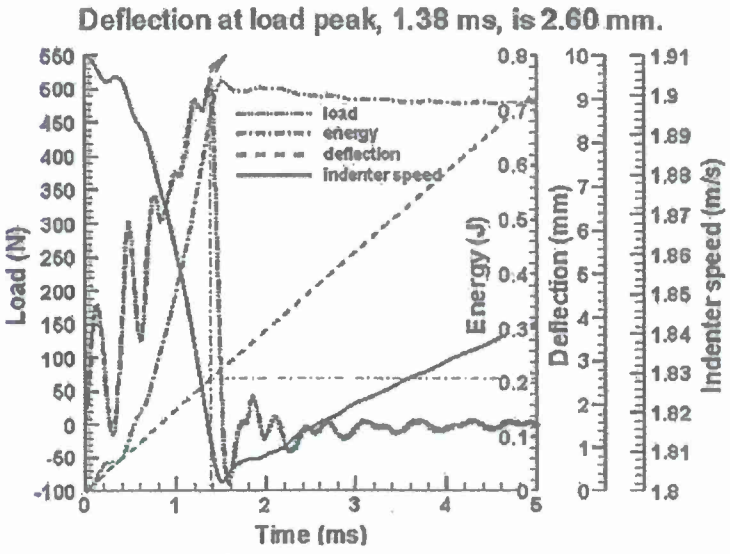


(a) Experimental observation

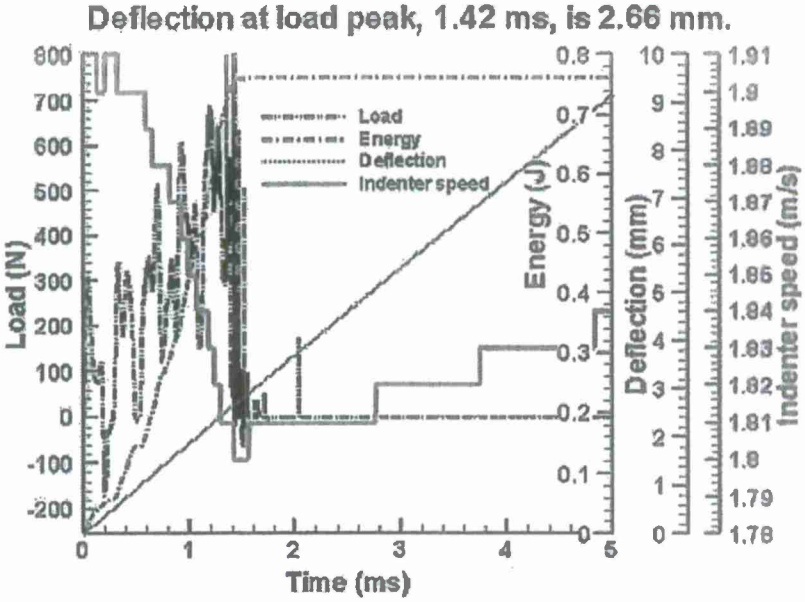


(b) HLPM simulation

**Fig. 4.** Comparison of HLPM result with the according experimental observation of the failure of vinyl ester due to the impact of a rigid indenter: (a) experimental observation and (b) HLPM simulation. Maximum drop velocity of indenter is 1.91 m/s.

We now postulate the equivalence of MD and PM models. From the mass conservation, we calculate the mass of each quasi-particle $m$ based on atomic mass $m_a$:

$$m = N^* \times m_a / N \tag{10}$$

From the energy conservation, we have:

$$(N \times \phi)_{r=r_0} = (N^* \times \phi_a)_{r=r_a} \tag{11}$$

Under the requirement:

$$F(r_0) = 0 \tag{12}$$

From Eqs. (11) and (12), we now derive Young's modulus $E$:

For $p = 1$:

$$G = Hr_a^{1-q}, \quad H = \frac{(N^* \times \phi_a)_{r=r_a}(1-q)}{N(1-q)r_0^{1-q}\ln r_0 - r_0^{1-q}}, \qquad E = -Gr_0^{-3} + qHr_0^{-q-2} \tag{13}$$

for $p > 1$:

$$G = Hr_a^{1-q}, \quad H = \frac{(N^* \times \phi_a)_{r=r_a}(1-p)(1-q)}{N(p-q)} r_0^{q-1}, \qquad E = -pGr_0^{-p-2} + qHr_0^{-q-2} \tag{14}$$

Similarly, tensile strength can be obtained under $dF(r_d)/dr = 0$. Evidently, the four parameters $(p, q)$, $r_0$ and $V$ affect $E$ and $\sigma_{TS}$.

We have established the equations for $G$, $H$, $p$ and $q$, and carried out a parametric study to find the differing effects on $p$, $q$, $V$ and $r_0$

(Wang and Ostoja-Starzewski, 2005). Herein, we summarize the obtained rules as follows:

(i) The larger the values of $(p, q)$ are adopted, the larger is $E$ generated. This is typically associated with the material becoming more brittle than ductile, albeit there is a range of toughness to choose from. Also, with $E$ going up, there is a fragmentation into a larger number of pieces.
(ii) In the case of $p = 1$, the larger $r_0$ spacing is adopted, the higher is Young's modulus of the PM material. On the contrary, in the special case of $p \neq 1$, there is an opposite trend. In any case, this increase or decrease does not change very much.
(iii) In the case of $p \neq 1$, while keeping the volume fixed, an increase of $r_0$ produces a decrease of Young's modulus. The situation is again opposite in the case of $p = 1$.
(iv) A uniform augmentation of volume $V$ by dilation in all three coordinate directions $(xyz)$, at any $(p, q)$ combination, results in Young's modulus increasing first strongly and then leveling off.

For elastic–brittle materials, a general format of linear dynamical equation is often employed for axial springs (Wang et al., 2008a),

$$F = \begin{cases} -S_0(r - r_0) & \text{for } r_c \leqslant r \leqslant r_t \\ 0 & \text{otherwise} \end{cases} \tag{15}$$

with $r$ being the distance between two particles, the axial stiffness $S_0 = E \cdot r_0$ by Eq. (2), $E$ the Young modulus and $r_0$ the equilibrium spacing between the contiguous particles.

In Eq. (15), $r_c$ and $r_t$ are the fracture positions applied for compression and tension, respectively, which in practice need to be empirically determined.

An analogous angular spring interaction scheme to Eq. (15) yields,

$$F_\beta = \begin{cases} -S_\varphi(\varphi - \varphi_0) & \text{for } \varphi_c \leqslant \varphi \leqslant \varphi_t \\ 0 & \text{otherwise} \end{cases} \tag{16}$$

with $\varphi_0$ the equilibrium angle between adjacent particles, and ce:italic>/ce:italic> the angular displacement. $\varphi_c$ and $\varphi_t$ in Eq. (16) are the angular fracture coefficients applied for compression and tension, respectively, which are also needed to be determined by empirical tests.

The angular stiffness $S_\varphi$ in Eq. (16) is after Wang et al. (2009),

$$S_\varphi = \frac{\sqrt{3}(1 - 3\nu)Er_0^2}{18(1 - \nu^2)} \tag{17}$$

with $\nu$ the Poisson's ratio.

The leapfrog method, with second-order accuracy, is employed in the HLPM simulations. The leapfrog formulas relating position, velocity and acceleration for particles $P_i$ $(i = 1, 2, \ldots, N)$ (Greenspan, 1997) are

$$\vec{V}_{i,1/2} = \vec{V}_{i,0} + \frac{(\Delta t)}{2}\vec{a}_{i,0} \quad \text{(starter formula)} \tag{18}$$

$$\vec{V}_{i,k+1/2} = \vec{V}_{i,k-1/2} + (\Delta t)\vec{a}_{i,k}, \quad k = 1, 2, 3, \ldots \tag{19}$$

$$\vec{r}_{i,k+1} = \vec{r}_{i,k} + (\Delta t)\vec{V}_{i,k+1/2}, \quad k = 0, 1, 2, \ldots \tag{20}$$

where $\vec{V}_{i,k}$, $\vec{a}_{i,k}$ and $\vec{r}_{i,k}$ are the velocity, acceleration and position vectors of particle $i$ at time $t_k = k\Delta t$, $\Delta t$ is the time step. $\vec{V}_{i,k+1/2}$ stands for the velocity of particle i at time $t_k = (k + 1/2)\Delta t$, and so on. Notably, the leapfrog method is of second-order accuracy: $O((\Delta t)^2)$.

The safe time step is after the derivation result by Hockney and Eastwood (1999):

$$\Omega\Delta t \ll 2, \quad \Omega = \left(\frac{1}{m}\left|\frac{dF}{dr}\right|_{\max}\right)^{1/2} \tag{21}$$

To readily describe the breakage effect on material, we define a concept of fracture density (Wang et al., 2008b). By this definition, the local fracture density of particle i, $f_{i_{\text{den.}}}$, is equal to the ratio of its current number of broken bonds, $N_{b_i}$ to its original number of bonds, $N_{o_i}$, i.e.,

$$f_{i_{\text{den.}}} = \frac{N_{b_i}}{N_{o_i}} \tag{22}$$

It is clearly seen that a big $f_{i_{\text{den.}}}$ value indicates a severe failure locally occurring at $i$.

Note that different failure criterion for inelastic and elastic materials shown in Eqs. (1) and (15) are employed as a cut-off for the axial interaction force. For instance, necking position, $dF(r_d)/dr = 0$, is adopted for inelastic material expressed in Eq. (1); for elastic–brittle material expressed in Eq. (15), using tensile stress, $\sigma_{TS}$, from Hooke's law, we determine the failure strain $\varepsilon_{\max}$

$$\frac{r_{\max} - r_0}{r_0} = \varepsilon_{\max} = \frac{\sigma_{TS}}{E} \tag{23}$$

and the displacement threshold for fracture to occur, $r_{\max}$.

Angular failure criterion follows the analogous scheme to Eq. (22) whereas shear strength is accounted for.

## 3. Results

In this section we first report a preliminary HLPM study of crack formation and propagation in a 2D, end-notched plate, subjected to a constant uniaxial tensile loading. The computational domain is a 2D 3.46 cm × 64 cm plate with an initial particle spacing $r_0 = 0.2$ cm, and a crack of length $l_0 = 0.8$ cm at the very left end; see Fig. 5. A fixed-grip condition with a constant vertical stretching rate $V = 40.0$ cm/s is applied to the two ends in the $Y$ direction. We assign $(p, q) = (3, 5), (5, 10)$ and $(7, 14)$ in Eq. (1) for three different inelastic materials. Table 2 illustrates the physical outcomes by using these three $(p, q)$ values under equilibrium lattice spacing $r_0 = 0.2$ cm. Fig. 6 displays the according interaction force profile vs. the three above-employed $(p, q)$ values. For simplicity, we assume the Poisson's ratios of the three materials are all equal to 1/3. Consequently, the angular spring effect is absent (Wang et al., 2009).

Table 2 illustrates that with the increase of $(p, q)$, the Young's modulus and tensile strength values of the resultant material also increase. So does the necking position of the interaction force pro-

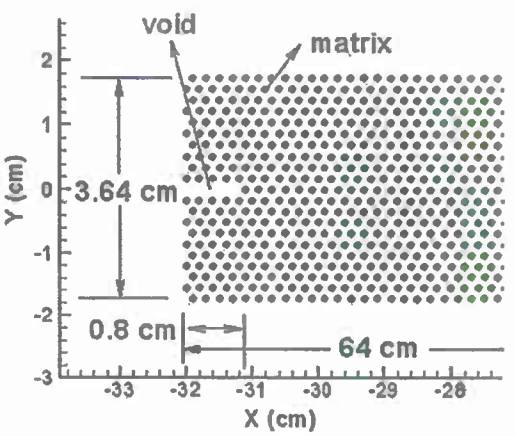


Fig. 5. Schematic of computational domain setup for a 2D plate with an initial crack. Particle spacing $r_0 = 0.2$ cm.

Table 2
Physical outcomes with $(p,q) = (3,5), (5,10)$ and $(7,14)$ under equilibrium lattice spacing $r_0 = 0.2$ cm.

| $(p,q)$ | (3,5) | (5,10) | (7,14) |
|---|---|---|---|
| $G$ | $2.473 \times 10^7$ | $1.781 \times 10^6$ | $1.102 \times 10^5$ |
| $H$ | $9.892 \times 10^5$ | $5.698 \times 10^2$ | 1.411 |
| $E$ (GPa) | 15.457 | 69.557 | 150.706 |
| $\sigma_{TS}$ (MN/m$^2$) | 86.205 | 263.570 | 441.534 |
| Necking position | $1.29 \cdot r_0$ | $1.15 \cdot r_0$ | $1.11 \cdot r_0$ |

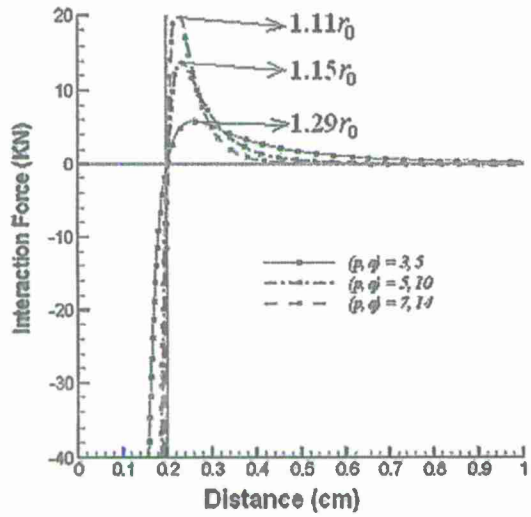


Fig. 6. Interaction force of HLPM under $r_0 = 0.2$ cm, with $(p,q) = (3,5), (5,10)$ and $(7,14)$.

file shown in Fig. 6 as well as in Table 2. This indicates that the material with big $(p,q)$ behave in low ductility and vice versa. Among these three materials indicated by the associated $(p,q)$, if we label $(p,q) = (3,5)$ as a ductile one (with high ductility), then $(p,q) = (5,10)$ and $(7,14)$ are in order labeled comparatively more brittle ones (with low ductility).

Fig. 7 shows the different stages of the crack propagation, from the initial crack formation, to the propagation, and to the final crack pattern, for the material, $(p,q) = (3,5)$, with high ductility. Figs. 8 and 9 show, respectively, the similar stages for $(p,q) = (5,10), (7,14)$, with comparatively low ductility.

Comparing Figs. 7–9, we observe:

(i) Crack develops sooner and propagates faster in material with low ductility (Fig. 8) than in material with high ductility (Fig. 7).
(ii) For low-ductility material, crack propagation tends to behave in an unstable manner by taking a zigzag path with varying speed (Figs. 8 and 9(c)). For high-ductility material, we observe a largely steady state growth with a smooth path (Fig. 7(c)).

Fig. 10 shows a zoomed section of the plate during the propagation stage, for comparatively the most brittle case among the three ones with $(p,q) = (7,14)$. It is observed that there are micro-cracks forming in a region ahead of the main crack (marked by circle and ellipses), attracting the main crack toward it, thus creating a zigzag path. This phenomenon was indeed observed in brittle-like materials, and not in ductile-like materials (Abraham, 1997). Fracture of this type is called a brittle fracture. We observe that the HLPM can truthfully capture this delicate phenomenon by simply prescribing a Lennard-Jones-type potential that corresponds to brittle materials. Hence the HLPM can serve an important function of correctly modeling the time dependent ductile and brittle crack propagation.

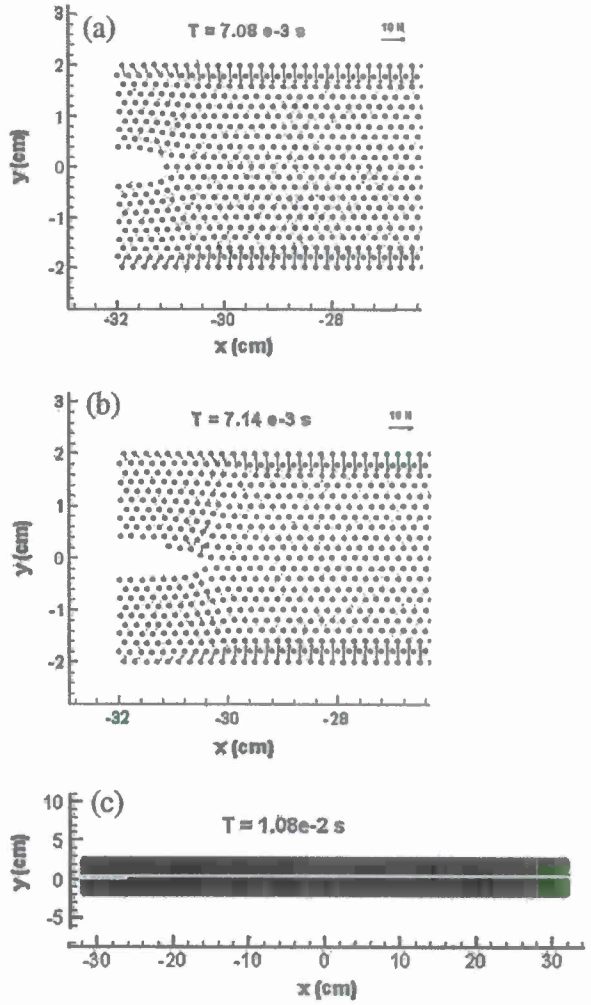


Fig. 7. Time-dependent fracture propagation of 2D plate with an initial crack, for ductile, $(p,q) = (5,10)$. Stretching rate = 40 cm/s. (a) $t = 7.08$ ms, (b) $t = 7.14$ ms, and (c) final crack pattern.

Next, we apply the HLPM to the investigation of some structure retrofitting ideas. First, we investigate an elastic–brittle beam subject to a point load at mid-span, with the two ends supported with permission of horizontal movement. The load is actually applied as a downward displacement at the constant rate of 50 cm/s. The two-dimensional beam is of the dimension 12.7 cm in length and 1.27 in thickness, with material properties corresponding to Young's modulus 3.0 GPa, and tensile strength 60 MPa. The dynamic interaction follows linear elastic formulas as described in Eq. (15). In Fig. 10, we present the deformation of the beam at $t = 5.6$ ms. We observe that the failure happens in the form of a zigzag fracture below the point load. The HLPM simulated crack pattern seems to agree well with the similar simulation by Cusatis and Cedolin (2006).

To investigate the retrofitting schemes, we protect the main structure as shown in Fig. 11 by a high-ductility material either on top, or at bottom of the beam, as shown in Fig. 12(a) and (b). The high-ductility material is characterized by $(p,q) = (3,5)$, which corresponds to $(E, \sigma_{TS}) = (15.5$ GPa,86.2 MPa), and a necking position equal to $r_d = 1.29 r_0$, see Fig. 5. The thickness of this ductile material is 0.3 cm. Applying the same loading condition, we demonstrate the result of simulation in Fig. 13(a) and (b).

Fig. 13(a) and (b) shows the result with the retrofitted layer on the top and at the bottom, at $t = 5.6$ ms. From Fig. 13(a), we

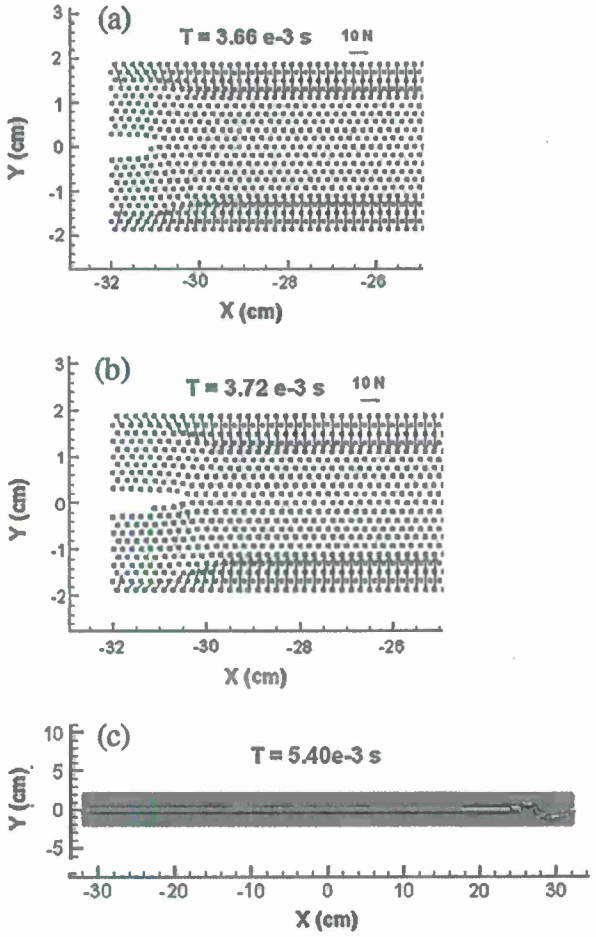


Fig. 8. Time-dependent fracture propagation of 2D plate with an initial crack, for ductile, $(p,q) = (5,10)$. Stretching rate = 40 cm/s. (a) $t = 3.66$ ms, (b) $t = 3.72$ ms, and (c) final crack pattern.

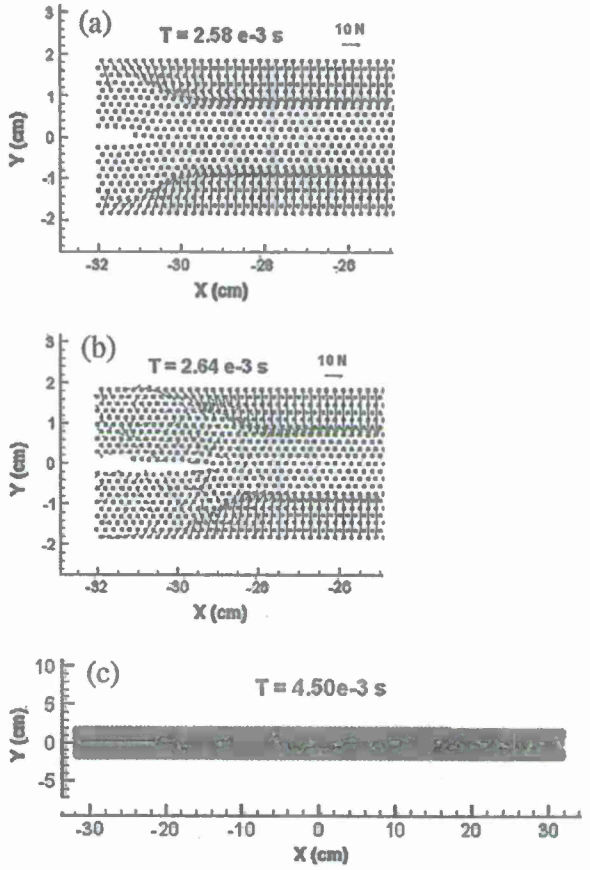


Fig. 9. Time-dependent fracture propagation of 2D plate with an initial crack, for brittle material, $(p,q) = (7,14)$. Stretching rate = 40 cm/s. (a) $t = 2.58$ ms, (b) $t = 2.64$ ms, and (c) final crack pattern.

observe that the vertical crack propagates upward toward the retrofitted layer, and is arrested without penetration. At the same time, the material starts to delaminate with interfacial crack propagating along the material interface; from Fig. 13(b), we observe an extended damaged area, in the form of a wedge, underneath the load, and also some delamination along the material interface. Viewing the two retrofitted simulation results in Fig. 13(a) and (b), we see that the infrastructure is fractured in each case under the action of the point-load; however, the entire integral structure is well sustained. Comparing the two retrofitting schemes, from the resultant minimum deflection in the mid-top of the structure, we conclude that putting the retrofitted material at the bottom works better.

## 4. Concluding remarks

In this paper, a hybrid lattice particle modeling (HLPM) method is employed for a study of crack formation and propagation in mode-I for a 2D end-notched plate subject to a fixed grip condition of a constant vertical uniaxial tensile loading. Different inelastic material properties, in terms of Young's modulus, tensile strength and also with varying ductility, are accounted for with the plate. From this study, the following benefits are obtained.

In the model capability aspect, the advantages of HLPM over the existing classical mechanics tools, such as finite element method (FEM), can be outlined as follows:

(1) No need for remeshing. Remishing is known as an overwhelming challenge for FEM whereas HLPM does not at all. In HLPM, fracture is created when a bond (spring) is broken by translational force. This provides HLPM a unique power to be able to quite easily overcome a "discontinuity of material" problem.
(2) No stress intensity required. In HLPM, a bond (spring) is broken and fracture is thus resulted wherever the critical failure strain reaches.
(3) HLPM can capture more realistic crack propagation. In this paper, we see that HLPM can capture micro-cracks appearing away from the main-crack path while the fracture develops in brittle materials or metals, whereas the continuum mechanics based models rarely report.

In the aspect of the problem explored itself, it is found that crack patterns and propagation is under strong influence of material constants. The obtained results can be outlined as follows:

(1) Crack develops sooner and propagates faster in low-ductility (brittle-like) materials than in high-ductility (ductile-like) materials.
(2) Crack propagation tends to behave in an unstable manner in low-ductility materials while in a steady fashion in high-ductility materials.

Following from the above-obtained results, we then apply the HLPM to the investigation of some structure retrofitting ideas.

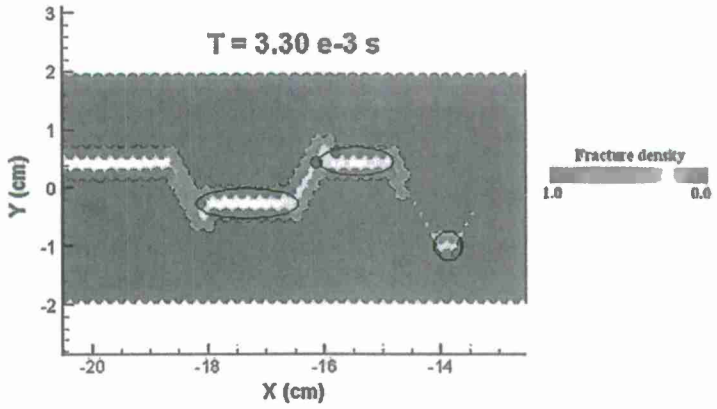


Fig. 10. Zooming of a HLPM simulated fracture during the propagation stage, at $t = 3.3$ ms, for brittle material, $(p, q) = (7, 14)$.

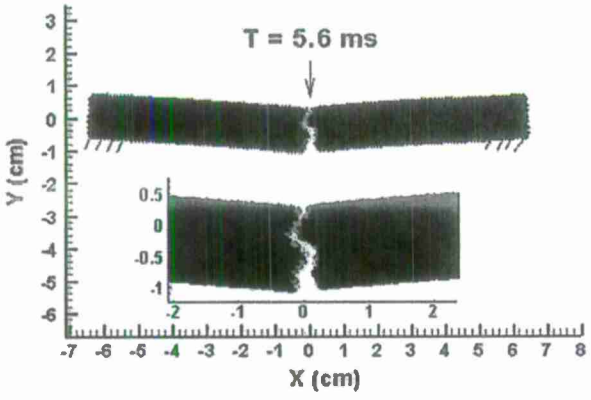


Fig. 11. HLPM simulation of failure of an elastic–brittle beam subject to a constant rate deformation at mid-span. Deformation rate = 50 cm/s. $t = 5.6$ ms.

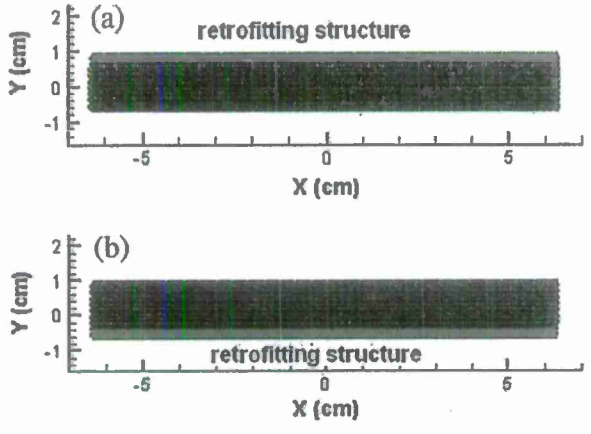


Fig. 12. An elastic–brittle plate coated with nonlinear ductile material: (a) retrofitted layer on the top and (b) retrofitted layer at the bottom.

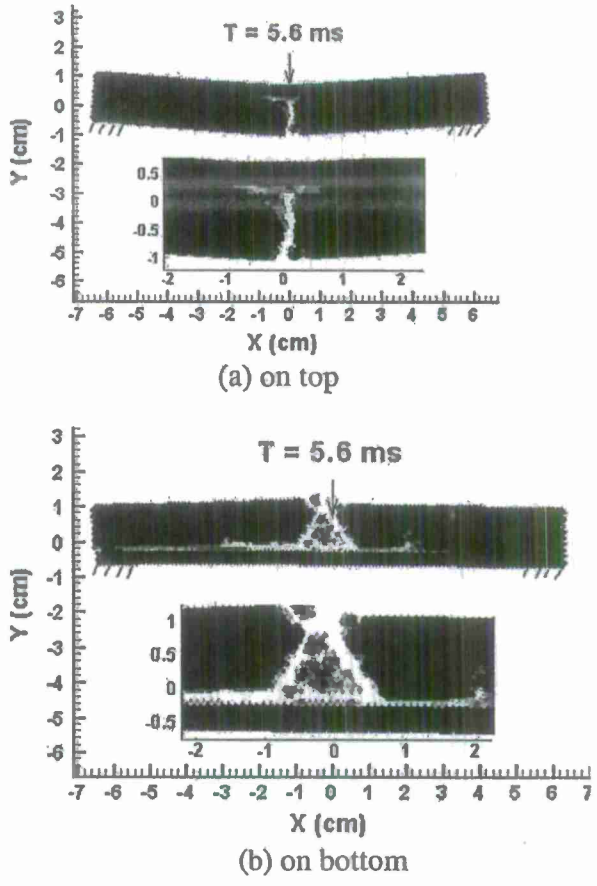


Fig. 13. HLPM simulated failure of an elastic–brittle plate coated with retrofitting material on top and at bottom, and subjected to a constant rate deformation at mid-span, (a) on top and (b) at bottom. Deformation rate = 50 cm/s. $t = 5.6$ ms.

We select putting a retrofitted material layer on the top and at the bottom of the infrastructure to find out a better protective effect. We conclude that integral structure with retrofitted material at the bottom produces a minimum deflection when subject to a point-load in the mid-span. The significance of this research may help guide to fabricate a high-resistance retrofitting layered structure optimally comprised of different materials. This fabricated enforcement structure is then coated to the infrastructure to effectively improve the performance of the retrofitting of failing infrastructure. In this paper, merely a preliminary simulation is attempted to identify the validation of this idea. We will report the detailed research progress of this topic in a separate paper.

## Acknowledgments

This work was partially supported by the funding received under a subcontract from the Department of Homeland Security-sponsored Southeast Region Research Initiative (SERRI) at the

Department of Energy's Oak Ridge National Laboratory, USA. The authors acknowledge the partial support for this research by ONR Grant No. N00014-07-1-1010, Office of Naval Research, Solid Mechanics Program (Dr. Yapa D.S. Rajapakse, Program Manager).

## References

Abraham, F.F., 1997. Some New Directions in Science on Computers. World Scientific, Singapore, pp. 91–113.
Alkhateb, H., Al-Ostaz, A., Alzebdeh, K.I., 2009. Developing a stochastic model to predict the strength and crack path of random composites. Composites B 40, 7–16.
Al-Ostaz, A., Jasiuk, I., 1997. Crack initiation and propagation in materials with randomly distributed holes. Engineering Fracture Mechanics 58, 395–420.
Ashby, M.F., Jones, D.R.H., 1980. Engineering Materials 1: An Introduction to Their Properties and Applications. Pergamon Press, Oxford.
Askar, A., 1985. Lattice Dynamical Foundations of Continuum Theories. World Scientific, Singapore.
Berton, S., Bolander, J.E., 2006. Crack band model of fracture in irregular lattices. Computer Methods in Applied Mechanics and Engineering 195, 7172–7181.
Berton, S., Bolander, J.E., 2006. Crack band model of fracture in irregular lattices. Computer Methods in Applied Mechanics and Engineering 195, 7172–7181.
Bolander, J.E., Sukumar, N., 2005. Irregular lattice model for quasi-static crack propagation. Physical Reviews B 71, 094106.
Cundall, P.A., 1988. Computer simulations of dense sphere assemblies. Micromechanics of Granular Materials, 113–123.
Cusatis, G., Cedolin, L., 2006. Two-scale study of concrete fracturing behavior. Engineering Fracture Mechanics 74, 3–17.
Greenspan, D., 1997. Particle Modeling. Birkhäuser Publishing, Basel.
Hockney, R.W., Eastwood, J.W., 1999. Computer Simulation Using Particles. Institute of Physics Publishing.
Meguro, M., Tagel-Din, H., 2000. Applied element method for structural analysis: theory and application for linear materials. Structural Engineering/Earthquake Engineering, JSCE 17 (1), 1–14.
Monaghan, J., 2005. Smoothed particle hydrodynamics. Reports on Progress in Physics 68 (1), 1703–1759.
Noor, A.K., 1988. Continuum modeling for repetitive lattice structures. Applied Mechanics in Reviews 41 (7), 285–296.
Oñate, E., Idelsohn, S.R., Pin, F.D., Aubry, R., 2004. The particle finite element method: an overview. International Journal Computational Method 1 (2), 267–307.
Ostoja-Starzewski, M., 2002. Lattice models in micromechanics. Applied Mechanics in Reviews 55 (1), 35–60.
Ostoja-Starzewski, M., 2007. Microstructural randomness and scaling in mechanics of materials. In: Modern Mechanics and Mathematics Series. Chapman & Hall/CRC Press/Taylor & Francis, London/Boca Raton, FL/London.
Ostoja-Starzewski, M., Wang, G., 2006. Particle modeling of random crack patterns in epoxy plates. Probabilistic Engineering Mechanics 21, 267–275.
Quan, X., Birnbaum, N.K., Cowler, M.S., Gerber, B.I., Clegg, R.A., Hayhurst, C.J., 2003. Numerical simulation of structural deformation under shock and impact loads using a coupled multi-solver approach. In: 5th Asia-Pacific Conference on Shock and Impact Loads on Structures, November 12–14, Human, China.
Wang, G., 2009. Particle modeling of polymeric material indentation study. Engineering Fracture Mechanics 76, 1386–1395.
Wang, G., Ostoja-Starzewski, M., 2005. Particle modeling of dynamic fragmentation – I: theoretical considerations. Computational Materials Science 33, 429–442.
Wang, G., Al-Ostaz, A., Cheng, A.H.-D., Mantena, P.R., 2008a. Particle modeling of a polymeric material (nylon-6,6) due to the impact of a rigid indenter. Computational Materials Science 44, 449–463.
Wang, G., Radziszewski, P., Ouellet, J., 2008b. Particle modeling simulation of thermal effects on ore breakage. Computational Materials Science 43, 892–901.
Wang, G., Al-Ostaz, A., Cheng, A.H.-D., Mantena, P.R., 2009. Hybrid lattice particle modeling: theoretical considerations for a 2-D elastic spring network for dynamic fracture simulations. Computational Materials Science 44, 1126–1134.

Comput. Methods Appl. Mech. Engrg. 199 (2009) 197–209

Contents lists available at ScienceDirect

Comput. Methods Appl. Mech. Engrg.

journal homepage: www.elsevier.com/locate/cma

# Hybrid lattice particle modeling of wave propagation induced fracture of solids

G. Wang [a,*], A. Al-Ostaz [a], A.H.-D. Cheng [a], P.R. Mantena [b]

[a] Department of Civil Engineering, University of Mississippi, University, MS 38677, United States
[b] Department of Mechanical Engineering, University of Mississippi, University, MS 38677, United States

ARTICLE INFO

*Article history:*
Received 13 July 2009
Received in revised form 2 October 2009
Accepted 6 October 2009
Available online 13 October 2009

*Keywords:*
Hybrid lattice particle modeling
Dynamic fracture
Wave propagation
Homogenous materials
Spall crack
Blast

ABSTRACT

This paper presents a discrete dynamic fracture model, hybrid lattice particle modeling (HLPM), and its applications in the wave propagation induced fracture problems of solids. The HLPM is established based on a combination of the first author's prior particle modeling (PM) technique with the conventional lattice modeling (LM) theory. The HLPM has the robustness of simulating the dynamic fragmentation of solids under high strain rate loadings at macro-scales with a varying Poisson's ratio. In this paper, first, the wave propagation in 1D and 2D homogenous materials with HLPM is modeled and the obtained results are validated by a comparison with the analytical solutions; then, two HLPM simulations of the wave propagation induced fracture, spall cracks, due to hyper-velocity impact and blasting, are completed. In the impact case, spall crack formation due to hyper-velocity impact is captured, and the HLPM results are in good agreement with the analogous molecular dynamics (MD) simulations by Krivtsov (1999) [27,28]. Moreover, a functionally designed infrastructure material coated with a high strength layer, but with different coating strengths at the interface, is also investigated to find out the protective effect of material from spallation. The modeling results demonstrate that prevention of a material from spallation under extreme loadings is difficult; it needs the coating material with a super strength. In the blasting study, the fracturing efficiency associated with different spatial explosive setup is investigated. This will benefit the explosive fracturing applications.

© 2009 Elsevier B.V. All rights reserved.

## 1. Introduction

Dynamic fracture and fragmentation under high strain rate loads (impact, blasting, crush, collapse, high speed puncture/penetration, comminution, etc.) has broad civilian/military applications, among which the explosive related applications, seismological studies, shock synthesis and ballistic impacts are currently the most challenging areas to the numerical models. In the above-listed areas, the wave propagation dominates the formation and evolution of the dynamic fracture pattern, and the fragments, e.g., spall cracks, are often induced by the internal wave interactions. Thus, a good model is required not only to be able to correctly predict wave but also the consequent induced fracture.

Static or quasi-static models have existed for several decades and successfully been used for micromechanics and macromechanics structure analysis. However, they fail to become a tool for dynamic fracture of solids. The reason arises from the fundamental differences between static (or quasi-static) and dynamic deformation. In a quasi-static deformation, at any time, a situation of static equilibrium holds, which implies that any element in the material body has a summation of forces acting on it close to zero. In contrast, in a dynamic deformation, when a high strain rate loading is applied to the boundary of the body, the stress propagates, that is, the stress has to travel through the body. This is called wave propagation, usually measured by Hopkinson bar test [1]. Thus, dynamic deformation often involves wave propagation. Consequently, a sequence of states of equilibrium defined by the well-known equations of mechanics of materials (summation of forces equal to zero, summation of moments equal to zero, compatibility of strain, constitutive relations, etc.) are no longer valid. In hyper-velocity impact and blast explorations, wave propagation of solids is the key to understand the resultant fracture and fragments. Moreover, wave propagation study can provide important outcomes for fracture control which has remarkable significance to engineering applications.

Current continuum mechanics based models (CMBM for short), e.g., a finite element method (FEM), can indeed accurately solve the wave propagation of solids even in case of large deformation. However, they limit to fracture/fragmentation. In principle, the FEM regards material as one continuum media, and constitutive equations are space-averagely applied within each element; hence, once the continuity of material is broken due to the presence of fracture or fragmentation, re-meshing is required for the next cycle of computation. When a material body is subject to extreme loadings, unexpected fragments are often produced. Herein, this offers

* Corresponding author. Tel.: +1 662 915 1975; fax: +1 662 915 5523.
*E-mail address:* gewang@olemiss.edu (G. Wang).

0045-7825/$ - see front matter © 2009 Elsevier B.V. All rights reserved.
doi:10.1016/j.cma.2009.10.002

FEM an extreme challenge in technique to deal with the dynamic re-meshing, and causes the computation highly expensive. Although FEM has constantly been developed to meet such requirements and several re-meshing techniques (i.e., Lagrange, Euler and Arbitrary Lagrange Euler) [2], and some hybrid sophisticated methods [3] have been well established and embedded into FEM, it still cannot simulate multi-cracks of materials, let alone fragmentation problems. Fig. 1 displays the comparison of using FEM and smoothed particle hydrodynamics (SPH), a discrete element based method (DEBM for short) [4], in simulating material penetration [2]. It is seen that, although the FEM employs powerful re-meshing techniques, the fragmentation of material is still not able to be predicted. Meanwhile, it illustrates that the DEBM is superior to the CMBM in solving the fragmentation of materials. As such, discrete element based methods (DEBM), e.g., SPH, particle flow code (PFC) [5], applied element method [6], particle modeling (PM) [7,8], and the further developed hybrid lattice particle modeling (HLPM) [9], have been established at a macroscopic level. DEBM is established based on treating material as an assemblage of mass particles. The constitutive equations are assigned to define the interactions among the discrete neighboring particles. Consequently, DEBM does not suffer from either the mesh tangling problem encountered when using Lagrangian mesh or the material flux conservation problem when using Eulerian mesh. This leads to DEBM unique robustness to solve the 'discontinuity of material' problems. Due to the irreplaceable superiority of DEBM to CMBM in solving the fragmentation of materials, the 'discrete material' concept is becoming more and more widely accepted by engineering fields, and the market for DEBM applications is increasingly growing. This gives rise to a more prosperous DEBM modeling research in this decade. Meanwhile, there are newly developed models that couple DEBM with CMBM, e.g., particle finite element method (PFEM) [10] and material point method (MPM) [11], in which the deformation is solved using CMBM while the fracture/fragmentation relies on DEBM. Since DEBM is the core in fracture/fragmentation simulations, to improve/develop techniques of various DEBMs is of significant importance and valuable.

All the current DEBMs can be classified into two categories: mesh free (or meshless) and lattice particle models. For example, SPH, PFC and their inherited subclass of methods are mesh free models since the computations do not rely on a meshing system. In contrast, the confinement-shear lattice model (CSLM for short) [12,13], PM and HLPM are lattice particle models since the simulations are carried out on a lattice structure. In lattice particle models, the neighborhood of each particle needs to be pre-defined, and the consequent evolution of deformation, fracture or fragmentation at each fracturing stage can be readily identified and predicted with the pre-defined neighborhood.

In the domain of meshless models, PFC and SPH are the two most notable techniques. Many new developed meshless models and the according hybrid CMBM–DEBM techniques originate from these two models. However, viewing from the current technological status of meshfree models, they are, in general, far less complete in technique. This imperfection partially arises from a fact of that the dynamic fracture mechanics model study is still at a quite fundamental stage, and partially from the technique limits inherently from each individual model which can be summarized as follows:

(1) In PFC and its inherited subclass of developed methods, each particle's size is physically accounted for, e.g., circular discs or spheres used for 2D or 3D, respectively. In summary, three disadvantages of PFC are obvious: (i) particle packing causes porosity of material. It is obviously not suitable for compact materials; (ii) material's Poisson's ratio cannot be related to the pattern of the packed particles; and (iii) expensive computation is spent in keeping track of the instantaneous contact positions and the evolving geometry of all elements.

(2) In SPH, a kernel density function, or weight function, is employed to define for each particle a reaction domain, and continuum constitutive equations are then applied to the particles within the domain. In the recent years, several new techniques have been established to modify the kernel function to improve the computation accuracy. These new techniques are element-free Galerkin method (EFGM) [14], reproducing kernel particle method (RKPM) [15] and partition of unity method (PUM) [16,17]. As was mentioned by Belytschko et al. [18], in most cases, these approaches are identical. Since the SPH was developed with in mind more fluid modeling than solid modeling, therefore, although SPH and its inherited subclass of developed techniques are in a good process of development, two fatal disadvantages inherently from the model is not easy to get rid of: (i) for solids, pre-fracture particle–particle interactions are different from the failed, while they are no difference in fluids. For instance, a blend of two separate parts of fluid follows the same constitutive equations, whereas a mixture of two separate solid parts does not follows the same interactive formulas as one integrated body applies. Consequently, post-fracture interaction of solids cannot be readily traced since the kernel density function cannot distinguish if the

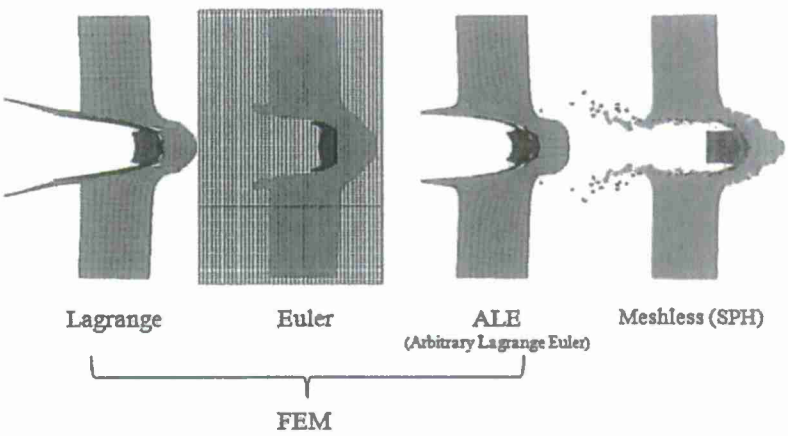


Fig. 1. A material impact simulation by using FEM accounting for different re-meshing skills, Lagrange, Euler and Arbitrary Lagrange Euler (ALE), and smoothed particle hydrodynamics (SPH) [2].

Q-211

Table 1
Comparison of the lattice model (LM), the particle model (PM) and the hybrid lattice particle model (HLPM).

| | Lattice model (LM) | Particle model (PM) | Hybrid lattice particle model (HLPM) |
|---|---|---|---|
| Particle interaction | Spring (axial/angular), beam, etc. | Leonard-Jones potential (axial only) | Spring (axial/angular) mimicking the Leonard-Jones potential |
| Interaction neighborhood | Not limited to nearest neighbor | Nearest neighbor only | Not limited to nearest neighbor |
| Mesh system | Small deformation | Large deformation | Large deformation |
| Poisson's ratio | Flexible | Fixed | Flexible |
| Time process | Static | Dynamic based on Newton's second law | Dynamic based on Newton's second law |
| Force–displacement relation | Displacement (strain) interpreted from force (stress) | Force interpreted from displacement (distance between particles) | Force interpreted from displacement (distance between particles) |

particles are pre-fractured or failed; and (ii) high expensive in computation. SPH is a time-consuming technique while the other meshless derivatives are more expensive [18].

Compared with the meshless techniques, dynamic lattice techniques are currently far less paid an attention and less developed, however, they are promising to be a more robust tool due to their unique advantages.

Cusatis's confinement-shear lattice model (CSLM) [12,13] conducted on a Delaunay triangulation mesh has demonstrated its ability in fracture predictions. However, the CSLM validations have so far been accomplished with quasi-static cases, ignoring the inertia term, rather than with high strain rate loadings. Else, the complex meshing technique in the model undoubtedly leads to a high expense in computations and limits it to the post-fracture applications.

Hybrid lattice particle modeling (HLPM) [9] has been proposed that combines the strengths of lattice model (LM) [19] and PM [8], in which the interaction potentials can be described by employing either linear (quadratic) or non-linear (Leonard-Jones or strain rate dependent polynomial) type to the axial/angular linkage. The defined spring constants are then mapped into lattice system, which are in turn matched with the material's continuum-level elastic moduli, strength and Poisson's ratio. Axial ($\alpha$-model) and axial–angular ($\alpha$–$\beta$-model) models have been developed together with considering triangular or rectangular lattice and various particle–particle interactions (nearest and two-layer neighboring). The theoretical derivations of different considerations associated with material's properties have been well addressed by Wang et al. [9].

The HLPM can readily simulate dynamic behaviors/fragmentation of materials at macro-scales with a varying Poisson's ratio. For instance, assigning the same $\alpha$ and $\beta$ to the axial and angular springs in 2D works for the Poisson's ratio ranging from $(-1,1/3]$ [9]; whereas for the Poisson's ratio ranging from [1/3,1), a 'triple honeycomb lattice' method ($\alpha$–$\beta$–$\gamma$-model) is provided [19]. The HLPM study of materials with a varying Poisson's ratio will be presented in the authors' another paper. Moreover, the HLPM can also efficiently solve a 'mesh bias' and 'lattice interpenetration problem' that bothers conventional LM [7,20]. The principle of HLPM can be described as follows: the particle–particle interaction is derived from lattice modeling (LM) theory, whereas the computational scheme follows the particle modeling (PM) technique. Once the translational strength is exceeded, the spring is broken and a fracture is created. The strength of HLPM over the traditional LM and PM is summarized and compared in Table 1.

The advantages of HLPM over the other existing DEBMs can be summarized as follows:

(1) Easy for the determination of input parameters. Five conservative/equivalent rules (mass, potential energy, Young's modulus, tensile/compression strength and Poisson's ratio) are required to determine the material's properties for the input datasheet.
(2) Easy for implementation and high computation efficiency. Since the physical size of each particle is ignored other than its equivalent mass, the algorithm of coding a HLPM computation is fairly easy; meanwhile, since no computation is spent in keeping track of the instantaneous contact positions and the evolving geometry of all elements, the HLPM computing cost is greatly reduced.
(3) Easy for tracing the post-fracture interactions. In HLPM, a pre-defined neighborhood in a lattice structure represents the integrated and non-fractured body of material. Any fractured member will change this originally defined neighborhood, and be defined with a different interaction rule from the non-fractured. Consequently, interactions among fragments can be readily and accurately predicted.
(4) A multi-scale model. In the case of lattice spacing decreasing to a few angstroms, we will recover a molecular dynamics (MD) model at zero Kelvin with, say, a Leonard-Jones potential. This implies that HLPM is an upscaled MD and can be flexibly applied to various length scale problems, if a proper equivalent macroscopic potential is provided.

Since its establishment, a successful HLPM simulation has been firstly achieved in predicting the fracture pattern of an epoxy plate with randomly distributed holes in tension, shown in Fig. 2a–c [21]. Here is pointed out that, in the simulation, the Poisson's ratio of epoxy was set to 1/3. This is a special case of HLPM in which all the angular interactions are absent [9]. As the figure illustrates, compared with the experimental observation, the HLPM prediction of crack pattern seems more accurate than that of the FEM solution. Moreover, two successful quantitative comparisons have been completed with the dynamic failure experiments of polymeric material (nylon-6,6 and vinyl ester) indentation, shown in Fig. 3a and b [20] and Fig. 4a and b [22], respectively.

A 3D HLPM has been built up, and a preliminarily quantitative comparison has recently been completed with the punch-shear experiment of a vinyl ester platelet under a low-velocity impact, 3.55 m/s. Fig. 5a and b shows the corresponding result comparisons. It is seen that the observed puncture area and shape on the specimen is similar to that of the HLPM prediction. Although the simulated load profile has a visual difference from the experiment, we observe similar characteristics, including the fluctuating profile with roughly the same tendency. Especially, the comparison is satisfactory at the *damage initiation stage* – from the moment of impact to the point of peak load, with the measured load peak equal to 10,000.0 N happening around a deflection of 2.1 mm while the two according HLPM results are 12,800.0 N vs. 1.6 mm. However, the HLPM underpredicts the duration of *puncture propagation stage* – from the point of peak load (puncture initiation) to the zero load point (puncture completion), and overpredicts the duration and magnitude of *post-puncture shear stage* – dominated by the shear effect of the available puncture peripheral surface of the specimen and the plunger surface.

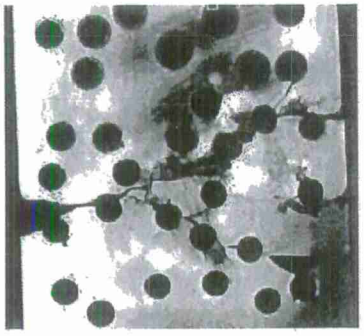

(a) Experimental result

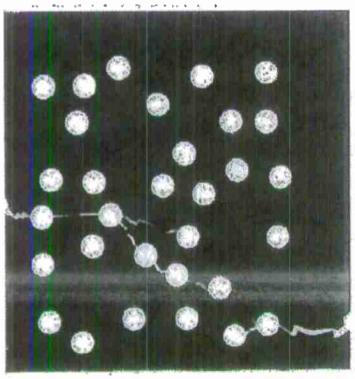

(b) FEM

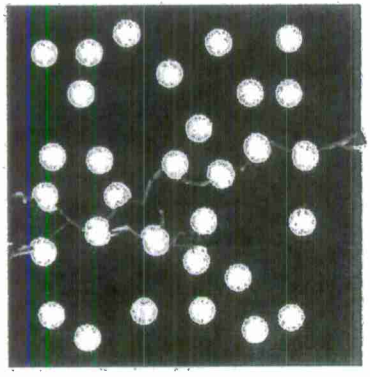

(c) HLPM

**Fig. 2.** Experimental and modeling results of epoxy in tension [21].

The above-mentioned discrepancies may come from two major factors. First, the 3D HLPM simulation shown here still employs the same contact method as in [20,22], in which a rigid plunger is assumed, and the particles interfacing with the plunger surface are assumed to be pushed away in the direction normal to plunger surface. This is a completely non-slip contact assumption. To improve the accuracy of HLPM at the *damage initiation stage*, a partial-slip contact mode may help. For the *puncture propagation stage* and the *post-puncture shear stage*, where the hinging effects of attached fragments with the surface of the plunger, the shear effect of the available puncture peripheral surface of the specimen and the plunger surface are dominant, our post-fractured particle-to-particle interaction scheme needs to be improved. It is well known that the post-failure simulations of material is currently a highly complex and challenging area. We will report our post-failure simulation progress in our future paper.

Nevertheless, we can conclude that the 3D HLPM can well predict the punch-shear process of a vinyl ester platelet, especially the damage initiation stage.

After gaining the confidence of HLPM from the above-mentioned fracture study cases, in this paper, we step forward to investigating the modeling capability of the HLPM on the wave propagation induced fracture problems. As the wave propagation in the lattice and the particle model (spring connections) is somewhat different from that of the continuum media, it is not clear if the physical phenomenon of wave propagation can be correctly predicted. Thus, to have confidence in HLPM model for simulating wave dominated problems, it needs to be tested and validated.

In what follows, we first briefly introduce the HLPM algorithm. It is then applied to one- and two-dimensional wave propagation problems. The obtained HLPM results are verified with the analytical solutions. Next, the HLPM is applied to the simulation of wave propagation induced fracture, spall cracks, due to hyper-velocity impact and blasting. In the impact case, a functionally designed infrastructure material coated with a high strength layer, but with different coating strengths at the interface, is also investigated to find out the protective effect of material from spallation. The ultimate application for HLPM is aimed at exploring shock synthesis.

## 2. Model description

The hybrid lattice particle model (HLPM)—also called lattice particle simulation, discrete modeling, or quasi-molecular modeling—is a dynamic simulation model that typically uses a relatively small number of particles of macroscopic sizes, representing solid and/or fluid mass. The particles' location and velocity evolves according to the laws of Newtonian mechanics. The axial force interaction between particles is modeled after Wang et al. [9], which is matched up with the Young's modulus and tensile strength of the material as well as energy and mass. The angular force interaction between the adjacent sides of each particle is modeled after Wang et al. [9], which is matched up with the Poisson's ratio of the material. The iterative calculating process is after Wang and Ostoja-Starzewski [8]. In principle, the distance of particle spacing can decrease to a few angstroms; in that case we recover a molecular dynamics like model. Hence the HLPM is fairly flexible in modeling physical phenomena of all sizes, limited only by the number of particles needed in the modeling (computational power).

The theoretical derivation of non-thermal-based HLPM can be briefly reviewed as follows.

In HLPM, the non-linear axial interaction force between neighboring (quasi-) particles, $F$, can alternatively take the same form as in MD:

$$F = -\frac{G}{r^p} + \frac{H}{r^q}. \tag{1}$$

Here $G$, $H$, $p$ and $q$ are positive constants, and $q > p \geqslant 1$ to obtain the repulsive effect that is necessarily (much) stronger than the attractive one, $r$ being the distance between two particles.

Ashby and Jones [23] presented a simple method to evaluate continuum-type Young's modulus $E$ and tensile stress $\sigma(r)$ of the material from $F(r)$, namely,

$$E = \frac{S_0}{r_0} \tag{2}$$

and

$$\sigma(r) = NF(r), \tag{3}$$

where $S_0 = (dF/dr)_{r=r_0}$, and $r_0$ is the equilibrium spacing between contiguous particles. $N$ is the number of bonds/unit area, equal to $1/r_0^2$. Tensile strength, $\sigma_{TS}$, results when $dF(r_d)/dr = 0$, that yields,

$$\sigma_{TS} = NF(r_d). \tag{4}$$

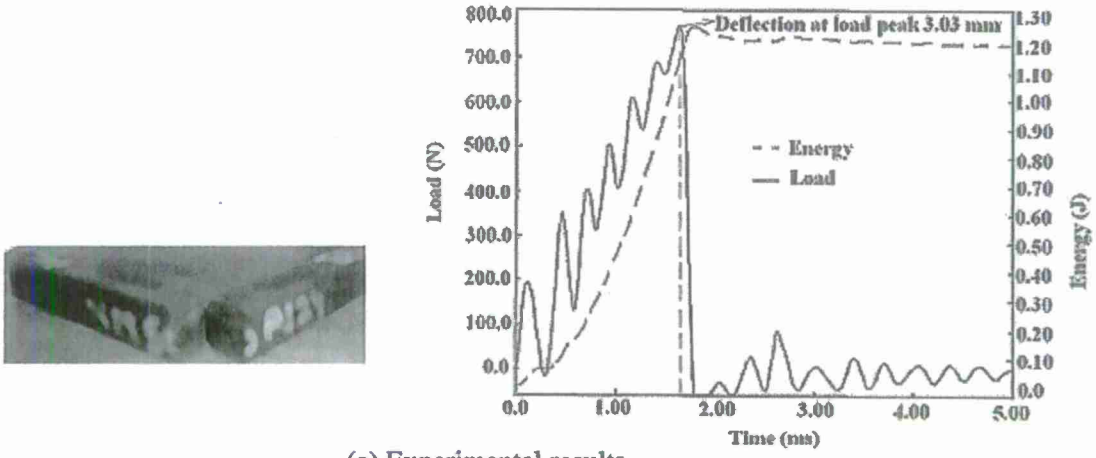


(a) Experimental results

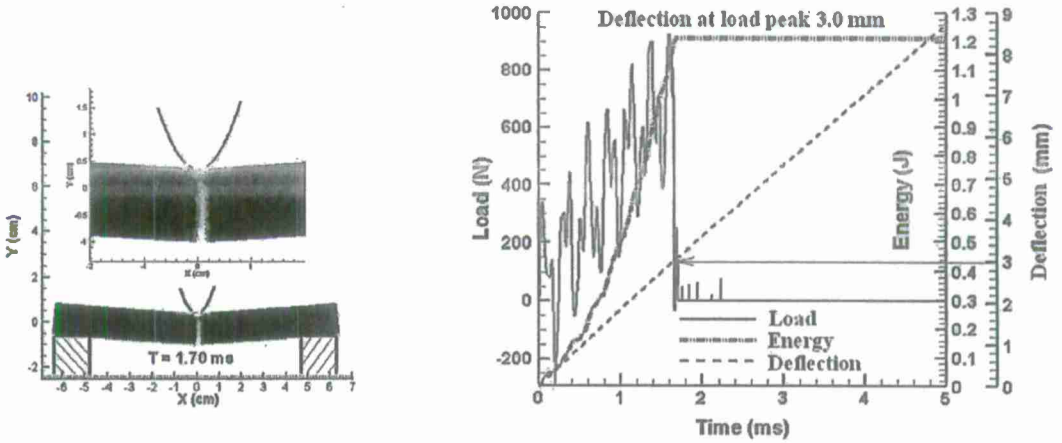


(b) HLPM results

**Fig. 3.** The study of the failure of nylon-6,6 due to the impact of a rigid indenter. Maximum drop velocity of indenter is 1.87 m/s [20].

Note that Eq. (2) has been demonstrated to be completely consistent with LM derivation [9].

Just as in MD, the non-linear dynamical equation of motion for each particle $P_i$ of the PM system is given by

$$m_i \frac{d^2 \vec{r}_i}{dt^2} = \sum \left[ \left( -\frac{G_i}{r_{ij}^p} + \frac{H_i}{r_{ij}^q} \right) \frac{\vec{r}_{ji}}{r_{ij}} \right], \quad i \neq j, \tag{5}$$

where $m_i$ and $\vec{r}_{ji}$ are mass of $P_i$ and the vector from $P_j$ to $P_i$; $K$ is the total number of ambient particles interacting with particle $i$. In the present study, only the nearest neighboring particles are considered which is addressed by Wang and Ostoja-Starzewski [8].

The derivation of four parameters in Eq. (1) from MD structures is conducted on a cubic body [8]. A face-centered cubic (f.c.c.) lattice for both atomic and quasi-particle structures is chosen. If $p$, $q$ and $r_0$ are given, then, by conditions of mass and energy conservation, $G$ and $H$ can be derived. Consequently, Young's modulus is evaluated by Eq. (2) and tensile strength by Eq. (4). To represent an expected material property, we would have to do many sets of testing until a unique $(p, q)$ is found to match both Young's modulus and tensile strength of the material. The complete derivation process is described below.

First, for the atomic structure (MD model), we have:Interaction potential energy (*ergs*):

$$\phi_a = \left( \frac{G_a r^{1-p_a}}{1-p_a} + \frac{H_a r^{1-q_a}}{1-q_a} \right) \times 10^{-8}. \tag{6}$$

Young's modulus (GPa) is obtained from Eq. (2) and tensile strength (MPa) from Eq. (4).

Total number of atoms in $A \times B \times C$ cubic material body:

$$N^* = \left( \frac{A \times 10^8}{r_a} + 1 \right) \times \left( \frac{B \times 10^8}{r_a \sin 60^\circ} + 1 \right) \times \left( \frac{C \times 10^8}{r_a \sqrt{6}/3} + 1 \right). \tag{7}$$

In Eqs. (6) and (7), $r_a$ is equilibrium position of the simulated material in atomic structure, and $p_a$, $q_a$ are the exponential parameters in atomic structure. Note that, for a Leonard-Jones interaction case, $p_a = 7$ and $q_a = 13$.

Next, for the quasi-particle structure (PM model), we have interaction force (dynes) as in Eq. (1).

Interaction potential energy (*ergs*):

$$\phi = \frac{G_r^{1-p}}{1-p} + \frac{H_r^{1-q}}{1-q}, \text{ for } p > 1; \quad \phi = G \ln r + \frac{H_r^{1-q}}{1-q}, \text{ for } p = 1. \tag{8}$$

Total number of quasi-particles in PM system:

$$N = i_{\max} \times j_{\max} \times k_{\max}. \tag{9}$$

We now postulate the equivalence of MD and PM models. From the mass conservation, we calculate the mass of each quasi-particle $m$ based on atomic mass $m_a$:

$$m = N^* \times m_a / N. \tag{10}$$

Q-214

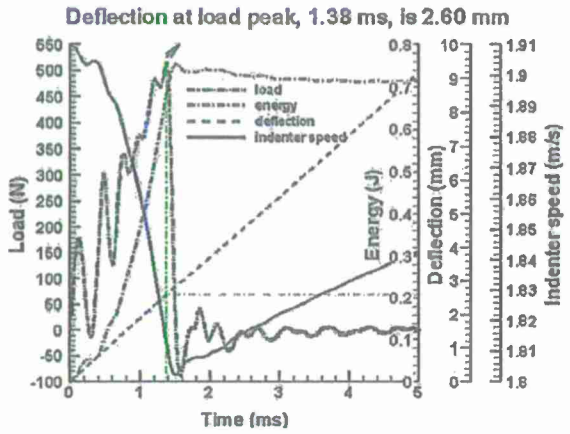


(a) Experimental observation

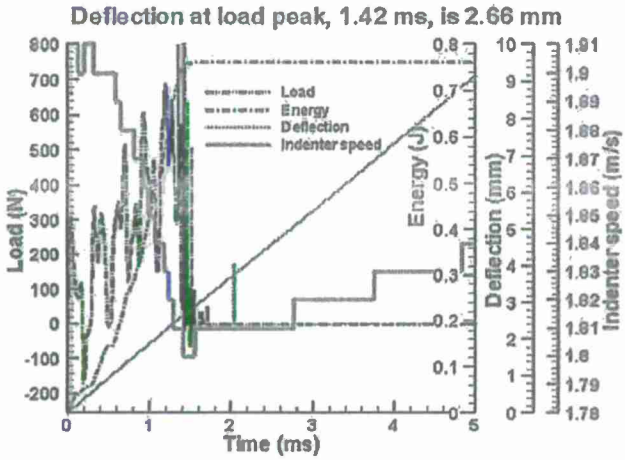


(b) HLPM simulation

Fig. 4. Comparison of HLPM result with the according experimental observation of the failure of vinyl ester due to the impact of a rigid indenter. Maximum drop velocity of indenter is 1.91 m/s [22].

From the energy conservation, we have:

$$(N \times \phi)_{r=r_0} = (N^* \times \phi_a)_{r=r_a}, \tag{11}$$

under the requirement:

$$F(r_0) = 0. \tag{12}$$

From Eqs. (11) and (12), we now derive Young's modulus $E$:

For $p = 1$:

$$G = Hr_0^{1-q}, \quad H = \frac{(N^* \times \phi_a)_{r=r_a}(1-q)}{N(1-q)r_0^{1-q}\ln r_0 - r_0^{1-q}},$$
$$E = -Gr_0^{-3} + qHr_0^{-q-2}. \tag{13}$$

For $p > 1$:

$$G = Hr_0^{1-q}, \quad H = \frac{(N^* \times \phi_a)_{r=r_a}(1-p)(1-q)}{N(p-q)}r_0^{q-1},$$
$$E = -pGr_0^{-p-2} + qHr_0^{-q-2}. \tag{14}$$

Similarly, tensile strength can be obtained under $dF(r_d)/dr = 0$. Evidently, the four parameters $(p,q)$, $r_0$ and $V$ affect $E$ and $\sigma_{TS}$.

We have established the equations for $G$, $H$, $p$ and $q$, and carried out a parametric study to find the differing effects on $p$, $q$, $V$ and $r_0$ [8]. Herein, we summarize the obtained rules as follows:

(i) The larger the values of $(p,q)$ are adopted, the larger is $E$ generated. This is typically associated with the material becoming more brittle than ductile, albeit there is a range of toughness to choose from. Also, with $E$ going up, there is a fragmentation into a larger number of pieces.

(ii) In the case of $p = 1$, the larger $r_0$ spacing is adopted, the higher is Young's modulus of the PM material. On the contrary, in the special case of $p \neq 1$, there is an opposite trend. In any case, this increase or decrease does not change very much.

(iii) In the case of $p \neq 1$, while keeping the volume fixed, an increase of $r_0$ produces a decrease of Young's modulus. The situation is again opposite in the case of $p = 1$.

(iv) A uniform augmentation of volume $V$ by dilation in all three coordinate directions $(xyz)$, at any $(p,q)$ combination, results in Young's modulus increasing first strongly and then leveling off.

For elastic-brittle materials, a general format of linear dynamical equation is often employed for axial springs [20],

$$F = \begin{cases} -S_0(r - r_0) & \text{for } r_c \leqslant r \leqslant r_t, \\ 0 & \text{otherwise} \end{cases} \tag{15}$$

with $r$ being the distance between two particles. Following the derivation rules in lattice models addressed in [9], we get the axial stiffness for 1D and 2D structure are $S_0 = E \cdot r_0/2$ and $E \cdot r_0$, respectively. $E$ the Young modulus and $r_0$ the equilibrium spacing between the contiguous particles.

In Eq. (14), $r_c$ and $r_t$ are the fracture positions applied for compression and tension, respectively, which in practice need to be empirically determined.

An analogous angular spring interaction scheme to Eq. (14) yields,

$$F_\beta = \begin{cases} -S_\varphi(\varphi - \varphi_0) & \text{for } \varphi_c \leqslant \varphi \leqslant \varphi_t, \\ 0 & \text{otherwise} \end{cases} \tag{16}$$

with $\varphi_0$ the equilibrium angle between adjacent particles, and $\varphi$ the angular displacement. $\varphi_c$ and $\varphi_t$ in Eq. (16) are the angular fracture coefficients applied for compression and tension, respectively, which are also needed to be determined by empirical tests.

The 2D angular stiffness $S_\varphi$ in Eq. (16) is after Wang et al. [9],

$$S_\varphi = \frac{\sqrt{3}(1-3\nu)Er_0^2}{18(1-\nu^2)} \tag{17}$$

with $\nu$ the Poisson's ratio.

The leapfrog method, with second-order accuracy, is employed in the HLPM simulations. The leapfrog formulas relating position, velocity and acceleration for particles $P_i$ $(i = 1,2,\ldots,N)$ [24] are

$$\vec{V}_{i,1/2} = \vec{V}_{i,0} + \frac{(\Delta t)}{2}\vec{a}_{i,0} \quad \text{(starter formula)}, \tag{18}$$

$$\vec{V}_{i,k+1/2} = \vec{V}_{i,k-1/2} + (\Delta t)\vec{a}_{i,k}, \quad k = 1,2,3,\ldots, \tag{19}$$

$$\vec{r}_{i,k+1} = \vec{r}_{i,k} + (\Delta t)\vec{V}_{i,k+1/2}, \quad k = 0,1,2,\ldots, \tag{20}$$

where $\vec{V}_{i,k}$, $\vec{a}_{i,k}$ and $\vec{r}_{i,k}$ are the velocity, acceleration and position vectors of particle $i$ at time $t_k = k\Delta t$, $\Delta t$ is the time step. $\vec{V}_{i,k+1/2}$ stands for the velocity of particle $i$ at time $t_k = (k+1/2)\Delta t$, and so on. Notably, the leapfrog method is of second-order accuracy: $O((\Delta t)^2)$.

The safe time step is after the derivation result by Hockney and Eastwood [24]:

$$\Omega \Delta t \ll 2, \quad \Omega = \left(\frac{1}{m}\left|\frac{dF}{dr}\right|_{\max}\right)^{1/2}. \tag{21}$$

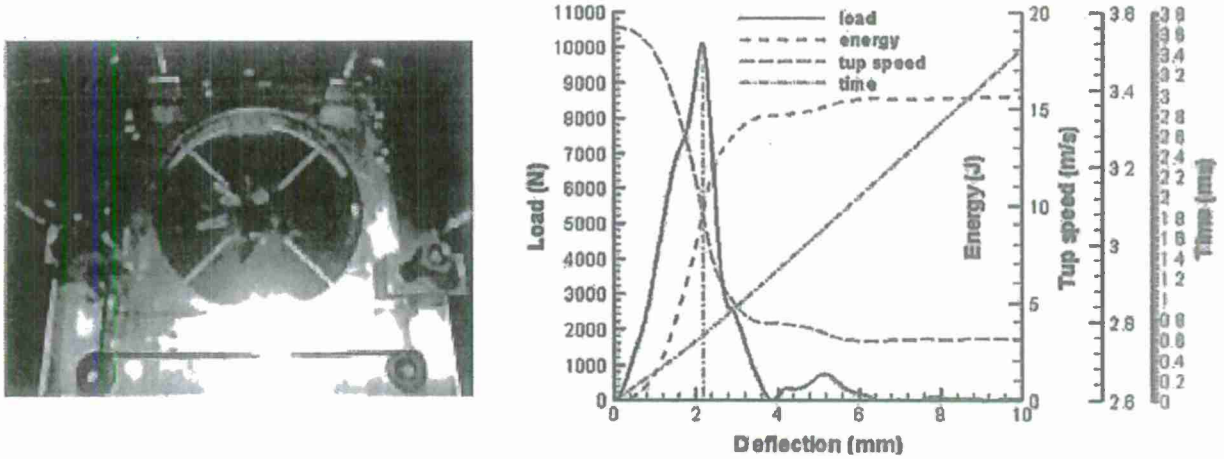


(a) Experimental results

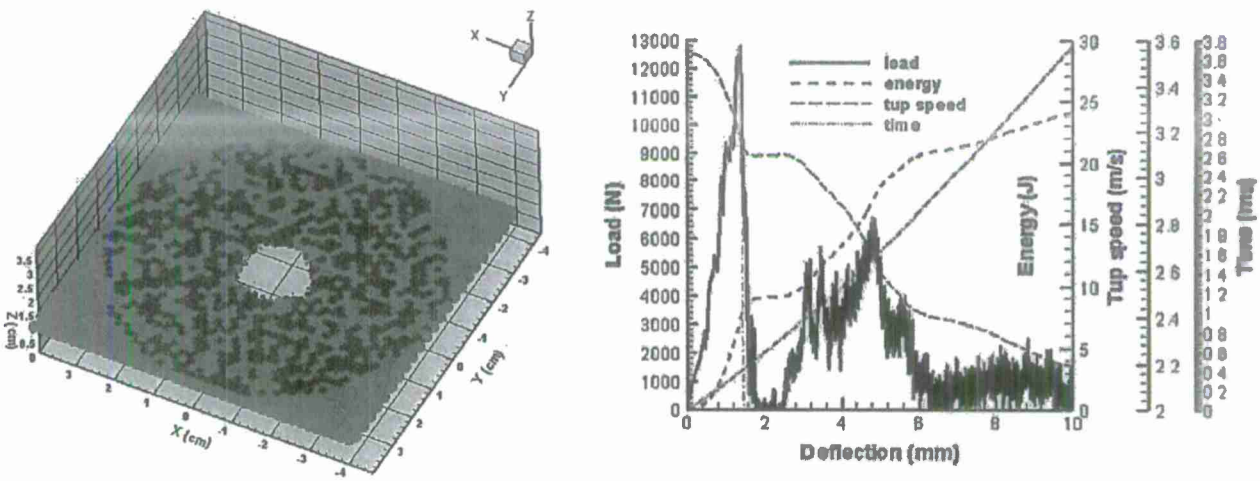


(b) 3D HLPM results

Fig. 5. The study of 3D punch-shear of vinyl ester. Maximum drop velocity of indenter is 3.55 m/s.

It is noted that the discretized scheme and deterministic time increment of HLPM as shown by Eqs. (18)–(21) is completely identical to what is used by PFC [5] and PFEM [10].

To readily describe the breakage effect on material, we define a concept of fracture density [25]. By this definition, the local fracture density of particle $i$, $f_{i_{den.}}$, is equal to the ratio of its current number of broken bonds, $N_{b_i}$ to its original number of bonds, $N_{o_i}$, i.e.,

$$f_{i_{den.}} = \frac{N_{b_i}}{N_{o_i}}. \tag{22}$$

It is clearly seen that a big $f_{i_{den.}}$ value indicates a severe failure locally occurring at $i$.

Note that different failure criterion for inelastic and elastic materials shown in Eqs. (1) and (15) are employed as a cut-off for the axial interaction force. For instance, necking position, $dF(r_d)/dr = 0$, is adopted for inelastic material expressed in Eq. (1); for elastic-brittle material expressed in Eq. (15), using tensile stress, $\sigma_{TS}$, from Hooke's law, we determine the failure strain $\varepsilon_{max}$:

$$\frac{r_{max} - r_0}{r_0} = \varepsilon_{max} = \frac{\sigma_{TS}}{E} \tag{23}$$

and the displacement threshold for fracture to occur, $r_{max}$.

Angular failure criterion follows the analogous scheme to Eq. (22), whereas shear strength is accounted for.

## 3. Results

### 3.1. HLPM prediction of wave propagation in 1D and 2D elastic-brittle material

In this section, we report a preliminary HLPM study of wave propagation in a 1D and 2D elastic-brittle bar, subjected to dynamic and kinematic loads, respectively. The computational domain for 1D and 2D are $L = 12.7$ cm in length (one layer of particles) and 12.7 cm × 1.27 cm (15 layers of particles), respectively, with an Initial particle spacing $r_0 = 0.1$ cm; two points are selected at $L/4$ and $L/2$ away from the left end for calculating the wave propagation speed. Dynamic and kinematic conditions are, respectively, applied to the left end at 97.8 MPa and constantly 60.0 m/s; the right end Is fixed and the remaining boundaries are traction free, shown in Fig. 6a and b. The material parameters are: Young's modulus $E = 3.0$ GPa, density $\rho = 1140$ kg/m$^3$, and failure strain $\varepsilon_{max} = 0.02$. For a simplicity, we assume that the Poisson's ratio of the material is equal to 1/3. Consequently, the angular

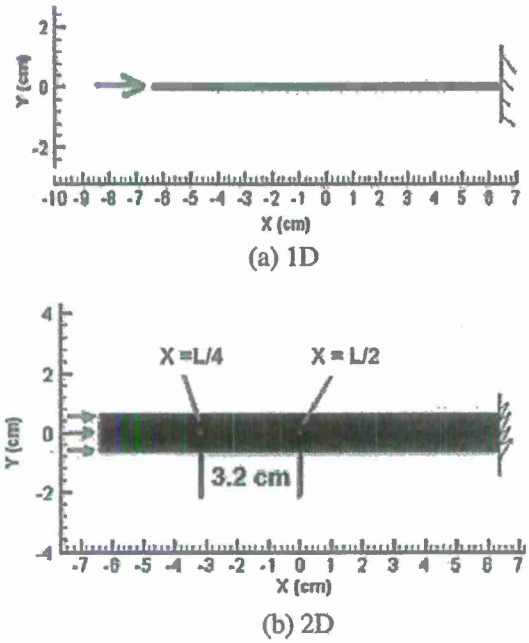


Fig. 6. Schematic of computational domain setup for (a) 1D and (b) 2D. Particle spacing $r_0 = 0.2$ cm.

spring effect is absent [9], and only the axial interaction is accounted for and determined after Eq. (15).

The classical wave theory gives that the wave propagation speeds in the above-mentioned 1D and 2D material bars are, respectively [26],

$$1D: \quad C_{p(1D)} = \sqrt{E/\rho} \approx 1622.0 \text{ m/s}, \tag{24}$$

$$2D: \quad C_{p(2D)} = \sqrt{(K + 4G/3)/\rho} \approx 1986.0 \text{ m/s} \tag{25}$$

with $K$ and $G$ the bulk and shear modulus, respectively.

*3.1.1. Dynamic boundary condition*

A dynamic boundary condition with 97.8 MPa is applied to the left end of 1D and 2D bar, respectively. Fig. 7 displays the HLPM results of the horizontal displacement for 1D and 2D at $X = L/2$. From Fig. 7a it is seen that the wave propagation profiles of 1D and 2D are different from each other due to the existing difference of wave propagation speed in 1D from in 2D structure; however, each profile of the two predictions is analogous to the Hopkinson bar test [1]. Via Fig. 7b, we can calculate that the horizontal wave speed values travelling in the 1D and 2D bar are equal to 1455.0 and 2133.0 m/s, respectively. These results indicate that, the 1D simulation result is smaller than the analytical solution, 1622.0 m/s, while the 2D result is bigger than the analytical value, 1986.0 m/s. The reason for the existing discrepancies is not very clear. It may arise from the difference of wave propagation in lattice-particle structure from that of the continuum media. However, we can still conclude that HLPM is able to correctly capture the wave propagation of solids.

Fig. 8 displays the HLPM results of the vertical displacement for the 1D and 2D cases at $X = L/2$. It is seen that an oscillation is emergent for the 2D simulation due to the reflection of wave from the lateral boundaries.

*3.1.2. Kinematic boundary condition*

A kinematic boundary condition with 60.0 cm/s is constantly applied to the left end of the 1D and 2D bar, respectively. Fig. 9 displays the HLPM results of the horizontal displacement for the 1D

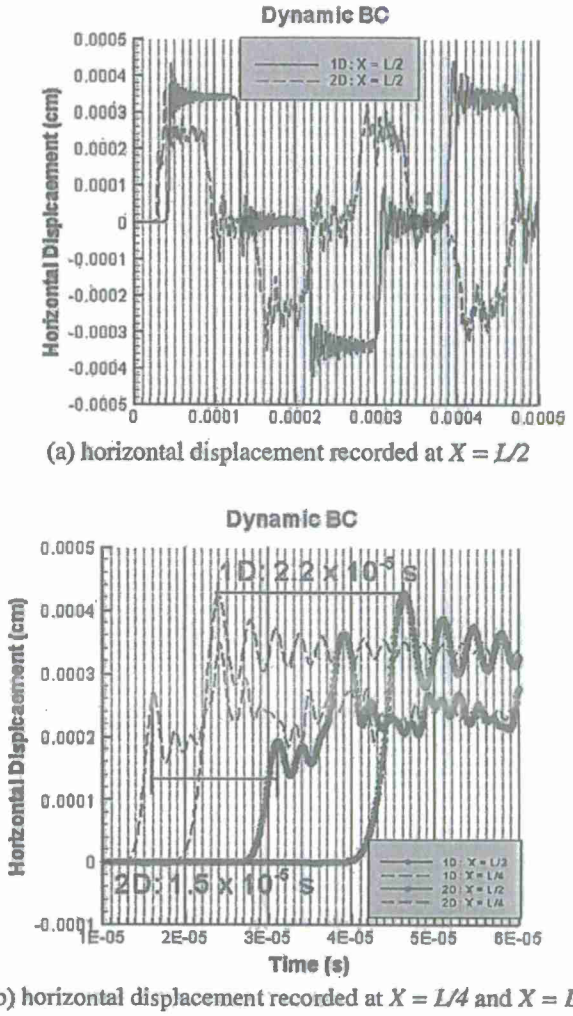


Fig. 7. HPLM prediction of horizontal displacement for 1D and 2D bar, respectively. Dynamic boundary condition is applied.

and 2D simulations at $X = L/2$. From Fig. 9a it is seen that the wave propagation profiles for both of the 1D and 2D cases are equally increased in amplitude after each period of wave reflection; this coincides with the knowledge of wave propagation with a constant load condition. Via Fig. 9b, we can calculate that the horizontal wave speed value for 1D and 2D cases are equal to 1455.0 and 2133.0 m/s, respectively. These values are identical to the above-shown 1D and 2D cases subject to a dynamic load.

Fig. 10 displays the HLPM results of the vertical displacement for 1D and 2D at $X = L/2$. Compared with the dynamic loading case in Fig. 8, it is seen that the vertical fluctuating amplitude is smaller when employing a kinematic loading than that of employing a dynamic load.

*3.1.3. HLPM of wave propagation with various loadings*

Within an elastic extent, wave speed should be identical and independent of the loading change. Therefore, next, we will employ different loading rates to the above-mentioned cases to test the reliability of HPLM.

We completely adopt the same geometry as what we have used for the above-mentioned 1D and 2D studies except that different dynamic and kinematic loading values are applied, respectively. Since the vertical effects are trivial, only the horizontal results are shown in the following.

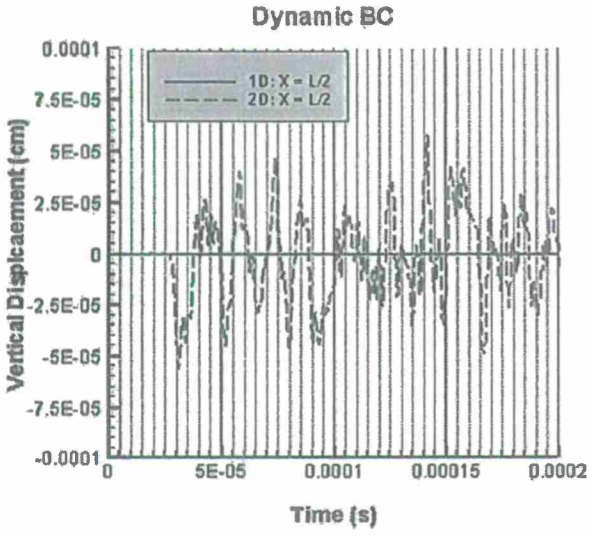


Fig. 8. HPLM prediction of vertical displacement recorded at $X = L/2$ for 1D and 2D bar, respectively. Dynamic boundary condition is applied.

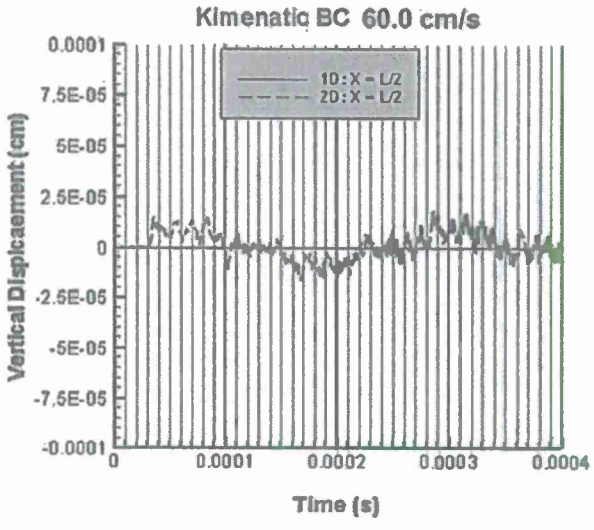


Fig. 10. HPLM prediction of vertical displacement recorded at $X = L/2$ for 1D and 2D bar, respectively. Kinematic boundary condition is applied.

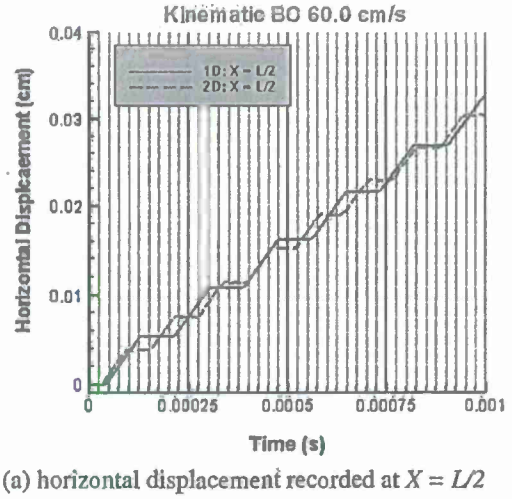


(a) horizontal displacement recorded at $X = L/2$

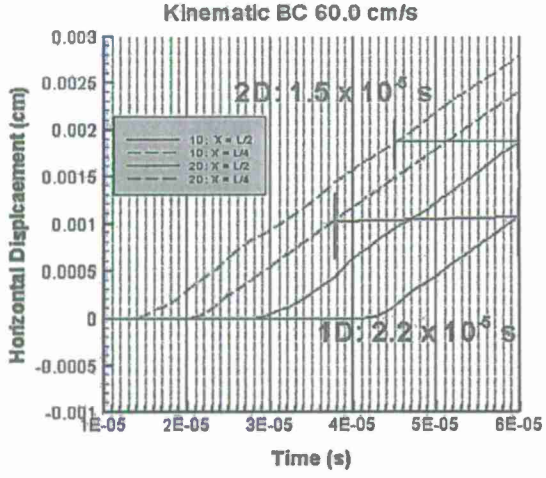


(b) horizontal displacement recorded at $X = L/4$ and $X = L/2$

Fig. 9. HPLM prediction of horizontal displacement for 1D and 2D bar, respectively. Kinematic boundary condition is applied.

For the dynamic loading test, 48.9 MPa is in addition applied to the left end of 1D and 2D bar, respectively. Fig. 11 illustrates the HPLM comparisons of horizontal displacement for 1D and 2D bar recorded at $X = L/2$, and dynamic boundary conditions, 48.9 and 97.8 MPa, are applied, respectively.

For the kinematic loading test, 50.0 cm/s is in addition applied to the left end of 1D and 2D bar, respectively. Fig. 12 illustrates the HPLM comparisons of horizontal displacement for 1D and 2D bar recorded at $X = L/2$, and kinematic boundary conditions, 50.0 and 60.0 cm/s are applied, respectively.

From Figs. 11 and 12, we clearly see that, for 1D and 2D simulations, either dynamic or kinematic loading is employed, the amplitude of particle displacement is dependent upon the loading rate change, while the wave propagation speed is independent of this change. Therefore, we conclude that HLPM is reliable in the wave prediction.

### 3.2. HLPM study of wave induced fracture – spall crack formation

Spall crack formation is the direct consequence arising from the wave (tension and compression wave) interactions in solids. The area will be highly stretched wherever the strong enough tension and compression wave meet, and a spall crack will consequently occur.

In the following, spall crack formations due to high speed impact and blasting load are preliminarily simulated, respectively.

#### 3.2.1. Spall crack formation due to high speed impact

The dimension of the target is set as 5.2 cm × 0.68 cm while the two different sizes of the flyer are set as 5.2 cm × 0.20 cm and 2.6 cm × 0.20 cm, respectively. The material properties of flyer and target are set to be identical, in which the Young's modulus is $E = 163.24$ GPa, the tensile strength $\sigma_{TS} = 478.25$ MPa, failure strain $\varepsilon_{max} = 0.10$, and density $\rho = 8900.0$ kg/m$^3$. The flyer's initial dropping speed is 260.0 m/s. Traction free boundary conditions are applied to all the boundaries.

Fig. 13 shows the qualitative comparison of spall crack formation of HPLM simulations with the results obtained from the analogous molecular dynamic (MD) simulations by Krivtsov [27,28]. As seen from Fig. 13b, the spall crack formation is clearly captured by HLPM. We see that the tension wave – the wave reflected from the bottom of the target, meets the compression wave – the wave

Q-218

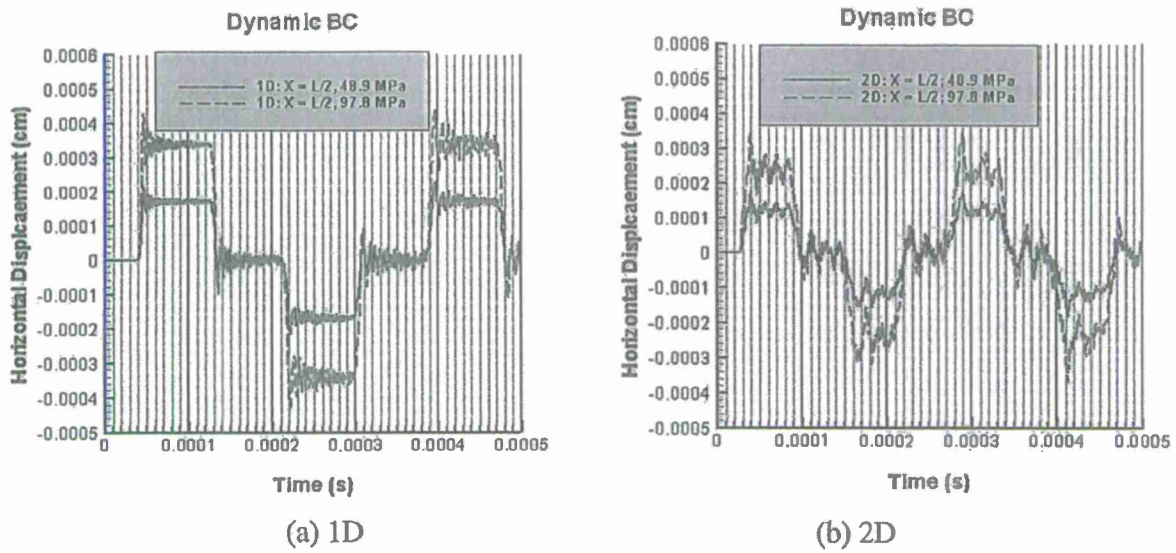


Fig. 11. HPLM prediction of horizontal displacement for 1D and 2D bar, respectively, recorded at $X = L/2$. Dynamic boundary conditions, 48.9 and 97.8 MPa are applied.

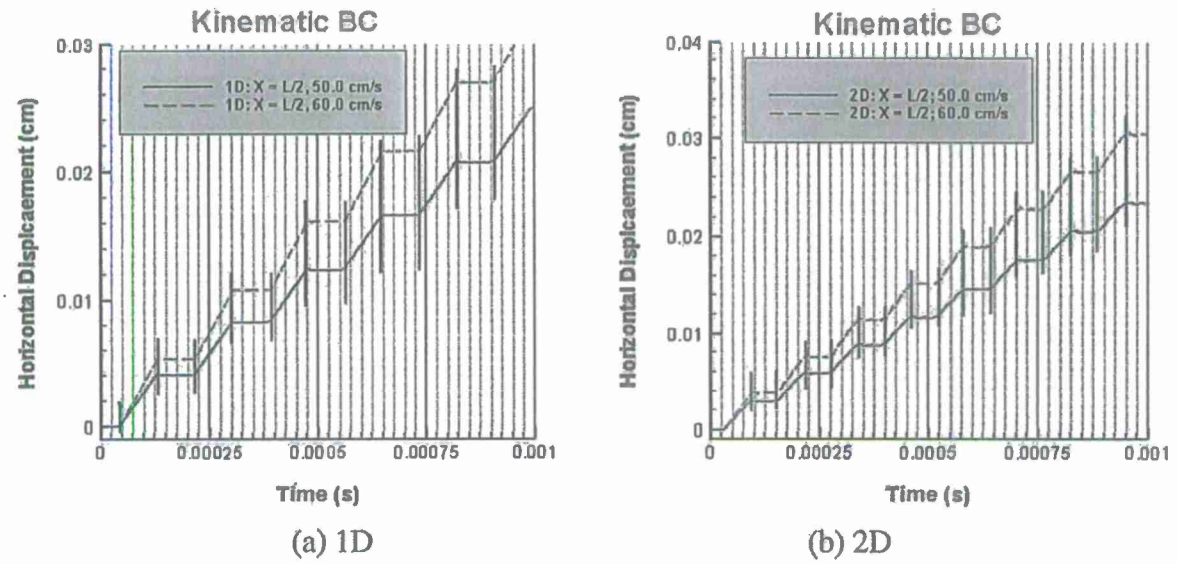


Fig. 12. HPLM prediction of horizontal displacement for 1D and 2D bar, respectively, recorded at $X = L/2$. Kinematic boundary conditions, 50.0 and 60.0 cm/s are applied.

reflected from the top of the flyer, at a thin layered area with a distance away from the bottom of the target. The two kinds of wave propagate in different directions alongside the $Y$-axis when they meet; this leads to a high stretching to the material herein, thus a spall crack zone is generated. It is also observed that the predicted length of spall crack formation is smaller than that of the flyer and the height of the lower spalling part is the same as that of the flyer. This matches with the MD results [27,28].

Next, the above-mentioned target coated with a high strength layer at the bottom of the target, but with different coating strength at the coating interface, is investigated to find out the protective effect of material from spallation.

We choose the coating layer with the same density as that of the above-mentioned flyer and target, but with more stronger material strength properties, i.e., the Young's modulus is $E = 380.89$ GPa, the tensile strength $\sigma_{TS} = 841.97$ MPa and failure strain $\varepsilon_{max} = 0.07$. Meanwhile, strong and weak coating strengths at the interface are attempted, respectively. The parameters of the strong coating treatment at the interface are the same as those of the flyer and target; while the parameters of the weak coating treatment are that the Young's modulus is $E = 16.74$ GPa, the tensile strength $\sigma_{TS} = 93.37$ MPa and failure strain $\varepsilon_{max} = 0.29$. The initial impact speed of the flyer is still 260 m/s.

Fig. 14a and b shows the HLPM simulations of employing weak and strong coating strengths at the interface, respectively. The modeling results display that, even when a high strength retrofitting material is coated at the target, spall crack formation is not prevent. This implies that prevention of material from spallation under extreme loadings is difficult; it needs the coating material with a super strength. Thus, the research is worth advancing. From Fig. 14, we also see that, for a weak coating case, the spall cracks occur not only inside the target, but also at the coating interface

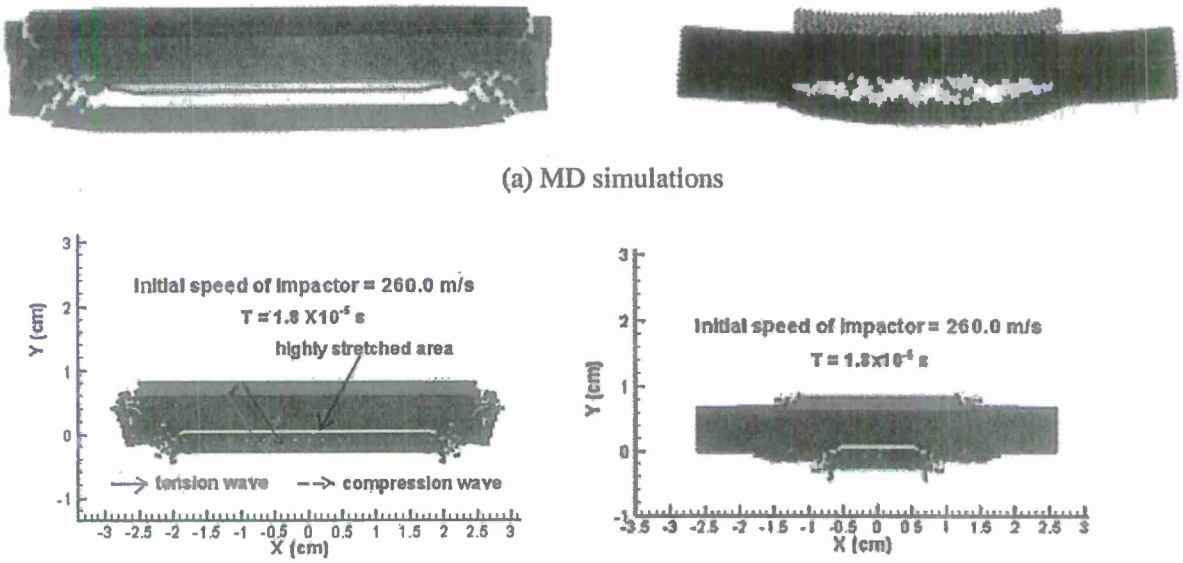


Fig. 13. Qualitative comparison of spall crack formation of HPLM with MD [27,28]. Impact speed = 260.0 m/s.

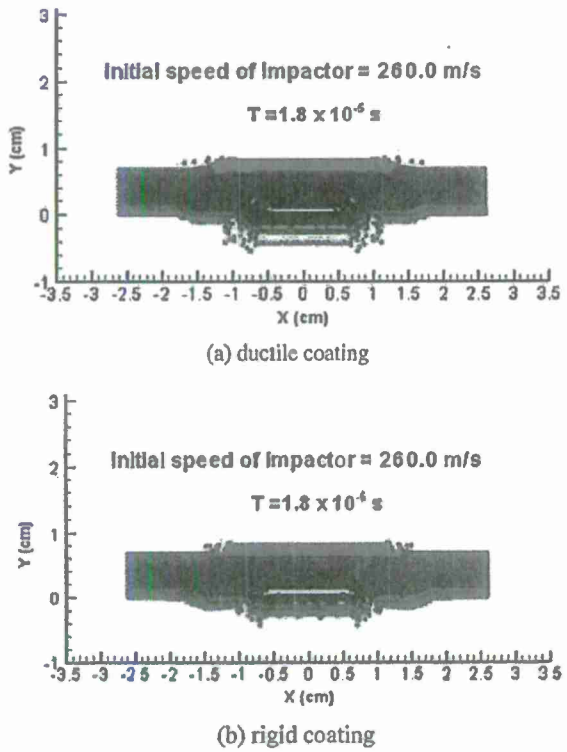


Fig. 14. HPLM of spall crack formation with bottom layer coating by (a) ductile material and (b) rigid material.

and inside the retrofitting material, whereas for a strong coating, the spall cracks are only formed inside the target.

*3.2.2. Spall crack formation due to blasting*

Preliminary HLPM simulations of spall crack formation with different spatial blasting sources are presented in the following.

Fig. 15a and b shows an α-mode HPLM simulation of spall crack formation during a blasting process with the detonation installed in one rectangular cavity. All the outer boundaries are traction free. The blasting wave trajectory in the material body is clearly captured as marked by an arrow in Fig. 15a. Fig. 15b displays the final fracture pattern. It is found that the spall cracks are mainly formed in the areas adjacent to the lateral boundaries due to the tension and compression wave interactions. Fig. 15a and b displays a 'mesh bias' problem which a regular triangular lattice model suffers from. It has been demonstrated that a two-layer neighboring particle interaction scheme can eliminate this mesh-related problem [20]. Alternatively, an irregular meshing system, such as a Delaunay triangulation mesh, can also solve this problem [12,13]. But it needs to be specially pointed out here that, since the location of the stress or pressure gradient in dynamic simulations is dependent upon time and space, thus, spurious wave reflection may arise from an irregular mesh system due to the presence of different limit to the wavelength generated by the irregular nodal spacing [14,29]. To prevent this problem, no less than 10% gradual difference between neighboring grid should be obeyed [30].

Fig. 16a and b shows the HPLM of spall crack formation during a blasting process with the detonation installed in two circular cavities located in parallel and diagonally, respectively. Fig. 16a indicates that explosive from two cavities set in parallel causes dominant spall crack formation horizontally, and the fragments are generated within the extent of circular diameter on the two vertical outer boundaries. Fig. 16b displays that explosive from two cavities set diagonally causes dominant spall crack formation diagonally on the lateral outer boundaries, and the resultant failure area coincides with the direction of the explosive source setting.

The spall crack formation in pattern and extent arises from the complicated tension–compression wave interactions in materials. Wherever the tension wave reacts with the strong enough compression wave, the material herein is highly stretched, and, thus, fracture or fragmentation is formed. Via the simulations, the fracturing efficiency associated with the spatial explosive source setup is exhibited. The underway research will benefit the explosive fracturing applications.

Q-220

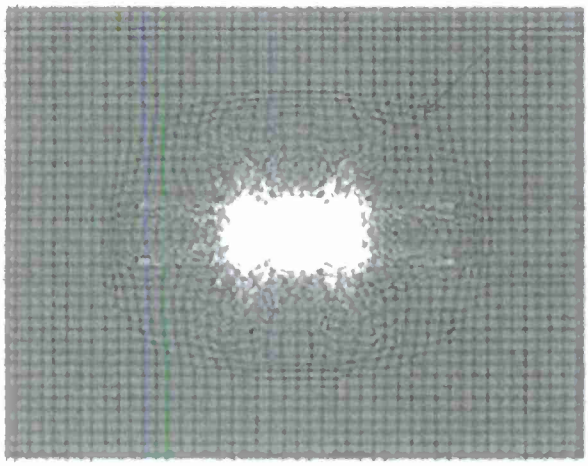

(a) blasting wave propagation

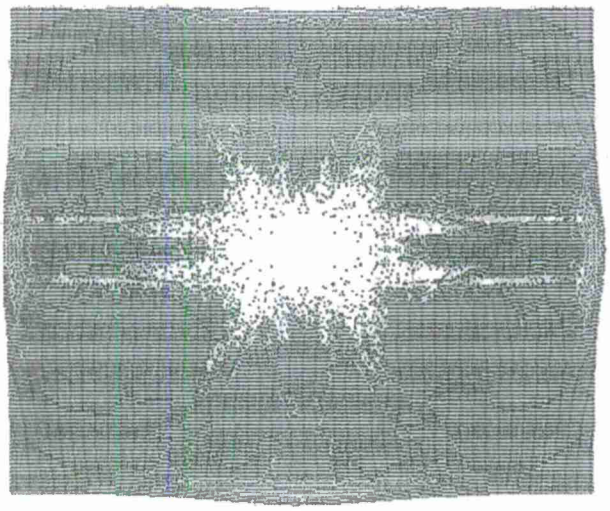

(b) final spall crack formation

Fig. 15. HPLM of spall crack formation during a blasting process with detonation installed from one cavity.

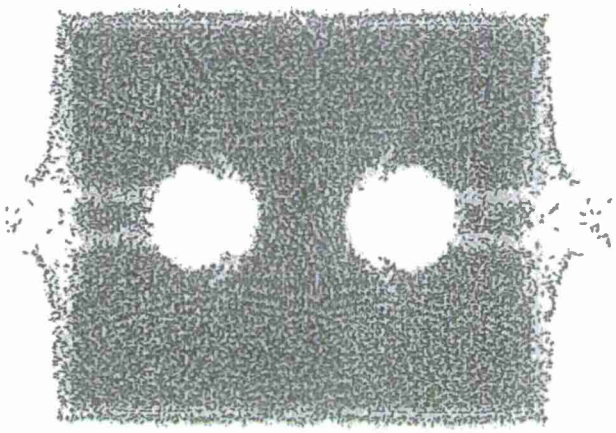

(a) detonation from two cavities located in parallel

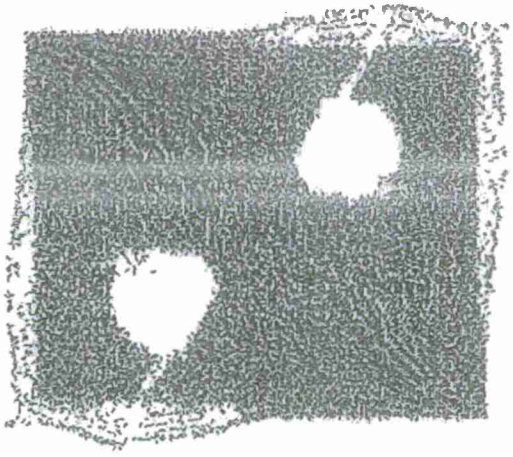

(b) detonation from two cavities located diagonally

Fig. 16. HPLM of spall crack formation during a blasting process with detonation installed from two cavities.

## 4. Concluding remarks

In this paper, a hybrid lattice particle modeling (HLPM) method is first employed for a study of wave propagation in 1D and 2D material bar, and the results are verified with the analytical solutions. Next, the HLPM is applied to the simulation of wave propagation induced fracture, spall cracks, due to hyper-velocity impact and blasting. In the hyper-velocity impact case, a functionally designed infrastructure material coated with a high strength layer, but with different coating strengths at the interface, is also investigated to find out the protective effect of material from spallation. Via this study, the following benefits are obtained.

From the serial analyses of the preliminary simulation results obtained by using HLPM, we obtain several important conclusions:

(1) No need for re-meshing. Re-meshing is known as an overwhelming challenge for FEM, whereas HLPM does not suffer from it at all. In HLPM, fracture is created when a bond (spring) is broken by translational force. This provides HLPM a unique power to be able to quite easily overcome a "discontinuity of material" problem.

(2) No stress intensity required. In HLPM, a bond (spring) is broken and fracture is thus resulted wherever the critical failure strain reaches.

(3) HLPM can correctly capture wave propagation of solids. From the HLPM applications of wave propagation induced fracture problems, spall cracks, due to hyper-velocity impact and blasting, we conclude that HLPM can successfully capture spall crack formation. In the hyper-velocity impact case, a functionally designed infrastructure material coated with a high strength layer, but with different coating strengths at the interface, is also investigated to find out the protective effect of material from spallation. The modeling results demonstrate that prevention of material from spallation under extreme loadings is difficult; it needs the coating material with a super strength. In the blasting study, the fracturing efficiency associated with the explosive setup is investigated. This will benefit the explosive fracturing applications.

In summary, the outcomes of this paper can provide important lessons for fracture control which has remarkable significance to engineering applications. Of course, more modeling validations and improvement work are required. The ultimate application for HLPM is aimed at exploring shock synthesis.

## Acknowledgements

This work was partially supported by the funding received under a subcontract from the Department of Homeland Security-sponsored Southeast Region Research Initiative (SERRI) at the Department of Energy's Oak Ridge National Laboratory, USA. Authors wish to acknowledge the partial support for this research by ONR Grant # N00014-07-1-1010, Office of Naval Research, Solid Mechanics Program (Dr. Yapa D.S. Rajapakse, Program Manager).

## References

[1] K.A. Kaiser, Advancements in the split Hopkinson bar test, Master Thesis, Virginia Polytechnic Institute, 1998.
[2] X. Quan, N.K. Birnbaum, M.S. Cowler, B.I. Gerber, R.A. Clegg, C.J. Hayhurst, Numerical simulation of structural deformation under shock and impact loads using a coupled multi-solver approach, in: Proceedings of the Fifth Asia-Pacific Conference on Shock and Impact Loads on Structures, Hunan, China, November 12–14, 2003.
[3] T. Belytschko, S. Loehnert, J.H. Song, Multiscale aggregating discontinuities: a method for circumventing loss of material stability, Int. J. Numer. Method Engrg. 73 (2008) 869–894.
[4] J. Monaghan, Smoothed particle hydrodynamics, Rep. Prog. Phys. 68 (1) (2005) 1703–1759.
[5] P.A. Cundall, Computer simulations of dense sphere assembles, Micromechanics of Granular Materials, 1988, pp. 113–123.
[6] M. Meguro, H. Tagel-Din, Applied element method for structural analysis: theory and application for linear materials, Struct. Engrg./Earthquake Engrg., JSCE 17 (1) (2000) 1–14.
[7] G. Wang, M. Ostoja-Starzewski, P. Radziszewski, M. Ourriban, Particle modeling of dynamic fragmentation – II: Fracture in single- and multi-phase materials, Comput. Mater. Sci. 35 (2006) 116–133.
[8] G. Wang, M. Ostoja-Starzewski, Particle modeling of dynamic fragmentation – I: Theoretical considerations, Comput. Mater. Sci. 33 (2005) 429–442.
[9] G. Wang, A. Al-Ostaz, A.H.-D. Cheng, P.R. Mantena, Hybrid lattice particle modeling: theoretical considerations for a 2-D elastic spring network for dynamic fracture simulations, Comput. Mater. Sci. 44 (2009) 1126–1134.
[10] E. Oñate, S.R. Idelsohn, F.D. Pin, R. Aubry, The particle finite element method. An overview, Int. J. Comput. Method 1 (2) (2004) 267–307.
[11] Z. Chen, R. Brannon, An evaluation of the material point method, Sand Report, Sandia National Laboratories, 2002.
[12] G. Cusatis, Z.P. Zdenek, L. Cedolin, Confinement-shear lattice model for concrete damage in tension and compression: I. Theory, ASCE J. Engrg. Mech. (2003) 1439–1448.
[13] G. Cusatis, Z.P. Zdenek, L. Cedolin, Confinement-shear lattice model for concrete damage in tension and compression: II. Computation and validation, ASCE J. Engrg. Mech. (2003) 1449–1458.
[14] T. Belytschko, D. Organ, C. Gerlach, Element-free Galerkin methods for dynamic fracture in concrete, Comput. Method Appl. Mech. Engrg. 187 (2000) 385–399.
[15] W.K. Liu, S. Jun, Y.F. Zhang, Reproducing kernel particle methods, Int. J. Numer. Method Fluid 20 (8–9) (2005) 1081–1106.
[16] J.M. Melenk, I. Babuska, The partition of unity finite element method: basic theory and applications, Comput. Method Appl. Mech. Engrg. 139 (1996) 289–314.
[17] I. Babuska, J.M. Melenk, The partition of unity method, Int. J. Numer. Method Engrg. 40 (1997) 727–758.
[18] T. Belytschko, Y. Krongauz, D. Organ, Meshless method: an overview and recent development, Comput. Method Appl. Mech. Engrg. 139 (1996) 3–47.
[19] M. Ostoja-Starzewski, Lattice models in micromechanics, Appl. Mech. Rev. 55 (1) (2002) 35–60.
[20] G. Wang, A. Al-Ostaz, A.H.-D. Cheng, P.R. Mantena, Particle modeling of a polymeric material (nylon-6,6) due to the impact of a rigid indenter, Comput. Mater. Sci. 44 (2008) 449–463.
[21] M. Ostoja-Starzewski, G. Wang, Particle modeling of random crack patterns in epoxy plates, Probabilist. Engrg. Mech. 21 (2006) 267–275.
[22] G. Wang, Particle modeling of polymeric material indentation study, Engrg. Fract. Mech. 76 (2009) 1386–1395.
[23] M.F. Ashby, D.R.H. Jones, Engineering Materials 1: An Introduction to Their Properties and Applications, Pergamon Press, 1980.
[24] G. Wang, P. Radziszewski, J. Ouellet, Particle modeling simulation of thermal effects on ore breakage, Comput. Mater. Sci. 43 (2008) 892–901.
[25] R.W. Hockney, J.W. Eastwood, Computer Simulation Using Particles, Institute of Physics Publishing, 1999.
[26] M.A. Meyers, Dynamic Behavior of Materials, A Wiley–Interscience Publication, 1994.
[27] A.M. Krivtsov, Relation between spall strength and mesoparticle velocity dispersion, Int. J. Impact Engrg. 23 (1999) 477–487.
[28] A.M. Krivtsov, Computer simulation of spall crack formation, in: Fryba, Naprstek (Eds.), Structural Dynamics – EURODYN '99, EURODYN '99, Balkema, Rotterdam, 1999, pp. 475–477.
[29] I. Fred, Numerical Simulation of Differential Equations, Academic Press, New York, 1979.
[30] J. Zukas, Introduction to Hydrocodes, Elsevier, 2004.

Q-222

Computational Materials Science 44 (2009) 1126–1134

Contents lists available at ScienceDirect

Computational Materials Science

journal homepage: www.elsevier.com/locate/commatsci

# Hybrid lattice particle modeling: Theoretical considerations for a 2D elastic spring network for dynamic fracture simulations

G. Wang [a,*], A. Al-Ostaz [a], A.H.-D. Cheng [a], P.R. Mantena [b]

[a] Department of Civil Engineering, University of Mississippi, Oxford, MS 38677-1848, United States
[b] Department of Mechanical Engineering, University of Mississippi, Oxford, MS 38677-1848, United States

ARTICLE INFO

*Article history:*
Received 30 May 2008
Received in revised form 1 July 2008
Accepted 23 July 2008
Available online 7 September 2008

*PACS:*
68.45.kg
61.43.Bn
40.30.My
46.30.Nz
83.20._d
83.80.Nb

*Keywords:*
Particle modeling
Lattice model
Dynamic fracture
Impact
Constitutive relations

ABSTRACT

A new hybrid lattice particle modeling (HLPM) scheme is proposed. The particle–particle interaction is derived from lattice modeling (LM) theory, whereas the computational scheme follows particle modeling (PM) technique. The newly proposed HLPM considers different particle interaction schemes, involving not only particles in the nearest neighborhood, but also the second nearest neighborhood. Different mesh structures with triangular or rectangular unit cells can be used. The current paper is concerned with the mathematical derivations of elastic interaction between contiguous particles in 2D lattice networks, accounting for different types of linkage mechanism and different shapes of lattice. Axial ($\alpha$) and combined axial-angular ($\alpha-\beta$) models are considered. Derivations are based on the equivalence of strain energy stored in a unit cell with its associated continuum structure in the case of in-plane elasticity. Conventional PM technique was restricted to a fixed Poisson's ratio and had a strong bias in crack propagation direction, as a result of the geometry of the adopted lattice network. The current HLPM is free from the above-mentioned deficiencies and can be applied to a wide range of impact and dynamic fracture failure problems. Although the current analysis is based on the linear elastic spring model, inelastic considerations can be easily implemented, as HLPM has the same force interaction scheme as PM, based on the Lennard–Jones potential.

© 2008 Elsevier B.V. All rights reserved.

## 1. Introduction

Since its introduction in the 1980s by Greenspan [1], particle modeling (PM) has found good success in a number of applications [2–10]. PM is a numerical technique similar to the molecular dynamic (MD) simulation; but rather than simulating actual atoms, it is based on lumped mass particles distributed on a grid to allow macro scale modeling. The PM utilizes an equivalent Lennard–Jones potential to model the nonlinear constitutive law at the continuum, macroscopic level. The mass has inertia that obeys Newton's second law of motion. It is a Lagrangian model that keeps track of particle location and velocity.

Despite its success, the PM has a few deficiencies. One major shortcoming is that in the modeling of solid, the potential type formulation allows only one elastic constant to be modeled, which is typically selected as the bulk modulus, or Young's modulus. The second elastic constant present in an isotropic material, say, Poisson's ratio, becomes the property of the grid system used, such as the triangular or rectangular networks.

The use of spring network model, or lattice model (LM), to model elastic solid has more than 60 years of history [11]. Literature review on the successive development of these models can be found in [12–15]. Lattice modeling technique has been widely applied in the computation of effective elastic moduli and simulation of brittle intergranular fracture (BIF) in ceramics, intermetallics, and refractory metals [16–21].

Lattice model, when applied in its original form, also has the deficiency that only one elastic constant can be modeled. For example, on a 2D equilateral triangular lattice, the equivalent Poisson's ratio is fixed to the value of 1/3. This situation can be remedied by the use of the more advanced lattice models. For example, Ostoja–Starzewski [14,15] has manipulated several types of spring systems, including central ($\alpha$), angular ($\beta$) and the mixed ($\alpha-\beta$) interactions, coupled with different lattice networks, triangular, rectangular, etc. that allows the modeling of two elastic constants of isotropic materials, as well as the potential for applying to anisotropic materials. Other deficiencies of the conventional LM include the fact that it is of an Eulerian model. It does not allow the particles to move around and even be fragmented from the main lattice. It is also basically a static model, and does not model the dynamic fracture process. In Table 1,

* Corresponding author. Tel.: +662 915 5369; fax: +662 915 5523.
*E-mail address:* gewang@olemiss.edu (G. Wang).

0927-0256/$ - see front matter © 2008 Elsevier B.V. All rights reserved.
doi:10.1016/j.commatsci.2008.07.032

the strengths and weaknesses of the traditional LM and PM are summarized and compared.

To extend the capability of both the LM and the PM, and to allow the modeling of dynamic fracture and fragmentation caused by impact, a hybrid lattice particle modeling (HLPM) has been proposed that combines the strengths of the LM and the PM [22]. Table 1 shows the selection of the modeling strategies of the HLPM. A preliminary version of the HLPM has been successfully applied to an impact induced dynamic fracture of a polymeric material, nylon-6,6 [23].

In the earlier implementations of HLPM (here we refer to our previous PM work addressed in [2–7]), however, the potential of the set of strategies outlined in Table 1 has not been fully utilized. For example, the capability of the different spring configurations ($\alpha$ and $\beta$ model), which allows the modeling of Poisson's ratio, was not implemented. Also, only the nearest neighborhood of particles has been defined in the dynamic interaction. One deficiency discovered in the applications is that there seems to be a bias in the fracture propagation direction inherent to the geometry of the lattice network employed, say, along the 60° direction for the equilateral triangular, nearest neighborhood network.

In the present work, we seek the improvement of the HLPM by implementing the $\alpha$, the $\beta$, and the $\alpha-\beta$-spring models, on difference lattices, triangular and rectangular. Multiple neighborhoods have been included for the particle dynamic interaction. Theoretical derivation is provided that established the explicit relations between the elastic material constants and the spring constants of the lattice system. Some of the resultant HLPM schemes are demonstrated to be free from the fracture propagation bias, and are adopted for the modeling. Validation of the HLPM is conducted by simulating the impact of a rigid indenter on a polymeric material (nylon-6,6). The modeling fracture pattern and dynamic results compares quite favorably with the associated laboratory test [23].

The current demonstration of the HLPM is based on a linear elastic model with an ultimate translational strength (i.e., tension/compression). Once the translational strength is exceeded, the spring is broken and a fracture is created. The linear model is created by using a quadratic form in the Lennard–Jones potential. The nonlinear constitutive laws are not implemented in the present study because the lack of independent measurement of the nonlinear material properties of the material tested. Once such constants are available, the implementation of nonlinear constitutive law is inherent in the Lennard–Jones potential approach of the PM, and is not a difficulty for the HLPM at all.

**Table 1**
Comparison of the lattice model (LM), the particle model (PM), and the hybrid lattice particle model (HLPM)

| | Lattice model (LM) | Particle model (PM) | Hybrid lattice particle model (HLPM) |
|---|---|---|---|
| Particle interaction | Spring (axial/angular), beam, etc. | Lennard–Jones potential (axial only) | Spring (axial/angular) mimicking the Lennard–Jones potential |
| Interaction neighborhood | Not limited to nearest neighbor | Nearest neighbor only | Not limited to nearest neighbor |
| Mesh system | Eulerian | Lagrangian | Lagrangian |
| Poisson's ratio | Flexible | Fixed | Flexible |
| Time process | Static | Dynamic based on Newton's second law | Dynamic based on Newton's second law |
| Force–displacement relation | Displacement (strain) interpreted from force (stress) | Force interpreted from displacement (distance between particles) | Force interpreted from displacement (distance between particles) |

## 2. Spring network representation

The basic idea of a spring network representation is based on the equivalence of strain energy, $U_{\text{cell}}$, stored in a unit cell of volume $V$, with the associated strain energy of the continuum system, $U_{\text{continuum}}$ (see Fig. 1),

$$U_{\text{cell}} \equiv U_{\text{continuum}} \tag{1}$$

These strain energies are given by the following relations

$$U_{\text{cell}} = \sum_b E_b = \frac{1}{2}\sum_b^{N_b} (\vec{F}\cdot\vec{u})^{(b)} \tag{2}$$

$$U_{\text{continuum}} = \frac{1}{2}\int_V \sigma\cdot\varepsilon \mathrm{d}V \tag{3}$$

where $\vec{F}$ is the axial force vector and $\vec{u}$ is the resultant displacement. The superscript $b$ in Eq. (2) is the $b$th spring (bond), and $N_b$ the total number of bonds. In this paper, we only account for 2D linear elastic springs and spatially linear displacement, i.e., uniform strain field $\varepsilon$. Thus, Eqs. (2) and (3) become

$$U_{\text{cell}} = \frac{1}{2}\sum_b^{N_b} (k\vec{u}\cdot\vec{u})^{(b)} \tag{4}$$

$$U_{\text{continuum}} = \frac{1}{2}\varepsilon\cdot C\cdot\varepsilon \tag{5}$$

where $k$ is the corresponding spring constant, $C$ is the stiffness tensor of the material.

## 3. α-Models

### 3.1. Triangular lattice

In this part, an equilateral triangular lattice is employed. Two interaction patterns of particles are considered: the nearest and two-layer (nearest and second nearest) neighboring particle interactions.

#### 3.1.1. Nearest neighboring particle interaction

The mesh structure is shown in Fig. 1. Assuming that each $\alpha$-spring is of length $l$, which is equal to the half-length of the spacing of a bond $r_0$. Therefore, the unit cell area is $V = 2\sqrt{3}l^2$. For each bond $b$, $\alpha^{(b)}$ is the spring constant of half-length of the bond, and the unit cell bond vectors $n^{(b)}$ at respective angles $\theta^{(b)}$ are given in Table 2.

The strain energy stored in a unit hexagonal cell (Fig. 1) is

$$U = \frac{l^2}{2}\sum_{b=1}^{6} \alpha^{(b)} n_i^{(b)} n_j^{(b)} n_k^{(b)} n_m^{(b)} \varepsilon_{ij}\varepsilon_{km} \tag{6}$$

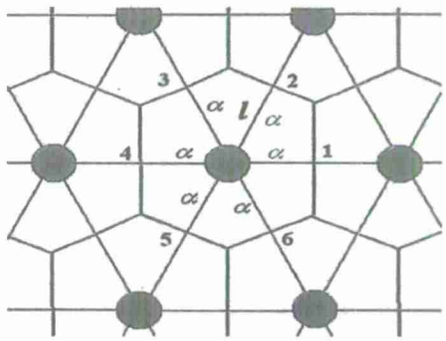


**Fig. 1.** A triangular lattice with hexagonal unit cell for α model, considering nearest neighboring particle interactions.

R-224

**Table 2**
Bond vectors $n^{(b)}$ with respect to angles $\theta^{(b)}$ in case of nearest particle interaction

| $b$ | $n^{(b)}$ |
|---|---|
| 1 | $(1, 0)$ |
| 2 | $(1/2, \sqrt{3}/2)$ |
| 3 | $(-1/2, \sqrt{3}/2)$ |
| 4 | $(-1, 0)$ |
| 5 | $(-1/2, -\sqrt{3}/2)$ |
| 6 | $(1/2, -\sqrt{3}/2)$ |

By Eq. (1), the stiffness tensor becomes

$$C^{\alpha}_{ijkm} = \frac{l^2}{V}\sum_{b=1}^{6}\alpha^{(b)} n_i^{(b)} n_j^{(b)} n_k^{(b)} n_m^{(b)} \tag{7}$$

In particular, taking all $\alpha^{(b)}$ the same, we get

$$\begin{aligned} C^{\alpha}_{1111} &= \frac{9l^2\alpha}{4V} = C^{\alpha}_{2222} \\ C^{\alpha}_{1122} &= \frac{3l^2\alpha}{4V} = C^{\alpha}_{2211} \\ C^{\alpha}_{1212} &= \frac{3l^2\alpha}{4V} \end{aligned} \tag{8}$$

Other $C^{\alpha}_{ijkm} = 0$.

First, Hooke's law in terms of stiffness tensor of 2D isotopic material is described as

$$\begin{bmatrix} \sigma_{11} \\ \sigma_{22} \\ \sigma_{12} \end{bmatrix} = \begin{bmatrix} C_{1111} & C_{1122} & C_{1112} \\ C_{2211} & C_{2222} & C_{2212} \\ C_{1211} & C_{1222} & C_{1212} \end{bmatrix} \begin{bmatrix} \varepsilon_{11} \\ \varepsilon_{22} \\ \varepsilon_{12} \end{bmatrix} \tag{9}$$

Second, Hooke's law in terms of engineering format in 2D isotopic material is described as

$$\begin{cases} \sigma_{11} = \frac{E}{1-\nu^2}\varepsilon_{11} + \frac{E\nu}{1-\nu^2}\varepsilon_{22} = C_{1111}\varepsilon_{11} + C_{1122}\varepsilon_{22} + C_{1112}\varepsilon_{12} \\ \sigma_{22} = \frac{E\nu}{1-\nu^2}\varepsilon_{11} + \frac{E}{1-\nu^2}\varepsilon_{22} = C_{2211}\varepsilon_{11} + C_{2222}\varepsilon_{22} + C_{2212}\varepsilon_{12} \\ \sigma_{12} = \mu\varepsilon_{12} = \frac{E}{2(1+\nu)}\varepsilon_{12} = C_{1211}\varepsilon_{11} + C_{1222}\varepsilon_{22} + C_{1212}\varepsilon_{12} \end{cases} \tag{10}$$

where $E$, $\nu$, $\mu$, $\sigma_{ij}$ and $\varepsilon_{ij}$ are Young's modulus, Poisson's ratio, shear modulus, stress and strain, respectively. From Eq. (10), we have

$$\begin{aligned} C^{\alpha}_{1111} &= \frac{9l^2\alpha}{4V} = C^{\alpha}_{2222} = \frac{E}{1-\nu^2} \\ C^{\alpha}_{1122} &= \frac{3l^2\alpha}{4V} = C^{\alpha}_{2211} = \frac{E\nu}{1-\nu^2} \\ C^{\alpha}_{1212} &= \frac{3l^2\alpha}{4V} = \mu = \frac{E}{2(1+\nu)} \end{aligned} \tag{11}$$

Other $C^{\alpha}_{ijkm} = 0$

By definition, Poisson's ratio yields

$$\nu = \frac{C^{\alpha}_{1122}}{C^{\alpha}_{1111}} = \frac{1}{3} \tag{12}$$

It is clearly seen that a fixed Poisson's ratio is reached by such a scheme.

Thus, we have

$$\alpha = \frac{4VE}{9(1-\nu^2)l^2} = \sqrt{3}E \tag{13}$$

Note that Eq. (10) holds only for isotropic materials. For anisotropic materials, the similar relationship can be founded following the mechanics of composite materials [24]. In the current paper, for simplicity, the continuum media is assumed to be isotropic even if the local cell can be anisotropic.

*3.1.2. Two-layer (nearest and second) neighboring particle interaction*

Now we consider a lattice made of two central force structures with structure I (three regular triangular networks with nearest neighbor particle interactions) and structure II (three regular triangular networks with second neighbor particle interactions). These two structures are superposed in a way shown in Fig. 2 [25]. In this structure system, each point communicates with six nearest neighbors via structure I, and with six second nearest neighbors via structure II. The spring constants for these two types of structures are $\alpha^{I}$ and $\alpha^{II}$, respectively. $S^{I} = 2l$ is the lattice spacing of structure I, while $S^{II} = S^{I}\sqrt{3}$ is that of structure II. The unit cell area is $V = \sqrt{3}l^2/2$.

Under the condition of uniform strain, and postulating the equivalence of strain energy in a unit cell due to all the spring constants to equal to the strain energy of an effective continuum, the following effective local-type stiffness tensor is determined [16],

$$C^{\alpha}_{ijkm} = C^{I}_{ijkm} + C^{II}_{ijkm} \tag{14}$$

where

$$\begin{aligned} C^{I}_{ijkm} &= \frac{2}{\sqrt{3}}\alpha^{I}\sum_{b=1,2,3} n_i^{I(b)} n_j^{I(b)} n_k^{I(b)} n_m^{I(b)} \\ C^{II}_{ijkm} &= \frac{6}{\sqrt{3}}\alpha^{II}\sum_{b=1,2,3} n_i^{II(b)} n_j^{II(b)} n_k^{II(b)} n_m^{II(b)} \end{aligned} \tag{15}$$

The unit vectors $n_i^{I(b)}$ and $n_i^{II(b)}$ in each structure are given in Table 3.

Hence,

$$\begin{aligned} C^{\alpha}_{1111} &= C^{\alpha}_{2222} = \frac{9}{4\sqrt{3}}\alpha^{I} + \frac{27}{4\sqrt{3}}\alpha^{II} = \frac{E}{1-\nu^2} \\ C^{\alpha}_{1122} &= C^{\alpha}_{2211} = \frac{3}{4\sqrt{3}}\alpha^{I} + \frac{9}{4\sqrt{3}}\alpha^{II} = \frac{E\nu}{1-\nu^2} \\ C^{\alpha}_{1212} &= \frac{3}{4\sqrt{3}}\alpha^{I} + \frac{9}{4\sqrt{3}}\alpha^{II} = \mu = \frac{E}{2(1+\nu)} \end{aligned} \tag{16}$$

Other $C^{\alpha}_{ijkm} = 0$

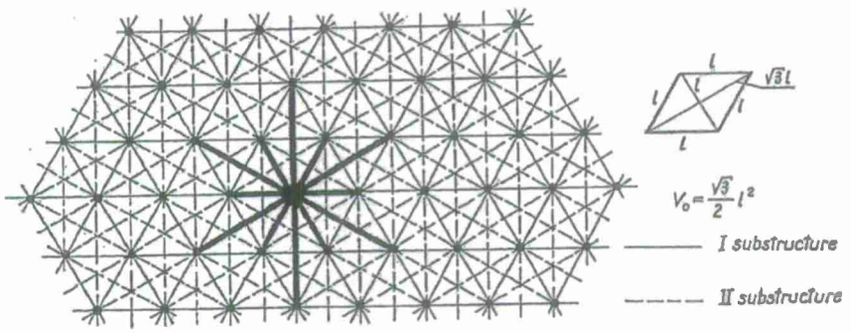


**Fig. 2.** Two structures for $\alpha$ model, I and II, resulting in a lattice with nearest neighbor and second neighbor particle interactions in central directions [21].

R-225

**Table 3**
Unit $n^{I(b)}$ and $n^{II(b)}$ with respect to angle $\theta^{I(b)}$ and $\theta^{II(b)}$

| Structure I: $b$ | Structure I: $n^{I(b)}$ | Structure II: $b$ | Structure II: $n^{II(b)}$ |
|---|---|---|---|
| 1 | $(1, 0)$ | 1 | $(\sqrt{3}/2, 1/2)$ |
| 2 | $(1/2, \sqrt{3}/2)$ | 2 | $(0, 1)$ |
| 3 | $(-1/2, \sqrt{3}/2)$ | 3 | $(-\sqrt{3}/2, 1/2)$ |

By definition, Poisson's ratio yields

$$\nu = \frac{C^{\alpha}_{1122}}{C^{\alpha}_{1111}} = \frac{1}{3} \tag{17}$$

We obtain that Poisson's ratio is independence of $\alpha^{I}$ and $\alpha^{II}$.

Assuming $\alpha^{II} = k\alpha^{I}$, from Eq. (16), we have

$$\alpha^{I} = \frac{\sqrt{3}E}{2(1+3k)}, \quad \alpha^{II} = \frac{\sqrt{3}Ek}{2(1+3k)}, \quad k > 0 \tag{18}$$

The physical meaning of $k$ is not certain at this stage; however, $k = 1$ is recommended for a simplicity.

### 3.2. Rectangular lattice

Fig. 3 shows a rectangular network. For a particle i, there are eight axial and diagonal neighboring particles to be accounted for. A unit rectangular cell area is $V = 4l^2$. All the spring constants of half-length of the axial bonds are $\alpha^{I}$, and $\alpha^{II}$ denote the spring constants in half-length of the diagonal bonds. The unit cell bond vectors $n^{(b)}$ at respective angles $\theta^{(b)}$ are given in Table 4.

Following the same derivation process as in Section 3.1, we have

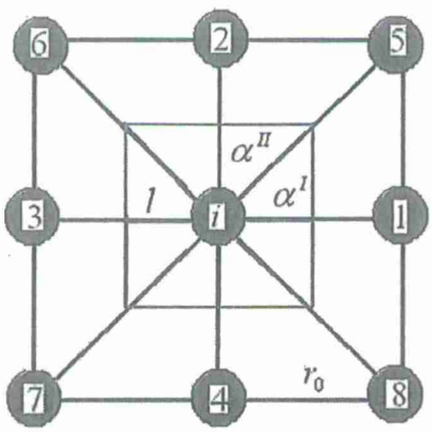


**Fig. 3.** A rectangular lattice with rectangular unit cell for $\alpha$ model, considering both axial and diagonal particles.

**Table 4**
Bond vectors $n^{(b)}$ with respect to angles $\theta^{(b)}$ in case of a rectangular network

| Axial: $b$ | Axial: $n^{(b)}$ | Diagonal: $b$ | Diagonal: $n^{(b)}$ |
|---|---|---|---|
| 1 | $(1, 0)$ | 5 | $(1, -1)$ |
| 2 | $(0, 1)$ | 6 | $(-1, 1)$ |
| 3 | $(-1, 0)$ | 7 | $(-1, -1)$ |
| 4 | $(0, -1)$ | 8 | $(1, -1)$ |

$$C^{\alpha}_{1111} = C^{\alpha}_{2222} = \frac{l^2}{V}(2\alpha^{I} + 4\alpha^{II}) = \frac{E}{1-\nu^2}$$
$$C^{\alpha}_{1122} = C^{\alpha}_{2211} = \frac{4\alpha^{II}l^2}{V} = \frac{E\nu}{1-\nu^2} \tag{19}$$
$$C^{\alpha}_{1212} = \frac{4\alpha^{II}l^2}{V} = \mu = \frac{E}{2(1+\nu)}$$
Other $C^{\alpha}_{ijkm} = 0$

By definition, Poisson's ratio yields

$$\nu = \frac{C^{\alpha}_{1122}}{C^{\alpha}_{1111}} = \frac{2\alpha^{II}}{\alpha^{I} + 2\alpha^{II}} \tag{20}$$

Hence, we have

$$\alpha^{I} = \frac{2E}{1+\nu}, \quad \alpha^{II} = \frac{E\nu}{1-\nu^2} \tag{21}$$

Substituting Eq. (21) into Eq. (19), also assuming $\alpha^{I}$ and $\alpha^{II}$ are both non-negative, then the following unique Poisson's ratio is resulted from this scheme,

$$\nu = 1/3 \tag{22}$$

This Poisson's ratio is the same as those resulted from triangular lattice models mentioned in Eqs. (12) and (17).

Substituting Eq. (22) into (20), $\alpha^{I} = 4\alpha^{II} = 3E/2$ must hold. This implies that putting other parameters into this model does not make it any physical meaning.

## 4. $\alpha - \beta$ models

Angular springs are used to consider the interactions between the contiguous bonds incident onto the same node. We assign angular spring constants $\beta^{(b)}$. With reference to Fig. 4, let $\Delta\theta^{(b)}$ be the infinitesimal angle change of the $b$th spring constant orientation from the non-deformed position. Noting that $\vec{n} \times \vec{n} = \vec{l}\Delta\theta$, we obtain

$$\Delta\theta^{(b)}_{k} = e_{kij}\varepsilon_{jp}n_i n_p \quad i,j,p = 1,2 \tag{23}$$

where $e_{kij}$ is the Levi–Civita permutation tensor. Then the angle change between two contiguous $\alpha$-springs ($b$ and $b+1$) is calculated by $\Delta\phi = \Delta\theta^{(b+1)} - \Delta\theta^{(b)}$, so that the strain energy stored in the spring $\beta^{(b)}$ is

$$E^{(b)} = \frac{1}{2}\beta^{(b)}|\Delta\phi|^2 = \frac{1}{2}\beta^{(b)}\left\{e_{kij}\varepsilon_{jp}(n^{(b+1)}_i n^{(b+1)}_p - n^{(b)}_i n^{(b)}_p)\right\}^2 \tag{24}$$

By superposing the strain energies of all angular and central bonds in Eq. (6), the effective stiffness tensors in a triangular lattice can be derived as follows

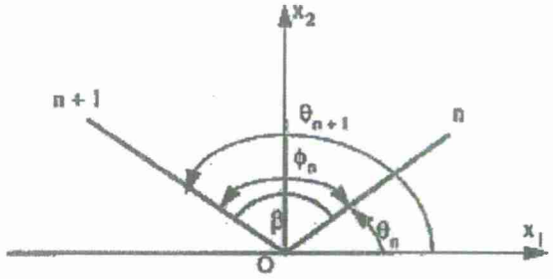


**Fig. 4.** A rectangular lattice with considering angular interactions.

R-226

$$C^{\alpha\beta}_{ijkm} = C^{\alpha}_{ijkm} + C^{\beta}_{ijkm}$$

$$= \underbrace{\frac{l^2}{V}\sum_{b=1}^{6}\alpha^{(b)} n_i^{(b)} n_j^{(b)} n_k^{(b)} n_m^{(b)}}_{\alpha\text{-spring}} + \left.\begin{aligned} &+\frac{1}{V}\sum_{b=1}^{6}\Big\{(\beta^{(b)}+\beta^{(b-1)})\delta_{ik} n_p^{(b)} n_j^{(b)} n_p^{(b)} n_m^{(b)} \\ &-(\beta^{(b)}+\beta^{(b-1)}) n_i^{(b)} n_j^{(b)} n_k^{(b)} n_m^{(b)} \\ &-\beta^{(b)}\delta_{ik} n_p^{(b)} n_j^{(b+1)} n_p^{(b+1)} n_m^{(b)} \\ &+\beta^{(b)} n_j^{(b)} n_j^{(b+1)} n_k^{(b+1)} n_m^{(b)} \\ &-\beta^{(b)}\delta_{ik} n_p^{(b)} n_j^{(b)} n_p^{(b+1)} n_m^{(b+1)} \\ &+\beta^{(b)} n_i^{(b+1)} n_j^{(b)} n_k^{(b)} n_m^{(b+1)}\Big\} \end{aligned}\right\}\beta\text{-spring} \tag{25}$$

where the position for $b = 0$ is the same as that of $b = 6$. Eq. (25) provides the basis for a spring network representation of an anisotropic material.

### 4.1. Triongular lattice

In this part, we consider two different particle interaction patterns, the nearest neighboring and two-layer particle (nearest and second neighbor) interactions.

#### 4.1.1. Nearest neighbor particle interaction

Here, we only account for the case of assigning the same $\alpha$ and $\beta$ to all the central and the angular springs, respectively. This generates a so-called Kirkwood model of an isotropic material [17]. The mesh structure is shown in Fig. 5. For each bond $b$, the direction vectors $n^{(b)}$ at respective angles $\theta^{(b)}$ are given in Table 2.

The stiffness tensors associated with $\alpha$-springs have been available from Eq. (11). According to Eq. (25), we get the stiffness tensors associated with $\beta$,

$$\begin{aligned} &C^{\beta}_{1111} = C^{\beta}_{2222} = \frac{9\beta}{4V} \\ &C^{\beta}_{1122} = C^{\beta}_{2211} = -\frac{9\beta}{4V} \\ &C^{\beta}_{1212} = \frac{9\beta}{4V} \\ &\text{Other } C^{\beta}_{ijkm} = 0 \end{aligned} \tag{26}$$

Hence, $\alpha - \beta$ stiffness tensors yield

$$\begin{aligned} &C^{\alpha\beta}_{1111} = C^{\alpha\beta}_{2222} = \frac{1}{2\sqrt{3}}\left(\frac{9\alpha}{4} + \frac{9\beta}{4l^2}\right) = \frac{E}{1-\nu^2} \\ &C^{\alpha\beta}_{1122} = C^{\alpha\beta}_{2211} = \frac{1}{2\sqrt{3}}\left(\frac{3\alpha}{4} - \frac{9\beta}{4l^2}\right) = \frac{E\nu}{1-\nu^2} \\ &C^{\alpha\beta}_{121} = \frac{1}{2\sqrt{3}}\left(\frac{3\alpha}{4} + \frac{9\beta}{4l^2}\right) = \mu = \frac{E}{2(1+\nu)} \\ &\text{Other } C^{\alpha\beta}_{ijkm} = 0 \end{aligned} \tag{27}$$

By definition, Poisson's ratio is resulted

$$\nu = \frac{C^{\alpha\beta}_{1122}}{C^{\alpha\beta}_{1111}} = \frac{1 - 3\beta/\alpha l^2}{3 + 3\beta/\alpha l^2} \tag{28}$$

$\alpha - \beta$spring constants are

$$\begin{aligned} &\alpha = \frac{2\sqrt{3}E}{3(1-\nu)} \\ &\beta = \frac{2\sqrt{3}(1-3\nu)El^2}{9(1-\nu^2)} \end{aligned} \tag{29}$$

From Eqs. (27) and (29), we obtain the Poisson's ratio range of this scheme is

$$-1 < \nu \leqslant \frac{1}{3} \tag{30}$$

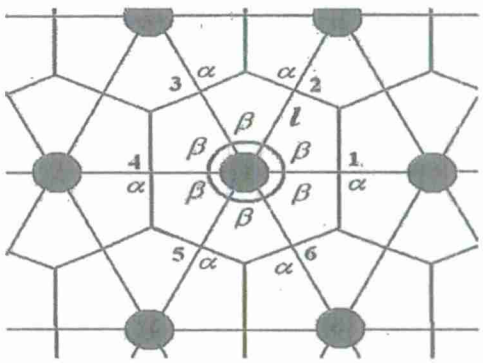


Fig. 5. A triangular lattice with hexagonal unit cell for $\alpha - \beta$ model, considering nearest neighboring particle interactions.

#### 4.1.2. Two-layer (nearest and second neighboring) particle interaction

The lattice system used is the same as the one described in Section 3.1.2. We assign the same $\beta$ to all the angular springs between the contiguous bonds incident to the same node. The stiffness tensors with respect to $\alpha^{I}$ and $\alpha^{II}$ is discussed in Section 3.1.2. Analogous process to Section 3.1.2 description and effort of $\beta$ is followed. The unit cell bond vectors $n^{I(b)}$, $n^{II(b)}$, at respective angles $\theta^{I(b)}$, $\theta^{II(b)}$ are given in Table 5.

From Eq. (25), $\beta$ constants are

$$\begin{aligned} &C^{\beta}_{1111} = C^{\beta}_{2222} = -\frac{4\beta}{\sqrt{3}l^2}, \quad C^{\beta}_{1122} = C^{\beta}_{2211} = \frac{4\beta}{\sqrt{3}l^2}, \\ &C^{\beta}_{1212} = \frac{45\beta}{12\sqrt{3}l^2} \end{aligned} \tag{31}$$

Hence, all $\alpha - \beta$ constants yield

$$\begin{aligned} &C^{\alpha\beta}_{1111} = C^{\alpha\beta}_{2222} = \frac{9}{4\sqrt{3}}\alpha^{I} + \frac{27}{4\sqrt{3}}\alpha^{II} - \frac{4\beta}{\sqrt{3}l^2} = \frac{E}{1-\nu^2} \\ &C^{\alpha\beta}_{1122} = C^{\alpha\beta}_{2211} = \frac{3}{4\sqrt{3}}\alpha^{I} + \frac{9}{4\sqrt{3}}\alpha^{II} + \frac{4\beta}{\sqrt{3}l^2} = \frac{E\nu}{1-\nu^2} \\ &C^{\alpha\beta}_{1212} = \frac{3}{4\sqrt{3}}\alpha^{I} + \frac{9}{4\sqrt{3}}\alpha^{II} + \frac{45\beta}{12\sqrt{3}l^2} = \mu = \frac{E}{2(1+\nu)} \\ &\text{Other } C^{\alpha\beta}_{ijkm} = 0 \end{aligned} \tag{32}$$

Assuming $\alpha^{II} = k\alpha^{I}$, from Eq. (32), the $\alpha$, $\beta$-spring constants are determined as follows:

$$\begin{aligned} &\alpha^{I} = \frac{\sqrt{3}E}{3(1+3k)(1-\nu)}, \quad \alpha^{II} = \frac{\sqrt{3}Ek}{3(1+3k)(1-\nu)}, \\ &\beta = \frac{\sqrt{3}(3\nu-1)El^2}{16(1-\nu^2)} \end{aligned} \tag{33}$$

Considering all the spring constants are non-negative, then the Poisson's ratio resulted from this scheme is $\nu = 1/3$. Consequently, $\beta = 0$, the same system as in Section 3.1.2 is recovered. This implies that using angular spring in this lattice system does not give a physical model.

**Table 5**
Bond vectors $n^{I(b)}$ and $n^{II(b)}$ with respect to angle $\theta^{I(b)}$ and $\theta^{II(b)}$

| Structure I: $b$ | Structure I: $n^{I(b)}$ | Structure II: $b$ | Structure II: $n^{II(b)}$ |
|---|---|---|---|
| 1 | $(1, 0)$ | 1 | $(3/2, \sqrt{3}/2)$ |
| 2 | $(1/2, \sqrt{3}/2)$ | 2 | $(0, \sqrt{3})$ |
| 3 | $(-1/2, \sqrt{3}/2)$ | 3 | $(-3/2, \sqrt{3}/2)$ |
| 4 | $(-1, 0)$ | 4 | $(-3/2, -\sqrt{3}/2)$ |
| 5 | $(-1/2, -\sqrt{3}/2)$ | 5 | $(0, -\sqrt{3})$ |
| 6 | $(1/2, -\sqrt{3}/2)$ | 6 | $(3/2, -\sqrt{3}/2)$ |

R-227

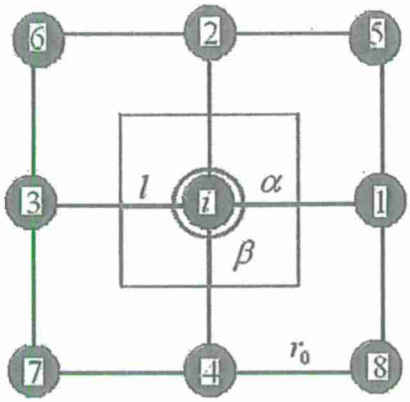


Fig. 6. A Rectangular lattice for $\alpha - \beta$ model, without considering diagonal particles.

### 4.2. Rectangular lattice

In this part, we consider the nearest neighboring interactions either containing axial or axial–diagonal particles.

#### 4.2.1. Axial interaction

Fig. 6 illustrates a mesh structure in which the diagonal particles are not involved into the interactions. The axial bond vectors for derivation are shown in Table 4. The cell area is $V = 4l^2$. The $\alpha - \beta$ stiffness tensors are determined

$$\begin{aligned} C^{\alpha\beta}_{1111} &= C^{\alpha\beta}_{2222} = \frac{2l^2}{V}\alpha = \frac{E}{1-\nu^2} \\ C^{\alpha\beta}_{1122} &= C^{\alpha\beta}_{2211} = 0 = \frac{E\nu}{1-\nu^2} \\ C^{\alpha\beta}_{1212} &= \frac{4\beta}{V} = \mu = \frac{E}{2(1+\nu)} \\ \text{Other } C^{\alpha\beta}_{ijkm} &= 0 \end{aligned} \tag{34}$$

From Eq. (34), we get

Poisson's ratio,

$$\nu = \frac{C^{\alpha}_{1122}}{C^{\alpha}_{1111}} = 0 \tag{35}$$

$$\alpha - \beta \text{ constants}: \quad \alpha = 2E, \ \beta = El^2/2 \tag{36}$$

#### 4.2.2. Axial-diagonal interaction consideration

We use the same lattice system as in Fig. 3, but all the angular springs are assigned as $\beta$. The bond vectors for derivation are completely the same values as in Table 4.

After conducting the analogous derivative process as above, the stiffness tensors yield

$$\begin{aligned} C^{\alpha\beta}_{1111} &= C^{\alpha\beta}_{2222} = \frac{l^2}{V}(2\alpha^{\mathrm{I}} + 4\alpha^{\mathrm{II}}) = \frac{E}{1-\nu^2} \\ C^{\alpha\beta}_{1122} &= C^{\alpha\beta}_{2211} = \frac{4\alpha^{\mathrm{II}}l^2}{V} = \frac{E\nu}{1-\nu^2} \\ C^{\alpha\beta}_{1212} &= \frac{4\alpha^{\mathrm{II}}l^2}{V} + \frac{4\beta}{V} = \mu = \frac{E}{2(1+\nu)} \\ \text{Other } C^{\alpha\beta}_{ijkm} &= 0 \end{aligned} \tag{37}$$

Thus, $\alpha - \beta$ constants are

$$\alpha^{\mathrm{I}} = \frac{2E}{1+\nu}, \quad \alpha^{\mathrm{II}} = \frac{E\nu}{1-\nu^2}, \quad \beta = \frac{(1-3\nu)El^2}{2(1-\nu^2)} \tag{38}$$

Eqs. (37) and (38) indicate the physical Poisson's ratio range resulted from this scheme is

$$-1 < \nu \leqslant \frac{1}{3}. \tag{39}$$

We find that this Poisson range is completely the same as that obtained by an $\alpha - \beta$ model in a triangular lattice mentioned in Section 4.1.1.

In contrast to the Poisson's ratio in Eq. (22) resulted by using the same lattice while without accounting for angular spring, we find that using $\beta$-springs in the rectangular lattice can greatly extend the Poisson's ratio range.

By definition, Poisson's ratio is

$$\nu = \frac{C^{\alpha\beta}_{1122}}{C^{\alpha\beta}_{1111}} = \frac{2\alpha^{\mathrm{II}}}{\alpha^{\mathrm{I}} + 2\alpha^{\mathrm{II}}} \tag{40}$$

We find that Eq. (40) is completely identified with Eq. (20), which implies, for this scheme, the resultant value of Poisson's ratio has nothing to do with the $\beta$-springs. However, $\beta$-springs affect the shear modulus, and therefore extend the range of Poisson's ratio.

Substituting Eqs. (38) and (40) into (39), we obtain

$$\alpha^{\mathrm{I}} \geqslant 4\alpha^{\mathrm{II}} \tag{41}$$

Eq. (41) indicates, a restricted ratio of $\alpha^{\mathrm{I}}$ to $\alpha^{\mathrm{II}}$ that must be satisfied in this lattice scheme.

Note that, for all the cases mentioned above, at interface of two materials, the axial effective spring constant, $\alpha_{\mathrm{eff}}$ can be approximately determined by a linear interpolation technique

$$\frac{1}{\alpha_{\mathrm{eff}}} = \frac{1}{\alpha^{\mathrm{phase\,1}}} + \frac{1}{\alpha^{\mathrm{phase\,2}}} \tag{42}$$

Where $\alpha^{\mathrm{phase\,1}}$ and $\alpha^{\mathrm{phase\,2}}$ are the spring constants of two different materials.

It is noted that the Poisson's ratios generated from all kinds of mesh networks and spring interaction manners mentioned above are varying from −1 up to 1/3. For the cases with Poisson's ratio ranging from 1/3 up to 1, a 'triple honeycomb lattice' is required [14]. As is shown in Fig. 7, this technique considers nearest neighbors but sets up three axial spring constants $\alpha_1$, $\alpha_2$ and $\alpha_3$ in each triangular unit cell, respectively. Synder et al. derived the Young's modulus and the Poisson's ratio from this technique as follows [18]:

$$E = \frac{2\sqrt{3}(\alpha_1 + \alpha_2 + \alpha_3)}{3\{1 + 2(\alpha_1 + \alpha_2 + \alpha_3)/9[(1/\alpha_1) + (1/\alpha_2) + (1/\alpha_3)]\}} \tag{43}$$

$$\nu = 1 - \frac{2}{\{1 + 2(\alpha_1 + \alpha_2 + \alpha_3)/9[(1/\alpha_1) + (1/\alpha_2) + (1/\alpha_3)]\}} \tag{44}$$

Then the spring constants $\alpha_1$, $\alpha_2$ and $\alpha_3$ are input into PM.

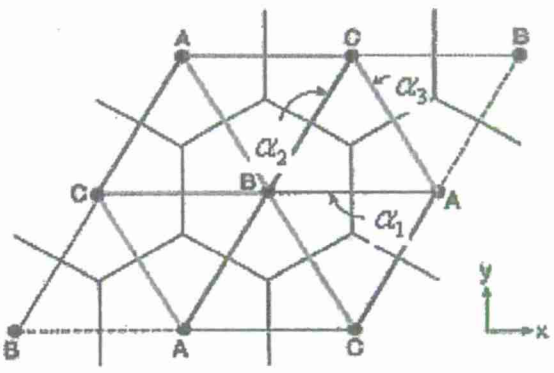


Fig. 7. A triangular lattice with hexagonal unit cell for $\alpha_1 - \alpha_2 - \alpha_3$ model, considering nearest neighbor particle interactions; after Snyder et al. [25].

## 5. PM dynamics associated with spring lattice derivations

In PM, a 2D linear axial dynamical equation with unit thickness is employed [24],

$$F_\alpha = \begin{cases} -S_0(r - r_0) & \text{for } r_c \leqslant r \leqslant r_t \\ 0 & \text{otherwise} \end{cases} \quad (45)$$

with $S_0$ the axial stiffness equal to $E{\cdot}r_0$ by the PM derivation, and $E$ the Young's modulus of material; $r$ is the distance between two particles, $r_0$ the equilibrium spacing between particles. $r_c$ and $r_t$ in Eq. (45) are the axial failure distance values applied for compression and tension, respectively, which are needed to be determined by empirical tests. For instance, the empirical tensile strain and compression failure strain values for concrete are $6.477 \times 10^{-5}$ and 0.003, respectively. Thus, for this case $r_c = (1. - 0.003) \cdot r_0$ and $r_t = (1. + 6.477 \times 10^{-5}) \cdot r_0$.

It has been introduced above that the conventional PM accounts for nearest neighboring particle interaction and runs in an equilateral triangular lattice system; this consideration leads to two deficiencies, fixed Poisson's ratio and biased mesh effect. It has been derived that using a variety of lattice structures and particle interactions, as introduced above, can extend PM to a larger range of Poisson's ratio as well as eliminate the so-called biased mesh effect. Once the lattice structure and the particle interaction manner are decided, the Poisson's ratio will be given. Hence, the remaining task for a dynamic problem lies in how to determine the stiffness $S_0$ in Eq. (45). In the following, we give only one example to illustrate how to determine $S_0$ demanded in PM under an equilateral triangular mesh and with one-layer particle interaction scheme. The analogous approach is followed for other cases.

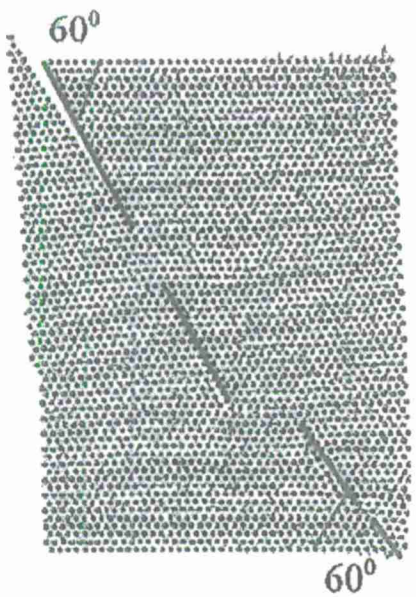


Fig. 8. Example of mesh effect by lattice model: compression simulation (red line indicates crack path). (For interpretation of the references to colour in this figure legend, the reader is referred to the web version of this article.)

In an equilateral triangular mesh structure, the spring constant $\alpha$ for one-layer particle interaction is determined by Eq. (13); the interface area of the unit cell between particles, illustrated in Fig. 1, is equal to $A = r_0/\sqrt{3}$ (note: $r_0 = 2l$ in Fig. 1). Thus, the effective stiffness is

$$S_0 = \alpha \cdot A = E \cdot r_0 \quad (46)$$

It is obvious that Eq. (46) describes a linear spring model that only limits to brittle materials. However, we find that Eq. (46) is completely identical to that is obtained from PM derivation [24]. The outcome of this result is that the already-existing nonlinear considerations of PM, such as Lennard–Jones potential (LJ), can be transferred into HLPM. In another word, we conclude that HLPM can be easily extended to inelastic systems.

In case of a $\beta$ interaction, an analogous angular spring interaction scheme to Eq. (45) yields

$$F_\beta = \begin{cases} -S_\phi(\phi - \phi_0) & \text{for} \phi_c \leqslant \phi \leqslant \phi_t \\ 0 & \text{otherwise} \end{cases} \quad (47)$$

with $\phi_0$ the equilibrium angle between adjacent particles, and $\phi$ the angular displacement. $\phi_c$ and $\phi_t$ in Eq. (47) are the angular fracture coefficients applied for compression and tension, respectively, which are also needed to be determined by empirical tests. At the current stage, due to a lack of the related empirical data, we have to leave them merely for the model tests. We believe that, for a specific material, default values for these two items could be found after elaborate numerical tests are conducted. By lattice model derivation, the angular stiffness $S_\phi = \beta$.

## 6. Example of using nearest and second neighbor particle interaction to eliminate mesh bias in a 2D triangular lattice

Mesh bias performs a fictitious crack path in the direction of crack propagation. It is well known that $\alpha$ model with an equilateral triangular mesh system often unavoidably derives such a mesh bias problem. For instance, in case of compression shown in Fig. 8, the simulated crack path propagates along a nearly 60° direction whereas the analytical result is 45° (crack path is indicated by read line). To deal with this problem, in this paper we adopt the scheme mentioned in Section 3.1.2, accounting for two-layer (nearest and second neighbor) particle interactions.

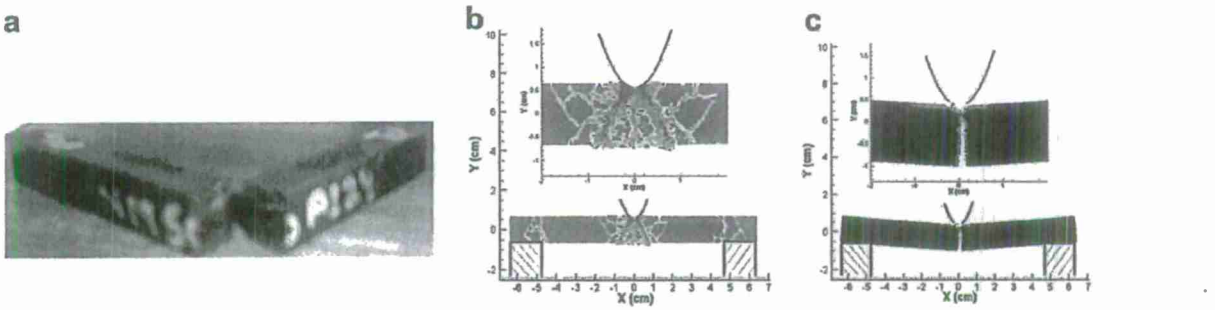


Fig. 9. Simulation of fracture pattern of a polymeric material (nylon-6,6) due to the impact of a rigid indenter: (a) experiment, (b) PM accounting for nearest particles and (c) PM accounting for two-layer of particles.

Fig. 9a shows the experimental result of fracture pattern of a polymeric material (nylon-6,6) due to the impact of a rigid indenter. Fig. 9b shows the particle modeling (PM) simulation result of this problem employing $\alpha$ model in a 2D triangular lattice which only considers the nearest particle interactions. It is obtained that a strong mesh bias behaves. This leads to the modeling result a low accuracy. While adopting a two-layer (nearest and second neighbor) particle interaction scheme, we see that HLPM successfully eliminates the mesh bias problem and the modeling crack path matches well with the experimental data (Fig. 9c).

Fig. 10a presents the measured load and energy history. It is measured that the load peak happens around $t \approx 1.70$ ms, and the deflection at the load peak is 3.03 mm, with the total impact energy equal to 1.2 J. The HLPM simulated result, Fig. 10b, shows that the load peak happens around $t \approx 1.66$ ms. The deflection at load peak is 3.0 mm, and the total impact energy calculated is 1.2 J. The simulated result can be compared to the experimental one shown in Fig. 10a. Although the simulated load profile is not exactly the same as the experiment, we observe similar characteristics, including the fluctuating profile with roughly the same period. The simulated peak load is also reasonable close to the experimental value. Hence, we conclude that the PM simulation compares favorably with the experimental measurements.

Here we expect that employment of $\alpha - \beta$ model may be another possible approach for eliminating a mesh effect. We will report the result to this study in our future papers.

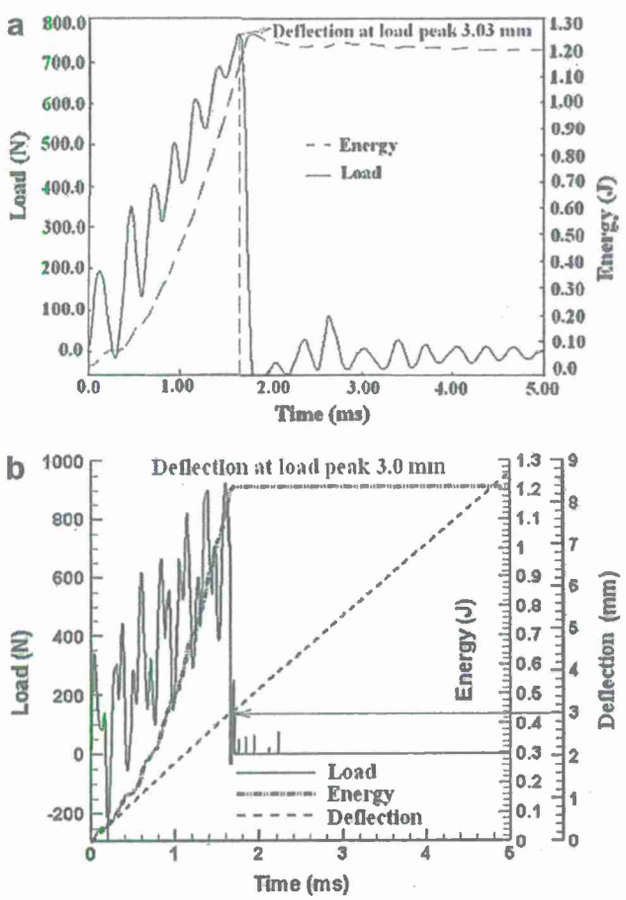


**Fig. 10.** Profile of load and energy of a polymeric material (nylon-6,6) due to the impact of a rigid indenter: (a) experiment and (b) PM accounting for two-layer of particles.

## 7. Conclusions

This paper proposes a hybrid lattice particle modeling (HLPM) approach for the simulation of dynamic fracture phenomena in homogeneous and heterogeneous materials at macro-scales with a variable Poisson's ratio effect. It is concerned with the mathematical derivations of employing elastic interaction formula between contiguous particles in 2D lattice networks accounting for different linkage mechanisms and different shapes of lattice. These lattice model (LM) techniques are then imported into the particle modeling (PM). Consequently, a hybrid model, HLPM is created. The principle of HLPM can be described as follows: the particle–particle interaction is derived from lattice modeling (LM) theory whereas the computational scheme follows particle modeling (PM) technique. Conventional PM technique was restricted to a fixed Poisson's ratio and had a strong bias in crack propagation direction, as a result of the geometry of the adopted lattice network. The newly proposed HLPM is free from the above-mentioned deficiencies and can be applied to a wide range of impact and dynamic fracture failure problems.

All the derivations follow the equivalence of strain energy stored in a unit cell with its associated continuum structure in the case of in-plane elasticity. In this paper, axial ($\alpha$) and combined axial-angular ($\alpha - \beta$) models are accounted for together with considering triangular or rectangular lattice. Through the study, a better understanding of the suitability of different lattice models is attained to adapt to various material properties and loading conditions. Consequently, equipped with these lattice derivations, HLPM can be extended to a wider spectrum of applications in dealing with different Poisson's ratios of materials at a continuum level with Poisson's ratios ranging from $(-1,1)$, no longer merely limited to 1/3 due to the application of an $\alpha$-model in a 2D equilateral triangular lattice. Meanwhile, a new particle interaction scheme (i.e., nearest and second neighbor particle interaction) is proposed in a triangular lattice. The adoption of this new particle linkage mechanism successfully eliminates a bias related to the lattice geometry in use. Overall, we have found the following results for elastic springs from the derivations of different considerations:

For $\alpha$-models:

(i) Nearest neighboring particle interaction:
  (a) In a uniform triangular lattice:Poisson's ratio is $\gamma = 1/3$; effective axial spring constant is $\alpha = \sqrt{3}E$. $E$ is the Young's modulus.
  (b) In a uniform rectangular lattice considering axial-diagonal particles:Poisson's ratio is $\gamma = 1/3$; effective axial and diagonal spring constants are $\alpha^{I} = 3E/2$, $\alpha^{II} = 3E/8$.

(ii) Two-layer (nearest and second) neighboring particle interaction in a uniform triangular lattice:Poisson's ratio is $\gamma = 1/3$; effective spring constants for the nearest and second neighboring particles are:
$\alpha^{I} = \sqrt{3}E/[2(1+3k)]$, $\alpha^{II} = \sqrt{3}Ek/[2(1+3k)]$, where $k$ is the ratio of the two spring constants.

For $\alpha - \beta$-models:

(i) Nearest neighboring particle interaction:
  (a) In a uniform triangular lattice:Poisson's ratio range is $-1 < \gamma \leqslant 1/3$; effective axial and angular spring constants are $\alpha = 2\sqrt{3}E/[3(1-\gamma)]$, $\beta = 2\sqrt{3}(1-3\gamma)El^2/[9(1-\gamma^2)]$, where $l$ is the half-length of the grid spacing.

R-230

(b) In a uniform rectangular lattice considering axial particles:Poisson's ratio $\gamma = 0.0$; effective axial and angular spring constants are $\alpha = 2E$, $\beta = El^2/2$.

(c) In a uniform rectangular lattice considering axial-diagonal particles:Poisson's ratio $-1 < \gamma \leqslant 1/3$; effective axial and angular spring constants are $\alpha^{I} = 2E/(1+\gamma)$, $\alpha^{II} = E\gamma/(1-\gamma^2)$, $\beta = (1-3\gamma)El^2/[2(1-\gamma^2)]$.

(ii) Two-layer (nearest and second) neighboring particle interaction in a uniform triangular lattice: angular spring is invalid for a realistic model.

Since HLPM and PM have the identical interaction force definition as illustrated in Eq. (46), inelastic considerations of PM are easily to be implemented into HLPM.

We finally transfer a two-layer neighboring particle interaction scheme into the PM model to simulate fracture pattern of a polymeric material (nylon-6,6) due to the impact of a rigid indenter. This treatment is found an efficient approach to eliminate a mesh bias effect in the direction of crack propagation.

Our future work will focus on implementing all the schemes mentioned above into PM. Calibrations of HLPM by aid of experimental data are also required.

## Acknowledgement

This work was partially supported by the funding received under a subcontract from the Department of Homeland Security-sponsored Southeast Region Research Initiative (SERRI) at the Department of Energy's Oak Ridge National Laboratory, USA. Authors wish to acknowledge the partial support for this research by ONR Grant No. N00014-07-1-1010, Office of Naval Research, Solid Mechanics Program (Dr. Yapa D.S. Rajapakse, Program Manager).

## References

[1] D. Greenspan, Computer-Oriented Mathematical Physics, University of Texas at Arlington, Pergamon Press, 1981.
[2] G. Wang, M. Ostoja-Starzewski, Comput. Mater. Sci. 33 (2005) 429–442.
[3] G. Wang, Particle modeling of dynamic fragmentation, Ph.D. dissertation, McGill University, 2005.
[4] G. Wang, M. Ostoja-Starzewski, P. Radziszewski, Particle modeling of comminution, 20th Canadian Congress of Applied Mechanics, May 30th to June 2nd, Montreal, Canada, 2005, pp. 149–150.
[5] G. Wang, M. Ostoja-Starzewski, P. Radziszewski, M. Ourriban, Comput. Mater. Sci. 35 (2006) 116–133.
[6] M. Ostoja-Starzewski, G. Wang, Probabilist. Eng. Mech. 21 (2006) 267–275.
[7] G. Wang, P. Radziszewski, J. Ouellet, Particle modeling simulation of thermal effects on ore breakage, Comput. Mater. Sci. (in press).
[8] D. Greenspan, J. Phys. Chem. Solids 50 (12) (1989) 1245–1249.
[9] D. Greenspan, Particle Modeling, Birkhäuser Publishing, 1997.
[10] D. Greenspan, Acta Appl. Math. 71 (2002) 279–313.
[11] A. Hrennikoff, ASME J. Appl. Mech. 8 (1941) A619–A715.
[12] A. Askar, Lattice Dynamical Foundations of Continuum Theories, World Scientific, Singapore, 1985.
[13] A.K. Noor, Appl. Mech. Rev. 41 (7) (1988) 285–296.
[14] M. Ostoja-Starzewski, Appl. Mech. Rev. 55 (1) (2002) 35–60.
[15] M. Ostoja-Starzewski, Microstructural randomness and scaling in mechanics of materials, in modern mechanics and mathematics series, Chapman & Hall/CRC/Taylor & Francis, 2007.
[16] M. Grah, K. Alzebdeh, P.Y. Sheng, M.D. Vaudin, K.J. Bowman, M. Ostoja-Starzewski, Acta Mater. 44 (10) (1996) 4003–4018.
[17] P.N. Keating, J. Mech. Phys. Solids 40 (1966) 1031–1051.
[18] K.A. Synder, E.J. Garboczi, A.R. Day, J. Mech. Phys. Solids 72 (1992) 5948–5955.
[19] M. Ostoja-Starzewski, Int. J. Solids Struct. 35 (19) (1998) 2429–2455.
[20] S. Bardenhagen, N. Triantafyllidis, J. Mech. Solids 42 (1994) 111–139.
[21] J.Y. Chen, Y. Huang, M. Ortiz, J. Mech. Phys. Solids 46 (1998) 789–828.
[22] G. Wang, A. Al-Ostaz, A.H.-D. Cheng, P.R. Mantena, A hybrid particle-lattice model for dynamic fracture problems, AAM'08, Louisiana, June 17–20, 2008.
[23] G. Wang, A. Al-Ostaz, A.H.-D. Cheng, P.R. Mantena, Particle modeling of a polymeric material (nylon-6, 6) due to the impact of a rigid indenter, Comput. Mater. Sci. (in press).
[24] K.K. Autar, Mechanics of composite materials, second ed., Taylor & Francis Group, 2005.
[25] J. Holnicki-Szulc, D. Rogula, Arch. Mech. 31 (6) (1979) 793–802.

# MICROWAVE CONDUCTIVITY MEASUREMENTS OF CARBON VEIL BY TWO DIFFERENT METHODS

**Shaya Karimkashi,[1] Darko Kajfez,[1] Ahmed A. Kishk,[1] and Shalmalee Vaidya[2]**
[1] Department of Electrical Engineering, Center of Applied Electromagnetic Systems Research, University of Mississippi, MS 38677; Corresponding author: skarimka@olemiss.edu
[2] Department of Materials Science and Engineering, University of Alabama at Birmingham, Birmingham, AL 35294

*Received 2 February 2009*

**ABSTRACT:** *Two measurement techniques to measure the conductivity of carbon veil sample, a new composite conductive material, are presented: the parallel plate cavity resonator method and the waveguide measurement method. Comparison between results obtained by these two methods is provided and an uncertainty analysis performed for both measurement methods.* © 2009 Wiley Periodicals, Inc. Microwave Opt Technol Lett 51: 2435–2438, 2009; Published online in Wiley InterScience (www.interscience.wiley.com). DOI 10.1002/mop.24661

**Key words:** *carbon veil; conductivity measurement; dielectric resonator; uncertainty; waveguides*

## 1. INTRODUCTION

In recent years, new categories of conductive materials including carbon fibers, carbon nanotubes, and carbon veils have become available. These new composite materials have a wide variety of applications in electromagnetic interference (EMI) and electromagnetic compatibility (EMC) [1–3]. The enhancement in utilizing these new conductive materials is because of their interesting electrical and mechanical properties achieved by combining different composites. For instance, they may have various levels of conductivity, lower weight, higher flexibility, and environmental durability in comparison with metal conductors [4, 5].

There is a lack of information about their electrical properties because of some difficulties in measuring their conductivity. However, reliable data on conductivities of these materials are needed to plan possible new applications.

Transmission line techniques are the simplest of the relatively accurate ways of measuring the electric properties of materials [2, 4, 6]. On the other hand, resonant cavity methods are very accurate for measuring the conductivity of metals or semiconductors [7, 8].

The main objective of this article is to measure the conductivity of carbon veil, one of the most available conductive composites, by using both waveguide and resonator cavity methods. Carbon veil can have a wide variety of applications in EMC and EMI because of its softness, flexibility, and low conductivity. Moreover, it is less subject to oxidation than its conductive counterparts like aluminum or copper.

Initially, we attempted to use the waveguide method described in [9] to determine the complex permittivity of the carbon veil, but the results were very inconclusive. After modifying the equations for interpretation of the waveguide procedure in the way described in Section 2.1., the results appeared to be more reliable. To verify the results by a different measurement procedure, we used a modified parallel-plate resonator containing a high-Q dielectric resonator with microstrip feeding, as described in Section 2.2. The measured results are presented and discussed in Section 3.

## 2. MEASUREMENT PRINCIPLES

### 2.1. Waveguide Method

Configuration of the waveguide fixture is depicted in Figure 1. The waveguide fixture consists of two coaxial to waveguide transitions connected to each other with waveguide flanges [9]. After TRL calibration, we put the thin layer of carbon veil sample between two waveguide flanges. This was done to insure a good contact of the carbon veil sample with the waveguide walls and to prevent the existence of any air gaps.

The novelty in the waveguide method implemented here consists of assuming that the material of the sample is essentially a conductor. To find a relation between S-parameters in the waveguide and conductivity of the sample, we start by some simple manipulation in Maxwell equations as follows:

$$\begin{aligned} \nabla \times H &= j\omega\varepsilon E + \sigma E \\ \nabla \times E &= -j\omega\mu H \end{aligned} \tag{1}$$

where $\sigma$ is the conductivity of the sample. We assume that for a conductive material $\sigma >> \omega\varepsilon$ and after using the method of separation of variables, we derive the propagation constant for TE modes as follows:

$$\gamma = \sqrt{-j\omega\mu\sigma - \left(\frac{m\pi}{a}\right)^2 - \left(\frac{n\pi}{b}\right)^2} \tag{2}$$

where $a$ and $b$ are waveguide cross section dimensions. Then, S-parameters for an assumed value of conductivity $\sigma$ can be calculated as follows:

$$S_{11} = \frac{\left(\frac{1}{R} - R\right)(e^{-\gamma l} - e^{\gamma l})}{D} \tag{3}$$

$$S_{21} = \frac{4}{D}. \tag{4}$$

Denominator $D$ is given by

$$D = \left(R + \frac{1}{R} + 2\right)e^{\gamma l} - \left(R + \frac{1}{R} - 2\right)e^{-\gamma l}. \tag{5}$$

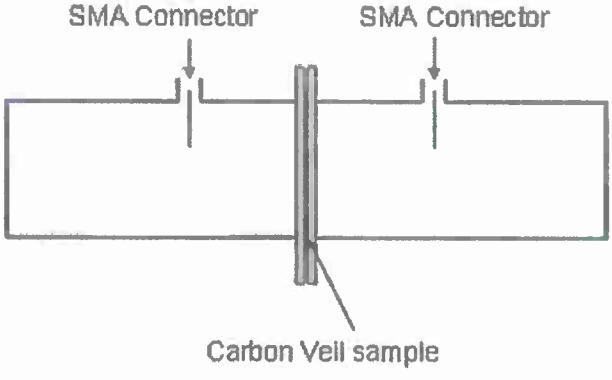


**Figure 1** Waveguide fixture with a thin carbon veil sample placed between two flanges. [Color figure can be viewed in the online issue, which is available at www.interscience.wiley.com]



S-232

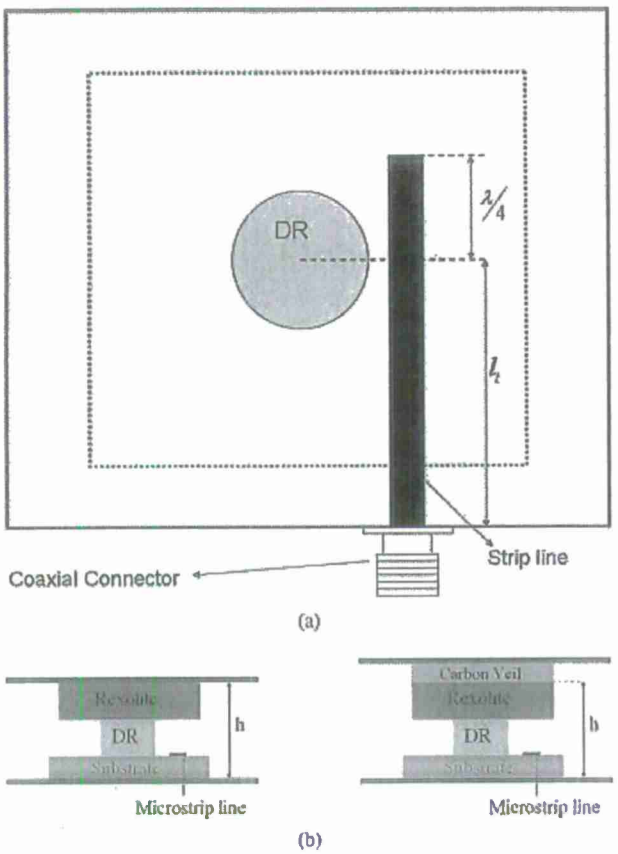


**Figure 2** Configuration of the cavity resonator (a) top view, (b) side view without carbon veil to measure, and (c) side view with carbon veil to measure. [Color figure can be viewed in the online issue, which is available at www.interscience.wiley.com]

$R$ is the ratio of the characteristic impedance of the filled waveguide and that of the empty waveguide for $TE_{01}$ mode:

$$R = \frac{\omega}{c}\sqrt{\frac{1-\left(\frac{f_c}{f}\right)^2}{-j\omega\mu\sigma-\left(\frac{\pi}{a}\right)^2}} \tag{6}$$

where $f_c$ is the cutoff frequency of the empty waveguide and $f$ is the frequency of operation.

The value of conductivity $\sigma$ is determined by minimizing the difference between the measured and computed S parameters of the sample.

### 2.2. *Cavity Resonator Method*

The difficulty of using the waveguide method is that carbon veil is very thin ($l$ = 0.254 mm) and also fuzzy type of material. At the same time, the measured value of the conductivity strongly depends on the accurate value of $l$. In contrast, the cavity resonator method, to be described here does not depend on the value of $l$, as long as this value is larger than one skin depth. Configuration of the parallel-plate resonator for measuring the conductivity is shown in Figure 2. This measuring equipment consists of two silver-plated conductors, a dielectric resonator, a microstrip transmission line, and a layer of Rexolite. The reason for this layer of dielectric between the resonator and the top conductor is to maintain a relatively high value of the unloaded $Q$-factor. Without this dielectric layer, the $Q$-factor of the resonator loaded with the carbon veil drops to as low value as 20. The traditional methods of the $Q$-factor measurement lose their accuracy when the unloaded $Q$-factor falls below about 100 [8].

To obtain impedance values associated with the dielectric resonator, the input impedance of the cavity is measured through the microstrip transmission line that is very close to the dielectric resonator [Fig. 2(a)]. Then, a de-embedding procedure is applied to determine the impedance close to the dielectric resonator to obtain accurate values of the unloaded $Q$-factors. Discontinuities in the coax-to-microstrip transition and also lossy propagation along the microstrip transmission line are taken into account in the de-embedding procedure [8, 10].

The de-embedded impedance values in the vicinity of resonant frequency are then curve-fitted to obtain an accurate value of the unloaded $Q$-factor of the resonator, $Q_{0s}$, when the top conductor is silver-plated [Fig. 2(b)], and another unloaded $Q$-factor, $Q_{0v}$, when a few thin layers of carbon veil are inserted between the Rexolite layer and the top conductor [Fig. 2(c)]. The difference of two unloaded $Q$-factors depends only on the two partial $Q$-factors $Q_{cv}$ and $Q_{cs}$, emanating from the conductivities of the carbon veil and silver, located on top of the Rexolite layer in Figures 2(b) and 2(c):

$$\frac{1}{Q_{0v}}-\frac{1}{Q_{0s}}=\frac{1}{Q_{cv}}-\frac{1}{Q_{cs}}. \tag{7}$$

The electric field of the $TE_{01\delta}$ mode is tangential to the top conductor surface, so that the partial $Q$-factors can be computed by the incremental inductance rule [11]:

$$Q_c=\frac{f_0}{\Delta f_0(\delta)}. \tag{8}$$

In other words, instead of integrating the power loss over the surface of the conductor, the partial $Q$-factor can be determined by computing the incremental frequency change when the perfect electric conductor surface is moved inwards by one skin depth $\delta$. Surface conductivity $\sigma$, which is to be measured, is related to skin depth $\delta$ as follows:

$$\delta=\frac{1}{\sqrt{\pi f\mu\sigma}}. \tag{9}$$

The incremental frequency change can be obtained by the numerical electromagnetic simulator. It is convenient to express the normalized change, which is the sensitivity of resonant frequency $f_0$, with respect to the change in $h$, the total height of the resonator:

$$C_h=\frac{h}{f_0}\cdot\frac{\partial f_0}{\partial h} \tag{10}$$

Substituting (8) to (10) into (7) and solving for the unknown skin depth of the carbon veil $\delta_v$, we obtain:

$$\frac{\delta_v}{h}=\frac{1}{C_h}\left(\frac{1}{Q_{0v}}-\frac{1}{Q_{0s}}\right)+\frac{\delta_s}{h} \tag{11}$$

The above equation enables us to determine the skin depth, and thus the surface conductivity of the carbon veil. The advantage of (11) is that all the terms entering the equation are dimensionless.

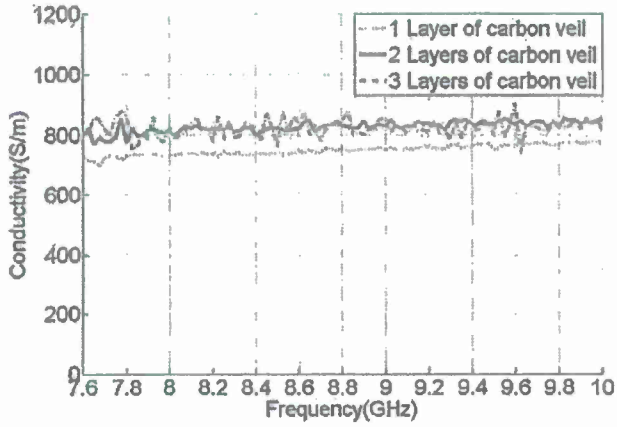


**Figure 3** Measured conductivity of carbon veil using waveguide method for different number of layers of carbon veil sample. [Color figure can be viewed in the online issue, which is available at www.interscience.wiley.com]

## 3. MEASUREMENT RESULTS

### *3.1. Waveguide Method*

Measurements were conducted using a square waveguide fixture of 20 × 20 cm cross section, over the frequency range of 7.6–10 GHz, with the Network Analyzer model HP 8510C. One, two, and three thin layers of carbon veil specimen with the thickness of 0.254 mm have been placed between two flanges and the measured two-port S-parameters have been referenced to the sample surfaces and then processed by minimization. Figure 3 shows the conductivity measured for three different cases. It can be seen that the measured conductivity is between 700 and 905 for three different cases in the frequency range.

### *3.2. Cavity Resonator Method*

A Trans-Tech dielectric resonator model D8700-0325-146 is used. The unloaded $Q$-factors, $Q_{0s}$, and $Q_{0v}$, are obtained by fitting the de-embedded measured S-parameters to the idealized $Q$-circles, as described in [8]. The de-embedding parameters of the transmission line are negligible except the attenuation constant, $\alpha$, which is estimated to be 1.005 ($Np/m$). Table 1 shows the measured and computed results for different number of carbon veil layers. Moreover, the heights and dielectric constants of different layers of the parallel-plate resonator are shown in Table 2.

After determination of $Q_{cv}$, incremental frequency rule for computing the conductivity of the carbon veil has been implemented by using HFSS software assuming PEC parallel plates. The reason for doing this is that HFSS fails to converge when a low conductivity value is used to model carbon veil sample. Measurements were conducted at the frequency of 7.66 GHz that is the resonant frequency of the resonator. Figure 4 shows the measured conductivity of the carbon veil for different number of carbon veil layers by assuming some uncertainties in the measurements. It can be seen that the mean value of the conductivity of the sample is between 790 and 870 for different cases.

**TABLE 1 The Measured ($Q_{0s}$, $Q_{0v}$) and Computed ($C_h$) Results of the Cavity Resonator for Different Number of Layers of Carbon Veil Sample**

| | 2 Layers | 3 Layers | 4 Layers | 5 Layers |
|---|---|---|---|---|
| $Q_{0s}$ | 3601 ± 200 | | | |
| $Q_{0v}$ | 468 ± 5.6 | 478 ± 6.1 | 463 ± 5.6 | 464 ± 7.1 |
| $C_h$ | 0.07157 | | | |

**TABLE 2 Properties of Different Sections of the Parallel-Plate Resonator**

| | Height (mm) | Dielectric Constant |
|---|---|---|
| Rexolite | 3.40 | 2.53 |
| Dielectric resonator | 3.71 | 28.5 |
| Substrate | 0.864 | 2.54 |

### *3.3. Uncertainty Analysis*

The measurement of the conductivity by using waveguide method is strongly affected by the thickness uncertainty of the thin carbon veil sample.

Assuming that the thickness uncertainty of each layer of the carbon veil sample is 0.0381 mm, about 15% of its measured value, the uncertainty in the carbon veil conductivity can be achieved by changing the thickness value of carbon veil sample, $l$, in (3) and (5). As shown in Figure 5, the percent uncertainty of the carbon veil conductivity is about 20%, 27%, and 27% for measurement with one, two, and three layers of carbon veil, respectively. It should be noted that the uncertainty analysis is done at the same frequency that conductivity is measured using resonant cavity method.

To estimate the uncertainty in measured conductivity using resonant cavity method, the inaccuracy of the HFSS simulation, the unloaded $Q$-factor when the top conductor is silver-plated, $Q_{0s}$, the other unloaded $Q$-factor when a few thin layers of carbon veil are inserted, $Q_{0v}$, and the microstrip attenuation constant, $\alpha$, can be identified as the sources of uncertainty. The uncertainty of these parameters will be denoted $\Delta C_h$, $\Delta Q_{0s}$, $\Delta Q_{0v}$, and $\Delta\alpha$.

For $\Delta C_h$, one can say that the error in the resonant frequency of the cavity structure affects the measured conductivity results. $\Delta Q_{0s}$ and $\Delta Q_{0v}$ are caused by the error in fitting the de-embedded measured S-parameters to the idealized $Q$-circles. The values are obtained by the software Qzero. In addition, $\Delta\alpha$ is caused by error in determining the unloaded $Q$-factor of the open ended microstrip line. As the four errors are uncorrelated, the total uncertainty of the carbon veil becomes

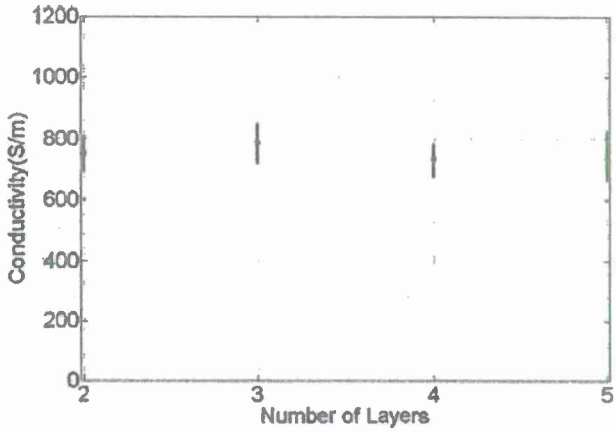


**Figure 4** Measured conductivity of carbon veil samples using cavity resonator method for different number of layers of carbon veil sample and by assuming some uncertainties in resonator cavity method. [Color figure can be viewed in the online issue, which is available at www.interscience.wiley.com]

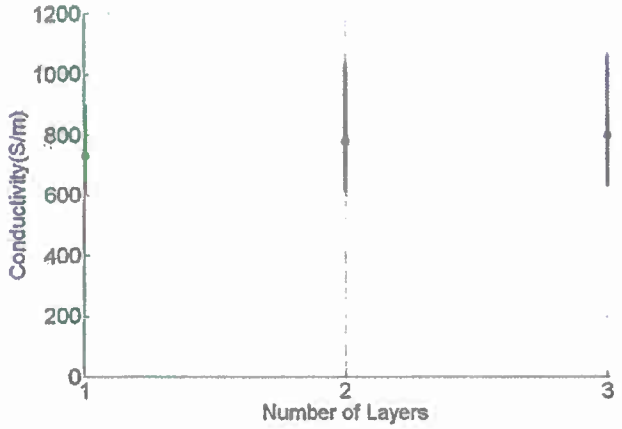


**Figure 5** Carbon veil conductivity measured using waveguide method by assuming a 15% of thickness uncertainty for one, two, and three layers of carbon veil sample. [Color figure can be viewed in the online issue, which is available at www.interscience.wiley.com]

$$\Delta\sigma = \sqrt{|\Delta C_b|^2 + |\Delta Q_{0s}|^2 + |\Delta Q_{0\sigma}|^2 + |\Delta\alpha|^2}\,. \qquad (12)$$

The total uncertainty of the carbon veil for different number of layers are also shown in Figure 4.

## 4. CONCLUSION

Two different techniques for measuring the conductivity of thin carbon veil samples were successfully implemented. After performing uncertainty analysis, the conductivity measured by using both methods agrees with each other. For the carbon veil sample used here, the resonant cavity method seems to be more accurate. However, by using waveguide method, it is possible to measure the conductivity at a wider frequency range.


## ACKNOWLEDGMENTS

Partial support for this research by ONR Grant # N00014-07-1-1010, Office of Naval Research, Solid Mechanics Program (Dr. Yapa D.S. Rajapakse, Program Manager) is acknowledged.


## REFERENCES


1. P.M. Raj, Processing and dielectric properties of nanocomposite thin film "supercapacitors" for high-frequency embedded decoupling, IEEE Trans Compon Packaging Technol 30 (2007), 569–578.
2. A. Saib, L. Bednarz, R. Daussin, C. Bailly, X. Lou, J.M. Thomassin, C. Pagnoulle, C. Detrembleur, R. Jérôme, and I. Huynen, Carbon nanotube composites for broadband microwave absorbing materials, IEEE Trans Microwave Theory Tech 54 (2006), 2745–2754.
3. C.P. Neo and V.K. Varadan, Optimization of carbon fiber composites for microwave absorbers, IEEE Trans Electromagn Compat 46 (2004), 102–106.
4. R.K. Challa, D. Kajfez, V. Demir, J.R. Gladden, and A.Z. Elsherbini, Characterization of multiwalled carbon nanotube (MWCNT) composites in a waveguide of square cross section, IEEE Microwave Wireless Compon Lett 18 (2008), 161–163.
5. R.J. Ramos, R.F. Bianchi, D.T. Balogh, and R.M. Faria, Conductivity of carbon black-PE composites as a function of temperature and UV aging, IEEE Trans Dielectrics Electrical Insulation 7 (2000), 855–859.
6. J. Baker-Jarvis, M.D Janezic, J.H. Grosvenor, and R.D. Geyer, Transmission/reflection and short-circuit line methods for measuring permittivity and permeability, NIST Technical Note 1335-R, 1993.
7. J. Mazierska, Dielectric resonator as possible standard for characterization of high temperature superconducting films for microwave applications, J Superconduct 10 (1997), 73–84.
8. D. Kajfez, Q factor, Vector Forum, Oxford, MS, 1994.
9. R.K. Challa, D. Kajfez, J.R. Gladden, and A.Z. Elsherbeni, Permittivity measurement with a non-standard waveguide by using TRL calibration and fractional linear Data fitting, Prog Electromagn Res B 2 (2008), 1–13.
10. W.P. Wheless, Jr., A Resonator impedance de-embedding procedure, IEEE Trans Microwave Theory Tech 38 (1989), 864–869.
11. D. Kajfez, Incremental frequency rule for computing the Q-factor of a shielded $TE_{0mp}$ dielectric resonator, IEEE Trans Microwave Theory Tech 32 (1984), 941–943.


© 2009 Wiley Periodicals, Inc.

# MEASUREMENT OF ELECTRIC POWER USING AN OPTICAL FIBER GRATING


**Chin-Hsing Cheng, Li-Min Lin, and Wen-Fung Liu**
Department of Electrical Engineering, Feng Chia University No.100, Wen Hwa Rd., Taichung 407, Taiwan, Republic of China;
Corresponding author: chcheng@fcu.edu.tw



*Received 3 February 2009*



**ABSTRACT:** *There is increasing motivation ta develap sensors and actuatars ta manage domestic electric power cansumption. This article demonstrates an optical fiber sensor using a superstructure fiber grating (SFG) to measure electric power cansumptian. The sensor head is based an SFG encapsulated in a palymer-half-field metal cylinder embedded a magnetic material at measure point. The operating mechanism is that the sensor can be attracted by the induced magnetic farce created by the electric power in the solenaid along one radial direction only, and respands to an axial force on the magnetic rod attached to the round plate, creating an axial attraction on the SFG. Therefore, variations in attractive farce cause center-wavelength variatians in SFB and long-period grating acts as an edge filter converting strain-induced wavelength variatian into aptical power measurement. Thus, the sensar can be used ta measure electric power without the use of power meter.* © 2009 Wiley Periodicals, Inc. Microwave Opt Technol Lett 51: 2438–2441, 2009; Published online in Wiley InterScience (www.interscience.wiley.com). DOI 10.1002/mop.24660



**Key words:** *electric power measurement; superstructure fiber grating (SFG); long-periad grating (LPG); pawer meter*


## 1. INTRODUCTION

Optical fiber gratings are currently being used as sensors for a number of physical magnitudes such as temperature, strain and pressure [1–2]; other magnitudes, such as current and magnetic field measurements can be detected by fiber gratings using appropriate transducers [3–8]. In particular, a superstructure fiber grating (SFG) has been used to measure pressure and temperature simultaneously [9–10]. The fabrication of an SFG generally exposes an ultraviolet laser beam passing through a periodic low-spatial-frequency amplitude mask and a phase mask into a fiber. Thus, an SFG includes the characteristics of both an FBG and a long-period grating (LPG). Based on this principle, the pressure and temperature can be measured simultaneously.

In various countries, there are presently attempts to replace electro-mechanical power meters with electronic ones [11]. Optical systems can replace electro-mechanical power meters for electric power measurements. As optical measurement systems tend to be much smaller and lighter than their conventional equivalents, this technique also makes it possible to produce portable equipment. In this article, we demonstrate a new approach to the measurement of electric power using a SFG. The LPG is used as



S-235

J Mater Sci (2008) 43:164–173
DOI 10.1007/s10853-007-2132-6

# Molecular dynamics simulation of SWCNT–polymer nanocomposite and its constituents

**Ahmed Al-Ostaz · Ghanshyam Pal · P. Raju Mantena · Alex Cheng**

Received: 31 March 2007 / Accepted: 27 August 2007 / Published online: 29 September 2007
© Springer Science+Business Media, LLC 2007

**Abstract** Elastic and engineering properties of nanoparticle enhanced composites and their constituents (matrix, reinforcement and interface) are calculated. The nanocomposites considered in this study consist of a single-wall carbon nanotube (SWCNT) embedded in polyethylene matrix. Molecular dynamics simulations are used to estimate the elastic properties of SWCNT, interfacial bonding, polyethylene matrix and composites with aligned and randomly distributed SWCNTs. The elastic properties of bundles with 7, 9, and 19 SWCNTs are also compared using a similar approach. In all simulations, the average density of SWCNT–polymer nanocomposite was maintained in the vicinity of CNTs, to match the experimentally observed density of a similar nanocomposite. Results are found to be in good agreement with experimentally obtained values by other researchers. The interface is an important constituent of CNT–polymer composites, which has been modeled in the present research with reasonable success.

## Nomenclature

| | |
|---|---|
| $H$ | Hamiltonian of the system |
| $\Psi$ | Wave function |
| $R$ | Position vector of atomic nucleus |
| $r_i$ | Position vector of an electron in the atom (or any particle in general) |
| $\Theta$ | Force field |
| $m$ | Mass of the particle |
| $t$ | Time |
| $E_{\text{total}}$, $U$ | Total potential energy of the system |
| $K_2$, $K_3$, $K_4$ | Force constants associated with bond length change |
| $b$ | Changed bond length |
| $b_o$ | Equilibrium bond length |
| $K_{2\theta}$, $K_{3\theta}$, $K_{4\theta}$ | Force constants associated with bond angle change |
| $\theta$ | Changed angle between two bonds |
| $\theta_o$ | Equilibrium angle between two bonds |
| $K_{1\phi}, K_{2\phi}, K_{3\phi}$ | Force constants associated with bond torsion |
| $\phi$ | Torsion angle |
| $K_{2\chi}$ | Force constants associated with out of plane angle change |
| $\chi$ | Out of plane angle |
| $\chi_0$ | Equilibrium out-of-plane angle |
| $K_{b\theta}$ | Force constants associated with bond length change and bond angle change coupling |
| $K_{1b}$, $K_{2b}$, $K_{3b}$ | Force constants associated with bond length change and bond torsion coupling |
| $K_{1\theta\phi}, K_{2\theta\phi}, K_{3\theta\phi}$ | Force constants associated with bond angle change and bond torsion coupling |
| $K_{\theta\phi}$ | Force constants associated with second order bond angle change and bond torsion coupling |
| $e$ | Charge of an electron |
| $C_{ijkl}$ | Stiffness matrix |
| $\sigma_{ij}$ | Stress component |

A. Al-Ostaz (✉)
Department of Civil Engineering, The University of Mississippi, 202 Carrier Hall, University, MS 38677, USA
e-mail: Alostaz@olemiss.edu

G. Pal · P. R. Mantena · A. Cheng
Composite Structures and Nano Engineering Research Group, The University of Mississippi, University, MS 38677, USA



T-236

| | |
|---|---|
| $\varepsilon_{kl}$ | Strain component |
| $A$ | Helmholtz free energy |
| $V$ | Volume of the simulation cell |
| $V_o$ | Undeformed volume of the simulation cell |
| $v$ | Velocity of the particle |
| $f_i$ | Force acting on the particle $i$ |
| $p_i$ | Momentum of the atom (particle) in original system |
| $\bar{F}, \bar{G}$ | Trajectory average of any thermodynamic property |
| $N$ | Total number of atoms in the system |
| $\rho_i$ | Position vector in the scaled coordinate system |
| $Q$ | Same as volume, $V$ |
| $\eta$, $M$ | Constants |
| $\pi_i$ | Momentum conjugate to $\rho_i$ |
| $\Pi$ | Momentum conjugate to $Q$ |
| S | Stochastic collision term for atoms |
| $\gamma$ | Mean rate of stochastic collision |
| $C_{ij}$ | Material stiffness matrix |
| $E_{ij}$, $\upsilon_{ij}$, $\mu_{ij}$, $K_{ij}$ | Engineering constants (Youngs modulus, Poisson's ratio, shear modulus and bulk modulus) |
| $E_{\text{pull-out}}$ | Pull-out energy |
| $\tau_i$ | Interfacial shear stress |
| $a$ | Radius of the nanotube |
| $L$ | Length of the nanotube |

## Introduction

The emergence of nano-sciences during the last decade has drastically altered the landscape of scientific research and technology development. Nano reinforcement of engineering materials can impart dramatic structural (e.g., stiffness) and physical (e.g., reduced CTE) property benefits without adding significant weight [1, 2]. For example, nanolayered reinforcement can impart greater thermal stability [3, 4] with reduced permeability, making the polymer less flammable, and improving barrier performance [5–7]. Ideally, the nanolayer reinforcement distributes internal stresses more uniformly allowing greater dimensional latitude in forming and shaping processes compared to conventional macroscale reinforcement. The unparalleled characteristics of clay nanolayers to boost mechanical properties of an engineering polymer (Nylon-6) were first demonstrated by Toyota researchers [8]. With only 4.2 wt.% of clay nanolayers, the modulus doubled and heat distortion temperature increased by 80 °C compared to the pristine polymer, along with a reduction in water permeability and an increase in flame retardant properties. These dramatic improvements in properties made it possible to extend the use of low-cost polymers in under-the-hood applications. In order to fully utilize this type of mechanical property improvement for structural applications, the resulting nanoreinforced composite materials must have high modulus, high heat deflection temperature, low thermal expansion coefficient, high tensile strength and low permeation rates.

A critical issue for nanotechnology is the ability to understand, model, and simulate the behavior of small structures and to make the connection between structure properties and functions. Most nanosystems are too small for direct measurements but too large to be described by current rigorous first principles in theoretical and computational methods. They exhibit too many statistical ensembles. This problem is even more challenging in the case of nanocomposites where carbon nanotubes are dispersed randomly in a polymeric (i.e., polystyrene, epoxy etc.) matrix. The vital role of molecular modeling in this field is to enable engineering design at the component and systems level, and to set objectives that could guide laboratory efforts of the physical implications. An important component in molecular mechanics calculations of nanostructured materials is the description of the forces between individual atoms which are characterized by force fields.

## Simulation of carbon nanotube composites using molecular dynamics approach

Many researchers have attempted to model the mechanical behavior of single wall carbon nanotube (SWCNT) taking input from molecular mechanics. Several new computational methods and their applications to nanostructures have been developed: equivalent continuum models [9–11], quasi-continuum models [12–18] using Tersoff and Brenner interatomic potential [19, 20], and molecular dynamics simulations [21, 22]. In this article we focus on modeling and simulation of SWCNT composites using the molecular dynamics approach.

### The Born–Oppenheimer approximation

The Born–Oppenheimer approximation is the foundation of molecular dynamics [23]. Noting that the electrons are several thousands of times lighter than the nuclei and therefore move much faster, Born and Oppenheimer proposed that the motion of the electrons can be decoupled from that of the nuclei, giving two separate equations. The first of these equations describes the electron motion where the energy is the function of coordinate of nucleus $E(R)$ only and is termed as potential energy surface. The second part of the equation describes the motion of the nucleus on this potential energy surface. The solution of the nucleus



T-237

motion is the basis of molecular dynamics. But prior to that, one needs to solve the equation pertaining to the motion of the electron for the expression of the $E(R; r)$. Solving the equation for electronic motion is not easy because the potential energy surface is not unique. Thus, an empirical fit to the potential energy surface, commonly called a force field ($E_{\text{total}}$), is usually used. Since the nuclei are relatively heavy objects, quantum mechanical effects are often insignificant and equation of motion for nuclei can be replaced by Newton's equation of motion given as:

$$-\frac{\mathrm{d}\Theta}{\mathrm{d}R} = m\frac{\mathrm{d}^2R}{\mathrm{d}t^2} \tag{1}$$

where, $\Theta$ is the force field, $R$ describes the location of the nuclei in space, $m$ is the mass of the nuclei and $t$ is time. The solution of the above equation is the term $R$ ($t$) called the trajectory of the system.

## The force field

A force field in molecular mechanics and molecular dynamics is the average description of the existing interactions among various atoms in a molecule or a group of molecules in terms of functions and parameters sets [24]. The electronic configuration around atoms is not included into the description of these atomic interactions. Generally, the force field parameters are empirical, derived from quantum modeling and, sometimes, from heuristics.

The functional forms of various interactions, summed together in order to yield the COMPASS force field can be achieved from the introductory paper on COMPASS by Sun [25].

$$\begin{aligned}
E_{\text{Total}} = & \sum_b [K_2(b-b_o)^2 + K_3(b-b_o)^3 + K_4(b-b_o)^4] \\
& + \sum_\theta [K_{2\theta}(\theta-\theta_o)^2 + K_{3\theta}(\theta-\theta_o)^3 + K_{4\theta}(\theta-\theta_o)^4] \\
& + \sum_\phi [K_{1\phi}(1-\cos\phi) + K_{2\phi}(1-\cos 2\phi) \\
& + K_{3\phi}(1-\cos 3\phi)] + \sum_\chi K_{2\chi}(\chi-\chi_o)^2 \\
& + \sum_{b,\theta} K_{b\theta}(b-b_o)(\theta-\theta_o) + \sum_{b,\phi}(b-b_o)[K_{1b}\cos\phi \\
& + K_{2b}\cos 2\phi + K_{3b}\cos 3\phi] + \sum_{\theta,\phi}(\theta-\theta_o)[K_{1\theta\phi}\cos\phi \\
& + K_{2\theta\phi}\cos 2\phi + K_{3\theta\phi}\cos 3\phi] + \sum_{b,\theta}(\theta'-\theta'_o)(\theta-\theta_o) \\
& + \sum_{\theta,\theta,\phi} K_{\theta\phi}(\theta'-\theta'_o)(\theta-\theta_o)\cos\phi \\
& + \sum_{i,j}\frac{q_i q_j e}{r_{ij}} + \sum_{i,j}\varepsilon_{ij}\left[2\left(\frac{r^o_{ij}}{r_{ij}}\right)^9 - 3\left(\frac{r^o_{ij}}{r_{ij}}\right)^6\right]
\end{aligned} \tag{2}$$

where the first 10 terms are "valence terms". The first through fourth terms represent the energy associated with bond ($b$), angle ($\theta$), torsion ($\phi$), and Wilson out-of-plane ($\chi$) internal coordinates respectively. The rest of the terms excluding the last two terms represent the energies of cross-coupled internal coordinates which are important for calculating the vibration frequencies and structural variations associated with conformational changes. The last two terms represent "nonbond" interaction between atoms separated by two or more intervening atoms, or belonging to different molecules. The second-to-last term is the Coloumb potential that represents electrostatic interactions. The last term of Eq. 2, that is the Lenard-Johns 9-6 (LJ 9-6) potential, represents the van der Waals interaction. The *LJ-9-6* function is considered as a soft function in the repulsive region compare to the conventional *LJ-12-6* function.

## Simulation of SWCNT composites and their constituents

In this article we use commercially available molecular dynamics software (Materials Studio® 4.1) by Accelrys [23] to simulate a nanocomposite and its constituents (e.g., reinforcement, matrix, and interface). The nanocomposite considered in this study consists of a single-wall carbon nanotube (SWCNT) embedded in polyethylene matrix. Molecular dynamics approaches are used to estimate the elastic properties of SWCNT, interfacial bonding, polyethylene matrix, and composites with aligned and randomly distributed SWCNTs. The elastic properties of bundles of 7, 9, and 19 SWCNTs are also compared using the same approach.

For each configuration submitted for static elastic constants analysis, the first step consists of energy minimization using conjugate gradients method. In this study, the target minimum derivative for the initial step is 0.1 kcal/Å. However, to reduce the time required for the calculation, a maximum of 1,000 steps are performed in attempting to satisfy the convergence criterion. Following the initial stage, three tensile and three pure shear deformations of magnitude ±0.0005 are applied to the minimized system and the system is re-minimized following each deformation. The internal stress tensor is then obtained from the analytically calculated virial, which is also used for obtaining estimates of the stiffness matrix.

As a result of these simulations, the elastic stiffness coefficients can be obtained by calculating $\Delta\sigma_i/\Delta\varepsilon_j$ for each of the applied strains, where $\sigma_i$ represents, in vector notation, elements of the stress tensor obtained analytically using the following expression:



T-238

$$\sigma = -\frac{1}{V_o}\left[\left(\sum_{i=1}^{N} m_i\left(v_i v_i^T\right)\right) + \left(\sum_{i<j} r_{ij} f_{ij}^T\right)\right] \quad (3)$$

where, index $i$ runs over all particles 1 through $N$; $m_i$, $v_i$ and $f_i$ denote the mass, velocity and force acting on particle $i$; and $V_o$ denotes the (undeformed) system volume.

Due to scaling problems and computational limitations, one can simulate the behavior of only a small number of particles (few thousand atoms) by using molecular dynamics. However, in order to eliminate the surface effects and to simulate the bulk material, periodic boundary conditions are imposed on the system.

## Results and discussion

### Molecular dynamics simulation of SWCNT–polymer constituents

#### *Molecular dynamics simulation of SWCNT*

One of the primary aims of the present study is to determine the elastic and/or engineering constants of single-wall carbon nano tubes of different chirality. Molecular dynamics simulation runs of SWCNT with (7,0) chirality (Fig. 1a) and (5,5) chirality (Fig. 1b) were carried out under the constant Number of particle, constant Pressure and constant Temperature (NPT) ensemble. These two chiralities were chosen because they have a similar radius of the CNT. The length of SWCNT was chosen as 105 Å so that an aspect ratio of 25:1 (length:diameter) could be maintained in order to capture the slender structure of SWCNTs. One SWCNT was then placed into a 105 Å × 8.7 Å × 8.7 Å simulation cell. The simulation parameters for NPT molecular dynamics of one SWCNT are given in Table 1.

Depending upon load conditions, the simulation was divided into three parts: axial, transverse, and shear loadings. The simulation cell was subjected to uniaxial tensile loading along the tube axis. The load was varied from $2.0265 \times 10^{-2}$ MPa to $1.01325 \times 10^{2}$ MPa during different simulation runs. In other simulation runs, the load was applied either in the transverse or shear direction with load varied between $2.0265 \times 10^{-2}$ MPa and $1.01325 \times 10^{2}$ MPa during different simulation runs. All of the runs gave similar results. For each configuration submitted for static elastic constants analysis, a total of 13 minimizations are performed. The first consists of a conjugate gradients minimization of the undeformed amorphous system. The target minimum derivative for this initial step is 0.1 kcal/Å. However, to reduce the time required by the calculation, a maximum of 1,000 steps are performed in attempting to satisfy the convergence criterion. Following this initial stage, three tensile and three pure shear deformations of magnitude ±0.0005 are applied to the minimized undeformed system and the system is re-minimized following each deformation. The internal stress tensor is then obtained from the analytically calculated virial and used to obtain estimates of the six columns of the elastic stiffness coefficients matrix. These are the default values in the software which are calculated automatically and this is why the choice of applied loading magnitude (as long as it is in the elastic limit) and direction are irrelevant. Typical elastic constants obtained for the case of 7,0 SWCNT are:

$$C_{ij} = \begin{bmatrix} 1027 & 25.18 & 19.45 & 0 & 0 & 0 \\ 26.78 & 43.11 & 20.54 & 0 & 0 & 0 \\ 20.33 & 28.08 & 37.43 & 0 & 0 & 0 \\ 0 & 0 & 0 & 7.28 & 0 & 0 \\ 0 & 0 & 0 & 0 & 5.59 & 0 \\ 0 & 0 & 0 & 0 & 0 & 7.14 \end{bmatrix} \text{GPa}$$

and for the 5,5 SWCNT case are:

$$C_{ij} = \begin{bmatrix} 729.8 & 1.123 & 1.489 & 0 & 0 & 0 \\ 1.494 & 2.320 & .016 & 0 & 0 & 0 \\ 1.463 & 0.341 & 0.766 & 0 & 0 & 0 \\ 0 & 0 & 0 & 11.81 & 0 & 0 \\ 0 & 0 & 0 & 0 & 1.435 & 0 \\ 0 & 0 & 0 & 0 & 0 & 11.86 \end{bmatrix} \text{GPa}$$

where $i,j$ = 1,2,3 with 1 representing the axial direction and 2, 3 representing plane of symmetry. Thus we have a

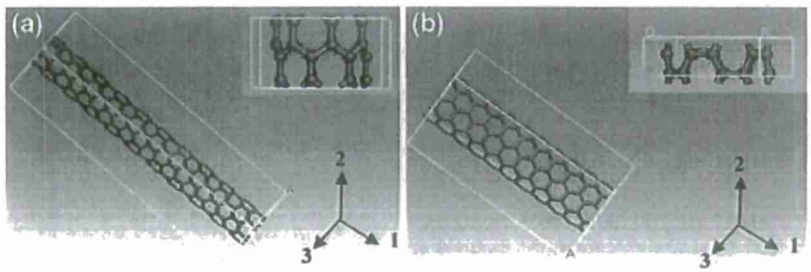


**Fig. 1** Molecular dynamic simulation of SWCNT with (a) 7,0 chirality, and (b) 5,5 chirality



T-239

**Table 1** Molecular dynamics simulation parameters for one SWCNT

| System | One (7,0) or (5,5) SWCNT, 105 Å length |
|---|---|
| MD ensemble | NPT |
| Temperature | 293 K |
| Time step | 1 femto second (fs) |
| Duration of simulation | 100 pico second (ps) |
| Periodic boundary condition | ON |

transversely isotropic problem. For this case, the five engineering constants may be calculated from elastic constants using the following relations [26]:

$$E_{11} = C_{11} - \frac{2C_{12}^2}{C_{22} + C_{23}}$$
$$E_{33} = E_{22} = C_{22} + \frac{C_{12}^2(-C_{22} + C_{23}) + C_{23}(-C_{11}C_{23} + C_{12}^2)}{C_{11}C_{22} - C_{12}^2}$$
$$\nu_{12} = \nu_{13} = \frac{C_{12}}{C_{22} + C_{23}}$$
$$\mu_{23} = \frac{1}{2}(C_{22} - C_{23})$$
$$K_{23} = \frac{1}{2}(C_{22} + C_{23}) \quad (4)$$

Thus, the axial Young's modulus of arm-chair CNT is 1007 GPa (≈1 TPa) whereas the axial Young's modulus of zigzag CNT is 728 GPa. These are in good agreement with experimentally obtained values by other researchers [27].

*Molecular dynamics simulation of clusters of SWCNT*

Carbon nanotubes naturally tend to form crystals of hexagonally packed bundles or ropes that exhibit transversely isotropic behavior. Determination of the effective mechanical properties of nanotube bundles is important so that their applicability as reinforcements in composite materials can be evaluated. Also, once the effective properties of the carbon nanotube bundles are determined, these values can be used as input parameters for the next step in case of multi level modeling of SWCNT–polymer matrix composites. In these bundles, the inter-tube force interactions are due to primarily nonbonding Van der Waals interactions. These weak cohesive properties of nanotube bundles are important in the prediction of mechanical properties of nanotube composite materials and those of fibers of woven carbon nanotubes.

Three clusters of (7,0) SWCNTs were examined using molecular dynamics. The first cluster consists of seven SWCNTs packed in hexagonal fashion in a simulation cell, the second cluster consists of nine, and third cluster consists of 19 SWCNTs packed in hexagonal fashion in a simulation cell as shown in Figs. 2, 3, and 4, respectively. Constant temperature–constant pressure (NPT) molecular dynamics was performed. In order to simulate normal temperature and pressure conditions during the simulation experiment, the temperature of the system was maintained at 298 K and an arbitrary chosen small hydrostatic pressure of magnitude 10 atm was applied on the simulation cell in all three experiments. The NPT MD simulation parameters are given in Table 2 and the results of MD simulation are reported in Table 3.

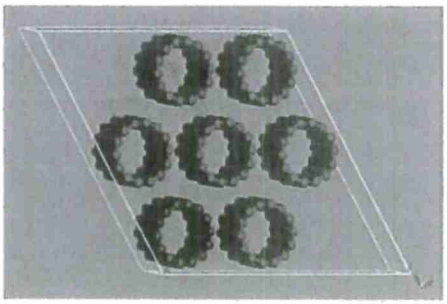

**Fig. 2** Cluster of seven (7,0) SWCNTs inside the simulation cell

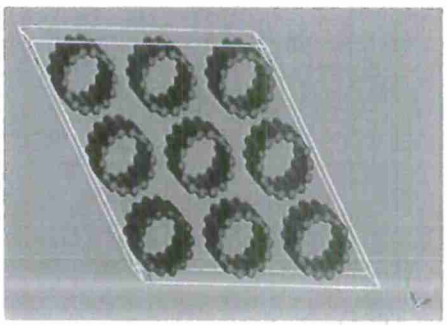

**Fig. 3** Cluster of nine (7,0) SWCNTs inside the simulation cell

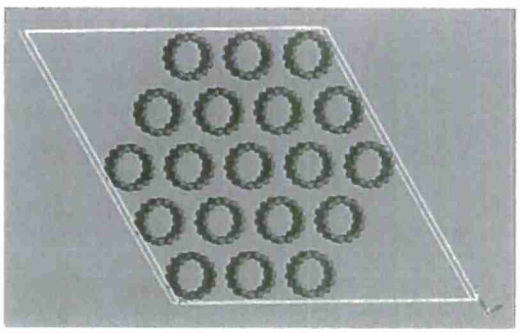

**Fig. 4** Cluster of 19 (7,0) SWCNTs inside the simulation cell



T-240

**Table 2** Molecular dynamics simulation parameters for SWCNT bundles

| System | Cluster of (7,0) SWCNTs, 105 Å length |
|---|---|
| MD ensemble | NPT |
| Temperature | 298 K |
| Time step | 1 femto second (fs) |
| Duration of simulation | 100 pico second (ps) |
| Periodic boundary condition | ON |

*Molecular dynamics simulation of matrix*

Polyethylene, a thermoplastic, has been chosen as the matrix material for construction of the composite. Polyethylene [IUPAC name—polyethene (PE)] is a thermoplastic commodity polymer [28] created through polymerization of ethylene. Its name originates from the monomer ethene, also known as ethylene, used to create the polymer. The ethylene molecule, $C_2H_4$ is $CH_2{=}CH_2$, two $CH_2$ connected by a double bond. The polymerized structure of the polyethylene is shown in Fig. 5.

Polyethylene is classified into several different categories based on its density and branching. Sometimes some of the carbons, instead of having hydrogen attached to them, they have long chains of polyethylene attached to them. This is called branched, or low-density polyethylene, or LDPE. When there is no branching, it is called linear polyethylene, or HDPE. Linear polyethylene is much stronger than branched polyethylene. The mechanical properties of PE depend significantly on variables such as the extent and type of branching, the crystal structure, and the molecular weight [28].

Simulation of the polymer consists of potential energy minimization followed by two steps of molecular dynamics. A single simulation cell of the polymer consists of eight chains of monomer comprising of total 1,216 atoms. This simulation cell was then subjected to periodic boundary conditions in order to simulate the behavior of the bulk polymer. Initially, during the actual chemical reaction the rate of the reaction is reported to be fast which gradually slows down as the chemical reaction proceeds. Therefore, in order to capture the complete trajectory of the polymer chains during molecular dynamics simulations, a two step molecular dynamics simulation was carried out.

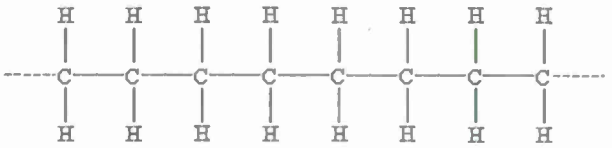

**Fig. 5** Polymerized structure of the polyethylene

The first stage of dynamics was carried out for 20 pico second (ps) with a smaller time step of 0.2 femto second (fs). This was followed by the second stage with a comparatively larger time step of 1.0 fs which lasted for 100 ps. The final density of the polymer matrix was maintained as 0.92 g/cc. The temperature of the system was maintained at 298 K throughout the simulation and a hydrostatic pressure of 1 atm pressure was applied to the system during the dynamics. Figures 6 and 7 show the polymer chains used in this simulation, and Table 4 shows final engineering properties of the simulated polymer system.

*Molecular dynamics simulation of the SWCNT–polymer interfacial bonding*

In case of composites, the effective transfer of load from matrix to reinforcement occurs via the interface. The extent of this load transfer depends upon the degree of adhesion between the nanotube and matrix material. The adhesive strength between the nanotubes and the polymeric matrix can be evaluated by the interfacial bonding energy. In case of nonfunctionalized SWCNT–polymer composites, the nature of interfacial bonding energy comes from electrostatic and Van der Waals force in the composite system.

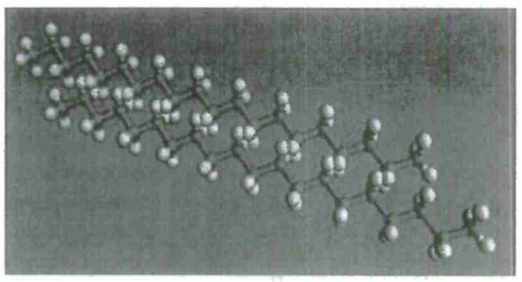

**Fig. 6** Simulated single polymer chain of polyethylene

**Table 3** Results of MD simulation of (7,0) SWCNT clusters

| Simulation conditions | $E_{11}$ (GPa) | $E_{22}$ (GPa) | $\nu_{12}$ | $\mu_{23}$ (GPa) | $K_{23}$ (GPa) |
|---|---|---|---|---|---|
| Seven nanotubes, NPT, 1.0 Mpa (hydrostatic), 293 K | 1021.7 | 26.85 | 0.31 | 8.41 | 33.7 |
| Nine nano-tubes (displaced from their equilibrium positions), NPT, 1.0 MPa (hydrostatic), 293 K | 1019.6 | 19.49 | 0.29 | 5.73 | 32.88 |
| 19 nanotubes, NPT, 1.0 Mpa (hydrostatic), 293 K | 931.3 | 14.96 | 0.29 | 4.44 | 23.9 |



T-241

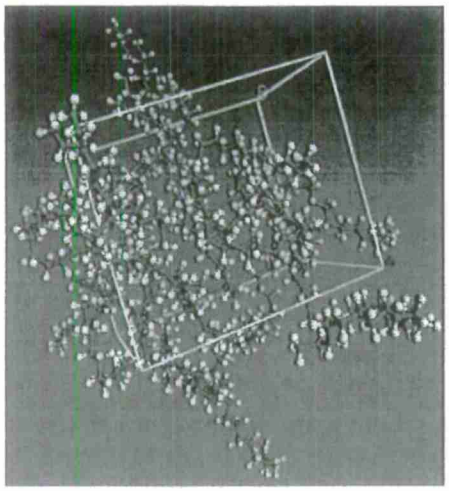

Fig. 7 Simulated polymer chains of polyethylene

Table 4 Engineering constants of the simulated polyethylene

| $E$ (GPa) | $\nu_{12}$ |
|---|---|
| 1.22 | 0.37 |

Molecular dynamics simulation of the interface for SWCNT–polymer composite was carried out by simulating the single fiber pull-out test. Figure 8 shows the atomistic model used for interfacial binding simulations. The polymer composite model used in this study was 10,0 SWCNT–polyethylene composite. The model has a total of 1,206 atoms and the final density of the composite was 1.3 g/cc. Before the start of pull-out test, the periodic boundary conditions imposed on the system were removed. The total energy of the system increases as the SWCNT is pulled out of the composite. This increase in total energy can be attributed to an increase in the potential energy of the system due to the formation of new surfaces. Figure 9 shows the variation in total energy, essentially the potential energy, of SWCNT–polyethylene resin composite as a function of the number of sub-units of SWCNT pulled out of the composite. Once, the whole SWCNT is pulled out of the matrix, the variation in total energy attains a plateau as the SWCNT is left far away from the matrix, because in such a situation the interaction between matrix and SWCNT is extremely weak.

According to Gou et al. [29], the pull-out energy, $E_{\text{pull-out}}$, is defined as the energy difference between the fully embedded nanotube and the complete pull-out

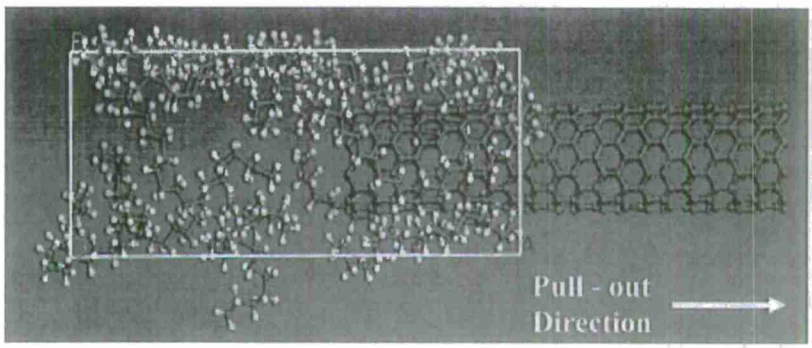


Fig. 8 Atomistic model of the composite for interfacial binding energy analysis

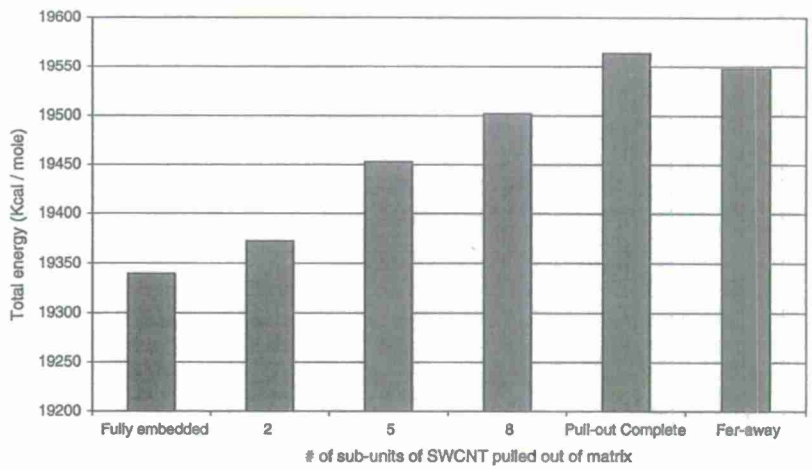


Fig. 9 Potential energy variation for SWCNT pull-out test from polyethylene matrix in single SWCNT composite



T-242

configuration. It can be related to the interfacial shear stress, $\tau_l$, by the following relation:

$$E_{\text{pull-out}} = \int_0^L 2\pi a(l-x)\tau_l \, dx = \pi a \tau_l L^2 \quad (5)$$

$$\Rightarrow \ \tau_l = E_{\text{pull-out}}/\pi a L^2 \quad (6)$$

where, $a$ and $L$ are the radius and length of the nanotube, respectively, and $x$ is the displacement of the nanotube.

The $E_{\text{pull-out}}$ for the system comes out to be 224 kcal/mol. The radius of the (10, 0) nanotube is 7.875 Å and the length of the SWCNT in the present system was 42.26 Å. The interfacial shear strength for the system under consideration comes out to be 133 MPa. This value of interfacial strength is comparable to interfacial strength value of 150 MPa for nanotube–polystyrene system reported in literature [30].

In another set of simulations, the same system was subjected to periodic boundary conditions. But, because of periodic boundary conditions of the system, when a SWCNT is pulled out from one end, another SWCNT enters from the opposite end into the simulation cell from its neighboring image cell. Therefore, the total energy of the system remains almost unaffected. Therefore, effect of the SWCNT pulling on the total energy of the system could not be studied in such a scenario.

## Molecular dynamics simulation of SWCNT–polyethylene composite

A key problem in the case of CNT polymer composites is the bonding between CNT and polymer matrix. On the one hand, the Van der Waals forces are too week to provide strong connections between CNT and the matrix such that attacks on CNT by chemical agents may result in development of covalent bonds with carbon atoms, which affect the structure of CNT. On the other hand, due to spatial mismatch between the atomic structure of CNT and matrix material, there can exist (by analogy with epitaxial growth) significant residual stresses, which in turn may cause defects in the matrix and deformation of CNT. These factors can change key properties of the CNT such as electrical and thermal conductivity. Figure 10 illustrates the deformed shape of a CNT (departure from circularity of cross-section) when surrounded by polymer chains, as obtained from molecular dynamics simulation.

Molecular dynamics simulation was carried out for the SWCNT–polyethylene matrix composite. The simulation cell for the composite consists of single 7,0 SWCNT embedded in polyethylene matrix. The dimensions of the simulation cell were maintained as 100 Å × 50 Å × 50 Å. The two-step NPT molecular dynamics, described in Section " MD simulation of matrix material", was applied to the present case as well. The temperature of the system was maintained at 298 K throughout the simulation and a hydrostatic pressure of 1 atm pressure was applied to the system. Figure 11 also shows the polymer chains used in this simulation and Table 5 shows final engineering constants of the simulated polymer system.

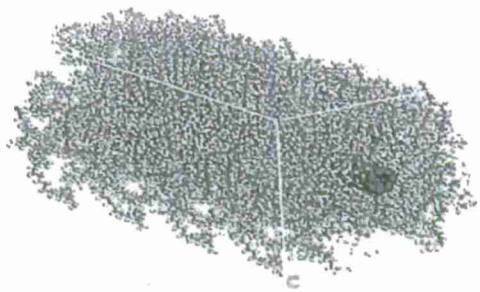

**Fig. 11** Molecular dynamics simulation cell for SWCNT–polyethylene matrix composite

**Table 5** Mechanical properties for SWCNT–polyethylene composite from molecular dynamics simulation

| $E_{11}$ (GPa) | $E_{22}$ (GPa) | $\nu_{12}$ | $\mu_{23}$(GPa) | $K_{23}$ (GPa) |
|---|---|---|---|---|
| 92.18 | 2.31 | 0.33 | 0.97 | 13.55 |

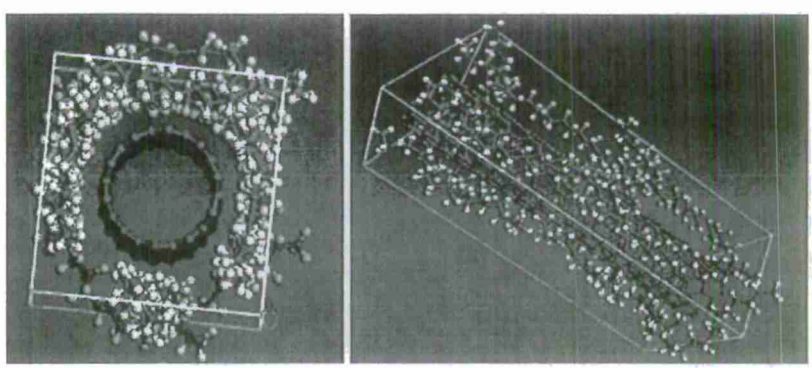

**Fig. 10** An arm chair CNT surrounded by ethylene molecules, before energy minimization



T-243

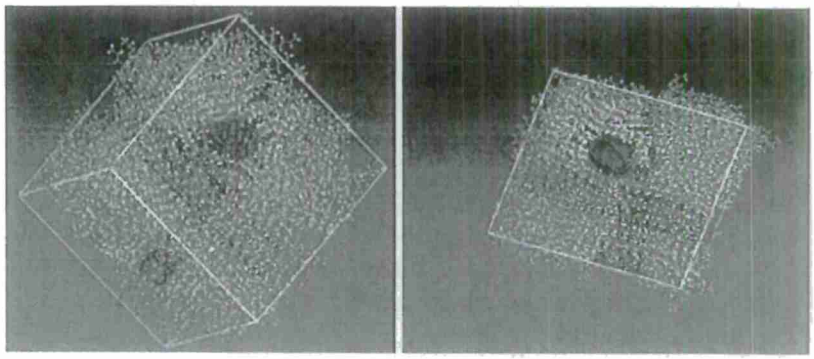

Fig. 12 Molecular dynamics simulation cell for three 7,0 SWCNTs embedded in polyethylene matrix

Table 6 Engineering constants of simulated composite with three 7,0 SWCNTs randomly embedded in polyethylene matrix

| $E$ (GPa) | $\nu_{12}$ |
|---|---|
| 24.62 | 0.36 |

In order to account for random distribution of CNTs in the polymeric matrix, molecular dynamics simulation was carried out for the three SWCNTs embedded in polyethylene matrix as shown in Fig. 12. The simulation cell for the composite consists of three single 7,0 SWCNTs embedded in the polyethylene matrix. The dimensions of the simulation cell were maintained as 100 Å × 100 Å × 100 Å. Two step NPT molecular dynamics was applied. The temperature of the system was maintained at 298 K through out the simulation and a hydrostatic pressure of 1 atm pressure was applied to the system. The same volume fraction used in the case of single CNT embedded in polyethylene matrix was maintained with a total of 13,414 atoms used in the simulation. The engineering constants obtained as a result of this simulation are summarized in Table 6.

## Conclusions

Results obtained from various types of loadings applied to SWCNT show that SWCNTs are transversely isotropic. Elastic constants are the same for SWCNT under various loadings. Thus, SWCNT behaves as a linear elastic material. The simulation of various SWCNT clusters establishes the fact that clusters of nanotubes have lower transverse properties when compared to individual nanotubes. SWCNTs lose their circularity when a polymer chain is placed in their vicinity. This shows that their transverse properties are comparatively poor. The interface is an important constituent of CNT–polymer composites, which has been modeled in the present research with reasonable success.

**Acknowledgement** Authors wish to acknowledge partial support for this research by ONR Grant#N00014-06-1-0577, Office of Naval Research, Solid Mechanics Program (Dr. Yapa D.S. Rajapakse, Program Manager); and by the NASA EPSCoR Research Infrastructure Grant.

## References

1. Deng CF, Wang DZ, Zhang XX, Li AB (2007) Mater Sci Eng A 444:138
2. Yoon PJ, Fornes TD, Paul DR (2002) Polymer 43:6727
3. Mishra S, Sonawane S, Chitodkar V (2005) Polym Plast Technol Eng 44:463–473
4. Gilman JW, Jackson CL, Morgan AB, Harris R Jr (2000) Chem Mater 12:1866
5. Strawhecker KE, Manias E (2000) Chem Mater 12:2943
6. Krishnamoorti R, Vaia RA, Giannelis EP (1996) Chem Mater 8:1728
7. Xu R, Manias E, Snyder AJ, Runt J (2001) Macromolecules 34:337
8. Kojima Y, Usuki A, Kawasumi M, Okada A, Fukushima Y, Kurauchi T, Kamigaito O (1993) J Mater Res 8:1185
9. Odegard GM, Gates TS, Nicholson LM, Wise C (2002) NASA ICASE report NASA/TM-2002-211454, March 2002
10. Odegard GM, Gates TS, Nicholson LM, Wise C (2001) NASA ICASE report NASA/TM-2001-210863, May 2001
11. Li C, Chou T (2003) Int J Solids Struct 40:2487
12. Zhang P, Huang Y, Geubelle PH, Klein PA, Hwang K (2002) Int J Solids Struct 39:3893
13. Zhang P, Huang Y, Gao H, Hwang K (2002) Trans ASME 69:454
14. Arroyo M, Belytschko T (2004) Phys Rev B 69:115415.1
15. Zhang P, Jiang H, Huang Y, Geubelle PH, Hwang KC (2004) J Mech Phys Solids 52:977
16. Jiang H, Zhang P, Liu B, Huang Y, Geubelle PH, Gao H, Hwang KC (2003) Comput Mater Sci 28:429
17. Jiang H, Feng XQ, Huang Y, Hwang KC, Wu PD (2004) Comput Methods Appl Mech Eng 193:3419
18. Arroyo M, Belytschko T (2003) Phys Rev Lett 91(21):215505.1
19. Tersoff J (1988) Phys Rev B 37:6991
20. Brenner DW (1990) Phys Rev B 42:9458
21. Yakobson BI, Cambell MP, Brabec CJ, Bernholc J (1997) Comput Mater Sci 8:341
22. Belytschko T, Xiao SP, Schatz GC (2002) Phys Rev B 65(23):235430.1
23. (2005) MS modeling 4.0 Online help manual, Accelrys Inc.
24. www.wikipedia.org, the free web based encyclopedia, accessed on 05-01-2006
25. Sun H (1998) J Phys Chem B 102:7338



T-244

26. Christensen R (1991) Mechanics of composite materials. Krieger Publishing Company, Malbar, Fl, p 74
27. Chou TW, Thostenson ET, Ren ZF (2001) Composit Sci Technol 61:1899
28. http://www.pslc.ws/macrog/pe.htm, Polymer science learning center, The University of Southern Mississippi
29. Gou J, Jiang S, Minaie B, Liang Z, Chuck Z, Wang B (2003) IMECE'03 – 41138, Proceedings of IMECE'03 international engineering congress and exposition. Washington, D.C., November 16–21, 2003, p 1
30. Liao K, Li S (2001) Appl Phys Lett 79(25):4225



T-245

*Progress In Electromagnetics Research, PIER 86, 111–134, 2008*

# A SYMMETRY-BASED FORMALISM FOR THE ELECTRODYNAMICS OF NANOTUBES

**S. M. Mikki and A. A. Kishk**

Center of Applied Electromagnetic Systems Research
Department of Electrical Engineering
University of Mississippi
University, MS 38677, USA

**Abstract**—In this paper, a general symmetry-based approach to the electrodynamics of a class of low-dimensional structures, carbon nanotubes, is proposed. The contribution of the microscopic configuration is handled using the symmetry group of the structure under consideration. An explicit form of the electromagnetic field is derived starting from a general nonlocal linear susceptibility model expressed as a low-dimensional phenomenological response function. The general form of the field obtained is used to devise new theoretical insights by providing a framework for the computation of the nanotube Green's functions.

## 1. INTRODUCTION

There is an increasing interest in employing applications from nanotechnology to develop new generation of materials and devices that can handle the growing demands of industry [1]. Of special importance is a class of low-dimensional structures called carbon nanotubes (CNT), which were discovered in 1991 by Iijima [1–3]. Since then, they have attracted the attention of both physicists and engineers who investigated extensively the possibility of using CNTs for various applications, ranging from mechanical shielding to nano-waveguide and transistors [5, 6]. One of the most attractive features in CNTs is their ability to function in either metallic or semi-conducting modes, depending on how the original graphite sheet is rolled to form the tube [6]. Such plethora of advantages suggest that CNTs may become the vital device of future nono-electronics when reaching the fundamental size limit of the current silicon micro-electronics industry.

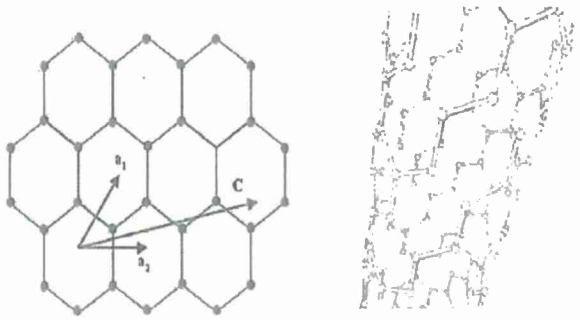


**Figure 1.** (a) Graphene sheet used in forming CNTs (The dots illustrate the carbon atoms positions). (b) Geometry of a single-wall carbon nanotube (SWCNT).

Our goal in this paper is to show systematically how nontrivial differences between conventional and nano-electromagnetics can be accounted for once the conceptual corrections of the nanoscale problem are taken into consideration. In order to keep the problem at the practical level, a concrete example, carbon nanotubes, has been chosen to function as a vehicle for the illustration of the various theoretical ideas we are proposing for nanoelectromagnetics. Those nanotubes demonstrate nicely several peculiarities unique in nanoscale problems. First, they are, obviously, microscopic structures, leading to the fact that a direct conventional electrodynamic approach will probably fail to account for the full nature of their physics. Second, since atoms in carbon nanotubes are arranged geometrically in a cylindrical fashion, with very high aspect ration, they serve as toy models illustrating the electrodynamics as taking place in a lower-dimensional space, in this case 1-D. Such interpretation may help in suggesting, at least theoretically, new ways of viewing Maxwell's equations, different from the bulk matter approach of conventional macroscopic electrodynamics. Third, as we mentioned above, carbon nanotubes are very promising stable microscopic structures that have found various mechanical and electrical applications and are expected to play important role in future nano-electronics and other industries. Therefore, the task of employing them in the demonstration of the peculiarities of nanoscale electromagnetics is advantageous by itself, since many of the results derived throughout can be easily adapted in future work.

## 2. GENERAL CONSIDERATIONS FOR THEORETICAL NANO-ELECTROMAGNETICS

The conventional approach to the discourse of engineering, macroscopic electromagnetics is summarized in Figure 2. The threefold process constituting the core of this discourse can be explicated in the the following way.

(i) Define an excitation, a macroscopic concentration of electric charge and current $\mathbf{J}_s$ and/or equivalent magnetic currents $\mathbf{M}_s$.

(ii) Define a macroscopic boundary $\Omega$ separating various regions in space, each modeled unambiguously by an effective dielectric and magnetic permeability.

(iii) Solve Maxwell's equations by formulating them as a boundary-value problem in mathematical physics. Step 1 above provides the source (driving) term in the partial differential equations, while Step 2 specifies the boundary condition imposed on those equations. The outcome of this solution process is the electromagnetic fields everywhere, $\mathbf{E}$ and $\mathbf{H}$.

This formulation is complete in the sense that once the constitutive relations $\mathbf{D} = \varepsilon\mathbf{E}$ and $\mathbf{B} = \mu\mathbf{H}$ are known, Maxwell's equations can be solved to produce the unique set of fields satisfying the boundary condition of the problem. Due to this mathematical completeness, engineering electromagnetics has progressed throughout most of the previous century with minimum contact with other branches in physics.

However, this autonomy has been possible only because the problem is *macroscopic*. That is, the devices used to measure the electromagnetic fields already perform an averaging process, which washes out the fast components of the fields. This leads to the ability to

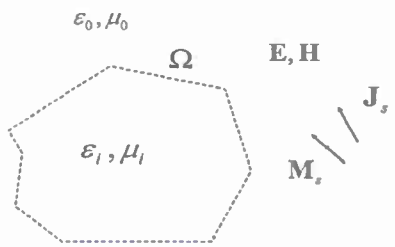


**Figure 2.** A general illustration of the formulation of macroscopic electromagnetic problems.

replace the inherently discontinues structure of matter by the smooth, continuous representation of the boundary $\Omega$ in Figure 2. Once the scale of the electromagnetic problem is pushed downward toward the nano-world, the discontinuity of matter becomes much more manifest. This leads to important corrections to be introduced to conventional (macroscopic) electromagnetics. Our claim is that those corrections are not just quantitative, in the sense that the numerical values of the effective medium functions $\epsilon$ and $\mu$ are going to change, but, most importantly, there are fundamental *conceptual* modifications that must be taken directly into considerations in order to understand why the problem at the nanoscale level presents something new to the electromagnetic community.

We mention two corrections to be taken into account for a successful description of the electrodynamics at the nanoscale level.

(i) The size effects (e.g., quantum confinement.)

(ii) The nonlocal effects (e.g., spatial dispersion.)

The size effects relate to the quantum mechanical phenomena of confinement. Since, according to the de Broglie's hypothesis, each particle has a wave associated with it, electrons (like photons) existing in very small dimensions will undergo resonator-type quantization effects, which are due to imposing the boundary condition of the spatial structure on the wavefunction. This usually results in new behavior that is not present in the original bulk material response functions.

The nonlocal effects (spatial dispersion) will be emphasized in this paper by demonstrating how the microscopic symmetry group can be used to take into consideration the higher-order Floquet modes.

One has always to remember that there is nothing orthodox in macroscopic Maxwell's equations. The true fundamental physical process is the microscopic equations of the fields *and* the mechanical models used to describe matter. Macroscopic Maxwell's equations are an *effective*-field theory, the outcome of combining these two aspects of reality, field and matter, as is shown in Figure 3. In other words, the electromagnetic process in material media can be visualized as a *coupled mode* of both radiation and matter. This picture applies equally to both bulk material electromagnetics and nanoscale lower-dimensional structures. However, the latter has the additional peculiarity of the so-called size effects of the lower scale. The treatment of the boundary of a lower-dimensional structure is tricky because there is no unique natural interface between different domains. The choice of the boundary condition depends on the way we decide to handle the *mechanical* problem at the aforementioned interface between different media [24].

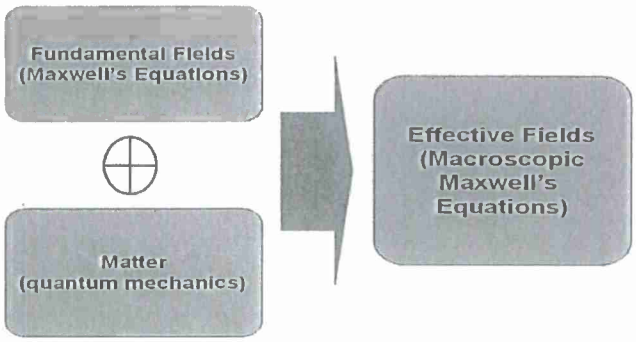


**Figure 3.** The anatomy of an effective-field electromagnetic theory.

We turn now to the important issue of averaging the fields and the role of quantum mechanics. The microscopic electric source consists of charged particles. Therefore, we can mathematically express this distribution in the following way

$$\rho^{\text{mic}}(\mathbf{r},t) = \sum_i q_i \delta\left[\mathbf{r} - \mathbf{r}_i(t)\right] \tag{1}$$

and

$$\mathbf{j}^{\text{mic}}(\mathbf{r},t) = \sum_i q_i \dot{\mathbf{r}}_i \delta\left[\mathbf{r} - \mathbf{r}_i(t)\right], \tag{2}$$

where $\mathbf{r}_i$ is the position vector if the $i$th charge $q_i$. The microscopic Maxwell's equations govern how these sources will generate a dynamics fields $\mathbf{e}$ and $\mathbf{h}$ in the space between the particles. However, the motion of a material particle is not a pure electromagnetic phenomena, but rather a mechanical process that must be described ultimately using quantum mechanics. This mechanics tells us something about the position appearing in (1) and the velocity appearing in (2): They can not be *both* determined with *arbitrary* accuracy, which is the content of Heisenberg's uncertainty relation. The more precise becomes the position, the more uncertain is the velocity (and vice versa.) Therefore, we can not know "exactly" both the charge and the current density. This leads to the problem of stochastic fluctuations, which is an inherently quantum phenomena, leading to the necessity of replacing the classical fields and variables by operators associated with statistical distributions.

Figure 4 illustrates the previous discussion. The fluctuations in the field emphasized there are the *statistical* fluctuations, not the fast-varying components of the fields, which are ultimately due to the

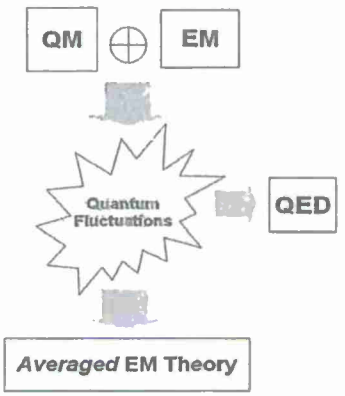


**Figure 4.** Quantum electrodynamic results from the effort to treat consistently the fluctuations in the electromagnetic fields resulting from talking into account the microscopic mechanical motion of the particles comprising the electric sources. The "averaged EM theory" here is a theory in which the fields variables are averaged only statistically over the ensemble of the quantum mechanically possible state.

nonlocality of the medium. It is important to distinguish between these two types of fluctuations. If a crude averaging procedure is applied to transform the microscopic fields $\mathbf{e}$ and $\mathbf{h}$ to $\mathbf{E}$ and $\mathbf{H}$, respectively, then all information about the microscopic structure will probably be lost. Clearly, for nanoscale device applications we *do* want to retain those non-statistical microscopic information, which are reflected in the high-order Floquet modes, which reflects in turn the spatial structure of the device under consideration. Therefore, we only average the fields statistically, i.e., using the Shrödinger wavefunction as a probability density function. The averaged field theory in Figure 4 refers then only to statistically averaged theory.

Aside from these general consideration, we will not perform any quantum electrodynamics calculations in this paper. The approach is semi-classical in the sense that the fields are going to be treated as classical variables.

## 3. STRUCTURE OF CARBON NANOTUBES

In this section, we provide a compact description of the structural properties of CNTs using the language of the associated symmetry group. The details of the symmetry operations will be used in the

remaining parts of this chapter to find the specific mathematical form of the eigenmodes appearing in the dielectric tensor of the nanotube. The crux of our approach is that the symmetry group will determine the boundary conditions of the problem [7]. These conditions can not be derived form the Hamiltonian of the CNT but should be obtained through an independent approach.

Figure 1(a) illustrates the honeycomb lattice structure of graphene (graphene is defined as a 2D layer of graphite). The unit cell is specified by two atoms located at the positions $1/3\,(\mathbf{a}_1+\mathbf{a}_2)$ and $2/3\,(\mathbf{a}_1+\mathbf{a}_2)$, where $\mathbf{a}_1$ and $\mathbf{a}_2$ are two unit vectors defining the lattice constants and $|\mathbf{a}_1| = |\mathbf{a}_2| = a_0 = 0.2461\,\mathrm{nm}$. The CNT is formed by rolling this sheet such that the circumference of the tube coincides with the *chiral vector* $\mathbf{c} = m\,\mathbf{a}_1 + n\,\mathbf{a}_2$. Here $m$ and $n$ are two integers that completely determine the structure and the properties of the CNT. If only one layer is used to form the tube, the resulting structure is called *single-wall* CNT (SWCNT). Alternatively, if the tube consists of several concentric cylinders, we call it *multi-wall* CNT (MWCNT). The chiral angle $\theta$ is defined as the angle between the chiral vector $\mathbf{c}$ and $\mathbf{a}_1$. The radius of the CNT is given by

$$b = \frac{|\mathbf{c}|}{2\pi} = \frac{a_0}{2\pi}\sqrt{m^2+mn+n^2}. \tag{3}$$

The first symmetry group for the CNT can be derived by writing $\mathbf{c} = N\,[(m/N)\,\mathbf{a}_1 + (n/N)\,\mathbf{a}_2] = N\,\mathbf{c}'$, where $N$ is the greatest common divider of $m$ and $n$. It is obvious that a rotation around the tube axis by $2\pi/N$ will preserve the original structure. Equivalently, we say that each CNT possess the symmetry operation $\mathbf{C}_N$.

Through knowledge of other symmetry operations, to be discussed in a moment, it is possible by following the original work of White et al. [17] to show that the entire tube can be constructed starting from two-atom unit cell and the chiral vector. The first atom in the unit cell will be mapped to an arbitrary location in the circumference of the CNT, call it $A$. The second atom will be mapped to other location $B$ obtained by rotating the first point by an angle $\gamma = 2\pi\,(\mathbf{a}_1+\mathbf{a}_2)\cdot\mathbf{c}/3\,|\mathbf{c}|^2$ and then translating the resulting point along the tube axis by a distance $d = |(\mathbf{a}_1+\mathbf{a}_2)\times\mathbf{c}|/3\,|\mathbf{c}|^2$. The two points obtained now can be used, together with the symmetry operation $\mathbf{C}_N$, to generate other $2(N-1)$ points by successive rotations around the tube axis by the angle $2\pi/N$. That is, atom $A$, together with $\mathbf{C}_N$, will generate other $N-1$ atoms. Atom $B$, again together with $\mathbf{C}_N$, will generate other set of $N-1$ atoms. Therefore, the total is $2\,(N-1)+N = 2N$ atoms. This set is called the *basic helical motif* of the CNT [17]. However, to complete the tube we need to use a *screw operator*, defined in [17], which is

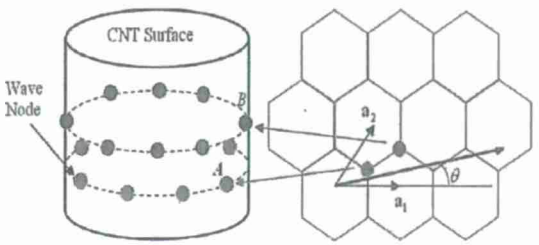


(a) (b)

**Figure 5.** (a) Illustration of two atomic circles in the translational unit cell of a SWCNT. Each circle corresponds to the symmetry operation $\mathbf{C}_N$. (b) The honeycomb lattice structure of graphene. The dots represent the arbitrary first two-atom unit cell.

denoted here by $\mathbf{T}_h^{\zeta}$. Its action on a specific point consists of rotation around the tube axis by an angle $\zeta$ and then translation along the tube axis by a distance $h$. Therefore, the screw operation is neither pure rotation nor pure translation, but a combination of both of them. A procedure for finding $\zeta$ and $h$ can be found in [17] and explicit closed form expressions in terms of Euler function are available as follow [18]

$$q = 2\frac{m^2 + mn + n^2}{NR}, \tag{4}$$

$$\xi = \frac{q}{N}\mathrm{Fr}\left[\frac{N}{qR}\left(3 - 2\frac{m-n}{m}\right) + \frac{N}{m}\left(\frac{m-n}{N}\right)^{\mathrm{E}(m/N)-1}\right], \tag{5}$$

$$\zeta = \frac{2\pi}{q}\xi, h = \frac{N}{\xi}a, \tag{6}$$

where $\mathrm{Fr}[x] = x - [x]$ gives the fractional part of the rational number $x$ and $\mathrm{E}(v)$ is the Euler function giving the co-primes less than $v$ ($a$ is defined in (8)). By repeated application of the screw operator $\mathbf{T}_h^{\zeta}$ on the basic helical motif, the entire tube can be reconstructed [17]. Therefore, the two-atom unit cell that we started with is enough to determine the full structure of the CNT.

It remains to present the translational symmetry of the CNT. Depending on the chirality, each CNT will have a characteristic length $a$ along its axis. Translations of multiples of $a$ will leave the tube

unchanged. This periodicity in the axial direction can be given by [18]

$$N_1 = -\frac{2n+m}{N\mathcal{R}}, N_2 = \frac{2m+n}{N\mathcal{R}}, \tag{7}$$

$$\mathbf{a} = N_1\mathbf{a}_1 + N_2\mathbf{a}_2, a = |\mathbf{a}| = \frac{\sqrt{3\left(m^2+mn+n^2\right)}}{N\mathcal{R}}a_0, \tag{8}$$

$$N_c = \frac{2\left(m^2+mn+n^2\right)}{N\mathcal{R}}, \tag{9}$$

where $N_c$ is the number of atomic pairs in the translational unit cell. Here, $\mathcal{R} = 3$ if $(n_1 - n_2)/3N$ is integer and $\mathcal{R} = 1$ otherwise. We denote here this symmetry operation by $\mathbf{T}_a$ and it means translation along the tube axis by distance $a$. The translational unit cell consists then of a cylindrical tube of radius $b$ and height $a$. The number of atoms in the unit cell is given by $N_c$.

To summarize, $\mathbf{C}_N$ is the symmetry operation of pure rotation (translations along the circumferential direction $\mathbf{c}$), $\mathbf{T}_a$ is the operation of pure translation, and $\mathbf{T}_h^\zeta$ is the (mixed) screw operation. It is worthy to mention that other symmetry operations were derived in [18] and [19] to fully characterize SWCNTs and MWCNTs. However, for the purpose of this paper, the previously mentioned three symmetry operations are enough to drive the basic mathematical form of the fields in the CNT environment. As will be shown in the next section, all other symmetry operations will alter only the number of terms taken in the resulted summations without changing the basic form.

## 4. GENERAL LINEAR PHENOMENOLOGICAL MODEL FOR THE ELECTROMAGNETIC FIELD INTERACTION WITH NANOTUBES

The main model we adopt to describe light-matter interaction in carbon nanotubes is given by the general susceptibility tensor $\overline{\overline{\chi}}$. Assuming that the external field is weak, it is possible to ignore nonlinear effects and write the polarization vector density as [22, 13]

$$\mathbf{P}(\mathbf{r},t) = \int_{t'} dt' \int_{\mathbf{r}'} d^3r' \overline{\overline{\chi}}(\mathbf{r},\mathbf{r}',t,t') \cdot \mathbf{E}(\mathbf{r}',t'), \tag{10}$$

where $\mathbf{E}$ is the *total* microscopic electric field. We list below some of the important observations about the linear model in (10) that should be taken into consideration.

Before considering some of the general properties of this model, a clarification of the coordinate system that is chosen to represent

relation (??) is in order. As we view the CNT as a low-dimensional structure, the medium described by the susceptibility tensor $\overline{\overline{\chi}}$ above is defined only for observation points lying on the cylindrical surface of the nanotube. This means that *local* cylindrical coordinates should be employed, instead of the typical cylindrical coordinates used to describe the 3D space. That is, a point on a cylinder is described locally by $\varphi$ and $z$. This allows us to write vectors located entirely on the cylinder surface. Strictly speaking, we consider a *curvilinear* coordinate system $u$, $z$, and $\varphi$, as shown in Figure 6. There, the two vectors traversed by $z$ and $\varphi$ are similar to those used to describe circular cylindrical geometrids. The reference direction for measuring the azimuthal direction is specified by the vector traversed by $u$. Thus, the CNT medium exists only at $u = b$, where $b$ is the radius of the nanotube given by (3). Throughout this paper, we write any vector expressed in terms of this local coordinate system in the form $\mathbf{r} = \langle z, \varphi, u \rangle$.

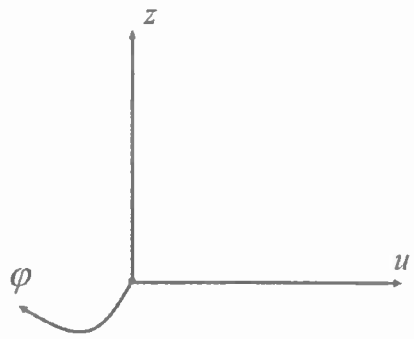


**Figure 6.** A local curvilinear coordinate system to describe the dynamics of carbon nanotubes. The $z$ and $\varphi$ correspond to the cylindrical variables, while $u$ here is a chosen reference direction for the azimuthal vector traversed by $\varphi$.

Some of the general properties of the linear model in (10) can be summarized as follows.

(i) Since no effect can precede its cause, we must have $t' < t$.

(ii) According to relativity theory, no signal can travel faster than the speed of light $c$. Thus, we have the additional light cone causal condition $|\mathbf{r} - \mathbf{r}'| \leq c|t - t'|$.

(iii) Since the CNT atoms exist only on the tube surface $u = b$, $\mathbf{P}$ must vanish for any observation point outside the tube. Therefore, we write $\overline{\overline{\chi}} = 0$ for $u \neq b$.

(iv) Since $\mathbf{r}'$ is the field (source) point, this need not to be within the matter. Any point $\mathbf{r}'$ satisfying the relativistic criterion above must be taken into consideration. In others words, we have in general $\overline{\overline{\chi}} \neq 0$ for $u \neq b$ provided $|\mathbf{r} - \mathbf{r}'| \leq c\,|t - t'|$.

It is readily noticed from (10) that the susceptibility model is nonlocal or, equivalently, exhibits *spatial* dispersion. This is reflected in the fact that the dependence of $\chi$ on spacial variables is retained in the model. This will lead naturally to the interesting possibility of applying directly the symmetry group of the CNT, a task we achieve in the next section.

## 5. APPLICATION OF THE NANOTUBE SYMMETRY TO THE RESPONSE FUNCTION

Since $\overline{\overline{\chi}}(\mathbf{r}, \mathbf{r}', t, t')$ is a response function, it must obey the same symmetry operations of the CNT itself. The Bravais vector of an atom located on the CNT is given by

$$\mathbf{R}_{\mathbf{l}} = \langle z_{\mathbf{l}}, \varphi_{\mathbf{l}} \rangle, \tag{11}$$

where we remind the reader again that we are using local (Dupin) vectors. Here, $\mathbf{l} = (l_1, l_2)$ is a vector index enumerating the atomic position $(l_1, l_2)$ on the CNT surface. $\varphi_{\mathbf{l}}$ and $z_{\mathbf{l}}$ are the $\varphi$- and $z$-locations of the $\mathbf{l}$th atom, respectively. The full microscopic structural information of the CNT can be taken into consideration by enforcing explicitly the symmetry group of CNTs. Therefore, by applying the symmetry operations $\mathbf{T}_a$ and $\mathbf{C}_N$, we find that the structure-preserving CNT displacements satisfy

$$\overline{\overline{\chi}}\left(z + l_1 a, \varphi + l_2 \frac{2\pi}{N}, z' + l_1 a, \varphi' + l_2 \frac{2\pi}{N}, u, u', t, t'\right) = \overline{\overline{\chi}}\left(\mathbf{r}, \mathbf{r}', t, t'\right), \tag{12}$$

where $l_{1,2} = 0, \pm 1, \pm 2, \ldots, \pm\infty$. Obviously, there is no periodicity in the radial direction. Equation (12) can be interpreted as the result of moving the primed and unprimed spatial coordinates according to the spatial symmetry operation of the CNT structure.

The mathematics of the coming parts can be simplified considerably if we re-write condition (12) above utilizing a different functional form for $\overline{\overline{\chi}}$. Namely, we have

$$\overline{\overline{\chi}}\left(z + l_1 a, \varphi + l_2 \frac{2\pi}{N}, u, \mathbf{r} - \mathbf{r}', t, t'\right) = \overline{\overline{\chi}}\left(\mathbf{r}, \mathbf{r} - \mathbf{r}', t, t'\right). \tag{13}$$

Therefore, from this equation we see that $\overline{\overline{\chi}}$ is (1) non-periodic in $\mathbf{r} - \mathbf{r}'$, (2) periodic with respect to $z$ and $\varphi$, and (3) vanish for $u \neq b$.

By expanding (13) using Fourier series in the periodic arguments, observing meanwhile that the CNT "medium" exist only on the tube cylindrical surface, we find

$$\overline{\overline{\chi}}\left(\mathbf{r},\mathbf{r}-\mathbf{r}',t,t'\right)=\sum_{l_1=-\infty}^{\infty}\sum_{l_2=-\infty}^{\infty}\overline{\overline{\chi}}^{l_1,l_2}\left(\mathbf{r}-\mathbf{r}',t,t'\right)\delta\left(u-b\right)e^{jl_1N\varphi}e^{j\frac{2\pi}{a}l_2z}, \tag{14}$$

where $\overline{\overline{\chi}}^{l_1,l_2}$ are the (tensor) coefficients of the Fourier series expansion. The summations in (14) can be further simplified by applying the screw symmetry operation $\mathbf{T}_h^{\zeta}$ as follow

$$\overline{\overline{\chi}}\left(\mathbf{r},\mathbf{r}-\mathbf{r}',t,t'\right)=\overline{\overline{\chi}}\left(z-h,\varphi-\zeta,u,\mathbf{r}-\mathbf{r}',t,t'\right), \tag{15}$$

where $\zeta$ and $h$ are the parameters of the screw operator defined in Section 3. Equations (14) and (15) give $\exp\left(-jl_1N\zeta-j\frac{2\pi}{a}l_2h\right)=1$, which translates to the following condition

$$\mathbf{C}:\ \ l_1N\zeta+l_2\frac{2\pi h}{a}=2\pi v,\ \ v=0,\pm1,\pm2,\ldots,\pm\infty. \tag{16}$$

In the next calculations, we write a summation over $\mathbf{l}=(l_1,l_2)$ that takes into consideration the condition (16) in the form $\sum_{\mathbf{l}|\mathbf{C}}$.

By applying the time symmetry condition (shift invariance), the final expression of the susceptibility can be written compactly as

$$\overline{\overline{\chi}}\left(\mathbf{r},\mathbf{r}-\mathbf{r}',t,t'\right)=\sum_{\mathbf{l}|\mathbf{C}}\overline{\overline{\chi}}^{\mathbf{l}}\left(\mathbf{r}-\mathbf{r}',t-t'\right)\delta\left(u-b\right)e^{jl_1N\varphi}e^{j\frac{2\pi}{a}l_2z}. \tag{17}$$

## 6. GENERAL EXPANSION FOR THE POLARIZATION DENSITY

Next, We expand the susceptibility tensor in the non-periodic arguments using Fourier integrals as follow

$$\begin{aligned}\overline{\overline{\chi}}\left(\mathbf{r},\mathbf{R},t,t'\right)\ =\ &\sum_{\mathbf{l}|\mathbf{C}}\int_{\mathbf{k}'}\int_{\omega'}\frac{d^3k'\,d\omega'}{\left(2\pi\right)^4}\overline{\overline{\chi}}^{\mathbf{l}}\left(\mathbf{k}',\omega'\right)\\ &\times\delta\left(u-b\right)e^{j\frac{2\pi}{a}l_1z}e^{jNl_2\varphi}e^{j\,\mathbf{k}'\cdot\mathbf{R}}e^{j\omega'\tau},\end{aligned} \tag{18}$$

where $\mathbf{R}=\mathbf{r}-\mathbf{r}'$ and $\tau=t-t'$. The Fourier transform of the polarization density $\mathbf{P}$ is defined as

$$\mathbf{P}\left(\mathbf{k},\omega\right)=\int_{\mathbf{r}}\int_{t}d^3rdt\,\mathbf{P}\left(\mathbf{r},t\right)e^{-j\mathbf{k}\cdot\mathbf{r}}e^{-j\omega t}. \tag{19}$$

By using (18) and (10), Equation (19) gives

$$\mathbf{P}(\mathbf{k},\omega) = \int_{\mathbf{r}}\int_{t}\int_{\mathbf{R}}\int_{\tau} d^3r\,dt\,d^3R\,d\tau\, e^{-j\,\mathbf{k}\cdot\mathbf{r}} e^{-j\omega t} e^{j\frac{2\pi}{a}l_1 z} e^{jNl_2\varphi} e^{j\,\mathbf{k}'\cdot\mathbf{R}} e^{j\omega'\tau} \times \sum_{\mathbf{l}|\mathbf{C}} \int_{\mathbf{k}'}\int_{\omega'} \frac{d^3k'd\omega'}{(2\pi)^4} \overline{\overline{\chi}}^{\mathbf{l}}(\mathbf{k}',\omega')\,\delta(u-b)\cdot\mathbf{E}(\mathbf{r}-\mathbf{R},t-\tau), \quad (20)$$

where we have used the transformation $d^3Rd\tau = d(\mathbf{r}-\mathbf{r}')\,d(t-t') = d^3r'dt'$. By first performing the integration with respect to $t$, we have

$$\int_t dt\, e^{-j\omega t}\mathbf{E}(\mathbf{r}-\mathbf{R},t-\tau) = e^{-j\omega\tau}\int_{\lambda} d\lambda\, e^{-j\omega\lambda}\mathbf{E}(\mathbf{r}-\mathbf{R},\lambda) = e^{-j\omega\tau}\mathbf{E}(\mathbf{r}-\mathbf{R},\omega), \quad (21)$$

where the transformation $\lambda = t-\tau$ was used. Performing now the integration with respect to $\mathbf{r}$, it is possible to write

$$\int_{\mathbf{r}} d^3r\, e^{-j\,\mathbf{k}\cdot\mathbf{r}}\mathbf{E}(\mathbf{r}-\mathbf{R},\omega)\,\delta(u-b)\,e^{j\frac{2\pi}{a}l_1 z}e^{jNl_2\varphi} = e^{-jk_u b}e^{-j(\mathbf{q}-\mathbf{g}_\mathbf{l})\cdot\mathbf{R}}\mathbf{E}(\mathbf{q}-\mathbf{g}_\mathbf{l},b,\omega) \quad (22)$$

where with the transformation $\mathbf{s} = \mathbf{r}-\mathbf{R}$ was used. Here, $\mathbf{q} = \langle k_z, k_\varphi\rangle$ and the CNT reciprocal lattice vector $\mathbf{g}_\mathbf{l}$ is given by

$$\mathbf{g}_\mathbf{l} = \left\langle l_1\frac{2\pi}{a}, l_2N\right\rangle \quad (23)$$

Here, the Fourier transform can be computed as

$$\mathbf{E}(\mathbf{q},b,\omega) = \int_{-\infty}^{\infty}\int_0^{2\pi} bd\varphi\,dz\,\mathbf{E}(z,\varphi,u=b,\omega)\,e^{-j\mathbf{q}\cdot\mathbf{r}}. \quad (24)$$

Therefore, by substituting (21) and (22) into (20) we arrive to

$$\mathbf{P}(\mathbf{k},\omega) = \int_{\mathbf{R}}\int_{\tau} d^3Rd\tau \sum_{\mathbf{l}|\mathbf{C}}\int_{\mathbf{k}'}\int_{\omega'} \frac{d^3k'd\omega'}{(2\pi)^4} e^{-j(\mathbf{q}-\mathbf{g}_\mathbf{l}-\mathbf{k}')\cdot\mathbf{R}} e^{j(\omega'-\omega)\tau} \times \overline{\overline{\chi}}^{\mathbf{l}}(\mathbf{k}',\omega')\cdot e^{-jk_u b}\mathbf{E}(\mathbf{q}-\mathbf{g}_\mathbf{l},b,\omega), \quad (25)$$

By using the sifting property of the Dirac delta function, it is possible to write

$$\int_{\mathbf{R}}\int_{\tau} d^3Rd\tau e^{-j(\mathbf{q}-\mathbf{g}_\mathbf{l}-\mathbf{k}')\cdot\mathbf{R}} e^{j(\omega'-\omega)\tau} = (2\pi)^4\,\delta(\mathbf{q}-\mathbf{g}_\mathbf{l}-\mathbf{k}')\,\delta(\omega'-\omega). \quad (26)$$

Plugging this integral into (25), we get

$$\mathbf{P}(\mathbf{k},\omega) = \sum_{\mathbf{l}|\mathbf{C}} \int_{\mathbf{k}'} \int_{\omega'} d^3k' d\omega' \delta(\mathbf{q}-\mathbf{g}_{\mathbf{l}}-\mathbf{k}') \delta(\omega'-\omega) \times \overline{\overline{\chi}}^{\mathbf{l}}(\mathbf{k}',\omega') \cdot e^{-jk_u b} \mathbf{E}(\mathbf{q}-\mathbf{g}_{\mathbf{l}},b,\omega). \quad (27)$$

Using the sifting property again, the integrations with respect to $\mathbf{k}'$ and $\omega'$ simplifies to single evaluations and finally we obtain

$$\mathbf{P}(\mathbf{k},\omega) = \sum_{\mathbf{l}|\mathbf{C}} \overline{\overline{\chi}}^{\mathbf{l}}(\mathbf{q}-\mathbf{g}_{\mathbf{l}},\omega) \cdot e^{-jk_u b} \mathbf{E}(\mathbf{q}-\mathbf{g}_{\mathbf{l}},b,\omega). \quad (28)$$

Thus, this key results tells us that the polarization $\mathbf{P}$ of the CNT induced by a field with spatial frequency $\mathbf{q}$ and temporal frequency $\omega$ appears as a function of the same temporal frequency but contains, in addition to the $\mathbf{q}$-component, an infinite set of harmonics of $\mathbf{g}_{\mathbf{l}}$, which are defined by (23). The spectral description of the electromagnetic interaction with nanotubes, which are viewed as low-dimensional structures, takes this simple form depicted in (28) because of the convenience of working with the local coordinate system introduced in Figure 6.

## 7. EIGENMODE EXCITATION OF THE NANOTUBE MEDIUM

To understand the physical meaning of Equation (28), let us assume that there is an eigenfunction wave mode impinging on the CNT medium given by

$$\mathbf{E}(\mathbf{r},t) = \mathbf{E}^0 e^{-j\mathbf{k}_0\cdot\mathbf{r}} e^{j\omega_0 t}, \quad (29)$$

where $\mathbf{k}_0 = (k_{z0}, k_{\varphi 0}, k_{u0})$. Its Fourier transform, evaluated using (24), is given by

$$\begin{aligned}\mathbf{E}(\mathbf{k},b,\omega) &= \int_{\mathbf{r}} \int_{\omega} d^2r\, dt\, \mathbf{E}^0 e^{-jk_{u0}b} e^{-j\mathbf{q}_0\cdot\mathbf{r}} e^{j\omega_0 t} e^{-j\,\mathbf{q}\cdot\mathbf{r}} e^{-j\omega t} \\ &= (2\pi)^4 \mathbf{E}^0 e^{-jk_{u0}b} \delta(\mathbf{q}+\mathbf{q}_0)\delta(\omega-\omega_0) \quad (30)\end{aligned}$$

where $\mathbf{q}_0 = (k_{z0}, k_{\varphi 0})$. Therefore, substituting (30) into Equation (28) we get

$$\mathbf{P}(\mathbf{k},\omega) = (2\pi)^4 \mathbf{E}^0 e^{-j(k_u+k_{u0})b} \sum_{\mathbf{l}|\mathbf{C}} \overline{\overline{\chi}}^{\mathbf{l}}(\mathbf{q}-\mathbf{g}_{\mathbf{l}},\omega)\delta(\mathbf{q}-\mathbf{g}_{\mathbf{l}}+\mathbf{q}_0)\delta(\omega-\omega_0). \quad (31)$$

Calculating now the inverse Fourier transform, we find

$$\begin{aligned}\mathbf{P}(\mathbf{r},t) &= \frac{1}{(2\pi)^4}\int\limits_{\mathbf{k}}\int\limits_{\omega} d^3k\, d\omega\, \mathbf{P}(\mathbf{k},\omega)\, e^{j\mathbf{k}\cdot\mathbf{r}} e^{j\omega t} \\ &= \mathbf{E}^0 \int\limits_{\mathbf{k}}\int\limits_{\omega} d^3k\, d\omega\, e^{-j(k_u+k_{u0})b} \sum_{\mathbf{n}|\mathbf{C}} \overline{\overline{\chi}}^{\mathbf{l}}(\mathbf{q}-\mathbf{g}_{\mathbf{l}},\omega) \\ &\quad \times \delta(\mathbf{q}-\mathbf{g}_{\mathbf{l}}+\mathbf{q}_0)\,\delta(\omega-\omega_0)\, e^{j\mathbf{k}\cdot\mathbf{r}} e^{j\omega t}. \end{aligned} \tag{32}$$

By evaluating the integrals, the final answer can be written in the following compact form

$$\mathbf{P}(\mathbf{r},t) = \mathbf{E}^0 \left[\sum_{\mathbf{l}|\mathbf{C}} \overline{\overline{\chi}}^{\mathbf{l}}(-\mathbf{q}_0,\omega_0)\ \delta(u-b)\, e^{-jk_{u0}b}\, e^{j\mathbf{g}_{\mathbf{l}}\cdot\mathbf{r}}\right] e^{-j\mathbf{q}_0\cdot\mathbf{r}} e^{j\omega_0 t}. \tag{33}$$

The term between the brackets in Equation (33) has the form of a Fourier series, and thus it represents a periodic function with a period $\mathbf{R}_{\mathbf{l}}$, i.e., the fundamental lattice vector. Therefore, the form of the induced polarization given in (33) can be easily interpreted as a Bloch theorem adapted to the lower-dimensional structure of the nanotube.

From the linearity of Maxwell's equations (superposition), it is readily established that the field response to the polarization density (33) can be expanded as

$$\mathbf{E}(\mathbf{r},t) = \sum_{\mathbf{l}|\mathbf{C}} T\, \overline{\overline{\chi}}^{\mathbf{l}}(-\mathbf{q}_0,\omega_0)\cdot \mathbf{E}^0 \delta(u-b)\, e^{-jk_{u0}b} e^{j\mathbf{g}_{\mathbf{l}}\cdot\mathbf{r}} e^{-j\mathbf{q}_0\cdot\mathbf{r}} e^{j\omega_0 t}, \tag{34}$$

where $T$ is to the radiation operator that relates the polarization to the field induced in the CNT medium. An explicit expression for this operator will be derived in the next section.

Equation (34) shows again that the response of the CNT to an eigenmode excitation is a new wave consisting of the spatial and temporal frequencies of the original mode, plus higher-order Floquet modes at harmonics of the reciprocal lattice vector. Direct averaging of the field may lead to removing the fast-varying components of (34). This means that the microscopic information, the mathematical solution which is truly satisfying the symmetry group of the structure, will be lost. For the determination of the optical and electrical characteristics of materials starting from the atomic model, it is exactly such rapid variations what constitute the *local* field acting on the medium particles [8, 9, 13, 15, 22]. Therefore, for a complete electrodynamic theory for CNTs, the full field in (34) must be used without direct averaging.

## 8. BOUNDARY-VALUE PROBLEM FORMULATION FOR THE ELECTRODYNAMICS OF NANOTUBES

Assume an environment consisting of a single CNT surrounded by free space. Our goal is to formulate the suitable boundary-value problem of the electromagnetic field interaction with this environment. Let us assume first that there is an external incident field given by $(\mathbf{E}^{\text{inc}}, \mathbf{H}^{\text{inc}})$, which can be microscopic or macroscopic[†], and are propagating in an infinite and homogenous (free) space. The incident field will produce an induced fields $\left(\mathbf{E}^{\text{ind}}, \mathbf{H}^{\text{ind}}\right)$ because of the perturbation caused by the existence of the CNT in free space. The total field is given by

$$\mathbf{E} = \mathbf{E}^{\text{ind}} + \mathbf{E}^{\text{inc}}, \quad \mathbf{H} = \mathbf{H}^{\text{ind}} + \mathbf{H}^{\text{inc}}. \tag{35}$$

Equation (10) connects the polarization density of the medium with the total field. Since only linear operators are considered here, the medium response will split into two parts satisfying

$$\mathbf{P} = \mathbf{P}^{\text{ind}} + \mathbf{P}^{\text{inc}}, \tag{36}$$

where we have

$$\mathbf{P}^{\text{inc}}(\mathbf{r},t) = \int_{t'} dt' \int_{\mathbf{r}'} d^3r' \overline{\overline{\chi}}(\mathbf{r},\mathbf{r}',t,t') \cdot \mathbf{E}^{\text{inc}}(\mathbf{r}',t') \tag{37}$$

and

$$\mathbf{P}^{\text{ind}}(\mathbf{r},t) = \int_{t'} dt' \int_{\mathbf{r}'} d^3r' \overline{\overline{\chi}}(\mathbf{r},\mathbf{r}',t,t') \cdot \mathbf{E}^{\text{ind}}(\mathbf{r}',t'). \tag{38}$$

The polarization density is connected to the current by [9]

$$\mathbf{J} = \frac{\partial \mathbf{P}}{\partial t}. \tag{39}$$

By combining the two curl Maxwell's equations together with (35)–(39) and arranging the resulted terms, we arrive to the following equations

$$\nabla \times \mathbf{H}^{\text{ind}}(\mathbf{r},t) = \varepsilon_0 \frac{\partial \mathbf{E}^{\text{ind}}(\mathbf{r},t)}{\partial t} + \mathbf{J}_{\text{eq}}(\mathbf{r},t) \tag{40}$$

and

$$\nabla \times \mathbf{E}^{\text{ind}}(\mathbf{r},t) = -\mu_0 \frac{\partial \mathbf{H}^{\text{ind}}(\mathbf{r},t)}{\partial t}, \tag{41}$$

[†] The theory developed here is general enough to handle both cases.

where the equivalent electric current is given by

$$\mathbf{J}_{\text{eq}}(\mathbf{r},t) = \frac{\partial}{\partial t}\int\limits_{t'} dt' \int\limits_{\mathbf{r}'} d^3r' \overline{\overline{\chi}}(\mathbf{r},\mathbf{r}',t,t') \cdot \left[\mathbf{E}^{\text{inc}}(\mathbf{r}',t') + \mathbf{E}^{\text{ind}}(\mathbf{r}',t')\right]. \tag{42}$$

Equations (40) and (41), together with $\nabla \cdot \mathbf{D} = \rho_{\text{ex}}$ and $\nabla \cdot \mathbf{B} = 0$, where $\rho_{\text{ex}}$ is the external charge, represent a complete time-domain boundary-value problem for the electrodynamics in the CNT environment that takes into consideration the microscopic nature of the nanotube. Moreover, by assuming that an accurate quantum-mechanical solution was used for the susceptibility tensor $\overline{\overline{\chi}}$ in (42), this formulation for the electrodynamics of the nanotube can be considered semi-classically exact.

By invoking the field decomposition (35), the system of equations (40) and (41) can be solved to provide the induced field as the response to the incident field as given by the following expression

$$\mathbf{E}^{\text{ind}} = \left[-\frac{\partial^2}{\partial t^2}\left(\frac{1}{c^2} + \Im\right) + \nabla \times \nabla \times\right]^{-1} \frac{\partial^2}{\partial t^2}\Im\mathbf{E}^{\text{inc}}, \tag{43}$$

where the action of the operator $\Im$ when applied to a field $\mathbf{F}$ is defined by

$$\Im\mathbf{F} = -\mu_0 \int\limits_{t'} dt' \int\limits_{\mathbf{r}'} d^3r' \overline{\overline{\chi}}(\mathbf{r},\mathbf{r}',t,t') \cdot \mathbf{F}(\mathbf{r}',t'). \tag{44}$$

By using (37), it follows that $\mathbf{P}^{\text{inc}} = (-1/\mu_0)\Im\mathbf{E}^{\text{ind}}$. Therefore, from (43), we arrive to the following expression for the radiation operator $T$ in the relation $\mathbf{E}^{\text{ind}} = T\mathbf{P}^{\text{inc}}$

$$T = -\mu_0 \left[-\frac{\partial^2}{\partial t^2}\left(\frac{1}{c^2} + \Im\right) + \nabla \times \nabla \times\right]^{-1} \frac{\partial^2}{\partial t^2}. \tag{45}$$

On the other hand, it is also possible to express Maxwell's equations directly in the spectral domain. In this case, we apply the Fourier transform to (40) and (41), making use of (28) to expand (38), arriving to the following equations

$$\mathbf{k} \times \mathbf{H}^{\text{ind}}(\mathbf{k},\omega) = \omega\varepsilon_0 \mathbf{E}^{\text{ind}}(\mathbf{k},\omega) + \mathbf{J}_{\text{eq}}(\mathbf{k},\omega) \tag{46}$$

and

$$\mathbf{k} \times \mathbf{E}^{\text{ind}}(\mathbf{k},\omega) = -\omega\mu_0 \mathbf{H}^{\text{ind}}(\mathbf{k},\omega), \tag{47}$$

where

$$\mathbf{J}_{\text{eq}}(\mathbf{k},\omega) = \omega \sum_{\mathbf{l}|\mathbf{C}} \overline{\overline{\chi}}(\mathbf{q}-\mathbf{g}_{\mathbf{l}},\omega)\cdot e^{-jk_u b} \times \left[\mathbf{E}^{\text{inc}}(\mathbf{q}-\mathbf{g}_{\mathbf{l}},b,\omega)+\mathbf{E}^{\text{ind}}(\mathbf{q}-\mathbf{g}_{\mathbf{l}},b,\omega)\right]. \quad (48)$$

It is worthy to mention that if the source is at infinity, then the incident field takes the simple form of plane wave. This allows for further simplification in the current of (42) if the expansion (34) is taken into account.

Equations (40) and (41) can be readily discretized using differential solvers, like Finite-Element Method (FEM) or Finite Difference Time-Domain Method (FDTD), which take advantage of the fact that the problem is set most generally in the time domain. Alternatively, one can exploit the equivalent currents of (42) to write spectral domain integral equations and solve them using the Method of Moment (MoM). Such direct numerical solutions are not attempted in this paper.

## 9. GREEN'S FUNCTIONS FOR CARBON NANOTUBES

The general microscopic expansion of the fields formulated previously can be used to derive the Green's functions of the CNT located in infinite homogenous environment. Such derivation is not based on the traditional boundary condition formulation familiar in electromagnetics [10, 11]. The motivation of the current work is the fact, established formally in the previous parts, that at the nanoscale level, the microscopic details of the spatial nonlocality should be fully taken into consideration [10]. Besides their theoretical importance, the Green's functions can be utilized to build a fast and efficient general Method of Moment code to compute both the CNT near- and far-fields.

Consider a point source lying outside the CNT as shown in Figure 7. The source radiates a wave that interacts with the CNT surface. The result of this interaction is three different waves. One is propagating along the nanotube surface and we call it the *refracted* wave. Another wave is transmitted inside the tube, called here *trapped* or *transmitted* field. The third part is reflected back and is duped *diffracted*[‡].

[‡] We refer here to 'diffraction' instead of "reflection" because, in contrast to the macroscopic case, there is no meaning for 'continuous surface' upon which the wave is reflected. The term 'diffraction' from individual atoms seems more convenient for a microscopic theory of light-matter interaction.

The incident wave interacts with the CNT medium, producing the polarization given by (28), which, according to the linear model of Section 4, is nonzero only on the nanotube cylindrical surface. This polarization, in turn, will radiate everywhere. We write the radiation operator responsible of transforming the induced polarization into refracted, trapped, and diffracted fields as $T_r$, $T_t$, and $T_d$, respectively. Those operators can be found by solving the boundary-value problem of (40)–(42). In the following parts, a time-harmonic dependence of the form $\exp(j\omega t)$ is assumed and suppressed everywhere.

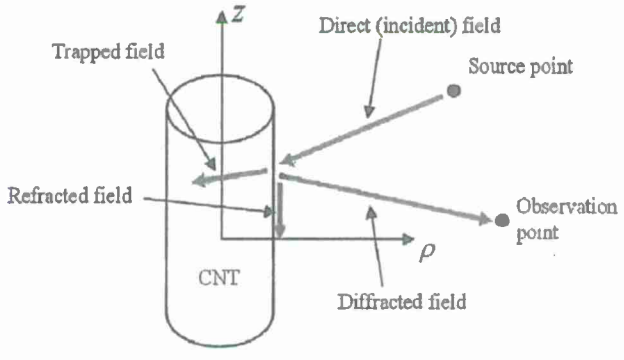


**Figure 7.** Source and observation points located outside the CNT. The point source radiates a direct wave that interacts with the CNT and results in refracted, trapped, and diffracted fields.

Let the source be an electric current located at the position $\mathbf{r}'$ and given by

$$\mathbf{J}(\mathbf{r}') = \hat{v}\delta(\mathbf{r} - \mathbf{r}'), \tag{49}$$

where $\hat{v}$ is a unit vector specifying the direction of the current. The electric field radiated by this source is given by [10]

$$\mathbf{E}(\mathbf{r}) = -j\omega\mu \int d^3r' \, \bar{\mathbf{G}}(\mathbf{r}, \mathbf{r}') \cdot \mathbf{J}(\mathbf{r}'), \tag{50}$$

where we have assumed that the source environment is an infinite homogeneous space, with characteristics $(\varepsilon, \mu)$ (i.e., remove the CNT from the source environment). The Dyadic Green's functions of free space can be written as [10]

$$\bar{\mathbf{G}}(\mathbf{r}, \mathbf{r}') = \left[\bar{\mathbf{I}} + \frac{\nabla'\nabla'}{k^2}\right] g(\mathbf{r}, \mathbf{r}'), \tag{51}$$

where $\overline{\mathbf{I}}$ is the identity dyad, $k = \omega\sqrt{\varepsilon\mu}$ is the free space wavenumber, and $g(\mathbf{r}, \mathbf{r}')$ is the scalar Green's function given by

$$g(\mathbf{r}, \mathbf{r}') = \frac{e^{-jk|\mathbf{r}-\mathbf{r}'|}}{4\pi|\mathbf{r}-\mathbf{r}'|}, \tag{52}$$

By substituting (49), (51), and (52) into (50), the incident field is simplified to

$$\mathbf{E}^{\text{inc}}(\mathbf{r}) = -j\omega\mu\left[\overline{\mathbf{I}} + \frac{\nabla'\nabla'}{k^2}\right] \cdot \hat{v}\frac{e^{-jk|\mathbf{r}-\mathbf{r}'|}}{4\pi|\mathbf{r}-\mathbf{r}'|}. \tag{53}$$

We will make use of the following form of Sommerfeld identify [10]

$$\frac{e^{-jk|\mathbf{r}-\mathbf{r}'|}}{|\mathbf{r}-\mathbf{r}'|} = -j\int_0^\infty dk_\rho \frac{k_\rho}{k_z} e^{-jk_z(z-z')} J_0\left(k_\rho|\rho-\rho'|\right), \tag{54}$$

where

$$k_z = \sqrt{k^2 - k_\rho^2} \tag{55}$$

and $J_0$ is the Bessel function of the first kind. Then, equation (53) can be written as

$$\mathbf{E}^{\text{inc}}(\mathbf{r}) = \mathbf{D}'\int_0^\infty dk_\rho \frac{k_\rho}{k_z} e^{-jk_z(z-z')} J_0\left(k_\rho|\rho-\rho'|\right), \tag{56}$$

where the differential operator $\mathbf{D}'$ is given by

$$\mathbf{D}' = -\frac{\omega\mu}{4\pi}\left[\overline{\mathbf{I}} + \frac{\nabla'\nabla'}{k^2}\right] \cdot \hat{v}. \tag{57}$$

Moreover, from the time-harmonic assumption and the particular expansion of the field in (56) we have

$$\nabla' = \hat{z}jk_z + \hat{\varphi}'\frac{jn}{\rho'} + \hat{\rho}'\frac{\partial}{\partial\rho'}. \tag{58}$$

By utilizing the addition theorem [10, 25], it is possible to expand the Bessel function of (56) in cylindrical harmonics as follow

$$J_0\left(k_\rho|\rho-\rho'|\right) = \sum_{n=-\infty}^{\infty} J_n\left(k_\rho\rho'\right) J_n\left(k_\rho\rho\right) e^{-jn(\varphi-\varphi')}. \tag{59}$$

Therefore, the primary field in (56) becomes

$$\mathbf{E}^{\text{inc}}(\mathbf{r}) = \mathbf{D}' \sum_{n=-\infty}^{\infty} \int_0^{\infty} dk_\rho \frac{k_\rho}{k_z} J_n(k_\rho \rho') J_n(k_\rho \rho) e^{-jn(\varphi-\varphi')} e^{-jk_z(z-z')}. \tag{60}$$

This means that the field radiated by a point source can be written as a sum of plane waves in the transverse direction and cylindrical wave in the radial direction.

According to (60), the point source will radiate a continuum of plane waves in both the transverse and radial directions. By identifying the cylindrical coordinates $z$ and $\varphi$ with those in the local coordinate system in Figure 6, the eigenfunction wave mode impinging on the CNT can be expressed as

$$J_n(k_\rho \rho) e^{-jk_z z - jn\varphi} = J_n(k_\rho \rho) e^{-j\,\mathbf{q}_0 \cdot \mathbf{r}}, \tag{61}$$

where

$$\mathbf{q}_0 = \langle k_z, n \rangle. \tag{62}$$

We expand now the cylindrical wave function $J_n(k_\rho \rho)$ using the following integral representation [12, 25]

$$J_n(k_\rho \rho) = \frac{j^{-n}}{2\pi} \int_0^{2\pi} d\alpha e^{jn\alpha} e^{jk_\rho \cos\alpha \rho}. \tag{63}$$

This integral representation can be interpreted in two equivalent ways. First, it may be taken to represent the cylindrical wave function $J_n(k_\rho \rho)$ as a superposition of plane waves, all with the same wavenumber $k_\rho$, but propagating in the directions $u(\alpha) = \rho \cos\alpha$. The second interpretation is that those plane waves have varying wavenumbers given by $k(\alpha) = k_\rho \cos\alpha$ but with fixed (arbitrary) spatial direction $\rho$. If we take the second interpretation, we can assume that the reference spatial direction coincides with our coordinate $u$ in the local system of Figure 6. Therefore, the wave in (61) can be written as

$$J_n(k_\rho u) e^{-j\mathbf{q}_0 \cdot \mathbf{r}} = \frac{j^{-n}}{2\pi} \int_0^{2\pi} \left( d\alpha e^{jn\alpha} \right) e^{-j\mathbf{q}_0 \cdot \mathbf{r} - jk'_\rho(\alpha) u}, \tag{64}$$

where

$$k'_\rho(\alpha) = -k_\rho \cos\alpha. \tag{65}$$

According to the key result (34), the microscopic field generated by the eigenmode $e^{-j\mathbf{q}_0\cdot\mathbf{r}-jk'_\rho u}$ takes the form

$$\sum_{l_1,l_2|\mathbf{C}} T_{r,t,d}\overline{\overline{\chi}}^{\mathrm{I}}(-\mathbf{q}_0)\cdot\mathbf{D}'e^{-jk'_\rho b}\delta(u-b)\,e^{j\frac{2\pi}{a}l_1 z}e^{jNl_2\varphi}\,e^{-j\,\mathbf{q}_0\cdot\mathbf{r}}$$
$$=\sum_{l_1,l_2|\mathbf{C}} T_{r,t,d}\overline{\overline{\chi}}^{\mathrm{I}}(-\mathbf{q}_0)\cdot\mathbf{D}'e^{-jk'_\rho b}\delta(u-b)e^{j\left(\frac{2\pi}{a}l_1-k_z\right)z}e^{j(Nl_2-n)\varphi}. \quad (66)$$

By using (61) and (66) in (56), the total electric Green's functions can be calculated by superposition. We have

$$\mathbf{G}^{e}_{r,t,d}(\mathbf{r},\mathbf{r}')=\mathbf{E}^{\mathrm{inc}}+\sum_{n=-\infty}^{\infty}\sum_{l_1|\mathbf{C}}\sum_{l_2|\mathbf{C}}\left\{\int_{-\infty}^{\infty}\int_{0}^{2\pi}d\alpha dk_\rho\frac{j^{-n}}{2\pi}\frac{k_\rho}{k_z}\right.$$
$$\times T_{r,t,d}\overline{\overline{\chi}}^{\mathrm{I}}(-\mathbf{q}_0)\cdot\mathbf{D}'J_n(k_\rho\rho')e^{-jk_\rho b\cos\alpha}\delta(u-b)\,e^{jn\varphi'}e^{jk_z z'}$$
$$\left.\times\, e^{jn\alpha}e^{j\left(\frac{2\pi}{a}l_1-k_z\right)z}e^{j(Nl_2-n)\varphi}\right\} \quad (67)$$

The magnetic Green's functions follows directly from Maxwell's equations and are given by

$$\mathbf{G}^{h}_{r,t,d}(\mathbf{r},\mathbf{r}')=\frac{1}{-j\omega\mu_0}\nabla\times\mathbf{G}^{\mathrm{e}}_{r,t,d}(\mathbf{r},\mathbf{r}'). \quad (68)$$

Because of the choice of the Sommerfeld integral adopted by (54), no modification is needed for the case when the source is inside the CNT. However, while evaluating the integral with respect to $k_\rho$, caution must be taken to avoid passing over the pole and branch point singularities of the integrand.

The apparent complexity of (67), compared with other problems in conventional engineering electromagnetics, is a natural consequence of the microscopic model introduced in Section 4. This is a price that must be paid for the abundance of the much simpler, but arguably potentially problematic, program of macroscopic Maxwell's equation[§].

## 10. CONCLUSION

In this paper, a formalism for the electrodynamics of carbon nanotubes was proposed. A general nonlocal linear phenomenological model

[§] For applications where the far-field response is the parameter of interest, the higher-order Floquet modes in the $z$-direction can be ignored, which amounts to a simple averaging operation applied to the Green's function in (67), removing hence the $l_1$ spatial modes.

was assumed in the study of the problem of the interaction of low-dimensional structure with electromagnetic fields. The symmetry group of the structure was employed to obtain the Bloch form of the spectral properties of the interaction. The derived expressions are then used to highlight a methodology for the computation of the Green's functions of the nanotube.

## ACKNOWLEDGMENT

This work was partially supported by the Department of Electrical Engineering, University of Mississippi and the National Science Foundation under Grant No. ECS-524293. Also, partial support for this research was provided by ONR Grant # N00014-07-1-1010, Office of Naval Research, Solid Mechanics Program (Dr. Yapa D.S. Rajapakse, Program Manager).

## REFERENCES

1. Poole, C. P. and F. J. Owens, *Introduction to Nanotechnology*, Wiley-Interscience, 2003.
2. Kong, F., K. Li, B.-I. Wu, H. Huang, H. Chen, and J. A. Kong, "Propagation properties of the SPP modes in nanoscale narrow metallic gap, channel, and hole geometries," *Progress In Electromagnetics Research*, PIER 76, 449–466, 2007.
3. Talele, K. and D. S. Patil, "Analysis of wave function, energy and transmission coefficients in GaN/ALGaN superlattice nanostructures," *Progress In Electromagnetics Research*, PIER 81, 237–252, 2008.
4. Iijima, S., "Helical microtabules of graphitic carbon," *Nature*, Vol. 354, 56–58, 1991.
5. Anantram, M. and F. Leonard, "Physics of carbon nanotube electronic devices," *Reports on Progress in Physics*, Vol. 69, 507–561, February 2006.
6. Smalley, R. E., M. S. Dresselhaus, G. Dresselhaus, and P. Avouris, *Carbon Nanotubes: Synthesis, Structure, Properties and Applications*, Springer, 2001.
7. Mikki, S. M. and A. A. Kishk, "Exact derivation of the dyadic Green's functions of carbon nanotubes using microscopic theory," *International IEEE APS Symposium*, Hawaii, June 2007.
8. Wooten, F., *Optical Properties of Solids*, Academic Press, 1972.
9. Jackson, J. D., *Classical Electrodynamics*, 3rd edition, John Wiley & Sons, 1999.

10. Chew, W. C., *Waves and Fields in Inhomogeneous Media*, re-print edition, IEEE Press, 1999.
11. Balanis, C., *Advanced Engineering Electromagnetics*, John Wiley & Sons, 1989.
12. Stratton, J., *Electromagnetic Theory*, McGraw-Hill, 1941.
13. Toyozawa, Y., *Optical Processes in Solids*, Cambridge University Press, 2003.
14. Brillouin, L., *Wave Propagation in Periodic Structures*, 1956.
15. Born, M. and K. Haung, *Dynamical Theory of Crystal Lattices*, 1st edition, Oxford University Press, London, 1954.
16. Grosso, G. and G. Parravicini, *Solid-State Physics*, Academic Press, 2000.
17. White, C. T., D. H. Robertson, and J. W. Mintmire, "Helical and rotational symmetries of nanoscale graphitic tubules," *Phys. Rev. B*, Vol. 47, No. 9, 5485–5488, March 1993.
18. Damnjanovic, M., I. Milosevic, T. Vukovic, and R. Sredanovic, "Full-symmetry, optical activity, and potentials of single-wall and multi-wall nanotubes," *Phys. Rev. B*, Vol. 60, No. 4, 2728–2739, July 1999.
19. Damnjanovic, M., I. Milosevic, T. Vukovic, and R. Sredanovic, "Symmetry and lattices of single-wall nanotubes," *J. Phys. A*, Vol. 32, 4097–4104, 1999.
20. Cohen-Tannoudjii, C., J. Dupont-Roc, and G. Grynberg, *Photons and Atoms: Introduction to Quantum Electrodynamics*, Wiley, 1989.
21. Pekar, S. I., "Theory of electromagnetic waves in a crystal in which excitons are produced," *Sov. Phys. JETP*, Vol. 6, 785, 1957.
22. Agranovich, V. M. and V. L Ginsburg, *Crystal Optics and Spatial Dispersion, and Excitons*, Springer, 1984.
23. Halevi, P. (ed.), *Spatial Dispersion in Solids and Plasmas*, Springer, 1992.
24. Cho, K., "Nonlocal theory of radiation-matter interaction: Boundary-condition-less treatment of Maxwell equations," *Prog. Theor. Phys. Suppl.*, No. 106, 225–233, 1991.
25. Abramowitz, M. and I. A. Stegun, *Handbook of Mathematical Functions*, Dover Publications, 1965.

U-269

*Progress In Electromagnetics Research B, Vol. 9, 1–26, 2008*

# DERIVATION OF THE CARBON NANOTUBE SUSCEPTIBILITY TENSOR USING LATTICE DYNAMICS FORMALISM

**S. M. Mikki and A. A. Kishk**

Center of Applied Electromagnetic Systems Research
Department of Electrical Engineering
University of Mississippi
University, MS 38677, USA

**Abstract**—We develop in this paper a theoretical approach to describe the electrodynamics of carbon nanotubes (CNTs). A lattice dynamics formalism is employed to model the mechanical response of matter to the radiation field. We start first by deriving the normal modes of the free lattice. Then, a simple and general microscopic model for light-matter interaction is proposed and the resulting mechanical equation of motion is derived using a suitable Lagrangian formalism. The symmetry group of the CNT is employed to explicitly probe the nonlocal structure of the fields and to carefully insure that higher-order Floquet modes are included in the derivation. The normal modes are then employed to perform an eigenmode expansion for the solution of the mechanical equation of motion, leading to the susceptibility tensor of the CNT medium. The final expression of this tensor describes the electrodynamics in the CNT viewed as a low-dimensional surface and is shown to be reduced effectively to a one-dimensional response function.

## 1. INTRODUCTION

The maturation of recent developments in measurement technology during the last 15 years has created a breakthrough in our capabilities to monitor and study structures at the nanoscale [1–3]. Of special importance is a class of low-dimensional structures called carbon nanotubes (CNT), which were discovered in 1991 by Iijima [4]. Since then, they have attracted the attention of both physicists and engineers who investigated extensively the possibility of using CNTs for various applications, ranging from mechanical shielding to nano-waveguide and transistors [5]. One of the most attractive features in CNTs is

their ability to function in either metallic or semi-conducting modes, depending on how the original graphite sheet is rolled to form the tube [6].

The electrodynamics of nanostructures differs considerably from the conventional scheme adopted in engineering electromagnetics. In this paper, we provide a theoretical study and various demonstrations of these differences by using a lattice dynamics formalism to derive the dielectric tensor of the CNT. We highlight in particular two major themes in the electrodynamics of nanometer structures.

- **Mechanics is Inevitable:** In the microscopic treatment of light-matter interaction, the mechanical response of matter represents the sole interaction with light. Therefore, any derivation of the dielectric tensor must use a mechanical model. In this paper we choose the linear lattice vibration approach for its conceptual simplicity, wide applicability, and the existence of an exact quantum mechanical analogy.
- **The Nonlocality of the Fields:** This point is less obvious than the previous one. At the nanometer level, the periodic arrangements of atoms in crystals (like nanotubes and graphenes) creates higher-order (Floquet) mode interactions which modify the structure of the applied fields. For a satisfactory derivation of the optical characteristics of CNTs, it is important to calculate these higher-order contributions and include them directly in the final expressions. We highlight this feature in our mathematical formulation throughout the paper.

Based on the theme above, we develop in this paper a theoretical description of the carbon nanotube electrodynamics starting from suitable microscopic considerations. Previous studies of the lattice dynamics of CNTs reported applications to the mechanical and acoustic aspects of the device [17]. Here, we provide a tentative treatment of the electromagnetic coupling between an external field and the mechanical lattice vibration modes. The contribution of the electronic response to the susceptibility is treated on a phenomenological level coupled with the lattice vibration of the nanotube.

This paper is organized as follow. We start by reviewing the structure of CNTs, which is summarized using basic symmetry groups developed previously in the literature. The normal modes of the free lattice are then derived carefully. Next, we formulate a general lattice dynamics microscopic model for the light-matter interaction. The equations of motion are derived using a full Lagrangian formalism. We enforce explicitly the nonlocal structure of the fields in the derived equation of motion. This equation is then solved using an

eigenvalue expansion in terms of the free lattice normal modes obtained previously, leading to an expression for the susceptibility tensor of the nanotube. Finally, conclusions are given.

## 2. STRUCTURE OF CARBON NANOTUBES

In this section, we provide a compact description of the structural properties of CNTs using the language of the associated symmetry group. The details of the symmetry operations will be used in the remaining parts of this paper to find the specific mathematical form of the eigenmodes appearing in the dielectric tensor of the nanotube. The crux of our approach is that the symmetry group will determine the boundary conditions of the problem [12]. These conditions can not be derived form the Hamiltonian of the CNT but should be obtained through an independent approach. Fig. 1 illustrates the honeycomb lattice structure of graphene (graphene is defined as a 2D layer of graphite). The unit cell is specified by two atoms located at the positions $1/3\,(\mathbf{a}_1 + \mathbf{a}_2)$ and $2/3\,(\mathbf{a}_1 + \mathbf{a}_2)$, where $\mathbf{a}_1$ and $\mathbf{a}_2$ are two unit vectors defining the lattice constants and $|\mathbf{a}_1| = |\mathbf{a}_2| = a_0 = 0.2461\,\text{nm}$. The CNT is formed by rolling this sheet such that the circumference of the tube coincides with the *chiral vector* $\mathbf{c} = m\,\mathbf{a}_1 + n\,\mathbf{a}_2$. Here $m$ and $n$ are two integers that completely determine the structure and the properties of the CNT. If only one layer is used to form the tube, the resulting structure is called *single-wall* CNT (SWCNT). Alternatively, if the tube consists of several concentric cylinders, we call it *multi-wall* CNT (MWCNT). The chiral angle $\theta$ is defined as the angle between

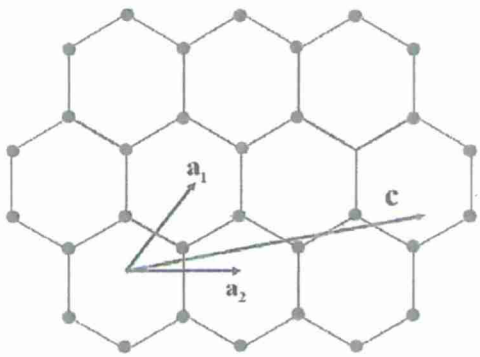


**Figure 1.** Graphene sheet used in forming a CNT. The dots illustrate the positions of carbon atoms.

the chiral vector $\mathbf{c}$ and $\mathbf{a}_1$. The radius of the CNT is given by

$$\rho_{\rm cn} = \frac{|\mathbf{c}|}{2\pi} = \frac{a_0}{2\pi}\sqrt{m^2+mn+n^2}. \tag{1}$$

The first symmetry group for the CNT can be derived by writing $\mathbf{c} = N\left[(m/N)\,\mathbf{a}_1 + (n/N)\,\mathbf{a}_2\right] = N\,\mathbf{c}'$, where $N$ is the greatest common divider of $m$ and $n$. It is obvious that a rotation around the tube axis by $2\pi/N$ will preserve the original structure. Equivalently, we say that each CNT possess the symmetry operation $\mathbf{C}_N$.

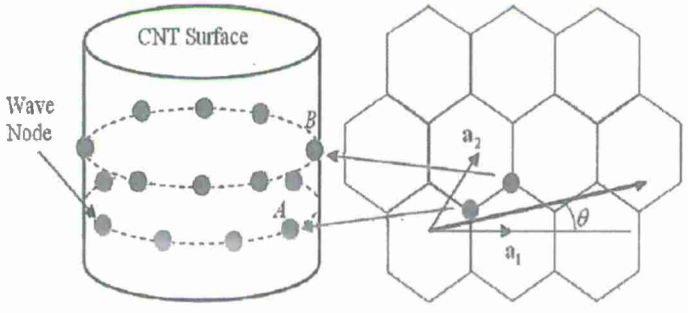


**Figure 2.** (a) Illustration of two atomic circles in the translational unit cell of a SWCNT. Each circle corresponds to the symmetry operation $\mathbf{C}_N$. (b) The honeycomb lattice structure of graphene. The dots represent the arbitrary first two-atom unit cell.

Through knowledge of other symmetry operations, to be discussed in a moment, it is possible by following the original work of White et al. [14] to show that the entire tube can be constructed starting from two-atom unit cell and the chiral vector. The first atom in the unit cell will be mapped to an arbitrary location in the circumference of the CNT, call it $A$. The second atom will be mapped to other location $B$ obtained by rotating the first point by an angle $\gamma = 2\pi\,(\mathbf{a}_1+\mathbf{a}_2)\cdot\mathbf{c}/3\,|\mathbf{c}|^2$ and then translating the resulting point along the tube axis by a distance $d = |(\mathbf{a}_1+\mathbf{a}_2)\times\mathbf{c}|/3\,|\mathbf{c}|^2$. The two points obtained now can be used, together with the symmetry operation $\mathbf{C}_N$, to generate other $2(N-1)$ points by successive rotations around the tube axis by the angle $2\pi/N$. That is, atom $A$, together with $\mathbf{C}_N$, will generate other $N-1$ atoms. Atom $B$, again together with $\mathbf{C}_N$, will generate other set of $N-1$ atoms. Therefore, the total is

$2(N-1)+N=2N$ atoms. This set is called the *basic helical motif* of the CNT [14]. However, to complete the tube we need to use a *screw operator*, defined in [14], which is denoted here by $\mathbf{T}_h^\zeta$. Its action on a specific point consists of rotation around the tube axis by an angle $\zeta$ and then translation along the tube axis by a distance $h$. Therefore, the screw operation is neither pure rotation nor pure translation, but a combination of both of them. A procedure for finding $\zeta$ and $h$ can be found in [14] and explicit closed form expressions in terms of Euler function are available as follow [15]

$$q = 2\frac{m^2+mn+n^2}{NR}, \tag{2}$$

$$\xi = \frac{q}{N}\mathrm{Fr}\left[\frac{N}{qR}\left(3-2\frac{m-n}{m}\right)+\frac{N}{m}\left(\frac{m-n}{N}\right)^{\mathrm{E}(m/N)-1}\right], \tag{3}$$

$$\zeta = \frac{2\pi}{q}\xi, \quad h = \frac{N}{\xi}a, \tag{4}$$

where $\mathrm{Fr}[x] = x - [x]$ gives the fractional part of the rational number $x$ and $\mathrm{E}(v)$ is the Euler function giving the co-primes less than $v$ ($a$ is defined in (6)). By repeated application of the screw operator $\mathbf{T}_h^\zeta$ on the basic helical motif, the entire tube can be reconstructed [14]. Therefore, the two-atom unit cell that we started with is enough to determine the full structure of the CNT.

It remains to present the translational symmetry of the CNT. Depending on the chirality, each CNT will have a characteristic length $a$ along its axis. Translations of multiples of $a$ will leave the tube unchanged. This periodicity in the axial direction can be given by [15]

$$N_1 = -\frac{2n+m}{N\mathcal{R}}, \quad N_2 = \frac{2m+n}{N\mathcal{R}}, \tag{5}$$

$$\mathbf{a} = N_1\mathbf{a}_1 + N_2\mathbf{a}_2, \quad a = |\mathbf{a}| = \frac{\sqrt{3\left(m^2+mn+n^2\right)}}{N\mathcal{R}}a_0, \tag{6}$$

$$N_c = \frac{2\left(m^2+mn+n^2\right)}{N\mathcal{R}}, \tag{7}$$

where $N_c$ is the number of atomic pairs in the translational unit cell. Here, $\mathcal{R} = 3$ if $(n_1-n_2)/3N$ is integer and $\mathcal{R} = 1$ otherwise. We denote here this symmetry operation by $\mathbf{T}_a$ and it means translation along the tube axis by distance $a$. The translational unit cell consists then of a cylindrical tube of radius $\rho_{\mathrm{cn}}$ and height $a$. The number of atoms in the unit cell is given by $N_c$.

To summarize, $\mathbf{C}_N$ is the symmetry operation of pure rotation (translations along the circumferential direction $\mathbf{c}$), $\mathbf{T}_a$ is the operation of pure translation, and $\mathbf{T}_h^\zeta$ is the (mixed) screw operation. It is worthy to mention that other symmetry operations were derived in [15] and [16] to fully characterize SWCNTs and MWCNTs. However, for the purpose of this paper the, previously mentioned three symmetry operations are enough to drive the basic mathematical form of the fields in the CNT environment. As will be shown in the next section, all other symmetry operations will alter only the number of terms taken in the resulted summations without changing the basic form.

## 3. LATTICE DYNAMICS FORMALISM

### 3.1. Motivation

The mathematical theory of lattice vibrations in solids is well-known since the original work of Max Born [11]. We start first in this section by providing a quick sketch of the theoretical background that motivates the application of lattice dynamics formalisms to study the optical properties in solids.

The exact solution for the problem of light-matter interaction requires applying quantum theory to describe the mechanical response of charged particles to the external fields. Such solution, however, implies dealing with the full Hamiltonian of the matter system, which complicates considerably the mathematical treatment. However, since the electron mass is much smaller than the nuclear mass, it is possible to write the Hamiltonian in the form $\mathcal{H}_0 = \mathcal{H}_{0e} + T$. Here, $\mathcal{H}_{0e}$ is the Hamiltonian of the electronic system and $T$ is the kinetic energy operator of the nuclear parts. Without going to the mathematical details (see [13] for example), a perturbation method can be applied to the previous Hamiltonian to obtain a solution accurate to the order of the smallness of $T$ with respect to $\mathcal{H}_0$. The approximation leading to this solution is called the *adiabatic approximation* and is one of the most fundamental tools in condensed matter physics. Within this approximation, the problem of the interaction of electromagnetic fields with CNT can be treated in terms of the lattice vibrations of the nuclei. It is as if we imagine at each moment that the nuclear motion is fixed and the electrons are responding by creating a nontrivial charge and current distribution. The nuclear motion is a *parameter* for the electronic state.

### 3.2. Hamiltonian of the Carbon Nanotube Free Lattice

The free lattice of carbon nanotubes is the periodic arrangement of atoms in the crystal structure as described by the exact symmetry groups of Section 2. The basic formulation of this paper will follow a classical Hamiltonian approach. Since we are going to proceed under the harmonic approximation assumption, an exact quantum-mechanical quantization of this classic solution can be obtained in a straightforward way.

Following the treatment of symmetry operations in Section 2, we write the position vector of the $\mathbf{n}s$th atom as

$$\mathbf{R}_{\mathbf{n}s} = S_{\mathbf{n}}^{\zeta,h}\mathbf{R}_{0s}, \tag{8}$$

where $\mathbf{R}_{0s}$ is the position vector of the $s$th atom ($s = 1, 2$) in the initial unit cell (atom pair) and the operator $S_{\mathbf{n}}^{\zeta,h}$ represents the repeated application of $\mathbf{C}_N$ followed by the skew operator, with parameters $\zeta$ and $h$, starting from the initial pair at $\mathbf{n} = \mathbf{0}$ and ending in the current pair $\mathbf{n}$. Equation (8) will be applied implicitly in all of the coming calculations.

We start with a crystal structure in the equilibrium state. Due to an external field, or any other source, the locations of the atoms will be disturbed. The resulting motion can be described as vibrations around a center defined by the undisturbed equilibrium locations, represented by a position vector $\mathbf{R}$. Let the displacement around this center be $\mathbf{u}$. By assuming that the external force is weak, the resulting displacement $\mathbf{u}$ can be considered as a small perturbation around the equilibrium position. Therefore, it is possible to expand the total potential energy of the lattice in power series as

$$\begin{aligned} U(\mathbf{R}+\mathbf{u}) &= U(\mathbf{R}) + \sum_{\mathbf{n}}\sum_{s}\frac{\partial U}{\partial \mathbf{R}_{\mathbf{n}s}}\mathbf{u}_{\mathbf{n}s} \\ &\quad + \frac{1}{2}\sum_{\mathbf{n}}\sum_{s}\sum_{\mathbf{n}'}\sum_{s'}\mathbf{u}_{\mathbf{n}'s'}\frac{\partial U}{\partial \mathbf{R}_{\mathbf{n}s}\partial \mathbf{R}_{\mathbf{n}'s'}}\mathbf{u}_{\mathbf{n}s} + \cdots, \end{aligned} \tag{9}$$

where $\partial^2 U/\partial \mathbf{R}_{\mathbf{n}s}\partial \mathbf{R}_{\mathbf{n}'s'}$ is a $3 \times 3$ matrix and all vectors are three-dimensional. The $\alpha\beta$th element of this matrix is the second-order derivative $\partial^2 U/\partial R_\alpha \partial R_\beta$ evaluated at the equilibrium positions $R_\alpha = R_{\mathbf{n}s\alpha}$ and $R_\beta = R_{\mathbf{n}'s'\beta}$, where $\alpha, \beta = 1, 2, 3$ enumerate the three orthogonal spatial directions.

Since we assume that $\mathbf{R}$ describes the equilibrium state of the lattice, the potential energy attains a minimum at this location. Consequently, the second term in (9) will vanish. If we keep only the

second-order terms in the series expansion, we obtain the well-known linear harmonic approximation Hamiltonian [7, 11]

$$\mathcal{H}=\sum_{\mathbf{n}}\sum_{s}\frac{\mathbf{P}_{\mathbf{n}s}\cdot\mathbf{P}_{\mathbf{n}s}}{2M}+\frac{1}{2}\sum_{\mathbf{n}}\sum_{s}\sum_{\mathbf{n}'}\sum_{s'}\mathbf{u}_{\mathbf{n}'s'}\frac{\partial^2 U}{\partial\mathbf{R}_{\mathbf{n}s}\partial\mathbf{R}_{\mathbf{n}'s'}}\mathbf{u}_{\mathbf{n}s}, \quad (10)$$

where $\mathbf{P}_{\mathbf{n}s}$ is the momentum of the $\mathbf{n}s$th atom. The first term corresponds to the total kinetic energy and the second term to the potential energy of the CNT lattice. Since the entire tube is constructed from identical atoms (carbon), we introduce $M$ to denote the atomic mass of carbon.

Once the Hamiltonian of the CNT is constructed, the dynamic equations follow directly

$$\dot{\mathbf{u}}_{\mathbf{n}s}=\frac{\partial\mathcal{H}}{\partial\mathbf{P}_{\mathbf{n}s}}, \qquad \dot{\mathbf{P}}_{\mathbf{n}s}=-\frac{\partial\mathcal{H}}{\partial\mathbf{u}_{\mathbf{n}s}}. \quad (11)$$

Thus, it follows from (10) and (11) that

$$M\ddot{\mathbf{u}}_{\mathbf{n}s}+\sum_{\mathbf{n}'}\sum_{s'}A^{ss'}_{\mathbf{n},\mathbf{n}'}u_{\mathbf{n}'s'}=0, \quad (12)$$

where the matrix $A^{s,s'}_{\mathbf{n},\mathbf{n}'}$ is defined as

$$A^{ss'}_{\mathbf{n},\mathbf{n}'}=\frac{\partial^2 U}{\partial\mathbf{R}_{\mathbf{n}s}\partial\mathbf{R}_{\mathbf{n}'s'}}. \quad (13)$$

Equation (12) captures the dynamics of the CNT lattice under no external electromagnetic field. Therefore, its solutions should provide the free vibrations, or the *normal modes*, from which we can later expand the (driven) response to the field.

### 3.3. Normal Modes

Assume that the axis of the CNT coincides with the $z$-direction. In light of Bloch's theorem, the general solution of Equation (12) can be written as [7, 9, 11]

$$\mathbf{u}_{\mathbf{n}s}=\mathbf{u}_s e^{-j\mathbf{k}\cdot\mathbf{R}_{\mathbf{n}}}e^{j\omega t}=\mathbf{u}_s e^{-jk_\phi\phi_{\mathbf{n}}}e^{-jk_z z_{\mathbf{n}}}e^{j\omega t}, \quad (14)$$

where we have used the notation $\mathbf{R}_{\mathbf{n}}=\langle z_{\mathbf{n}},\phi_{\mathbf{n}}\rangle$ and $\mathbf{k}=\langle k_z,k_\phi\rangle$. Here $\mathbf{u}_s$ is a constant of motion that depends on $\mathbf{k}$. We will show now that the symmetry group of the CNT leads to the result that $k_z$ must be continuous while $k_\phi$ is quantized.

Assume that the CNT is finite in the longitudinal (axial) direction, in which it consists of $L$ identical unit cells each with length $a$. By applying the periodic boundary condition of Born [11], we get $\mathbf{u}_{\mathbf{n}s}(z=0) = \mathbf{u}_{\mathbf{n}s}(z=La)$, which in light of (14) will give the condition $e^{-jk_zLa} = 1$. Thus, we can write $k_z = (2\pi/La)\,l'$, $l' = 0, 1, 2, \ldots, \infty$. For very large $L$, the ratio $2\pi/La$ becomes very small. Since the CNT structure is infinite in the $z$-direction, we require $L \to \infty$, and $k_z$ therefore becomes continuous.

For the transverse (circumferential) direction, we apply the symmetry operation $\mathbf{C}_N$, which states that rotations around the $z$-axis will preserve the structure. Therefore, we write $l \cdot \lambda = c = 2\pi\rho_{\mathrm{cn}}$, where $c$ is the circumference of the nanotube. This leads to the quantization rule

$$k_\phi = l, \ \forall\, l = 0, 1, 2, \ldots, N_c - 1. \tag{15}$$

We can now write the $l$th normal mode of the free lattice as

$$\mathbf{u}_{\mathbf{n}s} = \mathbf{u}_s e^{-jl\phi_{\mathbf{n}}} e^{-jk_z z_{\mathbf{n}}} e^{j\omega_{\mathbf{k}}t}, \tag{16}$$

where the function $\omega_{\mathbf{k}} = \omega(\mathbf{k})$ is the dispersion relation (to be found). Substituting (16) into (12), we get

$$-M\omega_{\mathbf{k}}^2 \mathbf{u}_s + \sum_{\mathbf{n}'} \sum_{s'} A_{\mathbf{n},\mathbf{n}'}^{ss'} \mathbf{u}_s e^{-jl(\phi_{\mathbf{n}'} - \phi_{\mathbf{n}})} e^{-jk_z(z_{\mathbf{n}'} - z_{\mathbf{n}})} = 0. \tag{17}$$

The above equation reduces to

$$-M\omega_{\mathbf{k}}^2 \mathbf{u}_s + \sum_{s'} \hat{A}^{ss'}(\mathbf{k})\, \mathbf{u}_s = 0, \tag{18}$$

where the dynamic matrix

$$\hat{A}^{ss'}(\mathbf{k}) = \sum_{\mathbf{m}} A_{\mathbf{m},\mathbf{n}}^{ss'} e^{j\,\mathbf{k}\cdot\mathbf{R}_{\mathbf{m}}} \tag{19}$$

can be interpreted as the discrete Fourier transform of the lattice force matrix $A_{\mathbf{m},\mathbf{n}}^{ss'}$. It can be shown that by employing the general symmetry properties of the dynamic matrix that this transform does not depend on $\mathbf{n}$ [13].

Equation (18) is an eigenvalue problem and can be set in the form

$$\left\| M\omega_{\mathbf{k}}^2 \delta_{ss'} \delta_{\alpha\alpha'} - \hat{A}_{\alpha\alpha'}^{ss'}(\mathbf{k}) \right\| = 0, \tag{20}$$

where the symbol $\|\cdot\|$ denotes the determinant and $\delta_{ss'}$ is the Kronecker delta function. Here, $\alpha = 1, 2, 3$ enumerates the three spatial direction

and $s = 1, 2$ enumerates the atom in the nth two-atom unit cell. Therefore, Equation (20) is of order 6. Its eigenvalues will determine the dispersion relation while the eigenvectors constitute a complete set of basis function for the representation of the full space of the lattice vibrations.

Let us introduce the canonical variables $\tilde{\mathbf{u}}_{\mathbf{n}s} = M^{1/2}\mathbf{u}_{\mathbf{n}s}$ and $\tilde{A}^{ss'}(\mathbf{k}) = M^{-1}\hat{A}^{ss'}(\mathbf{k})$. Now, the fact that the force matrix (13) is conjugate symmetric with respect to the transformation $\mathbf{n}s\alpha \longleftrightarrow \mathbf{n}'s'\alpha$ makes its Fourier transform (19) Hermitian. Following the standard diagonalization procedure in linear algebra, the eigenvalue problem (20) leads to a set of real eigenvalues $\omega^i(\mathbf{k})$ and complex eigenvectors $\tilde{e}^i_{s\alpha}(\mathbf{k})$ satisfying the following equations

$$\sum_s \sum_\alpha \tilde{e}^i_{s\alpha}(\mathbf{k})\,\tilde{e}^{*i'}_{s\alpha}(\mathbf{k}) = \delta_{ii'} \quad \text{(orthonormality)}, \tag{21}$$

$$\sum_i \tilde{e}^{*i}_{s\alpha}(\mathbf{k})\,\tilde{e}^{i}_{s'\alpha'}(\mathbf{k}) = \delta_{ss'}\delta_{\alpha\alpha'} \quad \text{(completeness)}, \tag{22}$$

$$\sum_{s,s'} \sum_{\alpha,\alpha'} \tilde{e}^{*i}_{s\alpha}(\mathbf{k})\,A^{ss'}_{\alpha\alpha'}\tilde{e}^{i'}_{s\alpha}(\mathbf{k}) = \delta_{ii'}\omega^i(\mathbf{k})^2 \quad \text{(diagonality)}. \tag{23}$$

Therefore, the most general solution to the lattice dynamics problem takes the following form

$$u_{\mathbf{n}s\alpha} = \sum_{i=1}^{6}\sum_{l=1}^{N_c}\int_{-\pi}^{\pi} dk_z \varsigma^i(k_z,l)\tilde{e}^i_{s\alpha}(k_z,l)\exp\left(j\omega^i_l(k_z)\,t\right)\exp(-jl\varphi_{\mathbf{n}} - jk_z z_{\mathbf{n}}), \tag{24}$$

where $\varsigma^i(k_z,l)$ are the expansion weights.

### 3.4. Expansion of the Force Matrix

To obtain numerical values for the eigenvalue and eigenvectors derived in the previous section, an estimation of the unknown force constants in (13) must be attempted. However, although the force matrix of the lattice vibration in CNTs is phenomenological, and experimental results are needed to accurately determine its values, we will show in this section that a considerable reduction in the complexity of the problem can be achieved if the symmetry operations of the CNT are applied. Since the potential function is a system characteristic, not a wave, the periodic boundary condition can not be applied to the axial direction; pure translations in the $z$-direction will maintain their discrete nature. Together with the rotational periodicity, we

expand the potential function as a Fourier series in both the $z$- and $\varphi$-directions as follow

$$U(z,\varphi,\rho) = \sum_{\mathbf{l}} \Gamma_{\mathbf{l}}(\rho)\, e^{j\mathbf{g_l}\cdot\mathbf{t}}, \tag{25}$$

where $\mathbf{l} = (l_1, l_2)$ and

$$\mathbf{g_l} = \left\langle \frac{2\pi}{a} l_2, N l_1 \right\rangle, \qquad \mathbf{t} = \langle z, \phi \rangle . \tag{26}$$

The summation in (25) can be further restricted by applying the screw symmetry condition

$$U(z,\phi,\rho) = U(z-h, \phi-\zeta, \rho), \tag{27}$$

with $\zeta$ and $h$ are the parameters of the screw operator defined in (4). Equation (27) gives $\exp\left(jl_1 N\zeta + j\frac{2\pi}{a} l_2 h\right) = 1$, which translates to the following condition

$$\mathbf{C}: \;\; l_1 N\zeta + l_2 \frac{2\pi h}{a} = 2\pi v, \;\; v = 0, \pm 1, \pm 2, \ldots, \pm\infty. \tag{28}$$

In the coming parts, we write a summation over $\mathbf{l}$ that takes into consideration the condition $\mathbf{C}$, as defined in (28), in the form $\sum_{\mathbf{l}|\mathbf{C}}$. Therefore, using the definition of the force matrix in (13), we can arrive to the reduced expansion shown in Appendix A. The attractive feature of this expansion is that all the functions are calculated at the same radial distance $\rho = \rho_{\mathrm{cn}}$, the radius of the CNT in (1). Therefore, the problem of determining the force constants for all dimensions is reduced to knowledge of sufficient number of the coefficients $\Gamma_{\mathbf{l}}$ and $\partial\Gamma_{\mathbf{l}}/\partial\rho$ evaluated at the single point $\rho = \rho_{\mathrm{cn}}$. This is a considerable reduction of the number of degrees of freedom in the original problem that was achieved by applying the symmetry group of CNTs.

## 4. INTERACTION WITH THE ELECTROMAGNETIC FIELD

### 4.1. Microscopic Model for the Interaction

In this section, we provide a simple atomic model for the interaction between external electromagnetic fields and the lattice of CNTs. The starting assumption is that the amplitude of the external source is weak, giving rise to small distortion in the electronic clouds

surrounding the vibrating nuclei in the lattice dynamics model formulated in the previous parts. To accomplish this formally, we assume that the motion of atoms in the lattice will introduce a small distribution of non-trivial electric charge density $\delta\rho$ and current density $\delta\mathbf{J}$. Therefore, based on the first-order approximation, we retain only the linear variation of the functional dependence of these quantities in their Taylor series expansion. It is possible then to write

$$\delta\rho = \sum_{\mathbf{n}} \sum_{s} \sum_{\alpha} \Upsilon_{\mathbf{n}s\alpha}(\mathbf{r})\, u_{\mathbf{n}s\alpha} \tag{29}$$

and

$$\delta J_{\alpha} = \sum_{\mathbf{n}} \sum_{s} \sum_{\beta} \Gamma^{\mathbf{n}s}_{\alpha\beta}(\mathbf{r})\, \dot{u}_{\mathbf{n}s\beta}, \tag{30}$$

where $\Upsilon_{\mathbf{n}s\alpha}$ and $\Gamma^{\mathbf{n}s}_{\alpha\beta}$ are phenomenological parameters describing the "rate" of the system response to the linear variation in the displacements $u_{\mathbf{n}s\alpha}$. These can be calculated using a suitable quantum-mechanical model. However, such calculations are beyond the scope of this paper and will not be carried out here. Notice that zero-order terms in the Taylor series are exactly zero because the overall CNT is electrically neutral.

It should be noticed that the assumptions behind the expansions (29) and (30) are quite general and apply to most of the practical cases encountered in the study of material response to weak electromagnetic fields, with exceptions mainly in laser applications where the nonlinear effects must be accounted for explicitly. Moreover, a quantum-mechanical treatment of the nontrivial charge and current distributions $\delta\rho$ and $\delta\mathbf{J}$ can be included implicitly in the functions $\Upsilon_{\mathbf{n}s\alpha}$ and $\Gamma_{\mathbf{n}s}$. Therefore, our model can include for pure quantum effects, like electronic transitions, as long as the adiabatic approximation is valid.

### 4.2. Coupling between External Fields and the Lattice Oscillators

Based on the microscopic model of Section 4.1, we derive the equation of motion under the influence of an applied electromagnetic field described by scalar and vector potentials $\phi$ and $\mathbf{A}$. Within the adiabatic approximation, we start from the following non-relativistic

Lagrangian [18]

$$L = \frac{1}{2}\sum_{\mathbf{n}}\sum_{s}\sum_{\alpha} M\left(\dot{u}_{ns\alpha}\right)^2 - \frac{1}{2}\sum_{\mathbf{n}}\sum_{s} \mathbf{u}_{\mathbf{n}'s'} A^{ss'}_{\mathbf{n},\mathbf{n}'} \mathbf{u}_{ns} + \sum_i e_i \mathbf{v}_i \cdot \mathbf{A}\left(\mathbf{r}_i, t\right) - \sum_i e_i \phi\left(\mathbf{r}_i, t\right) + \int \mathrm{d}^3 r \mathcal{L}_{EM}, \quad (31)$$

where $i$ enumerates the fundamental charges $e_i$ and $\mathcal{L}_{EM}$ is the field Lagrangian density given by

$$\begin{aligned}\mathcal{L}_{EM} &= \frac{\varepsilon_0}{2}\left[\left(\nabla\phi + \frac{\partial \mathbf{A}}{\partial t}\right)^2 - c^2\left(\nabla \times \mathbf{A}\right)^2\right] \\ &= \frac{\varepsilon_0}{2}\left(|\mathbf{E}|^2 - c^2|\mathbf{B}|^2\right). \end{aligned} \quad (32)$$

Due to the microscopic nature of the sources, we can write [8]

$$\begin{aligned}\delta\rho &= \sum_i e_i \delta\left[\mathbf{r} - \mathbf{r}_i\left(t\right)\right], \\ \delta\mathbf{J} &= \sum_i e_i \dot{\mathbf{r}}_i \delta\left[\mathbf{r} - \mathbf{r}_i\left(t\right)\right]. \end{aligned} \quad (33)$$

Therefore, the Lagrangian in (31) takes the form

$$L = \frac{1}{2}\sum_{\mathbf{n}}\sum_{s}\sum_{\alpha} M\left(\dot{u}_{ns\alpha}\right)^2 - \frac{1}{2}\sum_{\mathbf{n}}\sum_{s} \mathbf{u}_{\mathbf{n}'s'} A^{ss'}_{\mathbf{n},\mathbf{n}'} \mathbf{u}_{ns} + \int \mathrm{d}^3 r\, \mathbf{A}\left(\mathbf{r}, t\right) \cdot \delta\mathbf{J} - \int \mathrm{d}^3 r\, \phi\left(\mathbf{r}, t\right) \delta\rho + \int \mathrm{d}^3 r \mathcal{L}_{EM}. \quad (34)$$

The first and second terms represent the mechanical energies, kinetic and potential, respectively. The third and fourth terms capture the interaction between the external fields and the local lattice sources. The last term is a representation of the energy stored in the fields.

Applying Hamilton's principle, the equation of motion under the Lagrangian (34) is given by [8]

$$\frac{d}{dt}\left(\frac{\partial L}{\partial \dot{u}_{ns\alpha}}\right) - \frac{\partial L}{\partial u_{ns\alpha}} = 0. \quad (35)$$

In Appendix B, we show that the following equation of motion can be derived from the Lagrangian formalism above

$$M\ddot{u}_{ns\alpha} + \sum_{\mathbf{n}'}\sum_{s'}\sum_{\alpha'} A^{ss'\alpha\alpha'}_{\mathbf{n},\mathbf{n}'} u_{\mathbf{n}'s'\alpha'} = \int \mathrm{d}^3 r\, \Gamma^{ns}_{\alpha}\left(\mathbf{r}\right) \cdot \mathbf{E}\left(\mathbf{r}, t\right). \quad (36)$$

This is an inhomogeneous equation that governs the dynamics of the system under the influence of external electromagnetic field.

### 4.3. The Nonlocal Structure of the Fields

Following the general theoretical framework developed in [12], we emphasize that when applying the electromagnetic theory to problems at the nanometer scale it is of paramount importance to take into consideration the non-local relations between the fields and the induced polarization at different spacial locations. This is particularly important when dealing with crystal structures like CNTs where the prevailing characteristics are periodic, as exemplified by the associated symmetry group.

There is some confusion about non-locality in electromagnetic theory, which accompanies the nature of the field appearing in (36). Therefore, we will spend some time discussing the conceptual background of the problem. First, as we mentioned before, the correct mathematical treatment of the problem requires that we insert the *actual* field, which is different from the applied field [6, 7, 9]. Moreover, in [12] an explicit form for the field in the CNT medium was derived and showed that higher-order (Floquet) modes will emerge from the periodic structure of the problem. The main reason why such higher-order modes are sometimes ignored in literature is the fact that we usually apply conventional *macroscopic* electromagnetic theory, where the fields are averaged over spacial regions large compared to the microscopic scale but small in comparison to the macroscopic one. Therefore, all of the short-wavelength components will be washed out by the averaging in the theory. For a satisfactory derivation of the optical characteristics using microscopic models, this averaging, which amounts to loosing some of the important information in the field structure that may participate in determining the final observed value for the dielectric function must be avoided. Now, although this function itself is usually measured by a device that inherently averages the results, we should notice that such averaging in the final result is *not* equivalent to averaging the fields from the start using a macroscopic electromagnetic theory. The mathematical treatment of the incoming parts are designed to clearly demonstrate these claims in the particular example of nanotubes.

To summarize, what is needed for a correct microscopic derivation of the optical characteristics is two requirements

1. Distinction between the applied and actual (local) field.
2. Distinction between the "slow" part of the field (long-wavelength, fundamental mode, low-frequency part, etc) and the "fast" part

(short-wavelength, higher-order modes, high-frequency parts, etc).

In the present approach, we achieve the two requirements above simultaneously by using the microscopic model for the interaction in Section 4.1. We first translate the first requirement into the following equation

$$\mathbf{E} = \mathbf{E}^e + \delta\mathbf{E}, \tag{37}$$

where $\mathbf{E}$ refers here to the actual (local) field acting on the atoms in the CNT. $\mathbf{E}^e$ is the external (applied) field. The difference between the actual and the external field is denoted by $\delta\mathbf{E}$. The mechanism behind its existence is the distortion of the electronic wave functions and the nuclear displacements through the lattice vibrations that result in the build up of non-trivial charge and current distributions (29) and (30).

Without loss of generality, we assume that the external field has only long-wavelength component (averaged). The induced fields $\delta\mathbf{E}$, however, contains all the harmonics of the CNT structure due to the non-local effects [12]. Therefore, we expand the total field as

$$\mathbf{E} = \bar{\mathbf{E}} + \tilde{\mathbf{E}}, \tag{38}$$

where $\bar{\mathbf{E}}$ is the long-wavelength (slow) part and $\tilde{\mathbf{E}}$ is the short-wavelength (fast) part. We immediately obtain

$$\bar{\mathbf{E}} = \mathbf{E}^e + \delta\bar{\mathbf{E}} \tag{39}$$

and

$$\tilde{\mathbf{E}} = \delta\tilde{\mathbf{E}}. \tag{40}$$

Within the general assumption of the linear harmonic approximation of the lattice dynamics and the weakness of the external sources, we expand $\delta\mathbf{E}$ in Taylor series and retain only the linear terms

$$\delta E_\alpha = \sum_{\mathbf{n}'} \sum_{s'} \sum_{\alpha'} \Lambda_{\alpha\alpha'}^{\mathbf{n}'s'}(\mathbf{r})\, u_{\mathbf{n}'s'\alpha'}, \tag{41}$$

where $\Lambda_{\alpha\alpha'}^{\mathbf{n}s}(\mathbf{r})$ is some unknown function that represents the "rate" of the change in the system response to the linear displacements $u_{\mathbf{n}s\alpha}$. Now, this function is a characteristic of the original lattice (zero displacement). Therefore, it must obey the exact symmetry group introduced in Section 2. We can then expand it in a Fourier series like Equation (25). We write then (41) as

$$\delta E_\alpha = \sum_{\mathbf{n}'} \sum_{s'} \sum_{\alpha'} \sum_{\mathbf{l}|\mathbf{C}} \Lambda_{\alpha\alpha'}^{\mathbf{n}'s'\mathbf{l}}(\rho)\, e^{j\mathbf{g}_\mathbf{l}\cdot\mathbf{t}} u_{\mathbf{n}'s'\alpha'}, \tag{42}$$

where the Fourier expansion

$$\Lambda^{\mathbf{n}'s'}_{\alpha\alpha'}(\mathbf{r}) = \sum_{\mathbf{l}|\mathbf{C}} \Lambda^{\mathbf{n}'s'\mathbf{l}}_{\alpha\alpha'}(\rho)\, e^{j\mathbf{g}_\mathbf{l}\cdot\mathbf{t}}. \tag{43}$$

has been used. Here, $\mathbf{g}_\mathbf{l}$ and $\mathbf{t}$ are defined as in (26). Based on the previous discussion, we write the long-wavelength part as the component $\mathbf{l} = 0$ and the short-wavelength parts as all the other (higher) order modes. We find

$$\delta\bar{\mathbf{E}} = \sum_{\mathbf{n}'}\sum_{s'}\sum_{\alpha'} \Lambda^{\mathbf{n}'s'0}_{\alpha'}(\rho)\, u_{\mathbf{n}'s'\alpha'} \tag{44}$$

and

$$\delta\tilde{\mathbf{E}} = \sum_{\mathbf{n}'}\sum_{s'}\sum_{\alpha'}\sum_{\mathbf{l},\mathbf{l}\neq 0} \Lambda^{\mathbf{n}'s'\mathbf{l}}_{\alpha'}(\rho)\, e^{j\mathbf{g}_\mathbf{l}\cdot\mathbf{t}} u_{\mathbf{n}'s'\alpha'}. \tag{45}$$

Substituting Equations (37)–(45) into (36) we obtain

$$M\ddot{u}_{\mathbf{n}s\alpha} + \sum_{\mathbf{n}'}\sum_{s'}\sum_{\alpha'} A^{\prime ss'\alpha\alpha'}_{\mathbf{n},\mathbf{n}'} u_{\mathbf{n}'s'\alpha'} = \int \mathrm{d}^3 r\, \Gamma^{\mathbf{n}s}_{\alpha}(\mathbf{r})\cdot\bar{\mathbf{E}}(\mathbf{r},t), \tag{46}$$

where the new dynamic matrix is given by

$$A^{\prime ss'\alpha\alpha'}_{\mathbf{n},\mathbf{n}'} = A^{ss'\alpha\alpha'}_{\mathbf{n},\mathbf{n}'} - \sum_{\mathbf{l}\neq 0|\mathbf{C}} \int \mathrm{d}^3 r\, \Gamma^{\mathbf{n}s}_{\alpha}(\mathbf{r})\cdot\Lambda^{\mathbf{n}'s'\mathbf{l}}_{\alpha'}(\rho)\, e^{j\mathbf{g}_\mathbf{l}\cdot\mathbf{t}} \tag{47}$$

and represents the structure of the lattice dynamics with the short-wavelength contribution of the fields taken implicitly into consideration. This re-arrangement of the equation of motion will allow us to calculate the (measured) dielectric function due to a *macroscopic* field $\bar{\mathbf{E}}$ with the microscopic higher-order Floquet modes already handled properly by the new matrix (47). The important feature of Equation (46) is that it has exactly the same structure of (36), rendering the theory of lattice vibrations developed in Section 3 applicable. The only important difference, however, is that the eigenvalues in (21), (22), and (23) are now generally complex.

### 4.4. The Dielectric Tensor

We have now all the tools required to derive an expression for the dielectric function of the CNT. To accomplish this, we excite the nanotube by a wave in the form

$$\mathbf{E} = \mathbf{E}_0 e^{-j\mathbf{k}\cdot\mathbf{r}} e^{j\omega t} = \mathbf{E}_0 e^{-jk_z z - jk_\phi \phi} e^{j\omega t}. \tag{48}$$

The response of the medium consists of lattice vibrations propagating in the direction $\mathbf{k} = \langle k_z, k_\phi \rangle$. That is, we restrict ourselves to the electrodynamics in the CNT medium. Using the general formulation of Section 3.3, it is possible to expand the medium response in terms of eigenmodes of the homogenous equation of motion as follow

$$u_{ns\alpha} = \sum_i \eta_i(\mathbf{k}) e^{-j\mathbf{k}\cdot\mathbf{R_n}} e^{j\omega t} e^i_{s\alpha}(\mathbf{k}). \tag{49}$$

Substituting (49) into (46), employing the canonical transformations $\tilde{u} = \sqrt{M}u$ and $\tilde{A}^{ss'}_{\alpha\alpha'} = (1/M)\hat{A}^{ss'}_{\alpha\alpha'}$, we find

$$\begin{aligned} &-\omega^2 \sum_i \eta_i \tilde{e}^i_{s\alpha}(\mathbf{k}) + \sum_{s'}\sum_{\alpha'}\sum_i \tilde{A'}^{ss'}_{\alpha\alpha'} \eta_i \tilde{e}^i_{s'\alpha'}(\mathbf{k}) \\ &= \frac{1}{\sqrt{M}} \int \mathrm{d}^3 r\, \Gamma^{ns}_\alpha(\mathbf{r}) \cdot \mathbf{E}_0 e^{-j\mathbf{k}\cdot\mathbf{r}} e^{j\,\mathbf{k}\cdot\mathbf{R_n}}, \end{aligned} \tag{50}$$

where $\hat{A}'$ is the modified dynamic matrix defined exactly like (19). Multiplying (50) by $\tilde{e}^{*i'}_{s\alpha}$, summing over $s$ and $\alpha$, we obtain

$$\begin{aligned} &-\omega^2 \sum_i \sum_s \sum_\alpha \eta_i \tilde{e}^i_{s\alpha} \tilde{e}^{*i'}_{s\alpha} + \sum_i \eta_i \sum_s \sum_\alpha \sum_{s'} \sum_{\alpha'} \tilde{e}^{*i'}_{s\alpha} \tilde{A'}^{ss'}_{\alpha\alpha'} \tilde{e}^i_{s'\alpha'} \\ &= \frac{1}{\sqrt{M}} \sum_s \sum_\alpha \int \mathrm{d}^3 r\, \Gamma^{ns}_\alpha(\mathbf{r}) \cdot \mathbf{E}_0 e^{-j\,\mathbf{k}\cdot\mathbf{r}} e^{j\,\mathbf{k}\cdot\mathbf{R_n}} \tilde{e}^{*i'}_{s\alpha}. \end{aligned} \tag{51}$$

Applying (21) and (23) to the first and second terms in (51), respectively, we can arrive to the following expression for the expansion coefficients

$$\eta_i(\mathbf{k}) = \frac{\frac{1}{\sqrt{M}} \sum_s \sum_\alpha \int \mathrm{d}^3 r\, \Gamma^{ns}_\alpha(\mathbf{r}) \cdot \mathbf{E}_0 e^{-j\,\mathbf{k}\cdot(\mathbf{r}-\mathbf{R_n})} \tilde{e}^{*i'}_{s\alpha}(\mathbf{k})}{\omega_i^2(\mathbf{k}) - \omega^2}. \tag{52}$$

We proceed now to calculate the induced current in the medium. Using (30), the total current is written as

$$J_\alpha = \frac{j\omega}{\sqrt{M}} \sum_{\mathbf{n}} \sum_s \sum_\beta \sum_i \Gamma^{ns}_{\alpha\beta}(\mathbf{r})\, \eta_i e^{-j\,\mathbf{k}\cdot\mathbf{R_n}} e^{j\omega t} \tilde{e}^i_{s\alpha}, \tag{53}$$

where (49) has been used in writing (53). In order to simplify the forthcoming calculations, we resort to a the reasonable assumption that the coefficients of the Taylor series expansion $\Gamma^{ns}_\alpha(\mathbf{r})$ are centered

around the $n$sth unit cell. Thus, we write $\Gamma_{\alpha}^{ns}(\mathbf{r}) = \Gamma_{\alpha}^{s}(\mathbf{r} - \mathbf{R}_{ns})$. The Fourier transform of the current (53) is then written as

$$J_{\alpha}(\mathbf{k},t) = \frac{1}{V}\int d^3 r J_{\alpha}(\mathbf{r},t)\, e^{j\,\mathbf{k}\cdot\mathbf{r}}. \tag{54}$$

Therefore, we can compute the $\ell_1$th-component of the CNT medium response to the $\ell_2$th-component of the field ($\ell_1, \ell_2 = 1,2,3$) as

$$\begin{aligned} J_{\ell_1}(\mathbf{k},t) \;=\; & \frac{j\omega}{VM}\int d^3 r \sum_{\mathbf{n}}\sum_{s}\sum_{\beta}\sum_{i}\frac{E_{0l_2}\Xi_{\ell_2}^{i}}{\omega_i^2-\omega^2}\Gamma_{\ell_1\beta}^{s}(\mathbf{r}-\mathbf{R}_{ns}) \\ & \times e^{j\,\mathbf{k}\cdot(\mathbf{r}-\mathbf{R}_{\mathbf{n}})}e^{j\omega t}\tilde{e}_{s\ell_1}^{i}(\mathbf{k}), \end{aligned} \tag{55}$$

where we define the *effective charge* as

$$\Xi_{\ell}^{i}(\mathbf{k}) = \sum_{s}\sum_{\alpha}\int d^3 r\phi\,\Gamma_{\alpha\ell}^{s}(\mathbf{r}-\mathbf{R}_{ns})\, e^{-j\mathbf{k}\cdot(\mathbf{r}-\mathbf{R}_{\mathbf{n}})}\tilde{e}_{s\ell}^{*i}(\mathbf{k}). \tag{56}$$

It is clear that the integral in (56) can be made independent of $\mathbf{n}$ by the transformation $\mathbf{y} = \mathbf{r} - \mathbf{R}_{\mathbf{n}}$. Now, re-arranging (55), it is possible to write

$$\begin{aligned} J_{\ell_1}(k,t) \;=\; & \frac{j\omega}{VM}E_{0l_2}e^{j\omega t}\sum_{\mathbf{n}}\sum_{i}\frac{\Xi_{\ell_2}^{i}}{\omega_i^2-\omega^2} \\ & \times\left[\sum_{s}\sum_{\beta}\int d^3 r\,\Gamma_{\ell_1\beta}^{s}(\mathbf{r}-\mathbf{R}_{ns})\,\tilde{e}_{s\ell_1}^{i}e^{j\,\mathbf{k}\cdot(\mathbf{r}-\mathbf{R}_{\mathbf{n}})}\right]. \end{aligned} \tag{57}$$

Using the definition of the effective charge in (56) for the term between brackets in (57), we get

$$J_{\ell_1}(\mathbf{k},t) = \frac{j\omega}{VM}E_{0l_2}e^{j\omega t}\sum_{\mathbf{n}}\sum_{i}\frac{\Xi_{\ell_1}^{i*}(\mathbf{k})\,\Xi_{\ell_2}^{i}(\mathbf{k})}{\omega_i^2(\mathbf{k})-\omega^2}. \tag{58}$$

The polarization density $\mathbf{P}$ is connected to the volume current density $\mathbf{J}_v$ by the relation $\mathbf{J}_v(\mathbf{k},t) = (\partial/\partial t)\,\mathbf{P}(\mathbf{k},t)$. For the problem under consideration here, by restricting ourselves to the surface current and polarization density, we obtain

$$P_{\ell_1}(\mathbf{k},\omega) = \frac{1}{j\omega}\left(N_c/2\pi a\rho_{\mathrm{cn}}\right)J_{\ell_1}(\mathbf{k},\omega) = \chi_{\ell_1\ell_2}(\mathbf{k},\omega)\,E_{\ell_2}(\mathbf{k},\omega), \tag{59}$$

where $\chi_{\ell_1\ell_2}$ is the susceptibility tensor of the medium. Here, since the effective charges are independent of $\mathbf{n}$, the current density emerges

naturally from truncating the summation over $\mathbf{n}$ in (58) for a certain number of atoms in the CNT surface and then dividing over the area of this surface in order to get the density of the current. From Section 2, this ratio can be found to be $N_c/2\pi a\rho_{\rm cn}$. Applying (59) to (58), we finally arrive to the following expression for the susceptibility tensor of the CNT

$$\chi_{\ell_1\ell_2}(\mathbf{k},\omega) = \frac{N_c}{2\pi a\rho_{\rm cn}M}\sum_i \frac{\Xi^{i*}_{\ell_1}(\mathbf{k})\,\Xi^{i}_{\ell_2}(\mathbf{k})}{\omega_i^2(\mathbf{k})-\omega^2}. \tag{60}$$

We keep the information about the electronic contribution to the total dielectric function in the effective charges defined in (56). Strictly speaking, if electronic transitions represent the main contribution to the dielectric function at a certain frequency band in which the lattice interactions are insignificant, then a phenomenological model, or an accurate quantum calculation, can be used in the response functions in (29) and (30). Within this scheme, the total dielectric function for the CNT medium can be finally stated as

$$\varepsilon_{\ell_1\ell_2}(\mathbf{k},\omega) = \varepsilon_0 + \frac{N_c}{2\pi a\rho_{\rm cn}M}\sum_i \frac{\Xi^{i*}_{\ell_1}(\mathbf{k})\,\Xi^{i}_{\ell_2}(\mathbf{k})}{\omega_i^2(\mathbf{k})-\omega^2}. \tag{61}$$

This represents the key result of the paper. We have derived the electrodynamic responses of CNT media using a microscopic model of its interaction with the electromagnetic field. Since the derivation was achieved within the linear oscillator formalism, a direct quantization procedure for the above formulation is straightforward but lengthy and avoided here because of the limitation of space.

## 5. DISCUSSION OF THE RESULTS

There are certain interesting features in the derived expression (61) that are worthy to be mentioned here from the purely theoretical point of view.

1. We first notice that since $\mathbf{k} = \langle k_z, k_\phi\rangle$, the fields are propagating only on the tube surface. That does not mean that no actual field can impinge obliquely on the tube, but it illustrates the peculiar, although not quite surprising, fact that for low-dimensional structures the entire electrodynamics takes place in a reduced-dimensional space. The CNT medium does not exist for $\rho \neq \rho_{\rm cn}$, which prohibits mechanical vibrations to propagate in the radial direction. Notice that the displacements themselves may have three spatial components, but the vibrations can propagate only

along the tube surface. For the more general case where there is an incident field *outside* the CNT and it is desired to calculate the scattered field, one should go beyond the model developed in this paper. It is well-known that for nanometer structures, where the effect of spatial dispersion is important, the conventional boundary-condition approach to Maxwell's equations fails to solve for the unknown fields uniquely. One actually needs additional boundary-conditions (ABC) augmented to Maxwell's boundary conditions [19]. Although there has been many approaches to solve this problem [18–20], the determination of these ABCs for a general structure is still an open problem. One should resorts to microscopic models to provide a specification of how the mechanical movements of the microscopic sources behave at the interface between the two media. In the case illuminated in this paper, this means that a more sophisticated model is needed to describe the mechanical motion of the oscillators in the lattice vibrations at the boundary $\rho = \rho_{\text{cn}}$. It is not clear how to accomplish this with our formalism. One possibility would be to introduce a more detailed mathematical model for the distribution of the microscopic charges (29) and (30) that is not necessary localized over the CNT surface. Then, by describing how its radial dependences behave while the oscillations pass through the boundary $\rho = \rho_{\text{cn}}$ it may become possible to derive the required ABC. However, we leave such speculations to future work. To summarize, it is stated that the derivation of this paper is meant to deal with the electrodynamics *within* the CNT medium. An observer living on the CNT surface (the medium) simply can not "see" the space where $\rho \neq \rho_{\text{cn}}$, which explains the absence of $k_\rho$ in (61). The remarks here refers to the new situation where a dielectric constant for a sheet or a surface was derived rigorously without approximating the sheet as a limit of very small thin film.

2. The effective charges in $\Xi_\ell^i(\mathbf{k})$ are actually vectors. The tensor product $\Xi_{\ell_1}^{i*}(\mathbf{k})\,\Xi_{\ell_2}^{i}(\mathbf{k})$ is symmetric and does not reduce to scalar because the CNT has no cubic symmetry.
3. Although the susceptibility in (60) is written in terms of both $k_\phi$ and $k_z$, the problem is actually one-dimensional. As we saw in Section 3.3, $k_\phi$ is effectively quantized in the form $k_\phi = n$, where $n = 1, 2, \ldots, N_{\text{c}}$. Therefore, it is possible to write the field as

$$\mathbf{E} = \mathbf{E}_0 \sum_{n=1}^{N_{\text{c}}} a_n e^{-jn\phi} e^{-jk_z z}, \tag{62}$$

where $a_n$ is the expansion coefficients. Substituting (62) to (60),

we find

$$\mathbf{P} = \bar{\chi}(k_z, \omega) \cdot \mathbf{E}_0, \tag{63}$$

where the effective 1D susceptibility $\bar{\chi}(k_z, \omega)$ is given by

$$\bar{\chi}(k_z, \omega) = \sum_{n=1}^{N_c} a_n \bar{\chi}(k_\phi = n, k_z, \omega) . \tag{64}$$

Therefore, it may be instructive to think of the electrodynamics of the CNT as occurring effectively in one-dimensional space with the mapping from the full 2D space to the reduced 1D space accomplished by (64).

## 6. CONCLUSION

A general derivation for the dielectric tensor of carbon nanotubes was achieved using a lattice dynamics formalism. The derivation demonstrated the peculiar feature of CNTs as a low-dimensional structure. Specifically, we showed that the problem can be reduced to a one-dimensional case. The derivation was based on a microscopic model for the charge and current sources induced in the system because of the lattice vibrations. We developed a Lagrangian formalism to deal with the problem and solved for the resulting mechanical motion using the dynamic (retarded) interactions through the lattice sites. The final expression for the dielectric tensor rests on only three reasonable assumptions: (1) The adiabatic approximation, (2) the external field is weak so the system response is linear, and (3) the nontrivial sources induced in the lattice are localized on the surface of the CNT, each around the center of the atomic unit cell. The lattice dynamics model of this paper can be easily quantized, rendering the model quantum-mechanically complete within the three assumptions stated above.

## APPENDIX A. REDUCED FORM FOR THE FORCE MATRIX ELEMENTS

The list of the matrix elements calculated in Section 3.4 using the symmetry group of the CNT are listed here as follow

$$A^{ss'}_{\mathbf{n},\mathbf{n}'}(\alpha = 1, \alpha' = 1) = \sum_{\mathbf{l},\mathbf{l}'|\mathbf{C}} \left(\frac{2\pi}{a}\right)^2 (l_2 l'_2)\, \Gamma_{\mathbf{l}} \Gamma_{\mathbf{l}'} \Omega^{\mathbf{l}}_{\mathbf{n}\mathbf{n}'ss'}$$

$$A^{ss'}_{\mathbf{n},\mathbf{n}'}(\alpha = 1, \alpha' = 2) = \sum_{\mathbf{l},\mathbf{l}'|\mathbf{C}} \left(\frac{2\pi}{a} N l_2 l'_1\right) \Gamma_{\mathbf{l}} \Gamma_{\mathbf{l}'} \Omega^{\mathbf{l}}_{\mathbf{n}\mathbf{n}'ss'}$$

$$
\begin{aligned}
A^{ss'}_{\mathbf{n},\mathbf{n}'}\left(\alpha=1,\alpha'=3\right) &= \sum_{\mathbf{l},\mathbf{l}'|\mathbf{C}}\left(\frac{2\pi}{a}l_2\right)\Gamma_{\mathbf{l}}\frac{\partial\Gamma_{\mathbf{l}'}}{\partial\rho}\Omega^{\mathbf{l}}_{\mathbf{n}\mathbf{n}'ss'}\\
A^{ss'}_{\mathbf{n},\mathbf{n}'}\left(\alpha=2,\alpha'=1\right) &= \sum_{\mathbf{l},\mathbf{l}'|\mathbf{C}}\left(\frac{2\pi}{a}Nl_1l'_2\right)\Gamma_{\mathbf{l}}\Gamma_{\mathbf{l}'}\Omega^{\mathbf{l}}_{\mathbf{n}\mathbf{n}'ss'}\\
A^{ss'}_{\mathbf{n},\mathbf{n}'}\left(\alpha=2,\alpha'=2\right) &= \sum_{\mathbf{l},\mathbf{l}'|\mathbf{C}}\left(N^2l_2l'_2\right)\Gamma_{\mathbf{l}}\Gamma_{\mathbf{l}'}\Omega^{\mathbf{l}}_{\mathbf{n}\mathbf{n}'ss'}\\
A^{ss'}_{\mathbf{n},\mathbf{n}'}\left(\alpha=2,\alpha'=3\right) &= \sum_{\mathbf{l},\mathbf{l}'|\mathbf{C}}\left(Nl_2\right)\Gamma_{\mathbf{l}}\frac{\partial\Gamma_{\mathbf{l}'}}{\partial\rho}\Omega^{\mathbf{l}}_{\mathbf{n}\mathbf{n}'ss'}\\
A^{ss'}_{\mathbf{n},\mathbf{n}'}\left(\alpha=3,\alpha'=1\right) &= \sum_{\mathbf{l},\mathbf{l}'|\mathbf{C}}\left(\frac{2\pi}{a}l'_2\right)\frac{\partial\Gamma_{\mathbf{l}}}{\partial\rho}\Gamma_{\mathbf{l}'}\Omega^{\mathbf{l}}_{\mathbf{n}\mathbf{n}'ss'}\\
A^{ss'}_{\mathbf{n},\mathbf{n}'}\left(\alpha=3,\alpha'=2\right) &= \sum_{\mathbf{l},\mathbf{l}'|\mathbf{C}}\left(Nl'_2\right)\frac{\partial\Gamma_{\mathbf{l}}}{\partial\rho}\Gamma_{\mathbf{l}'}\Omega^{\mathbf{l}}_{\mathbf{n}\mathbf{n}'ss'}\\
A^{ss'}_{\mathbf{n},\mathbf{n}'}\left(\alpha=3,\alpha'=3\right) &= \sum_{\mathbf{l},\mathbf{l}'|\mathbf{C}}\frac{\partial\Gamma_{\mathbf{l}}}{\partial\rho}\frac{\partial\Gamma_{\mathbf{l}'}}{\partial\rho}\Omega^{\mathbf{l}}_{\mathbf{n}\mathbf{n}'ss'}
\end{aligned}
\tag{A1}
$$

where we used

$$
\Omega^{\mathbf{l}}_{\mathbf{n}\mathbf{n}'ss'} = e^{j\mathbf{g}_{\mathbf{l}}\cdot\mathbf{t}_{\mathbf{n}s}}e^{j\mathbf{g}_{\mathbf{l}}\cdot\mathbf{t}_{\mathbf{n}'s'}} = e^{j\mathbf{g}_{\mathbf{l}}\cdot\left(\mathbf{t}_{\mathbf{n}s}-\mathbf{t}_{\mathbf{n}'s'}\right)}. \tag{A2}
$$

## APPENDIX B. DERIVATION OF THE EQUATION OF MOTION UNDER EXTERNAL FIELDS

First, we convert the Lagrangian into an explicit function of the canonical variables $u$ and $\dot{u}$ by substituting (29) and (30) into (32) to get

$$
\begin{aligned}
L = \frac{1}{2}\sum_{\mathbf{n}}\sum_{s}\sum_{\alpha}M\left(\dot{u}_{\mathbf{n}s\alpha}\right)^2 - \frac{1}{2}\sum_{\mathbf{n}}\sum_{s}\mathbf{u}_{\mathbf{n}'s'}A^{ss'}_{\mathbf{n},\mathbf{n}'}\mathbf{u}_{\mathbf{n}s}\\
+\int \mathrm{d}^3r\sum_{\alpha}\sum_{\mathbf{n}}\sum_{s}\sum_{\beta}\Gamma^{\mathbf{n}s}_{\alpha\beta}\left(\mathbf{r}\right)A_{\beta}\left(\mathbf{r},t\right)\dot{u}_{\mathbf{n}s\beta}\\
-\int \mathrm{d}^3r\sum_{\mathbf{n}}\sum_{s}\sum_{\alpha}\Upsilon_{\mathbf{n}s\alpha}\left(\mathbf{r}\right)\phi\left(\mathbf{r},t\right)u_{\mathbf{n}s\alpha}.
\end{aligned}
\tag{B1}
$$

We start by calculating the individual terms in the Euler-Lagrange

Equation (35). Simple manipulations lead to

$$\frac{\partial L}{\partial \dot{u}_{\mathrm{n}s\alpha}} = M\dot{u}_{\mathrm{n}s\alpha} + \frac{\partial}{\partial \dot{u}_{\mathrm{n}s\alpha}} \int \mathrm{d}^3 r \sum_{\beta} \sum_{\mathrm{n}'} \sum_{s'} \sum_{\beta'} \Gamma_{\beta\beta'}^{\mathrm{n}'s'}(\mathrm{r})\, \delta J_{\beta} \dot{u}_{\mathrm{n}'s'\beta'}$$

$$= M\dot{u}_{\mathrm{n}s\alpha} + \int \mathrm{d}^3 r \sum_{\beta} \Gamma_{\beta\alpha}^{\mathrm{n}s}(\mathrm{r})\, A_{\beta}(\mathrm{r}, t), \tag{B2}$$

and

$$\frac{\partial L}{\partial u_{\mathrm{n}s\alpha}} = -\sum_{\mathrm{n}'} \sum_{s'} \sum_{\alpha'} A_{\mathrm{n},\mathrm{n}'}^{ss'\alpha\alpha'} u_{\mathrm{n}'s'\alpha'}$$

$$-\frac{\partial}{\partial u_{\mathrm{n}s\alpha}} \int \mathrm{d}^3 r \sum_{\mathrm{n}'} \sum_{s'} \sum_{\alpha'} \Upsilon_{\mathrm{n}'s'\alpha'} \phi u_{\mathrm{n}'s'\alpha'}$$

$$= -\sum_{\mathrm{n}'} \sum_{s'} \sum_{\alpha'} A_{\mathrm{n},\mathrm{n}'}^{ss'\alpha\alpha'} u_{\mathrm{n}'s'\alpha'} - \int \mathrm{d}^3 r\, \Upsilon_{\mathrm{n}s\alpha} \phi(\mathrm{r}, t). \tag{B3}$$

Substituting (B2) and (B3) into (35), we find

$$M\ddot{u}_{\mathrm{n}s\alpha} + \sum_{\mathrm{n}'} \sum_{s'} \sum_{\alpha'} A_{\mathrm{n},\mathrm{n}'}^{ss'\alpha\alpha'} u_{\mathrm{n}'s'\alpha'}$$

$$+ \int \mathrm{d}^3 r \left\{ \sum_{\beta} \Gamma_{\beta\alpha}^{\mathrm{n}s}(\mathrm{r}) \frac{\partial A_{\beta}}{\partial t} + \Upsilon_{\mathrm{n}s\alpha} \phi(\mathrm{r}, t) \right\} = 0. \tag{B4}$$

We need to use the equation of continuity

$$\frac{\partial \rho}{\partial t} + \nabla \cdot \mathrm{J} = 0. \tag{B5}$$

By plugging (29) and (30) into (B5), it is possible to write

$$\sum_{\mathrm{n}} \sum_{s} \sum_{\beta} \Upsilon_{\mathrm{n}s\beta}(\mathrm{r})\, \dot{u}_{\mathrm{n}s\beta}$$

$$= -\nabla \cdot \sum_{\mathrm{n}} \sum_{s} \sum_{\beta} \Gamma_{\alpha\beta}^{\mathrm{n}s}(\mathrm{r})\, \dot{u}_{\mathrm{n}s\beta}$$

$$= -\sum_{\alpha} \frac{\partial}{\partial x_{\alpha}} \sum_{\mathrm{n}} \sum_{s} \sum_{\beta} \Gamma_{\alpha\beta}^{\mathrm{n}s}(\mathrm{r})\, \dot{u}_{\mathrm{n}s\beta}$$

$$= -\sum_{\mathrm{n}} \sum_{s} \sum_{\beta} \left[ \sum_{\alpha} \frac{\partial}{\partial x_{\alpha}} \Gamma_{\alpha\beta}^{\mathrm{n}s}(\mathrm{r}) \right] \dot{u}_{\mathrm{n}s\beta}. \tag{B6}$$

Therefore, by equating like terms we obtain

$$\Upsilon_{\mathbf{n}s\beta}(\mathbf{r}) = -\sum_{\alpha} \frac{\partial}{\partial x_\alpha} \Gamma^{\mathbf{n}s}_{\alpha\beta}(\mathbf{r}) = -\nabla \cdot \Gamma^{\mathbf{n}s}_{\beta}, \tag{B7}$$

which transforms (B4) to

$$M\ddot{u}_{\mathbf{n}s\alpha} + \sum_{\mathbf{n}'} \sum_{s'} \sum_{\alpha'} A^{ss'\alpha\alpha'}_{\mathbf{n},\mathbf{n}'} u_{\mathbf{n}'s'\alpha'} + \int \mathrm{d}^3 r \left\{ \Gamma^{\mathbf{n}s}_{\alpha}(\mathbf{r}) \cdot \frac{\partial \mathbf{A}(\mathbf{r},t)}{\partial t} - \nabla \cdot \Gamma^{\mathbf{n}s}_{\alpha}(\mathbf{r}) \phi(\mathbf{r},t) \right\} = 0. \tag{B8}$$

Using the vector identity $\psi \nabla \cdot \mathbf{F} = \nabla \cdot (\psi \mathbf{F}) - \mathbf{F} \cdot \nabla \psi$, the last term in (B8) can be written as

$$\begin{aligned} \int \mathrm{d}^3 r \, \nabla \cdot \Gamma^{\mathbf{n}s}_{\alpha}(\mathbf{r}) \phi(\mathbf{r},t) &= \int \mathrm{d}^3 r \, \nabla \cdot (\phi \Gamma^{\mathbf{n}s}_{\alpha}) - \int \mathrm{d}^3 r \, \Gamma^{\mathbf{n}s}_{\alpha} \cdot \nabla \phi \\ &= \oint_S d\mathbf{s} \cdot \phi \Gamma^{\mathbf{n}s}_{\alpha} - \int \mathrm{d}^3 r \, \Gamma^{\mathbf{n}s}_{\alpha} \cdot \nabla \phi, \end{aligned} \tag{B9}$$

where the divergence theorem was utilized in the last step. By letting the surface $S$ goes to infinity, where the fields are asymptotically zero [8], the surface integral in (B9) will vanish and what left is

$$\int \mathrm{d}^3 r \, \nabla \cdot \Gamma^{\mathbf{n}s}_{\alpha}(\mathbf{r}) \phi(\mathbf{r},t) = -\int \mathrm{d}^3 r \, \Gamma^{\mathbf{n}s}_{\alpha} \cdot \nabla \phi. \tag{B10}$$

Substituting (B10) to (B8) and using $\mathbf{E} = -\partial \mathbf{A}/\partial t - \nabla \phi$, we finally arrive to (36).

## ACKNOWLEDGMENT

This work was partially supported by the Department of Electrical Engineering, University of Mississippi and the National Science Foundation under Grant No. ECS-524293. Also, partial support for this research was provided by ONR Grant No. N00014-07-1-1010, Office of Naval Research, Solid Mechanics Program (Dr. Yapa D. S. Rajapakse, Program Manager).

## REFERENCES

1. Poole, C. P. and F. J. Owens, *Introduction to Nanotechnology*, Wiley-Interscience, 2003.

2. Talele, K. and D. S. Patil, "Analysis of wave function, energy and transmission coefficients in GaN/ALGaN superlattice nanostructures," *Progress In Electromagnetics Research*, PIER 81, 237–252, 2008.
3. Kong, F. M., K. Li, B.-I. Wu, H. Huang, H. S. Chen, and J. A. Kong, "Propagation properties of the SPP modes in nanoscale narrow metallic gap, channel, and hole geometries," *Progress In Electromagnetics Research*, PIER 76, 449–466, 2007.
4. Iijima, S., "Helical microtabules of graphitic carbon," *Nature*, Vol. 354, 56–58, 1991.
5. Anantram, M. and F. Leonard, "Physics of carbon nanotube electronic devices," *Reports on Progress in Physics*, Vol. 69, 507–561, February 2006.
6. Smalley, R. E., M. S. Dresselhaus, G. Dresselhaus, and P. Avouris, *Carbon Nanotubes: Synthesis, Structure, Properties and Applications*, Springer, 2001.
7. Wooten, F., *Optical Properties of Solids*, Academic Press, 1972.
8. Jackson, J. D., *Classical Electrodynamics*, 3rd Edition, John Wiley & Sons, 1999.
9. Toyozawa, Y., *Optical Processes in Solids*, Cambridge University Press, 2003.
10. Brillouin, L., *Wave Propagation in Periodic Structures*, 1956.
11. Born, M. and K. Haung, *Dynamical Theory of Crystal Lattices*, 1st edition, Oxford University Press, London, 1954.
12. Mikki, S. M. and A. A. Kishk, "A symmetry-based formalism for the electrodynamics of nanotubes," submitted to *PIERS*.
13. Grosso, G. and G. Parravicini, *Solid-State Physics*, Academic Press, 2000.
14. White, C. T., D. H. Robertson, and J. W. Mintmire, "Helical and rotational symmetries of nanoscale graphitic tubules," *Phys. Rev. B*, Vol. 47, No. 9, 5485–5488, March 1993.
15. Damnjanovic, M., I. Milosevic, T. Vukovic, and R. Sredanovic, "Full-symmetry, optical activity, and potentials of single-wall and multi-wall nanotubes," *Phys. Rev. B*, Vol. 60, No. 4, 2728–2739, July 1999.
16. Damnjanovic, M., I. Milosevic, T. Vukovic, and R. Sredanovic, "Symmetry and lattices of single-wall nanotubes," *J. Phys. A*, Vol. 32, 4097–4104, 1999.
17. Popov, V. N. and V. E. van Doren, "Elastic properties of single-walled carbon nanotubes," *Phys. Rev. B*, Vol. 61, No. 4, 3078–3084, January 2000.

18. Cohen-Tannoudjii, C., J. Dupont-Roc, and G. Grynberg, *Photons and Atoms: Introduction to Quantum Electrodynamics*, Wiley, 1989.
19. Pekar, S. I., "Theory of electromagnetic waves in a crystal in which excitons are produced," *Sov. Phys. JETP*, Vol. 6, 785, 1957.
20. Agranovich, V. M. and V. L Ginsburg, *Crystal Optics and Spatial Dispersion, and Excitons*, Springer, 1984.
21. Halevi, P. (ed.), *Spatial Dispersion in Solids and Plasmas*, Springer, 1992.
22. Cho, K., "Nonlocal theory of radiation-matter interaction: Boundary-condition-less treatment of Maxwell equations," *Prog. Theor. Phys. Suppl.*, Vol. 106, 225–233, 1991.